НАУЧНОМ ВЕЋУ ИНСТИТУТА ЗА ФИЗИКУ

Предмет: Молба за покретање поступка за стицање звања научни сарадник

МОЛБА

Молим Научно веће Института за физику у Београду да покрене поступак за мој избор у звање научни сарадник, у складу са критеријумима које је прописало Министарство просвете, науке и технолошког развоја.

У прилогу достављам:

1. Мишљење руководиоца пројекта са предлогом чланова комисије за избор у звање
2. Стручну биографију
3. Преглед научне активности
4. Елементе за квалитативну оцену научног доприноса
5. Елементе за квантитативну оцену научног доприноса
6. Списак и фотокопије објављених научних радова
7. Уверење о одбрањеној докторској дисертацији

Београд, 30. август 2016.

С поштовањем,

Татјана Агатоновић Јовин

др Татјана Агатоновић Јовин

26. јули 2016

Научно веће Института за физику

Предмет: Мишљење руководиоца пројекта за избор Др Татјане Агатоновић Јовин у звање научни сарадник

Поштовани,

Татјана Агатоновић Јовин запослена је у Лабораторији за физику високих енергија Института за физику и ангажована је на пројекту основних истраживања Министарства просвете, науке и технолошког развоја 171004 под називом "АТЛАС експеримент и физика честица на ЛХЦ енергијама".

С обзиром да испуњава услове предвиђене Правилником за изборе у научно–истраживачка звања, сагласна сам са покретањем поступка за избор др Татјане Агатоновић Јовин у звање научни сарадник.

За чланове комисије за избор др Татјане Агатоновић Јовин у звање научни сарадник предлажем следећи састав:

1. др Љиљана Симић, научни саветник Института за физику;
2. др Јелена Крстић, научни саветник Института за физику;
3. проф. др Маја Бурић, редовни професор Физичког факултета;

Руководилац пројекта 171004,

др Лидија Живковић
Научни саветник

Стручна биографија – Татјана Агатоновић Јовин

Татјана Агатоновић Јовин рођена је 12. јула 1977. у Новом Саду где је завршила основну школу и гимназију. Основне студије уписала је академске 1998/1999 на Департману за физику, Природно-математичког факултета, Универзитета у Новом Саду, на смеру Дипломирани физичар. Дипломирала је 19.05.2005. године са просечном оценом 9.40 и дипломским радом на тему „Одређивање енергије и флукса космичких миона на нивоу мора". Академске 2008/2009 године уписала је Докторске академске студије на Физичком факултету, Универзитета у Београду, смер Физика језгара, честица и поља, где је положила све испите прописане статутом факултета, са просечном оценом 9.80.

У групи за експерименталну физику високих енергија, Лабораторије за физику, у Институту за нуклеарне науке „Винча" била је запослена као истраживач приправник од 01. априла 2009. године, где је била ангажована на пројекту Министарства, науке и технолошког развоја ОИ 171012 „Физика и развој детектора у експериментима са акцелераторима високих енергија". Била је ангажована у ATLAS експерименту на Великом хадронском сударачу (Large Hadron Collider - LHC), при Европском институту за нуклеарна истраживања (CERN) и у периоду 2009-2010 борави у Лабораторији за физику високих енергија (Laboratoire d'Annecy-le-Vieux de Physique des Particules - LAPP) у Ансију, Француска, као стипендиста француске владе. Од 01. маја 2011. квалификовани је аутор на радовима ATLAS колаборације. Такође учествовала је у раду на Међународном линеарном сударачу (International Linear Collider - ILC), где је била ангажована на мерењу луминозности користећи догађаје *Bhabha* расејања. Маја 2011. године изабрана је у звање истраживач сарадник. Од 01. фебруара 2014. запослена је у Лабораторији за физику високих енергија Института за физику у Земуну, као члан групе која уествује у ATLAS експерименту. Њена главна активност у оквиру ATLAS експеримента одвија се у области физике *beauty* мезона и односи се на мерење индиректног нарушења CP симетрије у распаду $B_s^0 \to J/\psi\phi$ у експерименту ATLAS. 07. јуна 2016. реизабрана је у звање истраживач сарадник.

По позиву ATLAS колаборације Татјана Агатоновић Јовин до сада је представљала резултате на више водећих међународних конференција из ове области. Током докторских студија похађала је више међународних школа из физике честица, у земљи и иностранству.

Докторску тезу под називом „Прецизно мерење нарушења CP симетрије у распаду $B_s^0 \to J/\psi\phi$ у ATLAS експерименту" одбранила је 10. јуна 2016. године на Физичком факултету, Универзитета у Београду.

Преглед научне активности – Татјана Агатоновић Јовин

Научно истраживачки рад Татјане Агатоновић Јовин одвија се у области физике високих енергија. Од 2009. ангажована је у ATLAS експерименту на Великом хадронском сударачу (Large Hadron Collider - LHC) у CERN-у. У периоду 2009-2010 године била је ангажована на Међународном линеарном сударачу (International Linear Collider - ILC) у оквиру једног од предложених концепата детекторског система (International Large Detector - ILD).

Први део свог истраживања у овој области посветила је раду на Међународном линеарном сударачу (International Linear Collider - ILC). Њена главна активност на ILC-у односила се на мерење луминозности користећи догађаје *Bhabha* расејања, који представљају доминантне QED процесе на енергији ILC-а. Татјана Агатоновић Јовин учествовала је у анализи четворо-фермионских (фонских) процеса, који предствљају један од главних извора систематске неодредјености у мерењима луминозности на ILC-у. Za generisanje dogadjaja sa leptonima u konachnom stanju korishćen je WHIZARD генератор, док је за генерисање *Bhabha* догађаја коришћен *Bhlumi* генератор. Одговор луминометра (LCAL) симулиран је користећи програмски пакет *Barbie*, заснован на Geant3 програму за симулацију детектора. Резултати ове анализе публиковани су у:

- H. Abramowicz, ... , T. Jovin et al., Forward instrumentation for ILC detectors, 2010 JINST **5** P12002.

- H. Stoeck, ... , T. Jovin, et al. [the ILD concept group], The International Large Detector: Letter of Intent, DESY 2009/87, Fermilab PUB-09-682-E, KEK Report 2009-6, ISSN 0418-9833; ISBN 978-3-935702-42-3 (2010), ILD (ILC) - Letter of Intent 2010.

У оквиру квалификације за ауторску листу ATLAS колаборације, од 2010. до 2011. године, радила је на развоју програма за симулацију одговора мионског спектрометра и анализи временске окупираности мионског детектора због присуства *pile-up* догађаја, за различите периоде прикупљања података на ATLAS детектору и рада LHC-а.

Основни део научно-истраживачког рада Татјане Агатоновиħц Јовин односи се на изучавање феномена нарушења CP симетрије у распаду $B_s^0 \to J/\psi\phi$ у ATLAS експерименту. У Стандардном моделу физике честица нарушење CP симетрије описано је комплексном фазом у *Cabbibo-Kobayashi-Maskawa* – CKM матрици и тестирање CKM механизма представља један од главних задатака у физици честица. Пошто је вредност фазе нарушења CP симетрије мала у Стандардном моделу, ово мерење представља веома осетљив тест на постојање физике изван

Стандардног модела, за шта је потребно извести што прецизније мерење. У овом мерењу до нарушења CP симетрије долази у интерференцији између осцилација B_s^0 мезона и директних распада. Да би се извело прецизно мерење фазе CP нарушења у $B_s^0 \to J/\psi\phi$ распаду помоћу ATLAS детектора примењена је *тагирана* временски зависна угаона анализа. Одговарајућа сепарација и моделовање фонских процеса у фиту максималне веродостојности који је примењен у анализи где је Татјана Агатоновић Јовин имала значајан допринос представља важан део ове анализе. Учествовала је у развоју модела фита који се односи на *специфични* B_d^0 фон и моделовање расподела масе и углова распада коначних продуката фонских процеса $B_d^0 \to J/\psi K^{*0}$ и $B_d^0 \to J/\psi K^+\pi^-$ у базису трансверзалитета. С обзиром да ови фонски процеси не могу бити елиминисани применом селекционих критеријума, важно је поред одређивања одговарајућих функција густине вероватноће у моделу фита, проценити и удео ових фонских процеса у области сигнала, на чему је Татјана Агатоновић Јовин такође радила. Поред развоја и имплементације функција густине вероватноће којима се описује B_d^0 фон у анализи, учествовала је и у процени систематксих ефеката услед моделовања B_d^0 фона у анализи. Такође, радила је на имплементацији и одређивању компоненти фита које описују допринос CP-непарног нерезонантног $B_s^0 \to J/K^+K^-$ S-*wave* stanja, као и на развоју алтернативних модела параметризације углова у базису трансверзалитета у анализи.

Резултати ове анализе публиковани су у:

- G. Aad, ... , T. Jovin et al. [ATLAS Collaboration], Time-dependent angular analysis of the decay $B_s^0 \to$J/$\psi\phi$ and extraction of $\Delta\Gamma_s$ and the CP-violating weak phase ϕ_s by ATLAS, JHEP **1212** (2012) 072.

- G. Aad, ... , T. Agatonovic-Jovin et al. [ATLAS Collaboration], Flavour tagged time dependent angular analysis of the $B_s^0 \to$J/$\psi\phi$ decay and extraction of $\Delta\Gamma_s$ and the weak phase ϕ_s in ATLAS, Phys. Rev. **D 90** (2014) 052007.

- G. Aad, ... , T. Agatonovic-Jovin *et al.* [ATLAS Collaboration], *Measurement of the CP-violating phase ϕ_s and the B_s^0 meson decay width difference with $B_s^0 \to J/\psi\phi$ decays in ATLAS*, JHEP **08** (2016) 147.

Елементи за квалитативну оцену научног доприноса

1.2 Квалитет научних резултата

Као члан ATLAS колаборације Татјана Агатоновић Јовин аутор је на 436 радова ATLAS колаборације. Оригиналан допринос дала је у три рада ATLAS колаборације публикована у врхунским међународним часописима (M21) JHEP са IF 5.618 у 2012. и IF 6.023 у 2015. и Phys. Rev. D са IF 4.643 у 2014. години. На међународним скуповима имала је четири предавања по позиву ATLAS колаборације штампана у целини (M33). Татјана Агатоновић Јовин коаутор је у раду ILD концепт групе на међународном линеарном сударачу (ILC) који је публикован у међународном часопису изузетних вредности (M21a) JINST са IF 3.148 у 2010. години, као и у монографској студији (M13) ILD-Letter of Intent публикованој 2010. године.

1.4 Нормирање броја коауторских радова

Др Татјана Агатоновић Јовин потписана је на свим радовима ATLAS колаборације од 2011. године. Сви добијени резултати објављени су или представљени на конференцијама по правилима ATLAS колаборације дефинисаним у документима: ATLAS Publication Policy и ATLAS Autorship Policy.

1.7 Утицај научних резултата

Три рада ATLAS колаборације са оригиналним доприносом Татјане Агатоновић Јовин публикована су у врхунским међународним часописима (M21), два рада у JHEP са IF 5.618 у 2012. и IF 6.023 у 2015. и један рад у Phys. Rev. D са IF 4.643 у 2014. години. Рад ILD (ILC) концепт групе у којем је Татјана Агатоновић Јовин имала такође оригиналан допринос публикован је у међународном часопису изузетних вредности (M21a) JINST са IF 3.148 у 2010. години. Укупан IF радова са оригиналним доприносом је 13.409. Према INSPIRE-HEP бази ови радови су до сада цитирани 166 пута, а према ISI/Web of Science 31 пут. Монографска студија у којој Татјана Агатоновић Јовин има оригиналан допринос (M13) ILD-Letter of Intent публикована је 2010. године и према INSPIRE-HEP бази до сада је цитирана 180 пута.

1.8 Конкретан допринос кандидата у реализацији радова у научним центрима у земљи и иностранству

Допринос др Татјане Агатоновић Јовин препознат је у оквиру ATLAS колаборације. Редовно је презентовала резултате свог рада на састанцима *BsJpsiphi* B-Physics радне групе, као и заједничке резултате радне групе $B_s^0 \to J/\psi$ на Physics & Performance ATLAS Weeks. Као резултат њеног рада Татјана је имала четири позива испред ATLAS колаборације да одржи предавање и прикаже резултате рада на међународним конференцијама.

Елементи за квантитативну оцену научног доприноса

Испуњеност квантитативних услова приказана је у следећој табели по класификацији коју је прописало Министарство просвете, науке и технолошког развоја. У табели су бодовани само радови са оригиналним и значајним доприносом Татјане Агатоновић Јовин.

Категорија	М бодова по раду	Број бодова	Укупно М бодова
М13	7	1	7
М21(a)	10	1	10
М21	8	3	24
М33	1	6	6
М63	1	3	3
М70	6	1	6

Поређење са минималним квантитативним условима за избор у звање научни сарадник.

Минималан број М бодова		Остварено
Укупно	16	56
М10 + М20 + М31 + М32 + М33 + М41 + М42	10	47
М11 + М21 + М21 + М22 + М23	6	41

Цитираност

Према INSPIRE-HEP бази научних радова др Татјане Агатоновић Јовин цитирани су 350 пута, а према ISI/Web of Science 16, 4, 11 пута, не рачунајући аутоцитате ATLAS колаборације.

Списак научних радова и саопштења са конференција

- **Радови у међународним часописима изузетних вредности (M21a):**

  (1) H. Abramowicz, ... , T. Jovin *et al.*, *Forward instrumentation for ILC detectors*, 2010 JINST **5** P12002.

- **Радови у врхунским међународним часописима (M21):**

  (1) G. Aad, ... , T. Jovin *et al.* [ATLAS Collaboration], *Time-dependent angular analysis of the decay* $B_s^0 \to J/\psi\phi$ *and extraction of* $\Delta\Gamma_s$ *and the CP-violating weak phase* ϕ_s *by ATLAS*, JHEP **1212** (2012) 072.

  (2) G. Aad, ... , T. Agatonovic-Jovin *et al.* [ATLAS Collaboration], *Flavour tagged time dependent angular analysis of the* $B_s^0 \to J/\psi\phi$ *decay and extraction of* $\Delta\Gamma_s$ *and the weak phase* ϕ_s *in ATLAS*, Phys. Rev. **D 90** (2014) 052007.

  (3) G. Aad, ... , T. Agatonovic-Jovin *et al.* [ATLAS Collaboration], *Measurement of the CP-violating phase* ϕ_s *and the* B_s^0 *meson decay width difference with* $B_s^0 \to J/\psi\phi$ *decays in ATLAS*, JHEP **08** (2016) 147.

- **Саопштења са међународних скупова штампана у целини (M33):**

  (1) T. Agatonovic-Jovin [On behalf of the ATLAS Collaboration], *Study of* Λ_b^0 *decay properties with the ATLAS detector*, PoS(DIS2014)182.

  (2) Tatjana Agatonovic-Jovin [On behalf of the ATLAS Collaboration], *Flavour Tagging and Systematics for* $B_s^0 \to J/\psi\phi$ *Measurement in ATLAS*, PoS(Beauty 2013)070.

  (3) Tatjana Jovin [On behalf of the ATLAS Collaboration], *CP Violation at ATLAS*, PoS(HQL 2012)038.

  (4) H. Abramowicz, P. Bambade, I. Bozovic-Jelisavcic, B. Pawlik, C. Rimbault, T. Jovin *et al.*, *Luminosity Measurement at ILC*, accepted as the eConf Proceedings of the International Linear Collider Workshop 2010 LCWS10 & ILC10, Beijing 2010, arXiv:1006.2539 [physics.ins-det].

  (5) I. Bozovic-Jelisavcic, M. Pandurovic, I. Smiljanic, T. Jovin, I. Sadeh, *Forward region studies for ILC*, 7th International Conference of the Balkan Physical Union, 9 - 13 September 2009, Alexandroupolis, Greece, AIP Conf. Proc. **1203**, 49 (2010).

  (6) I. Bikit, D. Mrdja, N. Todorovic, J. Slivka, M. Veskovic, M. Krmar, T. Jovin *et al.*, *Background reduction at an actively shielded gamma ray spectrometer*, Proceedings of the 20th Intenational Nuclear Physics Divisional Conference of the European Physical Society, Debrecen, Hungary, May 16 - 20, 2005, ISBN 2-914771-23-1 Vol.29A pp.83.

- **Саопштења са скупова националног значаја штампана у целини (M63):**

  (1) Т. Агатоновић-Јовин и др. [у име ATLAS колаборације], *Мерење фазе нарушења CP симетрије у распаду $B_s^0 \to J/\psi\phi$ у ATLAS експерименту*, 12. Конгрес физичара Србије, 28. април - 2. мај, 2013, Врњачка Бања, Србија, ISBN 978-86-86169-08-2, pp. 212-216 (2013).

  (2) Т. Јовин и др. [у име ATLAS колаборације], *Идентификација знака наелектрисања b-кварка у мерењу нарушења CP симетрије у ATLAS експерименту*, 12. Конгрес физичара Србије, април 28 - мај 2, 2013, Врњачка Бања, Србија, ISBN 978-86-86169-08-2, pp. 256-259 (2013).

  (3) Татјана Јовин, Наташа Жикић-Тодоровић, Софија Форкапић, Љиљана Чонкић, Миодраг Крмар, *Spektroskopija antimionskog plastičnog detektora*, 49. Конференција за електронику, телекомуникације, рачунарство, аутоматику и нуклеарну технику, ETPAH 2005, Будва, Србија и Црна Гора, 5. - 10. јун 2005, Proc. 49th ETRAN Conf., Vol. IV pp. 58 - 61 (2005).

- **Монографска студија/поглавље у књизи M11 или рад у тематском зборнику водећег међународног значаја (M13):**

  (1) H. Stoeck, ... , T. Jovin, *et al.* [the ILD concept group], *The International Large Detector: Letter of Intent*, DESY 2009/87, Fermilab PUB-09-682-E, KEK Report 2009-6, ISSN 0418-9833; ISBN 978-3-935702-42-3 (2010),
  ILD (ILC) - Letter of Intent 2010.

- **Јавне ноте ATLAS колаборације:**

  (1) A. Barton, ..., M. Smizanska, ... , T. Jovin *et al.*, *Flavour tagged time dependent angular analysis of the $B_s^0 \to J/\psi\phi$ decay and extraction of $\Delta\Gamma$ and the weak phase ϕ_s in ATLAS*, April 12, 2013, 18 pp., ATLAS-CONF-2013-039.

- **Интерне ноте ATLAS колаборације:**

  (1) A. Barton, ..., M. Smizanska, ... , T. Jovin *et al.*, *Time dependent angular analysis of $B_s^0 \to J/\psi\phi$ decay and extraction of $\Delta\Gamma_s$ and the CP violating weak phase ϕ_s in ATLAS*, May 10, 2012, 58 pp., ATL-COM-PHYS-2012-155 (restricted to ATLAS).

  (2) A. Barton, ..., M. Smizanska, ... , T. Agatonovic-Jovin *et al.*, *Time dependent angular analysis of $B_s^0 \to J/\psi\phi$ decay and extraction of $\Delta\Gamma_s$ and the weak phase of B_s^0 meson in ATLAS*, March 5, 2013, 77 pp., ATL-COM-PHYS-2013-293 (restricted to ATLAS).

  (3) A. Barton, ..., M. Smizanska, ... , T. Agatonovic-Jovin *et al.*, *Flavour tagged time dependent angular analysis of the $B_s^0 \to J/\psi\phi$ decays and extraction of $\Delta\Gamma_s$ and the*

weak phase ϕ_s in ATLAS, January 11, 2016, 106 pp., ATL-COM-PHYS-2014-598 (restricted to ATLAS).

- **Одбрањена докторска дисертација (M70):**

  (1) Т. Агатоновић-Јовин, *Прецизно мерење нарушења CP симетрије у распаду $B_s^0 \to J/\psi\phi$ у ATLAS експерименту*, Универзитет у Београду, Физички факултет, јун, 2016.

Универзитет у Београду ФИЗИЧКИ ФАКУЛТЕТ
Студентски трг 12, 11000 Београд
Поштански фах 44
Тел. 011 7158 151, 3281 375
ПИБ 100039173, Мат. бр. 07048190

University of Belgrade FACULTY OF PHYSICS
Studentski trg 12, 11000 Belgrade
Postal Box 44
Phone +381 11 7158 151, Fax +381 11 3282 619
www.ff.bg.ac.rs, dekanat@ff.bg.ac.rs

УНИВЕРЗИТЕТ У БЕОГРАДУ
ФИЗИЧКИ ФАКУЛТЕТ
Бр. 155/13
14. 6. 2016. год.
БЕОГРАД, СТУДЕНТСКИ ТРГ 12-16
П. ФАХ 44

На основу члана 161 Закона о општем управном поступку («Службени Лист СРЈ» број 33/97 и 31/01), и члана 120 Статута Универзитета у Београду - Физичког факултета, по захтеву ТАТЈАНЕ АГАТОНОВИЋ-ЈОВИН, дипломираног физичара, издаје се следеће

У В Е Р Е Њ Е

ТАТЈАНА АГАТОНОВИЋ-ЈОВИН, дипломирани физичар, дана 10. јуна 2016. године, одбранила је докторску дисертацију под називом

„ПРЕЦИЗНО МЕРЕЊЕ НАРУШЕЊА СР СИМЕТРИЈЕ У РАСПАДУ Bs→J/ψф
У АТЛАС ЕКСПЕРИМЕНТУ“

пред Комисијом Универзитета у Београду - Физичког факултета, и тиме испунила све услове за промоцију у ДОКТОРА НАУКА – ФИЗИЧКЕ НАУКЕ.

Уверење се издаје на лични захтев, а служи ради регулисања права из радног односа и важи до промоције, односно добијања докторске дипломе.

Уверење је ослобођено плаћања таксе.

ДЕКАН ФИЗИЧКОГ ФАКУЛТЕТА

Проф. др Јаблан Дојчиловић

Forward instrumentation for ILC detectors

2010 JINST 5 P12002

(http://iopscience.iop.org/1748-0221/5/12/P12002)

JINST

PUBLISHED BY IOP PUBLISHING FOR SISSA

RECEIVED: *September 15, 2010*
ACCEPTED: *November 12, 2010*
PUBLISHED: *December 7, 2010*

Forward instrumentation for ILC detectors

H. Abramowicz,[a] A. Abusleme,[b] K. Afanaciev,[c] J. Aguilar,[d] P. Ambalathankandy,[d] P. Bambade,[e] M. Bergholz,[f,1] I. Bozovic-Jelisavcic,[g] E. Castro,[f] G. Chelkov,[h] C. Coca,[i] W. Daniluk,[j] A. Dragone,[k] L. Dumitru,[i] K. Elsener,[l] I. Emeliantchik,[c] T. Fiutowski,[d] M. Gostkin,[h] C. Grah,[f,2] G. Grzelak,[j,3] G. Haller,[k] H. Henschel,[f] A. Ignatenko,[c,4] M. Idzik,[d] K. Ito,[m] T. Jovin,[g] E. Kielar,[j] J. Kotula,[j] Z. Krumstein,[h] S. Kulis,[d] W. Lange,[f] W. Lohmann,[f,1,5] A. Levy,[a] A. Moszczynski,[j] U. Nauenberg,[n] O. Novgorodova,[f,1] M. Ohlerich,[f,1] M. Orlandea,[i] G. Oleinik,[n] K. Oliwa,[j] A. Olshevski,[h] M. Pandurovic,[g] B. Pawlik,[j] D. Przyborowski,[d] Y. Sato,[m] I. Sadeh,[a] A. Sailer,[l] R. Schmidt,[f,1] B. Schumm,[o] S. Schuwalow,[f] I. Smiljanic,[g] K. Swientek,[d] Y. Takubo,[m] E. Teodorescu,[i] W. Wierba,[j] H. Yamamoto,[m] L. Zawiejski[j] and J. Zhang[p]

[a] *Tel Aviv University, Tel Aviv, Israel*
[b] *Stanford University, Stanford, U.S.A.*
[c] *NCPHEP, Minsk, Belarus*
[d] *AGH University of Science & Technology, Cracow, Poland*
[e] *Laboratoire de l Accelerateur Lineaire, Orsay, France*
[f] *DESY, Zeuthen, Germany*
[g] *Vinca Institute of Nuclear Sciences, University of Belgrade, Serbia*
[h] *JINR, Dubna, Russia*
[i] *IFIN-HH, Bucharest, Romania*
[j] *INP PAN, Cracow, Poland*
[k] *SLAC, Menlo Park, U.S.A.*
[l] *CERN, Geneva, Switzerland*
[m] *Tohoku University, Sendai, Japan*
[n] *University of Colorado, Boulder, U.S.A.*
[o] *UC California, Santa Cruz, U.S.A.*
[p] *ANL, Argonne, U.S.A.*

E-mail: Wolfgang.Lohmann@desy.de

[1] Also at Brandenburg University of Technology, Cottbus, Germany
[2] Now at BTO Consulting AG, Berlin, Germany
[3] Also at University of Warsaw, Poland
[4] Now at DESY, Hamburg, Germany
[5] Corresponding author.

doi:10.1088/1748-0221/5/12/P12002

2010 JINST 5 P12002

ABSTRACT: Two special calorimeters are foreseen for the instrumentation of the very forward region of the ILC detector, a luminometer designed to measure the rate of low angle Bhabha scattering events with a precision better than 10^{-3} and a low polar angle calorimeter, adjacent to the beam-pipe. The latter will be hit by a large amount of beamstrahlung remnants. The amount and shape of these depositions will allow a fast luminosity estimate and the determination of beam parameters. The sensors of this calorimeter must be radiation hard. Both devices will improve the hermeticity of the detector in the search for new particles. Finely segmented and very compact calorimeters will match the requirements. Due to the high occupancy fast front-end electronics is needed. The design of the calorimeters developed and optimised with Monte Carlo simulations is presented. Sensors and readout electronics ASICs have been designed and prototypes are available. Results on the performance of these major components are summarised.

KEYWORDS: Si microstrip and pad detectors; Radiation-hard detectors; Calorimeter methods; Detector modelling and simulations I (interaction of radiation with matter, interaction of photons with matter, interaction of hadrons with matter, etc)

ARXIV EPRINT: 1009.2433

2010 JINST 5 P12002

Contents

2010 JINST 5 P12002

1 Introduction and challenges

A high energy e^+e^- linear collider is considered to be the future research facility complementary to the LHC collider. Whereas LHC has a higher potential for discoveries, an e^+e^- collider will allow precision measurements to explore in detail the mechanism of electroweak symmetry breaking and the properties of the physics beyond the Standard Model, should it be found at the LHC. Two concepts of an e^+e^- linear collider are presently considered, the ILC [1] and CLIC [2]. For the ILC, with superconducting cavities, an engineering design report will be issued in 2012. The centre-of-mass energy will be 500 GeV, with the possibility of an upgrade to 1 TeV. CLIC is based on conventional cavities. A conceptional design report is foreseen in 2011. CLIC will allow to collide electrons and positrons up to energies of 3 TeV.

An R&D program is ongoing to develop the technologies for detectors for precision measurements in this new energy domain. Letters of Intent have been submitted for detectors at the ILC in 2009. Two detectors, the ILD [3] and the SiD [4], are reviewed and validated. In both detectors two specialised calorimeters are foreseen in the very forward region, LumiCal for the precise measurement of the luminosity and BeamCal for a fast estimate of the luminosity and for the control of beam parameters [5]. Both will also improve the hermeticity of the detector. To support beam-tuning an additional pair-monitor will be positioned just in front of BeamCal.

With LumiCal the luminosity will be measured using Bhabha scattering, $e^+e^- \to e^+e^-(\gamma)$, as a gauge process. To match the physics benchmarks, an accuracy of better than 10^{-3} is needed at a centre-of-mass energy of 500 GeV [3]. For the GigaZ option, where the ILC will be operated for precision measurements at centre-of-mass energies around the Z boson, an accuracy of 10^{-4} would be required [6]. To reach these accuracies, a precision device is needed, with particularly challenging requirements on the mechanics and position control.

BeamCal is positioned just outside the beam-pipe. At ILC energies we have to tackle here a new phenomenon — the beamstrahlung. When electron and positron bunches collide, the particles are accelerated in the magnetic field of the bunches towards the bunch centre. This so called pinch effect enhances the luminosity. However, electrons and positrons may radiate photons. A fraction of these photons converts in the Coulomb field of the bunch particles creating low energy e^+e^- pairs. A large amount of these pairs will deposit their energy after each bunch crossing in BeamCal. These depositions, useful for a bunch-by-bunch luminosity estimate and the determination of beam parameters [7], will lead, however, to a radiation dose of about one MGy per year in the sensors at lower polar angles. Hence radiation hard sensors are needed to instrument BeamCal. BeamCal is supplemented by a pair monitor, consisting of a layer of pixel sensors positioned just in front of it to measure the density of beamstrahlung pairs and give additional information for the beam parameter determination.

All detectors in the very forward region have to tackle relatively high occupancy, requiring special front-end electronics.

A small Molière radius is of importance for both calorimeters. It ensures high energy electron veto capability for BeamCal even at small polar angles. This is essential to suppress background in searches for new particles for which the signature consists of large missing energy and momentum. In LumiCal the precise reconstruction of electron, positron and photon showers in Bhabha events is facilitated. Both calorimeters also shield the inner tracking detectors from back-scattered particles

2010 JINST 5 P12002

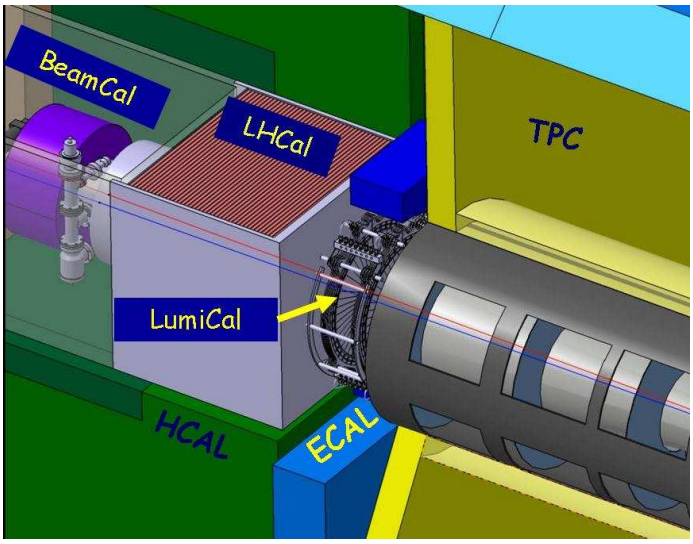

Figure 1: The very forward region of the ILD detector. LumiCal, BeamCal and LHCal are carried by the support tube for the final focusing quadrupole and the beam-pipe. LHCal extends the coverage of the hadron calorimeter to the polar angle range of LumiCal. TPC denotes the central track chamber, ECAL the electromagnetic and HCAL the hadron calorimeter.

induced by beamstrahlung pairs hitting the downstream beam-pipe and magnets.

2 Design of the very forward region

A sketch of the very forward region of the ILD detector [3] is shown in figure 1. LumiCal and BeamCal are designed as cylindrical sensor-tungsten sandwich electromagnetic calorimeters. Both consist of 30 absorber disks of 3.5 mm thickness, each corresponding to one radiation length, interspersed with sensor layers. Each sensor layer is segmented radially and azimuthally into pads. Front-end ASICs are positioned at the outer radius of the calorimeters. LumiCal is positioned in a circular hole of the end-cap electromagnetic calorimeter ECAL. BeamCal is placed just in front of the final focus quadrupole. BeamCal covers polar angles between 5 and 40 mrad and LumiCal between 31 and 77 mrad.

Colliding beams enter the interaction point, IP, with a crossing angle of 14 mrad. Both calorimeters are centred around the outgoing beam. In the design of BeamCal a hole for the incoming beam-pipe is foreseen.

2.1 LumiCal simulation studies

The differential cross section of Bhabha scattering, $\frac{d\sigma_B}{d\theta}$, can be calculated precisely from theory [8]. In leading order it reads,

$$\frac{d\sigma_B}{d\theta} = \frac{2\pi\alpha_{em}^2}{s}\frac{\sin\theta}{\sin^4(\theta/2)} \approx \frac{32\pi\alpha_{em}^2}{s}\frac{1}{\theta^3}\,, \tag{2.1}$$

where θ is the polar angle of the scattered electron with respect to the beam. The approximation holds at small θ.

2010 JINST 5 P12002

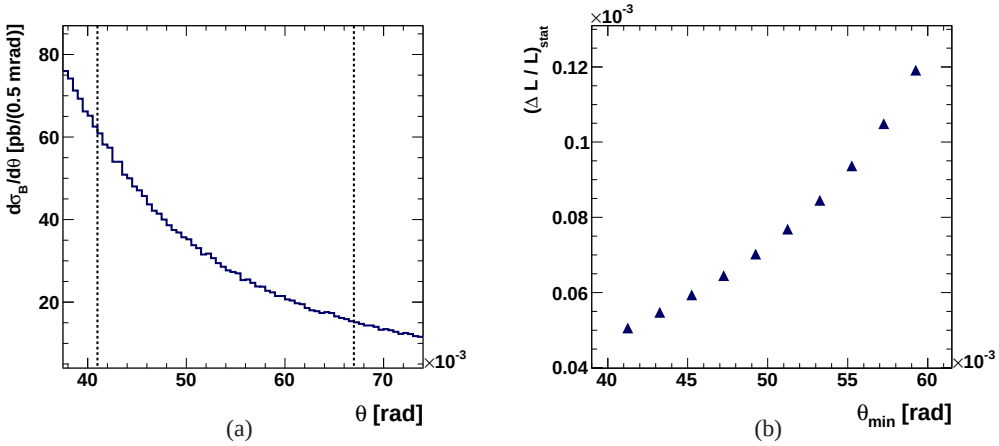

Figure 2: (a) Dependence of $d\sigma_B/d\theta$, the differential Bhabha cross-section, on the polar angle, θ, at $\sqrt{s} = 500$ GeV. The dashed lines mark the fiducial volume of LumiCal, $41 < \theta < 67$ mrad, which is defined in eq. (2.5) later in this section. (b) Dependence of the statistical uncertainty in counting the number of Bhabha events, $(\Delta L/L)_{stat}$, on the minimal polar angle of the fiducial volume, θ_{min}, while the upper limit is kept at 67 mrad. An integrated luminosity of 500 fb^{-1} is assumed.

For a given rate of Bhabha events, N_B, determined in a certain θ-range, the luminosity, L, is obtained as

$$L = \frac{N_B}{\sigma_B}, \tag{2.2}$$

where σ_B is the integral of the differential cross section, eq. (2.1), over the considered θ range. Because of the steep θ dependence of the cross section, as illustrated in figure 2a, the most critical quantity to control when counting Bhabha events is the inner acceptance radius of the calorimeter, defined as the lower cut in the polar angle, θ_{min}. Hence a very precise θ measurement is needed. Furthermore, the θ-range must be chosen such that the number of Bhabha events measured provides the required relative statistical uncertainty of 10^{-3}. By choosing the lower bound of the polar angle between 40 and 60 mrad the latter requirement can be easily reached as illustrated in figure 2b. Here a Bhabha event sample generated with the BHWIDE generator [9] was used. The generated sample corresponds to an integrated luminosity of 500 fb^{-1}, as expected in one year of running the collider at nominal luminosity.

Electromagnetic showers are simulated in LumiCal using the GEANT4 [10] based package Mokka [11]. Sensors consist of 300 μm thick silicon sectors covering an azimuthal angle of 30°. The depositions in each sensor pad are recorded, and a reconstruction of the shower is performed. The position of an electromagnetic shower in LumiCal is reconstructed by performing a weighted average over the energy deposits in individual pads. The weight, $\mathscr{W}_i$, of a given detector pad i is determined by logarithmic weighting [12], for which $\mathscr{W}_i = \max\{\, 0,\ \mathscr{C} + \ln(E_i/E_{tot}\,)\}$. Here E_i refers to the individual pad energy, E_{tot} is the total energy in all pads, and $\mathscr{C}$ is a constant. In this way, only pads which contain a sufficient fraction of the shower energy contribute to the reconstruction. The polar angle resolution, σ_θ, and a polar angle measurement bias, $\Delta\theta$, are defined as the Gaussian width and the central value of the difference between the reconstructed and the generated polar angles. There is an optimal value for $\mathscr{C}$, for which σ_θ is minimal [13, 14].

2010 JINST 5 P12002

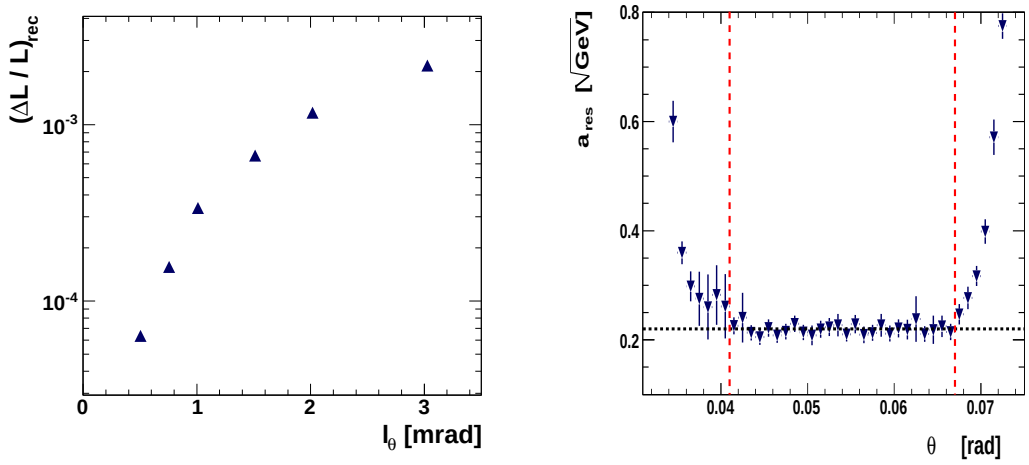

(a) (b)

Figure 3: (a) Dependence of $(\Delta L/L)_{rec}$, as defined in eq. (2.3), on the polar angle pad size, l_θ. (b) The energy resolution, a_{res}, for 250 GeV electrons as a function of the polar angle, θ, covering the polar angle range of the LumiCal.

Non-zero values of $\Delta\theta$ are due to the non-linear signal sharing on finite size pads with gaps between them. The bias and the resolution in the polar angle measurement depend on the polar angle pad size. The bias causes a shift in the luminosity measurement, since events may migrate into or out of the fiducial volume. This shift reads as

$$\left(\frac{\Delta L}{L}\right)_{rec} \approx 2\frac{\Delta\theta}{\theta_{min}} \,. \tag{2.3}$$

Figure 3a shows the relative shift in the luminosity as a function of the polar angular pad size, l_θ, using the optimal value of $\mathscr{C}$. For $l_\theta < 2$ mrad the shift in the luminosity measurement is smaller than 10^{-3}. As the baseline for the design we have chosen $l_\theta = 0.8$ mrad, which corresponds to 64 radial divisions of the sensor. For this segmentation the polar angle resolution and bias amount to $\sigma_\theta = (2.2 \pm 0.01) \times 10^{-2}$ and $\Delta\theta = (3.2 \pm 0.1) \times 10^{-3}$ mrad, respectively. The relative shift in the luminosity is $(\Delta L/L)_{rec} = 1.6 \times 10^{-4}$.

The polar angle bias needs careful understanding in test-beam measurements with sensors finally chosen for the calorimeter. Once its value is known, a correction can be applied to the luminosity measurement. The uncertainty of the luminosity measurement is then given by the uncertainty of the measured bias which may be smaller than the shift itself. The value of 1.6×10^{-4} can therefore be considered as an upper bound on the relative luminosity bias.

With 30 radiation lengths of tungsten as absorber, high energy electrons and photons deposit almost all of their energy in the detector. The relative energy resolution, σ_E/E, is parametrised as

$$\frac{\sigma_E}{E} = \frac{a_{res}}{\sqrt{E_{beam}\,(GeV)}}, \tag{2.4}$$

2010 JINST 5 P12002

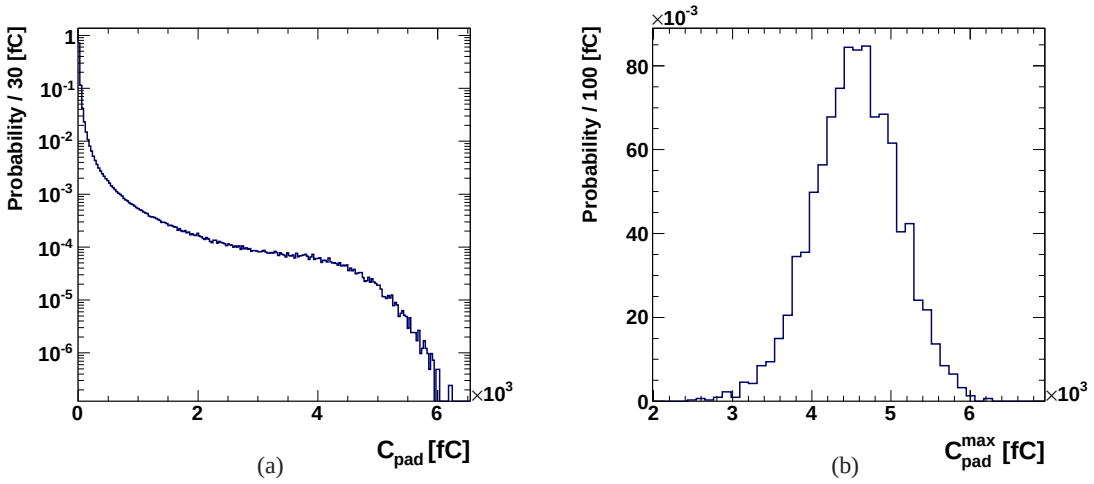

Figure 4: (a) Normalised distribution of the charge deposited in a detector pad, C_{pad}, by 250 GeV electron showers. (b) Normalised distribution of the maximal charge collected in a single pad per shower, C_{pad}^{max}, for 250 GeV electron showers.

where E and σ_E are, respectively, the central value and the standard deviation of the distribution of the energy deposited in the sensors for a beam of electrons with energy E_{beam}. The parameter a_{res} is usually quoted as the energy resolution, a convention which will be followed here.

Figure 3b shows the energy resolution as a function of the polar angle θ for electron showers with energy 250 GeV. The energy resolution parameter approaches minimal constant values between θ_{min} = 41 mrad and θ_{max} = 67 mrad, where the shower is fully contained inside the calorimeter. The fiducial volume of LumiCal is thus defined to be the polar angular range

$$41 < \theta < 67 \text{ mrad}, \tag{2.5}$$

as indicated by the dashed lines in figure 2a. Fiducial cuts on the minimal and maximal reconstructed polar angles of the particles used for the luminosity measurement reject events with shower leakage through the edges of LumiCal. For electron showers located inside the fiducial volume of LumiCal, the energy resolution is estimated to be $a_{res} = (0.21 \pm 0.02)\ \sqrt{\text{GeV}}$. No dependence on the electron energy is found in the energy range from 50 to 300 GeV. In order to determine the energy of showering particles, the integrated deposited energy in the detector has to be multiplied by a calibration factor. The calibration factor is found to be constant in the same energy range.

The expected range of energy depositions in the pads has been studied for the passage of minimum ionising particles, hereafter denoted as MIPs, and for showers of 250 GeV electrons [15]. The energy deposition in silicon is converted to released ionisation charge. The distribution of the charge in a single pad, C_{pad}, is shown in figure 4a. It ranges between $4 < C_{pad} < 6 \times 10^3$ fC. The distribution of the maximal charge collected in a single pad is shown in figure 4b. About 95 % of electron shower signals are less than 5.4×10^3 fC.

The impact of the digitisation of the detector signal on the LumiCal performance is investigated in ref. [15]. It is shown that an ADC with 8 bit resolution is sufficient to keep the energy resolution quoted above. No bias in the energy measurement is found.

2010 JINST 5 P12002

2.2 BeamCal simulation studies

BeamCal will be hit after each bunch-crossing by a large amount of beamstrahlung pairs. Their number, energy and spatial distribution depend on the beam parameters and the magnetic field inside the detector. For the nominal ILC beam-parameter set [16], beamstrahlung pairs are generated with the GUINEA-PIG program [17]. Inside the ILC detector an anti-DID field [18] is assumed. Beamstrahlung pairs are simulated in the detector, using a program based on GEANT4.

The energy deposited in the sensors of BeamCal per bunch crossing, about 150 GeV as shown in figure 5a, and the shape of these depositions allow a bunch-by-bunch luminosity estimate and the determination of beam parameters [7]. From the spatial distribution of the deposited energy a set of observables, e.g. radial and angular moments and asymmetries, is defined. These observables are related to beam parameters like bunch sizes, emittances and bunch offsets by a matrix equation. In the single parameter determination accuracies better than 10% [7] are obtained. In the multiparameter mode correlations appear. However, reasonable precision can still be obtained by using information from other diagnostics devices.

For search experiments it is important to detect single high energy electrons on top of the wider spread beamstrahlung pairs. Superimposed on the pair depositions in figure 5a is the deposition of an electron of 250 GeV, seen as the red spot on the right side. By performing an appropriate subtraction of the pair deposits and a shower-finding algorithm which takes into account the longitudinal shower profile, high energy electrons can be detected with high efficiency, as shown in figure 5b. This feature allows to suppress the background from two-photon processes in a search e.g. for super-symmetric tau-leptons [19] in a large fraction of the parameter space.

The range of signals expected on the pads was estimated. Including the depositions from beamstrahlung signals up to 40 pC are expected. Digitising the signals with an ADC with 10 bit resolution has no impact on the performance of the calorimeter.

GEANT4 simulations are also used to determine the expected dose and the neutron fluence in the sensors after one year of operation with nominal beam parameters. The dose in a sensor layer at the depths of the shower maximum as a function of the radius is shown in figure 6a. In the innermost ring of the calorimeter a dose of about 0.5 MGy is expected. Since the dose is non-uniformly distributed as a function of the azimuthal angle, it approaches 1 MGy per year in some sensor areas of the inner rings.

The neutron fluence is estimated using in GEANT4 the cascade model of Bertini [20]. The fluence per year of running at nominal beam parameters is shown in figure 6b as a function of the sensor layer number. Fluences up to 2×10^{15} per layer are expected near the shower maximum. Other GEANT4 models predict lower neutron fluences, particularly at low neutron energies [21]. The distribution of the fluence of neutrons in the sensor layer with the maximum fluence is shown in figure 7. With the cascade model of Bertini, a neutron fluence of 0.4×10^{12} neutrons per mm^2 and year is expected near the beam-pipe. Albeit this is still an order of magnitude less than predicted for LHC detectors near the beam pipe dedicated tests of sensors are planned.

2.3 Pair monitor simulations

Additional and independent information on beam parameters will be obtained from the pair monitor [22, 23]. The device will consist of one layer of silicon pixel sensors, with pixel size of 400×400

2010 JINST 5 P12002

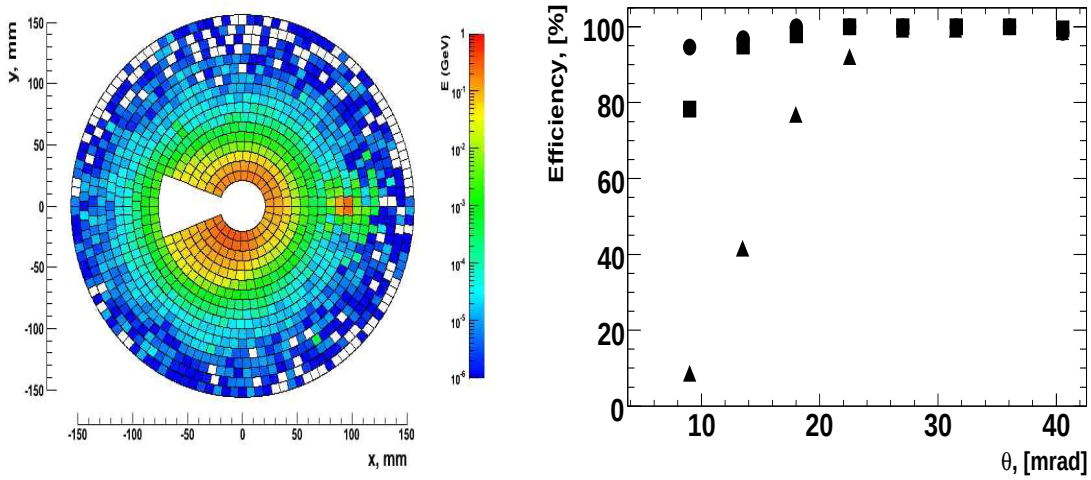

(a) (b)

Figure 5: (a) The distribution of the energy deposited by beamstrahlung pairs after one bunch crossing in the sensors of BeamCal. The depositions are integrated over pads of 7.65×7.65 mm^2 area. Superimposed is the deposition of a single high energy electron (red spot on the right side). The white area in the centre allows space for the beam-pipes. (b) The efficiency to detect single high energy electrons on top of the beamstrahlung background for electron energies of 75 (triangles), 150 (squares) and 250 (circles) GeV.

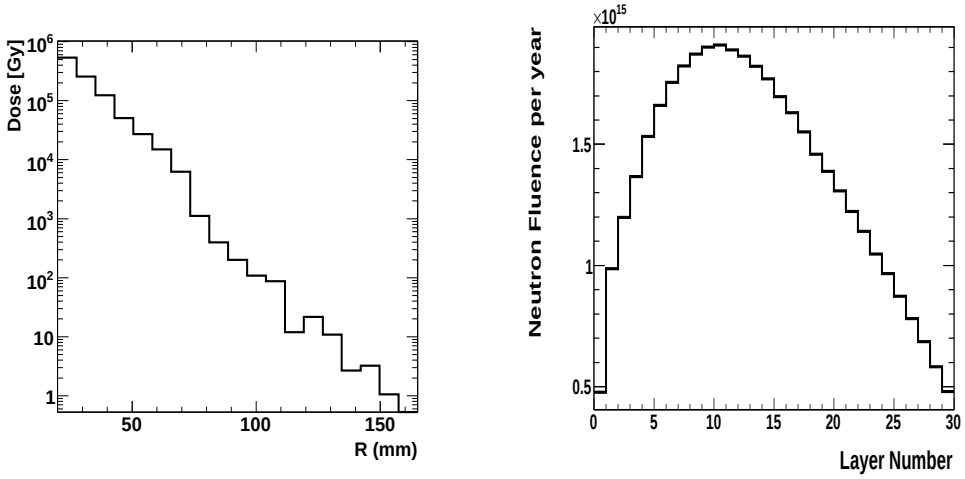

(a) (b)

Figure 6: (a) The dose in BeamCal sensors per year as a function of the radial distance from the beam. (b) The fluence of neutrons per year inside the sensors of BeamCal as a function of the sensor layer number using the cascade model of Bertini. An integrated luminosity of 500 fb^{-1} is assumed.

μm^2, just in front of BeamCal to measure the number density distribution of beamstrahlung pairs. Here we investigated the sensitivity to the horizontal and vertical bunch sizes, σ_x and σ_y, and the

2010 JINST 5 P12002

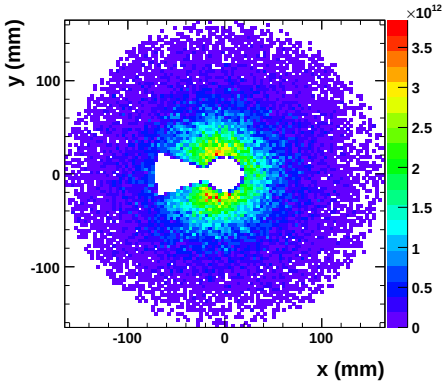

Figure 7: The fluence of neutrons per mm^2 and year crossing a sensor of BeamCal near the shower maximum using the cascade model of Bertini.

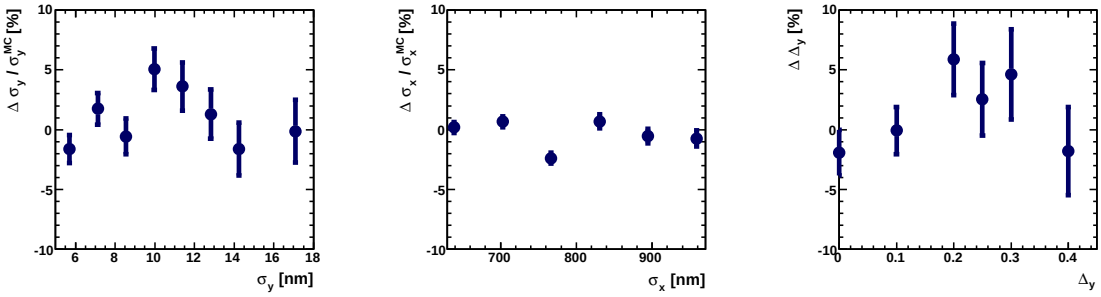

Figure 8: The relative deviations of the vertical, σ_y, and horizontal, σ_x, beam sizes, and the ratio of vertical displacement to the vertical beam size, Δ_y, averaged over 50 bunch crossings measured by the pair monitor.

ratio of the vertical displacement between bunches crossing to their vertical size, Δ_y.

To reconstruct the beam profile several observables characterising the number density of pairs at the front face of BeamCal are used [24]. Bunch crossings are simulated for certain ranges of σ_x, σ_y and Δ_y, and each of these observables is fitted with a second order polynomial. Then, several thousand bunch crossings are generated using different sets of beam parameters and σ_x, σ_y, and Δ_y are reconstructed with the inverse matrix method. Figure 8 shows a few examples of the results displayed as the difference between the beam parameters reconstructed and set in the simulation divided by the latter, averaged over 50 bunch crossings. These quantities are compatible with zero. The relative uncertainties, averaged over about 100 such reconstructions of vertical and horizontal beam sizes and the relative vertical displacement are 10.1%, 3.2% and 8.0%, respectively.

3 Mechanical concepts

On the basis of the simulation results mechanical designs of both calorimeters are developed. To allow their installation after the beam-pipe is in place, both calorimeters consist of two half-cylinders.

2010 JINST 5 P12002

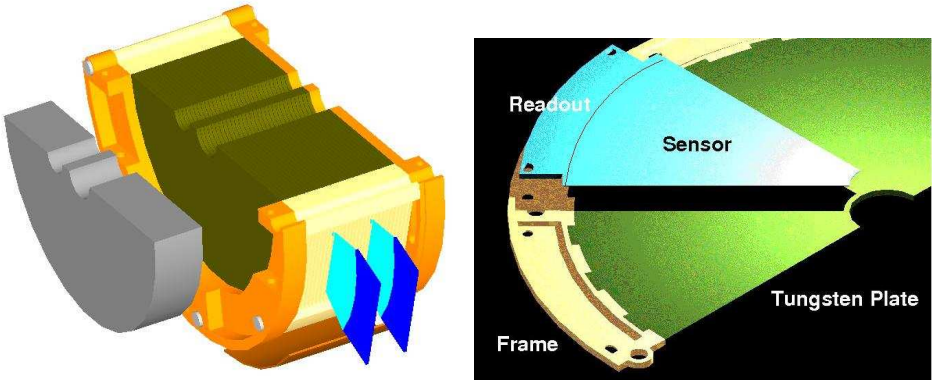

(a) (b)

Figure 9: (a) A half-cylinder of BeamCal. The brown block is the tungsten absorber structure interspersed with sensor layers. The orange structure represents the mechanical frame. The blue segments at the outer radius indicate the front-end electronics. In front of the calorimeter a graphite shield, shown in grey, reduces the amount of low energy particles back-scattered into the tracking detectors. (b) A half-layer of an absorber disk assembled with a sensor sector and the front-end readout.

A schematic of a half cylinder of BeamCal is shown in figure 9a. The tungsten absorber disks are embedded in a mechanical frame stabilised by steel rods. Each layer is composed of a tungsten half-disc surrounded by a brass half-ring as shown in figure 9b. Precise holes in the brass ring will ensure a position accuracy of better than 100μm. The sensors are fixed on the tungsten and connected via a flexible PCB to the front-end readout. The distance between two adjacent tungsten plates is kept to 1 mm to approach the smallest possible Molière radius. The sensors of BeamCal are structured into pads of about 8×8 mm^2 size allowing the maximum electron detection efficiency [25]. Due to the required high radiation tolerance, GaAs sensors are foreseen. For the innermost part of BeamCal, adjacent to the beam-pipes, also CVD[1] diamond is considered.

The design of LumiCal is similar [26]. Since it is a precision device, special care is devoted to the mechanical stability and position control. The tungsten half-discs are held by special bolts. For a barrel structure as shown in figure 10 a finite element simulation is performed. The calorimeter weight leads to a maximal vertical displacement of 20 μm. For a temperature difference of 1 K over a disk, the deformation of the shape of the tungsten plate is estimated to be 25 μm. To match the requirements on the precision of the lower polar angle measurement, the sensor positions at the inner acceptance radius must be controlled to better than 40 μm. Other critical quantities are the distance between the two calorimeters and the position of the beam with respect to the calorimeter axis. The former must be known to about 1 mm and the latter to 500 μm. A laser based position monitoring system has been developed [27] to control the position of LumiCal over short distances with μm precision.

For LumiCal, sensors made of high-ohmic n-type silicon are foreseen. The thickness of the sensors is about 300 μm. The p^+ side is segmented in polar and azimuthal pads and the backside

[1]Chemical Vapour Deposition.

2010 JINST 5 P12002

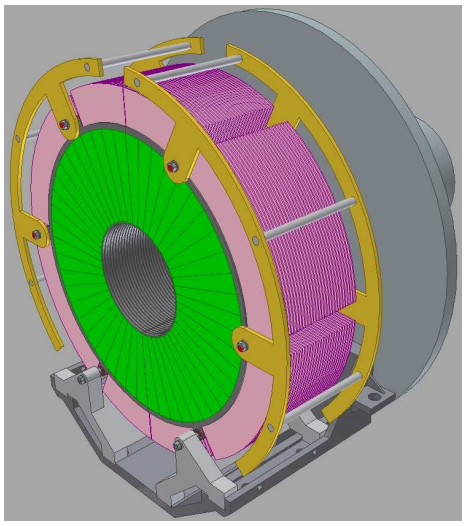

Figure 10: The mechanical structure of LumiCal. Tungsten disks are precisely positioned using 4 bolts which are stabilised by additional steel rings on both sides of the cylinder.

is fully metallised. To keep the Molière radius small the gap for the sensors is 1 mm. The signals on the pads of both calorimeters are led by thin copper strips on a Kapton foil to the front-end electronics positioned at the outer radius of the calorimeter.

4 Systematic effects in the luminosity measurement

Several phenomena which may have an impact on the luminosity measurement are considered. These are: pinch effect and beamstrahlung, background from two-photon processes, the resolution and scale of the electron energy measurement and the beam polarisation.

4.1 Pinch effect and beamstrahlung

Due to the pinch effect the luminosity for given bunch charges and sizes will be enhanced. However, electrons and positrons may radiate photons prior to Bhabha scattering. In addition, final state particles are deflected inside the bunch. The result is a reduction of the Bhabha event counting rate in a given range of low polar angles. The reduction is found to depend on the selection criteria for Bhabha events. For a selection optimised for nominal ILC beam parameters at 500 GeV centre-of-mass energy, it amounts to $1.51 \pm 0.05\%$ [28], where the quoted uncertainty stems from the statistics in the simulation. The dominant contribution to the loss is due to the reduction in the centre-of-mass energy caused by beamstrahlung. The latter leads to an effective centre-of-mass energy distribution called luminosity spectrum.

In the measurement of the luminosity, the loss of Bhabha events has to be corrected for. The impact of beamstrahlung can be estimated from the measured luminosity spectrum with a relative uncertainty of about 10^{-3} [28]. The impact of the deflection inside the bunch depends mainly on the horizontal bunch-size, σ_x, and the bunch length, σ_z. Assuming that one can control these two

2010 JINST 5 P12002

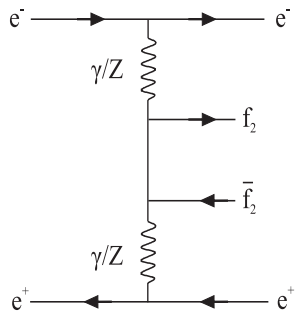

Figure 11: The Feynman graph for the dominant process in four-fermion production.

quantities with a relative uncertainty of 5%,[2] the uncertainty of a correction to the luminosity is about 1.5×10^{-3} [28].

4.2 Background from four-fermion production

Four-fermion production is known to have a large cross section with maxima at low polar angles.

It is dominated by the diagram shown in figure 11, where two virtual photons are exchanged between electron spectators. We used the WHIZARD [29] event generator to obtain samples of events for final states with leptons in the inner legs. The generator was tuned to experimental data of the process $e^+e^- \to e^+e^- c\bar{c}$ using data from LEP and other accelerators [30]. The cross-section of four-lepton production amounts to 12.0±0.5 nb at 500 GeV when the momenta of the exchanged photons are required to be larger than 0.1 GeV/c. The spectators remain at high energy. Less than 1% of them hit the luminosity calorimeter and become a background for Bhabha events. A Bhabha event sample has been generated with a cross-section of 4.70±0.03 nb at 500 GeV centre-of-mass energy, using the BHLUMI [31] event generator. The LumiCal response is simulated using BARBIE V4.3 [32], a GEANT3 based simulation program. The following event selection criteria are applied: the polar angle of the reconstructed shower must be within the LumiCal fiducial volume at one side and within $\theta_{\mathrm{min}} + 4$ mrad and $\theta_{\mathrm{max}} - 7$ mrad on the other. In addition, the total energy deposited in both calorimeters must be more than 80% of the center-of-mass energy. These criteria are optimised to reduce the impact of beamstrahlung and deflection on the Bhabha event counting to the amount given in the previous section [28]. The selection efficiency of Bhabha scattering events is about 68%.

Four-fermion events in the LumiCal are to a large fraction rejected by the Bhabha selection criteria. This is illustrated in figure 12 where the hits of particles from the four-fermion final states in the front plane of LumiCal per bunch crossing are shown before and after applying the Bhabha event selection. The fraction of four-fermion final states in the selected Bhabha event sample is 2.3×10^{-3}.

At LEP energies agreement between measurements and modelling of four-fermion processes was obtained within 20% [30]. Assuming that at 500 GeV it will be possible to model these processes with a precision of 40%, correcting the luminosity measurement correspondingly will lead to an uncertainty of 0.9×10^{-3}.

[2] In ref. [7] the estimated uncertainty of e.g. σ_x varies between 0.5% and 6.5%, depending on the number of free

2010 JINST 5 P12002

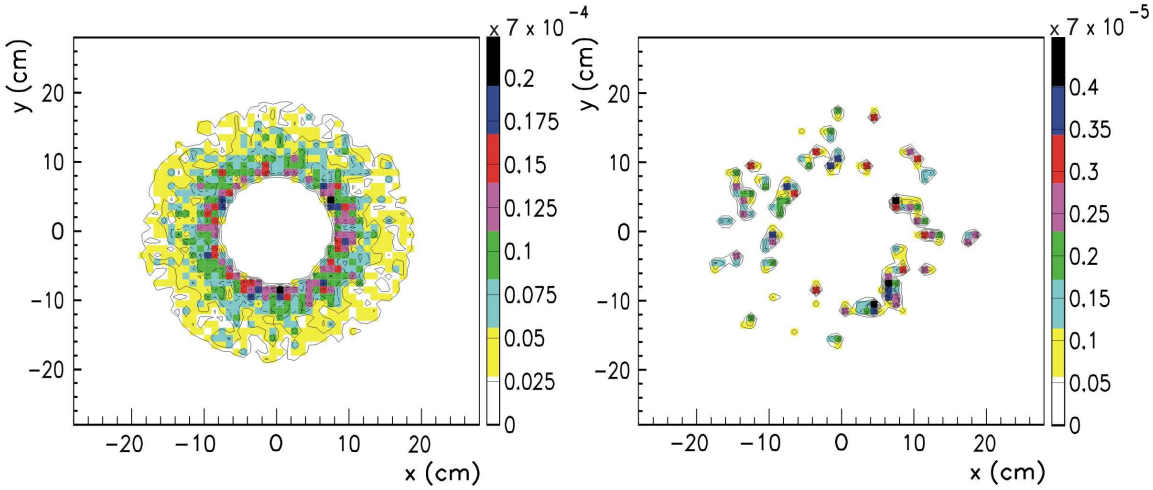

Figure 12: Average number of hits originating from four-fermion interactions per bunch crossing on the first plane of LumiCal at 500 GeV, before (left) and after (right) application of Bhabha event selection criteria.

4.3 Effects of a bias in the energy resolution and the energy scale

One of the criteria to select Bhabha events is the total energy measured in the calorimeters, required to be larger than 80% of the centre-of-mass energy. A possible bias in the energy resolution or the energy calibration will result in a change of the number of selected Bhabha events and hence in the measured luminosity.

The selection efficiency for Bhabha events as a function of the required energy in the calorimeters is shown in figure 13a. At the position of the cut in the measured calorimeter energy the slope of the tangent to the function is about -1.8×10^{-3}. To keep the shift of the luminosity below 10^{-3}, the cut in the measured calorimeter energy must be controlled with a precision of about 400 MeV. A study done allowing a constant offset in the measured energy leads to a similar requirement [33].

The effect of a bias in the energy resolution, a_{res} in eq. (2.4), is illustrated in figure 13b. We estimate that if a_{res} can be controlled within 20%, it will contribute to the luminosity uncertainty by about 10^{-4} .

4.4 Impact of electron and positron polarisation

To exploit the full physics potential of a linear collider, electron and positron beams will be polarised. Polarisation will also change the Bhabha cross section in the acceptance range of LumiCal up to a few per cent [34]. In the current design the maximum values for electron and positron polarisation are 0.8 and 0.6, respectively, with an uncertainty of 0.0025 [35]. Using these values the shift in the Bhabha cross section is 2.3×10^{-2} with an uncertainty of 1.9×10^{-4}.

4.5 Summary of systematic uncertainties

In addition to effects studied in this section also the impact of the polar angle resolution and polar angle bias as estimated in section 2.1 are included. All uncertainties based on the current level

beam parameters in the analysis. A similar range of precision is obtained for σ_z.

2010 JINST 5 P12002

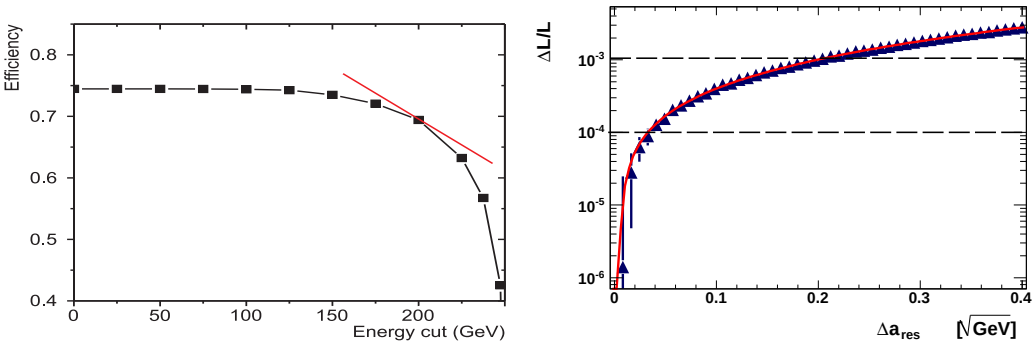

(a) (b)

Figure 13: (a) The selection efficiency for Bhabha events as a function of the measured shower energy, (b) the shift of the measured luminosity as a function of the bias in the energy resolution parameter a_{res}.

Table 1: The estimated systematic uncertainties on the luminosity measurement from all sources considered above at a centre-of-mass energy of 500 GeV.

Source	Value	Uncertainty	Luminosity Uncertainty
σ_θ	2.2×10^{-2}	100%	1.6×10^{-4}
Δ_θ	3.2×10^{-3}	100%	1.6×10^{-4}
$a_{\rm res}$	0.21	15%	10^{-4}
luminosity spectrum			10^{-3}
bunch sizes σ_x, σ_z,	655 nm, 300 μm	5%	1.5×10^{-3}
two photon events	2.3×10^{-3}	40%	0.9×10^{-3}
energy scale	400 MeV	100%	10^{-3}
polarisation, e^-, e^+	0.8, 0.6	0.0025	1.9×10^{-4}
total uncertainty			2.3×10^{-3}

of understanding are summarised in table 1. They are considered as being uncorrelated, leading currently to a total uncertainty of 2.3×10^{-3}. The reduction of the largest uncertainty, due to the deflections of final state electrons or positrons inside the bunch, needs further investigation. Also the energy scale uncertainty may be reduced by a proper calibration.

5 Sensor development

5.1 Sensors for BeamCal

The challenge of BeamCal is to find sensors tolerating about one MGy of dose per year. So far polycrystalline CVD diamond sensors of 1 cm^2 size and larger sectors of GaAs pad sensors, as shown in figure 14, have been studied. Irradiation is done using a 10 MeV electron beam at the S-

2010 JINST 5 P12002

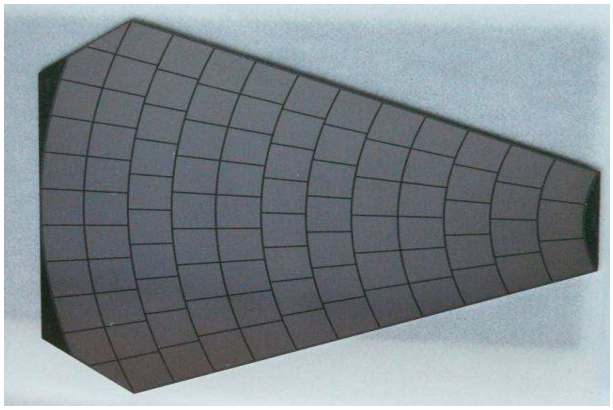

Figure 14: A prototype of a GaAs sensor sector for BeamCal with pads of about 30 mm^2 area.

DALINAC accelerator [36]. The intensity is varied between 10 and 100 nA corresponding to dose rates between 20 and 200 kGy/h. Since large area CVD diamond sensors are extremely expensive, they may be used only at the innermost part of BeamCal. At larger radii GaAs sensors appear to be a promising option.

5.1.1 GaAs sensors

Large area GaAs sensors are obtained from the Tomsk State University. They are produced using the liquid encapsulated Czochralski method and are doped with tin and tellur as shallow donors and chromium as a deep acceptor.

Three batches with different concentrations of dopants are irradiated up to 1.2 MGy and the charge collection efficiency, CCE, is measured as a function of the absorbed dose. The results are shown in figure 15. The charge collection efficiency depends slightly on the dopant concentration. The sensors with a lower donor concentration show a larger initial charge collection efficiency and the decrease of the charge collection efficiency as a function of the absorbed dose is less steep. The smallest decrease of the CCE as a function of the dose is observed for tin donor. A MIP signal is separated from the pedestal up to a dose of 600 kGy for the sensors with lower donor concentration. The leakage current of a pad at room temperature before irradiation is about 200 nA at an applied voltage of 50 V. After exposure of a dose of 1.2 MGy leakage currents of up to a factor 2 larger were found. The pad capacitance is measured to 12 pF. The results are consistent with previous measurements [37].

5.1.2 CVD diamond sensors

For polycrystalline diamond sensor samples of 1 cm^2 area and 500 μm thickness the linearity of the response and the leakage current and the signal collection efficiency have been investigated as a function of the absorbed dose [38]. The signal size depends linearly on the number of charged particles crossing the sensors for up to 5×10^6 particles in 10 ns. The leakage current, less than 1 pA at room temperature, depends only slightly on the absorbed dose up to 7 MGy. The charge collection efficiency rises by a factor of two for doses between 0.5 to 1 MGy, then drops smoothly

2010 JINST 5 P12002

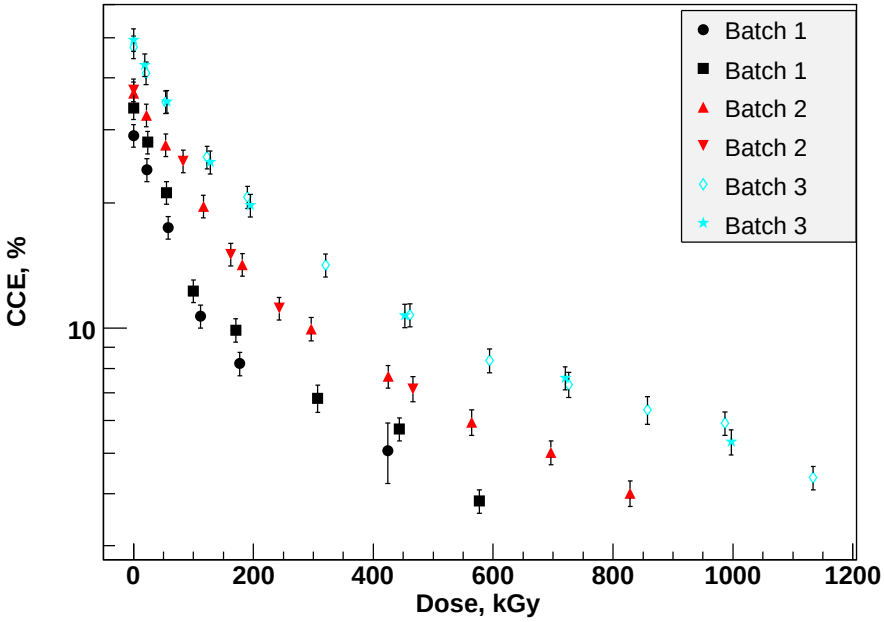

Figure 15: The CCE as a function of the absorbed dose for the GaAs sensors with different donor concentrations. The donor is tellur for batches 1 and 2 and tin for batch 3.

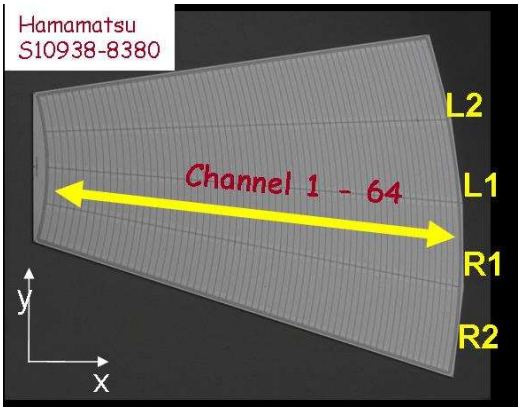

Figure 16: A prototype silicon sensor for LumiCal.

approaching the charge collection efficiency of a non-irradiated sensor. Provided the sensor is continuously irradiated, this efficiency is reached at about 7 MGy.

5.2 Sensors for LumiCal

Prototypes of LumiCal sensors have been designed [39] and then manufactured by Hamamatsu Photonics. A picture of a sensor is shown in figure 16. Its shape is a ring segment of 30°. The thickness of the n-type silicon bulk is 320 μm. The pitch of the concentric p^+ pads is 1.8 mm and the gap between two pads is 0.1 mm. The leakage current of a single pad as a function of the bias voltage is shown in figure 17a. Putting the neighbouring pads on ground stabilises the measurement and reduces the current values by a factor of two. The leakage currents of all the pads of one sensor

2010 JINST 5 P12002

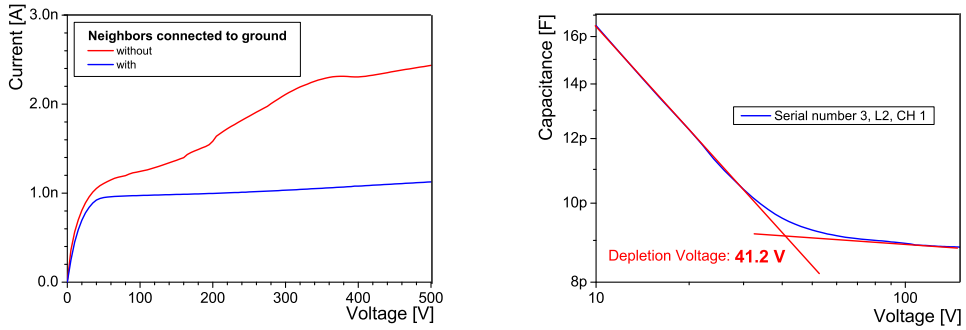

(a) (b)

Figure 17: (a) The dependence of the leakage current on the bias voltage for a single pad with and without grounded neighbours. (b) The capacitance of a pad as a function of the bias voltage.

have been measured at a bias voltage of 500 V. All pads except one have a leakage current in the range from 1 to 4 nA. Less than 5% of all pads have a break-through voltage below 500 V. For other sensors the results are similar. The capacitance as a function of the bias voltage for a pad is shown in figure 17b. Also shown is how the value of the full depletion voltage is obtained. Values from 39 V to 43 V were found. At a voltage of 100 V the pad capacitance values are between 8 pF for the smallest pads and 25 pF for the largest pads.

6 ASIC developments

Since the occupancy in BeamCal and LumiCal is relatively large they must be read-out after each bunch crossing. Therefore special front-end and ADC ASICs have been developed which match the timing of the ILC-bunch trains with a frequency of 5 Hz and about one ms duration with 300 ns between bunches. Since the ASICs are positioned at the outer radius of the calorimeters the expected radiation dose is noncritical. From Monte Carlo simulations less than 140 Gy and about one Gy are estimated for BeamCal and LumiCal, respectively, for one year of operation at 500 GeV centre-of-mass energy and nominal beam parameters.

6.1 LumiCal readout

The design of the LumiCal front-end electronics was performed for the proposed detector architecture [40]. The front-end ASIC is supposed to work in two modes, the physics mode and the calibration mode. In the physics mode, electromagnetic showers will be measured with large energy depositions on the pads. The front-end ASIC must process signals up to at least 6 pC per channel. In the calibration mode, MIP signals from single relativistic muons will be measured. The minimum size of these signals is 2 fC, corresponding to the low end of the Landau distribution for MIPs in 300 μm thick silicon. From the sensor segmentation a range of pad capacitances between 10 pF and 100 pF was obtained.[3] Because of the high expected occupancy, the front-end ASIC needs to be fast enough to resolve signals from subsequent bunch crossings which are separated in time by about 300 ns.

[3]The sensor segmentation was revised later, resulting in pad capacitances between 10 pF and 25 pF.

2010 JINST 5 P12002

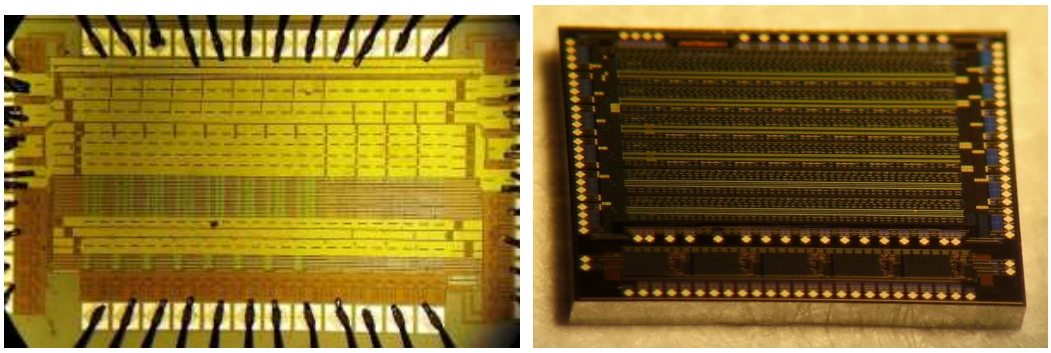

(a) (b)

Figure 18: Photograph of prototypes of the front-end ASIC (a) and the ADC ASIC (b)

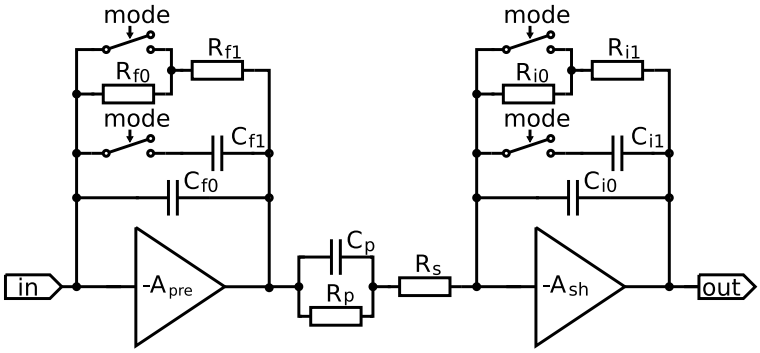

Figure 19: Block diagram of the single front-end channel

The simulations of LumiCal indicate that the shower reconstruction needs at least 8 bit precision. Severe requirements set on the readout electronics power dissipation may be strongly relaxed if switching of the power between bunch trains is done. This is feasible since in the ILC experiments after each 1 ms bunch train there will be a pause of about 200 ms [16].

The prototype ASICs, as shown in figures 18a and 18b, are fabricated in 0.35 μm CMOS technology.

6.1.1 Front-end electronics design

The chosen front-end architecture comprises a charge sensitive amplifier, a pole-zero cancellation circuit (PZC) and a shaper, as shown in figure 19. In order to cope with large charges in the physics mode and small ones in the calibration mode a variable gain in both the charge amplifier and the shaper is applied. The mode switch in figure 19 changes the effective values of the feedback circuit components R_f, C_f, R_i, C_i and therefore the transimpedance gain of the front-end ASIC is changed. The low gain (large C_f) is used for the physics mode when the front-end processes signals from large charge depositions in the sensor, while the high gain (small C_f) is used in the calibration mode. Assuming high enough open loop gain of the pre-amplifier (A_{pre}) and the shaper amplifier

2010 JINST 5 P12002

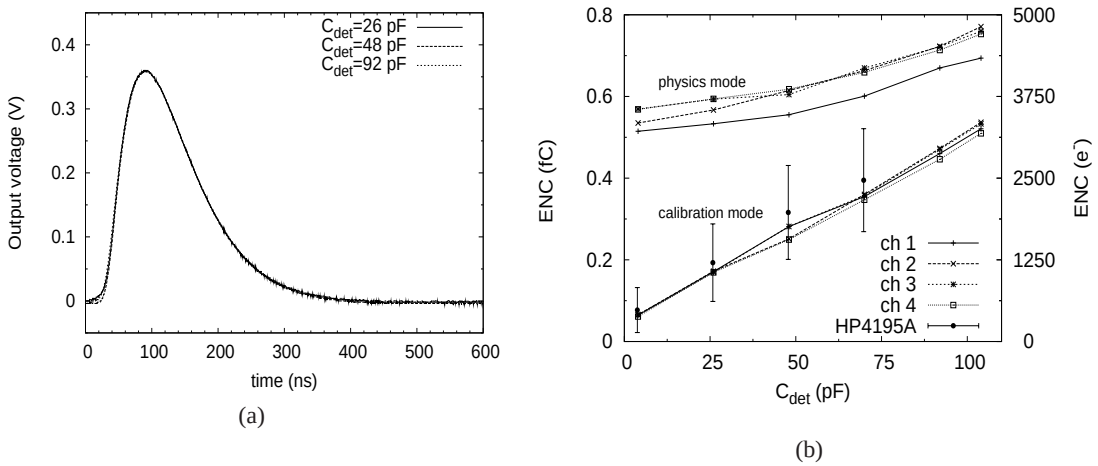

Figure 20: (a) Output pulses in physics mode as a function of the input capacitance for Q_{in}=3.3 pC. (b) Noise ENC measurements obtained with true r.m.s. meter for the front-end ASIC.

(A_{sh}), the transfer function of this circuit is given by

$$\frac{U_{out}(s)}{I_{in}(s)} = \frac{1}{C_f C_i R_s} \cdot \frac{s+1/C_p R_p}{s+1/C_f R_f} \cdot \frac{1}{(s+1/C_i R_i)(s+1/C_p(R_p||R_s))}. \quad (6.1)$$

By setting properly the PZC parameters ($C_f R_f = C_p R_p$) and by equalising the shaping time constants ($C_i R_i = C_p(R_p||R_s)$), one obtains the first order shaping, equivalent to a CR-RC filter, with a peaking time $T_{peak} = C_i R_i$. A simple first order shaping is chosen as a trade-off between the noise and the power dissipation. Regarding the noise, the main requirement is to obtain in calibration mode the signal to noise ratio of about 10 for the largest sensor capacitances. Both of the amplifying stages (A_{pre}, A_{sh}) are designed as folded cascodes [41] with active loads, followed by source followers. In the prototype ASIC, eight front-end channels are implemented. A more detailed discussions of the front-end ASICs can be found in ref. [42].

6.1.2 Front-end electronics measurements

Figure 20a shows the response of the front-end channel to charge injected through the input test capacitance for different values of the input capacitance, C_{det}, within the interesting range. The sensor capacitance is simulated with an external capacitor. It is seen that both the amplitude and the peaking time are not sensitive to the value of the input capacitance in agreement with HSPICE simulations.

The output noise has been measured using a HP3400 true r.m.s. meter [43]. The equivalent noise charge, ENC, as a function of input capacitance is shown in figure 20b. Results obtained for the physics and calibration modes are shown on the same plot. Since the HP3400 bandwidth is only up to 10 MHz the numbers may be underestimated by about 20%. The measured ENC as a function of C_{det} are in agreement with simulations. In particular, in the calibration mode the signal to noise ratio of 10 is maintained for input capacitances up to about 100 pF. For a few points additional noise measurements have been performed by measuring the output noise spectra using a HP4195A

2010 JINST 5 P12002

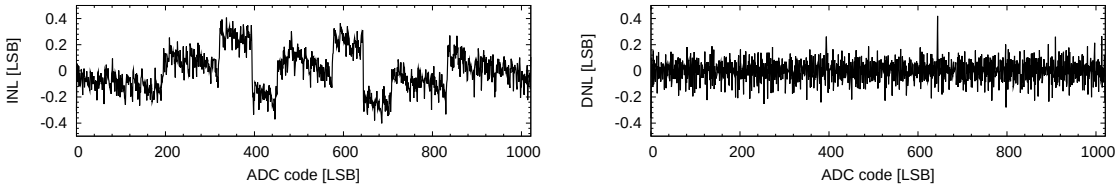

(a) (b)

Figure 21: Static measurements of (a) INL and (b) DNL at 20 MHz sampling frequency.

spectrum analyser [43] and then integrating it numerically. The results of such measurements are added in figure 20b. They agree within their uncertainties with the HP3400 measurements.

In order to test the effectiveness of the PZC circuit, the front-end response has been measured as a function of the rate of input pulses. To avoid input charges of both polarities when using a square-wave test signal, the staircase test waveforms are synthesised using the Tektronix AWG2021 waveform generator. It was found that the change in amplitude reaches 2% for input rates of about 3 MHz and is quite insensitive to the input capacitance. The power consumption of about 8.9 mW/channel is measured in accordance with expectations from simulation.

6.1.3 ADC design

As a compromise between speed, area and power consumption the ADC was designed using pipeline technology. A 1.5-bit per stage architecture is chosen because of its simplicity and immunity to the offsets in the comparator and amplifier circuits. The prototype ADC consists of an input sample and hold circuit, 9 pipeline stages and digital correction circuitry. In addition, the power switching feature is also implemented. More details about the ADC design can be found in ref. [44].

6.1.4 ADC performance measurements

The static measurements of the Integral Nonlinearity, INL, and the Differential Nonlinearity, DNL, obtained at a sampling frequency of 20 MHz, are shown in figures 21a and 21b, respectively. These parameters are calculated using the histogramming method. The measured INL is always less than 1 LSB while the DNL is below 0.5 LSB. These results attest to a very good ADC linearity. To estimate the dynamic performance, measurements with sinusoidal wave input are performed [45]. An example of a measured Fourier spectrum using a 1.8 MHz full scale (0 dB) input signal sampled at 20 MHz is shown in figure 22a. It is seen that the noise and harmonic components are small enough not to affect significantly the resolution. The signal to noise ratio, SNHR, is measured as a function of sampling frequency as shown in figure 22b. An SNHR of about 58 dB is obtained in the frequency range up to almost 25 MHz.

6.2 BeamCal readout

The BeamCal ASIC, designed for 180 nm TSMC technology, will be able to handle 32 channels. The two modes of operation require a front-end circuit capable of a wide performance envelope: high slew rate for standard data taking, and low noise for calibration. In standard data taking the occupancy is high, and therefore all data from a full bunch train must be recorded, to be read out between bunch trains. Because of its reliability, density and redundancy, a digital memory array will

2010 JINST 5 P12002

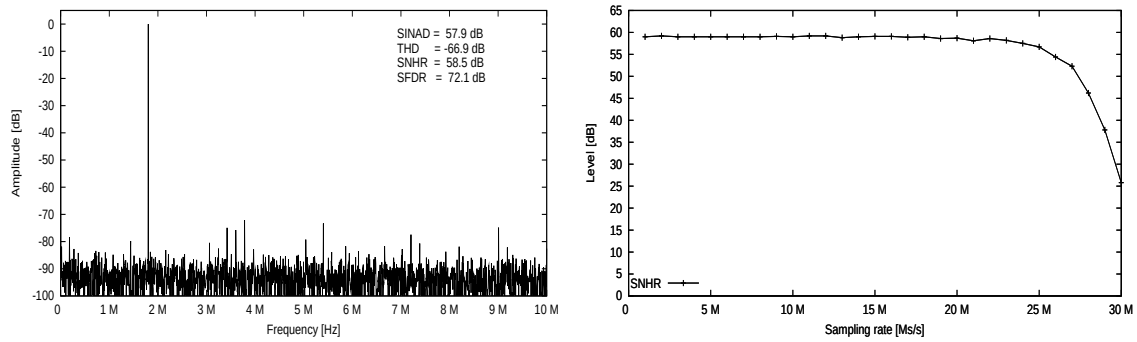

(a) (b)

Figure 22: (a) Example of the Fourier spectrum measurement with f_{in}=1.8 MHz and f_{clk}=20 MHz, (b) SNHR as a function of the sampling rate.

be used to store the data from all collisions in each bunch train. This choice requires a sampling rate of 3.25 MHz per channel, which is achieved by 10-bits, successive approximation analog-to-digital converters [46]. The small size of this ADC architecture allows to use one converter per channel.

In this front-end ASIC, the dominant noise source is the charge sensitive amplifier series noise. Assuming 40 pF input capacitance, high occupancy and the 300 ns period, a careful design of noise filtering and baseline restoration is necessary [47].

In order to take advantage of all the time available for signal processing, the filter for calibration operation has been implemented using switched-capacitor, SC, circuits [48]. This technique allows to precisely define the circuit time constants depending on the input clock frequency and the ratio of two capacitors. Baseline restoration is achieved by means of a fast gated reset, followed by a slow reset-release technique to reduce the effect of a split doublet. The slow reset-release is implemented using SC circuits.

In standard data taking operation, an adequate noise power is effectively achieved by means of a slow reset-release technique, similar to that used in calibration operation. An explicit filter for standard data taking operation is unnecessary, as the amplifier bandwidth suffices for noise filtering purposes.

Figure 23 shows a simplified block diagram for a single channel. In standard data taking operation, since filtering is unnecessary, the integrator is bypassed to reduce power consumption.

For design purposes, the transistor-level noise analysis has been carried out using the g_m/I_D technique [49], which takes noise coefficients directly from SPICE simulation results. As this is a gated front-end, the system-level noise analysis has been done using the weighting function approach.

Since the system's dominant noise source is series noise, a triangular-shaped weighting function effectively minimises the output noise power. The negative slope section of the triangular weighting function is easily implemented by means of an integrator — in this case, a SC integrator. The positive slope section is achieved by means of the slow reset-release technique mentioned earlier. The weighting function resulting from an ideal reset-release and a SC integrator is shown in figure 24, left; a more realistic weighting function, reconstructed from SPICE simulation results, is shown in the right plot. In both cases, the target noise level is effectively achieved.

2010 JINST 5 P12002

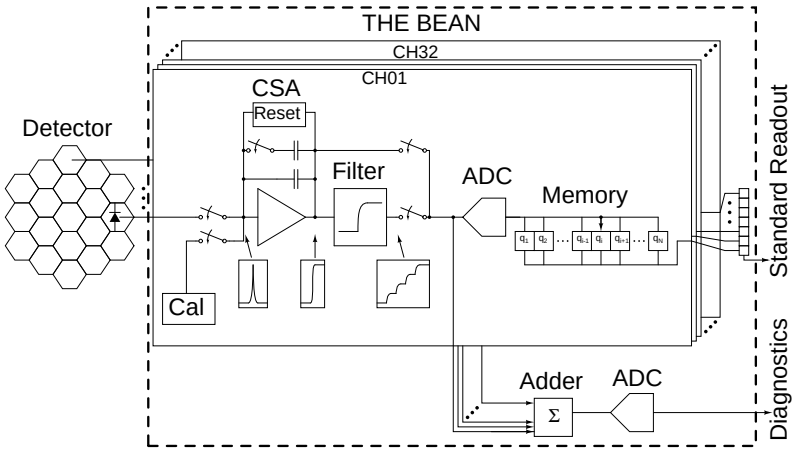

Figure 23: Simplified BeamCal ASIC block diagram of a single channel. In addition to the standard read-out a fast analog sum of groups of pads for beam-tuning is delivered by the Adder.

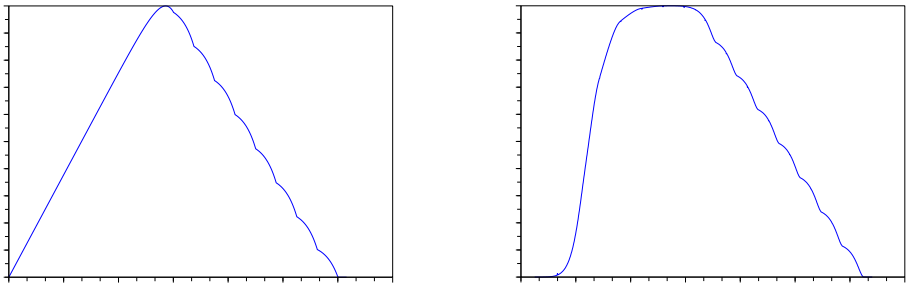

Figure 24: Front-end weighting function assuming ideal components (left) and simulation results (right) in the calibration mode

6.2.1 Circuit implementation

The charge sensitive amplifier is a folded-cascode amplifier with NMOS input device, connected to a switched-capacitor feedback network. The amplifier input transistor is biased at 450 μA whereas the load works at about 50 μA. The feedback network consist of two feedback capacitors of 0.9 pF and 44.1 pF for calibration and standard data taking modes, respectively. Both have a reset transistor, with a gate voltage driven by the switched-capacitor reset-release network. The amplifier output is pseudo-differential.

In order to isolate the amplifier from the filter's SC-related kickback noise, a buffer circuit is used. The buffer also allows signal shifting, producing a more adequate common-mode level for the filter. The buffer consumes 130 μA and consists of a source follower, with cascoded current source and an additional device to keep a nearly constant operational point in the input transistor. This serves the purpose of enhancing the buffer linearity.

The filter implemented is a fully-differential switched-capacitor integrator. Capacitor values were carefully designed in order to obtain the adequate noise performance. The core of the inte-

2010 JINST 5 P12002

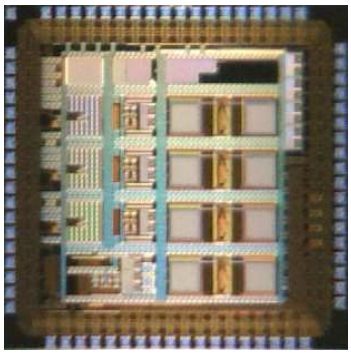

Figure 25: BeamCal Instrumentation ASIC Prototype

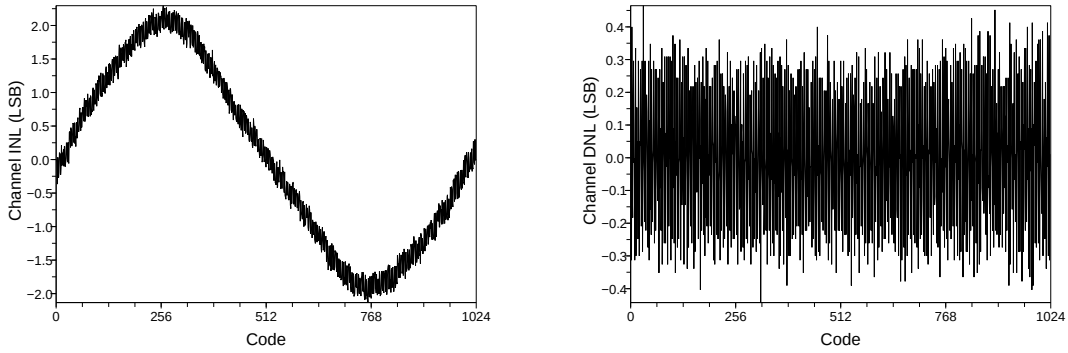

Figure 26: Results of (a) the INL and (b) the DNL using 2 fF unit capacitors.

grator is a class A/AB amplifier [50] that consumes 456 μA.

The converter is a 10-bit, fully-differential successive approximation register ADC. The one included in the BeamCal ASIC has 16 fF unit capacitances, and similar versions with 4 fF and 2 fF unit capacitances were also designed for individual characterisation.

The BeamCal ASIC prototype, similar to the ASIC described in figure 23, but including only three channels and no internal memory, was fabricated and is currently being tested. Figure 25 shows the 2.4 mm $\times$ 2.4 mm die.

6.2.2 Test results

The ADC in the BeamCal ASIC has been quantitatively characterised, along with the additional versions of the ADC using smaller unit capacitances. Figures 26a and 26b show the INL and DNL for the ADC using 2 fF capacitors. The measurements were done at the nominal sampling frequency of 3.125MHz. The ADC input was a ramp, generated by 16-bit DAC, and the static performance measurements were calculated using the histogram method on the ADC digital output. The results are consistent with unit capacitance matching better than 0.1%. The INL cubic-like shape in figure 26a is explained due to copper dishing effects, and will be corrected in future versions by re-arranging the capacitor array connections.

2010 JINST 5 P12002

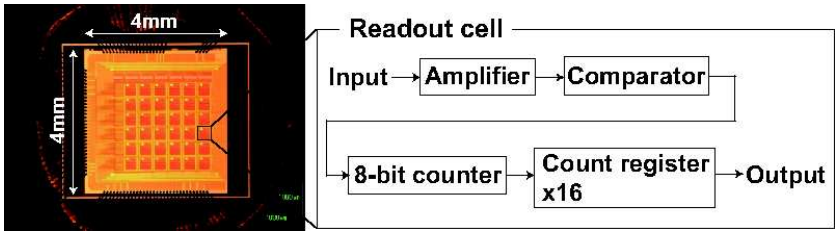

Figure 27: Picture of the prototype of the pair monitor readout ASIC and schematic diagram of the circuit in a readout cell. The readout cell consists of the amplifier, comparator, 8-bit counter, and 16 count-registers.

6.3 Pair monitor readout

A prototype ASIC has been designed with 36 readout cells arranged as an array of 6×6, as shown in figure 27. Each cell has an amplifier block, comparator, an 8-bit counter and a 16 count-registers. The amplifier block consists of a charge sensitive pre-amplifier, a threshold block and a differential-amplifier. The pre-amplifier is a constant-current feedback-type amplifier. The time-over-threshold of the output signal is proportional to the injected charge through the constant current feedback in the pre-amplifier. In the 8-bit counter, the Gray code is used to count the number of hits. The 16 count-registers are prepared to store hit counts in one bunch train subdivided in 16 time slices. There are also decoders which select a count-register to store and readout the hit count. A shift register to select a readout pixel, data transfer to the output line and distributor of the operation signals are arranged around the 36 readout cells as a glue logic. The bonding pad is prepared in each cell to be attached to a sensor with bump bonding. The prototype ASIC has been produced with TSMC 250 nm CMOS process. The chip size is 4×4 mm^2, and the readout cell size is 400×400 μm^2.

Figure 28 shows the response of the counter block. The state of the counter bits changes at each test pulse indicating a bunch crossing. The number of hits is measured in 16 time slices of a bunch train. The data stored will then be read-out during the inter-train time. The test is performed counting the hits in each time slice with a count rate of 4 MHz, larger than expected at the ILC. The number of hits was counted without any bit lost.

We also studied the noise level in the circuit. The count efficiency was investigated as a function of the threshold voltage at the comparator. Fitting the efficiency curve with the error function, a standard deviation of 0.94 mV was obtained. With the gain of 1.6×10^{-3} mV per electron, this corresponds to an ENC of about 600 electrons.

As the next step, a pair-monitor prototype will be built in Silicon On Insulator technology. The sensor and readout ASIC will be prepared on the same wafer. This prototype will be used to investigate not only the standard characteristics but also the radiation tolerance. Currently, an ASIC is developed in OKI 0.2 μm FD-SOI CMOS [51] technology.

2010 JINST 5 P12002

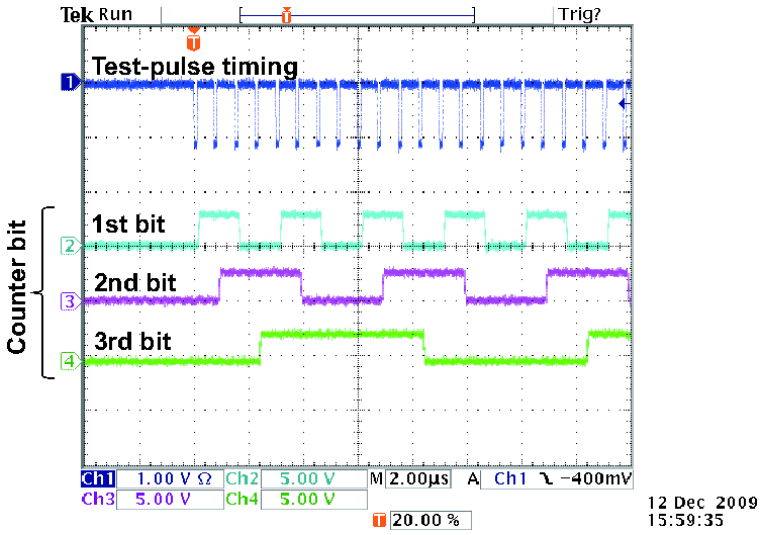

Figure 28: Output signals from the counter block. The lower 3 bits of the 8-bit counter are shown. The test-pulse timing corresponds to the bunch crossing frequency if the ILC.

7 Summary

A design for the instrumentation of the very forward region of a detector at the International Linear collider is presented. Two calorimeter are planned, LumiCal to measure precisely the luminosity and BeamCal, supplemented by a pair monitor, for a fast luminosity estimate and beam tuning. Both calorimeters extend the coverage of the detector to small polar angles. Parameters relevant for the physics program have been estimated by Monte Carlo simulations and found to match the requirements for the chosen geometry. Prototypes of the major components such as sensors, front-end ASICs and ADC ASICs are developed, produced and tested. Their measured performance fulfils the specifications derived from the Monte Carlo simulations. The results presented here demonstrate that the sensors and the ASICs are ready to be integrated into a fully functional prototype detector and to perform, as the next step, tests of fully assembled sensor plane prototypes.

Acknowledgments

This work is supported by the Commission of the European Communities under the 6^{th} Framework Program "Structuring the European Research Area", contract number RII3-026126. Tsukuba University is supported in part by the Creative Scientific Research Grant No. 18GS0202 of the Japan Society for Promotion of Science. The AGH-UST is supported by the Polish Ministry of Science and Higher Education under contract Nr. 372/6.PRUE/2007/7. The INP PAN is supported by the Polish Ministry of Science and Higher Education under contract Nr. 141/6.PR UE/2007/7. IFIN-HH is supported by the Romanian Ministry of Education, Research and Innovation through the Authority CNCSIS under contract IDEI-253/2007. The VINCA group is benefiting from the project "Physics and Detector R&D in HEP Experiments" supported by the Ministry of Science of

2010 JINST 5 P12002

the Republic of Serbia. J. Aguilar, P. Ambalathankandy and O. Novgorodova are supported by the 7th Framework Programme "Marie Curie ITN", grant agreement number 214560.

References

[1] *International Linearcollider Reference Report* (2007), http://www.linearcollider.org/about/Publications/Reference-Design-Report.

[2] *The Compact Linear Collider Study*, http://clic-study.web.cern.ch/clic-study/.

[3] T. Abe et al., *The International Large Detector: Letter of Intent*, FERMILAB-LOI-2010-01, FERMILAB-PUB-09-682-E, DESY-2009-87, KEK-REPORT-2009-6, arXiv:1006.3396 (2010).

[4] E.L. Berger et al., *SiD Letter of Intent* (2009), https://confluence.slac.stanford.edu/display/SiD/home.

[5] H. Abramowicz et al., *Instrumentation of the very forward region of a linear collider detector*, *IEEE Trans.Nucl.Sci.* **51** (2004) 2983.

[6] K. Mönig, *Physics needs for the forward region*, in *V. Workshop: Instrumentation of the Forward Region of a Linear Collider Detector*, August, 26–28 (2004) DESY, Zeuthen, Germany, http://www-zeuthen.desy.de/lcdet/Aug_04_WS/aug_04_ws.html.

[7] Ch. Grah and A. Sapronov, *Beam parameter determination using beamstrahlung photons and incoherent pairs*, 2008 *JINST* **3** P10004.

[8] R. Bonciani and A. Ferroglia, *Bhabha Scattering at NNLO*, *Nucl. Phys. B Proc. Suppl.* **181-182** (2008) 259;
T. Becher and K. Melnikov, *JHEP* **06** (2007) 084;
S. Actis, M. Czakon, J. Gluza and T. Riemann, *Fermionic NNLO contributions to Bhabha scattering*, *Acta Phys.Polon.* **B 38** (2007) 3517;
A.A. Penin, *Two-loop photonic corrections to massive Bhabha scattering*, *Nucl. Phys.* **B 734** (2006) 185;
M. Czakon, J. Gluza and T. Riemann, *The Planar four-point master integrals for massive two-loop Bhabha scattering*, *Nucl. Phys.* **B 751** (2006) 1.

[9] S. Jadach, W. Placzek and B.F.L. Ward, *BHWIDE 1.00: O(α) YFS exponentiated Monte Carlo for Bhabha scattering at wide angles for LEP1/SLC and LEP2*, *Phys. Lett.* **B 390** (1997) 298.

[10] S. Agostinelli et al., *Geant4 — a simulation toolkit*, *Nucl. Instrum. Meth.* **A 506** (2003) 250.

[11] *MOKKA, A simulation program for linear collider detectors*, http://polzope.in2p3.fr:8081/MOKKA/.

[12] T.C. Awes, F.E. Obenshain, F. Plasil, S. Saini, S.P. Sorensen and G.R. Young, *A simple method of shower localization and identification in laterally segmented calorimeters*, *Nucl. Instrum. Meth.* **311** (1992) 130.

[13] I. Sadeh, *Luminosity measurement at the International Linear Collider*, arXiv:1010.5992.

[14] H. Abramowicz et al., *Redefinition of the geometry of the luminosity calorimeter*, *EUDET-Memo-2008-09* (2008), http://www.eudet.org.

[15] H. Abramowicz et al., *Revised requirements on the readout of the luminosity calorimeter*. *EUDET-Memo-2008-08* (2008), http://www.eudet.org.

[16] J. Brau et al., *ILC Reference Design Report*, arXiv:0712.1950.

[17] D. Schulte, *Beam-beam simulations with guinea-pig*, CERN-PS-99-014LPCLIC-Note 387 (1998).

[18] A. Seryi, T. Maruyama and B. Parker, *IR optimization and anti-DID*, SLAC-PUB-11662 (2006).

2010 JINST 5 P12002

[19] P. Bambade, V. Drugakov and W. Lohmann, *The impact of Beamcal performance at different ILC beam parameters and crossing angles on stau searches*, *Pramana J. Phys.* **69** (2007) 1123.

[20] A. Heikkinen and N. Stepanov, *Bertini Intra-nuclear Cascade implementation in Geant4*, *Proceedings of CHEP03* (2003) La Jolla, California [nucl-th/0306008].

[21] C. Coca et al., *Expected electromagnetic and neutron doses for the BeamCal at ILD Rom. J.Phys* **55** (2010) 687.

[22] T. Tauchi and K. Yokoya, *Nanometer beam-size measurement during collisions at linear colliders*, *Phys. Rev.* **E 51** (1995) 6119.

[23] T. Tauchi, K. Yokoya and P. Chen, *Pair creation from beam-beam interaction in linear colliders*, *Part. Accel.* **41** (1993) 29.

[24] K. Ito, *Study of Beam Profile Measurement at Interaction Point in International Linear Collider*, arXiv:0901.4151.

[25] A. Elagin, *The optimized sensor segmentation for the very forward calorimeter*, in proceedings of *the 2005 International Linear Collider Physics and Detector Workshop*, Snowmass, Colorado, ECONF **C0508141** (2005) ALCPG0719.

[26] J. Blocki et al., *LumiCal new mechanical structure*, *EUDET-Memo-2009-10* (2009), http://www.eudet.org/.

[27] J. Blocki et al., *Laser alignment system for LumiCal*, *EUDET-Report-2008-05* (2008), http://www.eudet.org.

[28] C. Rimbault, P. Bambade, K. Monig and D. Schulte, *Impact of beam-beam effects on precision luminosity measurements at the ILC*, 2007 *JINST* **2** P09001.

[29] W. Kilian, *WHIZARD: A generic Monte-Carlo integration and event generation package for multi-particle processes*, LC-TOOL-2001-039 (2001).

[30] V.N. Pozdnyakov, *Two-photon interactions at LEP*, *Phys. Part. Nucl. Lett.* **4** (2007) 289.

[31] S. Jadach, E. Richter-Was, B.F.L. Ward and Z. Was, *Monte Carlo program BHLUMI for Bhabha scattering at low polar angle with Yennie-Frautschi-Suura exponentiation*, *Comp. Phys. Commun.* **70** (1992) 305.

[32] B. Pawlik et al., *BARBIE V4.3, Simulation-package of the LumiCal Detector*, http://www.ifj.edu.pl/dept/no1/nz13/barbi.php.

[33] I. Smiljanic et al., *Towards a final selection for luminosity measurement*, *Proceedings of the Workshop of the Collaboration on Forward Calorimetry at ILC* (2008), Belgrade Serbia.

[34] Ch. Grah et al., *Report to the Detector R&D Panel — Instrumentation of the Very Forward Region*, Hamburg, Germany (2007), http://www.desy.de/prc/docs_rd/prc_rd_02_01_update_05_07.pdf.

[35] S. Boogert et al., *Polarimeters and Energy Spectrometers for the ILC Beam Delivery System*, 2009 *JINST* **4** P10015.

[36] *S-DALINAC: Superconducting DArmstadt LInear ACcelerator*, http://www.ikp.tu-darmstadt.de/beschleuniger_1/S-DALINAC.de.jsp.

[37] Ch. Grah et al., *Radiation hard sensor for the BeamCal of the ILD detector*, *Proceedings of the IEEE conference*, October 27 – November 3 (2007) Honolulu, U.S.A.

[38] Ch. Grah et al., *Polycrystalline CVD Diamonds for the Beam Calorimeter of the ILC*, *IEEE Trans. Nucl. Sci.* **56** (2009) 462.

2010 JINST 5 P12002

[39] J. Blocki et al., *Silicon Sensors Prototype for LumiCal Calorimeter*, EUDET-Memo-2009-07 (2009), http://www.eudet.org.

[40] M. Idzik et al., *Status of VFCAL, EUDET-memo-2008-01* (2008), http://www.eudet.org.

[41] E. Beuville et al.. *AMPLEX, a low-noise, low-power analog CMOS signal processor for multi-element silicon particle detectors*, *Nucl. Instrum. Meth.* **A 288** (1990) 157.

[42] M. Idzik, Sz. Kulis and D. Przyborowski, *Development of front-end electronics for the luminosity detector at ILC*, *Nucl. Instrum. Meth.* **A 608** (2009) 169.

[43] http://www.home.agilent.com.

[44] M. Idzik, K. Swientek and Sz. Kulis, *Development of a Pipeline ADC for the Luminosity Detector at ILC*, 2010 *JINST* **5** P04006.

[45] *IEEE standard for terminology and test methods for analog-to-digital converters*, IEEE-STD-1241 (2000).

[46] J.L. McCreary and P.R. Gray, *All-MOS charge redistribution analog-to-digital conversion techniques. I*, *IEEE J. Solid-State Circ.* **10** (1975) 371.

[47] H. Spieler, *Semiconductor Detector Systems*. Oxford University Press, Oxford U.K. (2005).

[48] R. Gregorian, K.W. Martin and G.C. Temes, *Switched-capacitor circuit design*, *IEEE Proc.* **71** (1983) 941.

[49] F. Silveira, D. Flandre and P.G.A. Jespers, *A g_m/I_D based methodology for the design of CMOS analog circuits and its application to the synthesis of a silicon-on-insulator micropower OTA*, *IEEE J. Solid-State Cir.* **31** (1996) 1314.

[50] S. Rabii, *Design of Low-Voltage Low-Power Sigma-Delta Modulators*, PhD thesis, Stanford University (1998).

[51] Y. Arai, *Electronics and sensor study with the OKI SOI process*, in proceedings of the *Topical workshop on electronics for particle physics (TWEPP-07)*, September 3–7 (2007) Prague, Czech Republic.

2010 JINST 5 P12002

Published for SISSA by Springer

Received: *August 2, 2012*
Revised: *November 8, 2012*
Accepted: *November 23, 2012*
Published: *December 13, 2012*

Time-dependent angular analysis of the decay $B_s^0 \to J/\psi\phi$ and extraction of $\Delta\Gamma_s$ and the CP-violating weak phase ϕ_s by ATLAS

The ATLAS collaboration

E-mail: atlas.publications@cern.ch

Abstract: A measurement of $B_s^0 \to J/\psi\phi$ decay parameters, including the CP-violating weak phase ϕ_s and the decay width difference $\Delta\Gamma_s$ is reported, using 4.9 fb^{-1} of integrated luminosity collected in 2011 by the ATLAS detector from LHC pp collisions at a centre-of-mass energy $\sqrt{s} = 7$ TeV. The mean decay width Γ_s and the transversity amplitudes $|A_0(0)|^2$ and $|A_\parallel(0)|^2$ are also measured. The values reported for these parameters are:

$$\begin{aligned}
\phi_s &= 0.22 \pm 0.41 \text{ (stat.)} \pm 0.10 \text{ (syst.) rad} \\
\Delta\Gamma_s &= 0.053 \pm 0.021 \text{ (stat.)} \pm 0.010 \text{ (syst.) ps}^{-1} \\
\Gamma_s &= 0.677 \pm 0.007 \text{ (stat.)} \pm 0.004 \text{ (syst.) ps}^{-1} \\
|A_0(0)|^2 &= 0.528 \pm 0.006 \text{ (stat.)} \pm 0.009 \text{ (syst.)} \\
|A_\parallel(0)|^2 &= 0.220 \pm 0.008 \text{ (stat.)} \pm 0.007 \text{ (syst.)}
\end{aligned}$$

where the values quoted for ϕ_s and $\Delta\Gamma_s$ correspond to the solution compatible with the external measurements to which the strong phase $\delta_\perp$ is constrained and where $\Delta\Gamma_s$ is constrained to be positive. The fraction of S-wave KK or f_0 contamination through the decays $B_s^0 \to J/\psi K^+K^-(f_0)$ is measured as well and is found to be consistent with zero. Results for ϕ_s and $\Delta\Gamma_s$ are also presented as 68%, 90% and 95% likelihood contours, which show agreement with Standard Model expectations.

Keywords: Hadron-Hadron Scattering

doi:10.1007/JHEP12(2012)072

JHEP12(2012)072

Contents

JHEP12(2012)072

1 Introduction

New phenomena beyond the predictions of the Standard Model (SM) may alter CP violation in B-decays. A channel that is expected to be sensitive to new physics contributions is the decay $B_s^0 \to J/\psi\phi$. CP violation in the $B_s^0 \to J/\psi\phi$ decay occurs due to interference between direct decays and decays occurring through $B_s^0 - \overline{B_s^0}$ mixing. The oscillation frequency of B_s^0 meson mixing is characterized by the mass difference Δm_s of the heavy (B_H) and light (B_L) mass eigenstates. The CP-violating phase ϕ_s is defined as the weak phase difference between the $B_s^0 - \overline{B_s^0}$ mixing amplitude and the $b \to c\bar{c}s$ decay amplitude. In the absence of CP violation, the B_H state would correspond exactly to the CP-odd state and the B_L to the CP-even state. In the SM the phase ϕ_s is small and can be related to CKM quark mixing matrix elements via the relation $\phi_s \simeq -2\beta_s$, with $\beta_s = \arg[-(V_{ts}V_{tb}^*)/(V_{cs}V_{cb}^*)]$; a value of $\phi_s \simeq -2\beta_s = -0.0368 \pm 0.0018$ rad [1] is predicted in the SM. Many new physics models predict large ϕ_s values whilst satisfying all existing constraints, including the precisely measured value of Δm_s [2, 3].

Another physical quantity involved in $B_s^0 - \overline{B_s^0}$ mixing is the width difference $\Delta\Gamma_s = \Gamma_L - \Gamma_H$ of B_L and B_H. Physics beyond the SM is not expected to affect $\Delta\Gamma_s$ as significantly as ϕ_s [4]. Extracting $\Delta\Gamma_s$ from data is nevertheless useful as it allows theoretical predictions to be tested [4].

The decay of the pseudoscalar B_s^0 to the vector-vector final-state $J/\psi\phi$ results in an admixture of CP-odd and CP-even states, with orbital angular momentum $L = 0$, 1 or 2. The final states with orbital angular momentum $L = 0$ or 2 are CP-even while the state with $L = 1$ is CP-odd. No flavour tagging to distinguish between the initial B_s^0 and $\overline{B_s^0}$ states is used in this analysis; the CP states are separated statistically through the time-dependence of the decay and angular correlations amongst the final-state particles.

In this paper, measurements of ϕ_s, the average decay width $\Gamma_s = (\Gamma_L + \Gamma_H)/2$ and the value of $\Delta\Gamma_s$, using the fully reconstructed decay $B_s^0 \to J/\psi(\mu^+\mu^-)\phi(K^+K^-)$ are presented. Previous measurements of these quantities have been reported by the CDF and DØ collaborations [6, 5] and recently by the LHCb collaboration [7]. The analysis presented here uses data collected by the ATLAS detector from LHC pp collisions running at $\sqrt{s} = 7$ TeV in 2011, corresponding to an integrated luminosity of approximately 4.9 fb^{-1}.

2 ATLAS detector and Monte Carlo simulation

The ATLAS experiment [8] is a multipurpose particle physics detector with a forward-backward symmetric cylindrical geometry and near 4π coverage in solid angle. The inner tracking detector (ID) consists of a silicon pixel detector, a silicon microstrip detector and a transition radiation tracker. The ID is surrounded by a thin superconducting solenoid providing a 2 T axial magnetic field, and by high-granularity liquid-argon (LAr) sampling electromagnetic calorimeter. An iron/scintillator tile calorimeter provides hadronic coverage in the central rapidity range. The end-cap and forward regions are instrumented with LAr calorimeters for both electromagnetic and hadronic measurements. The muon spectrometer (MS) surrounds the calorimeters and consists of three large superconducting toroids with eight coils each, a system of tracking chambers, and detectors for triggering.

The muon and tracking systems are of particular importance in the reconstruction of B meson candidates. Only data where both systems were operating correctly and where the LHC beams were declared to be stable are used. The data were collected during a period of rising instantaneous luminosity at the LHC, and the trigger conditions varied over this time.

The triggers used to select events for this analysis are based on identification of a $J/\psi \to \mu^+\mu^-$ decay, with either a 4 GeV transverse momentum[1] (p_{T}) threshold for each muon or an asymmetric configuration that applies a higher p_{T} threshold ($4 - 10$ GeV) to one of the muons and a looser muon-identification requirement (p_{T} threshold below 4 GeV) to the second one.

Monte Carlo (MC) simulation is used to study the detector response, estimate backgrounds and model systematic effects. For this study, 12 million MC-simulated $B_s^0 \to J/\psi\phi$

[1]The ATLAS coordinate system and the definition of transverse momentum are described in reference [8].

JHEP12(2012)072

events were generated using PYTHIA [9] tuned with recent ATLAS data [10]. No p_{T} cuts were applied at the generator level. Detector responses for these events were simulated using an ATLAS simulation package based on GEANT4 [11, 12]. In order to take into account the varying trigger configurations during data-taking, the MC events were weighted to have the same trigger composition as the collected collision data. Additional samples of the background decay $B^0 \to J/\psi K^{0*}$ as well as the more general $bb \to J/\psi X$ and $pp \to J/\psi X$ backgrounds were also simulated using PYTHIA.

3 Reconstruction and candidate selection

Events passing the trigger and the data quality selections described in section 2 are required to pass the following additional criteria: the event must contain at least one reconstructed primary vertex built from at least four ID tracks in order to be considered in the subsequent analysis; the event must contain at least one pair of oppositely charged muon candidates that are reconstructed using two algorithms that combine the information from the MS and the ID [13]. In this analysis the muon track parameters are taken from the ID measurement alone, since the precision of the measured track parameters for muons in the p_{T} range of interest for this analysis is dominated by the ID track reconstruction. The pairs of muon tracks are refitted to a common vertex and accepted for further consideration if the fit results in $\chi^2/\text{d.o.f.} < 10$. The invariant mass of the muon pair is calculated from the refitted track parameters. To account for varying mass resolution, the J/ψ candidates are divided into three subsets according to the pseudorapidity η of the muons. A maximum likelihood fit is used to extract the J/ψ mass and the corresponding resolution for these three subsets. When both muons have $|\eta| < 1.05$, the di-muon invariant mass must fall in the range $(2.959 - 3.229)$ GeV to be accepted as a J/ψ candidate. When one muon has $1.05 < |\eta| < 2.5$ and the other muon $|\eta| < 1.05$, the corresponding signal region is $(2.913 - 3.273)$ GeV. For the third subset, where both muons have $1.05 < |\eta| < 2.5$, the signal region is $(2.852 - 3.332)$ GeV. In each case the signal region is defined so as to retain 99.8% of the J/ψ candidates identified in the fits.

The candidates for $\phi \to K^+K^-$ are reconstructed from all pairs of oppositely charged tracks with $p_{\mathrm{T}} > 0.5$ GeV and $|\eta| < 2.5$ that are not identified as muons. Candidates for $B_s^0 \to J/\psi(\mu^+\mu^-)\phi(K^+K^-)$ are sought by fitting the tracks for each combination of $J/\psi \to \mu^+\mu^-$ and $\phi \to K^+K^-$ to a common vertex. All four tracks are required to have at least one hit in the pixel detector and at least four hits in the silicon strip detector. The fit is further constrained by fixing the invariant mass calculated from the two muon tracks to the world average J/ψ mass [14]. These quadruplets of tracks are accepted for further analysis if the vertex fit has a $\chi^2/\text{d.o.f.} < 3$, the fitted p_{T} of each track from $\phi \to K^+K^-$ is greater than 1 GeV and the invariant mass of the track pairs (under the assumption that they are kaons) falls within the interval $1.0085\ \text{GeV} < m(K^+K^-) < 1.0305\ \text{GeV}$. In total 131k B_s^0 candidates are collected within a mass range of $5.15 < m(B_s^0) < 5.65$ GeV used in the fit.

JHEP12(2012)072

For each B_s^0 meson candidate the proper decay time t is determined by the expression:

$$t = \frac{L_{xy}\ M_B}{c\ p_{\mathrm{T}_B}},$$

where p_{T_B} is the reconstructed transverse momentum of the B_s^0 meson candidate and M_B denotes the world average mass value [14] of the B_s^0 meson (5.3663 GeV). The transverse decay length L_{xy} is the displacement in the transverse plane of the B_s^0 meson decay vertex with respect to the primary vertex, projected onto the direction of B_s^0 transverse momentum. The position of the primary vertex used to calculate this quantity is refitted following the removal of the tracks used to reconstruct the B_s^0 meson candidate.

For the selected events the average number of pileup interactions is 5.6, necessitating a choice of the best candidate for the primary vertex at which the B_s^0 meson is produced. The variable used is a three-dimensional impact parameter d_0, which is calculated as the distance between the line extrapolated from the reconstructed B_s^0 meson vertex in the direction of the B_s^0 momentum, and each primary vertex candidate. The chosen primary vertex is the one with the smallest d_0. Using MC simulation it is shown that the fraction of B_s^0 candidates which are assigned the wrong primary vertex is less than 1% and that the corresponding effect on the final results is negligible. No B_s^0 meson lifetime cut is applied in the analysis.

4 Maximum likelihood fit

An unbinned maximum likelihood fit is performed on the selected events to extract the parameters of the $B_s^0 \to J/\psi(\mu^+\mu^-)\phi(K^+K^-)$ decay. The fit uses information about the reconstructed mass m, the measured proper decay time t, the measured mass and proper decay time uncertainties σ_m and σ_t, and the transversity angles Ω of each $B_s^0 \to J/\psi\phi$ decay candidate. There are three transversity angles; $\Omega = (\theta_T, \psi_T, \varphi_T)$ and these are defined in section 4.1.

The likelihood function is defined as a combination of the signal and background probability density functions as follows:

$$\begin{aligned}\ln\ \mathcal{L} = \sum_{i=1}^{N} \Big\{ & w_i \cdot \ln\big(f_{\mathrm{s}} \cdot \mathcal{F}_{\mathrm{s}}(m_i, t_i, \Omega_i) + f_{\mathrm{s}} \cdot f_{B^0} \cdot \mathcal{F}_{B^0}(m_i, t_i, \Omega_i) \\ & + (1 - f_{\mathrm{s}} \cdot (1 + f_{B^0}))\mathcal{F}_{\mathrm{bkg}}(m_i, t_i, \Omega_i)\big) \Big\} + \ln P(\delta_\perp) \end{aligned} \tag{4.1}$$

where N is the number of selected candidates, w_i is a weighting factor to account for the trigger efficiency (described in section 4.5), f_{s} is the fraction of signal candidates, f_{B^0} is the fraction of peaking B^0 meson background events (described in section 4.2) calculated relative to the number of signal events; this parameter is fixed in the likelihood fit. The mass m_i, the proper decay time t_i and the decay angles Ω_i are the values measured from the data for each event i. $\mathcal{F}_{\mathrm{s}}$, $\mathcal{F}_{B^0}$ and $\mathcal{F}_{\mathrm{bkg}}$ are the probability density functions (PDF) modelling the signal, the specific B^0 background and the other background distributions, respectively. $P(\delta_\perp)$ is a constraint on the strong phase $\delta_\perp$. A detailed description of the PDF functions and other terms in the equation (4.1) is given in sections 4.1–4.5.

JHEP12(2012)072

4.1 Signal PDF

The PDF describing the signal events, $\mathcal{F}_{\rm s}$, has the form of a product of PDFs for each quantity measured from the data:

$$\mathcal{F}_{\rm s}(m_i, t_i, \Omega_i) = P_{\rm s}(m_i|\sigma_{m_i}) \cdot P_{\rm s}(\sigma_{m_i}) \cdot P_{\rm s}(\Omega_i, t_i|\sigma_{t_i}) \cdot P_{\rm s}(\sigma_{t_i}) \cdot A(\Omega_i, p_{{\rm T}i}) \cdot P_{\rm s}(p_{{\rm T}i}) \quad (4.2)$$

The terms $P_{\rm s}(m_i|\sigma_{m_i})$, $P_{\rm s}(\Omega_i, t_i|\sigma_{t_i})$ and $A(\Omega_i, p_{{\rm T}i})$ are explained in the current section, and the remaining per-candidate uncertainty terms $P_{\rm s}(\sigma_{m_i})$, $P_{\rm s}(\sigma_{t_i})$ and $P_{\rm s}(p_{{\rm T}i})$ are described in section 4.4. Ignoring detector effects, the joint distribution for the decay time t and the transversity angles Ω for the $B_s^0 \to J/\psi(\mu^+\mu^-)\phi(K^+K^-)$ decay is given by the differential decay rate [15]:

$$\frac{d^4\Gamma}{dt\, d\Omega} = \sum_{k=1}^{10} \mathcal{O}^{(k)}(t) g^{(k)}(\theta_T, \psi_T, \varphi_T), \quad (4.3)$$

where $\mathcal{O}^{(k)}(t)$ are the time-dependent amplitudes and $g^{(k)}(\theta_T, \psi_T, \varphi_T)$ are the angular functions, given in table 1. The time-dependent amplitudes are slightly different for decays of mesons that were initially $\overline{B_s^0}$. As an untagged analysis is performed here, all B_s^0 meson candidates are assumed to have had an equal chance of initially being either a particle or anti-particle. This leads to a significant simplification of the time-dependent amplitudes as any terms involving the mass splitting Δm_s cancel out. These simplified time-dependent amplitudes are given in table 1. $A_\perp(t)$ describes a CP-odd final-state configuration while both $A_0(t)$ and $A_\parallel(t)$ correspond to CP-even final-state configurations. A_S describes the contribution of CP-odd $B_s \to J/\psi K^+K^-(f_0)$, where the non-resonant KK or f_0 meson is an S-wave state. The corresponding amplitudes are given in the last four lines of table 1 (k=7-10) and follow the convention used in previous analysis [7]. The likelihood is independent of the invariant KK mass distribution.

The equations are normalised such that the squares of the amplitudes sum to unity; three of the four amplitudes are fit parameters and $|A_\perp(0)|^2$ is determined according to this constraint.

The angles $(\theta_T, \psi_T, \varphi_T)$, are defined in the rest frames of the final-state particles. The x-axis is determined by the direction of the ϕ meson in the J/ψ rest frame, the K^+K^- system defines the xy plane, where $p_y(K^+) > 0$. The three angles are defined:

- θ, the angle between $p(\mu^+)$ and the xy plane, in the J/ψ meson rest frame
- φ, the angle between the x-axis and $p_{xy}(\mu^+)$, the projection of the μ^+ momentum in the xy plane, in the J/ψ meson rest frame
- ψ, the angle between $p(K^+)$ and $-p(J/\psi)$ in the ϕ meson rest frame

It can be seen from table 1, that in the untagged analysis used in this study the time-dependent amplitudes depending on $\delta_\perp$ ($\mathcal{O}^{(k)}(t), k = 5, 6$) are multiplied by $\sin\phi_s$. Previous measurement by LHCb ref. [7] showed that ϕ_s is close to zero $(0.15 \pm 0.18 \pm 0.06)$ rad. For such a small value of ϕ_s the untagged analysis is not sensitive to $\delta_\perp$. A Gaussian constraint

JHEP12(2012)072

k	$\mathcal{O}^{(k)}(t)$	$g^{(k)}(\theta_T, \psi_T, \varphi_T)$
1	$\frac{1}{2}\lvert A_0(0)\rvert^2 \left[(1+\cos\phi_s)\, e^{-\Gamma_{\rm L}^{(s)}t} + (1-\cos\phi_s)\, e^{-\Gamma_{\rm H}^{(s)}t}\right]$	$2\cos^2\psi_T(1-\sin^2\theta_T\cos^2\varphi_T)$
2	$\frac{1}{2}\lvert A_\parallel(0)\rvert^2 \left[(1+\cos\phi_s)\, e^{-\Gamma_{\rm L}^{(s)}t} + (1-\cos\phi_s)\, e^{-\Gamma_{\rm H}^{(s)}t}\right]$	$\sin^2\psi_T(1-\sin^2\theta_T\sin^2\varphi_T)$
3	$\frac{1}{2}\lvert A_\perp(0)\rvert^2 \left[(1-\cos\phi_s)\, e^{-\Gamma_{\rm L}^{(s)}t} + (1+\cos\phi_s)\, e^{-\Gamma_{\rm H}^{(s)}t}\right]$	$\sin^2\psi_T\sin^2\theta_T$
4	$\frac{1}{2}\lvert A_0(0)\rvert\lvert A_\parallel(0)\rvert\cos\delta_\parallel$ $\left[(1+\cos\phi_s)\, e^{-\Gamma_{\rm L}^{(s)}t} + (1-\cos\phi_s)\, e^{-\Gamma_{\rm H}^{(s)}t}\right]$	$\frac{1}{\sqrt{2}}\sin 2\psi_T\sin^2\theta_T\sin 2\varphi_T$
5	$\frac{1}{2}\lvert A_\parallel(0)\rvert\lvert A_\perp(0)\rvert \left(e^{-\Gamma_{\rm H}^{(s)}t} - e^{-\Gamma_{\rm L}^{(s)}t}\right)\cos(\delta_\perp-\delta_\parallel)\sin\phi_s$	$\sin^2\psi_T\sin 2\theta_T\sin\varphi_T$
6	$-\frac{1}{2}\lvert A_0(0)\rvert\lvert A_\perp(0)\rvert \left(e^{-\Gamma_{\rm H}^{(s)}t} - e^{-\Gamma_{\rm L}^{(s)}t}\right)\cos\delta_\perp\sin\phi_s$	$\frac{1}{\sqrt{2}}\sin 2\psi_T\sin 2\theta_T\cos\varphi_T$
7	$\frac{1}{2}\lvert A_S(0)\rvert^2 \left[(1-\cos\phi_s)\, e^{-\Gamma_{\rm L}^{(s)}t} + (1+\cos\phi_s)\, e^{-\Gamma_{\rm H}^{(s)}t}\right]$	$\frac{2}{3}\left(1-\sin^2\theta_T\cos^2\varphi_T\right)$
8	$-\frac{1}{2}\lvert A_S(0)\rvert\lvert A_\parallel(0)\rvert \left(e^{-\Gamma_{\rm H}^{(s)}t} - e^{-\Gamma_{\rm L}^{(s)}t}\right)\sin(\delta_\parallel-\delta_S)\sin\phi_s$	$\frac{1}{3}\sqrt{6}\sin\psi_T\sin^2\theta_T\sin 2\varphi_T$
9	$\frac{1}{2}\lvert A_S(0)\rvert\lvert A_\perp(0)\rvert$ $\left[(1-\cos\phi_s)\, e^{-\Gamma_{\rm L}^{(s)}t} + (1+\cos\phi_s)\, e^{-\Gamma_{\rm H}^{(s)}t}\right]\sin(\delta_\perp-\delta_S)$	$\frac{1}{3}\sqrt{6}\sin\psi_T\sin 2\theta_T\cos\varphi_T$
10	$-\frac{1}{2}\lvert A_0(0)\rvert\lvert A_S(0)\rvert\sin(-\delta_S) \left(e^{-\Gamma_{\rm H}^{(s)}t} - e^{-\Gamma_{\rm L}^{(s)}t}\right)\sin\phi_s$	$\frac{4}{3}\sqrt{3}\cos\psi_T\left(1-\sin^2\theta_T\cos^2\varphi_T\right)$

Table 1. Table showing the ten time-dependent amplitudes, $\mathcal{O}^{(k)}(t)$ and the functions of the transversity angles $g^{(k)}(\theta_T, \psi_T, \varphi_T)$. The amplitudes $|A_0(0)|^2$ and $|A_\parallel(0)|^2$ are for the CP-even components of the $B_s^0 \to J/\psi\phi$ decay. $|A(0)_\perp|^2$ is the CP-odd amplitude. They have corresponding strong phases δ_0, $\delta_\parallel$ and $\delta_\perp$; by convention δ_0 is set to be zero. The S-wave amplitude $|A_S(0)|^2$ gives the fraction of $B_s^0 \to J/\psi K^+K^-(f_0)$ and has a related strong phase δ_S.

to the best measured value, $\delta_\perp = (2.95 \pm 0.39)$ rad [7], is therefore applied by adding a Gaussian function term $P(\delta_\perp)$ into the likelihood fit.

The signal PDF, $P_{\rm s}(\Omega_i, t_i|\sigma_{t_i})$ must take into account the time resolution and thus each time-dependent element in table 1 is convoluted with a Gaussian function. This convolution is performed numerically on an event-by-event basis where the width of the Gaussian is the proper decay time uncertainty σ_{t_i}, multiplied by an overall scale factor to account for any mis-measurements.

The angular sculpting of the detector and kinematic cuts on the angular distributions is included in the likelihood function through $A(\Omega_i, p_{{\rm T}i})$. This is calculated using a four-dimensional binned acceptance method, applying an event-by-event efficiency according to the transversity angles $(\theta_T, \psi_T, \varphi_T)$ and the $p_{\rm T}$ of the B_s^0. The acceptance was calculated from the $B_s^0 \to J/\psi\phi$ MC events. In the likelihood function, the acceptance is treated as an angular sculpting PDF, which is multiplied by the time- and angular-dependent PDF describing the $B_s^0 \to J/\psi(\mu^+\mu^-)\phi(K^+K^-)$ decays. Consequently, the complete angular function must be normalised as a whole as both the acceptance and the time-angular decay PDFs depend on the transversity angles. This normalisation is performed numerically in the likelihood fit.

JHEP12(2012)072

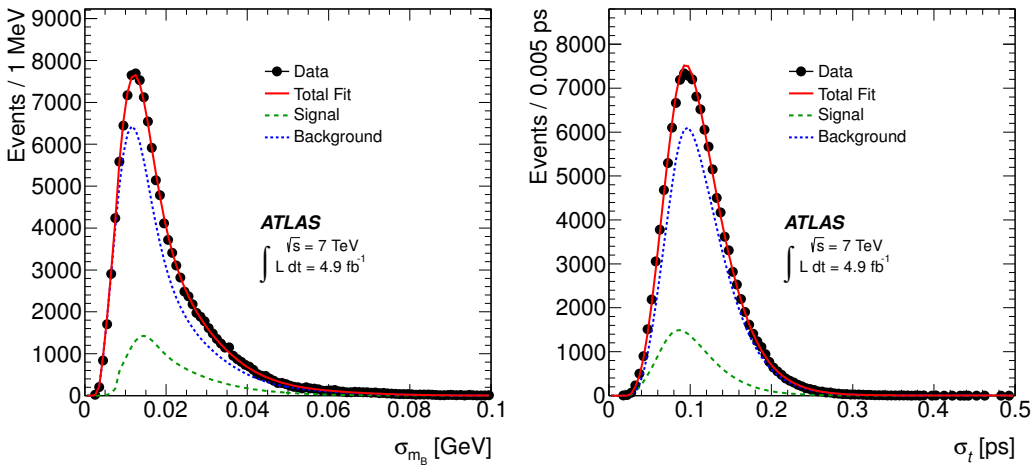

Figure 1. Left: mass uncertainty distribution for data, the fits to the background and the signal fractions and the sum of the two fits. Right: proper decay time uncertainty distribution for data, the fits to the background and the signal fractions and the sum of the two fits.

The signal mass PDF, $P_{\rm s}(m_i)$, is modelled as a single Gaussian function smeared with an event-by-event mass resolution σ_{m_i}, see figure 1, which is scaled using a factor to account for mis-estimation of the mass errors. The PDF is normalised over the range $5.15 < m(B_s^0) < 5.65$ GeV.

4.2 Specific B^0 background

The $B_s^0 \to J/\psi(\mu^+\mu^-)\phi(K^+K^-)$ sample is contaminated with mis-reconstructed $B^0 \to J/\psi K^*$ and $B^0 \to J/\psi K^+\pi^-$ (non-resonant) decays, where the final-state pion is mis-identified as a kaon. The two components of the background are referred to as B^0 reflections, since the B^0 is reconstructed as a B_s^0 meson and therefore lies within the B_s^0 meson mass window rather than in the usual B^0 mass range. The fractions of these components are fixed in the likelihood fit to values $(6.5\pm2.4)\%$ and $(4.5\pm2.8)\%$ respectively. These values are calculated from the relative production fractions of the B_s^0 and B^0 mesons and their decay probabilities taken from the PDG values [14] and from their selection efficiencies, which are determined from MC events. The corresponding uncertainties are dominated by uncertainties in the decay probabilities.

Mis-reconstructed B^0 decays are treated as part of the background and are described by a dedicated PDF:

$$\begin{aligned}\mathcal{F}_{B^0}(m_i, t_i, \Omega_i) = {} & P_{B^0}(m_i) \cdot P_{\rm s}(\sigma_{m_i}) \cdot P_{B^0}(t_i|\sigma_{t_i}) \\ & \cdot P_{B^0}(\theta_T) \cdot P_{B^0}(\varphi_T) \cdot P_{B^0}(\psi_T) \cdot P_{\rm s}(\sigma_{t_i}) \cdot P_{\rm s}(p_{{\rm T}i})\end{aligned} \tag{4.4}$$

The mass is described by the $P_{B^0}(m_i)$ term in the form of a Landau function due to the distortion caused by the incorrect mass assignment. The decay time is described in the term $P_{B^0}(t_i|\sigma_{t_i})$ by an exponential smeared with event-by-event Gaussian errors. The

JHEP12(2012)072

transversity angles are described using the same functions as the other backgrounds but with different values for the parameters obtained from the fit to MC data. The terms $P_{\rm s}(\sigma_{m_i})$, $P_{\rm s}(\sigma_{t_i})$ and $P_{\rm s}(p_{{\rm T}i})$ are described in section 4.4. All the PDFs describing these B^0 reflections have fixed shapes determined from the MC studies.

4.3 Background PDF

The background PDF has the following composition:

$$\begin{aligned}\mathcal{F}_{\rm bkg}(m_i, t_i, \Omega_i) = & P_{\rm b}(m_i) \cdot P_{\rm b}(\sigma_{m_i}) \cdot P_{\rm b}(t_i|\sigma_{t_i}) \\ & \cdot P_{\rm b}(\theta_T) \cdot P_{\rm b}(\varphi_T) \cdot P_{\rm b}(\psi_T) \cdot P_{\rm b}(\sigma_{t_i}) \cdot P_{\rm b}(p_{{\rm T}i})\end{aligned} \tag{4.5}$$

The proper decay time function $P_{\rm b}(t_i|\sigma_{t_i})$ is parameterised as a prompt peak modelled by a Gaussian distribution, two positive exponentials and a negative exponential. This function is smeared with the same resolution function as the signal decay time-dependence. The prompt peak models the combinatorial background events, which are expected to have reconstructed lifetime distributed around zero. The two positive exponentials represent a fraction of longer-lived backgrounds with non-prompt J/ψ, combined with hadrons from the primary vertex or from a B/D hadron in the same event. The negative exponential takes into account events with poor vertex resolution.

The shape of the background angular distributions, $P_{\rm b}(\theta_T)$, $P_{\rm b}(\varphi_T)$, and $P_{\rm b}(\psi_T)$ arise primarily from detector and kinematic sculpting. These are described by the following empirically determined functions:

$$\begin{aligned} f(\cos\theta_T) &= \frac{a_0 - a_1\cos^2(\theta_T) + a_2\cos^4(\theta_T)}{2a_0 - 2a_1/3 + 2a_2/5} \\ f(\varphi_T) &= \frac{1 + b_1\cos(2\varphi_T + b_0)}{2\pi} \\ f(\cos\psi_T) &= \frac{c_0 + c_1\cos^2(\psi_T)}{2c_0 + 2c_1/3} \end{aligned}$$

They are initially fitted to data from the B^0_s mass sidebands only, to find reasonable starting values for $a_{0,1,2}$, $b_{0,1}$ and $c_{0,1}$, then allowed to float freely in the full likelihood fit. The B^0_s mass sidebands, $(5.150 - 5.317)$ GeV and $(5.417 - 5.650)$ GeV, are defined to retain 0.02% of signal events identified in the fit. The correlations between the background angular shapes are neglected, but a systematic error arising from this simplification is evaluated in section 5. The background mass model, $P_{\rm b}(m)$ is a linear function.

4.4 Time and mass uncertainties of signal and background

The event-by-event proper decay time and mass uncertainty distributions differ significantly for signal and background, as shown in figure 1. The background PDFs cannot be factorized and it is necessary to include extra PDF terms describing the error distributions in the likelihood function to avoid significant biases [16].

The signal and background time and mass error distributions are described with Gamma functions:

$$P_{\rm s,b}(\sigma_{t(m)_i}) = \frac{(\sigma_{t(m)_i} - c)^{a_{\rm s,b}} e^{-(\sigma_{t(m)_i} - c)/b_{\rm s,b}}}{b_{\rm s,b}^{a_{\rm s,b}+1}\Gamma(a_{\rm s,b}+1)} \tag{4.6}$$

JHEP12(2012)072

where $a_{\rm s,b}$ and $b_{\rm s,b}$ are constants fitted from (b) sideband and (s) sideband-subtracted signal and fixed in the likelihood fit. Since $P_{\rm s,b}(\sigma_{t(m)_i})$ depend on transverse momentum of the B_s^0 meson, they were determined in six selected $p_{\rm T}$ bins, the choice of which is reflecting the natural $p_{\rm T}$ dependence of the detector resolution.

The same treatment is used for B_s^0 $p_{\rm T}$ signal and background, by introducing additional terms $P_{\rm s}(p_{{\rm T}i})$ and $P_{\rm b}(p_{{\rm T}i})$ into the PDF. These are described using the same functions as $P_{\rm s,b}(\sigma_{t(m)_i})$ but with different values for the parameters obtained from the fit to sideband and sideband-subtracted signal $p_{\rm T}$ distributions.

4.5 Muon trigger time-dependent efficiency

It has been observed that the muon trigger biases the transverse impact parameter of muons toward smaller values. The trigger selection efficiency was measured in data and MC simulation using a tag-and-probe method [17]. To account for this efficiency in the fit, the events are re-weighted by a factor w:

$$w = e^{-|t|/(\tau_{\rm sing}+\epsilon)}/e^{-|t|/\tau_{\rm sing}} \tag{4.7}$$

where the $\tau_{\rm sing}$ is a single B_s^0 lifetime measured before the correction, using unbinned mass-lifetime maximum likelihood fit. The weight form and the factor $\epsilon = 0.013 \pm 0.004$ ps are determined using MC events by comparing the B_s^0 lifetime distribution of an unbiased sample with the lifetime distribution obtained after including the dependence of the trigger efficiency on the muon transverse impact parameter as measured from the data. The value of ϵ is determined as the difference of exponential fits to the two distributions. The uncertainty 0.004 ps, which reflects the precision of the tag-and-probe method, is used to assign a systematic error due to this time efficiency correction.

5 Systematic uncertainties

Systematic uncertainties are assigned by considering several effects that are not accounted for in the likelihood fit. These are described below.

- **Inner Detector Alignment:** residual misalignments of the ID affect the impact parameter distribution with respect to the primary vertex. The effect of this residual misalignment on the measurement is estimated using events simulated with perfect and distorted ID geometries. The distorted geometry is produced by moving detector components to match the observed small shifts in data. The observable of interest is the impact parameter distribution with respect to the primary vertex as a function of η and ϕ. The mean value of this impact parameter distribution for a perfectly aligned detector is expected to be zero and in data a maximum deviation of less than 10 μm is observed. The difference between the measurement using simulated events reconstructed with a perfect geometry compared to the distorted geometry is used to assess the systematic uncertainty.

JHEP12(2012)072

- **Angular acceptance method:** the angular acceptance is calculated from a binned fit to MC data. In the kinematical region used in this analysis, the angular acceptance varies with the transversity angles by about ±10%. The statistical error in the acceptance is smaller than 1% in any bin, and data driven analyses show that systematic uncertainties in modelling detector and reconstruction are also at the level of 1% [18, 19]. Possible dependences of the results on the choice of the binning are tested by varying bin widths and central values. Taking all these arguments into consideration, the systematic uncertainties due to detector acceptance are found to be negligible.

- **Trigger efficiency:** to correct for the trigger lifetime bias the events are re-weighted according to equation (4.7). The uncertainty in the parameter ϵ is used to estimate the systematic uncertainty due to the time efficiency correction.

- **Fit model:** pseudo-experiments are used to estimate systematic uncertainties. In a first test, the results of 1000 pseudo-experiments are compared to the generated values, and the average of the differences are taken as systematic uncertainties. Additional sets of 1000 pseudo-experiments are generated with variations in the signal and background mass model, resolution model, background lifetime and background angles models, as discussed below. These sets are analysed with the default model, and average deviations in the results of the fit are taken as additional systematic errors. The following variations are considered:

  - The signal mass distribution is generated using a sum of two Gaussian functions. Their relative fractions and widths are determined from a likelihood fit to data. In the PDF for this fit, the mass of each event is modelled by two different Gaussians with widths equal to products of the scale factors multiplied by a per-candidate mass error.
  - The background mass is generated from an exponential function. The default fit uses a linear model for the mass of background events.
  - Two different scale factors instead of one are used to generate the lifetime uncertainty.
  - The values used for the background lifetime are generated by sampling data from the mass sidebands. The default fit uses a set of functions to describe the background lifetime.
  - Pseudo-experiments are performed using two methods of generating the background angles. The default method uses a set of functions describing the background angles of data without taking correlations between the angles into account. In the alternative fit the background angles are generated using a three dimensional histogram of the sideband-data angles.

- **B^0 contribution:** contamination from $B^0 \to J/\psi K^{*0}$ and $B^0 \to J/\psi K\pi$ events misreconstructed as $B_s^0 \to J/\psi\phi$ are accounted for in the default fit; the fractions of these

JHEP12(2012)072

contributions are fixed to values estimated from selection efficiencies in MC simulation and decay probabilities from ref. [14]. To estimate the systematic uncertainty arising from the precision of the fraction estimates, the data are fitted with these fractions increased and decreased by 1σ. The largest shift in the fitted values from the default case is taken as the systematic uncertainty for each parameter of interest.

The systematic uncertainties are summarised in table 4. In general, pseudo-experiments generated with the default model produce pull-distributions that show a negligible bias, and confirm that the uncertainties are correctly estimated by the fit. The largest average deviation in a residual divided by its fit uncertainty (or pull) is 0.32; the second largest is 0.26, while the remainder where much smaller. These two largest deviations were added in quadrature to those obtained by varying the model assumptions, resulting for each variable in a total systematic uncertainty shown in table 4.

6 Results

The full maximum likelihood fit contains 26 free parameters. This includes the eight physics parameters: $\Delta\Gamma_s$, ϕ_s, Γ_s, $|A_0(0)|^2$, $|A_\parallel(0)|^2$, $\delta_\parallel$, $|A_S(0)|^2$ and δ_S, and strong phase $\delta_\perp$ constrained by external data. The other free parameters in the likelihood function are the B_s^0 signal fraction f_s, the parameters describing the $J/\psi\phi$ mass distribution, the parameters describing the decay time and the angular distributions of the background, the parameters used to describe the estimated decay time uncertainty distributions for signal and background events, and the scale factors between the estimated decay-time and mass uncertainties and their true uncertainties, see equation (4.6).

As discussed in section 4.1, the strong phase $\delta_\perp$ is constrained to the value measured in ref. [7], as the fit in the absence of flavour tagging is not sufficiently sensitive to this value. The second strong phase, $\delta_\parallel$, is fitted very close to its symmetry point at π. Pull studies, based on pseudo-experiments using input values determined from the fit to data, return a non-Gaussian pull distribution for this parameter. For this reason the result for the strong phase $\delta_\parallel$ is given in the form of a 1σ confidence interval $[3.04, 3.24]$ rad. The strong phase of the S-wave component is fitted relative to $\delta_\perp$, as $\delta_\perp - \delta_S = (0.03 \pm 0.13)$ rad.

The number of signal B_s^0 meson candidates extracted from the fit is 22690 ± 160. The results and correlations for the measured physics parameters of the unbinned maximum likelihood fit are given in tables 2 and 3. Fit projections of the mass, proper decay time and angles are given in figures 2, 3 and 4 respectively.

7 Symmetries of the likelihood function and two-dimensional likelihood contours

The PDF describing the $B_s^0 \to J/\psi\phi$ decay is invariant under the following simultaneous transformations:

$$\{\phi_s, \Delta\Gamma_s, \delta_\perp, \delta_\parallel, \delta_S\} \to \{\pi - \phi_s, -\Delta\Gamma_s, \pi - \delta_\perp, -\delta_\parallel, -\delta_S\}.$$

JHEP12(2012)072

Parameter	Value	Statistical uncertainty	Systematic uncertainty
ϕ_s(rad)	0.22	0.41	0.10
$\Delta\Gamma_s(\text{ps}^{-1})$	0.053	0.021	0.010
$\Gamma_s(\text{ps}^{-1})$	0.677	0.007	0.004
$\lvert A_0(0)\rvert^2$	0.528	0.006	0.009
$\lvert A_\parallel(0)\rvert^2$	0.220	0.008	0.007
$\lvert A_S(0)\rvert^2$	0.02	0.02	0.02

Table 2. Fitted values for the physics parameters along with their statistical and systematic uncertainties.

	ϕ_s	$\Delta\Gamma_s$	Γ_s	$\lvert A_0(0)\rvert^2$	$\lvert A_\parallel(0)\rvert^2$	$\lvert A_S(0)\rvert^2$
ϕ_s	1.00	−0.13	0.38	−0.03	−0.04	0.02
$\Delta\Gamma_s$		1.00	−0.60	0.12	0.11	0.10
Γ_s			1.00	−0.06	−0.10	0.04
$\lvert A_0(0)\rvert^2$				1.00	−0.30	0.35
$\lvert A_\parallel(0)\rvert^2$					1.00	0.09
$\lvert A_S(0)\rvert^2$						1.00

Table 3. Correlations between the physics parameters.

Systematic Uncertainty	ϕ_s(rad)	$\Delta\Gamma_s(\text{ps}^{-1})$	$\Gamma_s(\text{ps}^{-1})$	$\lvert A_\parallel(0)\rvert^2$	$\lvert A_0(0)\rvert^2$	$\lvert A_S(0)\rvert^2$
Inner Detector alignment	0.04	< 0.001	0.001	< 0.001	< 0.001	< 0.01
Trigger efficiency	< 0.01	< 0.001	0.002	< 0.001	< 0.001	< 0.01
Default fit model	< 0.001	0.006	< 0.001	< 0.001	0.001	< 0.01
Signal mass model	0.02	0.002	< 0.001	< 0.001	< 0.001	< 0.01
Background mass model	0.03	0.001	< 0.001	0.001	< 0.001	< 0.01
Resolution model	0.05	< 0.001	0.001	< 0.001	< 0.001	< 0.01
Background lifetime model	0.02	0.002	< 0.001	< 0.001	< 0.001	< 0.01
Background angles model	0.05	0.007	0.003	0.007	0.008	0.02
B^0 contribution	0.05	< 0.001	< 0.001	< 0.001	0.005	< 0.01
Total	0.10	0.010	0.004	0.007	0.009	0.02

Table 4. Summary of systematic uncertainties assigned to parameters of interest.

In the absence of initial state flavour tagging the PDF is also invariant under

$$\{\phi_s, \Delta\Gamma_s, \delta_\perp, \delta_\parallel, \delta_S\} \to \{-\phi_s, \Delta\Gamma_s, \pi - \delta_\perp, -\delta_\parallel, -\delta_S\} \tag{7.1}$$

leading to a fourfold ambiguity.

The two-dimensional likelihood contours in the $\phi_s - \Delta\Gamma_s$ plane are calculated allowing all parameters to vary within their physical ranges. As discussed in section 6, the value for the Gaussian constraint on $\delta_\perp$ is taken from the LHCb measurement [7]. That paper quotes only two solutions with a positive ϕ_s and two $\Delta\Gamma_s$ values symmetric around zero, by using initial state flavour tagging to eliminate the symmetry defined in equation (7.1).

JHEP12(2012)072

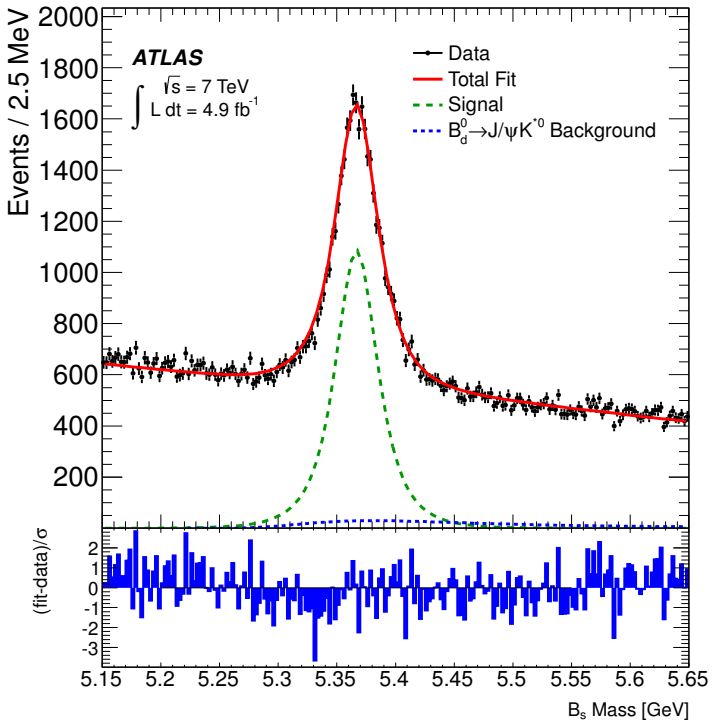

Figure 2. Mass fit projection for the B_s^0. The pull distribution at the bottom shows the difference between the data and fit value normalised to the data uncertainty.

Due to the accurate local determination of ϕ_s and $\Delta\Gamma_s$ in both this measurement and in the LHCb measurement [7], the other two solutions seen in the ATLAS analysis are not compatible with the observations of the two experiments. As such, two of the four minima fitted in the present non-flavour tagged analysis are excluded from the results presented here. Additionally a solution with negative $\Delta\Gamma_s$ is excluded following the LHCb measurement [20] which determines the $\Delta\Gamma_s$ to be positive. Therefore, the two-dimensional contour plot for ϕ_s and $\Delta\Gamma_s$ has been computed only for the solution consistent with the previous measurements. The resulting contours for the 68%, 90% and 95% confidence intervals are produced using a profile likelihood method and are shown in figure 5.

The systematic errors are not included in figure 5 but as seen from table 2 they are small compared to the statistical errors. The confidence levels are obtained using the corresponding $\Delta \ln \mathcal{L}$ intervals. Pseudo-experiments are used to study the coverage of the likelihood contours. This test suggests that the statistical uncertainty of our result is overestimated by about 5%. No correction to compensate for this overestimation is applied.

8 Conclusion

A measurement of CP violation in $B_s^0 \to J/\psi(\mu^+\mu^-)\phi(K^+K^-)$ decays from a 4.9 fb^{-1} data sample of pp collisions collected with the ATLAS detector during the 2011 $\sqrt{s} = 7$ TeV run was presented. Several parameters describing the B_s^0 meson system are measured. These

JHEP12(2012)072

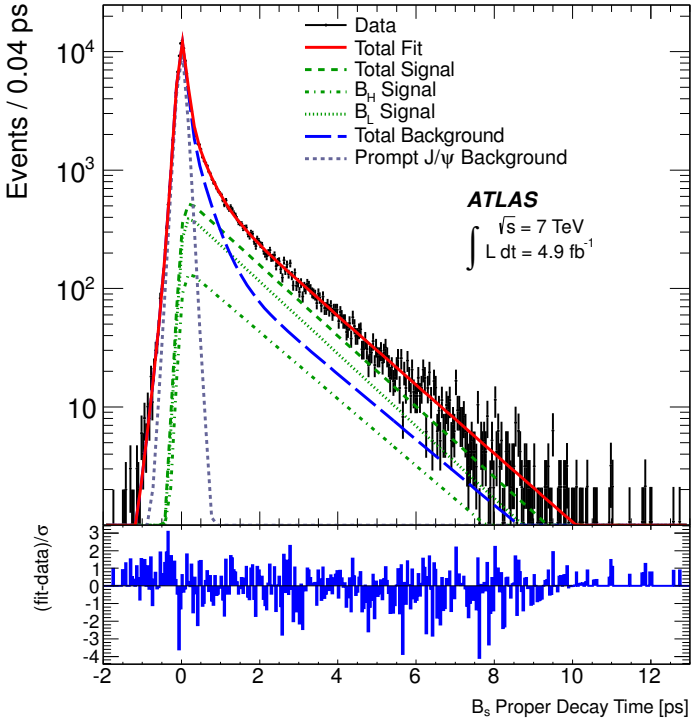

Figure 3. Proper decay time fit projection for the B_s^0. The pull distribution at the bottom shows the difference between the data and fit value normalised to the data uncertainty.

include the mean B_s^0 lifetime, the decay width difference $\Delta\Gamma_s$ between the heavy and light mass eigenstates, the transversity amplitudes $|A_0(0)|$ and $|A_\parallel(0)|$ and the CP-violating week phase ϕ_s. They are consistent with the world average values.

The measured values, for the minimum resulting from $\delta_\perp$ constrained to the LHCb value of 2.95 ± 0.39 rad [7] and $\Delta\Gamma_s$ being constrained to be positive following LHCb measurement [20], are:

$$\begin{aligned}
\phi_s &= 0.22 \pm 0.41 \text{ (stat.)} \pm 0.10 \text{ (syst.) rad} \\
\Delta\Gamma_s &= 0.053 \pm 0.021 \text{ (stat.)} \pm 0.010 \text{ (syst.) ps}^{-1} \\
\Gamma_s &= 0.677 \pm 0.007 \text{ (stat.)} \pm 0.004 \text{ (syst.) ps}^{-1} \\
|A_0(0)|^2 &= 0.528 \pm 0.006 \text{ (stat.)} \pm 0.009 \text{ (syst.)} \\
|A_\parallel(0)|^2 &= 0.220 \pm 0.008 \text{ (stat.)} \pm 0.007 \text{ (syst.)}
\end{aligned}$$

These values are consistent with theoretical expectations, in particular ϕ_s is within 1σ of the expected value in the Standard Model. A likelihood contour in the $\phi_s - \Delta\Gamma_s$ plane is also provided for the minimum compatible with the LHCb measurements [7, 20]. The fraction of S-wave KK or f_0 contamination is measured to be consistent with zero, at $|A_S(0)|^2 = 0.02 \pm 0.02$.

JHEP12(2012)072

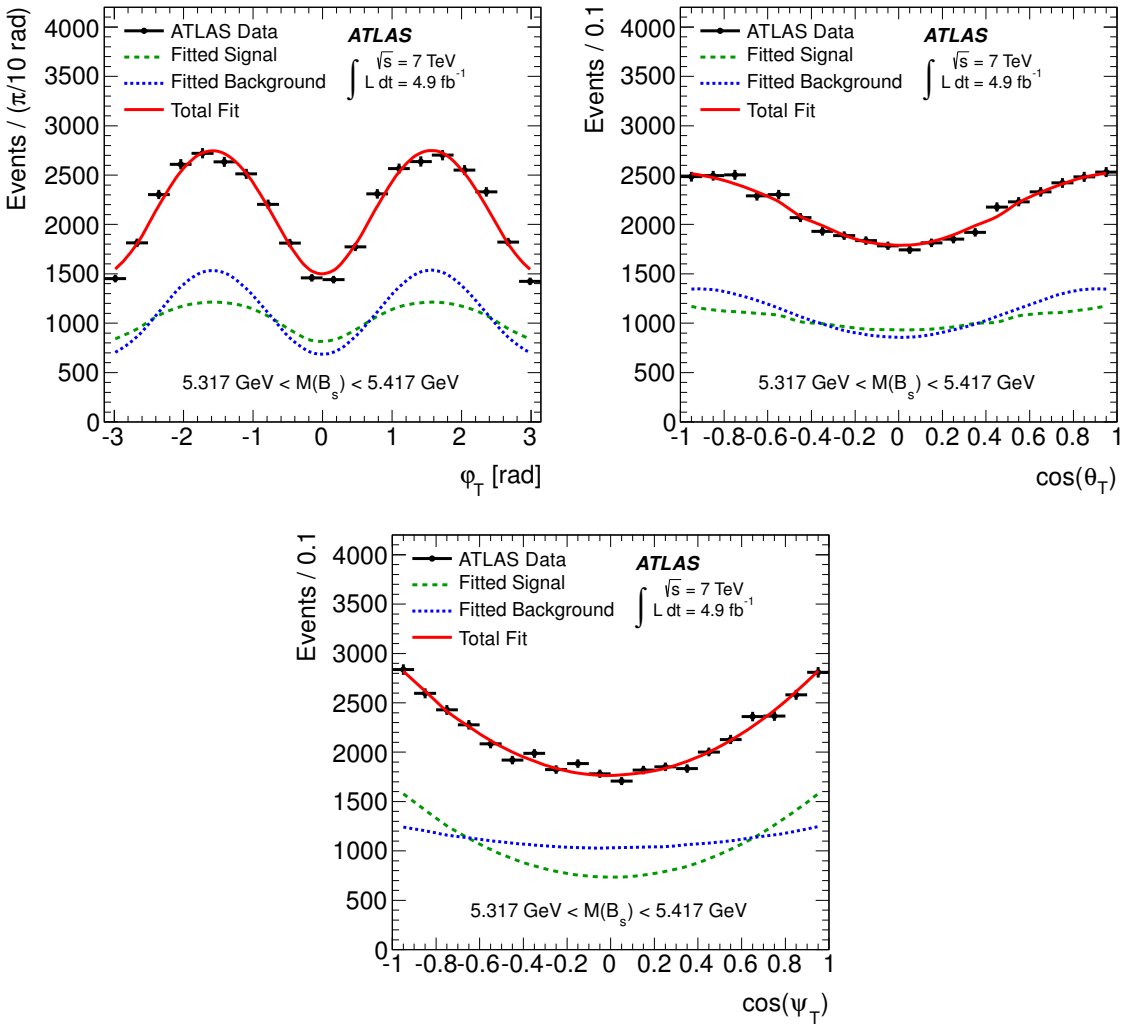

Figure 4. Fit projections for transversity angles. (Left): φ_T, (Right): $\cos\theta_T$, (Bottom): $\cos\psi_T$ for the events with B_s^0 mass from signal region (5.317–5.417) GeV.

Acknowledgments

We thank CERN for the very successful operation of the LHC, as well as the support staff from our institutions without whom ATLAS could not be operated efficiently.

We acknowledge the support of ANPCyT, Argentina; YerPhI, Armenia; ARC, Australia; BMWF, Austria; ANAS, Azerbaijan; SSTC, Belarus; CNPq and FAPESP, Brazil; NSERC, NRC and CFI, Canada; CERN; CONICYT, Chile; CAS, MOST and NSFC, China; COLCIENCIAS, Colombia; MSMT CR, MPO CR and VSC CR, Czech Republic; DNRF, DNSRC and Lundbeck Foundation, Denmark; EPLANET and ERC, European Union; IN2P3-CNRS, CEA-DSM/IRFU, France; GNAS, Georgia; BMBF, DFG, HGF, MPG and AvH Foundation, Germany; GSRT, Greece; ISF, MINERVA, GIF, DIP and Benoziyo Center, Israel; INFN, Italy; MEXT and JSPS, Japan; CNRST, Morocco; FOM

JHEP12(2012)072

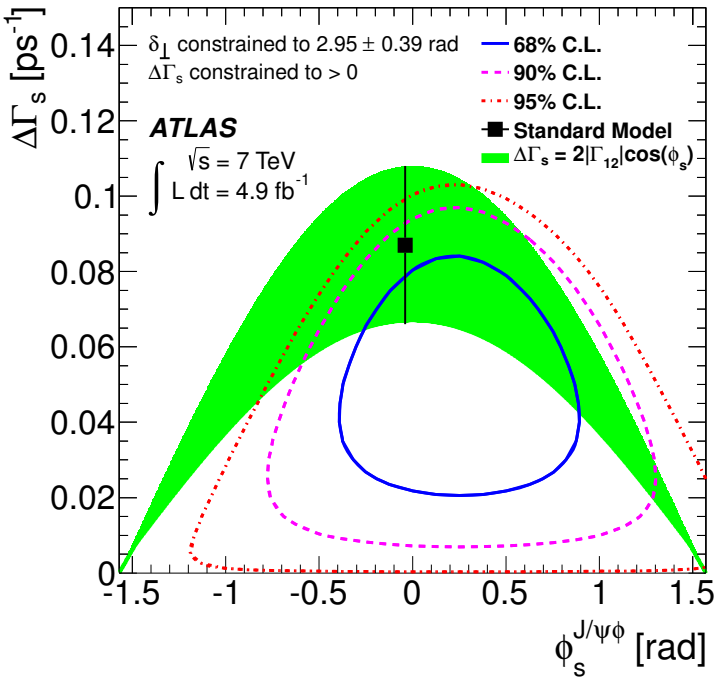

Figure 5. Likelihood contours in the $\phi_s - \Delta\Gamma_s$ plane. Three contours show the 68%, 90% and 95% confidence intervals (statistical errors only). The green band is the theoretical prediction of mixing- induced CP violation. The PDF contains a fourfold ambiguity. Three minima are excluded by applying the constraints from the LHCb measurements [7, 20].

and NWO, Netherlands; RCN, Norway; MNiSW, Poland; GRICES and FCT, Portugal; MERYS (MECTS), Romania; MES of Russia and ROSATOM, Russian Federation; JINR; MSTD, Serbia; MSSR, Slovakia; ARRS and MVZT, Slovenia; DST/NRF, South Africa; MICINN, Spain; SRC and Wallenberg Foundation, Sweden; SER, SNSF and Cantons of Bern and Geneva, Switzerland; NSC, Taiwan; TAEK, Turkey; STFC, the Royal Society and Leverhulme Trust, United Kingdom; DOE and NSF, United States of America.

The crucial computing support from all WLCG partners is acknowledged gratefully, in particular from CERN and the ATLAS Tier-1 facilities at TRIUMF (Canada), NDGF (Denmark, Norway, Sweden), CC-IN2P3 (France), KIT/GridKA (Germany), INFN-CNAF (Italy), NL-T1 (Netherlands), PIC (Spain), ASGC (Taiwan), RAL (U.K.) and BNL (U.S.A.) and in the Tier-2 facilities worldwide.

References

[1] UTfit collaboration, M. Bona et al., *Constraints on new physics from the quark mixing unitarity triangle*, *Phys. Rev. Lett.* **97** (2006) 151803 [hep-ph/0605213] [INSPIRE].

JHEP12(2012)072

[2] CDF collaboration, A. Abulencia et al., *Observation of $B_s^0 - \bar{B}_s^0$ Oscillations*, *Phys. Rev. Lett.* **97** (2006) 242003 [hep-ex/0609040] [INSPIRE].

[3] LHCb collaboration, R. Aaij et al., *Measurement of the $B_s^0 - \bar{B}_s^0$ oscillation frequency Δm_s in $B_s^0 \to D_s^-(3)\pi$ decays*, *Phys. Lett.* **B 709** (2012) 177 [arXiv:1112.4311] [INSPIRE].

[4] A. Lenz and U. Nierste, *Theoretical update of $B_s - \bar{B}_s$ mixing*, *JHEP* **06** (2007) 072 [hep-ph/0612167] [INSPIRE].

[5] D0 collaboration, V.M. Abazov et al., *Measurement of the CP-violating phase $\phi_s^{J/\psi\phi}$ using the flavor-tagged decay $B_s^0 \to J/\psi\phi$ in 8 fb^{-1} of $p\bar{p}$ collisions*, *Phys. Rev.* **D 85** (2012) 032006 [arXiv:1109.3166] [INSPIRE].

[6] CDF collaboration, T. Aaltonen et al., *Measurement of the CP-Violating Phase $\beta_s^{J/\Psi\phi}$ in $B_s^0 \to J/\Psi\phi$ Decays with the CDF II Detector*, *Phys. Rev.* **D 85** (2012) 072002 [arXiv:1112.1726] [INSPIRE].

[7] LHCb collaboration, R. Aaij et al., *Measurement of the CP-violating phase ϕ_s in the decay $B_s^0 \to J/\psi\phi$*, *Phys. Rev. Lett.* **108** (2012) 101803 [arXiv:1112.3183] [INSPIRE].

[8] ATLAS collaboration, *The ATLAS Experiment at the CERN Large Hadron Collider*, 2008 *JINST* **3** S08003 [INSPIRE].

[9] T. Sjöstrand, S. Mrenna and P.Z. Skands, *PYTHIA 6.4 Physics and Manual*, *JHEP* **05** (2006) 026 [hep-ph/0603175] [INSPIRE].

[10] ATLAS collaboration, *ATLAS tunes of PYTHIA 6 and PYTHIA 8 for MC11*, PHYS-PUB-2011-009 (2011).

[11] ATLAS collaboration, *The ATLAS Simulation Infrastructure*, *Eur. Phys. J.* **C 70** (2010) 823 [arXiv:1005.4568] [INSPIRE].

[12] GEANT4 collaboration, S. Agostinelli et al., *GEANT4: A Simulation toolkit*, *Nucl. Instrum. Meth.* **A 506** (2003) 250 [INSPIRE].

[13] ATLAS collaboration, *Measurement of the differential cross-sections of inclusive, prompt and non-prompt J/ψ production in proton-proton collisions at $\sqrt{s} = 7$ TeV*, *Nucl. Phys.* **B 850** (2011) 387 [arXiv:1104.3038] [INSPIRE].

[14] Particle Data Group collaboration, K. Nakamura et al., *Review of particle physics*, *J. Phys.* **G 37** (2010) 075021, and 2011 partial update for the 2012 edition [INSPIRE].

[15] A.S. Dighe, I. Dunietz and R. Fleischer, *Extracting CKM phases and $B_s - \bar{B}_s$ mixing parameters from angular distributions of nonleptonic B decays*, *Eur. Phys. J.* **C 6** (1999) 647 [hep-ph/9804253] [INSPIRE].

[16] G. Punzi, *Ordering algorithms and confidence intervals in the presence of nuisance parameters*, physics/0511202 [INSPIRE].

[17] ATLAS collaboration, *Measurement of the Λ_b lifetime and mass in the ATLAS experiment*, arXiv:1207.2284 [INSPIRE].

[18] ATLAS collaboration, *Charged-particle multiplicities in pp interactions measured with the ATLAS detector at the LHC*, *New J. Phys.* **13** (2011) S053033.

[19] ATLAS collaboration, *Measurement of Upsilon production in 7 TeV pp collisions at ATLAS*, arXiv:1211.7255 [INSPIRE].

[20] LHCb collaboration, R. Aaij et al., *Determination of the sign of the decay width difference in the B_s system*, *Phys. Rev. Lett.* **108** (2012) 241801 [arXiv:1202.4717] [INSPIRE].

JHEP12(2012)072

The ATLAS collaboration

G. Aad[48], T. Abajyan[21], B. Abbott[111], J. Abdallah[12], S. Abdel Khalek[115], A.A. Abdelalim[49], O. Abdinov[11], R. Aben[105], B. Abi[112], M. Abolins[88], O.S. AbouZeid[158], H. Abramowicz[153], H. Abreu[136], E. Acerbi[89a,89b], B.S. Acharya[164a,164b], L. Adamczyk[38], D.L. Adams[25], T.N. Addy[56], J. Adelman[176], S. Adomeit[98], P. Adragna[75], T. Adye[129], S. Aefsky[23], J.A. Aguilar-Saavedra[124b,a], M. Agustoni[17], M. Aharrouche[81], S.P. Ahlen[22], F. Ahles[48], A. Ahmad[148], M. Ahsan[41], G. Aielli[133a,133b], T. Akdogan[19a], T.P.A. Åkesson[79], G. Akimoto[155], A.V. Akimov[94], M.S. Alam[2], M.A. Alam[76], J. Albert[169], S. Albrand[55], M. Aleksa[30], I.N. Aleksandrov[64], F. Alessandria[89a], C. Alexa[26a], G. Alexander[153], G. Alexandre[49], T. Alexopoulos[10], M. Alhroob[164a,164c], M. Aliev[16], G. Alimonti[89a], J. Alison[120], B.M.M. Allbrooke[18], P.P. Allport[73], S.E. Allwood-Spiers[53], J. Almond[82], A. Aloisio[102a,102b], R. Alon[172], A. Alonso[79], F. Alonso[70], B. Alvarez Gonzalez[88], M.G. Alviggi[102a,102b], K. Amako[65], C. Amelung[23], V.V. Ammosov[128,*], A. Amorim[124a,b], N. Amram[153], C. Anastopoulos[30], L.S. Ancu[17], N. Andari[115], T. Andeen[35], C.F. Anders[58b], G. Anders[58a], K.J. Anderson[31], A. Andreazza[89a,89b], V. Andrei[58a], X.S. Anduaga[70], P. Anger[44], A. Angerami[35], F. Anghinolfi[30], A. Anisenkov[107], N. Anjos[124a], A. Annovi[47], A. Antonaki[9], M. Antonelli[47], A. Antonov[96], J. Antos[144b], F. Anulli[132a], M. Aoki[101], S. Aoun[83], L. Aperio Bella[5], R. Apolle[118,c], G. Arabidze[88], I. Aracena[143], Y. Arai[65], A.T.H. Arce[45], S. Arfaoui[148], J-F. Arguin[15], E. Arik[19a,*], M. Arik[19a], A.J. Armbruster[87], O. Arnaez[81], V. Arnal[80], C. Arnault[115], A. Artamonov[95], G. Artoni[132a,132b], D. Arutinov[21], S. Asai[155], R. Asfandiyarov[173], S. Ask[28], B. Åsman[146a,146b], L. Asquith[6], K. Assamagan[25], A. Astbury[169], M. Atkinson[165], B. Aubert[5], E. Auge[115], K. Augsten[127], M. Aurousseau[145a], G. Avolio[163], R. Avramidou[10], D. Axen[168], G. Azuelos[93,d], Y. Azuma[155], M.A. Baak[30], G. Baccaglioni[89a], C. Bacci[134a,134b], A.M. Bach[15], H. Bachacou[136], K. Bachas[30], M. Backes[49], M. Backhaus[21], E. Badescu[26a], P. Bagnaia[132a,132b], S. Bahinipati[3], Y. Bai[33a], D.C. Bailey[158], T. Bain[158], J.T. Baines[129], O.K. Baker[176], M.D. Baker[25], S. Baker[77], E. Banas[39], P. Banerjee[93], Sw. Banerjee[173], D. Banfi[30], A. Bangert[150], V. Bansal[169], H.S. Bansil[18], L. Barak[172], S.P. Baranov[94], A. Barbaro Galtieri[15], T. Barber[48], E.L. Barberio[86], D. Barberis[50a,50b], M. Barbero[21], D.Y. Bardin[64], T. Barillari[99], M. Barisonzi[175], T. Barklow[143], N. Barlow[28], B.M. Barnett[129], R.M. Barnett[15], A. Baroncelli[134a], G. Barone[49], A.J. Barr[118], F. Barreiro[80], J. Barreiro Guimarães da Costa[57], P. Barrillon[115], R. Bartoldus[143], A.E. Barton[71], V. Bartsch[149], A. Basye[165], R.L. Bates[53], L. Batkova[144a], J.R. Batley[28], A. Battaglia[17], M. Battistin[30], F. Bauer[136], H.S. Bawa[143,e], S. Beale[98], T. Beau[78], P.H. Beauchemin[161], R. Beccherle[50a], P. Bechtle[21], H.P. Beck[17], A.K. Becker[175], S. Becker[98], M. Beckingham[138], K.H. Becks[175], A.J. Beddall[19c], A. Beddall[19c], S. Bedikian[176], V.A. Bednyakov[64], C.P. Bee[83], L.J. Beemster[105], M. Begel[25], S. Behar Harpaz[152], M. Beimforde[99], C. Belanger-Champagne[85], P.J. Bell[49], W.H. Bell[49], G. Bella[153], L. Bellagamba[20a], F. Bellina[30], M. Bellomo[30], A. Belloni[57], O. Beloborodova[107,f], K. Belotskiy[96], O. Beltramello[30], O. Benary[153], D. Benchekroun[135a], K. Bendtz[146a,146b], N. Benekos[165], Y. Benhammou[153], E. Benhar Noccioli[49], J.A. Benitez Garcia[159b], D.P. Benjamin[45], M. Benoit[115], J.R. Bensinger[23], K. Benslama[130], S. Bentvelsen[105], D. Berge[30], E. Bergeaas Kuutmann[42], N. Berger[5], F. Berghaus[169], E. Berglund[105], J. Beringer[15], P. Bernat[77], R. Bernhard[48], C. Bernius[25], T. Berry[76], C. Bertella[83], A. Bertin[20a,20b], F. Bertolucci[122a,122b], M.I. Besana[89a,89b], G.J. Besjes[104], N. Besson[136], S. Bethke[99], W. Bhimji[46], R.M. Bianchi[30], M. Bianco[72a,72b], O. Biebel[98], S.P. Bieniek[77], K. Bierwagen[54], J. Biesiada[15], M. Biglietti[134a], H. Bilokon[47], M. Bindi[20a,20b], S. Binet[115], A. Bingul[19c], C. Bini[132a,132b], C. Biscarat[178], B. Bittner[99], K.M. Black[22], R.E. Blair[6], J.-B. Blanchard[136], G. Blanchot[30], T. Blazek[144a], C. Blocker[23], J. Blocki[39], A. Blondel[49], W. Blum[81], U. Blumenschein[54], G.J. Bobbink[105], V.B. Bobrovnikov[107], S.S. Bocchetta[79],

JHEP12(2012)072

A. Bocci[45], C.R. Boddy[118], M. Boehler[48], J. Boek[175], N. Boelaert[36], J.A. Bogaerts[30], A. Bogdanchikov[107], A. Bogouch[90,*], C. Bohm[146a], J. Bohm[125], V. Boisvert[76], T. Bold[38], V. Boldea[26a], N.M. Bolnet[136], M. Bomben[78], M. Bona[75], M. Boonekamp[136], C.N. Booth[139], S. Bordoni[78], C. Borer[17], A. Borisov[128], G. Borissov[71], I. Borjanovic[13a], M. Borri[82], S. Borroni[87], V. Bortolotto[134a,134b], K. Bos[105], D. Boscherini[20a], M. Bosman[12], H. Boterenbrood[105], J. Bouchami[93], J. Boudreau[123], E.V. Bouhova-Thacker[71], D. Boumediene[34], C. Bourdarios[115], N. Bousson[83], A. Boveia[31], J. Boyd[30], I.R. Boyko[64], I. Bozovic-Jelisavcic[13b], J. Bracinik[18], P. Branchini[134a], A. Brandt[8], G. Brandt[118], O. Brandt[54], U. Bratzler[156], B. Brau[84], J.E. Brau[114], H.M. Braun[175,*], S.F. Brazzale[164a,164c], B. Brelier[158], J. Bremer[30], K. Brendlinger[120], R. Brenner[166], S. Bressler[172], D. Britton[53], F.M. Brochu[28], I. Brock[21], R. Brock[88], F. Broggi[89a], C. Bromberg[88], J. Bronner[99], G. Brooijmans[35], T. Brooks[76], W.K. Brooks[32b], G. Brown[82], H. Brown[8], P.A. Bruckman de Renstrom[39], D. Bruncko[144b], R. Bruneliere[48], S. Brunet[60], A. Bruni[20a], G. Bruni[20a], M. Bruschi[20a], T. Buanes[14], Q. Buat[55], F. Bucci[49], J. Buchanan[118], P. Buchholz[141], R.M. Buckingham[118], A.G. Buckley[46], S.I. Buda[26a], I.A. Budagov[64], B. Budick[108], V. Büscher[81], L. Bugge[117], O. Bulekov[96], A.C. Bundock[73], M. Bunse[43], T. Buran[117], H. Burckhart[30], S. Burdin[73], T. Burgess[14], S. Burke[129], E. Busato[34], P. Bussey[53], C.P. Buszello[166], B. Butler[143], J.M. Butler[22], C.M. Buttar[53], J.M. Butterworth[77], W. Buttinger[28], S. Cabrera Urbán[167], D. Caforio[20a,20b], O. Cakir[4a], P. Calafiura[15], G. Calderini[78], P. Calfayan[98], R. Calkins[106], L.P. Caloba[24a], R. Caloi[132a,132b], D. Calvet[34], S. Calvet[34], R. Camacho Toro[34], P. Camarri[133a,133b], D. Cameron[117], L.M. Caminada[15], R. Caminal Armadans[12], S. Campana[30], M. Campanelli[77], V. Canale[102a,102b], F. Canelli[31,g], A. Canepa[159a], J. Cantero[80], R. Cantrill[76], L. Capasso[102a,102b], M.D.M. Capeans Garrido[30], I. Caprini[26a], M. Caprini[26a], D. Capriotti[99], M. Capua[37a,37b], R. Caputo[81], R. Cardarelli[133a], T. Carli[30], G. Carlino[102a], L. Carminati[89a,89b], B. Caron[85], S. Caron[104], E. Carquin[32b], G.D. Carrillo Montoya[173], A.A. Carter[75], J.R. Carter[28], J. Carvalho[124a,h], D. Casadei[108], M.P. Casado[12], M. Cascella[122a,122b], C. Caso[50a,50b,*], A.M. Castaneda Hernandez[173,i], E. Castaneda-Miranda[173], V. Castillo Gimenez[167], N.F. Castro[124a], G. Cataldi[72a], P. Catastini[57], A. Catinaccio[30], J.R. Catmore[30], A. Cattai[30], G. Cattani[133a,133b], S. Caughron[88], V. Cavaliere[165], P. Cavalleri[78], D. Cavalli[89a], M. Cavalli-Sforza[12], V. Cavasinni[122a,122b], F. Ceradini[134a,134b], A.S. Cerqueira[24b], A. Cerri[30], L. Cerrito[75], F. Cerutti[47], S.A. Cetin[19b], A. Chafaq[135a], D. Chakraborty[106], I. Chalupkova[126], K. Chan[3], P. Chang[165], B. Chapleau[85], J.D. Chapman[28], J.W. Chapman[87], E. Chareyre[78], D.G. Charlton[18], V. Chavda[82], C.A. Chavez Barajas[30], S. Cheatham[85], S. Chekanov[6], S.V. Chekulaev[159a], G.A. Chelkov[64], M.A. Chelstowska[104], C. Chen[63], H. Chen[25], S. Chen[33c], X. Chen[173], Y. Chen[35], A. Cheplakov[64], R. Cherkaoui El Moursli[135e], V. Chernyatin[25], E. Cheu[7], S.L. Cheung[158], L. Chevalier[136], G. Chiefari[102a,102b], L. Chikovani[51a,*], J.T. Childers[30], A. Chilingarov[71], G. Chiodini[72a], A.S. Chisholm[18], R.T. Chislett[77], A. Chitan[26a], M.V. Chizhov[64], G. Choudalakis[31], S. Chouridou[137], I.A. Christidi[77], A. Christov[48], D. Chromek-Burckhart[30], M.L. Chu[151], J. Chudoba[125], G. Ciapetti[132a,132b], A.K. Ciftci[4a], R. Ciftci[4a], D. Cinca[34], V. Cindro[74], C. Ciocca[20a,20b], A. Ciocio[15], M. Cirilli[87], P. Cirkovic[13b], M. Citterio[89a], M. Ciubancan[26a], A. Clark[49], P.J. Clark[46], R.N. Clarke[15], W. Cleland[123], J.C. Clemens[83], B. Clement[55], C. Clement[146a,146b], Y. Coadou[83], M. Cobal[164a,164c], A. Coccaro[138], J. Cochran[63], J.G. Cogan[143], J. Coggeshall[165], E. Cogneras[178], J. Colas[5], S. Cole[106], A.P. Colijn[105], N.J. Collins[18], C. Collins-Tooth[53], J. Collot[55], T. Colombo[119a,119b], G. Colon[84], P. Conde Muiño[124a], E. Coniavitis[118], M.C. Conidi[12], S.M. Consonni[89a,89b], V. Consorti[48], S. Constantinescu[26a], C. Conta[119a,119b], G. Conti[57], F. Conventi[102a,j], M. Cooke[15], B.D. Cooper[77], A.M. Cooper-Sarkar[118], K. Copic[15], T. Cornelissen[175], M. Corradi[20a], F. Corriveau[85,k], A. Cortes-Gonzalez[165], G. Cortiana[99], G. Costa[89a], M.J. Costa[167], D. Costanzo[139], D. Côté[30], L. Courneyea[169], G. Cowan[76], C. Cowden[28], B.E. Cox[82],

JHEP12(2012)072

K. Cranmer[108], F. Crescioli[122a,122b], M. Cristinziani[21], G. Crosetti[37a,37b], S. Crépé-Renaudin[55], C.-M. Cuciuc[26a], C. Cuenca Almenar[176], T. Cuhadar Donszelmann[139], M. Curatolo[47], C.J. Curtis[18], C. Cuthbert[150], P. Cwetanski[60], H. Czirr[141], P. Czodrowski[44], Z. Czyczula[176], S. D'Auria[53], M. D'Onofrio[73], A. D'Orazio[132a,132b], M.J. Da Cunha Sargedas De Sousa[124a], C. Da Via[82], W. Dabrowski[38], A. Dafinca[118], T. Dai[87], C. Dallapiccola[84], M. Dam[36], M. Dameri[50a,50b], D.S. Damiani[137], H.O. Danielsson[30], V. Dao[49], G. Darbo[50a], G.L. Darlea[26b], J.A. Dassoulas[42], W. Davey[21], T. Davidek[126], N. Davidson[86], R. Davidson[71], E. Davies[118,c], M. Davies[93], O. Davignon[78], A.R. Davison[77], Y. Davygora[58a], E. Dawe[142], I. Dawson[139], R.K. Daya-Ishmukhametova[23], K. De[8], R. de Asmundis[102a], S. De Castro[20a,20b], S. De Cecco[78], J. de Graat[98], N. De Groot[104], P. de Jong[105], C. De La Taille[115], H. De la Torre[80], F. De Lorenzi[63], L. de Mora[71], L. De Nooij[105], D. De Pedis[132a], A. De Salvo[132a], U. De Sanctis[164a,164c], A. De Santo[149], J.B. De Vivie De Regie[115], G. De Zorzi[132a,132b], W.J. Dearnaley[71], R. Debbe[25], C. Debenedetti[46], B. Dechenaux[55], D.V. Dedovich[64], J. Degenhardt[120], C. Del Papa[164a,164c], J. Del Peso[80], T. Del Prete[122a,122b], T. Delemontex[55], M. Deliyergiyev[74], A. Dell'Acqua[30], L. Dell'Asta[22], M. Della Pietra[102a,j], D. della Volpe[102a,102b], M. Delmastro[5], P.A. Delsart[55], C. Deluca[105], S. Demers[176], M. Demichev[64], B. Demirkoz[12,l], J. Deng[163], S.P. Denisov[128], D. Derendarz[39], J.E. Derkaoui[135d], F. Derue[78], P. Dervan[73], K. Desch[21], E. Devetak[148], P.O. Deviveiros[105], A. Dewhurst[129], B. DeWilde[148], S. Dhaliwal[158], R. Dhullipudi[25,m], A. Di Ciaccio[133a,133b], L. Di Ciaccio[5], A. Di Girolamo[30], B. Di Girolamo[30], S. Di Luise[134a,134b], A. Di Mattia[173], B. Di Micco[30], R. Di Nardo[47], A. Di Simone[133a,133b], R. Di Sipio[20a,20b], M.A. Diaz[32a], E.B. Diehl[87], J. Dietrich[42], T.A. Dietzsch[58a], S. Diglio[86], K. Dindar Yagci[40], J. Dingfelder[21], F. Dinut[26a], C. Dionisi[132a,132b], P. Dita[26a], S. Dita[26a], F. Dittus[30], F. Djama[83], T. Djobava[51b], M.A.B. do Vale[24c], A. Do Valle Wemans[124a,n], T.K.O. Doan[5], M. Dobbs[85], R. Dobinson[30,*], D. Dobos[30], E. Dobson[30,o], J. Dodd[35], C. Doglioni[49], T. Doherty[53], Y. Doi[65,*], J. Dolejsi[126], I. Dolenc[74], Z. Dolezal[126], B.A. Dolgoshein[96,*], T. Dohmae[155], M. Donadelli[24d], J. Donini[34], J. Dopke[30], A. Doria[102a], A. Dos Anjos[173], A. Dotti[122a,122b], M.T. Dova[70], A.D. Doxiadis[105], A.T. Doyle[53], M. Dris[10], J. Dubbert[99], S. Dube[15], E. Duchovni[172], G. Duckeck[98], D. Duda[175], A. Dudarev[30], F. Dudziak[63], M. Dührssen[30], I.P. Duerdoth[82], L. Duflot[115], M-A. Dufour[85], L. Duguid[76], M. Dunford[30], H. Duran Yildiz[4a], R. Duxfield[139], M. Dwuznik[38], F. Dydak[30], M. Düren[52], J. Ebke[98], S. Eckweiler[81], K. Edmonds[81], W. Edson[2], C.A. Edwards[76], N.C. Edwards[53], W. Ehrenfeld[42], T. Eifert[143], G. Eigen[14], K. Einsweiler[15], E. Eisenhandler[75], T. Ekelof[166], M. El Kacimi[135c], M. Ellert[166], S. Elles[5], F. Ellinghaus[81], K. Ellis[75], N. Ellis[30], J. Elmsheuser[98], M. Elsing[30], D. Emeliyanov[129], R. Engelmann[148], A. Engl[98], B. Epp[61], J. Erdmann[54], A. Ereditato[17], D. Eriksson[146a], J. Ernst[2], M. Ernst[25], J. Ernwein[136], D. Errede[165], S. Errede[165], E. Ertel[81], M. Escalier[115], H. Esch[43], C. Escobar[123], X. Espinal Curull[12], B. Esposito[47], F. Etienne[83], A.I. Etienvre[136], E. Etzion[153], D. Evangelakou[54], H. Evans[60], L. Fabbri[20a,20b], C. Fabre[30], R.M. Fakhrutdinov[128], S. Falciano[132a], Y. Fang[173], M. Fanti[89a,89b], A. Farbin[8], A. Farilla[134a], J. Farley[148], T. Farooque[158], S. Farrell[163], S.M. Farrington[170], P. Farthouat[30], F. Fassi[167], P. Fassnacht[30], D. Fassouliotis[9], B. Fatholahzadeh[158], A. Favareto[89a,89b], L. Fayard[115], S. Fazio[37a,37b], R. Febbraro[34], P. Federic[144a], O.L. Fedin[121], W. Fedorko[88], M. Fehling-Kaschek[48], L. Feligioni[83], D. Fellmann[6], C. Feng[33d], E.J. Feng[6], A.B. Fenyuk[128], J. Ferencei[144b], W. Fernando[6], S. Ferrag[53], J. Ferrando[53], V. Ferrara[42], A. Ferrari[166], P. Ferrari[105], R. Ferrari[119a], D.E. Ferreira de Lima[53], A. Ferrer[167], D. Ferrere[49], C. Ferretti[87], A. Ferretto Parodi[50a,50b], M. Fiascaris[31], F. Fiedler[81], A. Filipčič[74], F. Filthaut[104], M. Fincke-Keeler[169], M.C.N. Fiolhais[124a,h], L. Fiorini[167], A. Firan[40], G. Fischer[42], M.J. Fisher[109], M. Flechl[48], I. Fleck[141], J. Fleckner[81], P. Fleischmann[174], S. Fleischmann[175], T. Flick[175], A. Floderus[79], L.R. Flores Castillo[173], M.J. Flowerdew[99], T. Fonseca Martin[17], A. Formica[136], A. Forti[82],

JHEP12(2012)072

D. Fortin[159a], D. Fournier[115], H. Fox[71], P. Francavilla[12], M. Franchini[20a,20b], S. Franchino[119a,119b], D. Francis[30], T. Frank[172], S. Franz[30], M. Fraternali[119a,119b], S. Fratina[120], S.T. French[28], C. Friedrich[42], F. Friedrich[44], R. Froeschl[30], D. Froidevaux[30], J.A. Frost[28], C. Fukunaga[156], E. Fullana Torregrosa[30], B.G. Fulsom[143], J. Fuster[167], C. Gabaldon[30], O. Gabizon[172], T. Gadfort[25], S. Gadomski[49], G. Gagliardi[50a,50b], P. Gagnon[60], C. Galea[98], E.J. Gallas[118], V. Gallo[17], B.J. Gallop[129], P. Gallus[125], K.K. Gan[109], Y.S. Gao[143,e], A. Gaponenko[15], F. Garberson[176], M. Garcia-Sciveres[15], C. García[167], J.E. García Navarro[167], R.W. Gardner[31], N. Garelli[30], H. Garitaonandia[105], V. Garonne[30], C. Gatti[47], G. Gaudio[119a], B. Gaur[141], L. Gauthier[136], P. Gauzzi[132a,132b], I.L. Gavrilenko[94], C. Gay[168], G. Gaycken[21], E.N. Gazis[10], P. Ge[33d], Z. Gecse[168], C.N.P. Gee[129], D.A.A. Geerts[105], Ch. Geich-Gimbel[21], K. Gellerstedt[146a,146b], C. Gemme[50a], A. Gemmell[53], M.H. Genest[55], S. Gentile[132a,132b], M. George[54], S. George[76], P. Gerlach[175], A. Gershon[153], C. Geweniger[58a], H. Ghazlane[135b], N. Ghodbane[34], B. Giacobbe[20a], S. Giagu[132a,132b], V. Giakoumopoulou[9], V. Giangiobbe[12], F. Gianotti[30], B. Gibbard[25], A. Gibson[158], S.M. Gibson[30], D. Gillberg[29], A.R. Gillman[129], D.M. Gingrich[3,d], J. Ginzburg[153], N. Giokaris[9], M.P. Giordani[164c], R. Giordano[102a,102b], F.M. Giorgi[16], P. Giovannini[99], P.F. Giraud[136], D. Giugni[89a], M. Giunta[93], P. Giusti[20a], B.K. Gjelsten[117], L.K. Gladilin[97], C. Glasman[80], J. Glatzer[48], A. Glazov[42], K.W. Glitza[175], G.L. Glonti[64], J.R. Goddard[75], J. Godfrey[142], J. Godlewski[30], M. Goebel[42], T. Göpfert[44], C. Goeringer[81], C. Gössling[43], S. Goldfarb[87], T. Golling[176], A. Gomes[124a,b], L.S. Gomez Fajardo[42], R. Gonçalo[76], J. Goncalves Pinto Firmino Da Costa[42], L. Gonella[21], S. Gonzalez[173], S. González de la Hoz[167], G. Gonzalez Parra[12], M.L. Gonzalez Silva[27], S. Gonzalez-Sevilla[49], J.J. Goodson[148], L. Goossens[30], P.A. Gorbounov[95], H.A. Gordon[25], I. Gorelov[103], G. Gorfine[175], B. Gorini[30], E. Gorini[72a,72b], A. Gorišek[74], E. Gornicki[39], B. Gosdzik[42], A.T. Goshaw[6], M. Gosselink[105], M.I. Gostkin[64], I. Gough Eschrich[163], M. Gouighri[135a], D. Goujdami[135c], M.P. Goulette[49], A.G. Goussiou[138], C. Goy[5], S. Gozpinar[23], I. Grabowska-Bold[38], P. Grafström[20a,20b], K-J. Grahn[42], F. Grancagnolo[72a], S. Grancagnolo[16], V. Grassi[148], V. Gratchev[121], N. Grau[35], H.M. Gray[30], J.A. Gray[148], E. Graziani[134a], O.G. Grebenyuk[121], T. Greenshaw[73], Z.D. Greenwood[25,m], K. Gregersen[36], I.M. Gregor[42], P. Grenier[143], J. Griffiths[8], N. Grigalashvili[64], A.A. Grillo[137], S. Grinstein[12], Ph. Gris[34], Y.V. Grishkevich[97], J.-F. Grivaz[115], E. Gross[172], J. Grosse-Knetter[54], J. Groth-Jensen[172], K. Grybel[141], D. Guest[176], C. Guicheney[34], S. Guindon[54], U. Gul[53], H. Guler[85,p], J. Gunther[125], B. Guo[158], J. Guo[35], P. Gutierrez[111], N. Guttman[153], O. Gutzwiller[173], C. Guyot[136], C. Gwenlan[118], C.B. Gwilliam[73], A. Haas[143], S. Haas[30], C. Haber[15], H.K. Hadavand[40], D.R. Hadley[18], P. Haefner[21], F. Hahn[30], S. Haider[30], Z. Hajduk[39], H. Hakobyan[177], D. Hall[118], J. Haller[54], K. Hamacher[175], P. Hamal[113], M. Hamer[54], A. Hamilton[145b,q], S. Hamilton[161], L. Han[33b], K. Hanagaki[116], K. Hanawa[160], M. Hance[15], C. Handel[81], P. Hanke[58a], J.R. Hansen[36], J.B. Hansen[36], J.D. Hansen[36], P.H. Hansen[36], P. Hansson[143], K. Hara[160], G.A. Hare[137], T. Harenberg[175], S. Harkusha[90], D. Harper[87], R.D. Harrington[46], O.M. Harris[138], J. Hartert[48], F. Hartjes[105], T. Haruyama[65], A. Harvey[56], S. Hasegawa[101], Y. Hasegawa[140], S. Hassani[136], S. Haug[17], M. Hauschild[30], R. Hauser[88], M. Havranek[21], C.M. Hawkes[18], R.J. Hawkings[30], A.D. Hawkins[79], D. Hawkins[163], T. Hayakawa[66], T. Hayashi[160], D. Hayden[76], C.P. Hays[118], H.S. Hayward[73], S.J. Haywood[129], M. He[33d], S.J. Head[18], V. Hedberg[79], L. Heelan[8], S. Heim[88], B. Heinemann[15], S. Heisterkamp[36], L. Helary[22], C. Heller[98], M. Heller[30], S. Hellman[146a,146b], D. Hellmich[21], C. Helsens[12], R.C.W. Henderson[71], M. Henke[58a], A. Henrichs[54], A.M. Henriques Correia[30], S. Henrot-Versille[115], C. Hensel[54], T. Henß[175], C.M. Hernandez[8], Y. Hernández Jiménez[167], R. Herrberg[16], G. Herten[48], R. Hertenberger[98], L. Hervas[30], G.G. Hesketh[77], N.P. Hessey[105], E. Higón-Rodriguez[167], J.C. Hill[28], K.H. Hiller[42], S. Hillert[21], S.J. Hillier[18], I. Hinchliffe[15], E. Hines[120], M. Hirose[116], F. Hirsch[43], D. Hirschbuehl[175],

JHEP12(2012)072

J. Hobbs[148], N. Hod[153], M.C. Hodgkinson[139], P. Hodgson[139], A. Hoecker[30], M.R. Hoeferkamp[103], J. Hoffman[40], D. Hoffmann[83], M. Hohlfeld[81], M. Holder[141], S.O. Holmgren[146a], T. Holy[127], J.L. Holzbauer[88], T.M. Hong[120], L. Hooft van Huysduynen[108], S. Horner[48], J-Y. Hostachy[55], S. Hou[151], A. Hoummada[135a], J. Howard[118], J. Howarth[82], I. Hristova[16], J. Hrivnac[115], T. Hryn'ova[5], P.J. Hsu[81], S.-C. Hsu[15], D. Hu[35], Z. Hubacek[127], F. Hubaut[83], F. Huegging[21], A. Huettmann[42], T.B. Huffman[118], E.W. Hughes[35], G. Hughes[71], M. Huhtinen[30], M. Hurwitz[15], U. Husemann[42], N. Huseynov[64,r], J. Huston[88], J. Huth[57], G. Iacobucci[49], G. Iakovidis[10], M. Ibbotson[82], I. Ibragimov[141], L. Iconomidou-Fayard[115], J. Idarraga[115], P. Iengo[102a], O. Igonkina[105], Y. Ikegami[65], M. Ikeno[65], D. Iliadis[154], N. Ilic[158], T. Ince[21], J. Inigo-Golfin[30], P. Ioannou[9], M. Iodice[134a], K. Iordanidou[9], V. Ippolito[132a,132b], A. Irles Quiles[167], C. Isaksson[166], M. Ishino[67], M. Ishitsuka[157], R. Ishmukhametov[40], C. Issever[118], S. Istin[19a], A.V. Ivashin[128], W. Iwanski[39], H. Iwasaki[65], J.M. Izen[41], V. Izzo[102a], B. Jackson[120], J.N. Jackson[73], P. Jackson[1], M.R. Jaekel[30], V. Jain[60], K. Jakobs[48], S. Jakobsen[36], T. Jakoubek[125], J. Jakubek[127], D.K. Jana[111], E. Jansen[77], H. Jansen[30], A. Jantsch[99], M. Janus[48], G. Jarlskog[79], L. Jeanty[57], I. Jen-La Plante[31], D. Jennens[86], P. Jenni[30], A.E. Loevschall-Jensen[36], P. Ježˇ[36], S. Jézéquel[5], M.K. Jha[20a], H. Ji[173], W. Ji[81], J. Jia[148], Y. Jiang[33b], M. Jimenez Belenguer[42], S. Jin[33a], O. Jinnouchi[157], M.D. Joergensen[36], D. Joffe[40], M. Johansen[146a,146b], K.E. Johansson[146a], P. Johansson[139], S. Johnert[42], K.A. Johns[7], K. Jon-And[146a,146b], G. Jones[170], R.W.L. Jones[71], T.J. Jones[73], C. Joram[30], P.M. Jorge[124a], K.D. Joshi[82], J. Jovicevic[147], T. Jovin[13b], X. Ju[173], C.A. Jung[43], R.M. Jungst[30], V. Juranek[125], P. Jussel[61], A. Juste Rozas[12], S. Kabana[17], M. Kaci[167], A. Kaczmarska[39], P. Kadlecik[36], M. Kado[115], H. Kagan[109], M. Kagan[57], E. Kajomovitz[152], S. Kalinin[175], L.V. Kalinovskaya[64], S. Kama[40], N. Kanaya[155], M. Kaneda[30], S. Kaneti[28], T. Kanno[157], V.A. Kantserov[96], J. Kanzaki[65], B. Kaplan[108], A. Kapliy[31], J. Kaplon[30], D. Kar[53], M. Karagounis[21], K. Karakostas[10], M. Karnevskiy[42], V. Kartvelishvili[71], A.N. Karyukhin[128], L. Kashif[173], G. Kasieczka[58b], R.D. Kass[109], A. Kastanas[14], M. Kataoka[5], Y. Kataoka[155], E. Katsoufis[10], J. Katzy[42], V. Kaushik[7], K. Kawagoe[69], T. Kawamoto[155], G. Kawamura[81], M.S. Kayl[105], S. Kazama[155], V.A. Kazanin[107], M.Y. Kazarinov[64], R. Keeler[169], R. Kehoe[40], M. Keil[54], G.D. Kekelidze[64], J.S. Keller[138], M. Kenyon[53], O. Kepka[125], N. Kerschen[30], B.P. Kerševan[74], S. Kersten[175], K. Kessoku[155], J. Keung[158], F. Khalil-zada[11], H. Khandanyan[146a,146b], A. Khanov[112], D. Kharchenko[64], A. Khodinov[96], A. Khomich[58a], T.J. Khoo[28], G. Khoriauli[21], A. Khoroshilov[175], V. Khovanskiy[95], E. Khramov[64], J. Khubua[51b], H. Kim[146a,146b], S.H. Kim[160], N. Kimura[171], O. Kind[16], B.T. King[73], M. King[66], R.S.B. King[118], J. Kirk[129], A.E. Kiryunin[99], T. Kishimoto[66], D. Kisielewska[38], T. Kitamura[66], T. Kittelmann[123], K. Kiuchi[160], E. Kladiva[144b], M. Klein[73], U. Klein[73], K. Kleinknecht[81], M. Klemetti[85], A. Klier[172], P. Klimek[146a,146b], A. Klimentov[25], R. Klingenberg[43], J.A. Klinger[82], E.B. Klinkby[36], T. Klioutchnikova[30], P.F. Klok[104], S. Klous[105], E.-E. Kluge[58a], T. Kluge[73], P. Kluit[105], S. Kluth[99], N.S. Knecht[158], E. Kneringer[61], E.B.F.G. Knoops[83], A. Knue[54], B.R. Ko[45], T. Kobayashi[155], M. Kobel[44], M. Kocian[143], P. Kodys[126], K. Köneke[30], A.C. König[104], S. Koenig[81], L. Köpke[81], F. Koetsveld[104], P. Koevesarki[21], T. Koffas[29], E. Koffeman[105], L.A. Kogan[118], S. Kohlmann[175], F. Kohn[54], Z. Kohout[127], T. Kohriki[65], T. Koi[143], G.M. Kolachev[107,*], H. Kolanoski[16], V. Kolesnikov[64], I. Koletsou[89a], J. Koll[88], M. Kollefrath[48], A.A. Komar[94], Y. Komori[155], T. Kondo[65], T. Kono[42,s], A.I. Kononov[48], R. Konoplich[108,t], N. Konstantinidis[77], S. Koperny[38], K. Korcyl[39], K. Kordas[154], A. Korn[118], A. Korol[107], I. Korolkov[12], E.V. Korolkova[139], V.A. Korotkov[128], O. Kortner[99], S. Kortner[99], V.V. Kostyukhin[21], S. Kotov[99], V.M. Kotov[64], A. Kotwal[45], C. Kourkoumelis[9], V. Kouskoura[154], A. Koutsman[159a], R. Kowalewski[169], T.Z. Kowalski[38], W. Kozanecki[136], A.S. Kozhin[128], V. Kral[127], V.A. Kramarenko[97], G. Kramberger[74], M.W. Krasny[78], A. Krasznahorkay[108], J.K. Kraus[21], S. Kreiss[108], F. Krejci[127], J. Kretzschmar[73], N. Krieger[54], P. Krieger[158],

JHEP12(2012)072

K. Kroeninger[54], H. Kroha[99], J. Kroll[120], J. Kroseberg[21], J. Krstic[13a], U. Kruchonak[64], H. Krüger[21], T. Kruker[17], N. Krumnack[63], Z.V. Krumshteyn[64], T. Kubota[86], S. Kuday[4a], S. Kuehn[48], A. Kugel[58c], T. Kuhl[42], D. Kuhn[61], V. Kukhtin[64], Y. Kulchitsky[90], S. Kuleshov[32b], C. Kummer[98], M. Kuna[78], J. Kunkle[120], A. Kupco[125], H. Kurashige[66], M. Kurata[160], Y.A. Kurochkin[90], V. Kus[125], E.S. Kuwertz[147], M. Kuze[157], J. Kvita[142], R. Kwee[16], A. La Rosa[49], L. La Rotonda[37a,37b], L. Labarga[80], J. Labbe[5], S. Lablak[135a], C. Lacasta[167], F. Lacava[132a,132b], H. Lacker[16], D. Lacour[78], V.R. Lacuesta[167], E. Ladygin[64], R. Lafaye[5], B. Laforge[78], T. Lagouri[80], S. Lai[48], E. Laisne[55], M. Lamanna[30], L. Lambourne[77], C.L. Lampen[7], W. Lampl[7], E. Lancon[136], U. Landgraf[48], M.P.J. Landon[75], J.L. Lane[82], V.S. Lang[58a], C. Lange[42], A.J. Lankford[163], F. Lanni[25], K. Lantzsch[175], S. Laplace[78], C. Lapoire[21], J.F. Laporte[136], T. Lari[89a], A. Larner[118], M. Lassnig[30], P. Laurelli[47], V. Lavorini[37a,37b], W. Lavrijsen[15], P. Laycock[73], O. Le Dortz[78], E. Le Guirriec[83], C. Le Maner[158], E. Le Menedeu[12], T. LeCompte[6], F. Ledroit-Guillon[55], H. Lee[105], J.S.H. Lee[116], S.C. Lee[151], L. Lee[176], M. Lefebvre[169], M. Legendre[136], F. Legger[98], C. Leggett[15], M. Lehmacher[21], G. Lehmann Miotto[30], X. Lei[7], M.A.L. Leite[24d], R. Leitner[126], D. Lellouch[172], B. Lemmer[54], V. Lendermann[58a], K.J.C. Leney[145b], T. Lenz[105], G. Lenzen[175], B. Lenzi[30], K. Leonhardt[44], S. Leontsinis[10], F. Lepold[58a], C. Leroy[93], J-R. Lessard[169], C.G. Lester[28], C.M. Lester[120], J. Levêque[5], D. Levin[87], L.J. Levinson[172], A. Lewis[118], G.H. Lewis[108], A.M. Leyko[21], M. Leyton[16], B. Li[83], H. Li[173,u], S. Li[33b,v], X. Li[87], Z. Liang[118,w], H. Liao[34], B. Liberti[133a], P. Lichard[30], M. Lichtnecker[98], K. Lie[165], W. Liebig[14], C. Limbach[21], A. Limosani[86], M. Limper[62], S.C. Lin[151,x], F. Linde[105], J.T. Linnemann[88], E. Lipeles[120], A. Lipniacka[14], T.M. Liss[165], D. Lissauer[25], A. Lister[49], A.M. Litke[137], C. Liu[29], D. Liu[151], H. Liu[87], J.B. Liu[87], L. Liu[87], M. Liu[33b], Y. Liu[33b], M. Livan[119a,119b], S.S.A. Livermore[118], A. Lleres[55], J. Llorente Merino[80], S.L. Lloyd[75], E. Lobodzinska[42], P. Loch[7], W.S. Lockman[137], T. Loddenkoetter[21], F.K. Loebinger[82], A. Loginov[176], C.W. Loh[168], T. Lohse[16], K. Lohwasser[48], M. Lokajicek[125], V.P. Lombardo[5], R.E. Long[71], L. Lopes[124a], D. Lopez Mateos[57], J. Lorenz[98], N. Lorenzo Martinez[115], M. Losada[162], P. Loscutoff[15], F. Lo Sterzo[132a,132b], M.J. Losty[159a,*], X. Lou[41], A. Lounis[115], K.F. Loureiro[162], J. Love[6], P.A. Love[71], A.J. Lowe[143,e], F. Lu[33a], H.J. Lubatti[138], C. Luci[132a,132b], A. Lucotte[55], A. Ludwig[44], D. Ludwig[42], I. Ludwig[48], J. Ludwig[48], F. Luehring[60], G. Luijckx[105], W. Lukas[61], D. Lumb[48], L. Luminari[132a], E. Lund[117], B. Lund-Jensen[147], B. Lundberg[79], J. Lundberg[146a,146b], O. Lundberg[146a,146b], J. Lundquist[36], M. Lungwitz[81], D. Lynn[25], E. Lytken[79], H. Ma[25], L.L. Ma[173], G. Maccarrone[47], A. Macchiolo[99], B. Maček[74], J. Machado Miguens[124a], R. Mackeprang[36], R.J. Madaras[15], H.J. Maddocks[71], W.F. Mader[44], R. Maenner[58c], T. Maeno[25], P. Mättig[175], S. Mättig[81], L. Magnoni[163], E. Magradze[54], K. Mahboubi[48], S. Mahmoud[73], G. Mahout[18], C. Maiani[136], C. Maidantchik[24a], A. Maio[124a,b], S. Majewski[25], Y. Makida[65], N. Makovec[115], P. Mal[136], B. Malaescu[30], Pa. Malecki[39], P. Malecki[39], V.P. Maleev[121], F. Malek[55], U. Mallik[62], D. Malon[6], C. Malone[143], S. Maltezos[10], V. Malyshev[107], S. Malyukov[30], R. Mameghani[98], J. Mamuzic[13b], A. Manabe[65], L. Mandelli[89a], I. Mandić[74], R. Mandrysch[16], J. Maneira[124a], A. Manfredini[99], P.S. Mangeard[88], L. Manhaes de Andrade Filho[24b], J.A. Manjarres Ramos[136], A. Mann[54], P.M. Manning[137], A. Manousakis-Katsikakis[9], B. Mansoulie[136], A. Mapelli[30], L. Mapelli[30], L. March[80], J.F. Marchand[29], F. Marchese[133a,133b], G. Marchiori[78], M. Marcisovsky[125], C.P. Marino[169], F. Marroquim[24a], Z. Marshall[30], F.K. Martens[158], L.F. Marti[17], S. Marti-Garcia[167], B. Martin[30], B. Martin[88], J.P. Martin[93], T.A. Martin[18], V.J. Martin[46], B. Martin dit Latour[49], S. Martin-Haugh[149], M. Martinez[12], V. Martinez Outschoorn[57], A.C. Martyniuk[169], M. Marx[82], F. Marzano[132a], A. Marzin[111], L. Masetti[81], T. Mashimo[155], R. Mashinistov[94], J. Masik[82], A.L. Maslennikov[107], I. Massa[20a,20b], G. Massaro[105], N. Massol[5], P. Mastrandrea[148], A. Mastroberardino[37a,37b], T. Masubuchi[155], P. Matricon[115], H. Matsunaga[155], T. Matsushita[66], C. Mattravers[118,c], J. Maurer[83], S.J. Maxfield[73], A. Mayne[139], R. Mazini[151], M. Mazur[21],

JHEP12(2012)072

L. Mazzaferro[133a,133b], M. Mazzanti[89a], J. Mc Donald[85], S.P. Mc Kee[87], A. McCarn[165], R.L. McCarthy[148], T.G. McCarthy[29], N.A. McCubbin[129], K.W. McFarlane[56,*], J.A. Mcfayden[139], G. Mchedlidze[51b], T. Mclaughlan[18], S.J. McMahon[129], R.A. McPherson[169,k], A. Meade[84], J. Mechnich[105], M. Mechtel[175], M. Medinnis[42], R. Meera-Lebbai[111], T. Meguro[116], R. Mehdiyev[93], S. Mehlhase[36], A. Mehta[73], K. Meier[58a], B. Meirose[79], C. Melachrinos[31], B.R. Mellado Garcia[173], F. Meloni[89a,89b], L. Mendoza Navas[162], Z. Meng[151,u], A. Mengarelli[20a,20b], S. Menke[99], E. Meoni[161], K.M. Mercurio[57], P. Mermod[49], L. Merola[102a,102b], C. Meroni[89a], F.S. Merritt[31], H. Merritt[109], A. Messina[30,y], J. Metcalfe[25], A.S. Mete[163], C. Meyer[81], C. Meyer[31], J-P. Meyer[136], J. Meyer[174], J. Meyer[54], T.C. Meyer[30], J. Miao[33d], S. Michal[30], L. Micu[26a], R.P. Middleton[129], S. Migas[73], L. Mijović[136], G. Mikenberg[172], M. Mikestikova[125], M. Mikuž[74], D.W. Miller[31], R.J. Miller[88], W.J. Mills[168], C. Mills[57], A. Milov[172], D.A. Milstead[146a,146b], D. Milstein[172], A.A. Minaenko[128], M. Miñano Moya[167], I.A. Minashvili[64], A.I. Mincer[108], B. Mindur[38], M. Mineev[64], Y. Ming[173], L.M. Mir[12], G. Mirabelli[132a], J. Mitrevski[137], V.A. Mitsou[167], S. Mitsui[65], P.S. Miyagawa[139], J.U. Mjörnmark[79], T. Moa[146a,146b], V. Moeller[28], K. Mönig[42], N. Möser[21], S. Mohapatra[148], W. Mohr[48], R. Moles-Valls[167], J. Monk[77], E. Monnier[83], J. Montejo Berlingen[12], F. Monticelli[70], S. Monzani[20a,20b], R.W. Moore[3], G.F. Moorhead[86], C. Mora Herrera[49], A. Moraes[53], N. Morange[136], J. Morel[54], G. Morello[37a,37b], D. Moreno[81], M. Moreno Llácer[167], P. Morettini[50a], M. Morgenstern[44], M. Morii[57], A.K. Morley[30], G. Mornacchi[30], J.D. Morris[75], L. Morvaj[101], H.G. Moser[99], M. Mosidze[51b], J. Moss[109], R. Mount[143], E. Mountricha[10,z], S.V. Mouraviev[94,*], E.J.W. Moyse[84], F. Mueller[58a], J. Mueller[123], K. Mueller[21], T.A. Müller[98], T. Mueller[81], D. Muenstermann[30], Y. Munwes[153], W.J. Murray[129], I. Mussche[105], E. Musto[102a,102b], A.G. Myagkov[128], M. Myska[125], J. Nadal[12], K. Nagai[160], R. Nagai[157], K. Nagano[65], A. Nagarkar[109], Y. Nagasaka[59], M. Nagel[99], A.M. Nairz[30], Y. Nakahama[30], K. Nakamura[155], T. Nakamura[155], I. Nakano[110], G. Nanava[21], A. Napier[161], R. Narayan[58b], M. Nash[77,c], T. Nattermann[21], T. Naumann[42], G. Navarro[162], H.A. Neal[87], P.Yu. Nechaeva[94], T.J. Neep[82], A. Negri[119a,119b], G. Negri[30], M. Negrini[20a], S. Nektarijevic[49], A. Nelson[163], T.K. Nelson[143], S. Nemecek[125], P. Nemethy[108], A.A. Nepomuceno[24a], M. Nessi[30,aa], M.S. Neubauer[165], M. Neumann[175], A. Neusiedl[81], R.M. Neves[108], P. Nevski[25], P.R. Newman[18], V. Nguyen Thi Hong[136], R.B. Nickerson[118], R. Nicolaidou[136], B. Nicquevert[30], F. Niedercorn[115], J. Nielsen[137], N. Nikiforou[35], A. Nikiforov[16], V. Nikolaenko[128], I. Nikolic-Audit[78], K. Nikolics[49], K. Nikolopoulos[18], H. Nilsen[48], P. Nilsson[8], Y. Ninomiya[155], A. Nisati[132a], R. Nisius[99], T. Nobe[157], L. Nodulman[6], M. Nomachi[116], I. Nomidis[154], S. Norberg[111], M. Nordberg[30], P.R. Norton[129], J. Novakova[126], M. Nozaki[65], L. Nozka[113], I.M. Nugent[159a], A.-E. Nuncio-Quiroz[21], G. Nunes Hanninger[86], T. Nunnemann[98], E. Nurse[77], B.J. O'Brien[46], S.W. O'Neale[18,*], D.C. O'Neil[142], V. O'Shea[53], L.B. Oakes[98], F.G. Oakham[29,d], H. Oberlack[99], J. Ocariz[78], A. Ochi[66], S. Oda[69], S. Odaka[65], J. Odier[83], H. Ogren[60], A. Oh[82], S.H. Oh[45], C.C. Ohm[30], T. Ohshima[101], H. Okawa[25], Y. Okumura[31], T. Okuyama[155], A. Olariu[26a], A.G. Olchevski[64], S.A. Olivares Pino[32a], M. Oliveira[124a,h], D. Oliveira Damazio[25], E. Oliver Garcia[167], D. Olivito[120], A. Olszewski[39], J. Olszowska[39], A. Onofre[124a,ab], P.U.E. Onyisi[31], C.J. Oram[159a], M.J. Oreglia[31], Y. Oren[153], D. Orestano[134a,134b], N. Orlando[72a,72b], I. Orlov[107], C. Oropeza Barrera[53], R.S. Orr[158], B. Osculati[50a,50b], R. Ospanov[120], C. Osuna[12], G. Otero y Garzon[27], J.P. Ottersbach[105], M. Ouchrif[135d], E.A. Ouellette[169], F. Ould-Saada[117], A. Ouraou[136], Q. Ouyang[33a], A. Ovcharova[15], M. Owen[82], S. Owen[139], V.E. Ozcan[19a], N. Ozturk[8], A. Pacheco Pages[12], C. Padilla Aranda[12], S. Pagan Griso[15], E. Paganis[139], C. Pahl[99], F. Paige[25], P. Pais[84], K. Pajchel[117], G. Palacino[159b], C.P. Paleari[7], S. Palestini[30], D. Pallin[34], A. Palma[124a], J.D. Palmer[18], Y.B. Pan[173], E. Panagiotopoulou[10], P. Pani[105], N. Panikashvili[87], S. Panitkin[25], D. Pantea[26a], A. Papadelis[146a], Th.D. Papadopoulou[10], A. Paramonov[6], D. Paredes Hernandez[34],

JHEP12(2012)072

W. Park[25,ac], M.A. Parker[28], F. Parodi[50a,50b], J.A. Parsons[35], U. Parzefall[48], S. Pashapour[54], E. Pasqualucci[132a], S. Passaggio[50a], A. Passeri[134a], F. Pastore[134a,134b,*], Fr. Pastore[76], G. Pásztor[49,ad], S. Pataraia[175], N. Patel[150], J.R. Pater[82], S. Patricelli[102a,102b], T. Pauly[30], M. Pecsy[144a], S. Pedraza Lopez[167], M.I. Pedraza Morales[173], S.V. Peleganchuk[107], D. Pelikan[166], H. Peng[33b], B. Penning[31], A. Penson[35], J. Penwell[60], M. Perantoni[24a], K. Perez[35,ae], T. Perez Cavalcanti[42], E. Perez Codina[159a], M.T. Pérez García-Estañ[167], V. Perez Reale[35], L. Perini[89a,89b], H. Pernegger[30], R. Perrino[72a], P. Perrodo[5], V.D. Peshekhonov[64], K. Peters[30], B.A. Petersen[30], J. Petersen[30], T.C. Petersen[36], E. Petit[5], A. Petridis[154], C. Petridou[154], E. Petrolo[132a], F. Petrucci[134a,134b], D. Petschull[42], M. Petteni[142], R. Pezoa[32b], A. Phan[86], P.W. Phillips[129], G. Piacquadio[30], A. Picazio[49], E. Piccaro[75], M. Piccinini[20a,20b], S.M. Piec[42], R. Piegaia[27], D.T. Pignotti[109], J.E. Pilcher[31], A.D. Pilkington[82], J. Pina[124a,b], M. Pinamonti[164a,164c], A. Pinder[118], J.L. Pinfold[3], B. Pinto[124a], C. Pizio[89a,89b], M. Plamondon[169], M.-A. Pleier[25], E. Plotnikova[64], A. Poblaguev[25], S. Poddar[58a], F. Podlyski[34], L. Poggioli[115], D. Pohl[21], M. Pohl[49], G. Polesello[119a], A. Policicchio[37a,37b], A. Polini[20a], J. Poll[75], V. Polychronakos[25], D. Pomeroy[23], K. Pommès[30], L. Pontecorvo[132a], B.G. Pope[88], G.A. Popeneciu[26a], D.S. Popovic[13a], A. Poppleton[30], X. Portell Bueso[30], G.E. Pospelov[99], S. Pospisil[127], I.N. Potrap[99], C.J. Potter[149], C.T. Potter[114], G. Poulard[30], J. Poveda[60], V. Pozdnyakov[64], R. Prabhu[77], P. Pralavorio[83], A. Pranko[15], S. Prasad[30], R. Pravahan[25], S. Prell[63], K. Pretzl[17], D. Price[60], J. Price[73], L.E. Price[6], D. Prieur[123], M. Primavera[72a], K. Prokofiev[108], F. Prokoshin[32b], S. Protopopescu[25], J. Proudfoot[6], X. Prudent[44], M. Przybycien[38], H. Przysiezniak[5], S. Psoroulas[21], E. Ptacek[114], E. Pueschel[84], J. Purdham[87], M. Purohit[25,ac], P. Puzo[115], Y. Pylypchenko[62], J. Qian[87], A. Quadt[54], D.R. Quarrie[15], W.B. Quayle[173], F. Quinonez[32a], M. Raas[104], V. Radescu[42], P. Radloff[114], T. Rador[19a], F. Ragusa[89a,89b], G. Rahal[178], A.M. Rahimi[109], D. Rahm[25], S. Rajagopalan[25], M. Rammensee[48], M. Rammes[141], A.S. Randle-Conde[40], K. Randrianarivony[29], F. Rauscher[98], T.C. Rave[48], M. Raymond[30], A.L. Read[117], D.M. Rebuzzi[119a,119b], A. Redelbach[174], G. Redlinger[25], R. Reece[120], K. Reeves[41], E. Reinherz-Aronis[153], A. Reinsch[114], I. Reisinger[43], C. Rembser[30], Z.L. Ren[151], A. Renaud[115], M. Rescigno[132a], S. Resconi[89a], B. Resende[136], P. Reznicek[98], R. Rezvani[158], R. Richter[99], E. Richter-Was[5,af], M. Ridel[78], M. Rijpstra[105], M. Rijssenbeek[148], A. Rimoldi[119a,119b], L. Rinaldi[20a], R.R. Rios[40], I. Riu[12], G. Rivoltella[89a,89b], F. Rizatdinova[112], E. Rizvi[75], S.H. Robertson[85,k], A. Robichaud-Veronneau[118], D. Robinson[28], J.E.M. Robinson[82], A. Robson[53], J.G. Rocha de Lima[106], C. Roda[122a,122b], D. Roda Dos Santos[30], A. Roe[54], S. Roe[30], O. Røhne[117], S. Rolli[161], A. Romaniouk[96], M. Romano[20a,20b], G. Romeo[27], E. Romero Adam[167], N. Rompotis[138], L. Roos[78], E. Ros[167], S. Rosati[132a], K. Rosbach[49], A. Rose[149], M. Rose[76], G.A. Rosenbaum[158], E.I. Rosenberg[63], P.L. Rosendahl[14], O. Rosenthal[141], L. Rosselet[49], V. Rossetti[12], E. Rossi[132a,132b], L.P. Rossi[50a], M. Rotaru[26a], I. Roth[172], J. Rothberg[138], D. Rousseau[115], C.R. Royon[136], A. Rozanov[83], Y. Rozen[152], X. Ruan[33a,ag], F. Rubbo[12], I. Rubinskiy[42], N. Ruckstuhl[105], V.I. Rud[97], C. Rudolph[44], G. Rudolph[61], F. Rühr[7], A. Ruiz-Martinez[63], L. Rumyantsev[64], Z. Rurikova[48], N.A. Rusakovich[64], J.P. Rutherfoord[7], C. Ruwiedel[15,*], P. Ruzicka[125], Y.F. Ryabov[121], M. Rybar[126], G. Rybkin[115], N.C. Ryder[118], A.F. Saavedra[150], I. Sadeh[153], H.F-W. Sadrozinski[137], R. Sadykov[64], F. Safai Tehrani[132a], H. Sakamoto[155], G. Salamanna[75], A. Salamon[133a], M. Saleem[111], D. Salek[30], D. Salihagic[99], A. Salnikov[143], J. Salt[167], B.M. Salvachua Ferrando[6], D. Salvatore[37a,37b], F. Salvatore[149], A. Salvucci[104], A. Salzburger[30], D. Sampsonidis[154], B.H. Samset[117], A. Sanchez[102a,102b], V. Sanchez Martinez[167], H. Sandaker[14], H.G. Sander[81], M.P. Sanders[98], M. Sandhoff[175], T. Sandoval[28], C. Sandoval[162], R. Sandstroem[99], D.P.C. Sankey[129], A. Sansoni[47], C. Santamarina Rios[85], C. Santoni[34], R. Santonico[133a,133b], H. Santos[124a], J.G. Saraiva[124a], T. Sarangi[173], E. Sarkisyan-Grinbaum[8], F. Sarri[122a,122b], G. Sartisohn[175], O. Sasaki[65],

JHEP12(2012)072

Y. Sasaki[155], N. Sasao[67], I. Satsounkevitch[90], G. Sauvage[5,*], E. Sauvan[5], J.B. Sauvan[115], P. Savard[158,d], V. Savinov[123], D.O. Savu[30], L. Sawyer[25,m], D.H. Saxon[53], J. Saxon[120], C. Sbarra[20a], A. Sbrizzi[20a,20b], D.A. Scannicchio[163], M. Scarcella[150], J. Schaarschmidt[115], P. Schacht[99], D. Schaefer[120], U. Schäfer[81], S. Schaepe[21], S. Schaetzel[58b], A.C. Schaffer[115], D. Schaile[98], R.D. Schamberger[148], A.G. Schamov[107], V. Scharf[58a], V.A. Schegelsky[121], D. Scheirich[87], M. Schernau[163], M.I. Scherzer[35], C. Schiavi[50a,50b], J. Schieck[98], M. Schioppa[37a,37b], S. Schlenker[30], E. Schmidt[48], K. Schmieden[21], C. Schmitt[81], S. Schmitt[58b], M. Schmitz[21], B. Schneider[17], U. Schnoor[44], A. Schoening[58b], A.L.S. Schorlemmer[54], M. Schott[30], D. Schouten[159a], J. Schovancova[125], M. Schram[85], C. Schroeder[81], N. Schroer[58c], M.J. Schultens[21], J. Schultes[175], H.-C. Schultz-Coulon[58a], H. Schulz[16], M. Schumacher[48], B.A. Schumm[137], Ph. Schune[136], C. Schwanenberger[82], A. Schwartzman[143], Ph. Schwegler[99], Ph. Schwemling[78], R. Schwienhorst[88], R. Schwierz[44], J. Schwindling[136], T. Schwindt[21], M. Schwoerer[5], G. Sciolla[23], W.G. Scott[129], J. Searcy[114], G. Sedov[42], E. Sedykh[121], S.C. Seidel[103], A. Seiden[137], F. Seifert[44], J.M. Seixas[24a], G. Sekhniaidze[102a], S.J. Sekula[40], K.E. Selbach[46], D.M. Seliverstov[121], B. Sellden[146a], G. Sellers[73], M. Seman[144b], N. Semprini-Cesari[20a,20b], C. Serfon[98], L. Serin[115], L. Serkin[54], R. Seuster[99], H. Severini[111], A. Sfyrla[30], E. Shabalina[54], M. Shamim[114], L.Y. Shan[33a], J.T. Shank[22], Q.T. Shao[86], M. Shapiro[15], P.B. Shatalov[95], K. Shaw[164a,164c], D. Sherman[176], P. Sherwood[77], A. Shibata[108], S. Shimizu[101], M. Shimojima[100], T. Shin[56], M. Shiyakova[64], A. Shmeleva[94], M.J. Shochet[31], D. Short[118], S. Shrestha[63], E. Shulga[96], M.A. Shupe[7], P. Sicho[125], A. Sidoti[132a], F. Siegert[48], Dj. Sijacki[13a], O. Silbert[172], J. Silva[124a], Y. Silver[153], D. Silverstein[143], S.B. Silverstein[146a], V. Simak[127], O. Simard[136], Lj. Simic[13a], S. Simion[115], E. Simioni[81], B. Simmons[77], R. Simoniello[89a,89b], M. Simonyan[36], P. Sinervo[158], N.B. Sinev[114], V. Sipica[141], G. Siragusa[174], A. Sircar[25], A.N. Sisakyan[64,*], S.Yu. Sivoklokov[97], J. Sjölin[146a,146b], T.B. Sjursen[14], L.A. Skinnari[15], H.P. Skottowe[57], K. Skovpen[107], P. Skubic[111], M. Slater[18], T. Slavicek[127], K. Sliwa[161], V. Smakhtin[172], B.H. Smart[46], S.Yu. Smirnov[96], Y. Smirnov[96], L.N. Smirnova[97], O. Smirnova[79], B.C. Smith[57], D. Smith[143], K.M. Smith[53], M. Smizanska[71], K. Smolek[127], A.A. Snesarev[94], S.W. Snow[82], J. Snow[111], S. Snyder[25], R. Sobie[169,k], J. Sodomka[127], A. Soffer[153], C.A. Solans[167], M. Solar[127], J. Solc[127], E.Yu. Soldatov[96], U. Soldevila[167], E. Solfaroli Camillocci[132a,132b], A.A. Solodkov[128], O.V. Solovyanov[128], V. Solovyev[121], N. Soni[1], V. Sopko[127], B. Sopko[127], M. Sosebee[8], R. Soualah[164a,164c], A. Soukharev[107], S. Spagnolo[72a,72b], F. Spanò[76], R. Spighi[20a], G. Spigo[30], R. Spiwoks[30], M. Spousta[126,ah], T. Spreitzer[158], B. Spurlock[8], R.D. St. Denis[53], J. Stahlman[120], R. Stamen[58a], E. Stanecka[39], R.W. Stanek[6], C. Stanescu[134a], M. Stanescu-Bellu[42], S. Stapnes[117], E.A. Starchenko[128], J. Stark[55], P. Staroba[125], P. Starovoitov[42], R. Staszewski[39], A. Staude[98], P. Stavina[144a,*], G. Steele[53], P. Steinbach[44], P. Steinberg[25], I. Stekl[127], B. Stelzer[142], H.J. Stelzer[88], O. Stelzer-Chilton[159a], H. Stenzel[52], S. Stern[99], G.A. Stewart[30], J.A. Stillings[21], M.C. Stockton[85], K. Stoerig[48], G. Stoicea[26a], S. Stonjek[99], P. Strachota[126], A.R. Stradling[8], A. Straessner[44], J. Strandberg[147], S. Strandberg[146a,146b], A. Strandlie[117], M. Strang[109], E. Strauss[143], M. Strauss[111], P. Strizenec[144b], R. Ströhmer[174], D.M. Strom[114], J.A. Strong[76,*], R. Stroynowski[40], J. Strube[129], B. Stugu[14], I. Stumer[25,*], J. Stupak[148], P. Sturm[175], N.A. Styles[42], D.A. Soh[151,w], D. Su[143], HS. Subramania[3], A. Succurro[12], Y. Sugaya[116], C. Suhr[106], M. Suk[126], V.V. Sulin[94], S. Sultansoy[4d], T. Sumida[67], X. Sun[55], J.E. Sundermann[48], K. Suruliz[139], G. Susinno[37a,37b], M.R. Sutton[149], Y. Suzuki[65], Y. Suzuki[66], M. Svatos[125], S. Swedish[168], I. Sykora[144a], T. Sykora[126], J. Sánchez[167], D. Ta[105], K. Tackmann[42], A. Taffard[163], R. Tafirout[159a], N. Taiblum[153], Y. Takahashi[101], H. Takai[25], R. Takashima[68], H. Takeda[66], T. Takeshita[140], Y. Takubo[65], M. Talby[83], A. Talyshev[107,f], M.C. Tamsett[25], J. Tanaka[155], R. Tanaka[115], S. Tanaka[131], S. Tanaka[65], A.J. Tanasijczuk[142], K. Tani[66], N. Tannoury[83], S. Tapprogge[81],

JHEP12(2012)072

D. Tardif[158], S. Tarem[152], F. Tarrade[29], G.F. Tartarelli[89a], P. Tas[126], M. Tasevsky[125], E. Tassi[37a,37b], M. Tatarkhanov[15], Y. Tayalati[135d], C. Taylor[77], F.E. Taylor[92], G.N. Taylor[86], W. Taylor[159b], M. Teinturier[115], F.A. Teischinger[30], M. Teixeira Dias Castanheira[75], P. Teixeira-Dias[76], K.K. Temming[48], H. Ten Kate[30], P.K. Teng[151], S. Terada[65], K. Terashi[155], J. Terron[80], M. Testa[47], R.J. Teuscher[158,k], J. Therhaag[21], T. Theveneaux-Pelzer[78], S. Thoma[48], J.P. Thomas[18], E.N. Thompson[35], P.D. Thompson[18], P.D. Thompson[158], A.S. Thompson[53], L.A. Thomsen[36], E. Thomson[120], M. Thomson[28], W.M. Thong[86], R.P. Thun[87], F. Tian[35], M.J. Tibbetts[15], T. Tic[125], V.O. Tikhomirov[94], Y.A. Tikhonov[107,f], S. Timoshenko[96], P. Tipton[176], S. Tisserant[83], T. Todorov[5], S. Todorova-Nova[161], B. Toggerson[163], J. Tojo[69], S. Tokár[144a], K. Tokushuku[65], K. Tollefson[88], M. Tomoto[101], L. Tompkins[31], K. Toms[103], A. Tonoyan[14], C. Topfel[17], N.D. Topilin[64], I. Torchiani[30], E. Torrence[114], H. Torres[78], E. Torró Pastor[167], J. Toth[83,ad], F. Touchard[83], D.R. Tovey[139], T. Trefzger[174], L. Tremblet[30], A. Tricoli[30], I.M. Trigger[159a], S. Trincaz-Duvoid[78], M.F. Tripiana[70], N. Triplett[25], W. Trischuk[158], B. Trocmé[55], C. Troncon[89a], M. Trottier-McDonald[142], M. Trzebinski[39], A. Trzupek[39], C. Tsarouchas[30], J.C-L. Tseng[118], M. Tsiakiris[105], P.V. Tsiareshka[90], D. Tsionou[5,ai], G. Tsipolitis[10], S. Tsiskaridze[12], V. Tsiskaridze[48], E.G. Tskhadadze[51a], I.I. Tsukerman[95], V. Tsulaia[15], J.-W. Tsung[21], S. Tsuno[65], D. Tsybychev[148], A. Tua[139], A. Tudorache[26a], V. Tudorache[26a], J.M. Tuggle[31], M. Turala[39], D. Turecek[127], I. Turk Cakir[4e], E. Turlay[105], R. Turra[89a,89b], P.M. Tuts[35], A. Tykhonov[74], M. Tylmad[146a,146b], M. Tyndel[129], G. Tzanakos[9], K. Uchida[21], I. Ueda[155], R. Ueno[29], M. Ugland[14], M. Uhlenbrock[21], M. Uhrmacher[54], F. Ukegawa[160], G. Unal[30], A. Undrus[25], G. Unel[163], Y. Unno[65], D. Urbaniec[35], G. Usai[8], M. Uslenghi[119a,119b], L. Vacavant[83], V. Vacek[127], B. Vachon[85], S. Vahsen[15], J. Valenta[125], S. Valentinetti[20a,20b], A. Valero[167], S. Valkar[126], E. Valladolid Gallego[167], S. Vallecorsa[152], J.A. Valls Ferrer[167], P.C. Van Der Deijl[105], R. van der Geer[105], H. van der Graaf[105], R. Van Der Leeuw[105], E. van der Poel[105], D. van der Ster[30], N. van Eldik[30], P. van Gemmeren[6], I. van Vulpen[105], M. Vanadia[99], W. Vandelli[30], A. Vaniachine[6], P. Vankov[42], F. Vannucci[78], R. Vari[132a], T. Varol[84], D. Varouchas[15], A. Vartapetian[8], K.E. Varvell[150], V.I. Vassilakopoulos[56], F. Vazeille[34], T. Vazquez Schroeder[54], G. Vegni[89a,89b], J.J. Veillet[115], F. Veloso[124a], R. Veness[30], S. Veneziano[132a], A. Ventura[72a,72b], D. Ventura[84], M. Venturi[48], N. Venturi[158], V. Vercesi[119a], M. Verducci[138], W. Verkerke[105], J.C. Vermeulen[105], A. Vest[44], M.C. Vetterli[142,d], I. Vichou[165], T. Vickey[145b,aj], O.E. Vickey Boeriu[145b], G.H.A. Viehhauser[118], S. Viel[168], M. Villa[20a,20b], M. Villaplana Perez[167], E. Vilucchi[47], M.G. Vincter[29], E. Vinek[30], V.B. Vinogradov[64], M. Virchaux[136,*], J. Virzi[15], O. Vitells[172], M. Viti[42], I. Vivarelli[48], F. Vives Vaque[3], S. Vlachos[10], D. Vladoiu[98], M. Vlasak[127], A. Vogel[21], P. Vokac[127], G. Volpi[47], M. Volpi[86], G. Volpini[89a], H. von der Schmitt[99], H. von Radziewski[48], E. von Toerne[21], V. Vorobel[126], V. Vorwerk[12], M. Vos[167], R. Voss[30], T.T. Voss[175], J.H. Vossebeld[73], N. Vranjes[136], M. Vranjes Milosavljevic[105], V. Vrba[125], M. Vreeswijk[105], T. Vu Anh[48], R. Vuillermet[30], I. Vukotic[31], W. Wagner[175], P. Wagner[120], H. Wahlen[175], S. Wahrmund[44], J. Wakabayashi[101], S. Walch[87], J. Walder[71], R. Walker[98], W. Walkowiak[141], R. Wall[176], P. Waller[73], B. Walsh[176], C. Wang[45], H. Wang[173], H. Wang[33b,ak], J. Wang[151], J. Wang[55], R. Wang[103], S.M. Wang[151], T. Wang[21], A. Warburton[85], C.P. Ward[28], M. Warsinsky[48], A. Washbrook[46], C. Wasicki[42], I. Watanabe[66], P.M. Watkins[18], A.T. Watson[18], I.J. Watson[150], M.F. Watson[18], G. Watts[138], S. Watts[82], A.T. Waugh[150], B.M. Waugh[77], M.S. Weber[17], P. Weber[54], A.R. Weidberg[118], P. Weigell[99], J. Weingarten[54], C. Weiser[48], H. Wellenstein[23], P.S. Wells[30], T. Wenaus[25], D. Wendland[16], Z. Weng[151,w], T. Wengler[30], S. Wenig[30], N. Wermes[21], M. Werner[48], P. Werner[30], M. Werth[163], M. Wessels[58a], J. Wetter[161], C. Weydert[55], K. Whalen[29], S.J. Wheeler-Ellis[163], A. White[8], M.J. White[86], S. White[122a,122b], S.R. Whitehead[118], D. Whiteson[163], D. Whittington[60], F. Wicek[115], D. Wicke[175], F.J. Wickens[129], W. Wiedenmann[173], M. Wielers[129], P. Wienemann[21],

JHEP12(2012)072

C. Wiglesworth[75], L.A.M. Wiik-Fuchs[48], P.A. Wijeratne[77], A. Wildauer[99], M.A. Wildt[42,s], I. Wilhelm[126], H.G. Wilkens[30], J.Z. Will[98], E. Williams[35], H.H. Williams[120], W. Willis[35], S. Willocq[84], J.A. Wilson[18], M.G. Wilson[143], A. Wilson[87], I. Wingerter-Seez[5], S. Winkelmann[48], F. Winklmeier[30], M. Wittgen[143], S.J. Wollstadt[81], M.W. Wolter[39], H. Wolters[124a,h], W.C. Wong[41], G. Wooden[87], B.K. Wosiek[39], J. Wotschack[30], M.J. Woudstra[82], K.W. Wozniak[39], K. Wraight[53], M. Wright[53], B. Wrona[73], S.L. Wu[173], X. Wu[49], Y. Wu[33b,al], E. Wulf[35], B.M. Wynne[46], S. Xella[36], M. Xiao[136], S. Xie[48], C. Xu[33b,z], D. Xu[139], B. Yabsley[150], S. Yacoob[145a,am], M. Yamada[65], H. Yamaguchi[155], A. Yamamoto[65], K. Yamamoto[63], S. Yamamoto[155], T. Yamamura[155], T. Yamanaka[155], J. Yamaoka[45], T. Yamazaki[155], Y. Yamazaki[66], Z. Yan[22], H. Yang[87], U.K. Yang[82], Y. Yang[60], Z. Yang[146a,146b], S. Yanush[91], L. Yao[33a], Y. Yao[15], Y. Yasu[65], G.V. Ybeles Smit[130], J. Ye[40], S. Ye[25], M. Yilmaz[4c], R. Yoosoofmiya[123], K. Yorita[171], R. Yoshida[6], C. Young[143], C.J. Young[118], S. Youssef[22], D. Yu[25], J. Yu[8], J. Yu[112], L. Yuan[66], A. Yurkewicz[106], M. Byszewski[30], B. Zabinski[39], R. Zaidan[62], A.M. Zaitsev[128], Z. Zajacova[30], L. Zanello[132a,132b], D. Zanzi[99], A. Zaytsev[25], C. Zeitnitz[175], M. Zeman[125], A. Zemla[39], C. Zendler[21], O. Zenin[128], T. Ženiš[144a], Z. Zinonos[122a,122b], S. Zenz[15], D. Zerwas[115], G. Zevi della Porta[57], Z. Zhan[33d], D. Zhang[33b,ak], H. Zhang[88], J. Zhang[6], X. Zhang[33d], Z. Zhang[115], L. Zhao[108], T. Zhao[138], Z. Zhao[33b], A. Zhemchugov[64], J. Zhong[118], B. Zhou[87], N. Zhou[163], Y. Zhou[151], C.G. Zhu[33d], H. Zhu[42], J. Zhu[87], Y. Zhu[33b], X. Zhuang[98], V. Zhuravlov[99], D. Zieminska[60], N.I. Zimin[64], R. Zimmermann[21], S. Zimmermann[21], S. Zimmermann[48], M. Ziolkowski[141], R. Zitoun[5], L. Živković[35], V.V. Zmouchko[128,*], G. Zobernig[173], A. Zoccoli[20a,20b], M. zur Nedden[16], V. Zutshi[106], L. Zwalinski[30].

[1] *School of Chemistry and Physics, University of Adelaide, North Terrace Campus, 5000, SA, Australia*

[2] *Physics Department, SUNY Albany, Albany NY, United States of America*

[3] *Department of Physics, University of Alberta, Edmonton AB, Canada*

[4] [(a)] *Department of Physics, Ankara University, Ankara;* [(b)] *Department of Physics, Dumlupinar University, Kutahya;* [(c)] *Department of Physics, Gazi University, Ankara;* [(d)] *Division of Physics, TOBB University of Economics and Technology, Ankara;* [(e)] *Turkish Atomic Energy Authority, Ankara, Turkey*

[5] *LAPP, CNRS/IN2P3 and Université de Savoie, Annecy-le-Vieux, France*

[6] *High Energy Physics Division, Argonne National Laboratory, Argonne IL, United States of America*

[7] *Department of Physics, University of Arizona, Tucson AZ, United States of America*

[8] *Department of Physics, The University of Texas at Arlington, Arlington TX, United States of America*

[9] *Physics Department, University of Athens, Athens, Greece*

[10] *Physics Department, National Technical University of Athens, Zografou, Greece*

[11] *Institute of Physics, Azerbaijan Academy of Sciences, Baku, Azerbaijan*

[12] *Institut de Física d'Altes Energies and Departament de Física de la Universitat Autònoma de Barcelona and ICREA, Barcelona, Spain*

[13] [(a)] *Institute of Physics, University of Belgrade, Belgrade;* [(b)] *Vinca Institute of Nuclear Sciences, University of Belgrade, Belgrade, Serbia*

[14] *Department for Physics and Technology, University of Bergen, Bergen, Norway*

[15] *Physics Division, Lawrence Berkeley National Laboratory and University of California, Berkeley CA, United States of America*

[16] *Department of Physics, Humboldt University, Berlin, Germany*

[17] *Albert Einstein Center for Fundamental Physics and Laboratory for High Energy Physics, University of Bern, Bern, Switzerland*

[18] *School of Physics and Astronomy, University of Birmingham, Birmingham, United Kingdom*

[19] [(a)] *Department of Physics, Bogazici University, Istanbul;* [(b)] *Division of Physics, Dogus University, Istanbul;* [(c)] *Department of Physics Engineering, Gaziantep University, Gaziantep;* [(d)] *Department of Physics, Istanbul Technical University, Istanbul, Turkey*

JHEP12(2012)072

[20] [(a)] INFN Sezione di Bologna; [(b)] Dipartimento di Fisica, Università di Bologna, Bologna, Italy
[21] Physikalisches Institut, University of Bonn, Bonn, Germany
[22] Department of Physics, Boston University, Boston MA, United States of America
[23] Department of Physics, Brandeis University, Waltham MA, United States of America
[24] [(a)] Universidade Federal do Rio De Janeiro COPPE/EE/IF, Rio de Janeiro; [(b)] Federal University of Juiz de Fora (UFJF), Juiz de Fora; [(c)] Federal University of Sao Joao del Rei (UFSJ), Sao Joao del Rei; [(d)] Instituto de Fisica, Universidade de Sao Paulo, Sao Paulo, Brazil
[25] Physics Department, Brookhaven National Laboratory, Upton NY, United States of America
[26] [(a)] National Institute of Physics and Nuclear Engineering, Bucharest; [(b)] University Politehnica Bucharest, Bucharest; [(c)] West University in Timisoara, Timisoara, Romania
[27] Departamento de Física, Universidad de Buenos Aires, Buenos Aires, Argentina
[28] Cavendish Laboratory, University of Cambridge, Cambridge, United Kingdom
[29] Department of Physics, Carleton University, Ottawa ON, Canada
[30] CERN, Geneva, Switzerland
[31] Enrico Fermi Institute, University of Chicago, Chicago IL, United States of America
[32] [(a)] Departamento de Física, Pontificia Universidad Católica de Chile, Santiago; [(b)] Departamento de Física, Universidad Técnica Federico Santa María, Valparaíso, Chile
[33] [(a)] Institute of High Energy Physics, Chinese Academy of Sciences, Beijing; [(b)] Department of Modern Physics, University of Science and Technology of China, Anhui; [(c)] Department of Physics, Nanjing University, Jiangsu; [(d)] School of Physics, Shandong University, Shandong, China
[34] Laboratoire de Physique Corpusculaire, Clermont Université and Université Blaise Pascal and CNRS/IN2P3, Aubiere Cedex, France
[35] Nevis Laboratory, Columbia University, Irvington NY, United States of America
[36] Niels Bohr Institute, University of Copenhagen, Kobenhavn, Denmark
[37] [(a)] INFN Gruppo Collegato di Cosenza; [(b)] Dipartimento di Fisica, Università della Calabria, Arcavata di Rende, Italy
[38] AGH University of Science and Technology, Faculty of Physics and Applied Computer Science, Krakow, Poland
[39] The Henryk Niewodniczanski Institute of Nuclear Physics, Polish Academy of Sciences, Krakow, Poland
[40] Physics Department, Southern Methodist University, Dallas TX, United States of America
[41] Physics Department, University of Texas at Dallas, Richardson TX, United States of America
[42] DESY, Hamburg and Zeuthen, Germany
[43] Institut für Experimentelle Physik IV, Technische Universität Dortmund, Dortmund, Germany
[44] Institut für Kern- und Teilchenphysik, Technical University Dresden, Dresden, Germany
[45] Department of Physics, Duke University, Durham NC, United States of America
[46] SUPA - School of Physics and Astronomy, University of Edinburgh, Edinburgh, United Kingdom
[47] INFN Laboratori Nazionali di Frascati, Frascati, Italy
[48] Fakultät für Mathematik und Physik, Albert-Ludwigs-Universität, Freiburg, Germany
[49] Section de Physique, Université de Genève, Geneva, Switzerland
[50] [(a)] INFN Sezione di Genova; [(b)] Dipartimento di Fisica, Università di Genova, Genova, Italy
[51] [(a)] E. Andronikashvili Institute of Physics, Tbilisi State University, Tbilisi; [(b)] High Energy Physics Institute, Tbilisi State University, Tbilisi, Georgia
[52] II Physikalisches Institut, Justus-Liebig-Universität Giessen, Giessen, Germany
[53] SUPA - School of Physics and Astronomy, University of Glasgow, Glasgow, United Kingdom
[54] II Physikalisches Institut, Georg-August-Universität, Göttingen, Germany
[55] Laboratoire de Physique Subatomique et de Cosmologie, Université Joseph Fourier and CNRS/IN2P3 and Institut National Polytechnique de Grenoble, Grenoble, France
[56] Department of Physics, Hampton University, Hampton VA, United States of America
[57] Laboratory for Particle Physics and Cosmology, Harvard University, Cambridge MA, United States of America
[58] [(a)] Kirchhoff-Institut für Physik, Ruprecht-Karls-Universität Heidelberg, Heidelberg; [(b)] Physikalisches Institut, Ruprecht-Karls-Universität Heidelberg, Heidelberg; [(c)] ZITI Institut für technische Informatik, Ruprecht-Karls-Universität Heidelberg, Mannheim, Germany

JHEP12(2012)072

[59] Faculty of Applied Information Science, Hiroshima Institute of Technology, Hiroshima, Japan
[60] Department of Physics, Indiana University, Bloomington IN, United States of America
[61] Institut für Astro- und Teilchenphysik, Leopold-Franzens-Universität, Innsbruck, Austria
[62] University of Iowa, Iowa City IA, United States of America
[63] Department of Physics and Astronomy, Iowa State University, Ames IA, United States of America
[64] Joint Institute for Nuclear Research, JINR Dubna, Dubna, Russia
[65] KEK, High Energy Accelerator Research Organization, Tsukuba, Japan
[66] Graduate School of Science, Kobe University, Kobe, Japan
[67] Faculty of Science, Kyoto University, Kyoto, Japan
[68] Kyoto University of Education, Kyoto, Japan
[69] Department of Physics, Kyushu University, Fukuoka, Japan
[70] Instituto de Física La Plata, Universidad Nacional de La Plata and CONICET, La Plata, Argentina
[71] Physics Department, Lancaster University, Lancaster, United Kingdom
[72] [(a)] INFN Sezione di Lecce; [(b)] Dipartimento di Matematica e Fisica, Università del Salento, Lecce, Italy
[73] Oliver Lodge Laboratory, University of Liverpool, Liverpool, United Kingdom
[74] Department of Physics, Jožef Stefan Institute and University of Ljubljana, Ljubljana, Slovenia
[75] School of Physics and Astronomy, Queen Mary University of London, London, United Kingdom
[76] Department of Physics, Royal Holloway University of London, Surrey, United Kingdom
[77] Department of Physics and Astronomy, University College London, London, United Kingdom
[78] Laboratoire de Physique Nucléaire et de Hautes Energies, UPMC and Université Paris-Diderot and CNRS/IN2P3, Paris, France
[79] Fysiska institutionen, Lunds universitet, Lund, Sweden
[80] Departamento de Fisica Teorica C-15, Universidad Autonoma de Madrid, Madrid, Spain
[81] Institut für Physik, Universität Mainz, Mainz, Germany
[82] School of Physics and Astronomy, University of Manchester, Manchester, United Kingdom
[83] CPPM, Aix-Marseille Université and CNRS/IN2P3, Marseille, France
[84] Department of Physics, University of Massachusetts, Amherst MA, United States of America
[85] Department of Physics, McGill University, Montreal QC, Canada
[86] School of Physics, University of Melbourne, Victoria, Australia
[87] Department of Physics, The University of Michigan, Ann Arbor MI, United States of America
[88] Department of Physics and Astronomy, Michigan State University, East Lansing MI, United States of America
[89] [(a)] INFN Sezione di Milano; [(b)] Dipartimento di Fisica, Università di Milano, Milano, Italy
[90] B.I. Stepanov Institute of Physics, National Academy of Sciences of Belarus, Minsk, Republic of Belarus
[91] National Scientific and Educational Centre for Particle and High Energy Physics, Minsk, Republic of Belarus
[92] Department of Physics, Massachusetts Institute of Technology, Cambridge MA, United States of America
[93] Group of Particle Physics, University of Montreal, Montreal QC, Canada
[94] P.N. Lebedev Institute of Physics, Academy of Sciences, Moscow, Russia
[95] Institute for Theoretical and Experimental Physics (ITEP), Moscow, Russia
[96] Moscow Engineering and Physics Institute (MEPhI), Moscow, Russia
[97] Skobeltsyn Institute of Nuclear Physics, Lomonosov Moscow State University, Moscow, Russia
[98] Fakultät für Physik, Ludwig-Maximilians-Universität München, München, Germany
[99] Max-Planck-Institut für Physik (Werner-Heisenberg-Institut), München, Germany
[100] Nagasaki Institute of Applied Science, Nagasaki, Japan
[101] Graduate School of Science and Kobayashi-Maskawa Institute, Nagoya University, Nagoya, Japan
[102] [(a)] INFN Sezione di Napoli; [(b)] Dipartimento di Scienze Fisiche, Università di Napoli, Napoli, Italy
[103] Department of Physics and Astronomy, University of New Mexico, Albuquerque NM, United States of America

JHEP12(2012)072

[104] *Institute for Mathematics, Astrophysics and Particle Physics, Radboud University Nijmegen/Nikhef, Nijmegen, Netherlands*
[105] *Nikhef National Institute for Subatomic Physics and University of Amsterdam, Amsterdam, Netherlands*
[106] *Department of Physics, Northern Illinois University, DeKalb IL, United States of America*
[107] *Budker Institute of Nuclear Physics, SB RAS, Novosibirsk, Russia*
[108] *Department of Physics, New York University, New York NY, United States of America*
[109] *Ohio State University, Columbus OH, United States of America*
[110] *Faculty of Science, Okayama University, Okayama, Japan*
[111] *Homer L. Dodge Department of Physics and Astronomy, University of Oklahoma, Norman OK, United States of America*
[112] *Department of Physics, Oklahoma State University, Stillwater OK, United States of America*
[113] *Palacký University, RCPTM, Olomouc, Czech Republic*
[114] *Center for High Energy Physics, University of Oregon, Eugene OR, United States of America*
[115] *LAL, Université Paris-Sud and CNRS/IN2P3, Orsay, France*
[116] *Graduate School of Science, Osaka University, Osaka, Japan*
[117] *Department of Physics, University of Oslo, Oslo, Norway*
[118] *Department of Physics, Oxford University, Oxford, United Kingdom*
[119] [(a)] *INFN Sezione di Pavia;* [(b)] *Dipartimento di Fisica, Università di Pavia, Pavia, Italy*
[120] *Department of Physics, University of Pennsylvania, Philadelphia PA, United States of America*
[121] *Petersburg Nuclear Physics Institute, Gatchina, Russia*
[122] [(a)] *INFN Sezione di Pisa;* [(b)] *Dipartimento di Fisica E. Fermi, Università di Pisa, Pisa, Italy*
[123] *Department of Physics and Astronomy, University of Pittsburgh, Pittsburgh PA, United States of America*
[124] [(a)] *Laboratorio de Instrumentacao e Fisica Experimental de Particulas - LIP, Lisboa, Portugal;* [(b)] *Departamento de Fisica Teorica y del Cosmos and CAFPE, Universidad de Granada, Granada, Spain*
[125] *Institute of Physics, Academy of Sciences of the Czech Republic, Praha, Czech Republic*
[126] *Faculty of Mathematics and Physics, Charles University in Prague, Praha, Czech Republic*
[127] *Czech Technical University in Prague, Praha, Czech Republic*
[128] *State Research Center Institute for High Energy Physics, Protvino, Russia*
[129] *Particle Physics Department, Rutherford Appleton Laboratory, Didcot, United Kingdom*
[130] *Physics Department, University of Regina, Regina SK, Canada*
[131] *Ritsumeikan University, Kusatsu, Shiga, Japan*
[132] [(a)] *INFN Sezione di Roma I;* [(b)] *Dipartimento di Fisica, Università La Sapienza, Roma, Italy*
[133] [(a)] *INFN Sezione di Roma Tor Vergata;* [(b)] *Dipartimento di Fisica, Università di Roma Tor Vergata, Roma, Italy*
[134] [(a)] *INFN Sezione di Roma Tre;* [(b)] *Dipartimento di Fisica, Università Roma Tre, Roma, Italy*
[135] [(a)] *Faculté des Sciences Ain Chock, Réseau Universitaire de Physique des Hautes Energies - Université Hassan II, Casablanca;* [(b)] *Centre National de l'Energie des Sciences Techniques Nucleaires, Rabat;* [(c)] *Faculté des Sciences Semlalia, Université Cadi Ayyad, LPHEA-Marrakech;* [(d)] *Faculté des Sciences, Université Mohamed Premier and LPTPM, Oujda;* [(e)] *Faculté des sciences, Université Mohammed V-Agdal, Rabat, Morocco*
[136] *DSM/IRFU (Institut de Recherches sur les Lois Fondamentales de l'Univers), CEA Saclay (Commissariat a l'Energie Atomique), Gif-sur-Yvette, France*
[137] *Santa Cruz Institute for Particle Physics, University of California Santa Cruz, Santa Cruz CA, United States of America*
[138] *Department of Physics, University of Washington, Seattle WA, United States of America*
[139] *Department of Physics and Astronomy, University of Sheffield, Sheffield, United Kingdom*
[140] *Department of Physics, Shinshu University, Nagano, Japan*
[141] *Fachbereich Physik, Universität Siegen, Siegen, Germany*
[142] *Department of Physics, Simon Fraser University, Burnaby BC, Canada*

JHEP12(2012)072

[143] SLAC National Accelerator Laboratory, Stanford CA, United States of America
[144] [(a)] Faculty of Mathematics, Physics & Informatics, Comenius University, Bratislava; [(b)] Department of Subnuclear Physics, Institute of Experimental Physics of the Slovak Academy of Sciences, Kosice, Slovak Republic
[145] [(a)] Department of Physics, University of Johannesburg, Johannesburg; [(b)] School of Physics, University of the Witwatersrand, Johannesburg, South Africa
[146] [(a)] Department of Physics, Stockholm University; [(b)] The Oskar Klein Centre, Stockholm, Sweden
[147] Physics Department, Royal Institute of Technology, Stockholm, Sweden
[148] Departments of Physics & Astronomy and Chemistry, Stony Brook University, Stony Brook NY, United States of America
[149] Department of Physics and Astronomy, University of Sussex, Brighton, United Kingdom
[150] School of Physics, University of Sydney, Sydney, Australia
[151] Institute of Physics, Academia Sinica, Taipei, Taiwan
[152] Department of Physics, Technion: Israel Institute of Technology, Haifa, Israel
[153] Raymond and Beverly Sackler School of Physics and Astronomy, Tel Aviv University, Tel Aviv, Israel
[154] Department of Physics, Aristotle University of Thessaloniki, Thessaloniki, Greece
[155] International Center for Elementary Particle Physics and Department of Physics, The University of Tokyo, Tokyo, Japan
[156] Graduate School of Science and Technology, Tokyo Metropolitan University, Tokyo, Japan
[157] Department of Physics, Tokyo Institute of Technology, Tokyo, Japan
[158] Department of Physics, University of Toronto, Toronto ON, Canada
[159] [(a)] TRIUMF, Vancouver BC; [(b)] Department of Physics and Astronomy, York University, Toronto ON, Canada
[160] Institute of Pure and Applied Sciences, University of Tsukuba,1-1-1 Tennodai, Tsukuba, Ibaraki 305-8571, Japan
[161] Science and Technology Center, Tufts University, Medford MA, United States of America
[162] Centro de Investigaciones, Universidad Antonio Narino, Bogota, Colombia
[163] Department of Physics and Astronomy, University of California Irvine, Irvine CA, United States of America
[164] [(a)] INFN Gruppo Collegato di Udine; [(b)] ICTP, Trieste; [(c)] Dipartimento di Chimica, Fisica e Ambiente, Università di Udine, Udine, Italy
[165] Department of Physics, University of Illinois, Urbana IL, United States of America
[166] Department of Physics and Astronomy, University of Uppsala, Uppsala, Sweden
[167] Instituto de Física Corpuscular (IFIC) and Departamento de Física Atómica, Molecular y Nuclear and Departamento de Ingeniería Electrónica and Instituto de Microelectrónica de Barcelona (IMB-CNM), University of Valencia and CSIC, Valencia, Spain
[168] Department of Physics, University of British Columbia, Vancouver BC, Canada
[169] Department of Physics and Astronomy, University of Victoria, Victoria BC, Canada
[170] Department of Physics, University of Warwick, Coventry, United Kingdom
[171] Waseda University, Tokyo, Japan
[172] Department of Particle Physics, The Weizmann Institute of Science, Rehovot, Israel
[173] Department of Physics, University of Wisconsin, Madison WI, United States of America
[174] Fakultät für Physik und Astronomie, Julius-Maximilians-Universität, Würzburg, Germany
[175] Fachbereich C Physik, Bergische Universität Wuppertal, Wuppertal, Germany
[176] Department of Physics, Yale University, New Haven CT, United States of America
[177] Yerevan Physics Institute, Yerevan, Armenia
[178] Domaine scientifique de la Doua, Centre de Calcul CNRS/IN2P3, Villeurbanne Cedex, France

[a] Also at Laboratorio de Instrumentacao e Fisica Experimental de Particulas - LIP, Lisboa, Portugal
[b] Also at Faculdade de Ciencias and CFNUL, Universidade de Lisboa, Lisboa, Portugal
[c] Also at Particle Physics Department, Rutherford Appleton Laboratory, Didcot, United Kingdom

JHEP12(2012)072

[d] Also at TRIUMF, Vancouver BC, Canada
[e] Also at Department of Physics, California State University, Fresno CA, United States of America
[f] Also at Novosibirsk State University, Novosibirsk, Russia
[g] Also at Fermilab, Batavia IL, United States of America
[h] Also at Department of Physics, University of Coimbra, Coimbra, Portugal
[i] Also at Department of Physics, UASLP, San Luis Potosi, Mexico
[j] Also at Università di Napoli Parthenope, Napoli, Italy
[k] Also at Institute of Particle Physics (IPP), Canada
[l] Also at Department of Physics, Middle East Technical University, Ankara, Turkey
[m] Also at Louisiana Tech University, Ruston LA, United States of America
[n] Also at Dep Fisica and CEFITEC of Faculdade de Ciencias e Tecnologia, Universidade Nova de Lisboa, Caparica, Portugal
[o] Also at Department of Physics and Astronomy, University College London, London, United Kingdom
[p] Also at Group of Particle Physics, University of Montreal, Montreal QC, Canada
[q] Also at Department of Physics, University of Cape Town, Cape Town, South Africa
[r] Also at Institute of Physics, Azerbaijan Academy of Sciences, Baku, Azerbaijan
[s] Also at Institut für Experimentalphysik, Universität Hamburg, Hamburg, Germany
[t] Also at Manhattan College, New York NY, United States of America
[u] Also at School of Physics, Shandong University, Shandong, China
[v] Also at CPPM, Aix-Marseille Université and CNRS/IN2P3, Marseille, France
[w] Also at School of Physics and Engineering, Sun Yat-sen University, Guanzhou, China
[x] Also at Academia Sinica Grid Computing, Institute of Physics, Academia Sinica, Taipei, Taiwan
[y] Also at Dipartimento di Fisica, Università La Sapienza, Roma, Italy
[z] Also at DSM/IRFU (Institut de Recherches sur les Lois Fondamentales de l'Univers), CEA Saclay (Commissariat a l'Energie Atomique), Gif-sur-Yvette, France
[aa] Also at Section de Physique, Université de Genève, Geneva, Switzerland
[ab] Also at Departamento de Fisica, Universidade de Minho, Braga, Portugal
[ac] Also at Department of Physics and Astronomy, University of South Carolina, Columbia SC, United States of America
[ad] Also at Institute for Particle and Nuclear Physics, Wigner Research Centre for Physics, Budapest, Hungary
[ae] Also at California Institute of Technology, Pasadena CA, United States of America
[af] Also at Institute of Physics, Jagiellonian University, Krakow, Poland
[ag] Also at LAL, Université Paris-Sud and CNRS/IN2P3, Orsay, France
[ah] Also at Nevis Laboratory, Columbia University, Irvington NY, United States of America
[ai] Also at Department of Physics and Astronomy, University of Sheffield, Sheffield, United Kingdom
[aj] Also at Department of Physics, Oxford University, Oxford, United Kingdom
[ak] Also at Institute of Physics, Academia Sinica, Taipei, Taiwan
[al] Also at Department of Physics, The University of Michigan, Ann Arbor MI, United States of America
[am] Also at Discipline of Physics, University of KwaZulu-Natal, Durban, South Africa
[*] Deceased

JHEP12(2012)072

Flavor tagged time-dependent angular analysis of the $B_s^0 \to J/\psi\phi$ decay and extraction of $\Delta\Gamma_s$ and the weak phase ϕ_s in ATLAS

G. Aad *et al.*[*]
(ATLAS Collaboration)

(Received 8 July 2014; published 23 September 2014)

A measurement of the $B_s^0 \to J/\psi\phi$ decay parameters, updated to include flavor tagging is reported using 4.9 fb^{-1} of integrated luminosity collected by the ATLAS detector from $\sqrt{s} = 7$ TeV pp collisions recorded in 2011 at the LHC. The values measured for the physical parameters are

$$\begin{aligned}
\phi_s &= 0.12 \pm 0.25(\text{stat}) \pm 0.05(\text{syst}) \text{ rad} \\
\Delta\Gamma_s &= 0.053 \pm 0.021(\text{stat}) \pm 0.010(\text{syst}) \text{ ps}^{-1} \\
\Gamma_s &= 0.677 \pm 0.007(\text{stat}) \pm 0.004(\text{syst}) \text{ ps}^{-1} \\
|A_\parallel(0)|^2 &= 0.220 \pm 0.008(\text{stat}) \pm 0.009(\text{syst}) \\
|A_0(0)|^2 &= 0.529 \pm 0.006(\text{stat}) \pm 0.012(\text{syst}) \\
\delta_\perp &= 3.89 \pm 0.47(\text{stat}) \pm 0.11(\text{syst}) \text{ rad}
\end{aligned}$$

where the parameter $\Delta\Gamma_s$ is constrained to be positive. The S-wave contribution was measured and found to be compatible with zero. Results for ϕ_s and $\Delta\Gamma_s$ are also presented as 68% and 95% likelihood contours, which show agreement with the Standard Model expectations.

DOI: 10.1103/PhysRevD.90.052007 PACS numbers: 14.40.Nd

I. INTRODUCTION

New phenomena beyond the predictions of the Standard Model (SM) may alter CP violation in B-decays. A channel that is expected to be sensitive to new physics contributions is the decay $B_s^0 \to J/\psi\phi$. CP violation in the $B_s^0 \to J/\psi\phi$ decay occurs due to interference between direct decays and decays with $B_s^0 - \bar{B}_s^0$ mixing. The oscillation frequency of B_s^0 meson mixing is characterized by the mass difference Δm_s of the heavy (B_H) and light (B_L) mass eigenstates. The CP violating phase ϕ_s is defined as the weak phase difference between the $B_s^0 - \bar{B}_s^0$ mixing amplitude and the $b \to c\bar{c}s$ decay amplitude. In the absence of CP violation, the B_H state would correspond to the CP odd state and the B_L to the CP even state. In the SM the phase ϕ_s is small and can be related to Cabibbo-Kobayashi-Maskawa quark mixing matrix elements via the relation $\phi_s \simeq -2\beta_s$, with $\beta_s = \arg[-(V_{ts}V_{tb}^*)/(V_{cs}V_{cb}^*)]$; a value of $\phi_s \simeq -2\beta_s = -0.037 \pm 0.002$ rad [1] is predicted in the SM. Many new physics models predict large ϕ_s values while satisfying all existing constraints, including the precisely measured value of Δm_s [2,3].

Another physical quantity involved in $B_s^0 - \bar{B}_s^0$ mixing is the width difference $\Delta\Gamma_s = \Gamma_L - \Gamma_H$, which is predicted to be $\Delta\Gamma_s = 0.087 \pm 0.021$ ps^{-1} [4]. Physics beyond the SM is not expected to affect $\Delta\Gamma_s$ as significantly as ϕ_s [5]. Extracting $\Delta\Gamma_s$ from data is nevertheless useful as it allows theoretical predictions to be tested [5].

The decay of the pseudoscalar B_s^0 to the vector–vector final-state $J/\psi\phi$ results in an admixture of CP odd and CP even states, with orbital angular momentum $L = 0$, 1 or 2. The final states with orbital angular momentum $L = 0$ or 2 are CP even while the state with $L = 1$ is CP odd. Flavor tagging is used to distinguish between the initial B_s^0 and $\bar{B}_s^0$ states. The CP states are separated statistically using an angular analysis of the final-state particles.

In this paper, an update to the previous measurement [6] with the addition of flavor tagging is presented. Flavor tagging significantly reduces the uncertainty of the measured value of ϕ_s while also allowing a measurement of one of the strong phases. Previous measurements of these quantities have been reported by the D0, CDF and LHCb collaborations [7–9]. The analysis presented here uses 4.9 fb^{-1} of LHC pp data at $\sqrt{s} = 7$ TeV collected by the ATLAS detector in 2011.

II. ATLAS DETECTOR AND MONTE CARLO SIMULATION

The ATLAS experiment [10] is a multipurpose particle physics detector with a forward-backward symmetric cylindrical geometry and near 4π solid angle coverage. The inner tracking detector (ID) consists of a silicon pixel

[*] Full author list given at the end of the article.

detector, a silicon microstrip detector and a transition radiation tracker. The ID is surrounded by a thin superconducting solenoid providing a 2T axial magnetic field and by a high granularity liquid-argon sampling electromagnetic calorimeter. A steel/scintillator tile calorimeter provides hadronic coverage in the central rapidity range. The end cap and forward regions are instrumented with liquid-argon calorimeters for both electromagnetic and hadronic measurements. The muon spectrometer (MS) surrounds the calorimeters and consists of three large superconducting toroids with eight coils each, a system of tracking chambers, and detectors for triggering.

The muon and tracking systems are of particular importance in the reconstruction of B meson candidates. Only data for which both systems were operating correctly and for which the LHC beams were declared to be stable are used. A muon identified using a combination of MS and ID track parameters is referred to as *combined*. A muon formed by track segments which are not associated with an MS track, but which are matched to ID tracks extrapolated to the MS is referred to as *segment tagged*.

The data were collected during a period of rising instantaneous luminosity, and the trigger conditions varied over this time. The triggers used to select events for this analysis are based on identification of a $J/\psi \to \mu^+\mu^-$ decay, with either a 4 GeV transverse momentum [11] (p_{T}) threshold for each muon or an asymmetric configuration that applies a p_{T} threshold of 4 GeV to one of the muons while accepting a second muon with p_{T} as low as 2 GeV.

Monte Carlo (MC) simulation is used to study the detector response, estimate backgrounds and model systematic effects. For this study, 12 million MC-simulated $B_s^0 \to J/\psi\phi$ events were generated using PYTHIA 6 [12] tuned with recent ATLAS data [13]. No p_{T} cuts were applied at the generator level. Detector responses for these events were simulated using the ATLAS simulation package based on GEANT4 [14,15]. Pileup corresponding to the conditions during data taking was included. To take into account the varying trigger configurations during data taking, the MC events were weighted to have the same trigger composition as the collected collision data. Additional samples of the background decay $B^0 \to J/\psi K^{0*}$ as well as the more general $bb \to J/\psi X$ and $pp \to J/\psi X$ backgrounds were also simulated using PYTHIA.

III. RECONSTRUCTION AND CANDIDATE SELECTION

Events passing the trigger and the data quality selections described in Sec. II are required to pass the following additional criteria: the event must contain at least one reconstructed primary vertex, built from at least four ID tracks, and at least one pair of oppositely charged muon candidates that are reconstructed using information from the MS and the ID [16]. Both combined and segment tagged muons are used. In this analysis the muon track parameters are taken from the ID measurement alone, since the precision of the measured track parameters for muons in the p_{T} range of interest for this analysis is dominated by the ID track reconstruction. The pairs of muon tracks are refitted to a common vertex and accepted for further consideration if the fit results in $\chi^2/\mathrm{d.o.f.} < 10$. The invariant mass of the muon pair is calculated from the refitted track parameters. To account for varying mass resolution, the J/ψ candidates are divided into three subsets according to the pseudorapidity η of the muons. A maximum likelihood fit is used to extract the J/ψ mass and the corresponding resolution for these three subsets. When both muons have $|\eta| < 1.05$, the dimuon invariant mass must fall in the range (2.959–3.229) GeV to be accepted as a J/ψ candidate. When one muon has $1.05 < |\eta| < 2.5$ and the other muon $|\eta| < 1.05$, the corresponding signal region is (2.913–3.273) GeV. For the third subset, where both muons have $1.05 < |\eta| < 2.5$, the signal region is (2.852–3.332) GeV. In each case the signal region is defined so as to retain 99.8% of the J/ψ candidates identified in the fits.

The candidates for $\phi \to K^+K^-$ are reconstructed from all pairs of oppositely charged particles with $p_{\mathrm{T}} > 0.5$ GeV and $|\eta| < 2.5$ that are not identified as muons. Candidates for $B_s^0 \to J/\psi(\mu^+\mu^-)\phi(K^+K^-)$ are sought by fitting the tracks for each combination of $J/\psi \to \mu^+\mu^-$ and $\phi \to K^+K^-$ to a common vertex. Each of the four tracks is required to have at least one hit in the pixel detector and at least four hits in the silicon microstrip detector. The fit is further constrained by fixing the invariant mass calculated from the two muon tracks to the J/ψ mass [17]. These quadruplets of tracks are accepted for further analysis if the vertex fit has a $\chi^2/\mathrm{d.o.f.} < 3$, the fitted p_{T} of each track from $\phi \to K^+K^-$ is greater than 1 GeV and the invariant mass of the track pairs (under the assumption that they are kaons) falls within the interval $1.0085\ \mathrm{GeV} < m(K^+K^-) < 1.0305$ GeV. If there is more than one accepted candidate in the event, the candidate with the lowest $\chi^2/\mathrm{d.o.f.}$ is selected. In total 131513 B_s^0 candidates are collected within a mass range of $5.15 < m(B_s^0) < 5.65$ GeV.

For each B_s^0 meson candidate the proper decay time t is estimated by the expression

$$t = \frac{L_{xy} M_B}{p_{\mathrm{T}_B}},$$

where p_{T_B} is the reconstructed transverse momentum of the B_s^0 meson candidate and M_B denotes the world average mass value [17] of the B_s^0 meson. The transverse decay length, L_{xy}, is the displacement in the transverse plane of the B_s^0 meson decay vertex with respect to the primary vertex, projected onto the direction of the B_s^0 transverse momentum. The position of the primary vertex used to

calculate this quantity is refitted following the removal of the tracks used to reconstruct the B_s^0 meson candidate.

For the selected events the average number of pileup interactions is 5.6, necessitating a choice of the best candidate for the primary vertex at which the B_s^0 meson is produced. The variable used is the three-dimensional impact parameter d_0, which is calculated as the distance between the line extrapolated from the reconstructed B_s^0 meson vertex in the direction of the B_s^0 momentum and each primary vertex candidate. The chosen primary vertex is the one with the smallest d_0. Using MC simulation it is shown that the fraction of B_s^0 candidates which are assigned the wrong primary vertex is less than 1% and that the corresponding effect on the final results is negligible. No B_s^0 meson decay time cut is applied in the analysis.

IV. FLAVOR TAGGING

The determination of the initial flavor of neutral B-mesons can be inferred using information from the B-meson that is typically produced from the other b-quark in the event [18]. This is referred to as the opposite-side tagging (OST).

To study and calibrate the OST methods, events containing the decays of $B^\pm \to J/\psi K^\pm$ can be used, where flavor of the B-meson at production is provided by the kaon charge. Events from the entire 2011 run period satisfying the same data quality selections as described in Sec. II are used.

A. $B^\pm \to J/\psi K^\pm$ event selection

To be selected for use in the calibration analysis, events must satisfy a trigger condition requiring two oppositely charged muons within an invariant mass range around the nominal J/ψ mass. Candidate $B^\pm \to J/\psi K^\pm$ decays are identified using two oppositely charged combined muons forming a good vertex using information supplied by the inner detector. Each muon is required to have a transverse momentum of at least 4 GeV and pseudorapidity within $|\eta| < 2.5$. The invariant mass of the dimuon candidate is required to satisfy $2.8 < m(\mu^+\mu^-) < 3.4$ GeV. To form the B candidate an additional track with the charged kaon mass hypothesis, $p_{\mathrm{T}} > 1$ GeV and $|\eta| < 2.5$ is combined with the dimuon candidate, and a vertex fit is performed with the mass of the dimuon pair constrained to the known value of the J/ψ mass. To reduce the prompt component of the combinatorial background, the requirement $L_{xy} > 0.1$ mm is applied to the B candidate. The choice of primary vertex is determined using the same procedure as done for the B_s^0 candidates.

To study the distributions corresponding to the signal processes with the background component removed, a sideband subtraction method is defined. Events are separated into five equal regions of B candidate rapidity from 0–2.5 and three mass regions. The mass regions are defined as a signal region around the fitted peak signal mass position $\mu \pm 2\sigma$, and the sidebands are $[\mu - 5\sigma, \mu - 3\sigma]$ and $[\mu + 3\sigma, \mu + 5\sigma]$, where μ and σ are the mean and width of the Gaussian function describing the B signal mass, for each rapidity region. Individual binned extended maximum likelihood fits to the invariant mass distribution are performed in each region of rapidity.

The background is modelled by an exponential to describe combinatorial background and a hyperbolic tangent function to parametrize the low-mass contribution from incorrectly or partially reconstructed B decays. A Gaussian function is used to model the $B^\pm \to J/\psi\pi^\pm$ contribution. The contributions of noncombinatorial backgrounds are found to have a negligible effect in the tagging procedure. Figure 1 shows the invariant mass distribution of B candidates for all rapidity regions overlaid with the fit result for the combined data.

B. Tagging methods

Several methods are available to infer the flavor of the opposite-side b-quark, with varying efficiencies and discriminating powers. The measured charge of a muon from the semileptonic decay of the B meson provides strong separation power; however, the $b \to \mu$ transitions are diluted through neutral B meson oscillations, as well as by cascade decays $b \to c \to \mu$ which can alter the sign of the muon relative to the one from direct semileptonic decays $b \to \mu$. The separation power of tagging muons can be enhanced by considering a weighted sum of the charge of the tracks in a cone around the muon. If no muon is present, a weighted sum of the charge of tracks associated with the opposite-side

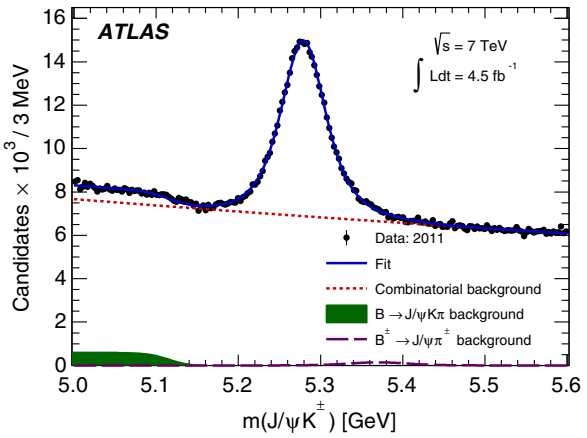

FIG. 1 (color online). The invariant mass distribution for $B^\pm \to J/\psi K^\pm$ candidates. Included in this plot are all events passing the selection criteria. The data are shown by points, and the overall result of the fit is given by the blue curve. The combinatorial background component is given by the red dotted line, partially reconstructed B decays by the green shaded area, and decays of $B^\pm \to J/\psi\pi^\pm$, where the pion is misassigned a kaon mass by a purple dashed line.

B meson decay will provide some separation. The tagging methods are described in detail below.

For muon-based tagging, an additional muon is required in the event, with $p_{\mathrm{T}} > 2.5$ GeV, $|\eta| < 2.5$ and with $|\Delta z| < 5$ mm from the primary vertex. Muons are classified according to their reconstruction class, combined or segment tagged and subsequently treated as distinct tagging methods. In the case of multiple muons, the muon with highest transverse momentum is selected.

A *muon cone charge* is defined as

$$Q_{\mu} = \frac{\sum_i^{N\mathrm{tracks}} q^i \cdot (p_{\mathrm{T}}^i)^{\kappa}}{\sum_i^{N\mathrm{tracks}} (p_{\mathrm{T}}^i)^{\kappa}},$$

where q is the charge of the track, $\kappa = 1.1$ and the sum is performed over the reconstructed ID tracks within a cone size of $\Delta R = 0.5$ [19] around the muon direction and the muon track is included as well. The reconstructed ID tracks must have a $p_{\mathrm{T}} > 0.5$ GeV and $|\eta| < 2.5$. The value of the parameter κ was determined while optimizing the tagging performance. Tracks associated with the signal decay are explicitly excluded from the sum. In Fig. 2 the opposite-side muon cone charge distributions are shown for candidates from $B^{\pm}$ signal decays. In the absence of a muon, a b-tagged jet [20] is required in the event, which is seeded from calorimeter clusters, with minimum energy threshold of 10 GeV, and where a minimum b-tag weight requirement of at least -0.5 is applied. The jet tracks are required to be associated with the same primary vertex as the signal decay, excluding those from the signal candidate. Jets within a cone of $\Delta R < 0.5$ of the signal momentum axis are excluded. The jet is reconstructed using the anti-k_t algorithm with a cone size of 0.6. In the case of multiple jets, the jet with the highest value of the b-tag weight is used.

A *jet charge* is defined as

$$Q_{\mathrm{jet}} = \frac{\sum_i^{N\mathrm{tracks}} q^i \cdot (p_T^i)^{\kappa}}{\sum_i^{N\mathrm{tracks}} (p_T^i)^{\kappa}},$$

where $\kappa = 1.1$, and the sum is over the tracks associated with the jet, using the method described in Ref. [21]. Figure 3 shows the distribution of charges for opposite-side jet charge from $B^{\pm}$ signal candidate events.

The efficiency ϵ of an individual tagger is defined as the ratio of the number of tagged events to the total number of candidates. A probability that a specific event has a signal decay containing a $\bar{b}$-quark given the value of the discriminating variable $P(B|Q)$ is constructed from the calibration samples for each of the B^+ and B^- samples, defining $P(Q|B^+)$ and $P(Q|B^-)$ respectively. The probability to tag a signal event as containing a $\bar{b}$-quark is therefore $P(B|Q) = P(Q|B^+)/(P(Q|B^+) + P(Q|B^-))$ and $P(\bar{B}|Q) = 1 - P(B|Q)$. The tagging power is defined as $\epsilon\mathcal{D}^2 = \sum_i \epsilon_i \cdot (2P_i(B|Q_i) - 1)^2$, where the sum is over the bins of the probability distribution as a function of the charge variable and ϵ_i is the number of tagged events in each bin divided by the total number of candidates. An

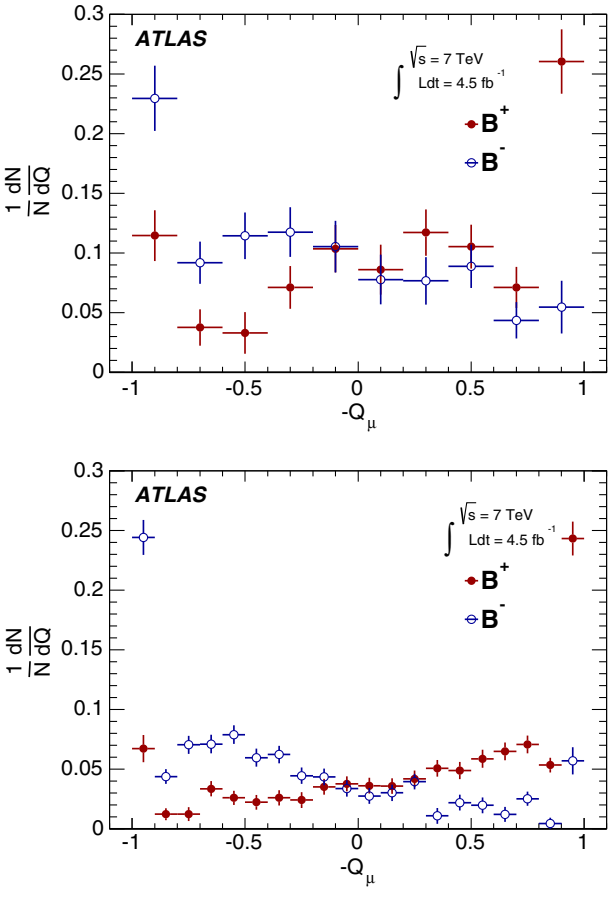

FIG. 2 (color online). The opposite-side muon cone charge distribution for $B^{\pm}$ signal candidates for segment tagged (top) and combined (bottom) muons.

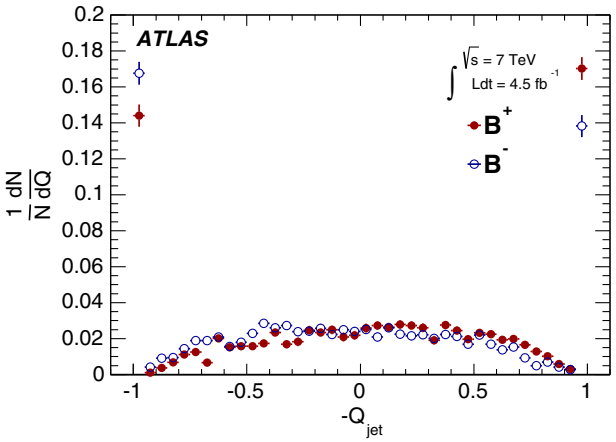

FIG. 3 (color online). Jet-charge distribution for $B^{\pm}$ signal candidates.

TABLE I. Summary of tagging performance for the different tagging methods described in the text. Uncertainties shown are statistical only. The efficiency and tagging power are each determined by summing over the individual bins of the charge distribution. The effective dilution is obtained from the measured efficiency and tagging power. The uncertainties are determined by combining the appropriate uncertainties on the individual bins of each charge distribution.

Tagger	Efficiency (%)	Dilution (%)	Tagging power (%)
Combined μ	3.37 ± 0.04	50.6 ± 0.5	0.86 ± 0.04
Segment tagged μ	1.08 ± 0.02	36.7 ± 0.7	0.15 ± 0.02
Jet charge	27.7 ± 0.1	12.68 ± 0.06	0.45 ± 0.03
Total	32.1 ± 0.1	21.3 ± 0.08	1.45 ± 0.05

effective dilution $\mathcal{D}$ is calculated from the tagging power and the efficiency.

The combination of the tagging methods is applied according to the hierarchy of performance, based on the dilution of the tagging method. The single best performing tagging measurement is taken, according to the order: combined muon cone charge, segment tagged muon cone charge, and jet charge. If it is not possible to provide a tagging response for the event, then a probability of 0.5 is assigned. A summary of the tagging performance is given in Table 1.

V. MAXIMUM LIKELIHOOD FIT

An unbinned maximum likelihood fit is performed on the selected events to extract the parameters of the $B_s^0 \to J/\psi(\mu^+\mu^-)\phi(K^+K^-)$ decay. The fit uses information about the reconstructed mass m and its uncertainty σ_m, the measured proper decay time t and its uncertainty σ_t, the tag probability, and the transversity angles Ω of each $B_s^0 \to J/\psi\phi$ decay candidate. There are three transversity angles; $\Omega = (\theta_T, \psi_T, \phi_T)$, and these are defined in Sec. V A.

The likelihood function is defined as a combination of the signal and background probability density functions as follows:

$$\begin{aligned}\ln \mathcal{L} = \sum_{i=1}^{N} \{ & w_i \cdot \ln(f_s \cdot \mathcal{F}_s(m_i, t_i, \Omega_i, P(B|Q)) \\ & + f_s \cdot f_{B^0} \cdot \mathcal{F}_{B^0}(m_i, t_i, \Omega_i, P(B|Q)) \\ & + (1 - f_s \cdot (1 + f_{B^0})) \cdot \mathcal{F}_{\rm bkg}(m_i, t_i, \Omega_i, P(B|Q))\}, \end{aligned} \quad (1)$$

where N is the number of selected candidates, w_i is a weighting factor to account for the trigger efficiency, f_s is the fraction of signal candidates and f_{B^0} is the fraction of B^0 ($B^0 \to J/\psi K^{0*}$ and $B^0 \to J/\psi K^{\pm}\pi^{\mp}$) mesons misidentified as B_s^0 candidates calculated relative to the number of signal events; this parameter is fixed in the likelihood fit. The mass m_i, the proper decay time t_i and the decay angles Ω_i are the values measured from the data for each event i. $\mathcal{F}_s$, $\mathcal{F}_{B^0}$ and $\mathcal{F}_{\rm bkg}$ are the probability density functions (PDF) modelling the signal, the specific B^0 background and the other background distributions, respectively. A detailed description of the signal PDF terms in Eq. (1) is given in Sec. V A. The two background functions are, with the exception of new terms dependent on $P(B|Q)$ which are explained in Sec. V B, unchanged from the previous analysis [6]. They are each described by the product of eight terms which describe the distribution of each measured parameter. With the exception of the lifetime and its uncertainty the background parameters are assumed uncorrelated.

A. Signal PDF

The PDF describing the signal events, $\mathcal{F}_s$, has the form of a product of PDFs for each quantity measured from the data:

$$\begin{aligned}\mathcal{F}_s(m_i, t_i, \Omega_i, P(B|Q)) = & P_s(m_i, \sigma_{m_i}) \cdot P_s(\sigma_{m_i}) \\ & \cdot P_s(\Omega_i, t_i, P(B|Q), \sigma_{t_i}) \cdot P_s(\sigma_{t_i}) \\ & \cdot P_s(P(B|Q)) \cdot A(\Omega_i, p_{{\rm T}i}) \cdot P_s(p_{{\rm T}i}).\end{aligned}$$

The terms $P_s(m_i, \sigma_{m_i})$, $P_s(\Omega_i, t_i, P(B|Q), \sigma_{t_i})$ and $A(\Omega_i, p_{{\rm T}i})$ are explained in the current section. The tagging probability term $P_s(P(B|Q))$ is described in Sec. V B. The remaining probability terms $P_s(\sigma_{m_i})$, $P_s(\sigma_{t_i})$ and $P_s(p_{{\rm T}i})$ are described by Gamma functions. They are unchanged from the previous analysis and explained in detail in Ref. [6]. Ignoring detector effects, the joint distribution for the decay time t and the transversity angles Ω for the $B_s^0 \to J/\psi(\mu^+\mu^-)\phi(K^+K^-)$ decay is given by the differential decay rate [22]:

$$\frac{d^4\Gamma}{dt d\Omega} = \sum_{k=1}^{10} \mathcal{O}^{(k)}(t) g^{(k)}(\theta_T, \psi_T, \phi_T),$$

where $\mathcal{O}^{(k)}(t)$ are the time-dependent amplitudes and $g^{(k)}(\theta_T, \psi_T, \phi_T)$ are the angular functions, given in Table II. The formulas for the time-dependent amplitudes have the same structure for B_s^0 and $\bar{B}_s^0$ but with a sign reversal in the terms containing Δm_s. The addition of flavor tagging to the analysis means that these terms no longer cancel, so there are more terms in the fit that contain ϕ_s. In addition to this, the strong phase variable $\delta_\perp$ becomes accessible, and one of the symmetries in the untagged fit is removed. $A_\perp(t)$ describes a CP odd final-state configuration while both $A_0(t)$ and $A_\parallel(t)$ correspond to CP even final-state configurations. $A_S(t)$ describes the contribution of the CP odd nonresonant $B_s^0 \to J/\psi K^+K^-$ S-wave state

TABLE II. Table showing the ten time-dependent amplitudes, $\mathcal{O}^{(k)}(t)$ and the functions of the transversity angles $g^{(k)}(\theta_T, \psi_T, \phi_T)$. The amplitudes $|A_0(0)|^2$ and $|A_\parallel(0)|^2$ are for the CP even components of the $B_s^0 \to J/\psi\phi$ decay, and $|A_\perp(0)|^2$ is the CP odd amplitude; they have corresponding strong phases δ_0, $\delta_\parallel$ and $\delta_\perp$, and by convention δ_0 is set to be zero. The S-wave amplitude $|A_S(0)|^2$ gives the fraction of $B_s^0 \to J/\psi K^+K^-(f_0)$ and has a related strong phase δ_S. The $\pm$ and $\mp$ terms denote two cases: the upper sign describes the decay of a meson that was initially a B_s^0, while the lower sign describes the decays of a meson that was initially $\bar{B}_s^0$.

k	$\mathcal{O}^{(k)}(t)$	$g^{(k)}(\theta_T, \psi_T, \phi_T)$
1	$\frac{1}{2}\lvert A_0(0)\rvert^2[(1+\cos\phi_s)e^{-\Gamma_{\rm L}^{(s)}t} + (1-\cos\phi_s)e^{-\Gamma_{\rm H}^{(s)}t} \pm 2e^{-\Gamma_s t}\sin(\Delta m_s t)\sin\phi_s]$	$2\cos^2\psi_T(1-\sin^2\theta_T\cos^2\phi_T)$
2	$\frac{1}{2}\lvert A_\parallel(0)\rvert^2[(1+\cos\phi_s)e^{-\Gamma_{\rm L}^{(s)}t} + (1-\cos\phi_s)e^{-\Gamma_{\rm H}^{(s)}t} \pm 2e^{-\Gamma_s t}\sin(\Delta m_s t)\sin\phi_s]$	$\sin^2\psi_T(1-\sin^2\theta_T\sin^2\phi_T)$
3	$\frac{1}{2}\lvert A_\perp(0)\rvert^2[(1-\cos\phi_s)e^{-\Gamma_{\rm L}^{(s)}t} + (1+\cos\phi_s)e^{-\Gamma_{\rm H}^{(s)}t} \mp 2e^{-\Gamma_s t}\sin(\Delta m_s t)\sin\phi_s]$	$\sin^2\psi_T\sin^2\theta_T$
4	$\frac{1}{2}\lvert A_0(0)\rvert\lvert A_\parallel(0)\rvert\cos\delta_\parallel$ $[(1+\cos\phi_s)e^{-\Gamma_{\rm L}^{(s)}t} + (1-\cos\phi_s)e^{-\Gamma_{\rm H}^{(s)}t} \pm 2e^{-\Gamma_s t}\sin(\Delta m_s t)\sin\phi_s]$	$-\frac{1}{\sqrt{2}}\sin 2\psi_T\sin^2\theta_T\sin 2\phi_T$
5	$\lvert A_\parallel(0)\rvert\lvert A_\perp(0)\rvert[\frac{1}{2}(e^{-\Gamma_{\rm L}^{(s)}t} - e^{-\Gamma_{\rm H}^{(s)}t})\cos(\delta_\perp-\delta_\parallel)\sin\phi_s$ $\pm e^{-\Gamma_s t}(\sin(\delta_\perp-\delta_\parallel)\cos(\Delta m_s t) - \cos(\delta_\perp-\delta_\parallel)\cos\phi_s\sin(\Delta m_s t))]$	$\sin^2\psi_T\sin 2\theta_T\sin\phi_T$
6	$\lvert A_0(0)\rvert\lvert A_\perp(0)\rvert[\frac{1}{2}(e^{-\Gamma_{\rm L}^{(s)}t} - e^{-\Gamma_{\rm H}^{(s)}t})\cos\delta_\perp\sin\phi_s$ $\pm e^{-\Gamma_s t}(\sin\delta_\perp\cos(\Delta m_s t) - \cos\delta_\perp\cos\phi_s\sin(\Delta m_s t))]$	$\frac{1}{\sqrt{2}}\sin 2\psi_T\sin 2\theta_T\cos\phi_T$
7	$\frac{1}{2}\lvert A_S(0)\rvert^2[(1-\cos\phi_s)e^{-\Gamma_{\rm L}^{(s)}t} + (1+\cos\phi_s)e^{-\Gamma_{\rm H}^{(s)}t} \mp 2e^{-\Gamma_s t}\sin(\Delta m_s t)\sin\phi_s]$	$\frac{2}{3}(1-\sin^2\theta_T\cos^2\phi_T)$
8	$\lvert A_S(0)\rvert\lvert A_\parallel(0)\rvert[\frac{1}{2}(e^{-\Gamma_{\rm L}^{(s)}t} - e^{-\Gamma_{\rm H}^{(s)}t})\sin(\delta_\parallel-\delta_S)\sin\phi_s$ $\pm e^{-\Gamma_s t}(\cos(\delta_\parallel-\delta_S)\cos(\Delta m_s t) - \sin(\delta_\parallel-\delta_S)\cos\phi_s\sin(\Delta m_s t))]$	$\frac{1}{3}\sqrt{6}\sin\psi_T\sin^2\theta_T\sin 2\phi_T$
9	$\frac{1}{2}\lvert A_S(0)\rvert\lvert A_\perp(0)\rvert\sin(\delta_\perp-\delta_S)$ $[(1-\cos\phi_s)e^{-\Gamma_{\rm L}^{(s)}t} + (1+\cos\phi_s)e^{-\Gamma_{\rm H}^{(s)}t} \mp 2e^{-\Gamma_s t}\sin(\Delta m_s t)\sin\phi_s]$	$\frac{1}{3}\sqrt{6}\sin\psi_T\sin 2\theta_T\cos\phi_T$
10	$\lvert A_0(0)\rvert\lvert A_S(0)\rvert[\frac{1}{2}(e^{-\Gamma_{\rm H}^{(s)}t} - e^{-\Gamma_{\rm L}^{(s)}t})\sin\delta_S\sin\phi_s$ $\pm e^{-\Gamma_s t}(\cos\delta_S\cos(\Delta m_s t) + \sin\delta_S\cos\phi_s\sin(\Delta m_s t))]$	$\frac{4}{3}\sqrt{3}\cos\psi_T(1-\sin^2\theta_T\cos^2\phi_T)$

as well as the $B_s^0 \to J/\psi f_0$ decays. The corresponding amplitudes are given in the last four lines of Table II ($k = 7$–10) and follow the convention used in the previous analysis [23]. The likelihood is independent of the K^+K^- mass distribution.

The equations are normalized, such that the squares of the amplitudes sum to unity; three of the four amplitudes are fit parameters, and $|A_\perp(0)|^2$ is determined according to this constraint.

The angles $(\theta_T, \psi_T, \phi_T)$ are defined in the rest frames of the final-state particles. The x axis is determined by the direction of the ϕ meson in the J/ψ rest frame, and the K^+K^- system defines the x–y plane, where $p_y(K^+) > 0$. The three angles are defined as follows:

(i) θ_T, the angle between $\vec{p}(\mu^+)$ and the normal to the x–y plane, in the J/ψ meson rest frame.
(ii) ϕ_T, the angle between the x axis and $\vec{p}_{xy}(\mu^+)$, the projection of the μ^+ momentum in the x–y plane, in the J/ψ meson rest frame.
(iii) ψ_T, the angle between $\vec{p}(K^+)$ and $-\vec{p}(J/\psi)$ in the ϕ meson rest frame.

The signal PDF, $P_s(\Omega, t, P(B|Q), \sigma_t)$, needs to take into account lifetime resolution, so each time element in Table II is smeared with a Gaussian function. This smearing is done numerically on an event-by-event basis where the width of the Gaussian function is the proper decay time uncertainty, measured for each event, multiplied by a scale factor to account for any mismeasurements.

The angular sculpting of the detector and kinematic cuts on the angular distributions are included in the likelihood function through $A(\Omega_i, p_{Ti})$. This is calculated using a four-dimensional binned acceptance method, applying an event-by-event efficiency according to the transversity angles $(\theta_T, \psi_T, \phi_T)$ and the $p_{\rm T}$ of the candidate. The $p_{\rm T}$ binning is necessary, because the angular sculpting is influenced by the $p_{\rm T}$ of the B_s^0. The acceptance was calculated from the $B_s^0 \to J/\psi\phi$ MC events. In the likelihood function, the acceptance is treated as an angular sculpting PDF, which is multiplied with the time- and angular-dependent PDF describing the $B_s^0 \to J/\psi(\mu^+\mu^-)\phi(K^+K^-)$ decays. As both the acceptance and time-angular decay PDFs depend on the transversity angles they must be normalized together. This normalization is done numerically during the likelihood fit.

The signal mass function, $P_s(m)$, is modelled using a single Gaussian function smeared with an event-by-event mass resolution. The PDF is normalized over the range $5.15 < m(B_s^0) < 5.65$ GeV.

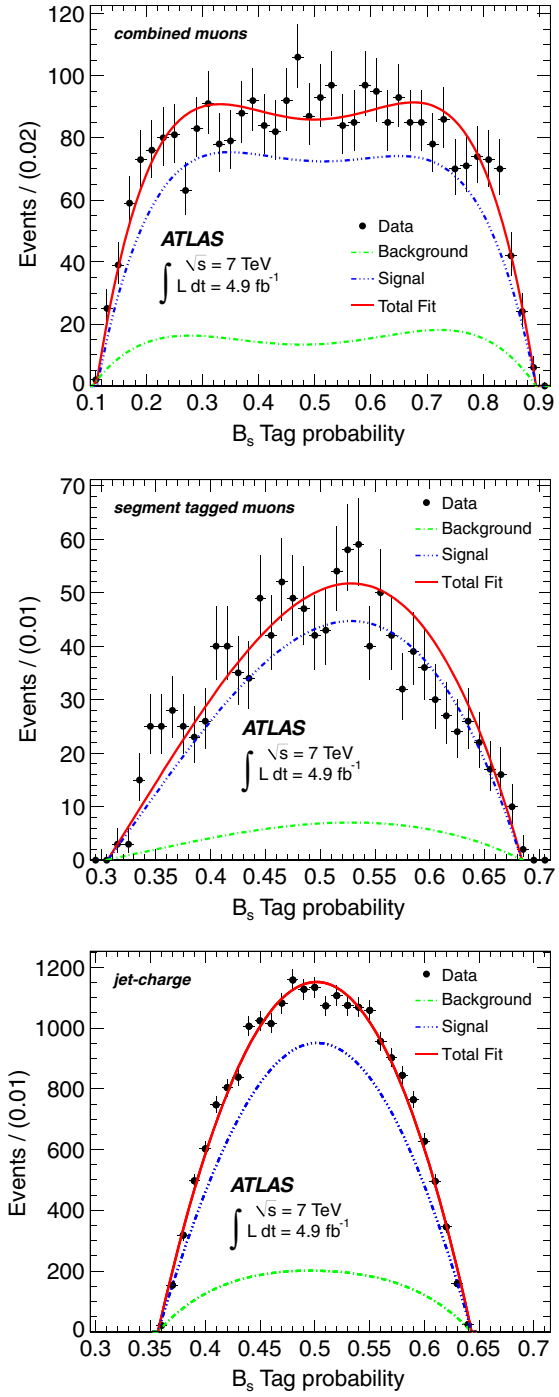

FIG. 4 (color online). The B_s^0-tag probability distribution for the events tagged with combined muons (top), segment tagged muons (middle) and jet charge (bottom). Black dots are data after removing spikes, blue is the fit to the sidebands, green is to the signal, and red is a sum of both fits.

B. Using tag information in the fit

The tag probability for each B_s^0 candidate is determined from a weighted sum of charged-particle tracks in a cone, as described in Sec. IV. The tag probability is obtained from this tag charge using the calibrations measured in the $B^{\pm} \to J/\psi K^{\pm}$ data. For the case where there is only one track, the cone charge can only be ± 1. This leads to a tag probability distribution with continuous and discrete parts (spikes), which are estimated separately. The distributions of tag probabilities for the signal and background are also different, and since the background cannot be factorized out, extra PDF terms are included to account for this difference. For each event with a given B_s^0 tag probability $P(B|Q)$, a relative PDF factor, $P_{S/B}(P(B|Q))$, that this is a signal or a background event is calculated using the parametrizations of the continuous parts, shown in Fig. 4. In the case of the spikes the relative PDF factor is calculated as given in Table III.

To describe the continuous parts, the sidebands are parametrized first. Sidebands are selected according to B_s^0 mass, i.e. $m(B_s^0) < 5.317$ GeV or $m(B_s^0) > 5.417$ GeV. In the fit the same function as for the sidebands is used to describe events in the signal region: background parameters are fixed to the values obtained in sidebands while signal parameters are free in this step. The ratio of background to signal (obtained from simultaneous mass–lifetime fit) is fixed as well. The function describing tagging using combined muons has the form of a fourth-order Chebychev polynomial. A third-order polynomial is used for the segment tagged muons' tagging algorithm. A fourth-order Chebychev polynomial is also applied for the jet charge tagging algorithm. In all three cases unbinned maximum likelihood fits are used. Results of fits projected on histograms are shown in Fig. 4.

The spikes have their origin in tagging objects formed from a single track, providing a tag charge of exactly $+1$ or -1. When a background candidate is formed from a random combination of a J/ψ and a pair of tracks, the positive and negative charges are equally probable. However, some of the background events are formed of partially reconstructed B hadrons, and in these cases tag charges of $+1$ or -1 are not equally probable. For signal events the tag charges are obviously not symmetric. The fractions f_{+1} and f_{-1} of events tagged with charges of $+1$ and -1 are derived separately for signal and background. The remaining $(1 - f_{+1} - f_{-1})$ is the fraction of events in the continuous region. The fractions f_{+1} and f_{-1} are determined using the same B_s^0 mass sidebands and signal regions as in case of continuous parts. Table III summarizes the obtained relative probabilities between tag charges $+1$ and -1 for signal and background events and for all tag methods.

Similarly, the sideband subtraction method is also used to determine, for signal and background events, the relative fraction of each tagging method. The results are summarized in Table IV.

If the tag-probability PDFs were ignored in the likelihood fit, equivalent to assuming identical signal and background behavior, the impact on the fit result would

TABLE III. Table summarizing the obtained relative probabilities between tag charges $+1$ and -1 for signal and background events for the different tagging methods. Only statistical errors are quoted. The asymmetry in the signal combined-muon tagging method has no impact on the results as it affects only 1% of the signal events (in addition to the negligible effect of the tag-probability distributions themselves).

	Signal		Background	
Tag method	f_{+1}	f_{-1}	f_{+1}	f_{-1}
Combined μ	0.106 ± 0.019	0.187 ± 0.022	0.098 ± 0.006	0.108 ± 0.006
Segment tag μ	0.152 ± 0.043	0.153 ± 0.043	0.098 ± 0.009	0.095 ± 0.008
Jet charge	0.167 ± 0.010	0.164 ± 0.010	0.176 ± 0.003	0.180 ± 0.003

TABLE IV. Table summarizing the relative population of the tagging methods in the background and signal events. Only statistical errors are quoted.

Tag method	Signal	Background
Combined μ	0.0372 ± 0.0023	0.0272 ± 0.0005
Segment tag μ	0.0111 ± 0.0014	0.0121 ± 0.0003
Jet charge	0.277 ± 0.007	0.254 ± 0.002
Untagged	0.675 ± 0.011	0.707 ± 0.003

TABLE V. Fitted values for the physical parameters with their statistical and systematic uncertainties. For the parameters $\delta_\parallel$ and $\delta_\perp - \delta_S$ a 68% confidence level interval is given. The reason for this is described in Sec. VIII.

Parameter	Value	Statistical uncertainty	Systematic uncertainty
ϕ_s [rad]	0.12	0.25	0.05
$\Delta\Gamma_s$[ps^{-1}]	0.053	0.021	0.010
Γ_s [ps^{-1}]	0.677	0.007	0.004
$\lvert A_\parallel(0)\rvert^2$	0.220	0.008	0.009
$\lvert A_0(0)\rvert^2$	0.529	0.006	0.012
$\lvert A_S(0)\rvert^2$	0.024	0.014	0.028
$\delta_\perp$	3.89	0.47	0.11
$\delta_\parallel$		[3.04, 3.23]	0.09
$\delta_\perp - \delta_S$		[3.02, 3.25]	0.04

be small, affecting the results by less than 10% of the statistical uncertainty.

VI. RESULTS

The full simultaneous maximum likelihood fit contains 25 free parameters. These include the nine physics parameters: $\Delta\Gamma_s$, ϕ_s, Γ_s, $|A_0(0)|^2$, $|A_\parallel(0)|^2$, $\delta_\parallel$, $\delta_\perp$, $|A_S|^2$ and δ_S. The other parameters in the likelihood function are the B_s^0 signal fraction f_s, the parameters describing the $J/\psi\phi$ mass distribution, the parameters describing the B_s^0 meson decay time plus angular distributions of background events, the parameters used to describe the estimated decay time uncertainty distributions for signal and background events, and scale factors between the estimated decay time and mass uncertainties and their true uncertainties.

The number of signal B_s^0 meson candidates extracted from the fits is 22670 ± 150. The results and correlations for the measured physics parameters of the simultaneous unbinned maximum likelihood fit are given in Tables V and VI. Fit projections of the mass, proper decay time and angles are given in Figs. 5 and 6 respectively.

VII. SYSTEMATIC UNCERTAINTIES

Systematic uncertainties are assigned by considering several effects that are not accounted for in the likelihood fit. These are described below:

(i) *Inner detector alignment:* Residual misalignments of the inner detector affect the impact parameter

TABLE VI. Correlations between the physics parameters. The physics parameters are, in general, uncorrelated to the remaining nuisance parameters in the fit. There are a few exceptions, but no correlation is greater than 0.12.

	ϕ_s	$\Delta\Gamma$	Γ_s	$\lvert A_\parallel(0)\rvert^2$	$\lvert A_0(0)\rvert^2$	$\lvert A_S(0)\rvert^2$	$\delta_\parallel$	$\delta_\perp$	$\delta_\perp - \delta_S$
ϕ_s	1.000	0.107	0.026	0.010	0.002	0.029	0.021	−0.043	−0.003
$\Delta\Gamma$		1.000	−0.617	0.105	0.103	0.069	0.006	−0.017	0.001
Γ_s			1.000	−0.093	−0.063	0.034	−0.003	0.001	−0.009
$\lvert A_\parallel(0)\rvert^2$				1.000	−0.316	0.077	0.008	0.005	−0.010
$\lvert A_0(0)\rvert^2$					1.000	0.283	−0.003	−0.016	−0.025
$\lvert A_S(0)\rvert^2$						1.000	−0.011	−0.054	−0.098
$\delta_\parallel$							1.000	0.038	0.007
$\delta_\perp$								1.000	0.081
$\delta_\perp - \delta_S$									1.000

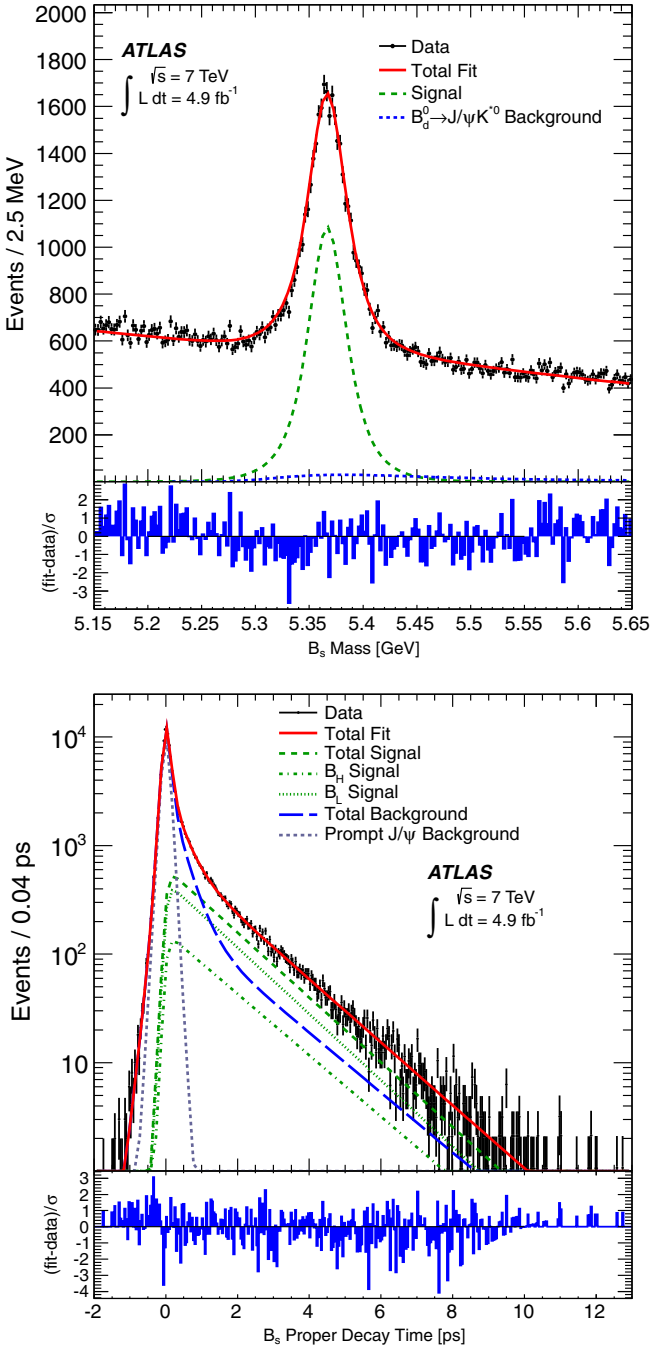

FIG. 5 (color online). (Top) Mass fit projection for the $B_s^0 \to J/\psi\phi$. The red line shows the total fit, the dashed green line shows the signal component while the dotted blue line shows the contribution from $B^0 \to J/\psi K^{0*}$ events. (Bottom) Proper decay time fit projection for the $B_s^0 \to J/\psi\phi$. The red line shows the total fit while the green dashed line shows the total signal. The light and heavy components of the signal are shown in green as a dotted and a dash-dotted line, respectively. The total background is shown as a blue dashed line with a grey dotted line showing the prompt J/ψ background. The pull distributions at the bottom show the difference between data and fit value normalized to the data statistical uncertainty.

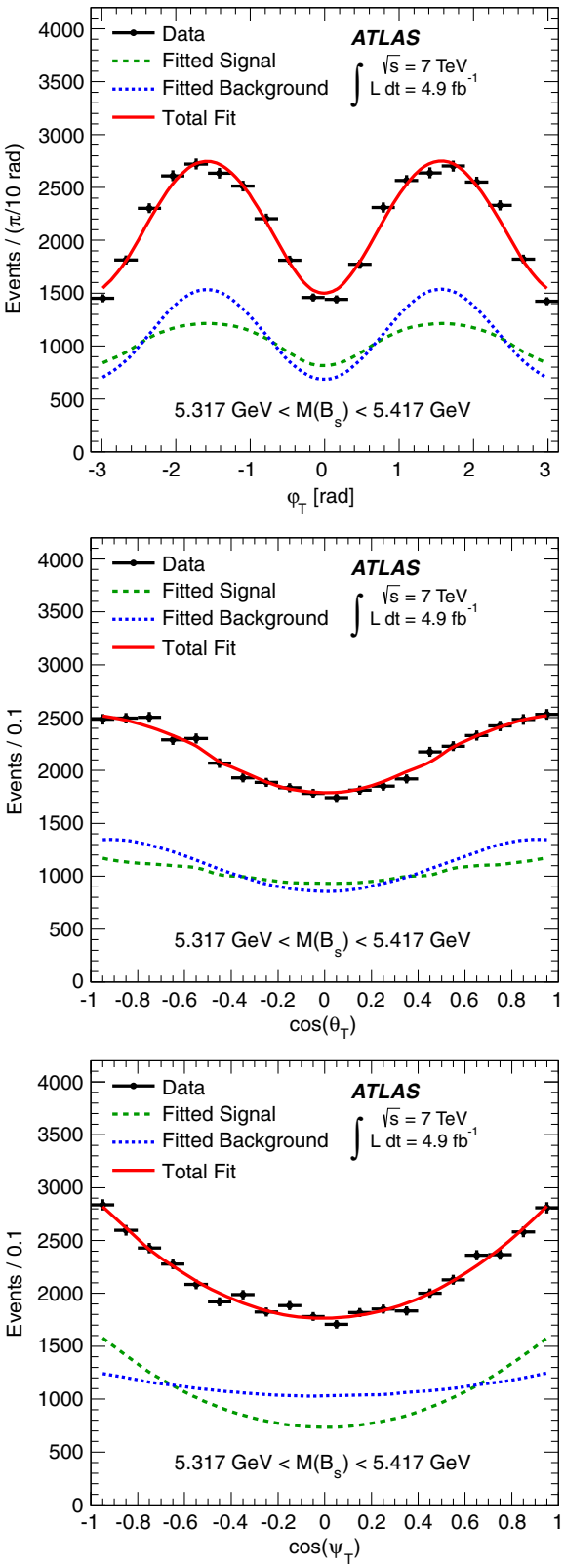

FIG. 6 (color online). Fit projections for transversity angles. (Top) ϕ_T, (middle) $\cos\theta_T$, (bottom) $\cos\psi_T$. In all three plots, the red line shows the total fit, the dashed green line shows the signal component, and the dotted blue line shows the background contribution.

distribution with respect to the primary vertex. The effect of the residual misalignment is estimated using simulated events with and without distorted geometry. For this, the impact parameter distribution with respect to the primary vertex is measured with data as a function of η and ϕ with the maximum deviation from zero being less than 10 μm. The measurement is used to distort the geometry for simulated events in order to reproduce the impact parameter distribution measured as a function of η and ϕ. The difference between the measurement using simulated events with and without the distorted geometry is used as the systematic uncertainty.

(ii) *Trigger efficiency:* It is observed that the muon trigger biases the transverse impact parameter of muons toward smaller values. To correct for this bias the events are reweighted according to

$$w = e^{-|t|/(\tau_{\rm sing}+\epsilon)}/e^{-|t|/\tau_{\rm sing}},$$

where $\tau_{\rm sing}$ is a single B_s^0 lifetime measured before the correction, using an unbinned mass–lifetime maximum likelihood fit. The value of the parameter ϵ and its uncertainty are described in Ref. [6]. The systematic uncertainty is calculated by varying the value of ϵ by its uncertainty and rerunning the fit.

(iii) B^0 *contribution:* Contaminations from $B^0 \to J/\psi K^{0*}$ and $B^0 \to J/\psi K\pi$ events misreconstructed as $B_s^0 \to J/\psi\phi$ are accounted for in the default fit. The fractions of $B^0 \to J/\psi K^{0*}$ and $B^0 \to J/\psi K\pi$ events in the default fit are $(6.5 +/- 2.4)\%$ and $(4.5 +/- 2.8)\%$ respectively. They were determined in MC simulation and using branching fractions from Ref. [17]. To estimate the systematic uncertainty arising from the precision of the fraction estimates, the data are fitted with these fractions increased and decreased by 1σ. The largest shifts in the fitted values from the default case are taken as the systematic uncertainty for each parameter of interest.

(iv) *Tagging:* For the uncertainties in the fit parameters due to uncertainty in the tagging, the statistical and systematic components are separated. The statistical uncertainty is due to the sample size of $B^{\pm} \to J/\psi K^{\pm}$ decays available and is included in the overall statistical error. The systematic uncertainty arises from the precision of the tagging calibration and is estimated by varying the model parametrizing the probability distribution, $P(B|Q)$, as a function of tag charge. The default model is a linear function. For the combined-muon cone-charge tag and the segment tagged muons the alternative fit function is a third-order polynomial. For the jet-charge tag with no muons, a third- and a fifth-order polynomial are used. The B_s^0 fit was repeated using the alternative models, and the largest difference was assigned as the systematic uncertainty.

(v) *Angular acceptance method:* The angular acceptance is calculated from a binned fit to Monte Carlo data. A separate set of Monte Carlo signal events were generated and fully simulated. Background was generated using pseudoexperiments as described below. There is sufficient data to perform 166 fits. The systematic uncertainty is calculated using the bias of the pull distribution multiplied by the statistical uncertainty of each parameter. To estimate the size of the systematic uncertainty introduced from the choice of binning, different acceptance functions are calculated using different bin widths and central values. These effects are found to be negligible.

(vi) *Signal and background mass model, resolution model, background lifetime and background angles model:* To estimate the size of systematic uncertainties caused by the assumptions made in the fit model, variations of the model are tested in pseudoexperiments. A set of 2400 pseudoexperiments is generated for each variation considered and fitted with the default model. The systematic error quoted for each effect is the difference between the mean shift of

TABLE VII. Summary of systematic uncertainties assigned to the physics parameters.

	ϕ_s [rad]	$\Delta\Gamma_s$ [ps^{-1}]	Γ_s [ps^{-1}]	$\lvert A_\parallel(0)\rvert^2$	$\lvert A_0(0)\rvert^2$	$\lvert A_S(0)\rvert^2$	$\delta_\perp$ [rad]	$\delta_\parallel$ [rad]	$\delta_\perp - \delta_S$ [rad]
ID alignment	$<10^{-2}$	$<10^{-3}$	$<10^{-3}$	$<10^{-3}$	$<10^{-3}$	...	$<10^{-2}$	$<10^{-2}$	...
Trigger efficiency	$<10^{-2}$	$<10^{-3}$	0.002	$<10^{-3}$	$<10^{-3}$	$<10^{-3}$	$<10^{-2}$	$<10^{-2}$	$<10^{-2}$
B^0 contribution	0.03	0.001	$<10^{-3}$	$<10^{-3}$	0.005	0.001	0.02	$<10^{-2}$	$<10^{-2}$
Tagging	0.03	$<10^{-3}$	$<10^{-3}$	$<10^{-3}$	$<10^{-3}$	$<10^{-3}$	0.04	$<10^{-2}$	$<10^{-2}$
Acceptance	0.02	0.004	0.002	0.002	0.004	...	...	$<10^{-2}$	...
Models:									
Default fit	$<10^{-2}$	0.003	$<10^{-3}$	0.001	0.001	0.006	0.07	0.01	0.01
Signal mass	$<10^{-2}$	0.001	$<10^{-3}$	$<10^{-3}$	0.001	$<10^{-3}$	0.03	0.04	0.01
Background mass	$<10^{-2}$	0.001	0.001	$<10^{-3}$	$<10^{-3}$	0.002	0.06	0.02	0.02
Resolution	0.02	$<10^{-3}$	0.001	0.001	$<10^{-3}$	0.002	0.04	0.02	0.01
Background time	0.01	0.001	$<10^{-3}$	0.001	$<10^{-3}$	0.002	0.01	0.02	0.02
Background angles	0.02	0.008	0.002	0.008	0.009	0.027	0.06	0.07	0.03
Total	0.05	0.010	0.004	0.009	0.012	0.028	0.11	0.09	0.04

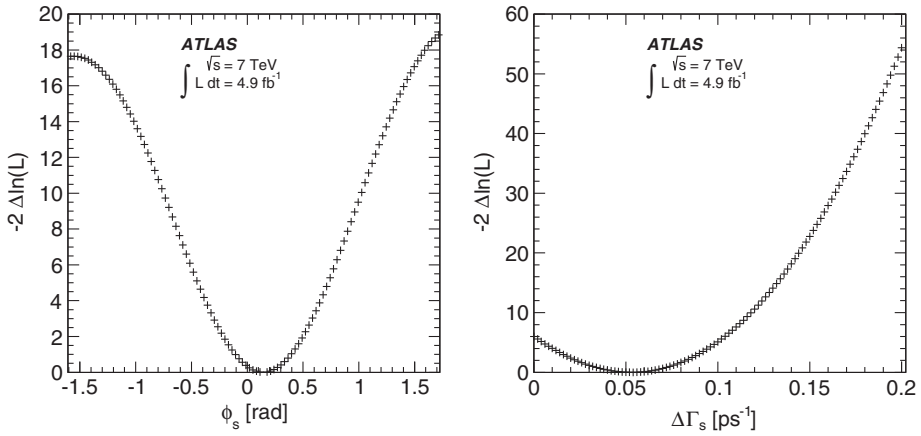

FIG. 7. One-dimensional likelihood scans for ϕ_s (left) and $\Delta\Gamma_s$ (right).

the fitted value of each parameter from its input value for the pseudoexperiments with the systematic alteration included. The variations are as follows. Two different scale factors are used to generate the signal mass. The background mass is generated from an exponential function. Two different scale factors are used to generate the lifetime uncertainty. The background lifetimes are generated by sampling data from the mass sidebands. Pseudoexperiments are generated with background angles taken from histograms from sideband data and are fitted with the default fit model to assess the systematic uncertainty to the parameterization of the background angles in the fit.

(vii) *Default fit model:* The systematic uncertainty of the default fit model is calculated using the bias of the pull distribution of 2400 pseudoexperiments, multiplied by the statistical uncertainty of each parameter.

The systematic uncertainties are provided in Table VII. For each variable, the total systematic error is obtained by adding in quadrature the different contributions.

VIII. DISCUSSION

The PDF describing the $B_s^0 \to J/\psi\phi$ decay is invariant under the following simultaneous transformations:

$$\{\phi_s, \Delta\Gamma_s, \delta_\perp, \delta_\parallel\} \to \{\pi - \phi_s, -\Delta\Gamma_s, \pi - \delta_\perp, 2\pi - \delta_\parallel\}.$$

$\Delta\Gamma_s$ has been determined to be positive [24]. Therefore, there is a unique solution, and only the case $\Delta\Gamma_s > 0$ is considered. Uncertainties on individual parameters were studied in detail in likelihood scans. Figure 7 shows the one-dimensional likelihood scans for ϕ_s and $\Delta\Gamma_s$. Figure 8 shows the likelihood contours in the $\phi_s - \Delta\Gamma_s$ plane.

The behavior of the amplitudes around their fitted values is Gaussian; however, the strong phases are more complicated. Figure 9 shows the one-dimensional likelihood scans for the three measured strong phases.

The likelihood behavior of $\delta_\perp$ appears Gaussian, and therefore it is reasonable to quote $\delta_\perp = 3.89 \pm 0.47(\text{stat})$ rad. For $\delta_\perp - \delta_S$ the scan shows a minimum close to π; however, it is insensitive over the rest of the scan at the level of 2.1σ. Therefore, the measured value of the difference $\delta_\perp - \delta_S$ is only given as 1σ confidence interval [3.02, 3.25] rad. It should be noted that both $|A_S(0)|^2$ and the strong phase δ_S are determined for the K^+K^- invariant mass range $1.0085\ \text{GeV} < m(K^+K^-) < 1.0305\ \text{GeV}$ used in this analysis. For the strong phase $\delta_\parallel$ the central fit value is

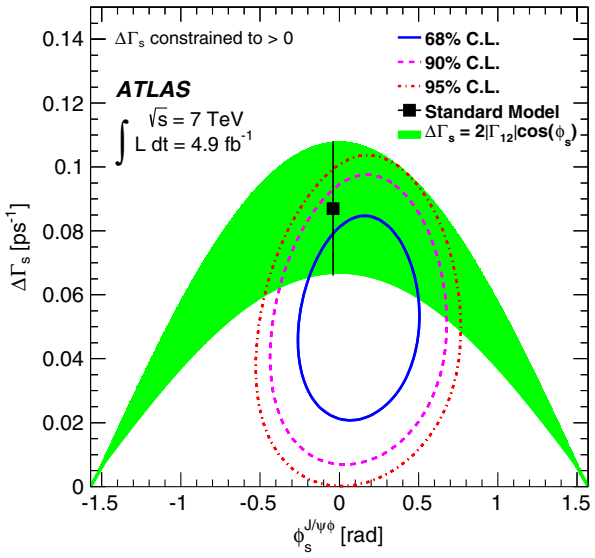

FIG. 8 (color online). Likelihood contours in the $\phi_s - \Delta\Gamma_s$ plane. The blue line shows the 68% likelihood contour, the dashed pink line shows the 90% likelihood contour, and the red dotted line shows the 95% likelihood contour (statistical errors only). The green band is the theoretical prediction of mixing-induced CP violation.

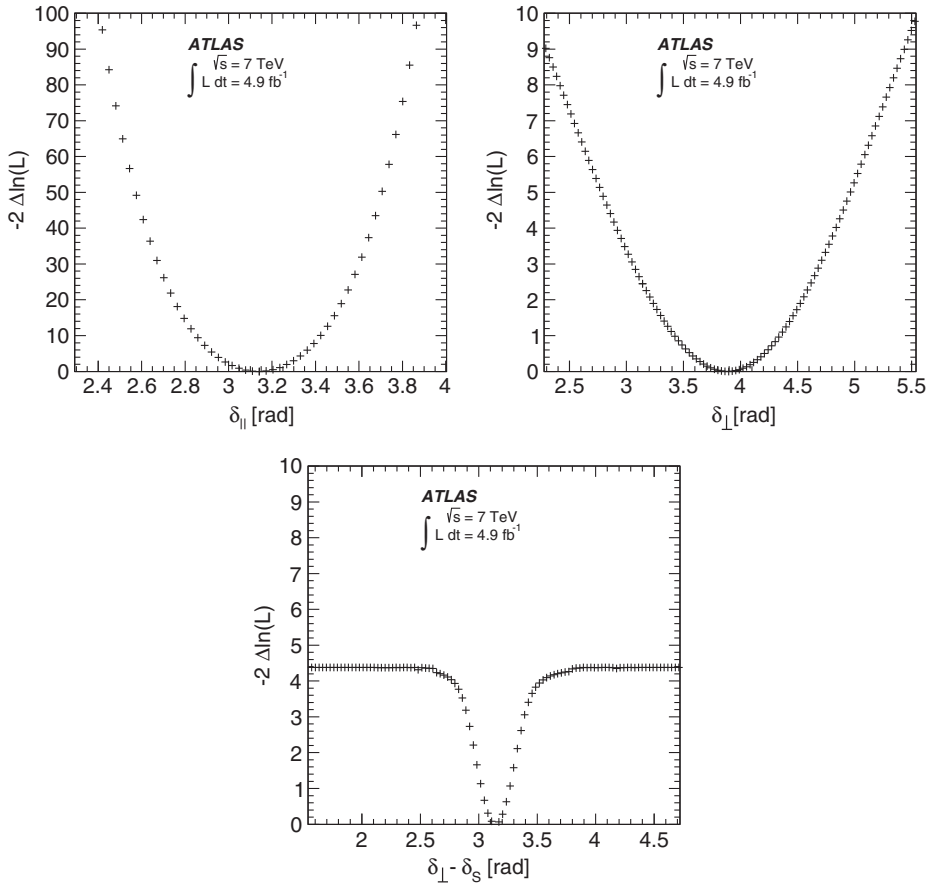

FIG. 9. One-dimensional likelihood scans for $\delta_{||}$ (top left), $\delta_{\perp}$ (top right) and $\delta_{\perp} - \delta_S$ (bottom).

close to π (3.14 ± 0.10), and the one-dimensional likelihood scan shows normal Gaussian behavior around this minimum. However, the systematic pull plot based on 2400 pseudoexperiments fits reveals a double-Gaussian shape with 68% of the results included in the interval [2.92, 3.35] rad, and so we quote the result in the form of a 68% C.L. interval $\delta_{||} \in [2.92, 3.35]$ rad (statistical only).

IX. CONCLUSION

A measurement of time-dependent CP asymmetry parameters in $B_s^0 \to J/\psi(\mu^+\mu^-)\phi(K^+K^-)$ decays from a 4.9 fb^{-1} data sample of pp collisions collected with the ATLAS detector during the 2011 $\sqrt{s} = 7$ TeV LHC run is presented. Several parameters describing the B_s^0 meson system are measured. These include the mean B_s^0 lifetime $1/\Gamma_s$, the decay width difference $\Delta\Gamma_s$ between the heavy and light mass eigenstates, and the transversity amplitudes $|A_0(0)|$ and $|A_{\|}(0)|$. Each of these is consistent with its respective world average. Likelihood contours in the ϕ_s - $\Delta\Gamma_s$ plane are also provided. The fraction $|A_S(0)|^2$, the signal contribution from $B_s^0 \to J/\psi K^+K^-$ and $B_s^0 \to J/\psi f_0$ decays, is measured to be consistent with zero, at $0.024 \pm 0.014(\text{stat}) \pm 0.028(\text{syst})$.

The results are

$$\begin{aligned}
\phi_s &= 0.12 \pm 0.25(\text{stat}) \pm 0.05(\text{syst}) \text{ rad} \\
\Delta\Gamma_s &= 0.053 \pm 0.021(\text{stat}) \pm 0.010(\text{syst}) \text{ ps}^{-1} \\
\Gamma_s &= 0.677 \pm 0.007(\text{stat}) \pm 0.004(\text{syst}) \text{ ps}^{-1} \\
|A_{\|}(0)|^2 &= 0.220 \pm 0.008(\text{stat}) \pm 0.009(\text{syst}) \\
|A_0(0)|^2 &= 0.529 \pm 0.006(\text{stat}) \pm 0.012(\text{syst}) \\
\delta_{\perp} &= 3.89 \pm 0.47(\text{stat}) \pm 0.11(\text{syst}) \text{ rad}.
\end{aligned}$$

The values are consistent with those obtained in our untagged analysis [6] and significantly reduce the overall uncertainty on ϕ_s. These results are consistent with the values predicted in the Standard Model.

ACKNOWLEDGMENTS

We thank CERN for the very successful operation of the LHC, as well as the support staff from our institutions without whom ATLAS could not be operated efficiently. We acknowledge the support of ANPCyT, Argentina; YerPhI, Armenia; ARC, Australia; BMWF and FWF, Austria; ANAS, Azerbaijan; SSTC, Belarus; CNPq and

FAPESP, Brazil; NSERC, NRC and CFI, Canada; CERN; CONICYT, Chile; CAS, MOST and NSFC, China; COLCIENCIAS, Colombia; MSMT CR, MPO CR and VSC CR, Czech Republic; DNRF, DNSRC and Lundbeck Foundation, Denmark; EPLANET, ERC and NSRF, European Union; IN2P3-CNRS, CEA-DSM/IRFU, France; GNSF, Georgia; BMBF, DFG, HGF, MPG and AvH Foundation, Germany; GSRT and NSRF, Greece; ISF, MINERVA, GIF, I-CORE and Benoziyo Center, Israel; INFN, Italy; MEXT and JSPS, Japan; CNRST, Morocco; FOM and NWO, Netherlands; BRF and RCN, Norway; MNiSW and NCN, Poland; GRICES and FCT, Portugal; MNE/IFA, Romania; MES of Russia and ROSATOM, Russian Federation; JINR; MSTD, Serbia; MSSR, Slovakia; ARRS and MIZŠ, Slovenia; DST/NRF, South Africa; MINECO, Spain; SRC and Wallenberg Foundation, Sweden; SER, SNSF and Cantons of Bern and Geneva, Switzerland; NSC, Taiwan; TAEK, Turkey; STFC, the Royal Society and Leverhulme Trust, United Kingdom; DOE and NSF, United States of America. The crucial computing support from all WLCG partners is acknowledged gratefully, in particular from CERN and the ATLAS Tier-1 facilities at TRIUMF (Canada), NDGF (Denmark, Norway, Sweden), CC-IN2P3 (France), KIT/GridKA (Germany), INFN-CNAF (Italy), NL-T1 (Netherlands), PIC (Spain), ASGC (Taiwan), RAL (UK) and BNL (USA) and in the Tier-2 facilities worldwide.

[1] M. Bona *et al.* (UTfit Collaboration), Phys. Rev. Lett. **97**, 151803 (2006).
[2] A. Abulencia *et al.* (CDF Collaboration), Phys. Rev. Lett. **97**, 242003 (2006).
[3] R. Aaij *et al.* (LHCb Collaboration), Phys. Lett. B **709**, 177 (2012).
[4] A. Lenz and U. Nierste, arXiv:1102.4274.
[5] A. Lenz and U. Nierste, J. High Energy Phys. 06 (2007) 072.
[6] ATLAS Collaboration, J. High Energy Phys. 12 (2012) 072.
[7] V. M. Abazov *et al.* (D0 Collaboration), Phys. Rev. D **85** (2012) 032006.
[8] T. Aaltonen *et al.* (CDF Collaboration), Phys. Rev. Lett. **109**, 171802 (2012).
[9] R. Aaij *et al.* (LHCb Collaboration), Phys. Rev. D **87**, 112010 (2013).
[10] ATLAS Collaboration, JINST **3**, S08003 (2008).
[11] ATLAS uses a right-handed coordinate system with its origin at the nominal interaction point in the center of the detector and the z axis along the beam pipe. The x axis points from the IP to the center of the LHC ring, and the y axis points upward. Cylindrical coordinates (r, ϕ) are used in the transverse plane, ϕ being the azimuthal angle around the beam pipe. The pseudorapidity is defined in terms of the polar angle θ as $\eta = -\ln\tan(\theta/2)$.
[12] T. Sjostrand, S. Mrenna, and P. Z. Skands, J. High Energy Phys. 05 (2006) 026.
[13] ATLAS Collaboration, Report No. ATL-PHYS-PUB-2011-009, http://cds.cern.ch/record/1363300.
[14] ATLAS Collaboration, Eur. Phys. J. C **70**, 823 (2010).
[15] S. Agostinelli *et al.* (GEANT4 Collaboration), Nucl. Instrum. Methods Phys. Res., Sect. A **506**, 250 (2003).
[16] ATLAS Collaboration, Nucl. Phys. **B850**, 387 (2011).
[17] J. Beringer *et al.* (Particle Data Group Collaboration), Phys. Rev. D **86**, 010001 (2012) (and 2013 partial update for the 2014 edition).
[18] R. Field and R. Feynman, Nucl. Phys. **B136**, 1 (1978).
[19] $\Delta R^2 = \Delta\phi^2 + \Delta\eta^2$, where $\Delta\phi$ and $\Delta\eta$ are the differences between the measured ϕ and η of the tracks respectively.
[20] ATLAS Collaboration, Report No. ATLAS-CONF-2011-102, http://cds.cern.ch/record/1369219.
[21] ATLAS Collaboration, arXiv:0901.0512.
[22] A. S. Dighe, I. Dunietz, and R. Fleischer, Eur. Phys. J. C **6**, 647 (1999).
[23] R. Aaij *et al.* (LHCb Collaboration), Phys. Rev. Lett. **108**, 101803 (2012).
[24] R. Aaij *et al.*, Phys. Rev. Lett. **108**, 241801 (2012).

G. Aad,[84] T. Abajyan,[21] B. Abbott,[112] J. Abdallah,[152] S. Abdel Khalek,[116] O. Abdinov,[11] R. Aben,[106] B. Abi,[113] M. Abolins,[89] O. S. AbouZeid,[159] H. Abramowicz,[154] H. Abreu,[137] Y. Abulaiti,[147a,147b] B. S. Acharya,[165a,165b,b] L. Adamczyk,[38a] D. L. Adams,[25] T. N. Addy,[56] J. Adelman,[177] S. Adomeit,[99] T. Adye,[130] T. Agatonovic-Jovin,[13b] J. A. Aguilar-Saavedra,[125f,125a] M. Agustoni,[17] S. P. Ahlen,[22] A. Ahmad,[149] F. Ahmadov,[64,c] G. Aielli,[134a,134b] T. P. A. Åkesson,[80] G. Akimoto,[156] A. V. Akimov,[95] J. Albert,[170] S. Albrand,[55] M. J. Alconada Verzini,[70] M. Aleksa,[30] I. N. Aleksandrov,[64] C. Alexa,[26a] G. Alexander,[154] G. Alexandre,[49] T. Alexopoulos,[10] M. Alhroob,[165a,165c] G. Alimonti,[90a] L. Alio,[84] J. Alison,[31] B. M. M. Allbrooke,[18] L. J. Allison,[71] P. P. Allport,[73] S. E. Allwood-Spiers,[53] J. Almond,[83] A. Aloisio,[103a,103b] R. Alon,[173] A. Alonso,[36] F. Alonso,[70] C. Alpigiani,[75] A. Altheimer,[35] B. Alvarez Gonzalez,[89]

M. G. Alviggi,[103a,103b] K. Amako,[65] Y. Amaral Coutinho,[24a] C. Amelung,[23] D. Amidei,[88] V. V. Ammosov,[129,a] S. P. Amor Dos Santos,[125a,125c] A. Amorim,[125a,125b] S. Amoroso,[48] N. Amram,[154] G. Amundsen,[23] C. Anastopoulos,[140] L. S. Ancu,[17] N. Andari,[30] T. Andeen,[35] C. F. Anders,[58b] G. Anders,[30] K. J. Anderson,[31] A. Andreazza,[90a,90b] V. Andrei,[58a] X. S. Anduaga,[70] S. Angelidakis,[9] P. Anger,[44] A. Angerami,[35] F. Anghinolfi,[30] A. V. Anisenkov,[108] N. Anjos,[125a] A. Annovi,[47] A. Antonaki,[9] M. Antonelli,[47] A. Antonov,[97] J. Antos,[145b] F. Anulli,[133a] M. Aoki,[65] L. Aperio Bella,[18] R. Apolle,[119,d] G. Arabidze,[89] I. Aracena,[144] Y. Arai,[65] J. P. Araque,[125a] A. T. H. Arce,[45] J-F. Arguin,[94] S. Argyropoulos,[42] M. Arik,[19a] A. J. Armbruster,[30] O. Arnaez,[82] V. Arnal,[81] O. Arslan,[21] A. Artamonov,[96] G. Artoni,[23] S. Asai,[156] N. Asbah,[94] A. Ashkenazi,[154] S. Ask,[28] B. Åsman,[147a,147b] L. Asquith,[6] K. Assamagan,[25] R. Astalos,[145a] M. Atkinson,[166] N. B. Atlay,[142] B. Auerbach,[6] E. Auge,[116] K. Augsten,[127] M. Aurousseau,[146b] G. Avolio,[30] G. Azuelos,[94,e] Y. Azuma,[156] M. A. Baak,[30] C. Bacci,[135a,135b] A. M. Bach,[15] H. Bachacou,[137] K. Bachas,[155] M. Backes,[30] M. Backhaus,[30] J. Backus Mayes,[144] E. Badescu,[26a] P. Bagiacchi,[133a,133b] P. Bagnaia,[133a,133b] Y. Bai,[33a] D. C. Bailey,[159] T. Bain,[35] J. T. Baines,[130] O. K. Baker,[177] S. Baker,[77] P. Balek,[128] F. Balli,[137] E. Banas,[39] Sw. Banerjee,[174] D. Banfi,[30] A. Bangert,[151] A. A. E. Bannoura,[176] V. Bansal,[170] H. S. Bansil,[18] L. Barak,[173] S. P. Baranov,[95] T. Barber,[48] E. L. Barberio,[87] D. Barberis,[50a,50b] M. Barbero,[84] T. Barillari,[100] M. Barisonzi,[176] T. Barklow,[144] N. Barlow,[28] B. M. Barnett,[130] R. M. Barnett,[15] Z. Barnovska,[5] A. Baroncelli,[135a] G. Barone,[49] A. J. Barr,[119] F. Barreiro,[81] J. Barreiro Guimarães da Costa,[57] R. Bartoldus,[144] A. E. Barton,[71] P. Bartos,[145a] V. Bartsch,[150] A. Bassalat,[116] A. Basye,[166] R. L. Bates,[53] L. Batkova,[145a] J. R. Batley,[28] M. Battistin,[30] F. Bauer,[137] H. S. Bawa,[144,f] T. Beau,[79] P. H. Beauchemin,[162] R. Beccherle,[123a,123b] P. Bechtle,[21] H. P. Beck,[17] K. Becker,[176] S. Becker,[99] M. Beckingham,[139] C. Becot,[116] A. J. Beddall,[19c] A. Beddall,[19c] S. Bedikian,[177] V. A. Bednyakov,[64] C. P. Bee,[149] L. J. Beemster,[106] T. A. Beermann,[176] M. Begel,[25] K. Behr,[119] C. Belanger-Champagne,[86] P. J. Bell,[49] W. H. Bell,[49] G. Bella,[154] L. Bellagamba,[20a] A. Bellerive,[29] M. Bellomo,[85] A. Belloni,[57] O. L. Beloborodova,[108,g] K. Belotskiy,[97] O. Beltramello,[30] O. Benary,[154] D. Benchekroun,[136a] K. Bendtz,[147a,147b] N. Benekos,[166] Y. Benhammou,[154] E. Benhar Noccioli,[49] J. A. Benitez Garcia,[160b] D. P. Benjamin,[45] J. R. Bensinger,[23] K. Benslama,[131] S. Bentvelsen,[106] D. Berge,[106] E. Bergeaas Kuutmann,[16] N. Berger,[5] F. Berghaus,[170] E. Berglund,[106] J. Beringer,[15] C. Bernard,[22] P. Bernat,[77] C. Bernius,[78] F. U. Bernlochner,[170] T. Berry,[76] P. Berta,[128] C. Bertella,[84] F. Bertolucci,[123a,123b] M. I. Besana,[90a] G. J. Besjes,[105] O. Bessidskaia,[147a,147b] N. Besson,[137] C. Betancourt,[48] S. Bethke,[100] W. Bhimji,[46] R. M. Bianchi,[124] L. Bianchini,[23] M. Bianco,[30] O. Biebel,[99] S. P. Bieniek,[77] K. Bierwagen,[54] J. Biesiada,[15] M. Biglietti,[135a] J. Bilbao De Mendizabal,[49] H. Bilokon,[47] M. Bindi,[54] S. Binet,[116] A. Bingul,[19c] C. Bini,[133a,133b] C. W. Black,[151] J. E. Black,[144] K. M. Black,[22] D. Blackburn,[139] R. E. Blair,[6] J.-B. Blanchard,[137] T. Blazek,[145a] I. Bloch,[42] C. Blocker,[23] W. Blum,[82,a] U. Blumenschein,[54] G. J. Bobbink,[106] V. S. Bobrovnikov,[108] S. S. Bocchetta,[80] A. Bocci,[45] C. R. Boddy,[119] M. Boehler,[48] J. Boek,[176] T. T. Boek,[176] J. A. Bogaerts,[30] A. G. Bogdanchikov,[108] A. Bogouch,[91,a] C. Bohm,[147a] J. Bohm,[126] V. Boisvert,[76] T. Bold,[38a] V. Boldea,[26a] A. S. Boldyrev,[98] N. M. Bolnet,[137] M. Bomben,[79] M. Bona,[75] M. Boonekamp,[137] A. Borisov,[129] G. Borissov,[71] M. Borri,[83] S. Borroni,[42] J. Bortfeldt,[99] V. Bortolotto,[135a,135b] K. Bos,[106] D. Boscherini,[20a] M. Bosman,[12] H. Boterenbrood,[106] J. Boudreau,[124] J. Bouffard,[2] E. V. Bouhova-Thacker,[71] D. Boumediene,[34] C. Bourdarios,[116] N. Bousson,[113] S. Boutouil,[136d] A. Boveia,[31] J. Boyd,[30] I. R. Boyko,[64] I. Bozovic-Jelisavcic,[13b] J. Bracinik,[18] P. Branchini,[135a] A. Brandt,[8] G. Brandt,[15] O. Brandt,[58a] U. Bratzler,[157] B. Brau,[85] J. E. Brau,[115] H. M. Braun,[176,a] S. F. Brazzale,[165a,165c] B. Brelier,[159] K. Brendlinger,[121] A. J. Brennan,[87] R. Brenner,[167] S. Bressler,[173] K. Bristow,[146c] T. M. Bristow,[46] D. Britton,[53] F. M. Brochu,[28] I. Brock,[21] R. Brock,[89] C. Bromberg,[89] J. Bronner,[100] G. Brooijmans,[35] T. Brooks,[76] W. K. Brooks,[32b] J. Brosamer,[15] E. Brost,[115] G. Brown,[83] J. Brown,[55] P. A. Bruckman de Renstrom,[39] D. Bruncko,[145b] R. Bruneliere,[48] S. Brunet,[60] A. Bruni,[20a] G. Bruni,[20a] M. Bruschi,[20a] L. Bryngemark,[80] T. Buanes,[14] Q. Buat,[143] F. Bucci,[49] P. Buchholz,[142] R. M. Buckingham,[119] A. G. Buckley,[53] S. I. Buda,[26a] I. A. Budagov,[64] F. Buehrer,[48] L. Bugge,[118] M. K. Bugge,[118] O. Bulekov,[97] A. C. Bundock,[73] H. Burckhart,[30] S. Burdin,[73] B. Burghgrave,[107] S. Burke,[130] I. Burmeister,[43] E. Busato,[34] V. Büscher,[82] P. Bussey,[53] C. P. Buszello,[167] B. Butler,[57] J. M. Butler,[22] A. I. Butt,[3] C. M. Buttar,[53] J. M. Butterworth,[77] P. Butti,[106] W. Buttinger,[28] A. Buzatu,[53] M. Byszewski,[10] S. Cabrera Urbán,[168] D. Caforio,[20a,20b] O. Cakir,[4a] P. Calafiura,[15] G. Calderini,[79] P. Calfayan,[99] R. Calkins,[107] L. P. Caloba,[24a] D. Calvet,[34] S. Calvet,[34] R. Camacho Toro,[49] S. Camarda,[42] D. Cameron,[118] L. M. Caminada,[15] R. Caminal Armadans,[12] S. Campana,[30] M. Campanelli,[77] A. Campoverde,[149] V. Canale,[103a,103b] A. Canepa,[160a] J. Cantero,[81] R. Cantrill,[76] T. Cao,[40] M. D. M. Capeans Garrido,[30] I. Caprini,[26a] M. Caprini,[26a] M. Capua,[37a,37b] R. Caputo,[82] R. Cardarelli,[134a] T. Carli,[30] G. Carlino,[103a] L. Carminati,[90a,90b] S. Caron,[105] E. Carquin,[32a] G. D. Carrillo-Montoya,[146c] A. A. Carter,[75] J. R. Carter,[28] J. Carvalho,[125a,125c] D. Casadei,[77] M. P. Casado,[12] E. Castaneda-Miranda,[146b] A. Castelli,[106] V. Castillo Gimenez,[168]

N. F. Castro,[125a] P. Catastini,[57] A. Catinaccio,[30] J. R. Catmore,[71] A. Cattai,[30] G. Cattani,[134a,134b] S. Caughron,[89] V. Cavaliere,[166] D. Cavalli,[90a] M. Cavalli-Sforza,[12] V. Cavasinni,[123a,123b] F. Ceradini,[135a,135b] B. Cerio,[45] K. Cerny,[128] A. S. Cerqueira,[24b] A. Cerri,[150] L. Cerrito,[75] F. Cerutti,[15] M. Cerv,[30] A. Cervelli,[17] S. A. Cetin,[19b] A. Chafaq,[136a] D. Chakraborty,[107] I. Chalupkova,[128] K. Chan,[3] P. Chang,[166] B. Chapleau,[86] J. D. Chapman,[28] D. Charfeddine,[116] D. G. Charlton,[18] C. C. Chau,[159] C. A. Chavez Barajas,[150] S. Cheatham,[86] A. Chegwidden,[89] S. Chekanov,[6] S. V. Chekulaev,[160a] G. A. Chelkov,[64] M. A. Chelstowska,[88] C. Chen,[63] H. Chen,[25] K. Chen,[149] L. Chen,[33d,h] S. Chen,[33c] X. Chen,[146c] Y. Chen,[35] H. C. Cheng,[88] Y. Cheng,[31] A. Cheplakov,[64] R. Cherkaoui El Moursli,[136e] V. Chernyatin,[25,a] E. Cheu,[7] L. Chevalier,[137] V. Chiarella,[47] G. Chiefari,[103a,103b] J. T. Childers,[6] A. Chilingarov,[71] G. Chiodini,[72a] A. S. Chisholm,[18] R. T. Chislett,[77] A. Chitan,[26a] M. V. Chizhov,[64] S. Chouridou,[9] B. K. B. Chow,[99] I. A. Christidi,[77] D. Chromek-Burckhart,[30] M. L. Chu,[152] J. Chudoba,[126] L. Chytka,[114] G. Ciapetti,[133a,133b] A. K. Ciftci,[4a] R. Ciftci,[4a] D. Cinca,[62] V. Cindro,[74] A. Ciocio,[15] P. Cirkovic,[13b] Z. H. Citron,[173] M. Citterio,[90a] M. Ciubancan,[26a] A. Clark,[49] P. J. Clark,[46] R. N. Clarke,[15] W. Cleland,[124] J. C. Clemens,[84] B. Clement,[55] C. Clement,[147a,147b] Y. Coadou,[84] M. Cobal,[165a,165c] A. Coccaro,[139] J. Cochran,[63] L. Coffey,[23] J. G. Cogan,[144] J. Coggeshall,[166] B. Cole,[35] S. Cole,[107] A. P. Colijn,[106] C. Collins-Tooth,[53] J. Collot,[55] T. Colombo,[58c] G. Colon,[85] G. Compostella,[100] P. Conde Muiño,[125a,125b] E. Coniavitis,[167] M. C. Conidi,[12] S. H. Connell,[146b] I. A. Connelly,[76] S. M. Consonni,[90a,90b] V. Consorti,[48] S. Constantinescu,[26a] C. Conta,[120a,120b] G. Conti,[57] F. Conventi,[103a,i] M. Cooke,[15] B. D. Cooper,[77] A. M. Cooper-Sarkar,[119] N. J. Cooper-Smith,[76] K. Copic,[15] T. Cornelissen,[176] M. Corradi,[20a] F. Corriveau,[86,j] A. Corso-Radu,[164] A. Cortes-Gonzalez,[12] G. Cortiana,[100] G. Costa,[90a] M. J. Costa,[168] D. Costanzo,[140] D. Côté,[8] G. Cottin,[28] G. Cowan,[76] B. E. Cox,[83] K. Cranmer,[109] G. Cree,[29] S. Crépé-Renaudin,[55] F. Crescioli,[79] M. Crispin Ortuzar,[119] M. Cristinziani,[21] G. Crosetti,[37a,37b] C.-M. Cuciuc,[26a] C. Cuenca Almenar,[177] T. Cuhadar Donszelmann,[140] J. Cummings,[177] M. Curatolo,[47] C. Cuthbert,[151] H. Czirr,[142] P. Czodrowski,[3] Z. Czyczula,[177] S. D'Auria,[53] M. D'Onofrio,[73] M. J. Da Cunha Sargedas De Sousa,[125a,125b] C. Da Via,[83] W. Dabrowski,[38a] A. Dafinca,[119] T. Dai,[88] O. Dale,[14] F. Dallaire,[94] C. Dallapiccola,[85] M. Dam,[36] A. C. Daniells,[18] M. Dano Hoffmann,[137] V. Dao,[105] G. Darbo,[50a] G. L. Darlea,[26c] S. Darmora,[8] J. A. Dassoulas,[42] W. Davey,[21] C. David,[170] T. Davidek,[128] E. Davies,[119,d] M. Davies,[94] O. Davignon,[79] A. R. Davison,[77] P. Davison,[77] Y. Davygora,[58a] E. Dawe,[143] I. Dawson,[140] R. K. Daya-Ishmukhametova,[23] K. De,[8] R. de Asmundis,[103a] S. De Castro,[20a,20b] S. De Cecco,[79] J. de Graat,[99] N. De Groot,[105] P. de Jong,[106] C. De La Taille,[116] H. De la Torre,[81] F. De Lorenzi,[63] L. De Nooij,[106] D. De Pedis,[133a] A. De Salvo,[133a] U. De Sanctis,[165a,165c] A. De Santo,[150] J. B. De Vivie De Regie,[116] G. De Zorzi,[133a,133b] W. J. Dearnaley,[71] R. Debbe,[25] C. Debenedetti,[46] B. Dechenaux,[55] D. V. Dedovich,[64] J. Degenhardt,[121] I. Deigaard,[106] J. Del Peso,[81] T. Del Prete,[123a,123b] F. Deliot,[137] M. Deliyergiyev,[74] A. Dell'Acqua,[30] L. Dell'Asta,[22] M. Dell'Orso,[123a,123b] M. Della Pietra,[103a,i] D. della Volpe,[49] M. Delmastro,[5] P. A. Delsart,[55] C. Deluca,[106] S. Demers,[177] M. Demichev,[64] A. Demilly,[79] S. P. Denisov,[129] D. Derendarz,[39] J. E. Derkaoui,[136d] F. Derue,[79] P. Dervan,[73] K. Desch,[21] C. Deterre,[42] P. O. Deviveiros,[106] A. Dewhurst,[130] S. Dhaliwal,[106] A. Di Ciaccio,[134a,134b] L. Di Ciaccio,[5] A. Di Domenico,[133a,133b] C. Di Donato,[103a,103b] A. Di Girolamo,[30] B. Di Girolamo,[30] A. Di Mattia,[153] B. Di Micco,[135a,135b] R. Di Nardo,[47] A. Di Simone,[48] R. Di Sipio,[20a,20b] D. Di Valentino,[29] M. A. Diaz,[32a] E. B. Diehl,[88] J. Dietrich,[42] T. A. Dietzsch,[58a] S. Diglio,[87] A. Dimitrievska,[13a] J. Dingfelder,[21] C. Dionisi,[133a,133b] P. Dita,[26a] S. Dita,[26a] F. Dittus,[30] F. Djama,[84] T. Djobava,[51b] M. A. B. do Vale,[24c] A. Do Valle Wemans,[125a,125g] T. K. O. Doan,[5] D. Dobos,[30] E. Dobson,[77] C. Doglioni,[49] T. Doherty,[53] T. Dohmae,[156] J. Dolejsi,[128] Z. Dolezal,[128] B. A. Dolgoshein,[97,a] M. Donadelli,[24d] S. Donati,[123a,123b] P. Dondero,[120a,120b] J. Donini,[34] J. Dopke,[30] A. Doria,[103a] A. Dos Anjos,[174] M. T. Dova,[70] A. T. Doyle,[53] M. Dris,[10] J. Dubbert,[88] S. Dube,[15] E. Dubreuil,[34] E. Duchovni,[173] G. Duckeck,[99] O. A. Ducu,[26a] D. Duda,[176] A. Dudarev,[30] F. Dudziak,[63] L. Duflot,[116] L. Duguid,[76] M. Dührssen,[30] M. Dunford,[58a] H. Duran Yildiz,[4a] M. Düren,[52] A. Durglishvili,[51b] M. Dwuznik,[38a] M. Dyndal,[38a] J. Ebke,[99] W. Edson,[2] N. C. Edwards,[46] W. Ehrenfeld,[21] T. Eifert,[144] G. Eigen,[14] K. Einsweiler,[15] T. Ekelof,[167] M. El Kacimi,[136c] M. Ellert,[167] S. Elles,[5] F. Ellinghaus,[82] N. Ellis,[30] J. Elmsheuser,[99] M. Elsing,[30] D. Emeliyanov,[130] Y. Enari,[156] O. C. Endner,[82] M. Endo,[117] R. Engelmann,[149] J. Erdmann,[177] A. Ereditato,[17] D. Eriksson,[147a] G. Ernis,[176] J. Ernst,[2] M. Ernst,[25] J. Ernwein,[137] D. Errede,[166] S. Errede,[166] E. Ertel,[82] M. Escalier,[116] H. Esch,[43] C. Escobar,[124] B. Esposito,[47] A. I. Etienvre,[137] E. Etzion,[154] H. Evans,[60] L. Fabbri,[20a,20b] G. Facini,[30] R. M. Fakhrutdinov,[129] S. Falciano,[133a] Y. Fang,[33a] M. Fanti,[90a,90b] A. Farbin,[8] A. Farilla,[135a] T. Farooque,[12] S. Farrell,[164] S. M. Farrington,[171] P. Farthouat,[30] F. Fassi,[168] P. Fassnacht,[30] D. Fassouliotis,[9] A. Favareto,[50a,50b] L. Fayard,[116] P. Federic,[145a] O. L. Fedin,[122,k] W. Fedorko,[169] M. Fehling-Kaschek,[48] S. Feigl,[30] L. Feligioni,[84] C. Feng,[33d] E. J. Feng,[6] H. Feng,[88] A. B. Fenyuk,[129] S. Fernandez Perez,[30] W. Fernando,[6] S. Ferrag,[53] J. Ferrando,[53] V. Ferrara,[42] A. Ferrari,[167]

P. Ferrari,[106] R. Ferrari,[120a] D. E. Ferreira de Lima,[53] A. Ferrer,[168] D. Ferrere,[49] C. Ferretti,[88] A. Ferretto Parodi,[50a,50b] M. Fiascaris,[31] F. Fiedler,[82] A. Filipčič,[74] M. Filipuzzi,[42] F. Filthaut,[105] M. Fincke-Keeler,[170] K. D. Finelli,[151] M. C. N. Fiolhais,[125a,125c] L. Fiorini,[168] A. Firan,[40] J. Fischer,[176] M. J. Fisher,[110] W. C. Fisher,[89] E. A. Fitzgerald,[23] M. Flechl,[48] I. Fleck,[142] P. Fleischmann,[175] S. Fleischmann,[176] G. T. Fletcher,[140] G. Fletcher,[75] T. Flick,[176] A. Floderus,[80] L. R. Flores Castillo,[174] A. C. Florez Bustos,[160b] M. J. Flowerdew,[100] A. Formica,[137] A. Forti,[83] D. Fortin,[160a] D. Fournier,[116] H. Fox,[71] S. Fracchia,[12] P. Francavilla,[12] M. Franchini,[20a,20b] S. Franchino,[30] D. Francis,[30] M. Franklin,[57] S. Franz,[61] M. Fraternali,[120a,120b] S. T. French,[28] C. Friedrich,[42] F. Friedrich,[44] D. Froidevaux,[30] J. A. Frost,[28] C. Fukunaga,[157] E. Fullana Torregrosa,[82] B. G. Fulsom,[144] J. Fuster,[168] C. Gabaldon,[55] O. Gabizon,[173] A. Gabrielli,[20a,20b] A. Gabrielli,[133a,133b] S. Gadatsch,[106] S. Gadomski,[49] G. Gagliardi,[50a,50b] P. Gagnon,[60] C. Galea,[105] B. Galhardo,[125a,125c] E. J. Gallas,[119] V. Gallo,[17] B. J. Gallop,[130] P. Gallus,[127] G. Galster,[36] K. K. Gan,[110] R. P. Gandrajula,[62] J. Gao,[33b,h] Y. S. Gao,[144,f] F. M. Garay Walls,[46] F. Garberson,[177] C. García,[168] J. E. García Navarro,[168] M. Garcia-Sciveres,[15] R. W. Gardner,[31] N. Garelli,[144] V. Garonne,[30] C. Gatti,[47] G. Gaudio,[120a] B. Gaur,[142] L. Gauthier,[94] P. Gauzzi,[133a,133b] I. L. Gavrilenko,[95] C. Gay,[169] G. Gaycken,[21] E. N. Gazis,[10] P. Ge,[33d] Z. Gecse,[169] C. N. P. Gee,[130] D. A. A. Geerts,[106] Ch. Geich-Gimbel,[21] K. Gellerstedt,[147a,147b] C. Gemme,[50a] A. Gemmell,[53] M. H. Genest,[55] S. Gentile,[133a,133b] M. George,[54] S. George,[76] D. Gerbaudo,[164] A. Gershon,[154] H. Ghazlane,[136b] N. Ghodbane,[34] B. Giacobbe,[20a] S. Giagu,[133a,133b] V. Giangiobbe,[12] P. Giannetti,[123a,123b] F. Gianotti,[30] B. Gibbard,[25] S. M. Gibson,[76] M. Gilchriese,[15] T. P. S. Gillam,[28] D. Gillberg,[30] D. M. Gingrich,[3,e] N. Giokaris,[9] M. P. Giordani,[165a,165c] R. Giordano,[103a,103b] F. M. Giorgi,[16] P. F. Giraud,[137] D. Giugni,[90a] C. Giuliani,[48] M. Giulini,[58b] B. K. Gjelsten,[118] I. Gkialas,[155,l] L. K. Gladilin,[98] C. Glasman,[81] J. Glatzer,[30] P. C. F. Glaysher,[46] A. Glazov,[42] G. L. Glonti,[64] M. Goblirsch-Kolb,[100] J. R. Goddard,[75] J. Godfrey,[143] J. Godlewski,[30] C. Goeringer,[82] S. Goldfarb,[88] T. Golling,[177] D. Golubkov,[129] A. Gomes,[125a,125b,125d] L. S. Gomez Fajardo,[42] R. Gonçalo,[125a] J. Goncalves Pinto Firmino Da Costa,[42] L. Gonella,[21] S. González de la Hoz,[168] G. Gonzalez Parra,[12] M. L. Gonzalez Silva,[27] S. Gonzalez-Sevilla,[49] L. Goossens,[30] P. A. Gorbounov,[96] H. A. Gordon,[25] I. Gorelov,[104] G. Gorfine,[176] B. Gorini,[30] E. Gorini,[72a,72b] A. Gorišek,[74] E. Gornicki,[39] A. T. Goshaw,[6] C. Gössling,[43] M. I. Gostkin,[64] M. Gouighri,[136a] D. Goujdami,[136c] M. P. Goulette,[49] A. G. Goussiou,[139] C. Goy,[5] S. Gozpinar,[23] H. M. X. Grabas,[137] L. Graber,[54] I. Grabowska-Bold,[38a] P. Grafström,[20a,20b] K-J. Grahn,[42] J. Gramling,[49] E. Gramstad,[118] F. Grancagnolo,[72a] S. Grancagnolo,[16] V. Grassi,[149] V. Gratchev,[122] H. M. Gray,[30] E. Graziani,[135a] O. G. Grebenyuk,[122] Z. D. Greenwood,[78,m] K. Gregersen,[36] I. M. Gregor,[42] P. Grenier,[144] J. Griffiths,[8] N. Grigalashvili,[64] A. A. Grillo,[138] K. Grimm,[71] S. Grinstein,[12,n] Ph. Gris,[34] Y. V. Grishkevich,[98] J.-F. Grivaz,[116] J. P. Grohs,[44] A. Grohsjean,[42] E. Gross,[173] J. Grosse-Knetter,[54] G. C. Grossi,[134a,134b] J. Groth-Jensen,[173] Z. J. Grout,[150] K. Grybel,[142] L. Guan,[33b] F. Guescini,[49] D. Guest,[177] O. Gueta,[154] C. Guicheney,[34] E. Guido,[50a,50b] T. Guillemin,[116] S. Guindon,[2] U. Gul,[53] C. Gumpert,[44] J. Gunther,[127] J. Guo,[35] S. Gupta,[119] P. Gutierrez,[112] N. G. Gutierrez Ortiz,[53] C. Gutschow,[77] N. Guttman,[154] C. Guyot,[137] C. Gwenlan,[119] C. B. Gwilliam,[73] A. Haas,[109] C. Haber,[15] H. K. Hadavand,[8] N. Haddad,[136e] P. Haefner,[21] S. Hageboeck,[21] Z. Hajduk,[39] H. Hakobyan,[178] M. Haleem,[42] D. Hall,[119] G. Halladjian,[89] K. Hamacher,[176] P. Hamal,[114] K. Hamano,[87] M. Hamer,[54] A. Hamilton,[146a] S. Hamilton,[162] P. G. Hamnett,[42] L. Han,[33b] K. Hanagaki,[117] K. Hanawa,[156] M. Hance,[15] P. Hanke,[58a] J. R. Hansen,[36] J. B. Hansen,[36] J. D. Hansen,[36] P. H. Hansen,[36] K. Hara,[161] A. S. Hard,[174] T. Harenberg,[176] S. Harkusha,[91] D. Harper,[88] R. D. Harrington,[46] O. M. Harris,[139] P. F. Harrison,[171] F. Hartjes,[106] A. Harvey,[56] S. Hasegawa,[102] Y. Hasegawa,[141] A. Hasib,[112] S. Hassani,[137] S. Haug,[17] M. Hauschild,[30] R. Hauser,[89] M. Havranek,[126] C. M. Hawkes,[18] R. J. Hawkings,[30] A. D. Hawkins,[80] T. Hayashi,[161] D. Hayden,[89] C. P. Hays,[119] H. S. Hayward,[73] S. J. Haywood,[130] S. J. Head,[18] T. Heck,[82] V. Hedberg,[80] L. Heelan,[8] S. Heim,[121] T. Heim,[176] B. Heinemann,[15] L. Heinrich,[109] S. Heisterkamp,[36] J. Hejbal,[126] L. Helary,[22] C. Heller,[99] M. Heller,[30] S. Hellman,[147a,147b] D. Hellmich,[21] C. Helsens,[30] J. Henderson,[119] R. C. W. Henderson,[71] C. Hengler,[42] A. Henrichs,[177] A. M. Henriques Correia,[30] S. Henrot-Versille,[116] C. Hensel,[54] G. H. Herbert,[16] Y. Hernández Jiménez,[168] R. Herrberg-Schubert,[16] G. Herten,[48] R. Hertenberger,[99] L. Hervas,[30] G. G. Hesketh,[77] N. P. Hessey,[106] R. Hickling,[75] E. Higón-Rodriguez,[168] J. C. Hill,[28] K. H. Hiller,[42] S. Hillert,[21] S. J. Hillier,[18] I. Hinchliffe,[15] E. Hines,[121] M. Hirose,[117] D. Hirschbuehl,[176] J. Hobbs,[149] N. Hod,[106] M. C. Hodgkinson,[140] P. Hodgson,[140] A. Hoecker,[30] M. R. Hoeferkamp,[104] J. Hoffman,[40] D. Hoffmann,[84] J. I. Hofmann,[58a] M. Hohlfeld,[82] T. R. Holmes,[15] T. M. Hong,[121] L. Hooft van Huysduynen,[109] J-Y. Hostachy,[55] S. Hou,[152] A. Hoummada,[136a] J. Howard,[119] J. Howarth,[42] M. Hrabovsky,[114] I. Hristova,[16] J. Hrivnac,[116] T. Hryn'ova,[5] P. J. Hsu,[82] S.-C. Hsu,[139] D. Hu,[35] X. Hu,[25] Y. Huang,[42] Z. Hubacek,[30] F. Hubaut,[84] F. Huegging,[21] T. B. Huffman,[119] E. W. Hughes,[35] G. Hughes,[71] M. Huhtinen,[30] T. A. Hülsing,[82] M. Hurwitz,[15] N. Huseynov,[64,c] J. Huston,[89] J. Huth,[57] G. Iacobucci,[49] G. Iakovidis,[10] I. Ibragimov,[142] L. Iconomidou-Fayard,[116] J. Idarraga,[116] E. Ideal,[177]

P. Iengo,[103a] O. Igonkina,[106] T. Iizawa,[172] Y. Ikegami,[65] K. Ikematsu,[142] M. Ikeno,[65] D. Iliadis,[155] N. Ilic,[159] Y. Inamaru,[66] T. Ince,[100] P. Ioannou,[9] M. Iodice,[135a] K. Iordanidou,[9] V. Ippolito,[57] A. Irles Quiles,[168] C. Isaksson,[167] M. Ishino,[67] M. Ishitsuka,[158] R. Ishmukhametov,[110] C. Issever,[119] S. Istin,[19a] J. M. Iturbe Ponce,[83] A. V. Ivashin,[129] W. Iwanski,[39] H. Iwasaki,[65] J. M. Izen,[41] V. Izzo,[103a] B. Jackson,[121] J. N. Jackson,[73] M. Jackson,[73] P. Jackson,[1] M. R. Jaekel,[30] V. Jain,[2] K. Jakobs,[48] S. Jakobsen,[36] T. Jakoubek,[126] J. Jakubek,[127] D. O. Jamin,[152] D. K. Jana,[78] E. Jansen,[77] H. Jansen,[30] J. Janssen,[21] M. Janus,[171] G. Jarlskog,[80] T. Javůrek,[48] L. Jeanty,[15] G.-Y. Jeng,[151] D. Jennens,[87] P. Jenni,[48,o] J. Jentzsch,[43] C. Jeske,[171] S. Jézéquel,[5] H. Ji,[174] W. Ji,[82] J. Jia,[149] Y. Jiang,[33b] M. Jimenez Belenguer,[42] S. Jin,[33a] A. Jinaru,[26a] O. Jinnouchi,[158] M. D. Joergensen,[36] K. E. Johansson,[147a] P. Johansson,[140] K. A. Johns,[7] K. Jon-And,[147a,147b] G. Jones,[171] R. W. L. Jones,[71] T. J. Jones,[73] J. Jongmanns,[58a] P. M. Jorge,[125a,125b] K. D. Joshi,[83] J. Jovicevic,[148] X. Ju,[174] C. A. Jung,[43] R. M. Jungst,[30] P. Jussel,[61] A. Juste Rozas,[12,n] M. Kaci,[168] A. Kaczmarska,[39] M. Kado,[116] H. Kagan,[110] M. Kagan,[144] E. Kajomovitz,[45] S. Kama,[40] N. Kanaya,[156] M. Kaneda,[30] S. Kaneti,[28] T. Kanno,[158] V. A. Kantserov,[97] J. Kanzaki,[65] B. Kaplan,[109] A. Kapliy,[31] D. Kar,[53] K. Karakostas,[10] N. Karastathis,[10] M. Karnevskiy,[82] S. N. Karpov,[64] K. Karthik,[109] V. Kartvelishvili,[71] A. N. Karyukhin,[129] L. Kashif,[174] G. Kasieczka,[58b] R. D. Kass,[110] A. Kastanas,[14] Y. Kataoka,[156] A. Katre,[49] J. Katzy,[42] V. Kaushik,[7] K. Kawagoe,[69] T. Kawamoto,[156] G. Kawamura,[54] S. Kazama,[156] V. F. Kazanin,[108] M. Y. Kazarinov,[64] R. Keeler,[170] P. T. Keener,[121] R. Kehoe,[40] M. Keil,[54] J. S. Keller,[42] H. Keoshkerian,[5] O. Kepka,[126] B. P. Kerševan,[74] S. Kersten,[176] K. Kessoku,[156] J. Keung,[159] F. Khalil-zada,[11] H. Khandanyan,[147a,147b] A. Khanov,[113] A. Khodinov,[97] A. Khomich,[58a] T. J. Khoo,[28] G. Khoriauli,[21] A. Khoroshilov,[176] V. Khovanskiy,[96] E. Khramov,[64] J. Khubua,[51b] H. Y. Kim,[8] H. Kim,[147a,147b] S. H. Kim,[161] N. Kimura,[172] O. Kind,[16] B. T. King,[73] M. King,[168] R. S. B. King,[119] S. B. King,[169] J. Kirk,[130] A. E. Kiryunin,[100] T. Kishimoto,[66] D. Kisielewska,[38a] F. Kiss,[48] T. Kitamura,[66] T. Kittelmann,[124] K. Kiuchi,[161] E. Kladiva,[145b] M. Klein,[73] U. Klein,[73] K. Kleinknecht,[82] P. Klimek,[147a,147b] A. Klimentov,[25] R. Klingenberg,[43] J. A. Klinger,[83] E. B. Klinkby,[36] T. Klioutchnikova,[30] P. F. Klok,[105] E.-E. Kluge,[58a] P. Kluit,[106] S. Kluth,[100] E. Kneringer,[61] E. B. F. G. Knoops,[84] A. Knue,[53] T. Kobayashi,[156] M. Kobel,[44] M. Kocian,[144] P. Kodys,[128] P. Koevesarki,[21] T. Koffas,[29] E. Koffeman,[106] L. A. Kogan,[119] S. Kohlmann,[176] Z. Kohout,[127] T. Kohriki,[65] T. Koi,[144] H. Kolanoski,[16] I. Koletsou,[5] J. Koll,[89] A. A. Komar,[95,a] Y. Komori,[156] T. Kondo,[65] K. Köneke,[48] A. C. König,[105] S. König,[82] T. Kono,[65,p] R. Konoplich,[109,q] N. Konstantinidis,[77] R. Kopeliansky,[153] S. Koperny,[38a] L. Köpke,[82] A. K. Kopp,[48] K. Korcyl,[39] K. Kordas,[155] A. Korn,[77] A. A. Korol,[108] I. Korolkov,[12] E. V. Korolkova,[140] V. A. Korotkov,[129] O. Kortner,[100] S. Kortner,[100] V. V. Kostyukhin,[21] S. Kotov,[100] V. M. Kotov,[64] A. Kotwal,[45] C. Kourkoumelis,[9] V. Kouskoura,[155] A. Koutsman,[160a] R. Kowalewski,[170] T. Z. Kowalski,[38a] W. Kozanecki,[137] A. S. Kozhin,[129] V. Kral,[127] V. A. Kramarenko,[98] G. Kramberger,[74] D. Krasnopevtsev,[97] M. W. Krasny,[79] A. Krasznahorkay,[30] J. K. Kraus,[21] A. Kravchenko,[25] S. Kreiss,[109] M. Kretz,[58c] J. Kretzschmar,[73] K. Kreutzfeldt,[52] P. Krieger,[159] K. Kroeninger,[54] H. Kroha,[100] J. Kroll,[121] J. Kroseberg,[21] J. Krstic,[13a] U. Kruchonak,[64] H. Krüger,[21] T. Kruker,[17] N. Krumnack,[63] Z. V. Krumshteyn,[64] A. Kruse,[174] M. C. Kruse,[45] M. Kruskal,[22] T. Kubota,[87] S. Kuday,[4a] S. Kuehn,[48] A. Kugel,[58c] A. Kuhl,[138] T. Kuhl,[42] V. Kukhtin,[64] Y. Kulchitsky,[91] S. Kuleshov,[32b] M. Kuna,[133a,133b] J. Kunkle,[121] A. Kupco,[126] H. Kurashige,[66] Y. A. Kurochkin,[91] R. Kurumida,[66] V. Kus,[126] E. S. Kuwertz,[148] M. Kuze,[158] J. Kvita,[143] A. La Rosa,[49] L. La Rotonda,[37a,37b] L. Labarga,[81] C. Lacasta,[168] F. Lacava,[133a,133b] J. Lacey,[29] H. Lacker,[16] D. Lacour,[79] V. R. Lacuesta,[168] E. Ladygin,[64] R. Lafaye,[5] B. Laforge,[79] T. Lagouri,[177] S. Lai,[48] H. Laier,[58a] L. Lambourne,[77] S. Lammers,[60] C. L. Lampen,[7] W. Lampl,[7] E. Lançon,[137] U. Landgraf,[48] M. P. J. Landon,[75] V. S. Lang,[58a] C. Lange,[42] A. J. Lankford,[164] F. Lanni,[25] K. Lantzsch,[30] S. Laplace,[79] C. Lapoire,[21] J. F. Laporte,[137] T. Lari,[90a] M. Lassnig,[30] P. Laurelli,[47] V. Lavorini,[37a,37b] W. Lavrijsen,[15] A. T. Law,[138] P. Laycock,[73] B. T. Le,[55] O. Le Dortz,[79] E. Le Guirriec,[84] E. Le Menedeu,[12] T. LeCompte,[6] F. Ledroit-Guillon,[55] C. A. Lee,[152] H. Lee,[106] J. S. H. Lee,[117] S. C. Lee,[152] L. Lee,[177] G. Lefebvre,[79] M. Lefebvre,[170] F. Legger,[99] C. Leggett,[15] A. Lehan,[73] M. Lehmacher,[21] G. Lehmann Miotto,[30] X. Lei,[7] A. G. Leister,[177] M. A. L. Leite,[24d] R. Leitner,[128] D. Lellouch,[173] B. Lemmer,[54] K. J. C. Leney,[77] T. Lenz,[106] G. Lenzen,[176] B. Lenzi,[30] R. Leone,[7] K. Leonhardt,[44] S. Leontsinis,[10] C. Leroy,[94] C. G. Lester,[28] C. M. Lester,[121] J. Levêque,[5] D. Levin,[88] L. J. Levinson,[173] M. Levy,[18] A. Lewis,[119] G. H. Lewis,[109] A. M. Leyko,[21] M. Leyton,[41] B. Li,[33b,r] B. Li,[84] H. Li,[149] H. L. Li,[31] S. Li,[45] X. Li,[88] Y. Li,[33c,s] Z. Liang,[119,t] H. Liao,[34] B. Liberti,[134a] P. Lichard,[30] K. Lie,[166] J. Liebal,[21] W. Liebig,[14] C. Limbach,[21] A. Limosani,[87] M. Limper,[62] S. C. Lin,[152,u] F. Linde,[106] B. E. Lindquist,[149] J. T. Linnemann,[89] E. Lipeles,[121] A. Lipniacka,[14] M. Lisovyi,[42] T. M. Liss,[166] D. Lissauer,[25] A. Lister,[169] A. M. Litke,[138] B. Liu,[152] D. Liu,[152] J. B. Liu,[33b] K. Liu,[33b,v] L. Liu,[88] M. Liu,[45] M. Liu,[33b] Y. Liu,[33b] M. Livan,[120a,120b] S. S. A. Livermore,[119] A. Lleres,[55] J. Llorente Merino,[81] S. L. Lloyd,[75] F. Lo Sterzo,[152] E. Lobodzinska,[42] P. Loch,[7] W. S. Lockman,[138] T. Loddenkoetter,[21] F. K. Loebinger,[83] A. E. Loevschall-Jensen,[36] A. Loginov,[177] C. W. Loh,[169] T. Lohse,[16] K. Lohwasser,[48] M. Lokajicek,[126]

V. P. Lombardo,[5] J. D. Long,[88] R. E. Long,[71] L. Lopes,[125a] D. Lopez Mateos,[57] B. Lopez Paredes,[140] J. Lorenz,[99] N. Lorenzo Martinez,[60] M. Losada,[163] P. Loscutoff,[15] M. J. Losty,[160a,a] X. Lou,[41] A. Lounis,[116] J. Love,[6] P. A. Love,[71] A. J. Lowe,[144,f] F. Lu,[33a] H. J. Lubatti,[139] C. Luci,[133a,133b] A. Lucotte,[55] F. Luehring,[60] W. Lukas,[61] L. Luminari,[133a] O. Lundberg,[147a,147b] B. Lund-Jensen,[148] M. Lungwitz,[82] D. Lynn,[25] R. Lysak,[126] E. Lytken,[80] H. Ma,[25] L. L. Ma,[33d] G. Maccarrone,[47] A. Macchiolo,[100] B. Maček,[74] J. Machado Miguens,[125a,125b] D. Macina,[30] D. Madaffari,[84] R. Madar,[48] H. J. Maddocks,[71] W. F. Mader,[44] A. Madsen,[167] M. Maeno,[8] T. Maeno,[25] E. Magradze,[54] K. Mahboubi,[48] J. Mahlstedt,[106] S. Mahmoud,[73] C. Maiani,[137] C. Maidantchik,[24a] A. Maio,[125a,125b,125d] S. Majewski,[115] Y. Makida,[65] N. Makovec,[116] P. Mal,[137,w] B. Malaescu,[79] Pa. Malecki,[39] V. P. Maleev,[122] F. Malek,[55] U. Mallik,[62] D. Malon,[6] C. Malone,[144] S. Maltezos,[10] V. M. Malyshev,[108] S. Malyukov,[30] J. Mamuzic,[13b] B. Mandelli,[30] L. Mandelli,[90a] I. Mandić,[74] R. Mandrysch,[62] J. Maneira,[125a,125b] A. Manfredini,[100] L. Manhaes de Andrade Filho,[24b] J. A. Manjarres Ramos,[160b] A. Mann,[99] P. M. Manning,[138] A. Manousakis-Katsikakis,[9] B. Mansoulie,[137] R. Mantifel,[86] L. Mapelli,[30] L. March,[168] J. F. Marchand,[29] F. Marchese,[134a,134b] G. Marchiori,[79] M. Marcisovsky,[126] C. P. Marino,[170] C. N. Marques,[125a] F. Marroquim,[24a] S. P. Marsden,[83] Z. Marshall,[15] L. F. Marti,[17] S. Marti-Garcia,[168] B. Martin,[30] B. Martin,[89] J. P. Martin,[94] T. A. Martin,[171] V. J. Martin,[46] B. Martin dit Latour,[49] H. Martinez,[137] M. Martinez,[12,n] S. Martin-Haugh,[130] A. C. Martyniuk,[77] M. Marx,[139] F. Marzano,[133a] A. Marzin,[30] L. Masetti,[82] T. Mashimo,[156] R. Mashinistov,[95] J. Masik,[83] A. L. Maslennikov,[108] I. Massa,[20a,20b] N. Massol,[5] P. Mastrandrea,[149] A. Mastroberardino,[37a,37b] T. Masubuchi,[156] P. Matricon,[116] H. Matsunaga,[156] T. Matsushita,[66] P. Mättig,[176] S. Mättig,[42] J. Mattmann,[82] J. Maurer,[26a] S. J. Maxfield,[73] D. A. Maximov,[108,g] R. Mazini,[152] L. Mazzaferro,[134a,134b] G. Mc Goldrick,[159] S. P. Mc Kee,[88] A. McCarn,[88] R. L. McCarthy,[149] T. G. McCarthy,[29] N. A. McCubbin,[130] K. W. McFarlane,[56,a] J. A. Mcfayden,[77] G. Mchedlidze,[54] T. Mclaughlan,[18] S. J. McMahon,[130] R. A. McPherson,[170,j] A. Meade,[85] J. Mechnich,[106] M. Medinnis,[42] S. Meehan,[31] R. Meera-Lebbai,[112] S. Mehlhase,[36] A. Mehta,[73] K. Meier,[58a] C. Meineck,[99] B. Meirose,[80] C. Melachrinos,[31] B. R. Mellado Garcia,[146c] F. Meloni,[90a,90b] L. Mendoza Navas,[163] A. Mengarelli,[20a,20b] S. Menke,[100] E. Meoni,[162] K. M. Mercurio,[57] S. Mergelmeyer,[21] N. Meric,[137] P. Mermod,[49] L. Merola,[103a,103b] C. Meroni,[90a] F. S. Merritt,[31] H. Merritt,[110] A. Messina,[30,x] J. Metcalfe,[25] A. S. Mete,[164] C. Meyer,[82] C. Meyer,[31] J-P. Meyer,[137] J. Meyer,[30] R. P. Middleton,[130] S. Migas,[73] L. Mijović,[137] G. Mikenberg,[173] M. Mikestikova,[126] M. Mikuž,[74] D. W. Miller,[31] C. Mills,[46] A. Milov,[173] D. A. Milstead,[147a,147b] D. Milstein,[173] A. A. Minaenko,[129] M. Miñano Moya,[168] I. A. Minashvili,[64] A. I. Mincer,[109] B. Mindur,[38a] M. Mineev,[64] Y. Ming,[174] L. M. Mir,[12] G. Mirabelli,[133a] T. Mitani,[172] J. Mitrevski,[99] V. A. Mitsou,[168] S. Mitsui,[65] A. Miucci,[49] P. S. Miyagawa,[140] J. U. Mjörnmark,[80] T. Moa,[147a,147b] K. Mochizuki,[84] V. Moeller,[28] S. Mohapatra,[35] W. Mohr,[48] S. Molander,[147a,147b] R. Moles-Valls,[168] K. Mönig,[42] C. Monini,[55] J. Monk,[36] E. Monnier,[84] J. Montejo Berlingen,[12] F. Monticelli,[70] S. Monzani,[133a,133b] R. W. Moore,[3] C. Mora Herrera,[49] A. Moraes,[53] N. Morange,[62] J. Morel,[54] D. Moreno,[82] M. Moreno Llácer,[54] P. Morettini,[50a] M. Morgenstern,[44] M. Morii,[57] S. Moritz,[82] A. K. Morley,[148] G. Mornacchi,[30] J. D. Morris,[75] L. Morvaj,[102] H. G. Moser,[100] M. Mosidze,[51b] J. Moss,[110] R. Mount,[144] E. Mountricha,[25] S. V. Mouraviev,[95,a] E. J. W. Moyse,[85] S. Muanza,[84] R. D. Mudd,[18] F. Mueller,[58a] J. Mueller,[124] K. Mueller,[21] T. Mueller,[28] T. Mueller,[82] D. Muenstermann,[49] Y. Munwes,[154] J. A. Murillo Quijada,[18] W. J. Murray,[171,130] E. Musto,[153] A. G. Myagkov,[129,y] M. Myska,[126] O. Nackenhorst,[54] J. Nadal,[54] K. Nagai,[61] R. Nagai,[158] Y. Nagai,[84] K. Nagano,[65] A. Nagarkar,[110] Y. Nagasaka,[59] M. Nagel,[100] A. M. Nairz,[30] Y. Nakahama,[30] K. Nakamura,[65] T. Nakamura,[156] I. Nakano,[111] H. Namasivayam,[41] G. Nanava,[21] R. Narayan,[58b] T. Nattermann,[21] T. Naumann,[42] G. Navarro,[163] R. Nayyar,[7] H. A. Neal,[88] P. Yu. Nechaeva,[95] T. J. Neep,[83] A. Negri,[120a,120b] G. Negri,[30] M. Negrini,[20a] S. Nektarijevic,[49] A. Nelson,[164] T. K. Nelson,[144] S. Nemecek,[126] P. Nemethy,[109] A. A. Nepomuceno,[24a] M. Nessi,[30,z] M. S. Neubauer,[166] M. Neumann,[176] R. M. Neves,[109] P. Nevski,[25] F. M. Newcomer,[121] P. R. Newman,[18] D. H. Nguyen,[6] R. B. Nickerson,[119] R. Nicolaidou,[137] B. Nicquevert,[30] J. Nielsen,[138] N. Nikiforou,[35] A. Nikiforov,[16] V. Nikolaenko,[129,y] I. Nikolic-Audit,[79] K. Nikolics,[49] K. Nikolopoulos,[18] P. Nilsson,[8] Y. Ninomiya,[156] A. Nisati,[133a] R. Nisius,[100] T. Nobe,[158] L. Nodulman,[6] M. Nomachi,[117] I. Nomidis,[155] S. Norberg,[112] M. Nordberg,[30] J. Novakova,[128] S. Nowak,[100] M. Nozaki,[65] L. Nozka,[114] K. Ntekas,[10] G. Nunes Hanninger,[87] T. Nunnemann,[99] E. Nurse,[77] F. Nuti,[87] B. J. O'Brien,[46] F. O'grady,[7] D. C. O'Neil,[143] V. O'Shea,[53] F. G. Oakham,[29,e] H. Oberlack,[100] T. Obermann,[21] J. Ocariz,[79] A. Ochi,[66] M. I. Ochoa,[77] S. Oda,[69] S. Odaka,[65] H. Ogren,[60] A. Oh,[83] S. H. Oh,[45] C. C. Ohm,[30] H. Ohman,[167] T. Ohshima,[102] W. Okamura,[117] H. Okawa,[25] Y. Okumura,[31] T. Okuyama,[156] A. Olariu,[26a] A. G. Olchevski,[64] S. A. Olivares Pino,[46] D. Oliveira Damazio,[25] E. Oliver Garcia,[168] D. Olivito,[121] A. Olszewski,[39] J. Olszowska,[39] A. Onofre,[125a,125e] P. U. E. Onyisi,[31,aa] C. J. Oram,[160a] M. J. Oreglia,[31] Y. Oren,[154] D. Orestano,[135a,135b] N. Orlando,[72a,72b] C. Oropeza Barrera,[53] R. S. Orr,[159] B. Osculati,[50a,50b] R. Ospanov,[121] G. Otero y Garzon,[27] H. Otono,[69]

M. Ouchrif,[136d] E. A. Ouellette,[170] F. Ould-Saada,[118] A. Ouraou,[137] K. P. Oussoren,[106] Q. Ouyang,[33a] A. Ovcharova,[15] M. Owen,[83] V. E. Ozcan,[19a] N. Ozturk,[8] K. Pachal,[119] A. Pacheco Pages,[12] C. Padilla Aranda,[12] M. Pagáčová,[48] S. Pagan Griso,[15] E. Paganis,[140] C. Pahl,[100] F. Paige,[25] P. Pais,[85] K. Pajchel,[118] G. Palacino,[160b] S. Palestini,[30] D. Pallin,[34] A. Palma,[125a,125b] J. D. Palmer,[18] Y. B. Pan,[174] E. Panagiotopoulou,[10] J. G. Panduro Vazquez,[76] P. Pani,[106] N. Panikashvili,[88] S. Panitkin,[25] D. Pantea,[26a] L. Paolozzi,[134a,134b] Th. D. Papadopoulou,[10] K. Papageorgiou,[155,l] A. Paramonov,[6] D. Paredes Hernandez,[34] M. A. Parker,[28] F. Parodi,[50a,50b] J. A. Parsons,[35] U. Parzefall,[48] E. Pasqualucci,[133a] S. Passaggio,[50a] A. Passeri,[135a] F. Pastore,[135a,135b,a] Fr. Pastore,[76] G. Pásztor,[49,bb] S. Pataraia,[176] N. D. Patel,[151] J. R. Pater,[83] S. Patricelli,[103a,103b] T. Pauly,[30] J. Pearce,[170] M. Pedersen,[118] S. Pedraza Lopez,[168] R. Pedro,[125a,125b] S. V. Peleganchuk,[108] D. Pelikan,[167] H. Peng,[33b] B. Penning,[31] J. Penwell,[60] D. V. Perepelitsa,[25] E. Perez Codina,[160a] M. T. Pérez García-Estañ,[168] V. Perez Reale,[35] L. Perini,[90a,90b] H. Pernegger,[30] R. Perrino,[72a] R. Peschke,[42] V. D. Peshekhonov,[64] K. Peters,[30] R. F. Y. Peters,[83] B. A. Petersen,[87] J. Petersen,[30] T. C. Petersen,[36] E. Petit,[42] A. Petridis,[147a,147b] C. Petridou,[155] E. Petrolo,[133a] F. Petrucci,[135a,135b] M. Petteni,[143] N. E. Pettersson,[158] R. Pezoa,[32b] P. W. Phillips,[130] G. Piacquadio,[144] E. Pianori,[171] A. Picazio,[49] E. Piccaro,[75] M. Piccinini,[20a,20b] S. M. Piec,[42] R. Piegaia,[27] D. T. Pignotti,[110] J. E. Pilcher,[31] A. D. Pilkington,[77] J. Pina,[125a,125b,125d] M. Pinamonti,[165a,165c,cc] A. Pinder,[119] J. L. Pinfold,[3] A. Pingel,[36] B. Pinto,[125a] S. Pires,[79] C. Pizio,[90a,90b] M.-A. Pleier,[25] V. Pleskot,[128] E. Plotnikova,[64] P. Plucinski,[147a,147b] S. Poddar,[58a] F. Podlyski,[34] R. Poettgen,[82] L. Poggioli,[116] D. Pohl,[21] M. Pohl,[49] G. Polesello,[120a] A. Policicchio,[37a,37b] R. Polifka,[159] A. Polini,[20a] C. S. Pollard,[45] V. Polychronakos,[25] K. Pommès,[30] L. Pontecorvo,[133a] B. G. Pope,[89] G. A. Popeneciu,[26b] D. S. Popovic,[13a] A. Poppleton,[30] X. Portell Bueso,[12] G. E. Pospelov,[100] S. Pospisil,[127] K. Potamianos,[15] I. N. Potrap,[64] C. J. Potter,[150] C. T. Potter,[115] G. Poulard,[30] J. Poveda,[60] V. Pozdnyakov,[64] R. Prabhu,[77] P. Pralavorio,[84] A. Pranko,[15] S. Prasad,[30] R. Pravahan,[8] S. Prell,[63] D. Price,[83] J. Price,[73] L. E. Price,[6] D. Prieur,[124] M. Primavera,[72a] M. Proissl,[46] K. Prokofiev,[47] F. Prokoshin,[32b] E. Protopapadaki,[137] S. Protopopescu,[25] J. Proudfoot,[6] M. Przybycien,[38a] H. Przysiezniak,[5] E. Ptacek,[115] E. Pueschel,[85] D. Puldon,[149] M. Purohit,[25,dd] P. Puzo,[116] Y. Pylypchenko,[62] J. Qian,[88] G. Qin,[53] A. Quadt,[54] D. R. Quarrie,[15] W. B. Quayle,[165a,165b] D. Quilty,[53] A. Qureshi,[160b] V. Radeka,[25] V. Radescu,[42] S. K. Radhakrishnan,[149] P. Radloff,[115] P. Rados,[87] F. Ragusa,[90a,90b] G. Rahal,[179] S. Rajagopalan,[25] M. Rammensee,[30] M. Rammes,[142] A. S. Randle-Conde,[40] C. Rangel-Smith,[79] K. Rao,[164] F. Rauscher,[99] T. C. Rave,[48] T. Ravenscroft,[53] M. Raymond,[30] A. L. Read,[118] D. M. Rebuzzi,[120a,120b] A. Redelbach,[175] G. Redlinger,[25] R. Reece,[138] K. Reeves,[41] L. Rehnisch,[16] A. Reinsch,[115] H. Reisin,[27] M. Relich,[164] C. Rembser,[30] Z. L. Ren,[152] A. Renaud,[116] M. Rescigno,[133a] S. Resconi,[90a] B. Resende,[137] P. Reznicek,[128] R. Rezvani,[94] R. Richter,[100] M. Ridel,[79] P. Rieck,[16] M. Rijssenbeek,[149] A. Rimoldi,[120a,120b] L. Rinaldi,[20a] E. Ritsch,[61] I. Riu,[12] F. Rizatdinova,[113] E. Rizvi,[75] S. H. Robertson,[86,j] A. Robichaud-Veronneau,[119] D. Robinson,[28] J. E. M. Robinson,[83] A. Robson,[53] C. Roda,[123a,123b] L. Rodrigues,[30] S. Roe,[30] O. Røhne,[118] S. Rolli,[162] A. Romaniouk,[97] M. Romano,[20a,20b] G. Romeo,[27] E. Romero Adam,[168] N. Rompotis,[139] L. Roos,[79] E. Ros,[168] S. Rosati,[133a] K. Rosbach,[49] A. Rose,[150] M. Rose,[76] P. L. Rosendahl,[14] O. Rosenthal,[142] V. Rossetti,[147a,147b] E. Rossi,[103a,103b] L. P. Rossi,[50a] R. Rosten,[139] M. Rotaru,[26a] I. Roth,[173] J. Rothberg,[139] D. Rousseau,[116] C. R. Royon,[137] A. Rozanov,[84] Y. Rozen,[153] X. Ruan,[146c] F. Rubbo,[12] I. Rubinskiy,[42] V. I. Rud,[98] C. Rudolph,[44] M. S. Rudolph,[159] F. Rühr,[48] A. Ruiz-Martinez,[63] Z. Rurikova,[48] N. A. Rusakovich,[64] A. Ruschke,[99] J. P. Rutherfoord,[7] N. Ruthmann,[48] Y. F. Ryabov,[122] M. Rybar,[128] G. Rybkin,[116] N. C. Ryder,[119] A. F. Saavedra,[151] S. Sacerdoti,[27] A. Saddique,[3] I. Sadeh,[154] H. F-W. Sadrozinski,[138] R. Sadykov,[64] F. Safai Tehrani,[133a] H. Sakamoto,[156] Y. Sakurai,[172] G. Salamanna,[75] A. Salamon,[134a] M. Saleem,[112] D. Salek,[106] P. H. Sales De Bruin,[139] D. Salihagic,[100] A. Salnikov,[144] J. Salt,[168] B. M. Salvachua Ferrando,[6] D. Salvatore,[37a,37b] F. Salvatore,[150] A. Salvucci,[105] A. Salzburger,[30] D. Sampsonidis,[155] A. Sanchez,[103a,103b] J. Sánchez,[168] V. Sanchez Martinez,[168] H. Sandaker,[14] H. G. Sander,[82] M. P. Sanders,[99] M. Sandhoff,[176] T. Sandoval,[28] C. Sandoval,[163] R. Sandstroem,[100] D. P. C. Sankey,[130] A. Sansoni,[47] C. Santoni,[34] R. Santonico,[134a,134b] H. Santos,[125a] I. Santoyo Castillo,[150] K. Sapp,[124] A. Sapronov,[64] J. G. Saraiva,[125a,125d] B. Sarrazin,[21] G. Sartisohn,[176] O. Sasaki,[65] Y. Sasaki,[156] I. Satsounkevitch,[91] G. Sauvage,[5,a] E. Sauvan,[5] P. Savard,[159,e] D. O. Savu,[30] C. Sawyer,[119] L. Sawyer,[78,m] D. H. Saxon,[53] J. Saxon,[121] C. Sbarra,[20a] A. Sbrizzi,[3] T. Scanlon,[30] D. A. Scannicchio,[164] M. Scarcella,[151] J. Schaarschmidt,[173] P. Schacht,[100] D. Schaefer,[121] R. Schaefer,[42] A. Schaelicke,[46] S. Schaepe,[21] S. Schaetzel,[58b] U. Schäfer,[82] A. C. Schaffer,[116] D. Schaile,[99] R. D. Schamberger,[149] V. Scharf,[58a] V. A. Schegelsky,[122] D. Scheirich,[128] M. Schernau,[164] M. I. Scherzer,[35] C. Schiavi,[50a,50b] J. Schieck,[99] C. Schillo,[48] M. Schioppa,[37a,37b] S. Schlenker,[30] E. Schmidt,[48] K. Schmieden,[30] C. Schmitt,[82] C. Schmitt,[99] S. Schmitt,[58b] B. Schneider,[17] Y. J. Schnellbach,[73] U. Schnoor,[44] L. Schoeffel,[137] A. Schoening,[58b] B. D. Schoenrock,[89] A. L. S. Schorlemmer,[54] M. Schott,[82] D. Schouten,[160a] J. Schovancova,[25] M. Schram,[86] S. Schramm,[159] M. Schreyer,[175] C. Schroeder,[82] N. Schuh,[82]

M. J. Schultens,[21] H.-C. Schultz-Coulon,[58a] H. Schulz,[16] M. Schumacher,[48] B. A. Schumm,[138] Ph. Schune,[137] A. Schwartzman,[144] Ph. Schwegler,[100] Ph. Schwemling,[137] R. Schwienhorst,[89] J. Schwindling,[137] T. Schwindt,[21] M. Schwoerer,[5] F. G. Sciacca,[17] E. Scifo,[116] G. Sciolla,[23] W. G. Scott,[130] F. Scuri,[123a,123b] F. Scutti,[21] J. Searcy,[88] G. Sedov,[42] E. Sedykh,[122] S. C. Seidel,[104] A. Seiden,[138] F. Seifert,[127] J. M. Seixas,[24a] G. Sekhniaidze,[103a] S. J. Sekula,[40] K. E. Selbach,[46] D. M. Seliverstov,[122,a] G. Sellers,[73] N. Semprini-Cesari,[20a,20b] C. Serfon,[30] L. Serin,[116] L. Serkin,[54] T. Serre,[84] R. Seuster,[160a] H. Severini,[112] F. Sforza,[100] A. Sfyrla,[30] E. Shabalina,[54] M. Shamim,[115] L. Y. Shan,[33a] J. T. Shank,[22] Q. T. Shao,[87] M. Shapiro,[15] P. B. Shatalov,[96] K. Shaw,[165a,165b] P. Sherwood,[77] S. Shimizu,[66] C. O. Shimmin,[164] M. Shimojima,[101] T. Shin,[56] M. Shiyakova,[64] A. Shmeleva,[95] M. J. Shochet,[31] D. Short,[119] S. Shrestha,[63] E. Shulga,[97] M. A. Shupe,[7] S. Shushkevich,[42] P. Sicho,[126] D. Sidorov,[113] A. Sidoti,[133a] F. Siegert,[44] Dj. Sijacki,[13a] O. Silbert,[173] J. Silva,[125a,125d] Y. Silver,[154] D. Silverstein,[144] S. B. Silverstein,[147a] V. Simak,[127] O. Simard,[5] Lj. Simic,[13a] S. Simion,[116] E. Simioni,[82] B. Simmons,[77] R. Simoniello,[90a,90b] M. Simonyan,[36] P. Sinervo,[159] N. B. Sinev,[115] V. Sipica,[142] G. Siragusa,[175] A. Sircar,[78] A. N. Sisakyan,[64,a] S. Yu. Sivoklokov,[98] J. Sjölin,[147a,147b] T. B. Sjursen,[14] L. A. Skinnari,[15] H. P. Skottowe,[57] K. Yu. Skovpen,[108] P. Skubic,[112] M. Slater,[18] T. Slavicek,[127] K. Sliwa,[162] V. Smakhtin,[173] B. H. Smart,[46] L. Smestad,[118] S. Yu. Smirnov,[97] Y. Smirnov,[97] L. N. Smirnova,[98,ee] O. Smirnova,[80] K. M. Smith,[53] M. Smizanska,[71] K. Smolek,[127] A. A. Snesarev,[95] G. Snidero,[75] J. Snow,[112] S. Snyder,[25] R. Sobie,[170,j] F. Socher,[44] J. Sodomka,[127] A. Soffer,[154] D. A. Soh,[152,t] C. A. Solans,[30] M. Solar,[127] J. Solc,[127] E. Yu. Soldatov,[97] U. Soldevila,[168] E. Solfaroli Camillocci,[133a,133b] A. A. Solodkov,[129] O. V. Solovyanov,[129] V. Solovyev,[122] P. Sommer,[48] H. Y. Song,[33b] N. Soni,[1] A. Sood,[15] V. Sopko,[127] B. Sopko,[127] V. Sorin,[12] M. Sosebee,[8] R. Soualah,[165a,165c] P. Soueid,[94] A. M. Soukharev,[108] D. South,[42] S. Spagnolo,[72a,72b] F. Spanò,[76] W. R. Spearman,[57] R. Spighi,[20a] G. Spigo,[30] M. Spousta,[128] T. Spreitzer,[159] B. Spurlock,[8] R. D. St. Denis,[53] S. Staerz,[44] J. Stahlman,[121] R. Stamen,[58a] E. Stanecka,[39] R. W. Stanek,[6] C. Stanescu,[135a] M. Stanescu-Bellu,[42] M. M. Stanitzki,[42] S. Stapnes,[118] E. A. Starchenko,[129] J. Stark,[55] P. Staroba,[126] P. Starovoitov,[42] R. Staszewski,[39] P. Stavina,[145a,a] G. Steele,[53] P. Steinberg,[25] I. Stekl,[127] B. Stelzer,[143] H. J. Stelzer,[30] O. Stelzer-Chilton,[160a] H. Stenzel,[52] S. Stern,[100] G. A. Stewart,[53] J. A. Stillings,[21] M. C. Stockton,[86] M. Stoebe,[86] K. Stoerig,[48] G. Stoicea,[26a] P. Stolte,[54] S. Stonjek,[100] A. R. Stradling,[8] A. Straessner,[44] J. Strandberg,[148] S. Strandberg,[147a,147b] A. Strandlie,[118] E. Strauss,[144] M. Strauss,[112] P. Strizenec,[145b] R. Ströhmer,[175] D. M. Strom,[115] R. Stroynowski,[40] S. A. Stucci,[17] B. Stugu,[14] N. A. Styles,[42] D. Su,[144] J. Su,[124] HS. Subramania,[3] R. Subramaniam,[78] A. Succurro,[12] Y. Sugaya,[117] C. Suhr,[107] M. Suk,[127] V. V. Sulin,[95] S. Sultansoy,[4c] T. Sumida,[67] X. Sun,[33a] J. E. Sundermann,[48] K. Suruliz,[140] G. Susinno,[37a,37b] M. R. Sutton,[150] Y. Suzuki,[65] M. Svatos,[126] S. Swedish,[169] M. Swiatlowski,[144] I. Sykora,[145a] T. Sykora,[128] D. Ta,[89] K. Tackmann,[42] J. Taenzer,[159] A. Taffard,[164] R. Tafirout,[160a] N. Taiblum,[154] Y. Takahashi,[102] H. Takai,[25] R. Takashima,[68] H. Takeda,[66] T. Takeshita,[141] Y. Takubo,[65] M. Talby,[84] A. A. Talyshev,[108,g] J. Y. C. Tam,[175] M. C. Tamsett,[78,ff] K. G. Tan,[87] J. Tanaka,[156] R. Tanaka,[116] S. Tanaka,[132] S. Tanaka,[65] A. J. Tanasijczuk,[143] K. Tani,[66] N. Tannoury,[84] S. Tapprogge,[82] S. Tarem,[153] F. Tarrade,[29] G. F. Tartarelli,[90a] P. Tas,[128] M. Tasevsky,[126] T. Tashiro,[67] E. Tassi,[37a,37b] A. Tavares Delgado,[125a,125b] Y. Tayalati,[136d] C. Taylor,[77] F. E. Taylor,[93] G. N. Taylor,[87] W. Taylor,[160b] F. A. Teischinger,[30] M. Teixeira Dias Castanheira,[75] P. Teixeira-Dias,[76] K. K. Temming,[48] H. Ten Kate,[30] P. K. Teng,[152] S. Terada,[65] K. Terashi,[156] J. Terron,[81] S. Terzo,[100] M. Testa,[47] R. J. Teuscher,[159,j] J. Therhaag,[21] T. Theveneaux-Pelzer,[34] S. Thoma,[48] J. P. Thomas,[18] J. Thomas-Wilsker,[76] E. N. Thompson,[35] P. D. Thompson,[18] P. D. Thompson,[159] A. S. Thompson,[53] L. A. Thomsen,[36] E. Thomson,[121] M. Thomson,[28] W. M. Thong,[87] R. P. Thun,[88,a] F. Tian,[35] M. J. Tibbetts,[15] V. O. Tikhomirov,[95,gg] Yu. A. Tikhonov,[108,g] S. Timoshenko,[97] E. Tiouchichine,[84] P. Tipton,[177] S. Tisserant,[84] T. Todorov,[5] S. Todorova-Nova,[128] B. Toggerson,[164] J. Tojo,[69] S. Tokár,[145a] K. Tokushuku,[65] K. Tollefson,[89] L. Tomlinson,[83] M. Tomoto,[102] L. Tompkins,[31] K. Toms,[104] N. D. Topilin,[64] E. Torrence,[115] H. Torres,[143] E. Torró Pastor,[168] J. Toth,[84,bb] F. Touchard,[84] D. R. Tovey,[140] H. L. Tran,[116] T. Trefzger,[175] L. Tremblet,[30] A. Tricoli,[30] I. M. Trigger,[160a] S. Trincaz-Duvoid,[79] M. F. Tripiana,[70] N. Triplett,[25] W. Trischuk,[159] B. Trocmé,[55] C. Troncon,[90a] M. Trottier-McDonald,[143] M. Trovatelli,[135a,135b] P. True,[89] M. Trzebinski,[39] A. Trzupek,[39] C. Tsarouchas,[30] J. C-L. Tseng,[119] P. V. Tsiareshka,[91] D. Tsionou,[137] G. Tsipolitis,[10] N. Tsirintanis,[9] S. Tsiskaridze,[12] V. Tsiskaridze,[48] E. G. Tskhadadze,[51a] I. I. Tsukerman,[96] V. Tsulaia,[15] S. Tsuno,[65] D. Tsybychev,[149] A. Tua,[140] A. Tudorache,[26a] V. Tudorache,[26a] A. N. Tuna,[121] S. A. Tupputi,[20a,20b] S. Turchikhin,[98,ee] D. Turecek,[127] I. Turk Cakir,[4d] R. Turra,[90a,90b] P. M. Tuts,[35] A. Tykhonov,[74] M. Tylmad,[147a,147b] M. Tyndel,[130] K. Uchida,[21] I. Ueda,[156] R. Ueno,[29] M. Ughetto,[84] M. Ugland,[14] M. Uhlenbrock,[21] F. Ukegawa,[161] G. Unal,[30] A. Undrus,[25] G. Unel,[164] F. C. Ungaro,[48] Y. Unno,[65] D. Urbaniec,[35] P. Urquijo,[21] G. Usai,[8] A. Usanova,[61] L. Vacavant,[84] V. Vacek,[127] B. Vachon,[86] N. Valencic,[106] S. Valentinetti,[20a,20b] A. Valero,[168] L. Valery,[34] S. Valkar,[128] E. Valladolid Gallego,[168] S. Vallecorsa,[49] J. A. Valls Ferrer,[168] R. Van Berg,[121] P. C. Van Der Deijl,[106] R. van der Geer,[106]

H. van der Graaf,[106] R. Van Der Leeuw,[106] D. van der Ster,[30] N. van Eldik,[30] P. van Gemmeren,[6] J. Van Nieuwkoop,[143] I. van Vulpen,[106] M. C. van Woerden,[30] M. Vanadia,[133a,133b] W. Vandelli,[30] A. Vaniachine,[6] P. Vankov,[42] F. Vannucci,[79] G. Vardanyan,[178] R. Vari,[133a] E. W. Varnes,[7] T. Varol,[85] D. Varouchas,[79] A. Vartapetian,[8] K. E. Varvell,[151] V. I. Vassilakopoulos,[56] F. Vazeille,[34] T. Vazquez Schroeder,[54] J. Veatch,[7] F. Veloso,[125a,125c] S. Veneziano,[133a] A. Ventura,[72a,72b] D. Ventura,[85] M. Venturi,[48] N. Venturi,[159] A. Venturini,[23] V. Vercesi,[120a] M. Verducci,[139] W. Verkerke,[106] J. C. Vermeulen,[106] A. Vest,[44] M. C. Vetterli,[143,e] O. Viazlo,[80] I. Vichou,[166] T. Vickey,[146c,hh] O. E. Vickey Boeriu,[146c] G. H. A. Viehhauser,[119] S. Viel,[169] R. Vigne,[30] M. Villa,[20a,20b] M. Villaplana Perez,[168] E. Vilucchi,[47] M. G. Vincter,[29] V. B. Vinogradov,[64] J. Virzi,[15] O. Vitells,[173] I. Vivarelli,[150] F. Vives Vaque,[3] S. Vlachos,[10] D. Vladoiu,[99] M. Vlasak,[127] A. Vogel,[21] P. Vokac,[127] G. Volpi,[123a,123b] M. Volpi,[87] H. von der Schmitt,[100] H. von Radziewski,[48] E. von Toerne,[21] V. Vorobel,[128] M. Vos,[168] R. Voss,[30] J. H. Vossebeld,[73] N. Vranjes,[137] M. Vranjes Milosavljevic,[106] V. Vrba,[126] M. Vreeswijk,[106] T. Vu Anh,[48] R. Vuillermet,[30] I. Vukotic,[31] Z. Vykydal,[127] W. Wagner,[176] P. Wagner,[21] S. Wahrmund,[44] J. Wakabayashi,[102] J. Walder,[71] R. Walker,[99] W. Walkowiak,[142] R. Wall,[177] P. Waller,[73] B. Walsh,[177] C. Wang,[152,ii] C. Wang,[45] F. Wang,[174] H. Wang,[15] H. Wang,[40] J. Wang,[42] J. Wang,[33a] K. Wang,[86] R. Wang,[104] S. M. Wang,[152] T. Wang,[21] X. Wang,[177] A. Warburton,[86] C. P. Ward,[28] D. R. Wardrope,[77] M. Warsinsky,[48] A. Washbrook,[46] C. Wasicki,[42] I. Watanabe,[66] P. M. Watkins,[18] A. T. Watson,[18] I. J. Watson,[151] M. F. Watson,[18] G. Watts,[139] S. Watts,[83] B. M. Waugh,[77] S. Webb,[83] M. S. Weber,[17] S. W. Weber,[175] J. S. Webster,[31] A. R. Weidberg,[119] P. Weigell,[100] B. Weinert,[60] J. Weingarten,[54] C. Weiser,[48] H. Weits,[106] P. S. Wells,[30] T. Wenaus,[25] D. Wendland,[16] Z. Weng,[152,t] T. Wengler,[30] S. Wenig,[30] N. Wermes,[21] M. Werner,[48] P. Werner,[30] M. Wessels,[58a] J. Wetter,[162] K. Whalen,[29] A. White,[8] M. J. White,[1] R. White,[32b] S. White,[123a,123b] D. Whiteson,[164] D. Wicke,[176] F. J. Wickens,[130] W. Wiedenmann,[174] M. Wielers,[130] P. Wienemann,[21] C. Wiglesworth,[36] L. A. M. Wiik-Fuchs,[21] P. A. Wijeratne,[77] A. Wildauer,[100] M. A. Wildt,[42,jj] H. G. Wilkens,[30] J. Z. Will,[99] H. H. Williams,[121] S. Williams,[28] C. Willis,[89] S. Willocq,[85] J. A. Wilson,[18] A. Wilson,[88] I. Wingerter-Seez,[5] S. Winkelmann,[48] F. Winklmeier,[115] M. Wittgen,[144] T. Wittig,[43] J. Wittkowski,[99] S. J. Wollstadt,[82] M. W. Wolter,[39] H. Wolters,[125a,125c] B. K. Wosiek,[39] J. Wotschack,[30] M. J. Woudstra,[83] K. W. Wozniak,[39] M. Wright,[53] S. L. Wu,[174] X. Wu,[49] Y. Wu,[88] E. Wulf,[35] T. R. Wyatt,[83] B. M. Wynne,[46] S. Xella,[36] M. Xiao,[137] D. Xu,[33a] L. Xu,[33b,kk] B. Yabsley,[151] S. Yacoob,[146b,ll] M. Yamada,[65] H. Yamaguchi,[156] Y. Yamaguchi,[156] A. Yamamoto,[65] K. Yamamoto,[63] S. Yamamoto,[156] T. Yamamura,[156] T. Yamanaka,[156] K. Yamauchi,[102] Y. Yamazaki,[66] Z. Yan,[22] H. Yang,[33e] H. Yang,[174] U. K. Yang,[83] Y. Yang,[110] S. Yanush,[92] L. Yao,[33a] W-M. Yao,[15] Y. Yasu,[65] E. Yatsenko,[42] K. H. Yau Wong,[21] J. Ye,[40] S. Ye,[25] A. L. Yen,[57] E. Yildirim,[42] M. Yilmaz,[4b] R. Yoosoofmiya,[124] K. Yorita,[172] R. Yoshida,[6] K. Yoshihara,[156] C. Young,[144] C. J. S. Young,[30] S. Youssef,[22] D. R. Yu,[15] J. Yu,[8] J. M. Yu,[88] J. Yu,[113] L. Yuan,[66] A. Yurkewicz,[107] B. Zabinski,[39] R. Zaidan,[62] A. M. Zaitsev,[129,y] A. Zaman,[149] S. Zambito,[23] L. Zanello,[133a,133b] D. Zanzi,[100] A. Zaytsev,[25] C. Zeitnitz,[176] M. Zeman,[127] A. Zemla,[38a] K. Zengel,[23] O. Zenin,[129] T. Ženiš,[145a] D. Zerwas,[116] G. Zevi della Porta,[57] D. Zhang,[88] F. Zhang,[174] H. Zhang,[89] J. Zhang,[6] L. Zhang,[152] X. Zhang,[33d] Z. Zhang,[116] Z. Zhao,[33b] A. Zhemchugov,[64] J. Zhong,[119] B. Zhou,[88] L. Zhou,[35] N. Zhou,[164] C. G. Zhu,[33d] H. Zhu,[33a] J. Zhu,[88] Y. Zhu,[33b] X. Zhuang,[33a] A. Zibell,[99] D. Zieminska,[60] N. I. Zimine,[64] C. Zimmermann,[82] R. Zimmermann,[21] S. Zimmermann,[21] S. Zimmermann,[48] Z. Zinonos,[54] M. Ziolkowski,[142] R. Zitoun,[5] G. Zobernig,[174] A. Zoccoli,[20a,20b] M. zur Nedden,[16] G. Zurzolo,[103a,103b] V. Zutshi[107] and L. Zwalinski[30]

(ATLAS Collaboration)

[1]*Department of Physics, University of Adelaide, Adelaide, Australia*
[2]*Physics Department, SUNY Albany, Albany, New York, USA*
[3]*Department of Physics, University of Alberta, Edmonton, AB, Canada*
[4a]*Department of Physics, Ankara University, Ankara, Turkey*
[4b]*Department of Physics, Gazi University, Ankara, Turkey*
[4c]*Division of Physics, TOBB University of Economics and Technology, Ankara, Turkey*
[4d]*Turkish Atomic Energy Authority, Ankara, Turkey*
[5]*LAPP, CNRS/IN2P3 and Université de Savoie, Annecy-le-Vieux, France*
[6]*High Energy Physics Division, Argonne National Laboratory, Argonne, Illinois, USA*
[7]*Department of Physics, University of Arizona, Tucson, Arizona, USA*
[8]*Department of Physics, The University of Texas at Arlington, Arlington, Texas, USA*
[9]*Physics Department, University of Athens, Athens, Greece*
[10]*Physics Department, National Technical University of Athens, Zografou, Greece*
[11]*Institute of Physics, Azerbaijan Academy of Sciences, Baku, Azerbaijan*

[12]*Institut de Física d'Altes Energies and Departament de Física de la Universitat Autònoma de Barcelona, Barcelona, Spain*
[13a]*Institute of Physics, University of Belgrade, Belgrade, Serbia*
[13b]*Vinca Institute of Nuclear Sciences, University of Belgrade, Belgrade, Serbia*
[14]*Department for Physics and Technology, University of Bergen, Bergen, Norway*
[15]*Physics Division, Lawrence Berkeley National Laboratory and University of California, Berkeley, California, USA*
[16]*Department of Physics, Humboldt University, Berlin, Germany*
[17]*Albert Einstein Center for Fundamental Physics and Laboratory for High Energy Physics, University of Bern, Bern, Switzerland*
[18]*School of Physics and Astronomy, University of Birmingham, Birmingham, United Kingdom*
[19a]*Department of Physics, Bogazici University, Istanbul, Turkey*
[19b]*Department of Physics, Dogus University, Istanbul, Turkey*
[19c]*Department of Physics Engineering, Gaziantep University, Gaziantep, Turkey*
[20a]*INFN Sezione di Bologna, Bologna, Italy*
[20b]*Dipartimento di Fisica e Astronomia, Università di Bologna, Bologna, Italy*
[21]*Physikalisches Institut, University of Bonn, Bonn, Germany*
[22]*Department of Physics, Boston University, Boston, Massachusetts, USA*
[23]*Department of Physics, Brandeis University, Waltham, Massachusetts, USA*
[24a]*Universidade Federal do Rio De Janeiro COPPE/EE/IF, Rio de Janeiro, Brazil*
[24b]*Federal University of Juiz de Fora (UFJF), Juiz de Fora, Brazil*
[24c]*Federal University of Sao Joao del Rei (UFSJ), Sao Joao del Rei, Brazil*
[24d]*Instituto de Fisica, Universidade de Sao Paulo, Sao Paulo, Brazil*
[25]*Physics Department, Brookhaven National Laboratory, Upton, New York, USA*
[26a]*National Institute of Physics and Nuclear Engineering, Bucharest, Romania*
[26b]*National Institute for Research and Development of Isotopic and Molecular Technologies, Physics Department, Cluj Napoca, Romania*
[26c]*University Politehnica Bucharest, Bucharest, Romania*
[26d]*West University in Timisoara, Timisoara, Romania*
[27]*Departamento de Física, Universidad de Buenos Aires, Buenos Aires, Argentina*
[28]*Cavendish Laboratory, University of Cambridge, Cambridge, United Kingdom*
[29]*Department of Physics, Carleton University, Ottawa, ON, Canada*
[30]*CERN, Geneva, Switzerland*
[31]*Enrico Fermi Institute, University of Chicago, Chicago, Illinois, USA*
[32a]*Departamento de Física, Pontificia Universidad Católica de Chile, Santiago, Chile*
[32b]*Departamento de Física, Universidad Técnica Federico Santa María, Valparaíso, Chile*
[33a]*Institute of High Energy Physics, Chinese Academy of Sciences, Beijing, China*
[33b]*Department of Modern Physics, University of Science and Technology of China, Anhui, China*
[33c]*Department of Physics, Nanjing University, Jiangsu, China*
[33d]*School of Physics, Shandong University, Shandong, China*
[33e]*Physics Department, Shanghai Jiao Tong University, Shanghai, China*
[34]*Laboratoire de Physique Corpusculaire, Clermont Université and Université Blaise Pascal and CNRS/IN2P3, Clermont-Ferrand, France*
[35]*Nevis Laboratory, Columbia University, Irvington, New York, USA*
[36]*Niels Bohr Institute, University of Copenhagen, Kobenhavn, Denmark*
[37a]*INFN Gruppo Collegato di Cosenza, Laboratori Nazionali di Frascati, Italy*
[37b]*Dipartimento di Fisica, Università della Calabria, Rende, Italy*
[38a]*AGH University of Science and Technology, Faculty of Physics and Applied Computer Science, Krakow, Poland*
[38b]*Marian Smoluchowski Institute of Physics, Jagiellonian University, Krakow, Poland*
[39]*The Henryk Niewodniczanski Institute of Nuclear Physics, Polish Academy of Sciences, Krakow, Poland*
[40]*Physics Department, Southern Methodist University, Dallas, Texas, USA*
[41]*Physics Department, University of Texas at Dallas, Richardson Texas, USA*
[42]*DESY, Hamburg and Zeuthen, Germany*
[43]*Institut für Experimentelle Physik IV, Technische Universität Dortmund, Dortmund, Germany*
[44]*Institut für Kern- und Teilchenphysik, Technische Universität Dresden, Dresden, Germany*
[45]*Department of Physics, Duke University, Durham, North Carolina, USA*
[46]*SUPA - School of Physics and Astronomy, University of Edinburgh, Edinburgh, United Kingdom*
[47]*INFN Laboratori Nazionali di Frascati, Frascati, Italy*
[48]*Fakultät für Mathematik und Physik, Albert-Ludwigs-Universität, Freiburg, Germany*

[49]Section de Physique, Université de Genève, Geneva, Switzerland
[50a]INFN Sezione di Genova, Genova, Italy
[50b]Dipartimento di Fisica, Università di Genova, Genova, Italy
[51a]E. Andronikashvili Institute of Physics, Iv. Javakhishvili Tbilisi State University, Tbilisi, Georgia
[51b]High Energy Physics Institute, Tbilisi State University, Tbilisi, Georgia
[52]II Physikalisches Institut, Justus-Liebig-Universität Giessen, Giessen, Germany
[53]SUPA-School of Physics and Astronomy, University of Glasgow, Glasgow, United Kingdom
[54]II Physikalisches Institut, Georg-August-Universität, Göttingen, Germany
[55]Laboratoire de Physique Subatomique et de Cosmologie, Université Grenoble-Alpes, CNRS/IN2P3, Grenoble, France
[56]Department of Physics, Hampton University, Hampton, Virginia, USA
[57]Laboratory for Particle Physics and Cosmology, Harvard University, Cambridge, Massachusetts, USA
[58a]Kirchhoff-Institut für Physik, Ruprecht-Karls-Universität Heidelberg, Heidelberg, Germany
[58b]Physikalisches Institut, Ruprecht-Karls-Universität Heidelberg, Heidelberg, Germany
[58c]ZITI Institut für technische Informatik, Ruprecht-Karls-Universität Heidelberg, Mannheim, Germany
[59]Faculty of Applied Information Science, Hiroshima Institute of Technology, Hiroshima, Japan
[60]Department of Physics, Indiana University, Bloomington, Indiana, USA
[61]Institut für Astro- und Teilchenphysik, Leopold-Franzens-Universität, Innsbruck, Austria
[62]University of Iowa, Iowa City, Iowa, USA
[63]Department of Physics and Astronomy, Iowa State University, Ames, Iowa, USA
[64]Joint Institute for Nuclear Research, JINR Dubna, Dubna, Russia
[65]KEK, High Energy Accelerator Research Organization, Tsukuba, Japan
[66]Graduate School of Science, Kobe University, Kobe, Japan
[67]Faculty of Science, Kyoto University, Kyoto, Japan
[68]Kyoto University of Education, Kyoto, Japan
[69]Department of Physics, Kyushu University, Fukuoka, Japan
[70]Instituto de Física La Plata, Universidad Nacional de La Plata and CONICET, La Plata, Argentina
[71]Physics Department, Lancaster University, Lancaster, United Kingdom
[72a]INFN Sezione di Lecce, Lecce, Italy
[72b]Dipartimento di Matematica e Fisica, Università del Salento, Lecce, Italy
[73]Oliver Lodge Laboratory, University of Liverpool, Liverpool, United Kingdom
[74]Department of Physics, Jožef Stefan Institute and University of Ljubljana, Ljubljana, Slovenia
[75]School of Physics and Astronomy, Queen Mary University of London, London, United Kingdom
[76]Department of Physics, Royal Holloway University of London, Surrey, United Kingdom
[77]Department of Physics and Astronomy, University College London, London, United Kingdom
[78]Louisiana Tech University, Ruston, Louisiana, USA
[79]Laboratoire de Physique Nucléaire et de Hautes Energies, UPMC and Université Paris-Diderot and CNRS/IN2P3, Paris, France
[80]Fysiska institutionen, Lunds universitet, Lund, Sweden
[81]Departamento de Fisica Teorica C-15, Universidad Autonoma de Madrid, Madrid, Spain
[82]Institut für Physik, Universität Mainz, Mainz, Germany
[83]School of Physics and Astronomy, University of Manchester, Manchester, United Kingdom
[84]CPPM, Aix-Marseille Université and CNRS/IN2P3, Marseille, France
[85]Department of Physics, University of Massachusetts, Amherst, Massachusetts, USA
[86]Department of Physics, McGill University, Montreal, QC, Canada
[87]School of Physics, University of Melbourne, Victoria, Australia
[88]Department of Physics, The University of Michigan, Ann Arbor Michigan, USA
[89]Department of Physics and Astronomy, Michigan State University, East Lansing, Michigan, USA
[90a]INFN Sezione di Milano, Milano, Italy
[90b]Dipartimento di Fisica, Università di Milano, Milano, Italy
[91]B.I. Stepanov Institute of Physics, National Academy of Sciences of Belarus, Minsk, Republic of Belarus
[92]National Scientific and Educational Centre for Particle and High Energy Physics, Minsk, Republic of Belarus
[93]Department of Physics, Massachusetts Institute of Technology, Cambridge, Massachusetts, USA
[94]Group of Particle Physics, University of Montreal, Montreal, QC, Canada
[95]P.N. Lebedev Institute of Physics, Academy of Sciences, Moscow, Russia
[96]Institute for Theoretical and Experimental Physics (ITEP), Moscow, Russia
[97]Moscow Engineering and Physics Institute (MEPhI), Moscow, Russia
[98]D.V. Skobeltsyn Institute of Nuclear Physics, M.V. Lomonosov Moscow State University, Moscow, Russia
[99]Fakultät für Physik, Ludwig-Maximilians-Universität München, München, Germany

[100]*Max-Planck-Institut für Physik (Werner-Heisenberg-Institut), München, Germany*
[101]*Nagasaki Institute of Applied Science, Nagasaki, Japan*
[102]*Graduate School of Science and Kobayashi-Maskawa Institute, Nagoya University, Nagoya, Japan*
[103a]*INFN Sezione di Napoli, Napoli, Italy*
[103b]*Dipartimento di Fisica, Università di Napoli, Napoli, Italy*
[104]*Department of Physics and Astronomy, University of New Mexico, Albuquerque, New Mexico, USA*
[105]*Institute for Mathematics, Astrophysics and Particle Physics, Radboud University Nijmegen/Nikhef, Nijmegen, Netherlands*
[106]*Nikhef National Institute for Subatomic Physics and University of Amsterdam, Amsterdam, Netherlands*
[107]*Department of Physics, Northern Illinois University, DeKalb, Illinois, USA*
[108]*Budker Institute of Nuclear Physics, SB RAS, Novosibirsk, Russia*
[109]*Department of Physics, New York University, New York, New York, USA*
[110]*Ohio State University, Columbus, Ohio, USA*
[111]*Faculty of Science, Okayama University, Okayama, Japan*
[112]*Homer L. Dodge Department of Physics and Astronomy, University of Oklahoma, Norman, Oklahoma, USA*
[113]*Department of Physics, Oklahoma State University, Stillwater Oklahoma, USA*
[114]*Palacký University, RCPTM, Olomouc, Czech Republic*
[115]*Center for High Energy Physics, University of Oregon, Eugene, Oregon, USA*
[116]*LAL, Université Paris-Sud and CNRS/IN2P3, Orsay, France*
[117]*Graduate School of Science, Osaka University, Osaka, Japan*
[118]*Department of Physics, University of Oslo, Oslo, Norway*
[119]*Department of Physics, Oxford University, Oxford, United Kingdom*
[120a]*INFN Sezione di Pavia, Pavia, Italy*
[120b]*Dipartimento di Fisica, Università di Pavia, Pavia, Italy*
[121]*Department of Physics, University of Pennsylvania, Philadelphia, Pennsylvania, USA*
[122]*Petersburg Nuclear Physics Institute, Gatchina, Russia*
[123a]*INFN Sezione di Pisa, Pisa, Italy*
[123b]*Dipartimento di Fisica E. Fermi, Università di Pisa, Pisa, Italy*
[124]*Department of Physics and Astronomy, University of Pittsburgh, Pittsburgh, Pennsylvania, USA*
[125a]*Laboratorio de Instrumentacao e Fisica Experimental de Particulas - LIP, Lisboa, Portugal*
[125b]*Faculdade de Ciências, Universidade de Lisboa, Lisboa, Portugal*
[125c]*Department of Physics, University of Coimbra, Coimbra, Portugal*
[125d]*Centro de Física Nuclear da Universidade de Lisboa, Lisboa, Portugal*
[125e]*Departamento de Fisica, Universidade do Minho, Braga, Portugal*
[125f]*Departamento de Fisica Teorica y del Cosmos and CAFPE, Universidad de Granada, Granada (Spain), Portugal*
[125g]*Dep Fisica and CEFITEC of Faculdade de Ciencias e Tecnologia, Universidade Nova de Lisboa, Caparica, Portugal*
[126]*Institute of Physics, Academy of Sciences of the Czech Republic, Praha, Czech Republic*
[127]*Czech Technical University in Prague, Praha, Czech Republic*
[128]*Faculty of Mathematics and Physics, Charles University in Prague, Praha, Czech Republic*
[129]*State Research Center Institute for High Energy Physics, Protvino, Russia*
[130]*Particle Physics Department, Rutherford Appleton Laboratory, Didcot, United Kingdom*
[131]*Physics Department, University of Regina, Regina, SK, Canada*
[132]*Ritsumeikan University, Kusatsu, Shiga, Japan*
[133a]*INFN Sezione di Roma, Roma, Italy*
[133b]*Dipartimento di Fisica, Sapienza Università di Roma, Roma, Italy*
[134a]*INFN Sezione di Roma Tor Vergata, Roma, Italy*
[134b]*Dipartimento di Fisica, Università di Roma Tor Vergata, Roma, Italy*
[135a]*INFN Sezione di Roma Tre, Roma, Italy*
[135b]*Dipartimento di Matematica e Fisica, Università Roma Tre, Roma, Italy*
[136a]*Faculté des Sciences Ain Chock, Réseau Universitaire de Physique des Hautes Energies - Université Hassan II, Casablanca, Morocco*
[136b]*Centre National de l'Energie des Sciences Techniques Nucleaires, Rabat, Morocco*
[136c]*Faculté des Sciences Semlalia, Université Cadi Ayyad, LPHEA-Marrakech, Morocco*
[136d]*Faculté des Sciences, Université Mohamed Premier and LPTPM, Oujda, Morocco*
[136e]*Faculté des sciences, Université Mohammed V-Agdal, Rabat, Morocco*
[137]*DSM/IRFU (Institut de Recherches sur les Lois Fondamentales de l'Univers), CEA Saclay (Commissariat à l'Energie Atomique et aux Energies Alternatives), Gif-sur-Yvette, France*

[138]Santa Cruz Institute for Particle Physics, University of California Santa Cruz, Santa Cruz, California, USA
[139]Department of Physics, University of Washington, Seattle, Washington, USA
[140]Department of Physics and Astronomy, University of Sheffield, Sheffield, United Kingdom
[141]Department of Physics, Shinshu University, Nagano, Japan
[142]Fachbereich Physik, Universität Siegen, Siegen, Germany
[143]Department of Physics, Simon Fraser University, Burnaby, BC, Canada
[144]SLAC National Accelerator Laboratory, Stanford, California, USA
[145a]Faculty of Mathematics, Physics & Informatics, Comenius University, Bratislava, Slovak Republic
[145b]Department of Subnuclear Physics, Institute of Experimental Physics of the Slovak Academy of Sciences, Kosice, Slovak Republic
[146a]Department of Physics, University of Cape Town, Cape Town, South Africa
[146b]Department of Physics, University of Johannesburg, Johannesburg, South Africa
[146c]School of Physics, University of the Witwatersrand, Johannesburg, South Africa
[147a]Department of Physics, Stockholm University, Stockholm, Sweden
[147b]The Oskar Klein Centre, Stockholm, Sweden
[148]Physics Department, Royal Institute of Technology, Stockholm, Sweden
[149]Departments of Physics & Astronomy and Chemistry, Stony Brook University, Stony Brook, New York, USA
[150]Department of Physics and Astronomy, University of Sussex, Brighton, United Kingdom
[151]School of Physics, University of Sydney, Sydney, Australia
[152]Institute of Physics, Academia Sinica, Taipei, Taiwan
[153]Department of Physics, Technion: Israel Institute of Technology, Haifa, Israel
[154]Raymond and Beverly Sackler School of Physics and Astronomy, Tel Aviv University, Tel Aviv, Israel
[155]Department of Physics, Aristotle University of Thessaloniki, Thessaloniki, Greece
[156]International Center for Elementary Particle Physics and Department of Physics, The University of Tokyo, Tokyo, Japan
[157]Graduate School of Science and Technology, Tokyo Metropolitan University, Tokyo, Japan
[158]Department of Physics, Tokyo Institute of Technology, Tokyo, Japan
[159]Department of Physics, University of Toronto, Toronto, ON, Canada
[160a]TRIUMF, Vancouver, BC, Canada
[160b]Department of Physics and Astronomy, York University, Toronto, ON, Canada
[161]Faculty of Pure and Applied Sciences, University of Tsukuba, Tsukuba, Japan
[162]Department of Physics and Astronomy, Tufts University, Medford, Massachusetts, USA
[163]Centro de Investigaciones, Universidad Antonio Narino, Bogota, Colombia
[164]Department of Physics and Astronomy, University of California Irvine, Irvine, California, USA
[165a]INFN Gruppo Collegato di Udine, Sezione di Trieste, Udine, Italy
[165b]ICTP, Trieste, Italy
[165c]Dipartimento di Chimica, Fisica e Ambiente, Università di Udine, Udine, Italy
[166]Department of Physics, University of Illinois, Urbana, Illinois, USA
[167]Department of Physics and Astronomy, University of Uppsala, Uppsala, Sweden
[168]Instituto de Física Corpuscular (IFIC) and Departamento de Física Atómica, Molecular y Nuclear and Departamento de Ingeniería Electrónica and Instituto de Microelectrónica de Barcelona (IMB-CNM), University of Valencia and CSIC, Valencia, Spain
[169]Department of Physics, University of British Columbia, Vancouver, BC, Canada
[170]Department of Physics and Astronomy, University of Victoria, Victoria, BC, Canada
[171]Department of Physics, University of Warwick, Coventry, United Kingdom
[172]Waseda University, Tokyo, Japan
[173]Department of Particle Physics, The Weizmann Institute of Science, Rehovot, Israel
[174]Department of Physics, University of Wisconsin, Madison, Wisconsin, USA
[175]Fakultät für Physik und Astronomie, Julius-Maximilians-Universität, Würzburg, Germany
[176]Fachbereich C Physik, Bergische Universität Wuppertal, Wuppertal, Germany
[177]Department of Physics, Yale University, New Haven, Connecticut, USA
[178]Yerevan Physics Institute, Yerevan, Armenia
[179]Centre de Calcul de l'Institut National de Physique Nucléaire et de Physique des Particules (IN2P3), Villeurbanne, France

[a]Deceased.
[b]Also at Department of Physics, King's College London, London, United Kingdom.
[c]Also at Institute of Physics, Azerbaijan Academy of Sciences, Baku, Azerbaijan.

[d]Also at Particle Physics Department, Rutherford Appleton Laboratory, Didcot, United Kingdom.
[e]Also at TRIUMF, Vancouver, BC, Canada.
[f]Also at Department of Physics, California State University, Fresno, CA, USA.
[g]Also at Novosibirsk State University, Novosibirsk, Russia.
[h]Also at CPPM, Aix-Marseille Université and CNRS/IN2P3, Marseille, France.
[i]Also at Università di Napoli Parthenope, Napoli, Italy.
[j]Also at Institute of Particle Physics (IPP), Canada.
[k]Also at Department of Physics, St. Petersburg State Polytechnical University, St. Petersburg, Russia.
[l]Also at Department of Financial and Management Engineering, University of the Aegean, Chios, Greece.
[m]Also at Louisiana Tech University, Ruston LA, USA.
[n]Also at Institucio Catalana de Recerca i Estudis Avancats, ICREA, Barcelona, Spain.
[o]Also at CERN, Geneva, Switzerland.
[p]Also at Ochadai Academic Production, Ochanomizu University, Tokyo, Japan.
[q]Also at Manhattan College, New York, NY, USA.
[r]Also at Institute of Physics, Academia Sinica, Taipei, Taiwan.
[s]Also at LAL, Université Paris-Sud and CNRS/IN2P3, Orsay, France.
[t]Also at School of Physics and Engineering, Sun Yat-sen University, Guangzhou, China.
[u]Also at Academia Sinica Grid Computing, Institute of Physics, Academia Sinica, Taipei, Taiwan.
[v]Also at Laboratoire de Physique Nucléaire et de Hautes Energies, UPMC and Université Paris-Diderot and CNRS/IN2P3, Paris, France.
[w]Also at School of Physical Sciences, National Institute of Science Education and Research, Bhubaneswar, India.
[x]Also at Dipartimento di Fisica, Sapienza Università di Roma, Roma, Italy.
[y]Also at Moscow Institute of Physics and Technology State University, Dolgoprudny, Russia.
[z]Also at Section de Physique, Université de Genève, Geneva, Switzerland.
[aa]Also at Department of Physics, The University of Texas at Austin, Austin, TX, USA.
[bb]Also at Institute for Particle and Nuclear Physics, Wigner Research Centre for Physics, Budapest, Hungary.
[cc]Also at International School for Advanced Studies (SISSA), Trieste, Italy.
[dd]Also at Department of Physics and Astronomy, University of South Carolina, Columbia, SC, USA.
[ee]Also at Faculty of Physics, M.V. Lomonosov Moscow State University, Moscow, Russia.
[ff]Also at Physics Department, Brookhaven National Laboratory, Upton, NY, USA.
[gg]Also at Moscow Engineering and Physics Institute (MEPhI), Moscow, Russia.
[hh]Also at Department of Physics, Oxford University, Oxford, United Kingdom.
[ii]Also at Department of Physics, Nanjing University, Jiangsu, China.
[jj]Also at Institut für Experimentalphysik, Universität Hamburg, Hamburg, Germany.
[kk]Also at Department of Physics, The University of Michigan, Ann Arbor, MI, USA.
[ll]Also at Discipline of Physics, University of KwaZulu-Natal, Durban, South Africa.

JHEP

Published for SISSA by Springer

Received: *January 14, 2016*
Revised: *July 8, 2016*
Accepted: *August 20, 2016*
Published: *August 24, 2016*

Measurement of the CP-violating phase ϕ_s and the B_s^0 meson decay width difference with $B_s^0 \to J/\psi\phi$ decays in ATLAS

The ATLAS collaboration

E-mail: atlas.publications@cern.ch

Abstract: A measurement of the B_s^0 decay parameters in the $B_s^0 \to J/\psi\phi$ channel using an integrated luminosity of $14.3\,\text{fb}^{-1}$ collected by the ATLAS detector from 8 TeV pp collisions at the LHC is presented. The measured parameters include the CP-violating phase ϕ_s, the decay width Γ_s and the width difference between the mass eigenstates $\Delta\Gamma_s$. The values measured for the physical parameters are statistically combined with those from $4.9\,\text{fb}^{-1}$ of 7 TeV data, leading to the following:

$$\begin{aligned}\phi_s &= -0.090 \pm 0.078\ (\text{stat.}) \pm 0.041\ (\text{syst.})\ \text{rad}\\ \Delta\Gamma_s &= 0.085 \pm 0.011\ (\text{stat.}) \pm 0.007\ (\text{syst.})\ \text{ps}^{-1}\\ \Gamma_s &= 0.675 \pm 0.003\ (\text{stat.}) \pm 0.003\ (\text{syst.})\ \text{ps}^{-1}.\end{aligned}$$

In the analysis the parameter $\Delta\Gamma_s$ is constrained to be positive. Results for ϕ_s and $\Delta\Gamma_s$ are also presented as 68% and 95% likelihood contours in the ϕ_s-$\Delta\Gamma_s$ plane. Also measured in this decay channel are the transversity amplitudes and corresponding strong phases. All measurements are in agreement with the Standard Model predictions.

Keywords: B physics, CP violation, Flavor physics, Hadron-Hadron scattering (experiments)

ArXiv ePrint: 1601.03297

doi:10.1007/JHEP08(2016)147

Contents

JHEP08(2016)147

1 Introduction

New phenomena beyond the predictions of the Standard Model (SM) may alter CP violation in b-hadron decays. A channel that is expected to be sensitive to new physics contributions is the decay $B_s^0 \to J/\psi\phi$. CP violation in the $B_s^0 \to J/\psi\phi$ decay occurs due to interference between direct decays and decays with B_s^0-$\bar{B}_s^0$ mixing. The oscillation frequency of B_s^0 meson mixing is characterized by the mass difference Δm_s of the heavy ($B_{\rm H}$) and light ($B_{\rm L}$) mass eigenstates. The CP violating phase ϕ_s is defined as the weak phase difference between the B_s^0-$\bar{B}_s^0$ mixing amplitude and the $b \to c\bar{c}s$ decay amplitude. In the absence of CP violation, the $B_{\rm H}$ state would correspond to the CP-odd state and the $B_{\rm L}$ to the CP-even state. In the SM the phase ϕ_s is small and can be related to Cabibbo-Kobayashi-Maskawa (CKM) quark mixing matrix elements via the relation $\phi_s \simeq -2\beta_s$,

with $\beta_s = \arg[-(V_{ts}V_{tb}^*)/(V_{cs}V_{cb}^*)]$; assuming no physics beyond the SM contributions to B_s^0 mixing and decays, a value of $-2\beta_s = -0.0363^{+0.0016}_{-0.0015}$ rad can be predicted by combining beauty and kaon physics observables [1].

Other physical quantities involved in B_s^0-$\bar{B}_s^0$ mixing are the decay width $\Gamma_s = (\Gamma_{\rm L} + \Gamma_H)/2$ and the width difference $\Delta\Gamma_s = \Gamma_{\rm L} - \Gamma_H$, where $\Gamma_{\rm L}$ and Γ_H are the decay widths of the different eigenstates. The width difference is predicted to be $\Delta\Gamma_s = 0.087 \pm 0.021$ ps^{-1} [2]. Physics beyond the SM is not expected to affect $\Delta\Gamma_s$ as significantly as ϕ_s [3]. However, extracting $\Delta\Gamma_s$ from data is interesting as it allows theoretical predictions to be tested [3]. Previous measurements of these quantities have been reported by the DØ, CDF, LHCb, ATLAS and CMS collaborations [4–9].

The decay of the pseudoscalar B_s^0 to the vector-vector $J/\psi(\mu^+\mu^-)\phi(K^+K^-)$ final state results in an admixture of CP-odd and CP-even states, with orbital angular momentum $L = 0$, 1 or 2. The final states with orbital angular momentum $L = 0$ or 2 are CP-even, while the state with $L = 1$ is CP-odd. The same final state can also be produced with K^+K^- pairs in an S-wave configuration [10]. This S-wave final state is CP-odd. The CP states are separated statistically using an angular analysis of the final-state particles. Flavour tagging is used to distinguish between the initial B_s^0 and $\bar{B}_s^0$ states.

The analysis presented here provides a measurement of the $B_s^0 \to J/\psi\phi$ decay parameters using 14.3 fb^{-1} of LHC pp data collected by the ATLAS detector during 2012 at a centre-of-mass energy of 8 TeV. This is an update of the previous flavour-tagged time-dependent angular analysis of $B_s^0 \to J/\psi\phi$ [8] that was performed using 4.9 fb^{-1} of data collected at 7 TeV. Electrons are now included, in addition to final-state muons, for the flavour tagging using leptons.

2 ATLAS detector and Monte Carlo simulation

The ATLAS detector [11] is a multi-purpose particle physics detector with a forward-backward symmetric cylindrical geometry and nearly 4π coverage in solid angle.[1] The inner tracking detector (ID) consists of a silicon pixel detector, a silicon microstrip detector and a transition radiation tracker. The ID is surrounded by a thin superconducting solenoid providing a 2 T axial magnetic field, and by a high-granularity liquid-argon (LAr) sampling electromagnetic calorimeter. A steel/scintillator tile calorimeter provides hadronic coverage in the central rapidity range. The end-cap and forward regions are instrumented with LAr calorimeters for electromagnetic and hadronic measurements. The muon spectrometer (MS) surrounds the calorimeters and consists of three large superconducting toroids with eight coils each, a system of tracking chambers, and detectors for triggering.

The muon and tracking systems are of particular importance in the reconstruction of B meson candidates. Only data collected when both these systems were operating

[1] ATLAS uses a right-handed coordinate system with its origin at the nominal interaction point (IP) in the centre of the detector and the z-axis along the beam pipe. The x-axis points from the IP to the centre of the LHC ring, and the y-axis points upward. Cylindrical coordinates (r, ϕ) are used in the transverse plane, ϕ being the azimuthal angle around the beam pipe. The pseudorapidity is defined in terms of the polar angle θ as $\eta = -\ln\tan(\theta/2)$.

JHEP08(2016)147

correctly and when the LHC beams were declared to be stable are used in the analysis. The data were collected during a period of rising instantaneous luminosity, and the trigger conditions varied over this time. The triggers used to select events for this analysis are based on identification of a $J/\psi \to \mu^+\mu^-$ decay, with transverse momentum (p_{T}) thresholds of either 4 GeV or 6 GeV for the muons. The measurement uses 14.3 fb^{-1} of pp collision data collected with the ATLAS detector at a centre-of-mass energy of 8 TeV. Data collected at the beginning of the 8 TeV data-taking period are not included in the analysis due to a problem with the trigger tracking algorithm. The trigger was subsequently changed to use a different tracking algorithm that did not have this problem.

To study the detector response, estimate backgrounds and model systematic effects, 12 million Monte Carlo (MC) simulated $B_s^0 \to J/\psi\phi$ events were generated using Pythia 8 [12, 13] tuned with ATLAS data [14]. No p_{T} cuts were applied at the generator level. The detector response was simulated using the ATLAS simulation framework based on GEANT4 [15, 16]. In order to take into account the varying number of proton-proton interactions per bunch crossing (pile-up) and trigger configurations during data-taking, the MC events were weighted to reproduce the same pile-up and trigger conditions in data. Additional samples of the background decay $B_d^0 \to J/\psi K^{0*}$, as well as the more general $b\bar{b} \to J/\psi X$ and $pp \to J/\psi X$ backgrounds were also simulated using Pythia 8.

3 Reconstruction and candidate selection

Events must pass the trigger selections described in section 2. In addition, each event must contain at least one reconstructed primary vertex, formed from at least four ID tracks, and at least one pair of oppositely charged muon candidates that are reconstructed using information from the MS and the ID [17]. A muon identified using a combination of MS and ID track parameters is referred to as a *combined-muon*. A muon formed from a MS track segment that is not associated with a MS track but is matched to an ID track extrapolated to the MS is referred to as a *segment-tagged muon*. The muon track parameters are determined from the ID measurement alone, since the precision of the measured track parameters is dominated by the ID track reconstruction in the p_{T} range of interest for this analysis. Pairs of oppositely charged muon tracks are refitted to a common vertex and the pair is accepted for further consideration if the quality of the fit meets the requirement $\chi^2/\mathrm{d.o.f.} < 10$. The invariant mass of the muon pair is calculated from the refitted track parameters. In order to account for varying mass resolution in different parts of the detector, the J/ψ candidates are divided into three subsets according to the pseudorapidity η of the muons. A maximum-likelihood fit is used to extract the J/ψ mass and the corresponding mass resolution for these three subsets. When both muons have $|\eta| < 1.05$, the dimuon invariant mass must fall in the range 2.959–3.229 GeV to be accepted as a J/ψ candidate. When one muon has $1.05 < |\eta| < 2.5$ and the other muon $|\eta| < 1.05$, the corresponding signal region is 2.913–3.273 GeV. For the third subset, where both muons have $1.05 < |\eta| < 2.5$, the signal region is 2.852–3.332 GeV. In each case the signal region is defined so as to retain 99.8% of the J/ψ candidates identified in the fits.

JHEP08(2016)147

The candidates for the decay $\phi \to K^+K^-$ are reconstructed from all pairs of oppositely charged particles with $p_{\rm T} > 1$ GeV and $|\eta| < 2.5$ that are not identified as muons. Candidate events for $B_s^0 \to J/\psi(\mu^+\mu^-)\phi(K^+K^-)$ decays are selected by fitting the tracks for each combination of $J/\psi \to \mu^+\mu^-$ and $\phi \to K^+K^-$ to a common vertex. Each of the four tracks is required to have at least one hit in the pixel detector and at least four hits in the silicon microstrip detector. The fit is further constrained by fixing the invariant mass calculated from the two muon tracks to the J/ψ mass [18]. A quadruplet of tracks is accepted for further analysis if the vertex fit has a χ^2/d.o.f. < 3, the fitted $p_{\rm T}$ of each track from $\phi \to K^+K^-$ is greater than 1 GeV and the invariant mass of the track pairs (assuming that they are kaons) falls within the interval 1.0085 GeV $< m(K^+K^-) <$ 1.0305 GeV. If there is more than one accepted candidate in the event, the candidate with the lowest χ^2/d.o.f. is selected. In total, 375,987 B_s^0 candidates are collected within a mass range of 5.150–5.650 GeV.

For each B_s^0 meson candidate the proper decay time t is estimated using the expression:

$$t = \frac{L_{xy}\ m_{_B}}{p_{{\rm T}_B}},$$

where $p_{{\rm T}_B}$ is the reconstructed transverse momentum of the B_s^0 meson candidate and $m_{_B}$ denotes the mass of the B_s^0 meson, taken from [18]. The transverse decay length, L_{xy}, is the displacement in the transverse plane of the B_s^0 meson decay vertex with respect to the primary vertex, projected onto the direction of the B_s^0 transverse momentum. The position of the primary vertex used to calculate this quantity is determined from a refit following the removal of the tracks used to reconstruct the B_s^0 meson candidate.

For the selected events the average number of pile-up proton-proton interactions is 21, necessitating a choice of the best candidate for the primary vertex at which the B_s^0 meson is produced. The variable used is the three-dimensional impact parameter d_0, which is calculated as the distance between the line extrapolated from the reconstructed B_s^0 meson vertex in the direction of the B_s^0 momentum, and each primary vertex candidate. The chosen primary vertex is the one with the smallest d_0.

A study [19] made using a MC simulated dataset has shown that the precision of the reconstructed B_s^0 proper decay time remains stable over the range of pile-up encountered during 2012 data-taking. No B_s^0 meson decay-time cut is applied in this analysis.

4 Flavour tagging

The initial flavour of a neutral B meson can be inferred using information from the opposite-side B meson that contains the other pair-produced b-quark in the event [20, 21]. This is referred to as opposite-side tagging (OST).

To study and calibrate the OST methods, events containing $B^\pm \to J/\psi K^\pm$ decays are used, where the flavour of the $B^\pm$-meson is provided by the kaon charge. A sample of $B^\pm \to J/\psi K^\pm$ candidates is selected from the entire 2012 dataset satisfying the data-quality selection described in section 2. Since the OST calibration is not affected by the trigger problem at the start of the 8 TeV data-taking period, the tagging measurement uses 19.5 fb^{-1} of integrated luminosity of pp collision data.

JHEP08(2016)147

4.1 $B^{\pm} \to J/\psi K^{\pm}$ event selection

In order to select candidate $B^{\pm} \to J/\psi K^{\pm}$ decays, firstly J/ψ candidates are selected from pairs of oppositely charged combined-muons forming a good vertex, following the criteria described in section 3. Each muon is required to have a transverse momentum of at least 4 GeV and pseudorapidity within $|\eta| < 2.5$. The invariant mass of the dimuon candidate is required to satisfy 2.8 GeV $< m(\mu^+\mu^-) <$ 3.4 GeV. To form the B candidate, an additional track, satisfying the same quality requirements described for tracks in section 3, is combined with the dimuon candidate using the charged kaon mass hypothesis, and a vertex fit is performed with the mass of the dimuon pair constrained to the known value of the J/ψ mass. To reduce the prompt component of the combinatorial background, a requirement is applied to the transverse decay length of the B candidate of $L_{xy} > 0.1$ mm.

A sideband subtraction method is used in order to study parameter distributions corresponding to the $B^{\pm}$ signal processes with the background component subtracted. Events are divided into sub-sets into five intervals in the pseudorapidity of the B candidate and three mass regions. The mass regions are defined as a signal region around the fitted peak signal mass position $\mu \pm 2\sigma$ and the sideband regions are defined as $[\mu - 5\sigma, \mu - 3\sigma]$ and $[\mu + 3\sigma, \mu + 5\sigma]$, where μ and σ are the mean and width of the Gaussian function describing the B signal mass. Separate binned extended maximum-likelihood fits are performed to the invariant mass distribution in each region of pseudorapidity.

An exponential function is used to model the combinatorial background and a hyperbolic tangent function to parameterize the low-mass contribution from incorrectly or partially reconstructed B decays. A Gaussian function is used to model the $B^{\pm} \to J/\psi\pi^{\pm}$ contribution. The contribution from non-combinatorial background is found to have a negligible effect on the tagging procedure. Figure 1 shows the invariant mass distribution of B candidates for all rapidity regions overlaid with the fit result for the combined data.

4.2 Flavour tagging methods

Several methods that differ in efficiency and discriminating power are available to infer the flavour of the opposite-side b-quark. The measured charge of a muon or electron from a semileptonic decay of the B meson provides strong separation power; however, the $b \to \ell$ transitions are diluted through neutral B meson oscillations, as well as by cascade decays $b \to c \to \ell$, which can alter the charge of the lepton relative to those from direct $b \to \ell$ decays. The separation power of lepton tagging is enhanced by considering a weighted sum of the charge of the tracks in a cone around the lepton, where the weighting function is determined separately for each tagging method by optimizing the tagging performance. If no lepton is present, a weighted sum of the charge of tracks in a jet associated with the opposite-side B meson decay provides some separation. The flavour tagging methods are described in detail below.

For muon-based tagging, an additional muon is required in the event, with $p_{\mathrm{T}} > 2.5$ GeV, $|\eta| < 2.5$ and with $|\Delta z| < 5$ mm from the primary vertex. Muons are classified according to their reconstruction class, *combined* or *segment-tagged*, and subsequently treated as

JHEP08(2016)147

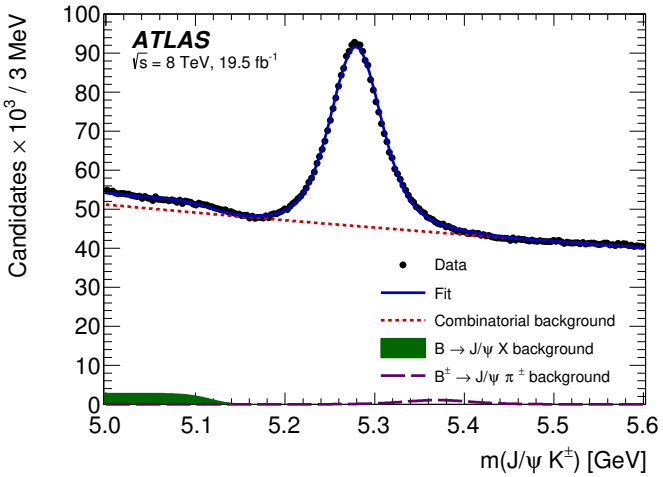

Figure 1. The invariant mass distribution for $B^{\pm} \to J/\psi K^{\pm}$ candidates satisfying the selection criteria, used to study the flavour tagging. Data are shown as points, and the overall result of the fit is given by the blue curve. The contribution from the combinatorial background component is indicated by the red dotted line, partially reconstructed B decays by the green shaded area, and decays of $B^{\pm} \to J/\psi\pi^{\pm}$, where the pion is mis-assigned a kaon mass, by the purple dashed line.

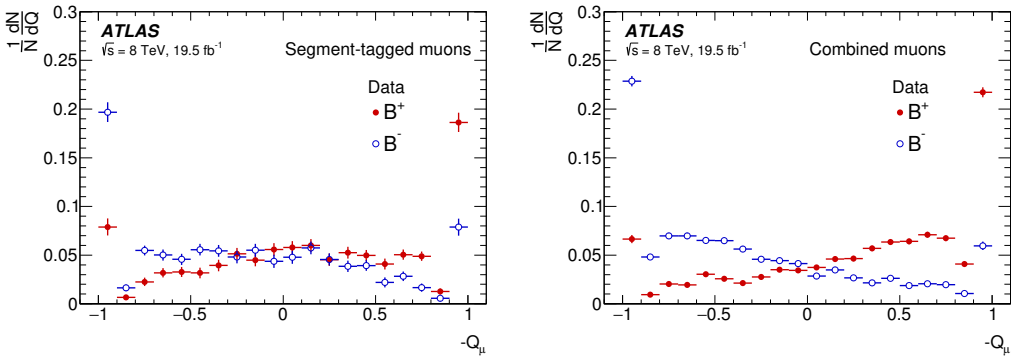

Figure 2. The opposite-side muon cone charge distribution for $B^{\pm}$ signal candidates for *segment-tagged* (left) and *combined* (right) muons. The $B^{\pm}$ charge is determined from the kaon charge.

distinct flavour tagging methods. In the case of multiple muons, the muon with the highest transverse momentum is selected.

A muon *cone charge* variable is constructed, defined as

$$Q_{\mu} = \frac{\sum_i^{N\ \text{tracks}} q_i \cdot (p_{\mathrm{T}i})^{\kappa}}{\sum_i^{N\ \text{tracks}} (p_{\mathrm{T}i})^{\kappa}},$$

where q is the charge of the track, $\kappa = 1.1$ and the sum is performed over the reconstructed ID tracks within a cone, $\Delta R = \sqrt{(\Delta\phi)^2 + (\Delta\eta)^2} < 0.5$, around the muon direction. The reconstructed ID tracks must have $p_{\mathrm{T}} > 0.5$ GeV and $|\eta| < 2.5$. Tracks associated with the $B^{\pm}$ signal decay are excluded from the sum. In figure 2 the opposite-side muon cone charge distributions are shown for candidates from $B^{\pm}$ signal decays.

JHEP08(2016)147

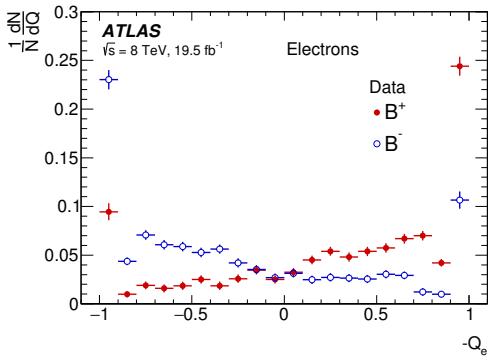

Figure 3. The opposite-side electron cone charge distribution for $B^{\pm}$ signal candidates.

For electron-based tagging, an electron is identified using information from the inner detector and calorimeter and is required to satisfy the tight electron quality criteria [22]. The inner detector track associated with the electron is required to have $p_{\mathrm{T}} > 0.5$ GeV and $|\eta| < 2.5$. It is required to pass within $|\Delta z| < 5$ mm of the primary vertex to remove electrons from non-signal interactions. To exclude electrons associated with the signal-side of the decay, electrons are rejected that have momenta within a cone of size $\Delta R = 0.4$ around the signal B candidate direction in the laboratory frame and opening angle between the B candidate and electron momenta, ζ_b, of $\cos(\zeta_b) > 0.98$. In the case of more than one electron passing the selection, the electron with the highest transverse momentum is chosen. As in the case of muon tagging, additional tracks within a cone of size $\Delta R = 0.5$ are used to form the electron cone charge Q_e with $\kappa = 1.0$. If there are no additional tracks within the cone, the charge of the electron is used. The resulting opposite-side electron cone charge distribution is shown in figure 3 for B^+ and B^- signal events.

In the absence of a muon or electron, *b-tagged* jets (i.e. jets that are the product of a b-quark) are identified using a multivariate tagging algorithm [23], which is a combination of several b-tagging algorithms using an artificial neural network and outputs a *b-tag* weight classifier. Jets are selected that exceed a *b-tag* weight of 0.7. This value is optimized to maximize the tagging power of the calibration sample. Jets are reconstructed from track information using the anti-k_t algorithm [24] with a radius parameter $R = 0.8$. In the case of multiple jets, the jet with the highest value of the b-tag weight is used.

The *jet charge* is defined as

$$Q_{\mathrm{jet}} = \frac{\sum_i^{N\ \mathrm{tracks}} q_i \cdot (p_{\mathrm{T}i})^{\kappa}}{\sum_i^{N\ \mathrm{tracks}} (p_{\mathrm{T}i})^{\kappa}},$$

where $\kappa = 1.1$ and the sum is over the tracks associated with the jet, excluding those tracks associated with a primary vertex other than that of the signal decay and tracks from the signal candidate. Figure 4 shows the distribution of the opposite-side jet-charge for $B^{\pm}$ signal candidates.

The efficiency, ϵ, of an individual tagging method is defined as the ratio of the number of events tagged by that method to the total number of candidates. A probability $P(B|Q)$ ($P(\bar{B}|Q)$) that a specific event has a signal decay containing a $\bar{b}$-quark (b-quark)

JHEP08(2016)147

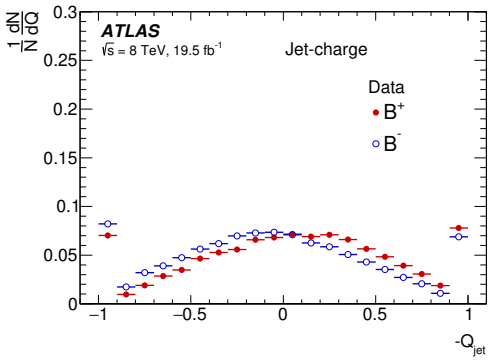

Figure 4. Opposite-side jet-charge distribution for $B^{\pm}$ signal candidates.

given the value of the discriminating variable is constructed from the calibration samples for each of the B^+ and B^- samples, which defines $P(Q|B^+)$ and $P(Q|B^-)$, respectively. The probability to tag a signal event as containing a $\bar{b}$-quark is therefore $P(B|Q) = P(Q|B^+)/(P(Q|B^+) + P(Q|B^-))$, and correspondingly $P(\bar{B}|Q) = 1 - P(B|Q)$. It is possible to define a quantity called the dilution $\mathcal{D} = P(B|Q) - P(\bar{B}|Q) = 2P(B|Q) - 1$, which represents the strength of a particular flavour tagging method. The tagging power of a particular tagging method is defined as $T = \epsilon\mathcal{D}^2 = \sum_i \epsilon_i \cdot (2P_i(B|Q_i) - 1)^2$, where the sum is over the bins of the probability distribution as a function of the charge variable. An effective dilution, $D = \sqrt{T/\epsilon}$, is calculated from the measured tagging power and efficiency.

The flavour tagging method applied to each B_s^0 candidate event is taken from the information contained in a given event. By definition there is no overlap between lepton-tagged and jet-charge-tagged events. The overlap between muon- and electron-tagged events, corresponding to 0.4% of all tagged events, is negligibly small. In the case of doubly tagged events, the tagger with the highest tagging power is selected; however, the choice of hierarchy between muon- and electron-tagged events is shown to have negligible impact on the final fit results. If it is not possible to provide a tagging response for the event, then a probability of 0.5 is assigned. A summary of the tagging performance is given in table 1.

4.3 Using tag information in the B_s^0 fit

The tag-probability for each B_s^0 candidate is determined from calibrations derived from a sample of $B^{\pm} \to J/\psi K^{\pm}$ candidates, as described in section 4.2. The distributions of tag-probabilities for the signal and background are different and since the background cannot be factorized out, additional probability terms, $P_{\rm s}(P(B|Q))$ and $P_{\rm b}(P(B|Q))$ for signal and background, respectively, are included in the fit. The distributions of tag-probabilities for the B_s^0 candidates consist of continuous and discrete parts (events with a tag charge of ± 1); these are treated separately as described below.

To describe the continuous part, a fit is first performed to the sideband data, i.e., 5.150 GeV $< m(B_s^0) <$ 5.317 GeV or 5.417 GeV $< m(B_s^0) <$ 5.650 GeV, where $m(B_s^0)$ is the mass of the B_s^0 candidate. Different functions are used for the different tagging methods. For the combined-muon tagging method, the function has the form of the sum of a

JHEP08(2016)147

Tagger	Efficiency [%]	Dilution [%]	Tagging Power [%]
Combined μ	4.12 ± 0.02	47.4 ± 0.2	0.92 ± 0.02
Electron	1.19 ± 0.01	49.2 ± 0.3	0.29 ± 0.01
Segment-tagged μ	1.20 ± 0.01	28.6 ± 0.2	0.10 ± 0.01
Jet-charge	13.15 ± 0.03	11.85 ± 0.03	0.19 ± 0.01
Total	19.66 ± 0.04	27.56 ± 0.06	1.49 ± 0.02

Table 1. Summary of tagging performance for the different flavour tagging methods described in the text. Uncertainties shown are statistical only. The efficiency and tagging power are each determined by summing over the individual bins of the charge distribution. The effective dilution is obtained from the measured efficiency and tagging power. For the efficiency, dilution, and tagging power, the corresponding uncertainty is determined by combining the appropriate uncertainties in the individual bins of each charge distribution.

fourth-order polynomial and two exponential functions. A second-order polynomial and two exponential functions are applied for the electron tagging algorithm. A sum of three Gaussian functions is used for the segment-tagged muons. For the jet-charge tagging algorithm an eighth-order polynomial is used. In all four cases unbinned maximum-likelihood fits to data are used. In the next step, the same function as applied to the sidebands is used to describe the distributions for events in the signal region: the background parameters are fixed to the values obtained from the fits to the sidebands while the signal parameters are free in this step. The ratio of background to signal (obtained from a simultaneous mass-lifetime fit) is fixed as well. The results of the fits projected onto histograms of B_s^0 tag-probability for the different tagging methods are shown in figure 5.

To account for possible deviations between data and the selected fit models a number of alternative fit functions are used to determine systematic uncertainties in the B_s^0 fit. These fit variations are described in section 7.

The discrete components of the tag-probability distribution originate from cases where the tag is derived from a single track, giving a tag charge of exactly $+1$ or -1. The fractions of events f_{+1} and f_{-1} with charges $+1$ and -1, respectively, are determined separately for signal and background using events from the same B_s^0 mass signal and sideband regions. Positive and negative charges are equally probable for background candidates formed from a random combination of a J/ψ and a pair of tracks, but this is not the case for background candidates formed from a partially reconstructed b-hadron. For signal and background contributions, similar fractions of events that are tagged with $+1$ or -1 tagging charge are observed for each of the tagging methods. The remaining fraction of events, $1 - f_{+1} - f_{-1}$, constitute the continuous part of the distributions. Table 2 summarizes the fractions f_{+1} and f_{-1} obtained for signal and background events and for the different tag methods.

To estimate the fractions of signal and background events which have tagging, a similar sideband-subtraction method is used to determine the relative fraction of signal and background events tagged using the different methods. These fractions are also included in the maximum-likelihood fit, described in section 5. The results are summarized in table 3.

JHEP08(2016)147

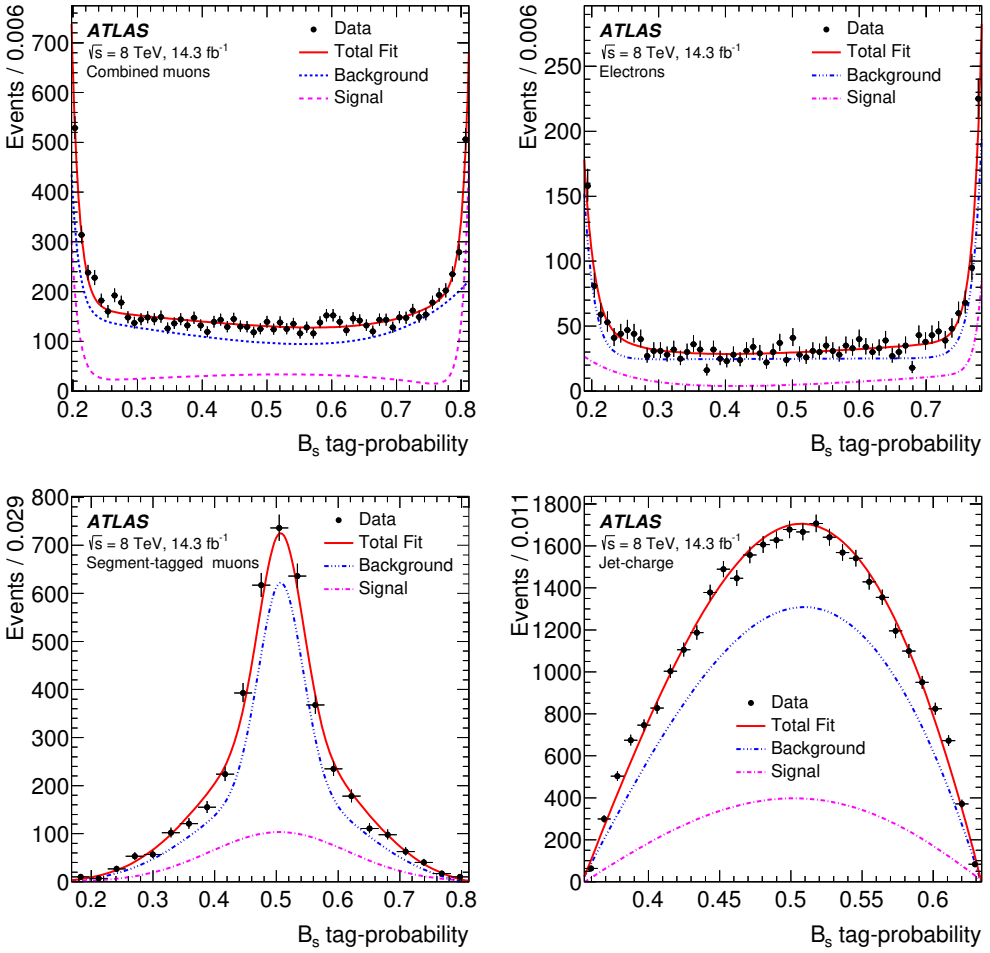

Figure 5. The continuous part of tag-probability for tagging using combined-muons (top-left), electrons (top-right), segment-tagged muons (bottom-left) and jet-charge (bottom-right). Black dots are data, blue is a fit to the sidebands, purple to the signal and red is a sum of both fits.

Tag method	Signal		Background	
	f_{+1}	f_{-1}	f_{+1}	f_{-1}
Combined μ	0.124 ± 0.012	0.127 ± 0.012	0.093 ± 0.003	0.095 ± 0.003
Electron	0.105 ± 0.020	0.139 ± 0.021	0.110 ± 0.007	0.110 ± 0.007
Segment-tagged μ	0.147 ± 0.024	0.118 ± 0.023	0.083 ± 0.004	0.084 ± 0.004
Jet-charge	0.071 ± 0.005	0.069 ± 0.005	0.068 ± 0.002	0.069 ± 0.002

Table 2. Table summarizing the fraction of events f_{+1} and f_{-1} with tag charges of $+1$ and -1, respectively for signal and background events and for the different tag methods. Only statistical errors are quoted.

JHEP08(2016)147

Tag method	Signal	Background
Combined μ	0.047 ± 0.003	0.038 ± 0.001
Electron	0.012 ± 0.001	0.008 ± 0.001
Segment-tagged μ	0.013 ± 0.001	0.015 ± 0.001
Jet-charge	0.135 ± 0.003	0.100 ± 0.001
Untagged	0.793 ± 0.002	0.839 ± 0.002

Table 3. Table summarizing the relative fractions of signal and background events tagged using the different tag methods. The fractions include both the continuous and discrete contributions. Only statistical errors are quoted.

5 Maximum likelihood fit

An unbinned maximum-likelihood fit is performed on the selected events to extract the parameter values of the $B_s^0 \to J/\psi(\mu^+\mu^-)\phi(K^+K^-)$ decay. The fit uses information about the reconstructed mass m, the measured proper decay time t, the measured proper decay time uncertainty σ_t, the tagging probability, and the transversity angles Ω of each $B_s^0 \to J/\psi\phi$ decay candidate. The measured proper decay time uncertainty σ_t is calculated from the covariance matrix associated with the vertex fit of each candidate event. The transversity angles $\Omega = (\theta_T, \psi_T, \phi_T)$ are defined in section 5.1. The likelihood is independent of the K^+K^- mass distribution. The likelihood function is defined as a combination of the signal and background probability density functions as follows:

$$\begin{aligned}\ln \mathcal{L} = \sum_{i=1}^{N} \{ & w_i \cdot \ln(f_{\rm s} \cdot \mathcal{F}_{\rm s}(m_i, t_i, \sigma_{t_i}, \Omega_i, P(B|Q), p_{{\rm T}_i}) \\ & + f_{\rm s} \cdot f_{B^0} \cdot \mathcal{F}_{B^0}(m_i, t_i, \sigma_{t_i}, \Omega_i, P(B|Q), p_{{\rm T}_i}) \\ & + f_{\rm s} \cdot f_{\Lambda_b} \cdot \mathcal{F}_{\Lambda_b}(m_i, t_i, \sigma_{t_i}, \Omega_i, P(B|Q), p_{{\rm T}_i}) \\ & + (1 - f_{\rm s} \cdot (1 + f_{B^0} + f_{\Lambda_b})) \mathcal{F}_{\rm bkg}(m_i, t_i, \sigma_{t_i}, \Omega_i, P(B|Q), p_{{\rm T}_i}))\}, \end{aligned} \tag{5.1}$$

where N is the number of selected candidates, w_i is a weighting factor to account for the trigger efficiency (described in section 5.3), and $f_{\rm s}$ is the fraction of signal candidates. The background fractions f_{B^0} and f_{Λ_b} are the fractions of B^0 mesons and Λ_b baryons mis-identified as B_s^0 candidates calculated relative to the number of signal events; these parameters are fixed to their MC values and varied as part of the systematic uncertainties. The mass m_i, the proper decay time t_i and the decay angles Ω_i are the values measured from the data for each event i. $\mathcal{F}_{\rm s}$, $\mathcal{F}_{B^0}$, $\mathcal{F}_{\Lambda_b}$ and $\mathcal{F}_{\rm bkg}$ are the probability density functions (PDF) modelling the signal, B^0 background, Λ_b background, and the other background distributions, respectively. A detailed description of the signal PDF terms in equation (5.1) is given in section 5.1. The three background functions are described in section 5.2.

JHEP08(2016)147

5.1 Signal PDF

The PDF used to describe the signal events, $\mathcal{F}_{\rm s}$, has the following composition:

$$\begin{aligned}\mathcal{F}_{\rm s}(m_i, t_i, \sigma_{t_i}, \Omega_i, P(B|Q), p_{{\rm T}_i}) = & \; P_{\rm s}(m_i) \cdot P_{\rm s}(\Omega_i, t_i, P(B|Q), \sigma_{t_i}) \\ & \cdot P_{\rm s}(\sigma_{t_i}) \cdot P_{\rm s}(P(B|Q)) \cdot A(\Omega_i, p_{{\rm T}_i}) \cdot P_{\rm s}(p_{{\rm T}_i}). \end{aligned} \quad (5.2)$$

The mass function $P_{\rm s}(m_i)$ is modelled by a sum of three Gaussian distributions. The probability terms $P_{\rm s}(\sigma_{t_i})$ and $P_{\rm s}(p_{{\rm T}i})$ are described by gamma functions and are unchanged from the analysis described in ref. [25]. The tagging probability term for signal $P_{\rm s}(P(B|Q))$ is described in section 4.3.

The term $P_{\rm s}(\Omega_i, t_i, P(B|Q), \sigma_{t_i})$ is a joint PDF for the decay time t and the transversity angles Ω for the $B_s^0 \to J/\psi(\mu^+\mu^-)\phi(K^+K^-)$ decay. Ignoring detector effects, the distribution for the time t and the angles Ω is given by the differential decay rate [26]:

$$\frac{{\rm d}^4\Gamma}{{\rm dt}\ {\rm d}\Omega} = \sum_{k=1}^{10} \mathcal{O}^{(k)}(t) g^{(k)}(\theta_T, \psi_T, \phi_T),$$

where $\mathcal{O}^{(k)}(t)$ are the time-dependent functions corresponding to the contributions of the four different amplitudes (A_0, $A_{||}$, $A_\perp$, and A_S) and their interference terms, and $g^{(k)}(\theta_T, \psi_T, \phi_T)$ are the angular functions. Table 4 shows these time-dependent functions and the angular functions of the transversity angles. The formulae for the time-dependent functions have the same structure for B_s^0 and $\bar{B}_s^0$ but with a sign reversal in the terms containing Δm_s. In table 4, the parameter $A_\perp(t)$ is the time-dependent amplitude for the CP-odd final-state configuration while $A_0(t)$ and $A_{||}(t)$ correspond to CP-even final-state configurations. The amplitude $A_S(t)$ gives the contribution from the CP-odd non-resonant $B_s^0 \to J/\psi K^+K^-$ S-wave state (which includes the f_0). The corresponding functions are given in the last four lines of table 4 (k = 7–10). The amplitudes are parameterized by $|A_i|e^{i\delta_i}$, where $i = \{0, ||, \perp, S\}$, with $\delta_0 = 0$ and are normalized such that $|A_0(0)|^2 + |A_\perp(0)|^2 + |A_{||}(0)|^2 = 1$. $|A_\perp(0)|$ is determined according to this condition, while the remaining three amplitudes are parameters of the fit. The formalism used throughout this analysis assumes no direct CP violation.

The angles $(\theta_T, \psi_T, \phi_T)$, are defined in the rest frames of the final-state particles. The x-axis is determined by the direction of the ϕ meson in the J/ψ rest frame, and the K^+K^- system defines the x–y plane, where $p_y(K^+) > 0$. The three angles are defined as:

- θ_T, the angle between $\vec{p}(\mu^+)$ and the normal to the x–y plane, in the J/ψ meson rest frame,
- ϕ_T, the angle between the x-axis and $\vec{p}_{xy}(\mu^+)$, the projection of the μ^+ momentum in the x–y plane, in the J/ψ meson rest frame,
- ψ_T, the angle between $\vec{p}(K^+)$ and $-\vec{p}(J/\psi)$ in the ϕ meson rest frame.

The PDF term $P_{\rm s}(\Omega_i, t_i, P(B|Q), \sigma_{t_i})$ takes into account the lifetime resolution, so each time element in table 4 is smeared with a Gaussian function. This smearing is performed

JHEP08(2016)147

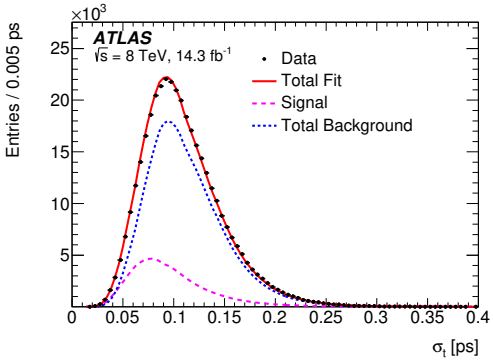

Figure 6. The proper decay time uncertainty distribution for data (black), and the fits to the background (blue) and the signal (purple) contributions. The total fit is shown as a red curve.

numerically on an event-by-event basis where the width of the Gaussian function is the proper decay time uncertainty, measured for each event, multiplied by a scale factor to account for any mis-measurements. The proper decay time uncertainty distribution for data, including the fits to the background and the signal contributions is shown in figure 6. The average value of this uncertainty for signal events is 97 fs.

The angular acceptance of the detector and kinematic cuts on the angular distributions are included in the likelihood function through $A(\Omega_i, p_{Ti})$. This is calculated using a 4D binned acceptance method, applying an event-by-event efficiency according to the transversity angles $(\theta_T, \psi_T, \phi_T)$ and the $p_{\rm T}$ of the candidate. The $p_{\rm T}$ binning is necessary, because the angular acceptance is influenced by the $p_{\rm T}$ of the B_s^0 candidate. The acceptance is calculated from the $B_s^0 \to J/\psi\phi$ MC events. Taking the small discrepancies between data and MC events into account have negligible effect on the fit results. In the likelihood function, the acceptance is treated as an angular acceptance PDF, which is multiplied with the time- and angle-dependent PDF describing the $B_s^0 \to J/\psi(\mu^+\mu^-)\phi(K^+K^-)$ decays. As both the acceptance and time- and angle-dependent decay PDFs depend on the transversity angles they must be normalized together. This normalization is done numerically during the likelihood fit. The PDF is normalized over the entire B_s^0 mass range 5.150–5.650 GeV.

5.2 Background PDF

The background PDF has the following composition:

$$\begin{aligned}\mathcal{F}_{\rm bkg}(m_i, t_i, \sigma_{t_i}, \Omega_i, P(B|Q), p_{{\rm T}_i}) = {} & P_{\rm b}(m_i) \cdot P_{\rm b}(t_i|\sigma_{t_i}) \cdot P_{\rm b}(P(B|Q)) \\ & \cdot P_{\rm b}(\Omega_i) \cdot P_{\rm b}(\sigma_{t_i}) \cdot P_{\rm b}(p_{{\rm T}i}). \end{aligned} \tag{5.3}$$

The proper decay time function $P_{\rm b}(t_i|\sigma_{t_i})$ is parameterized as a prompt peak modelled by a Gaussian distribution, two positive exponential functions and a negative exponential function. These functions are smeared with the same resolution function as the signal decay time-dependence. The prompt peak models the combinatorial background events, which are expected to have reconstructed lifetimes distributed around zero. The two positive exponential functions represent a fraction of longer-lived backgrounds with non-prompt

JHEP08(2016)147

k	$\mathcal{O}^{(k)}(t)$	$g^{(k)}(\theta_T, \psi_T, \phi_T)$
1	$\frac{1}{2}\lvert A_0(0)\rvert^2 \left[(1+\cos\phi_s)\, e^{-\Gamma_{\rm L}^{(s)}t} + (1-\cos\phi_s)\, e^{-\Gamma_{\rm H}^{(s)}t} \pm 2e^{-\Gamma_s t}\sin(\Delta m_s t)\sin\phi_s\right]$	$2\cos^2\psi_T(1-\sin^2\theta_T\cos^2\phi_T)$
2	$\frac{1}{2}\lvert A_\parallel(0)\rvert^2 \left[(1+\cos\phi_s)\, e^{-\Gamma_{\rm L}^{(s)}t} + (1-\cos\phi_s)\, e^{-\Gamma_{\rm H}^{(s)}t} \pm 2e^{-\Gamma_s t}\sin(\Delta m_s t)\sin\phi_s\right]$	$\sin^2\psi_T(1-\sin^2\theta_T\sin^2\phi_T)$
3	$\frac{1}{2}\lvert A_\perp(0)\rvert^2 \left[(1-\cos\phi_s)\, e^{-\Gamma_{\rm L}^{(s)}t} + (1+\cos\phi_s)\, e^{-\Gamma_{\rm H}^{(s)}t} \mp 2e^{-\Gamma_s t}\sin(\Delta m_s t)\sin\phi_s\right]$	$\sin^2\psi_T\sin^2\theta_T$
4	$\frac{1}{2}\lvert A_0(0)\rvert\lvert A_\parallel(0)\rvert\cos\delta_\parallel$ $\left[(1+\cos\phi_s)\, e^{-\Gamma_{\rm L}^{(s)}t} + (1-\cos\phi_s)\, e^{-\Gamma_{\rm H}^{(s)}t} \pm 2e^{-\Gamma_s t}\sin(\Delta m_s t)\sin\phi_s\right]$	$\frac{1}{\sqrt{2}}\sin 2\psi_T\sin^2\theta_T\sin 2\phi_T$
5	$\lvert A_\parallel(0)\rvert\lvert A_\perp(0)\rvert[\frac{1}{2}(e^{-\Gamma_{\rm L}^{(s)}t} - e^{-\Gamma_{\rm H}^{(s)}t})\cos(\delta_\perp-\delta_\parallel)\sin\phi_s$ $\pm e^{-\Gamma_s t}(\sin(\delta_\perp-\delta_\parallel)\cos(\Delta m_s t) - \cos(\delta_\perp-\delta_\parallel)\cos\phi_s\sin(\Delta m_s t))]$	$-\sin^2\psi_T\sin 2\theta_T\sin\phi_T$
6	$\lvert A_0(0)\rvert\lvert A_\perp(0)\rvert[\frac{1}{2}(e^{-\Gamma_{\rm L}^{(s)}t} - e^{-\Gamma_{\rm H}^{(s)}t})\cos\delta_\perp\sin\phi_s$ $\pm e^{-\Gamma_s t}(\sin\delta_\perp\cos(\Delta m_s t) - \cos\delta_\perp\cos\phi_s\sin(\Delta m_s t))]$	$\frac{1}{\sqrt{2}}\sin 2\psi_T\sin 2\theta_T\cos\phi_T$
7	$\frac{1}{2}\lvert A_S(0)\rvert^2 \left[(1-\cos\phi_s)\, e^{-\Gamma_{\rm L}^{(s)}t} + (1+\cos\phi_s)\, e^{-\Gamma_{\rm H}^{(s)}t} \mp 2e^{-\Gamma_s t}\sin(\Delta m_s t)\sin\phi_s\right]$	$\frac{2}{3}\left(1-\sin^2\theta_T\cos^2\phi_T\right)$
8	$\lvert A_S(0)\rvert\lvert A_\parallel(0)\rvert[\frac{1}{2}(e^{-\Gamma_{\rm L}^{(s)}t} - e^{-\Gamma_{\rm H}^{(s)}t})\sin(\delta_\parallel-\delta_S)\sin\phi_s$ $\pm e^{-\Gamma_s t}(\cos(\delta_\parallel-\delta_S)\cos(\Delta m_s t) - \sin(\delta_\parallel-\delta_S)\cos\phi_s\sin(\Delta m_s t))]$	$\frac{1}{3}\sqrt{6}\sin\psi_T\sin^2\theta_T\sin 2\phi_T$
9	$\frac{1}{2}\lvert A_S(0)\rvert\lvert A_\perp(0)\rvert\sin(\delta_\perp-\delta_S)$ $\left[(1-\cos\phi_s)\, e^{-\Gamma_{\rm L}^{(s)}t} + (1+\cos\phi_s)\, e^{-\Gamma_{\rm H}^{(s)}t} \mp 2e^{-\Gamma_s t}\sin(\Delta m_s t)\sin\phi_s\right]$	$\frac{1}{3}\sqrt{6}\sin\psi_T\sin 2\theta_T\cos\phi_T$
10	$\lvert A_0(0)\rvert\lvert A_S(0)\rvert[\frac{1}{2}(e^{-\Gamma_{\rm H}^{(s)}t} - e^{-\Gamma_{\rm L}^{(s)}t})\sin\delta_S\sin\phi_s$ $\pm e^{-\Gamma_s t}(\cos\delta_S\cos(\Delta m_s t) + \sin\delta_S\cos\phi_s\sin(\Delta m_s t))]$	$\frac{4}{3}\sqrt{3}\cos\psi_T\left(1-\sin^2\theta_T\cos^2\phi_T\right)$

Table 4. Table showing the ten time-dependent functions, $\mathcal{O}^{(k)}(t)$ and the functions of the transversity angles $g^{(k)}(\theta_T, \psi_T, \phi_T)$. The amplitudes $|A_0(0)|^2$ and $|A_\parallel(0)|^2$ are for the CP-even components of the $B_s^0 \to J/\psi\phi$ decay, $|A_\perp(0)|^2$ is the CP-odd amplitude; they have corresponding strong phases δ_0, $\delta_\parallel$ and $\delta_\perp$. By convention δ_0 is set to be zero. The S-wave amplitude $|A_S(0)|^2$ gives the fraction of $B_s^0 \to J/\psi K^+K^-(f_0)$ and has a related strong phase δ_S. The $\pm$ and $\mp$ terms denote two cases: the upper sign describes the decay of a meson that was initially a B_s^0 meson, while the lower sign describes the decays of a meson that was initially $\bar{B}_s^0$.

JHEP08(2016)147

J/ψ, combined with hadrons from the primary vertex or from a B/D meson in the same event. The negative exponential function takes into account events with poor vertex resolution. The probability terms $P_{\rm b}(\sigma_{t_i})$ and $P_{\rm b}(p_{{\rm T}i})$ are described by gamma functions. They are unchanged from the analysis described in ref. [25] and explained in detail there. The tagging probability term for background $P_{\rm b}(P(B|Q))$ is described in section 4.3.

The shape of the background angular distribution, $P_{\rm b}(\Omega_i)$ arises primarily from detector and kinematic acceptance effects. These are described by Legendre polynomial functions:

$$
\begin{aligned}
Y_l^m(\theta_T) &= \sqrt{(2l+1)/(4\pi)}\sqrt{(l-m)!/(l+m)!}P_l^{|m|}(\cos\theta_T) \\
P_k(x) &= \frac{1}{2^k k!}\frac{{\rm d}^{\rm k}}{{\rm dx}^{\rm k}}(x^2-1)^k \qquad (5.4)\\
\mathscr{P}_{\rm b}(\theta_T,\psi_T,\phi_T) &= \sum_{k=0}^{6}\sum_{l=0}^{6}\sum_{m=-l}^{l}\begin{cases} a_{k,l,m}\sqrt{2}Y_l^m(\theta_T)\cos(m\phi_T)P_k(\cos\psi_T) & \text{where } m>0 \\ a_{k,l,m}\sqrt{2}Y_l^{-m}(\theta_T)\sin(m\phi_T)P_k(\cos\psi_T) & \text{where } m<0 \\ a_{k,l,m}\sqrt{2}Y_l^0(\theta_T)P_k(\cos\psi_T) & \text{where } m=0 \end{cases}
\end{aligned}
$$

where the coefficients $a_{k,l,m}$ are adjusted to give the best fit to the angular distributions for events in the B_s^0 mass sidebands. These parameters are then fixed in the main fit. The B_s^0 mass interval used for the background fit is between 5.150 and 5.650 GeV excluding the signal mass region $|(m(B_s^0) - 5.366\ \text{GeV}| < 0.110$ GeV. The background mass model, $P_{\rm b}(m_i)$ is an exponential function with a constant term added.

Contamination from $B_d \to J/\psi K^{0*}$ and $\Lambda_b \to J/\psi p K^-$ events mis-reconstructed as $B_s^0 \to J/\psi\phi$ are accounted for in the fit through the $\mathcal{F}_{B^0}$ and $\mathcal{F}_{\Lambda_b}$ terms in the PDF function described in equation (5.1). The fraction of these contributions, $f_{B^0} = (3.3 \pm 0.5)\%$ and $f_{\Lambda_b} = (1.8 \pm 0.6)\%$, are evaluated from MC simulation using production and branching fractions from refs. [18, 27–31]. MC simulated events are also used to determine the shape of the mass and transversity angle distributions. The 3D angular distributions of $B_d^0 \to J/\psi K^{*0}$ and of the conjugate decay are modelled using input from ref. [32], while angular distributions for $\Lambda_b \to J/\psi p K^-$ and the conjugate decay are modelled as flat. These distributions are sculpted for detector acceptance effects and then described by Legendre polynomial functions, equation (5.4), as in the case of the background described by equation (5.3). These shapes are fixed in the fit. The B_d and Λ_b lifetimes are accounted for in the fit by adding additional exponential terms, scaled by the ratio of B_d/B_s^0 or Λ_b/B_s^0 masses as appropriate, where the lifetimes and masses are taken from ref. [18]. Systematic uncertainties due to the background from $B_d \to J/\psi K^{0*}$ and $\Lambda_b \to J/\psi p K^-$ decays are described in section 7. The contribution of $B_d \to J/\psi K\pi$ events as well as their interference with $B_d \to J/\psi K^{0*}$ events is not included in the fit and is instead assigned as a systematic uncertainty.

To account for possible deviations between data and the selected fit models a number of alternative fit functions and mass selection criteria are used to determine systematic uncertainties in the B_s^0 fit. These fit variations are described in section 7.

JHEP08(2016)147

5.3 Muon trigger proper time-dependent efficiency

It was observed that the muon trigger biases the transverse impact parameter of muons, resulting in a minor inefficiency at large values of the proper decay time. This inefficiency is measured using MC simulated events, by comparing the B_s^0 proper decay time distribution of an unbiased sample with the distribution obtained including the trigger. To account for this inefficiency in the fit, the events are re-weighted by a factor w:

$$w = p_0 \cdot [1 - p_1 \cdot (\mathrm{Erf}((\mathrm{t} - \mathrm{p_3})/\mathrm{p_2}) + 1)], \tag{5.5}$$

where p_0, p_1, p_2 and p_3 are parameters determined in the fit to MC events. No significant bias or inefficiency due to off-line track reconstruction, vertex reconstruction, or track quality selection criteria is observed.

6 Results

The full simultaneous unbinned maximum-likelihood fit contains nine physical parameters: $\Delta\Gamma_s$, ϕ_s, Γ_s, $|A_0(0)|^2$, $|A_{\|}(0)|^2$, $\delta_{||}$, $\delta_{\perp}$, $|A_S(0)|^2$ and δ_S. The other parameters in the likelihood function are the B_s^0 signal fraction f_s, parameters describing the $J/\psi\phi$ mass distribution, parameters describing the B_s^0 meson decay time plus angular distributions of background events, parameters used to describe the estimated decay time uncertainty distributions for signal and background events, and scale factors between the estimated decay time uncertainties and their true uncertainties. In addition there are also 353 nuisance parameters describing the background and acceptance functions that are fixed at the time of the fit. The fit model is tested using pseudo-experiments as described in section 7. These tests show no significant bias, as well as no systematic underestimation of the statistical errors reported from the fit to data.

Multiplying the total number of events supplied to the fit with the extracted signal fraction and its statistical uncertainty provides an estimate for the total number of B_s^0 meson candidates of 74900 ± 400. The results and correlations of the physics parameters obtained from the fit are given in tables 5 and 6. Fit projections of the mass, proper decay time and angles are given in figures 7 and 8, respectively.

7 Systematic uncertainties

Systematic uncertainties are assigned by considering effects that are not accounted for in the likelihood fit. These are described below.

- **Flavour tagging:** there are two contributions to the uncertainties in the fit parameters due to the flavour tagging procedure, the statistical and systematic components. The statistical uncertainty due to the size of the sample of $B^{\pm} \to J/\psi K^{\pm}$ decays is included in the overall statistical error. The systematic uncertainty arising from the precision of the tagging calibration is estimated by changing the model used to parameterize the probability distribution, $P(B|Q)$, as a function of tag charge from the third-order polynomial function used by default to one of several alternative

JHEP08(2016)147

Parameter	Value	Statistical uncertainty	Systematic uncertainty
ϕ_s[rad]	-0.110	0.082	0.042
$\Delta\Gamma_s[\mathrm{ps}^{-1}]$	0.101	0.013	0.007
$\Gamma_s[\mathrm{ps}^{-1}]$	0.676	0.004	0.004
$\lvert A_{\parallel}(0)\rvert^2$	0.230	0.005	0.006
$\lvert A_0(0)\rvert^2$	0.520	0.004	0.007
$\lvert A_S(0)\rvert^2$	0.097	0.008	0.022
$\delta_\perp$ [rad]	4.50	0.45	0.30
$\delta_{\parallel}$ [rad]	3.15	0.10	0.05
$\delta_\perp - \delta_S$ [rad]	-0.08	0.03	0.01

Table 5. Fitted values for the physical parameters of interest with their statistical and systematic uncertainties.

	$\Delta\Gamma$	Γ_s	$\lvert A_{\parallel}(0)\rvert^2$	$\lvert A_0(0)\rvert^2$	$\lvert A_S(0)\rvert^2$	$\delta_{\parallel}$	$\delta_\perp$	$\delta_\perp - \delta_S$
ϕ_s	0.097	-0.085	0.030	0.029	0.048	0.067	0.035	-0.008
$\Delta\Gamma$	1	-0.414	0.098	0.136	0.045	0.009	0.008	-0.011
Γ_s		1	-0.119	-0.042	0.167	-0.027	-0.009	0.018
$\lvert A_{\parallel}(0)\rvert^2$			1	-0.330	0.072	0.105	0.025	-0.018
$\lvert A_0(0)\rvert^2$				1	0.234	-0.011	0.007	0.014
$\lvert A_S(0)\rvert^2$					1	-0.046	0.004	0.052
$\delta_{\parallel}$						1	0.158	-0.006
$\delta_\perp$							1	0.018

Table 6. Fit correlations between the physical parameters of interest.

functions. The alternatives used are: a linear function; a fifth-order polynomial; or two third-order polynomials describing the positive and negative regions that share the constant and linear terms but have independent quadratic and cubic terms. For the combined-muon tagging, an additional model consisting of two third-order polynomials sharing the constant term but with independent linear, quadratic and cubic terms is also used. The B_s^0 fit is repeated using the alternative models and the largest difference is assigned as the systematic uncertainty.

- **Angular acceptance method:** the angular acceptance (from the detector and kinematic effects mentioned in section 5.1) is calculated from a binned fit to MC simulated data. In order to estimate the size of the systematic uncertainty introduced from the choice of binning, different acceptance functions are calculated using different bin widths and central values. These effects are found to be negligible.

JHEP08(2016)147

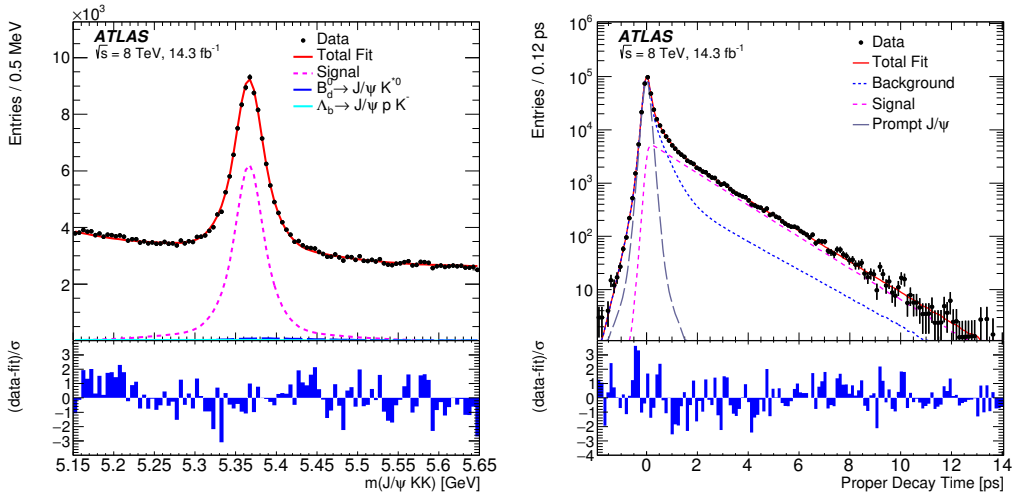

Figure 7. (Left) Mass fit projection for the $B_s^0 \to J/\psi\phi$ sample. The red line shows the total fit, the dashed purple line shows the signal component, the long-dashed dark blue line shows the $B_d^0 \to J/\psi K^{0*}$ component, while the solid light blue line shows the contribution from $\Lambda_b \to J/\psi p K^-$ events. (Right) Proper decay time fit projection for the $B_s^0 \to J/\psi\phi$ sample. The red line shows the total fit while the purple dashed line shows the total signal. The total background is shown as a blue dashed line with a long-dashed grey line showing the prompt J/ψ background. Below each figure is a ratio plot that shows the difference between each data point and the total fit line divided by the statistical uncertainty (σ) of that point.

- **Inner detector alignment:** residual misalignments of the ID affect the impact parameter, d_0, distribution with respect to the primary vertex. The effect of a radial expansion on the measured d_0 is determined from data collected at 8 TeV, with a trigger requirement of at least one muon with a transverse momentum greater than or equal to 4 GeV. The radial expansion uncertainties determined in this way are 0.14% for $|\eta| < 1.5$ and 0.55% for $1.5 < |\eta| < 2.5$. These values are used to estimate the effect on the fitted B_s^0 parameter values. Small deviations are seen in some parameters, and these are included as systematic uncertainties.

- **Trigger efficiency:** to correct for the trigger lifetime bias the events are re-weighted according to equation (5.5). The uncertainty of the parameters p_0, p_1, p_2 and p_3 are used to estimate the systematic uncertainty due to the time efficiency correction. These uncertainties originate from the following sources: the limited size of the MC simulated dataset, the choice of bin-size for the proper decay time distributions and variations between different triggers. The systematic effects are found to be negligible.

- **Background angles model, choice of p_{T} bins:** the shape of the background angular distribution, $P_{\mathrm{b}}(\theta_T, \varphi_T, \psi_T)$, is described by the Legendre polynomial functions given in equation (5.4). The shapes arise primarily from detector and kinematic acceptance effects and are sensitive to the p_{T} of the B_s^0 meson candidate. For this reason, the parameterization using the Legendre polynomial functions is performed in four p_{T} intervals: 0–13 GeV, 13–18 GeV, 18–25 GeV and >25 GeV. The system-

JHEP08(2016)147

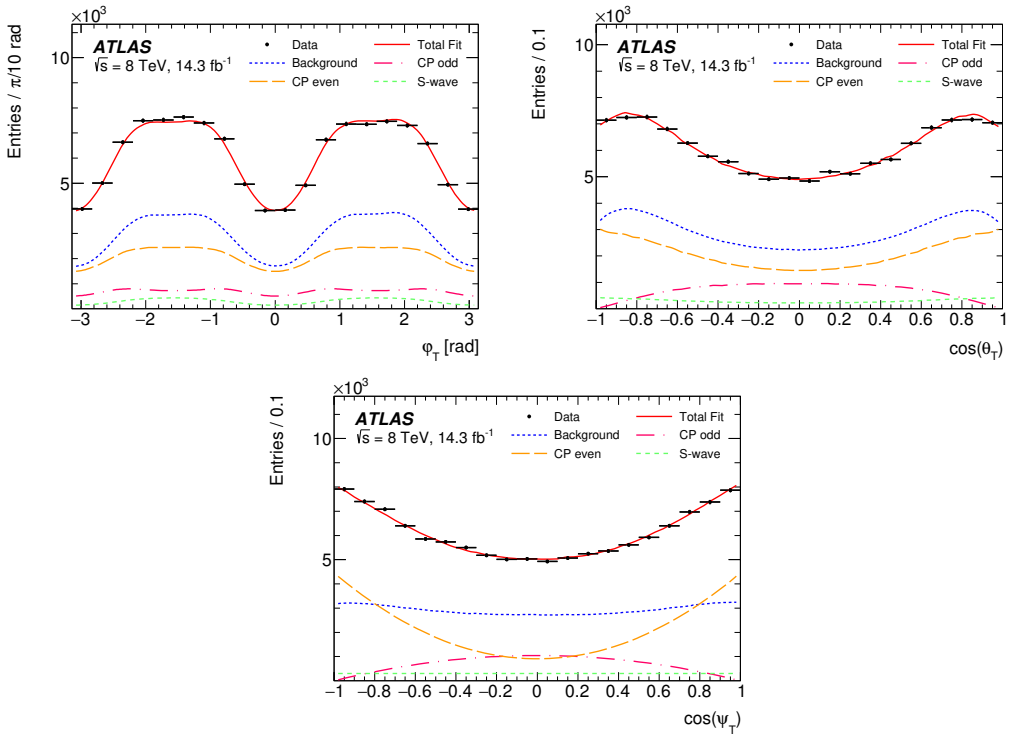

Figure 8. Fit projections for the transversity angles of events with 5.317 GeV $< m(J/\psi KK) <$ 5.417 GeV for ϕ_T (top left), $\cos(\theta_T)$ (top right), and $\cos(\psi_T)$ (bottom). In all three plots the red solid line shows the total fit, the CP-odd and CP-even signal components are shown by the red dot-dashed and orange dashed lines respectively, the S-wave component is given by the green dashed line and the blue dotted line shows the background contribution. The contributions of the interference terms are negligible in these projections and are not shown.

atic uncertainties due to the choice of $p_{\rm T}$ intervals are estimated by repeating the fit, varying these intervals. The biggest deviations observed in the fit results were taken to represent the systematic uncertainties.

- **Background angles model, choice of mass sidebands:** the parameters of the Legendre polynomial functions given in equation (5.4) are adjusted to give the best fit to the angular distributions for events in the B_s^0 mass sidebands. To test the sensitivity of the fit results to the choice of sideband regions, the fit is repeated with alternative choices for the excluded signal mass regions: $|m(B_s^0) - 5.366| > 0.085$ GeV and $|m(B_s^0) - 5.366| > 0.160$ GeV (instead of $|m(B_s^0) - 5.366| > 0.110$ GeV). The differences in the fit results are assigned as systematic uncertainties.

- ***B_d* contribution:** the contamination from $B_d \to J/\psi K^{0*}$ events mis-reconstructed as $B_s^0 \to J/\psi\phi$ is accounted for in the final fit. Studies are performed to evaluate the effect of the uncertainties in the $B_d \to J/\psi K^{0*}$ fraction, and the shapes of the mass and transversity angles distribution. In the MC events the angular distribution of the $B_d \to J/\psi K^{0*}$ decay is modelled using parameters taken from ref. [32]. The uncertainties of these parameters are taken into account in the estimation of systematic

JHEP08(2016)147

uncertainty. After applying the B_s^0 signal selection cuts, the angular distributions are fitted using Legendre polynomial functions. The uncertainties of this fit are included in the systematic tests. The impact of all these uncertainties is found to have a negligible effect on the B_s^0 fit results. The contribution of $B_d \to J/\psi K\pi$ events as well as their interference with $B_d \to J/\psi K^{0*}$ events is not included in the fit and is instead assigned as a systematic uncertainty. To evaluate this uncertainty, the MC background events are modelled using both the P-wave $B_d \to J/\psi K^{0*}$ and S-wave $B_d \to J/\psi K\pi$ decays and their interference, using the input parameters taken from ref. [32]. The B_s^0 fit using this input was compared to the default fit, and differences are included in table 7.

- **Λ_b contribution:** the contamination from $\Lambda_b \to J/\psi p K^-$ events mis-reconstructed as $B_s^0 \to J/\psi\phi$ is accounted for in the final fit. Studies are performed to evaluate the effect of the uncertainties in the $\Lambda_b \to J/\psi p K^-$ fraction f_{Λ_b}, and the shapes of the mass, transversity angles, and lifetime distributions. Additional studies are performed to determine the effect of the uncertainties in the $\Lambda_b \to J/\psi\Lambda^*$ branching ratios used to reweight the generated MC. These are uncertainties are included in table 7.

- **Fit model variations:** to estimate the systematic uncertainties due to the fit model, variations of the model are tested in pseudo-experiments. A set of ≈2500 pseudo-experiments is generated for each variation considered, and fitted with the default model. The systematic error quoted for each effect is the difference between the mean shift of the fitted value of each parameter from its input value for the pseudo-experiments altered for each source of systematic uncertainty. In the first variation tested, the signal mass is generated using the fitted B_s^0 mass convolved with a Gaussian function using the measured per-candidate mass errors. In another test, the background mass is generated from an exponential function with the addition of a first-degree polynomial function instead of an exponential function plus a constant term. The time resolution model was varied by using two different scale factors to generate the lifetime uncertainty, instead of the single scale factor used in the default model. The non-negligible uncertainties derived from these tests are included in the systematic uncertainties shown in table 7. To determine the possible systematics effects of mis-modelling of the background events by the fitted background model, as seen in the low mass side-band region (5.150–5.210 GeV) of figure 7, left, alternative mass selection cuts are used with the default fit model. The effect of these changes on the fit results are found to be negligible.

- **Default fit model:** due to its complexity, the fit model is less sensitive to some nuisance parameters. This limited sensitivity could potentially lead to a bias in the measured physics parameters, even when the model perfectly describes the fitted data. To estimate the systematic uncertainty due to the choice of default fit model, a set of pseudo-experiments were conducted using the default model in both the generation and fit. The systematic uncertainties are determined from the mean of

JHEP08(2016)147

	ϕ_s [rad]	$\Delta\Gamma_s$ [ps^{-1}]	Γ_s [ps^{-1}]	$\lvert A_\parallel(0)\rvert^2$	$\lvert A_0(0)\rvert^2$	$\lvert A_S(0)\rvert^2$	$\delta_\perp$ [rad]	$\delta_\parallel$ [rad]	$\delta_\perp - \delta_S$ [rad]
Tagging	0.025	0.003	$<10^{-3}$	$<10^{-3}$	$<10^{-3}$	0.001	0.236	0.014	0.004
Acceptance	$<10^{-3}$	$<10^{-3}$	$<10^{-3}$	0.003	$<10^{-3}$	0.001	0.004	0.008	$<10^{-3}$
Inner detector alignment	0.005	$<10^{-3}$	0.002	$<10^{-3}$	$<10^{-3}$	$<10^{-3}$	0.134	0.007	$<10^{-3}$
Background angles model:									
Choice of p_{T} bins	0.020	0.006	0.003	0.003	$<10^{-3}$	0.008	0.004	0.006	0.008
Choice of mass interval	0.008	0.001	0.001	$<10^{-3}$	$<10^{-3}$	0.002	0.021	0.005	0.003
B_d^0 background model	0.023	0.001	$<10^{-3}$	0.002	0.002	0.017	0.090	0.011	0.009
Λ_b background model	0.011	0.002	0.001	0.001	0.007	0.009	0.045	0.006	0.007
Fit model:									
Mass signal model	0.004	$<10^{-3}$	$<10^{-3}$	0.002	$<10^{-3}$	0.001	0.015	0.017	$<10^{-3}$
Mass background model	$<10^{-3}$	0.002	$<10^{-3}$	0.002	$<10^{-3}$	0.002	0.027	0.038	$<10^{-3}$
Time resolution model	0.003	$<10^{-3}$	0.001	0.002	$<10^{-3}$	0.002	0.057	0.011	0.001
Default fit model	0.001	0.002	$<10^{-3}$	0.002	$<10^{-3}$	0.002	0.025	0.015	0.002
Total	0.042	0.007	0.004	0.006	0.007	0.022	0.30	0.05	0.01

Table 7. Summary of systematic uncertainties assigned to the physical parameters of interest.

the pull distributions of the pseudo-experiments scaled by the statistical error of that parameter on the fit to data. These tests show no significant bias in the fit model, and no systematic underestimation of the statistical errors reported from the fit to data.

The systematic uncertainties are listed in table 7. For each parameter, the total systematic error is obtained by adding all of the contributions in quadrature.

8 Discussion

The PDF describing the $B_s^0 \to J/\psi\phi$ decay is invariant under the following simultaneous transformations:

$$\{\phi_s, \Delta\Gamma_s, \delta_\perp, \delta_\parallel\} \to \{\pi - \phi_s, -\Delta\Gamma_s, \pi - \delta_\perp, 2\pi - \delta_\parallel\}.$$

Since $\Delta\Gamma_s$ was determined to be positive [33], there is a unique solution. Figure 9 shows the 1D log-likelihood scans of ϕ_s, $\Delta\Gamma_s$ and of the three measured strong phases $\delta_{||}$, $\delta_\perp$ and $\delta_\perp - \delta_S$. The variable on vertical axis, $2\Delta\ln(\mathrm{L}) \equiv 2(\ln(\mathrm{L^G}) - \ln(\mathrm{L^i}))$, is a difference between the likelihood values of a default fit, $(\mathrm{L^G})$, and of the fit in which the physical parameter is fixed to a value shown on horizontal axis, $(\mathrm{L^i})$. $2\Delta\ln(\mathrm{L}) = 1$ corresponds to the estimated 1σ confidence level. There are a small asymmetries in the likelihood curves, however at the level of one statistical σ these are small compared to the corresponding statistical uncertainties of the physical variables, for which the scan is done. Therefore symmetric statistical uncertainties are quoted. Figure 10 shows the likelihood contours in the ϕ_s–$\Delta\Gamma_s$ plane. The region predicted by the Standard Model is also shown.

JHEP08(2016)147

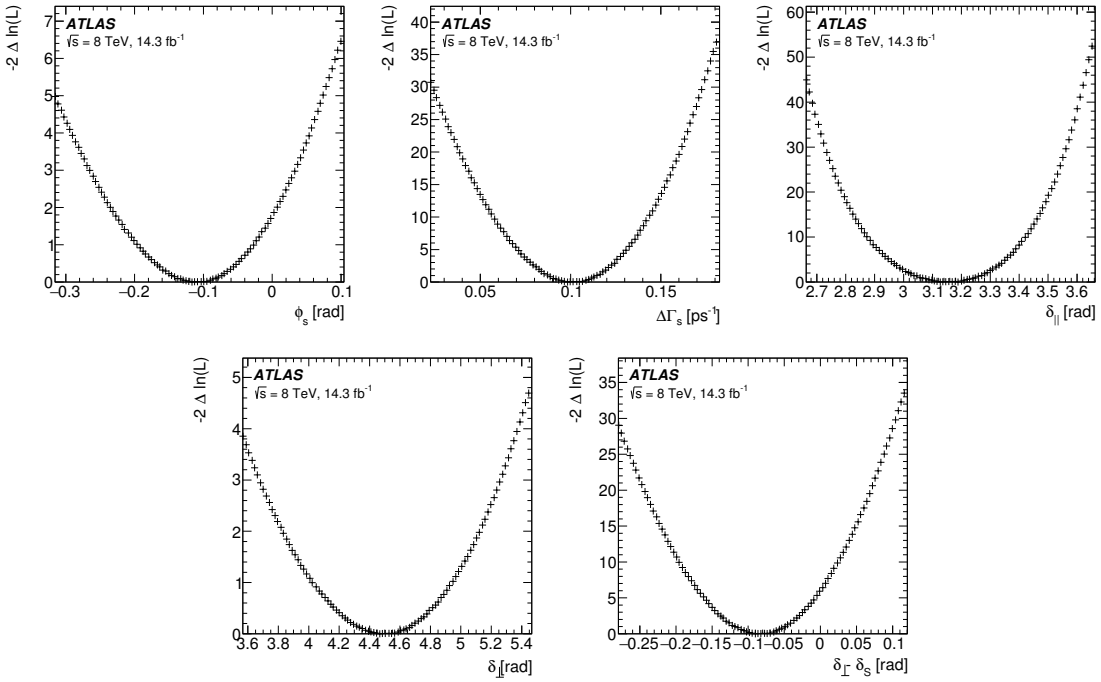

Figure 9. 1D likelihood contours (statistical errors only) for ϕ_s (top left), $\Delta\Gamma_s$ (top centre), $\delta_{||}$ (top right), $\delta_\perp$ (bottom left) and $\delta_\perp - \delta_S$ (bottom right).

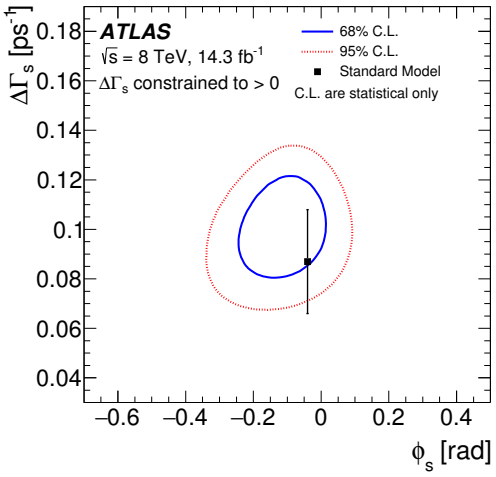

Figure 10. Likelihood contours in the ϕ_s–$\Delta\Gamma_s$ plane for 8 TeV data. The blue line shows the 68% likelihood contour, while the red dotted line shows the 95% likelihood contour (statistical errors only). The SM prediction is taken from ref. [1], at this scale the uncertainty on ϕ_s is not visible on the figure.

JHEP08(2016)147

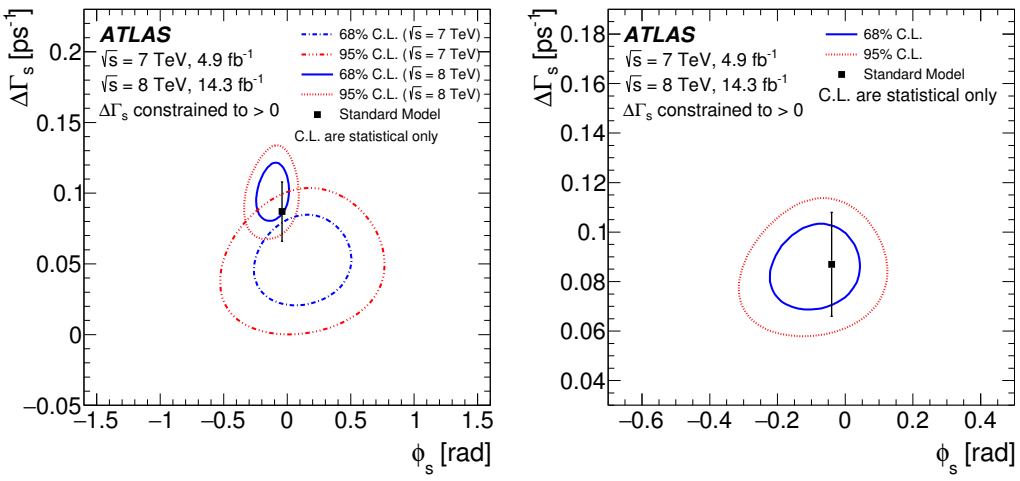

Figure 11. Likelihood contours in the ϕ_s–$\Delta\Gamma_s$ plane for individual results from 7 TeV and 8 TeV data (left) and a final statistical combination of the results from 7 TeV and 8 TeV data (right). The blue line shows the 68% likelihood contour, while the red dotted line shows the 95% likelihood contour (statistical errors only). The SM prediction is taken from ref. [1], at this scale the uncertainty on ϕ_s is not visible on the figure.

9 Combination of 7 TeV and 8 TeV results

The measured values are consistent with those obtained in a previous analysis [8], using ATLAS data collected in 2011 at a centre-of-mass energy of 7 TeV. This consistency is also clear from a comparison of the likelihood contours in the ϕ_s–$\Delta\Gamma_s$ projection shown in figure 11. A Best Linear Unbiased Estimate (BLUE) combination [34] is used to combine the 7 TeV and 8 TeV measurements to give an overall result for Run 1. In ref. [8] the strong phases $\delta_{\parallel}$ and $\delta_{\perp}$–δ_S were given as 1σ confidence intervals. These are not considered in the combination and the 8 TeV result is taken as the Run 1 result.

The BLUE combination requires the measured values and uncertainties of the parameters in question as well as the correlations between them. These are provided by the fits separately in the 7 TeV and 8 TeV measurements. The statistical correlation between these two measurements is zero as the events are different. The correlations of the systematic uncertainties between the two measurements are estimated by splitting the uncertainty into several categories.

The trigger efficiency is included as a systematic uncertainty only in the 7 TeV measurement, so there is no correlation with the 8 TeV measurement. Similarly, the systematic uncertainties arising from the $\Lambda_b \to J/\psi p K^-$ background, and the choice of p_{T} bins and mass sidebands in the modelling of background angles, are included as systematic uncertainties only in the 8 TeV measurement so there is no correlation with the 7 TeV measurement. In both the 7 TeV and 8 TeV results, a systematic uncertainty is assigned to the inner detector alignment and B_d contribution. The inner detector alignment systematic uncertainties are highly correlated and small. The assumed correlation between these systematics made no difference to the final combined result and was set to 100%. For the B_d

JHEP08(2016)147

Par	8 TeV data			7 TeV data			Run1 combined		
	Value	Stat	Syst	Value	Stat	Syst	Value	Stat	Syst
ϕ_s[rad]	-0.110	0.082	0.042	0.12	0.25	0.05	-0.090	0.078	0.041
$\Delta\Gamma_s[\mathrm{ps}^{-1}]$	0.101	0.013	0.007	0.053	0.021	0.010	0.085	0.011	0.007
$\Gamma_s[\mathrm{ps}^{-1}]$	0.676	0.004	0.004	0.677	0.007	0.004	0.675	0.003	0.003
$\lvert A_\parallel(0)\rvert^2$	0.230	0.005	0.006	0.220	0.008	0.009	0.227	0.004	0.006
$\lvert A_0(0)\rvert^2$	0.520	0.004	0.007	0.529	0.006	0.012	0.522	0.003	0.007
$\lvert A_S\rvert^2$	0.097	0.008	0.022	0.024	0.014	0.028	0.072	0.007	0.018
$\delta_\perp$ [rad]	4.50	0.45	0.30	3.89	0.47	0.11	4.15	0.32	0.16
$\delta_\parallel$ [rad]	3.15	0.10	0.05	[3.04, 3.23]		0.09	3.15	0.10	0.05
$\delta_\perp - \delta_S$ [rad]	-0.08	0.03	0.01	[3.02, 3.25]		0.04	-0.08	0.03	0.01

Table 8. Current measurement using data from 8 TeV pp collisions, the previous measurement using data taken at centre of mass energy of 7 TeV and the values for the parameters of the two measurements, statistically combined.

contribution, while the systematic uncertainty tests are different, they are both performed to account for an imprecise knowledge of the B_d contribution and are therefore assumed to be 100%. The tagging, acceptance and fit model uncertainties are quoted for both 7 TeV and 8 TeV. For the fit model, there are several different model variations each with their own uncertainty. For each year, these are summed in quadrature to produce a single fit model systematic uncertainty.

The tagging, acceptance and fit model systematic uncertainties are each assigned a variable (ρ_i, where $i = \mathrm{tag}, \mathrm{acc}, \mathrm{mod}$) corresponding to the correlation between the 7 TeV and 8 TeV results. Several different combinations were tried with different values of $\rho_i = 0, 0.25, 0.5, 0.75, 1.0$. The acceptance systematic uncertainty is small and therefore regardless of what value of ρ_{acc} is chosen the combination stays the same. For the 8 TeV measurement, electron tagging is added, therefore the systematic uncertainty is not 100% correlated. For $\rho_{\mathrm{tag}} = 0.25, 0.5, 0.75$ there is negligible difference between the results. The fit model was changed between the 7 TeV and 8 TeV measurement, the most significant change is that the mass uncertainty modelling was removed and the event-by-event Gaussian error distribution was replaced with a sum of three Gaussian distributions. It would be incorrect to estimate the correlation as 100% and there is negligible difference between the results for $\rho_{\mathrm{mod}} = 0.25, 0.5, 0.75$.

The combined results for the fit parameters and their uncertainties for Run 1 are given in table 8. Due to the negative correlation between Γ_s and $\Delta\Gamma_s$, and the change in the value of $\Delta\Gamma_s$ between the 7 TeV and 8 TeV results, the combined value of Γ_s is less than either individual result. The Run 1 likelihood contours in the ϕ_s–$\Delta\Gamma_s$ plane are shown in figure 11. They agree with the Standard Model predictions.

JHEP08(2016)147

10 Summary

A measurement of the time-dependent CP asymmetry parameters in $B_s^0 \to J/\psi(\mu^+\mu^-)\phi(K^+K^-)$ decays from a 14.3 fb^{-1} data sample of pp collisions collected with the ATLAS detector during the 8 TeV LHC run is presented. The values from the 8 TeV analysis are consistent with those obtained in the previous analysis using 7 TeV ATLAS data [8]. The two measurements are statistically combined leading to the following results:

$$\begin{aligned}
\phi_s &= -0.090 \pm 0.078\ (\text{stat.}) \pm 0.041\ (\text{syst.})\ \text{rad} \\
\Delta\Gamma_s &= 0.085 \pm 0.011\ (\text{stat.}) \pm 0.007\ (\text{syst.})\ \text{ps}^{-1} \\
\Gamma_s &= 0.675 \pm 0.003\ (\text{stat.}) \pm 0.003\ (\text{syst.})\ \text{ps}^{-1} \\
|A_\parallel(0)|^2 &= 0.227 \pm 0.004\ (\text{stat.}) \pm 0.006\ (\text{syst.}) \\
|A_0(0)|^2 &= 0.522 \pm 0.003\ (\text{stat.}) \pm 0.007\ (\text{syst.}) \\
|A_S(0)|^2 &= 0.072 \pm 0.007\ (\text{stat.}) \pm 0.018\ (\text{syst.}) \\
\delta_\perp &= 4.15 \pm 0.32\ (\text{stat.}) \pm\ 0.16\ (\text{syst.})\ \text{rad} \\
\delta_\parallel &= 3.15 \pm 0.10\ (\text{stat.}) \pm\ 0.05\ (\text{syst.})\ \text{rad} \\
\delta_\perp - \delta_S &= -0.08 \pm 0.03\ (\text{stat.}) \pm 0.01\ (\text{syst.})\ \text{rad}.
\end{aligned}$$

The ATLAS Run 1 results for the $B_s^0 \to J/\psi\phi$ decay are consistent with the SM.

Acknowledgments

We thank CERN for the very successful operation of the LHC, as well as the support staff from our institutions without whom ATLAS could not be operated efficiently.

We acknowledge the support of ANPCyT, Argentina; YerPhI, Armenia; ARC, Australia; BMWFW and FWF, Austria; ANAS, Azerbaijan; SSTC, Belarus; CNPq and FAPESP, Brazil; NSERC, NRC and CFI, Canada; CERN; CONICYT, Chile; CAS, MOST and NSFC, China; COLCIENCIAS, Colombia; MSMT CR, MPO CR and VSC CR, Czech Republic; DNRF and DNSRC, Denmark; IN2P3-CNRS, CEA-DSM/IRFU, France; GNSF, Georgia; BMBF, HGF, and MPG, Germany; GSRT, Greece; RGC, Hong Kong SAR, China; ISF, I-CORE and Benoziyo Center, Israel; INFN, Italy; MEXT and JSPS, Japan; CNRST, Morocco; FOM and NWO, Netherlands; RCN, Norway; MNiSW and NCN, Poland; FCT, Portugal; MNE/IFA, Romania; MES of Russia and NRC KI, Russian Federation; JINR; MESTD, Serbia; MSSR, Slovakia; ARRS and MIZŠ, Slovenia; DST/NRF, South Africa; MINECO, Spain; SRC and Wallenberg Foundation, Sweden; SERI, SNSF and Cantons of Bern and Geneva, Switzerland; MOST, Taiwan; TAEK, Turkey; STFC, United Kingdom; DOE and NSF, United States of America. In addition, individual groups and members have received support from BCKDF, the Canada Council, CANARIE, CRC, Compute Canada, FQRNT, and the Ontario Innovation Trust, Canada; EPLANET, ERC, FP7, Horizon 2020 and Marie Skłodowska-Curie Actions, European Union; Investissements d'Avenir Labex and Idex, ANR, Région Auvergne and Fondation Partager le Savoir, France; DFG and AvH Foundation, Germany; Herakleitos, Thales and Aristeia programmes co-financed by EU-ESF and the Greek NSRF; BSF, GIF and Minerva, Israel; BRF, Norway;

JHEP08(2016)147

Generalitat de Catalunya, Generalitat Valenciana, Spain; the Royal Society and Leverhulme Trust, United Kingdom.

The crucial computing support from all WLCG partners is acknowledged gratefully, in particular from CERN, the ATLAS Tier-1 facilities at TRIUMF (Canada), NDGF (Denmark, Norway, Sweden), CC-IN2P3 (France), KIT/GridKA (Germany), INFN-CNAF (Italy), NL-T1 (Netherlands), PIC (Spain), ASGC (Taiwan), RAL (U.K.) and BNL (U.S.A.), the Tier-2 facilities worldwide and large non-WLCG resource providers. Major contributors of computing resources are listed in ref. [35].

JHEP08(2016)147

References

[1] J. Charles et al., *Predictions of selected flavour observables within the standard model*, *Phys. Rev.* **D 84** (2011) 033005 [arXiv:1106.4041] [INSPIRE].

[2] A. Lenz and U. Nierste, *Numerical updates of lifetimes and mixing parameters of B mesons*, arXiv:1102.4274 [INSPIRE].

[3] A. Lenz and U. Nierste, *Theoretical update of B_s-$\bar{B}_s$ mixing*, *JHEP* **06** (2007) 072 [hep-ph/0612167] [INSPIRE].

[4] D0 collaboration, V.M. Abazov et al., *Measurement of the CP-violating phase $\phi_s^{J/\psi\phi}$ using the flavor-tagged decay $B_s^0 \to J/\psi\phi$ in 8 fb^{-1} of $p\bar{p}$ collisions*, *Phys. Rev.* **D 85** (2012) 032006 [arXiv:1109.3166] [INSPIRE].

[5] CDF collaboration, T. Aaltonen et al., *Measurement of the bottom-strange meson mixing phase in the full CDF data set*, *Phys. Rev. Lett.* **109** (2012) 171802 [arXiv:1208.2967] [INSPIRE].

[6] LHCb collaboration, *Measurement of CP-violation and the B_s^0 meson decay width difference with $B_s^0 \to J/\psi K^+K^-$ and $B_s^0 \to J/\psi\pi^+\pi^-$ decays*, *Phys. Rev.* **D 87** (2013) 112010 [arXiv:1304.2600] [INSPIRE].

[7] LHCb collaboration, *Precision measurement of CP violation in $B_s^0 \to J/\psi K^+K^-$ decays*, *Phys. Rev. Lett.* **114** (2015) 041801 [arXiv:1411.3104] [INSPIRE].

[8] ATLAS collaboration, *Flavor tagged time-dependent angular analysis of the $B_s \to J/\psi\phi$ decay and extraction of $\Delta\Gamma_s$ and the weak phase ϕ_s in ATLAS*, *Phys. Rev.* **D 90** (2014) 052007 [arXiv:1407.1796] [INSPIRE].

[9] CMS collaboration, *Measurement of the CP-violating weak phase ϕ_s and the decay width difference $\Delta\Gamma_s$ using the $B_s^0 \to J/\psi\phi(1020)$ decay channel in pp collisions at $\sqrt{s} = 8$ TeV*, *Phys. Lett.* **B 757** (2016) 97 [arXiv:1507.07527] [INSPIRE].

[10] S. Stone and L. Zhang, *S-waves and the measurement of CP-violating phases in B_s decays*, *Phys. Rev.* **D 79** (2009) 074024 [arXiv:0812.2832] [INSPIRE].

[11] ATLAS collaboration, *The ATLAS experiment at the CERN Large Hadron Collider*, 2008 *JINST* **3** S08003 [INSPIRE].

[12] T. Sjöstrand, S. Mrenna and P.Z. Skands, *PYTHIA* 6.4 *physics and manual*, *JHEP* **05** (2006) 026 [hep-ph/0603175] [INSPIRE].

[13] T. Sjöstrand, S. Mrenna and P.Z. Skands, *A brief introduction to PYTHIA* 8.1, *Comput. Phys. Commun.* **178** (2008) 852 [arXiv:0710.3820] [INSPIRE].

[14] ATLAS collaboration, *ATLAS tunes of PYTHIA* 6 *and PYTHIA* 8 *for MC*11, ATL-PHYS-PUB-2011-009, CERN, Geneva Switzerland (2011).

[15] ATLAS collaboration, *The ATLAS simulation infrastructure*, *Eur. Phys. J.* **C 70** (2010) 823 [arXiv:1005.4568] [INSPIRE].

[16] GEANT4 collaboration, S. Agostinelli et al., *GEANT4: a simulation toolkit*, *Nucl. Instrum. Meth.* **A 506** (2003) 250 [INSPIRE].

[17] ATLAS collaboration, *Measurement of the differential cross-sections of inclusive, prompt and non-prompt J/ψ production in proton-proton collisions at $\sqrt{s} = 7$ TeV*, *Nucl. Phys.* **B 850** (2011) 387 [arXiv:1104.3038] [INSPIRE].

[18] Particle Data Group collaboration, K.A. Olive et al., *Review of particle physics*, *Chin. Phys.* **C 38** (2014) 090001 [INSPIRE].

[19] ATLAS collaboration, *ATLAS B-physics studies at increased LHC luminosity, potential for CP-violation measurement in the $B_s^0 \to J/\psi\phi$ decay*, ATL-PHYS-PUB-2013-010, CERN, Geneva Switzerland (2013).

[20] R.D. Field and R.P. Feynman, *A parametrization of the properties of quark jets*, *Nucl. Phys.* **B 136** (1978) 1 [INSPIRE].

[21] ATLAS collaboration, *Jet charge studies with the ATLAS detector using $\sqrt{s} = 8$ TeV proton-proton collision data*, ATLAS-CONF-2013-086, CERN, Geneva Switzerland (2013).

[22] ATLAS collaboration, *Electron performance measurements with the ATLAS detector using the* 2010 *LHC proton-proton collision data*, *Eur. Phys. J.* **C 72** (2012) 1909 [arXiv:1110.3174] [INSPIRE].

[23] ATLAS collaboration, *Calibration of the performance of b-tagging for c and light-flavour jets in the* 2012 *ATLAS data*, ATLAS-CONF-2014-046, CERN, Geneva Switzerland (2014).

[24] M. Cacciari, G.P. Salam and G. Soyez, *The anti-k_t jet clustering algorithm*, *JHEP* **04** (2008) 063 [arXiv:0802.1189] [INSPIRE].

[25] ATLAS collaboration, *Time-dependent angular analysis of the decay $B_s^0 \to J/\psi\phi$ and extraction of $\Delta\Gamma_s$ and the CP-violating weak phase ϕ_s by ATLAS*, *JHEP* **12** (2012) 072 [arXiv:1208.0572] [INSPIRE].

[26] A.S. Dighe, I. Dunietz and R. Fleischer, *Extracting CKM phases and B_s^0-$\bar{B}_s^0$ mixing parameters from angular distributions of nonleptonic B decays*, *Eur. Phys. J.* **C 6** (1999) 647 [hep-ph/9804253] [INSPIRE].

[27] LHCb collaboration, *Updated average f_s/f_d b-hadron production fraction ratio for* 7 *TeV pp collisions*, LHCb-CONF-2013-011, CERN, Geneva Switzerland (2013).

[28] BaBar collaboration, B. Aubert et al., *Search for the $Z(4430)^-$ at BABAR*, *Phys. Rev.* **D 79** (2009) 112001 [arXiv:0811.0564] [INSPIRE].

[29] LHCb collaboration, *Study of the kinematic dependences of Λ_b^0 production in pp collisions and a measurement of the $\Lambda_b^0 \to \Lambda_c^+\pi^-$ branching fraction*, *JHEP* **08** (2014) 143 [arXiv:1405.6842] [INSPIRE].

JHEP08(2016)147

[30] LHCb collaboration, *Study of the production of Λ_b^0 and $\overline{B}^0$ hadrons in pp collisions and first measurement of the $\Lambda_b^0 \to J/\psi p K^-$ branching fraction*, *Chin. Phys.* **C 40** (2016) 011001 [arXiv:1509.00292] [INSPIRE].

[31] LHCb collaboration, *Observation of $J/\psi p$ resonances consistent with pentaquark states in $\Lambda_b^0 \to J/\psi K^- p$ decays*, *Phys. Rev. Lett.* **115** (2015) 072001 [arXiv:1507.03414] [INSPIRE].

[32] LHCb collaboration, *Measurement of the polarization amplitudes in $B^0 \to J/\psi K^*(892)^0$ decays*, *Phys. Rev.* **D 88** (2013) 052002 [arXiv:1307.2782] [INSPIRE].

[33] LHCb collaboration, *Determination of the sign of the decay width difference in the B_s system*, *Phys. Rev. Lett.* **108** (2012) 241801 [arXiv:1202.4717] [INSPIRE].

[34] R. Nisius, *On the combination of correlated estimates of a physics observable*, *Eur. Phys. J.* **C 74** (2014) 3004 [arXiv:1402.4016] [INSPIRE].

[35] ATLAS collaboration, *ATLAS computing acknowledgements* 2016–2017, ATL-GEN-PUB-2016-002, CERN, Geneva Switzerland (2016).

JHEP08(2016)147

The ATLAS collaboration

G. Aad[85], B. Abbott[113], J. Abdallah[151], O. Abdinov[11], R. Aben[107], M. Abolins[90], O.S. AbouZeid[158], H. Abramowicz[153], H. Abreu[152], R. Abreu[116], Y. Abulaiti[146a,146b], B.S. Acharya[164a,164b,a], L. Adamczyk[38a], D.L. Adams[25], J. Adelman[108], S. Adomeit[100], T. Adye[131], A.A. Affolder[74], T. Agatonovic-Jovin[13], J. Agricola[54], J.A. Aguilar-Saavedra[126a,126f], S.P. Ahlen[22], F. Ahmadov[65,b], G. Aielli[133a,133b], H. Akerstedt[146a,146b], T.P.A. Åkesson[81], A.V. Akimov[96], G.L. Alberghi[20a,20b], J. Albert[169], S. Albrand[55], M.J. Alconada Verzini[71], M. Aleksa[30], I.N. Aleksandrov[65], C. Alexa[26a], G. Alexander[153], T. Alexopoulos[10], M. Alhroob[113], G. Alimonti[91a], L. Alio[85], J. Alison[31], S.P. Alkire[35], B.M.M. Allbrooke[149], P.P. Allport[74], A. Aloisio[104a,104b], A. Alonso[36], F. Alonso[71], C. Alpigiani[76], A. Altheimer[35], B. Alvarez Gonzalez[30], D. Álvarez Piqueras[167], M.G. Alviggi[104a,104b], B.T. Amadio[15], K. Amako[66], Y. Amaral Coutinho[24a], C. Amelung[23], D. Amidei[89], S.P. Amor Dos Santos[126a,126c], A. Amorim[126a,126b], S. Amoroso[48], N. Amram[153], G. Amundsen[23], C. Anastopoulos[139], L.S. Ancu[49], N. Andari[108], T. Andeen[35], C.F. Anders[58b], G. Anders[30], J.K. Anders[74], K.J. Anderson[31], A. Andreazza[91a,91b], V. Andrei[58a], S. Angelidakis[9], I. Angelozzi[107], P. Anger[44], A. Angerami[35], F. Anghinolfi[30], A.V. Anisenkov[109,c], N. Anjos[12], A. Annovi[124a,124b], M. Antonelli[47], A. Antonov[98], J. Antos[144b], F. Anulli[132a], M. Aoki[66], L. Aperio Bella[18], G. Arabidze[90], Y. Arai[66], J.P. Araque[126a], A.T.H. Arce[45], F.A. Arduh[71], J-F. Arguin[95], S. Argyropoulos[42], M. Arik[19a], A.J. Armbruster[30], O. Arnaez[30], V. Arnal[82], H. Arnold[48], M. Arratia[28], O. Arslan[21], A. Artamonov[97], G. Artoni[23], S. Asai[155], N. Asbah[42], A. Ashkenazi[153], B. Åsman[146a,146b], L. Asquith[149], K. Assamagan[25], R. Astalos[144a], M. Atkinson[165], N.B. Atlay[141], K. Augsten[128], M. Aurousseau[145b], G. Avolio[30], B. Axen[15], M.K. Ayoub[117], G. Azuelos[95,d], M.A. Baak[30], A.E. Baas[58a], M.J. Baca[18], C. Bacci[134a,134b], H. Bachacou[136], K. Bachas[154], M. Backes[30], M. Backhaus[30], P. Bagiacchi[132a,132b], P. Bagnaia[132a,132b], Y. Bai[33a], T. Bain[35], J.T. Baines[131], O.K. Baker[176], E.M. Baldin[109,c], P. Balek[129], T. Balestri[148], F. Balli[84], E. Banas[39], Sw. Banerjee[173], A.A.E. Bannoura[175], H.S. Bansil[18], L. Barak[30], E.L. Barberio[88], D. Barberis[50a,50b], M. Barbero[85], T. Barillari[101], M. Barisonzi[164a,164b], T. Barklow[143], N. Barlow[28], S.L. Barnes[84], B.M. Barnett[131], R.M. Barnett[15], Z. Barnovska[5], A. Baroncelli[134a], G. Barone[23], A.J. Barr[120], F. Barreiro[82], J. Barreiro Guimarães da Costa[57], R. Bartoldus[143], A.E. Barton[72], P. Bartos[144a], A. Basalaev[123], A. Bassalat[117], A. Basye[165], R.L. Bates[53], S.J. Batista[158], J.R. Batley[28], M. Battaglia[137], M. Bauce[132a,132b], F. Bauer[136], H.S. Bawa[143,e], J.B. Beacham[111], M.D. Beattie[72], T. Beau[80], P.H. Beauchemin[161], R. Beccherle[124a,124b], P. Bechtle[21], H.P. Beck[17,f], K. Becker[120], M. Becker[83], S. Becker[100], M. Beckingham[170], C. Becot[117], A.J. Beddall[19b], A. Beddall[19b], V.A. Bednyakov[65], C.P. Bee[148], L.J. Beemster[107], T.A. Beermann[175], M. Begel[25], J.K. Behr[120], C. Belanger-Champagne[87], W.H. Bell[49], G. Bella[153], L. Bellagamba[20a], A. Bellerive[29], M. Bellomo[86], K. Belotskiy[98], O. Beltramello[30], O. Benary[153], D. Benchekroun[135a], M. Bender[100], K. Bendtz[146a,146b], N. Benekos[10], Y. Benhammou[153], E. Benhar Noccioli[49], J.A. Benitez Garcia[159b], D.P. Benjamin[45], J.R. Bensinger[23], S. Bentvelsen[107], L. Beresford[120], M. Beretta[47], D. Berge[107], E. Bergeaas Kuutmann[166], N. Berger[5], F. Berghaus[169], J. Beringer[15], C. Bernard[22], N.R. Bernard[86], C. Bernius[110], F.U. Bernlochner[21], T. Berry[77], P. Berta[129], C. Bertella[83], G. Bertoli[146a,146b], F. Bertolucci[124a,124b], C. Bertsche[113], D. Bertsche[113], M.I. Besana[91a], G.J. Besjes[36], O. Bessidskaia Bylund[146a,146b], M. Bessner[42], N. Besson[136], C. Betancourt[48], S. Bethke[101], A.J. Bevan[76], W. Bhimji[15], R.M. Bianchi[125], L. Bianchini[23], M. Bianco[30], O. Biebel[100], D. Biedermann[16], S.P. Bieniek[78], M. Biglietti[134a], J. Bilbao De Mendizabal[49], H. Bilokon[47], M. Bindi[54], S. Binet[117], A. Bingul[19b], C. Bini[132a,132b], S. Biondi[20a,20b], C.W. Black[150], J.E. Black[143], K.M. Black[22], D. Blackburn[138], R.E. Blair[6], J.-B. Blanchard[136],

JHEP08(2016)147

J.E. Blanco[77], T. Blazek[144a], I. Bloch[42], C. Blocker[23], W. Blum[83,*], U. Blumenschein[54], G.J. Bobbink[107], V.S. Bobrovnikov[109,c], S.S. Bocchetta[81], A. Bocci[45], C. Bock[100], M. Boehler[48], J.A. Bogaerts[30], D. Bogavac[13], A.G. Bogdanchikov[109], C. Bohm[146a], V. Boisvert[77], T. Bold[38a], V. Boldea[26a], A.S. Boldyrev[99], M. Bomben[80], M. Bona[76], M. Boonekamp[136], A. Borisov[130], G. Borissov[72], S. Borroni[42], J. Bortfeldt[100], V. Bortolotto[60a,60b,60c], K. Bos[107], D. Boscherini[20a], M. Bosman[12], J. Boudreau[125], J. Bouffard[2], E.V. Bouhova-Thacker[72], D. Boumediene[34], C. Bourdarios[117], N. Bousson[114], A. Boveia[30], J. Boyd[30], I.R. Boyko[65], I. Bozic[13], J. Bracinik[18], A. Brandt[8], G. Brandt[54], O. Brandt[58a], U. Bratzler[156], B. Brau[86], J.E. Brau[116], H.M. Braun[175,*], S.F. Brazzale[164a,164c], W.D. Breaden Madden[53], K. Brendlinger[122], A.J. Brennan[88], L. Brenner[107], R. Brenner[166], S. Bressler[172], K. Bristow[145c], T.M. Bristow[46], D. Britton[53], D. Britzger[42], F.M. Brochu[28], I. Brock[21], R. Brock[90], J. Bronner[101], G. Brooijmans[35], T. Brooks[77], W.K. Brooks[32b], J. Brosamer[15], E. Brost[116], J. Brown[55], P.A. Bruckman de Renstrom[39], D. Bruncko[144b], R. Bruneliere[48], A. Bruni[20a], G. Bruni[20a], M. Bruschi[20a], N. Bruscino[21], L. Bryngemark[81], T. Buanes[14], Q. Buat[142], P. Buchholz[141], A.G. Buckley[53], S.I. Buda[26a], I.A. Budagov[65], F. Buehrer[48], L. Bugge[119], M.K. Bugge[119], O. Bulekov[98], D. Bullock[8], H. Burckhart[30], S. Burdin[74], B. Burghgrave[108], S. Burke[131], I. Burmeister[43], E. Busato[34], D. Büscher[48], V. Büscher[83], P. Bussey[53], J.M. Butler[22], A.I. Butt[3], C.M. Buttar[53], J.M. Butterworth[78], P. Butti[107], W. Buttinger[25], A. Buzatu[53], A.R. Buzykaev[109,c], S. Cabrera Urbán[167], D. Caforio[128], V.M. Cairo[37a,37b], O. Cakir[4a], N. Calace[49], P. Calafiura[15], A. Calandri[136], G. Calderini[80], P. Calfayan[100], L.P. Caloba[24a], D. Calvet[34], S. Calvet[34], R. Camacho Toro[31], S. Camarda[42], P. Camarri[133a,133b], D. Cameron[119], R. Caminal Armadans[165], S. Campana[30], M. Campanelli[78], A. Campoverde[148], V. Canale[104a,104b], A. Canepa[159a], M. Cano Bret[33e], J. Cantero[82], R. Cantrill[126a], T. Cao[40], M.D.M. Capeans Garrido[30], I. Caprini[26a], M. Caprini[26a], M. Capua[37a,37b], R. Caputo[83], R. Cardarelli[133a], F. Cardillo[48], T. Carli[30], G. Carlino[104a], L. Carminati[91a,91b], S. Caron[106], E. Carquin[32a], G.D. Carrillo-Montoya[8], J.R. Carter[28], J. Carvalho[126a,126c], D. Casadei[78], M.P. Casado[12], M. Casolino[12], E. Castaneda-Miranda[145b], A. Castelli[107], V. Castillo Gimenez[167], N.F. Castro[126a,g], P. Catastini[57], A. Catinaccio[30], J.R. Catmore[119], A. Cattai[30], J. Caudron[83], V. Cavaliere[165], D. Cavalli[91a], M. Cavalli-Sforza[12], V. Cavasinni[124a,124b], F. Ceradini[134a,134b], B.C. Cerio[45], K. Cerny[129], A.S. Cerqueira[24b], A. Cerri[149], L. Cerrito[76], F. Cerutti[15], M. Cerv[30], A. Cervelli[17], S.A. Cetin[19c], A. Chafaq[135a], D. Chakraborty[108], I. Chalupkova[129], P. Chang[165], J.D. Chapman[28], D.G. Charlton[18], C.C. Chau[158], C.A. Chavez Barajas[149], S. Cheatham[152], A. Chegwidden[90], S. Chekanov[6], S.V. Chekulaev[159a], G.A. Chelkov[65,h], M.A. Chelstowska[89], C. Chen[64], H. Chen[25], K. Chen[148], L. Chen[33d,i], S. Chen[33c], X. Chen[33f], Y. Chen[67], H.C. Cheng[89], Y. Cheng[31], A. Cheplakov[65], E. Cheremushkina[130], R. Cherkaoui El Moursli[135e], V. Chernyatin[25,*], E. Cheu[7], L. Chevalier[136], V. Chiarella[47], G. Chiarelli[124a,124b], J.T. Childers[6], G. Chiodini[73a], A.S. Chisholm[18], R.T. Chislett[78], A. Chitan[26a], M.V. Chizhov[65], K. Choi[61], S. Chouridou[9], B.K.B. Chow[100], V. Christodoulou[78], D. Chromek-Burckhart[30], J. Chudoba[127], A.J. Chuinard[87], J.J. Chwastowski[39], L. Chytka[115], G. Ciapetti[132a,132b], A.K. Ciftci[4a], D. Cinca[53], V. Cindro[75], I.A. Cioara[21], A. Ciocio[15], Z.H. Citron[172], M. Ciubancan[26a], A. Clark[49], B.L. Clark[57], P.J. Clark[46], R.N. Clarke[15], W. Cleland[125], C. Clement[146a,146b], Y. Coadou[85], M. Cobal[164a,164c], A. Coccaro[49], J. Cochran[64], L. Coffey[23], J.G. Cogan[143], L. Colasurdo[106], B. Cole[35], S. Cole[108], A.P. Colijn[107], J. Collot[55], T. Colombo[58c], G. Compostella[101], P. Conde Muiño[126a,126b], E. Coniavitis[48], S.H. Connell[145b], I.A. Connelly[77], S.M. Consonni[91a,91b], V. Consorti[48], S. Constantinescu[26a], C. Conta[121a,121b], G. Conti[30], F. Conventi[104a,j], M. Cooke[15], B.D. Cooper[78], A.M. Cooper-Sarkar[120], T. Cornelissen[175], M. Corradi[20a], F. Corriveau[87,k], A. Corso-Radu[163], A. Cortes-Gonzalez[12], G. Cortiana[101], G. Costa[91a], M.J. Costa[167], D. Costanzo[139], D. Côté[8], G. Cottin[28], G. Cowan[77], B.E. Cox[84], K. Cranmer[110], G. Cree[29],

JHEP08(2016)147

S. Crépé-Renaudin[55], F. Crescioli[80], W.A. Cribbs[146a,146b], M. Crispin Ortuzar[120], M. Cristinziani[21], V. Croft[106], G. Crosetti[37a,37b], T. Cuhadar Donszelmann[139], J. Cummings[176], M. Curatolo[47], C. Cuthbert[150], H. Czirr[141], P. Czodrowski[3], S. D'Auria[53], M. D'Onofrio[74], M.J. Da Cunha Sargedas De Sousa[126a,126b], C. Da Via[84], W. Dabrowski[38a], A. Dafinca[120], T. Dai[89], O. Dale[14], F. Dallaire[95], C. Dallapiccola[86], M. Dam[36], J.R. Dandoy[31], N.P. Dang[48], A.C. Daniells[18], M. Danninger[168], M. Dano Hoffmann[136], V. Dao[48], G. Darbo[50a], S. Darmora[8], J. Dassoulas[3], A. Dattagupta[61], W. Davey[21], C. David[169], T. Davidek[129], E. Davies[120,l], M. Davies[153], P. Davison[78], Y. Davygora[58a], E. Dawe[88], I. Dawson[139], R.K. Daya-Ishmukhametova[86], K. De[8], R. de Asmundis[104a], A. De Benedetti[113], S. De Castro[20a,20b], S. De Cecco[80], N. De Groot[106], P. de Jong[107], H. De la Torre[82], F. De Lorenzi[64], L. De Nooij[107], D. De Pedis[132a], A. De Salvo[132a], U. De Sanctis[149], A. De Santo[149], J.B. De Vivie De Regie[117], W.J. Dearnaley[72], R. Debbe[25], C. Debenedetti[137], D.V. Dedovich[65], I. Deigaard[107], J. Del Peso[82], T. Del Prete[124a,124b], D. Delgove[117], F. Deliot[136], C.M. Delitzsch[49], M. Deliyergiyev[75], A. Dell'Acqua[30], L. Dell'Asta[22], M. Dell'Orso[124a,124b], M. Della Pietra[104a,j], D. della Volpe[49], M. Delmastro[5], P.A. Delsart[55], C. Deluca[107], D.A. DeMarco[158], S. Demers[176], M. Demichev[65], A. Demilly[80], S.P. Denisov[130], D. Derendarz[39], J.E. Derkaoui[135d], F. Derue[80], P. Dervan[74], K. Desch[21], C. Deterre[42], P.O. Deviveiros[30], A. Dewhurst[131], S. Dhaliwal[23], A. Di Ciaccio[133a,133b], L. Di Ciaccio[5], A. Di Domenico[132a,132b], C. Di Donato[104a,104b], A. Di Girolamo[30], B. Di Girolamo[30], A. Di Mattia[152], B. Di Micco[134a,134b], R. Di Nardo[47], A. Di Simone[48], R. Di Sipio[158], D. Di Valentino[29], C. Diaconu[85], M. Diamond[158], F.A. Dias[46], M.A. Diaz[32a], E.B. Diehl[89], J. Dietrich[16], S. Diglio[85], A. Dimitrievska[13], J. Dingfelder[21], P. Dita[26a], S. Dita[26a], F. Dittus[30], F. Djama[85], T. Djobava[51b], J.I. Djuvsland[58a], M.A.B. do Vale[24c], D. Dobos[30], M. Dobre[26a], C. Doglioni[81], T. Dohmae[155], J. Dolejsi[129], Z. Dolezal[129], B.A. Dolgoshein[98,*], M. Donadelli[24d], S. Donati[124a,124b], P. Dondero[121a,121b], J. Donini[34], J. Dopke[131], A. Doria[104a], M.T. Dova[71], A.T. Doyle[53], E. Drechsler[54], M. Dris[10], E. Dubreuil[34], E. Duchovni[172], G. Duckeck[100], O.A. Ducu[26a,85], D. Duda[107], A. Dudarev[30], L. Duflot[117], L. Duguid[77], M. Dührssen[30], M. Dunford[58a], H. Duran Yildiz[4a], M. Düren[52], A. Durglishvili[51b], D. Duschinger[44], M. Dyndal[38a], C. Eckardt[42], K.M. Ecker[101], R.C. Edgar[89], W. Edson[2], N.C. Edwards[46], W. Ehrenfeld[21], T. Eifert[30], G. Eigen[14], K. Einsweiler[15], T. Ekelof[166], M. El Kacimi[135c], M. Ellert[166], S. Elles[5], F. Ellinghaus[175], A.A. Elliot[169], N. Ellis[30], J. Elmsheuser[100], M. Elsing[30], D. Emeliyanov[131], Y. Enari[155], O.C. Endner[83], M. Endo[118], J. Erdmann[43], A. Ereditato[17], G. Ernis[175], J. Ernst[2], M. Ernst[25], S. Errede[165], E. Ertel[83], M. Escalier[117], H. Esch[43], C. Escobar[125], B. Esposito[47], A.I. Etienvre[136], E. Etzion[153], H. Evans[61], A. Ezhilov[123], L. Fabbri[20a,20b], G. Facini[31], R.M. Fakhrutdinov[130], S. Falciano[132a], R.J. Falla[78], J. Faltova[129], Y. Fang[33a], M. Fanti[91a,91b], A. Farbin[8], A. Farilla[134a], T. Farooque[12], S. Farrell[15], S.M. Farrington[170], P. Farthouat[30], F. Fassi[135e], P. Fassnacht[30], D. Fassouliotis[9], M. Faucci Giannelli[77], A. Favareto[50a,50b], L. Fayard[117], P. Federic[144a], O.L. Fedin[123,m], W. Fedorko[168], S. Feigl[30], L. Feligioni[85], C. Feng[33d], E.J. Feng[6], H. Feng[89], A.B. Fenyuk[130], L. Feremenga[8], P. Fernandez Martinez[167], S. Fernandez Perez[30], J. Ferrando[53], A. Ferrari[166], P. Ferrari[107], R. Ferrari[121a], D.E. Ferreira de Lima[53], A. Ferrer[167], D. Ferrere[49], C. Ferretti[89], A. Ferretto Parodi[50a,50b], M. Fiascaris[31], F. Fiedler[83], A. Filipčič[75], M. Filipuzzi[42], F. Filthaut[106], M. Fincke-Keeler[169], K.D. Finelli[150], M.C.N. Fiolhais[126a,126c], L. Fiorini[167], A. Firan[40], A. Fischer[2], C. Fischer[12], J. Fischer[175], W.C. Fisher[90], E.A. Fitzgerald[23], N. Flaschel[42], I. Fleck[141], P. Fleischmann[89], S. Fleischmann[175], G.T. Fletcher[139], G. Fletcher[76], R.R.M. Fletcher[122], T. Flick[175], A. Floderus[81], L.R. Flores Castillo[60a], M.J. Flowerdew[101], A. Formica[136], A. Forti[84], D. Fournier[117], H. Fox[72], S. Fracchia[12], P. Francavilla[80], M. Franchini[20a,20b], D. Francis[30], L. Franconi[119], M. Franklin[57], M. Frate[163], M. Fraternali[121a,121b], D. Freeborn[78], S.T. French[28], F. Friedrich[44], D. Froidevaux[30],

JHEP08(2016)147

J.A. Frost[120], C. Fukunaga[156], E. Fullana Torregrosa[83], B.G. Fulsom[143], T. Fusayasu[102], J. Fuster[167], C. Gabaldon[55], O. Gabizon[175], A. Gabrielli[20a,20b], A. Gabrielli[132a,132b], G.P. Gach[38a], S. Gadatsch[107], S. Gadomski[49], G. Gagliardi[50a,50b], P. Gagnon[61], C. Galea[106], B. Galhardo[126a,126c], E.J. Gallas[120], B.J. Gallop[131], P. Gallus[128], G. Galster[36], K.K. Gan[111], J. Gao[33b,85], Y. Gao[46], Y.S. Gao[143,e], F.M. Garay Walls[46], F. Garberson[176], C. García[167], J.E. García Navarro[167], M. Garcia-Sciveres[15], R.W. Gardner[31], N. Garelli[143], V. Garonne[119], C. Gatti[47], A. Gaudiello[50a,50b], G. Gaudio[121a], B. Gaur[141], L. Gauthier[95], P. Gauzzi[132a,132b], I.L. Gavrilenko[96], C. Gay[168], G. Gaycken[21], E.N. Gazis[10], P. Ge[33d], Z. Gecse[168], C.N.P. Gee[131], D.A.A. Geerts[107], Ch. Geich-Gimbel[21], M.P. Geisler[58a], C. Gemme[50a], M.H. Genest[55], S. Gentile[132a,132b], M. George[54], S. George[77], D. Gerbaudo[163], A. Gershon[153], S. Ghasemi[141], H. Ghazlane[135b], B. Giacobbe[20a], S. Giagu[132a,132b], V. Giangiobbe[12], P. Giannetti[124a,124b], B. Gibbard[25], S.M. Gibson[77], M. Gilchriese[15], T.P.S. Gillam[28], D. Gillberg[30], G. Gilles[34], D.M. Gingrich[3,d], N. Giokaris[9], M.P. Giordani[164a,164c], F.M. Giorgi[20a], F.M. Giorgi[16], P.F. Giraud[136], P. Giromini[47], D. Giugni[91a], C. Giuliani[48], M. Giulini[58b], B.K. Gjelsten[119], S. Gkaitatzis[154], I. Gkialas[154], E.L. Gkougkousis[117], L.K. Gladilin[99], C. Glasman[82], J. Glatzer[30], P.C.F. Glaysher[46], A. Glazov[42], M. Goblirsch-Kolb[101], J.R. Goddard[76], J. Godlewski[39], S. Goldfarb[89], T. Golling[49], D. Golubkov[130], A. Gomes[126a,126b,126d], R. Gonçalo[126a], J. Goncalves Pinto Firmino Da Costa[136], L. Gonella[21], S. González de la Hoz[167], G. Gonzalez Parra[12], S. Gonzalez-Sevilla[49], L. Goossens[30], P.A. Gorbounov[97], H.A. Gordon[25], I. Gorelov[105], B. Gorini[30], E. Gorini[73a,73b], A. Gorišek[75], E. Gornicki[39], A.T. Goshaw[45], C. Gössling[43], M.I. Gostkin[65], D. Goujdami[135c], A.G. Goussiou[138], N. Govender[145b], E. Gozani[152], H.M.X. Grabas[137], L. Graber[54], I. Grabowska-Bold[38a], P.O.J. Gradin[166], P. Grafström[20a,20b], K-J. Grahn[42], J. Gramling[49], E. Gramstad[119], S. Grancagnolo[16], V. Grassi[148], V. Gratchev[123], H.M. Gray[30], E. Graziani[134a], Z.D. Greenwood[79,n], K. Gregersen[78], I.M. Gregor[42], P. Grenier[143], J. Griffiths[8], A.A. Grillo[137], K. Grimm[72], S. Grinstein[12,o], Ph. Gris[34], J.-F. Grivaz[117], J.P. Grohs[44], A. Grohsjean[42], E. Gross[172], J. Grosse-Knetter[54], G.C. Grossi[79], Z.J. Grout[149], L. Guan[89], J. Guenther[128], F. Guescini[49], D. Guest[176], O. Gueta[153], E. Guido[50a,50b], T. Guillemin[117], S. Guindon[2], U. Gul[53], C. Gumpert[44], J. Guo[33e], Y. Guo[33b], S. Gupta[120], G. Gustavino[132a,132b], P. Gutierrez[113], N.G. Gutierrez Ortiz[78], C. Gutschow[44], C. Guyot[136], C. Gwenlan[120], C.B. Gwilliam[74], A. Haas[110], C. Haber[15], H.K. Hadavand[8], N. Haddad[135e], P. Haefner[21], S. Hageböck[21], Z. Hajduk[39], H. Hakobyan[177], M. Haleem[42], J. Haley[114], D. Hall[120], G. Halladjian[90], G.D. Hallewell[85], K. Hamacher[175], P. Hamal[115], K. Hamano[169], M. Hamer[54], A. Hamilton[145a], G.N. Hamity[145c], P.G. Hamnett[42], L. Han[33b], K. Hanagaki[66,p], K. Hanawa[155], M. Hance[15], P. Hanke[58a], R. Hanna[136], J.B. Hansen[36], J.D. Hansen[36], M.C. Hansen[21], P.H. Hansen[36], K. Hara[160], A.S. Hard[173], T. Harenberg[175], F. Hariri[117], S. Harkusha[92], R.D. Harrington[46], P.F. Harrison[170], F. Hartjes[107], M. Hasegawa[67], S. Hasegawa[103], Y. Hasegawa[140], A. Hasib[113], S. Hassani[136], S. Haug[17], R. Hauser[90], L. Hauswald[44], M. Havranek[127], C.M. Hawkes[18], R.J. Hawkings[30], A.D. Hawkins[81], T. Hayashi[160], D. Hayden[90], C.P. Hays[120], J.M. Hays[76], H.S. Hayward[74], S.J. Haywood[131], S.J. Head[18], T. Heck[83], V. Hedberg[81], L. Heelan[8], S. Heim[122], T. Heim[175], B. Heinemann[15], L. Heinrich[110], J. Hejbal[127], L. Helary[22], S. Hellman[146a,146b], D. Hellmich[21], C. Helsens[12], J. Henderson[120], R.C.W. Henderson[72], Y. Heng[173], C. Hengler[42], S. Henkelmann[168], A. Henrichs[176], A.M. Henriques Correia[30], S. Henrot-Versille[117], G.H. Herbert[16], Y. Hernández Jiménez[167], R. Herrberg-Schubert[16], G. Herten[48], R. Hertenberger[100], L. Hervas[30], G.G. Hesketh[78], N.P. Hessey[107], J.W. Hetherly[40], R. Hickling[76], E. Higón-Rodriguez[167], E. Hill[169], J.C. Hill[28], K.H. Hiller[42], S.J. Hillier[18], I. Hinchliffe[15], E. Hines[122], R.R. Hinman[15], M. Hirose[157], D. Hirschbuehl[175], J. Hobbs[148], N. Hod[107], M.C. Hodgkinson[139], P. Hodgson[139], A. Hoecker[30], M.R. Hoeferkamp[105], F. Hoenig[100], M. Hohlfeld[83], D. Hohn[21], T.R. Holmes[15],

JHEP08(2016)147

M. Homann[43], T.M. Hong[125], L. Hooft van Huysduynen[110], W.H. Hopkins[116], Y. Horii[103], A.J. Horton[142], J-Y. Hostachy[55], S. Hou[151], A. Hoummada[135a], J. Howard[120], J. Howarth[42], M. Hrabovsky[115], I. Hristova[16], J. Hrivnac[117], T. Hryn'ova[5], A. Hrynevich[93], C. Hsu[145c], P.J. Hsu[151,q], S.-C. Hsu[138], D. Hu[35], Q. Hu[33b], X. Hu[89], Y. Huang[42], Z. Hubacek[128], F. Hubaut[85], F. Huegging[21], T.B. Huffman[120], E.W. Hughes[35], G. Hughes[72], M. Huhtinen[30], T.A. Hülsing[83], N. Huseynov[65,b], J. Huston[90], J. Huth[57], G. Iacobucci[49], G. Iakovidis[25], I. Ibragimov[141], L. Iconomidou-Fayard[117], E. Ideal[176], Z. Idrissi[135e], P. Iengo[30], O. Igonkina[107], T. Iizawa[171], Y. Ikegami[66], K. Ikematsu[141], M. Ikeno[66], Y. Ilchenko[31,r], D. Iliadis[154], N. Ilic[143], T. Ince[101], G. Introzzi[121a,121b], P. Ioannou[9], M. Iodice[134a], K. Iordanidou[35], V. Ippolito[57], A. Irles Quiles[167], C. Isaksson[166], M. Ishino[68], M. Ishitsuka[157], R. Ishmukhametov[111], C. Issever[120], S. Istin[19a], J.M. Iturbe Ponce[84], R. Iuppa[133a,133b], J. Ivarsson[81], W. Iwanski[39], H. Iwasaki[66], J.M. Izen[41], V. Izzo[104a], S. Jabbar[3], B. Jackson[122], M. Jackson[74], P. Jackson[1], M.R. Jaekel[30], V. Jain[2], K. Jakobs[48], S. Jakobsen[30], T. Jakoubek[127], J. Jakubek[128], D.O. Jamin[114], D.K. Jana[79], E. Jansen[78], R. Jansky[62], J. Janssen[21], M. Janus[170], G. Jarlskog[81], N. Javadov[65,b], T. Javůrek[48], L. Jeanty[15], J. Jejelava[51a,s], G.-Y. Jeng[150], D. Jennens[88], P. Jenni[48,t], J. Jentzsch[43], C. Jeske[170], S. Jézéquel[5], H. Ji[173], J. Jia[148], Y. Jiang[33b], S. Jiggins[78], J. Jimenez Pena[167], S. Jin[33a], A. Jinaru[26a], O. Jinnouchi[157], M.D. Joergensen[36], P. Johansson[139], K.A. Johns[7], K. Jon-And[146a,146b], G. Jones[170], R.W.L. Jones[72], T.J. Jones[74], J. Jongmanns[58a], P.M. Jorge[126a,126b], K.D. Joshi[84], J. Jovicevic[159a], X. Ju[173], C.A. Jung[43], P. Jussel[62], A. Juste Rozas[12,o], M. Kaci[167], A. Kaczmarska[39], M. Kado[117], H. Kagan[111], M. Kagan[143], S.J. Kahn[85], E. Kajomovitz[45], C.W. Kalderon[120], S. Kama[40], A. Kamenshchikov[130], N. Kanaya[155], S. Kaneti[28], V.A. Kantserov[98], J. Kanzaki[66], B. Kaplan[110], L.S. Kaplan[173], A. Kapliy[31], D. Kar[53], K. Karakostas[10], A. Karamaoun[3], N. Karastathis[10,107], M.J. Kareem[54], E. Karentzos[10], M. Karnevskiy[83], S.N. Karpov[65], Z.M. Karpova[65], K. Karthik[110], V. Kartvelishvili[72], A.N. Karyukhin[130], L. Kashif[173], R.D. Kass[111], A. Kastanas[14], Y. Kataoka[155], C. Kato[155], A. Katre[49], J. Katzy[42], K. Kawagoe[70], T. Kawamoto[155], G. Kawamura[54], S. Kazama[155], V.F. Kazanin[109,c], R. Keeler[169], R. Kehoe[40], J.S. Keller[42], J.J. Kempster[77], H. Keoshkerian[84], O. Kepka[127], B.P. Kerševan[75], S. Kersten[175], R.A. Keyes[87], F. Khalil-zada[11], H. Khandanyan[146a,146b], A. Khanov[114], A.G. Kharlamov[109,c], T.J. Khoo[28], V. Khovanskiy[97], E. Khramov[65], J. Khubua[51b,u], H.Y. Kim[8], H. Kim[146a,146b], S.H. Kim[160], Y.K. Kim[31], N. Kimura[154], O.M. Kind[16], B.T. King[74], M. King[167], S.B. King[168], J. Kirk[131], A.E. Kiryunin[101], T. Kishimoto[67], D. Kisielewska[38a], F. Kiss[48], K. Kiuchi[160], O. Kivernyk[136], E. Kladiva[144b], M.H. Klein[35], M. Klein[74], U. Klein[74], K. Kleinknecht[83], P. Klimek[146a,146b], A. Klimentov[25], R. Klingenberg[43], J.A. Klinger[139], T. Klioutchnikova[30], E.-E. Kluge[58a], P. Kluit[107], S. Kluth[101], J. Knapik[39], E. Kneringer[62], E.B.F.G. Knoops[85], A. Knue[53], A. Kobayashi[155], D. Kobayashi[157], T. Kobayashi[155], M. Kobel[44], M. Kocian[143], P. Kodys[129], T. Koffas[29], E. Koffeman[107], L.A. Kogan[120], S. Kohlmann[175], Z. Kohout[128], T. Kohriki[66], T. Koi[143], H. Kolanoski[16], I. Koletsou[5], A.A. Komar[96,*], Y. Komori[155], T. Kondo[66], N. Kondrashova[42], K. Köneke[48], A.C. König[106], T. Kono[66], R. Konoplich[110,v], N. Konstantinidis[78], R. Kopeliansky[152], S. Koperny[38a], L. Köpke[83], A.K. Kopp[48], K. Korcyl[39], K. Kordas[154], A. Korn[78], A.A. Korol[109,c], I. Korolkov[12], E.V. Korolkova[139], O. Kortner[101], S. Kortner[101], T. Kosek[129], V.V. Kostyukhin[21], V.M. Kotov[65], A. Kotwal[45], A. Kourkoumeli-Charalampidi[154], C. Kourkoumelis[9], V. Kouskoura[25], A. Koutsman[159a], R. Kowalewski[169], T.Z. Kowalski[38a], W. Kozanecki[136], A.S. Kozhin[130], V.A. Kramarenko[99], G. Kramberger[75], D. Krasnopevtsev[98], M.W. Krasny[80], A. Krasznahorkay[30], J.K. Kraus[21], A. Kravchenko[25], S. Kreiss[110], M. Kretz[58c], J. Kretzschmar[74], K. Kreutzfeldt[52], P. Krieger[158], K. Krizka[31], K. Kroeninger[43], H. Kroha[101], J. Kroll[122], J. Kroseberg[21], J. Krstic[13], U. Kruchonak[65], H. Krüger[21], N. Krumnack[64], A. Kruse[173], M.C. Kruse[45], M. Kruskal[22], T. Kubota[88], H. Kucuk[78], S. Kuday[4b], S. Kuehn[48], A. Kugel[58c],

JHEP08(2016)147

F. Kuger[174], A. Kuhl[137], T. Kuhl[42], V. Kukhtin[65], Y. Kulchitsky[92], S. Kuleshov[32b], M. Kuna[132a,132b], T. Kunigo[68], A. Kupco[127], H. Kurashige[67], Y.A. Kurochkin[92], V. Kus[127], E.S. Kuwertz[169], M. Kuze[157], J. Kvita[115], T. Kwan[169], D. Kyriazopoulos[139], A. La Rosa[137], J.L. La Rosa Navarro[24d], L. La Rotonda[37a,37b], C. Lacasta[167], F. Lacava[132a,132b], J. Lacey[29], H. Lacker[16], D. Lacour[80], V.R. Lacuesta[167], E. Ladygin[65], R. Lafaye[5], B. Laforge[80], T. Lagouri[176], S. Lai[54], L. Lambourne[78], S. Lammers[61], C.L. Lampen[7], W. Lampl[7], E. Lançon[136], U. Landgraf[48], M.P.J. Landon[76], V.S. Lang[58a], J.C. Lange[12], A.J. Lankford[163], F. Lanni[25], K. Lantzsch[21], A. Lanza[121a], S. Laplace[80], C. Lapoire[30], J.F. Laporte[136], T. Lari[91a], F. Lasagni Manghi[20a,20b], M. Lassnig[30], P. Laurelli[47], W. Lavrijsen[15], A.T. Law[137], P. Laycock[74], T. Lazovich[57], O. Le Dortz[80], E. Le Guirriec[85], E. Le Menedeu[12], M. LeBlanc[169], T. LeCompte[6], F. Ledroit-Guillon[55], C.A. Lee[145b], S.C. Lee[151], L. Lee[1], G. Lefebvre[80], M. Lefebvre[169], F. Legger[100], C. Leggett[15], A. Lehan[74], G. Lehmann Miotto[30], X. Lei[7], W.A. Leight[29], A. Leisos[154,w], A.G. Leister[176], M.A.L. Leite[24d], R. Leitner[129], D. Lellouch[172], B. Lemmer[54], K.J.C. Leney[78], T. Lenz[21], B. Lenzi[30], R. Leone[7], S. Leone[124a,124b], C. Leonidopoulos[46], S. Leontsinis[10], C. Leroy[95], C.G. Lester[28], M. Levchenko[123], J. Levêque[5], D. Levin[89], L.J. Levinson[172], M. Levy[18], A. Lewis[120], A.M. Leyko[21], M. Leyton[41], B. Li[33b,x], H. Li[148], H.L. Li[31], L. Li[45], L. Li[33e], S. Li[45], Y. Li[33c,y], Z. Liang[137], H. Liao[34], B. Liberti[133a], A. Liblong[158], P. Lichard[30], K. Lie[165], J. Liebal[21], W. Liebig[14], C. Limbach[21], A. Limosani[150], S.C. Lin[151,z], T.H. Lin[83], F. Linde[107], B.E. Lindquist[148], J.T. Linnemann[90], E. Lipeles[122], A. Lipniacka[14], M. Lisovyi[58b], T.M. Liss[165], D. Lissauer[25], A. Lister[168], A.M. Litke[137], B. Liu[151,aa], D. Liu[151], H. Liu[89], J. Liu[85], J.B. Liu[33b], K. Liu[85], L. Liu[165], M. Liu[45], M. Liu[33b], Y. Liu[33b], M. Livan[121a,121b], A. Lleres[55], J. Llorente Merino[82], S.L. Lloyd[76], F. Lo Sterzo[151], E. Lobodzinska[42], P. Loch[7], W.S. Lockman[137], F.K. Loebinger[84], A.E. Loevschall-Jensen[36], A. Loginov[176], T. Lohse[16], K. Lohwasser[42], M. Lokajicek[127], B.A. Long[22], J.D. Long[89], R.E. Long[72], K.A. Looper[111], L. Lopes[126a], D. Lopez Mateos[57], B. Lopez Paredes[139], I. Lopez Paz[12], J. Lorenz[100], N. Lorenzo Martinez[61], M. Losada[162], P. Loscutoff[15], P.J. Lösel[100], X. Lou[33a], A. Lounis[117], J. Love[6], P.A. Love[72], N. Lu[89], H.J. Lubatti[138], C. Luci[132a,132b], A. Lucotte[55], F. Luehring[61], W. Lukas[62], L. Luminari[132a], O. Lundberg[146a,146b], B. Lund-Jensen[147], D. Lynn[25], R. Lysak[127], E. Lytken[81], H. Ma[25], L.L. Ma[33d], G. Maccarrone[47], A. Macchiolo[101], C.M. Macdonald[139], J. Machado Miguens[122,126b], D. Macina[30], D. Madaffari[85], R. Madar[34], H.J. Maddocks[72], W.F. Mader[44], A. Madsen[166], S. Maeland[14], T. Maeno[25], A. Maevskiy[99], E. Magradze[54], K. Mahboubi[48], J. Mahlstedt[107], C. Maiani[136], C. Maidantchik[24a], A.A. Maier[101], T. Maier[100], A. Maio[126a,126b,126d], S. Majewski[116], Y. Makida[66], N. Makovec[117], B. Malaescu[80], Pa. Malecki[39], V.P. Maleev[123], F. Malek[55], U. Mallik[63], D. Malon[6], C. Malone[143], S. Maltezos[10], V.M. Malyshev[109], S. Malyukov[30], J. Mamuzic[42], G. Mancini[47], B. Mandelli[30], L. Mandelli[91a], I. Mandić[75], R. Mandrysch[63], J. Maneira[126a,126b], A. Manfredini[101], L. Manhaes de Andrade Filho[24b], J. Manjarres Ramos[159b], A. Mann[100], P.M. Manning[137], A. Manousakis-Katsikakis[9], B. Mansoulie[136], R. Mantifel[87], M. Mantoani[54], L. Mapelli[30], L. March[145c], G. Marchiori[80], M. Marcisovsky[127], C.P. Marino[169], M. Marjanovic[13], D.E. Marley[89], F. Marroquim[24a], S.P. Marsden[84], Z. Marshall[15], L.F. Marti[17], S. Marti-Garcia[167], B. Martin[90], T.A. Martin[170], V.J. Martin[46], B. Martin dit Latour[14], M. Martinez[12,o], S. Martin-Haugh[131], V.S. Martoiu[26a], A.C. Martyniuk[78], M. Marx[138], F. Marzano[132a], A. Marzin[30], L. Masetti[83], T. Mashimo[155], R. Mashinistov[96], J. Masik[84], A.L. Maslennikov[109,c], I. Massa[20a,20b], L. Massa[20a,20b], N. Massol[5], P. Mastrandrea[148], A. Mastroberardino[37a,37b], T. Masubuchi[155], P. Mättig[175], J. Mattmann[83], J. Maurer[26a], S.J. Maxfield[74], D.A. Maximov[109,c], R. Mazini[151], S.M. Mazza[91a,91b], L. Mazzaferro[133a,133b], G. Mc Goldrick[158], S.P. Mc Kee[89], A. McCarn[89], R.L. McCarthy[148], T.G. McCarthy[29], N.A. McCubbin[131], K.W. McFarlane[56,*], J.A. Mcfayden[78], G. Mchedlidze[54], S.J. McMahon[131], R.A. McPherson[169,k], M. Medinnis[42],

JHEP08(2016)147

S. Meehan[145a], S. Mehlhase[100], A. Mehta[74], K. Meier[58a], C. Meineck[100], B. Meirose[41], B.R. Mellado Garcia[145c], F. Meloni[17], A. Mengarelli[20a,20b], S. Menke[101], E. Meoni[161], K.M. Mercurio[57], S. Mergelmeyer[21], P. Mermod[49], L. Merola[104a,104b], C. Meroni[91a], F.S. Merritt[31], A. Messina[132a,132b], J. Metcalfe[25], A.S. Mete[163], C. Meyer[83], C. Meyer[122], J-P. Meyer[136], J. Meyer[107], R.P. Middleton[131], S. Miglioranzi[164a,164c], L. Mijović[21], G. Mikenberg[172], M. Mikestikova[127], M. Mikuž[75], M. Milesi[88], A. Milic[30], D.W. Miller[31], C. Mills[46], A. Milov[172], D.A. Milstead[146a,146b], A.A. Minaenko[130], Y. Minami[155], I.A. Minashvili[65], A.I. Mincer[110], B. Mindur[38a], M. Mineev[65], Y. Ming[173], L.M. Mir[12], T. Mitani[171], J. Mitrevski[100], V.A. Mitsou[167], A. Miucci[49], P.S. Miyagawa[139], J.U. Mjörnmark[81], T. Moa[146a,146b], K. Mochizuki[85], S. Mohapatra[35], W. Mohr[48], S. Molander[146a,146b], R. Moles-Valls[21], K. Mönig[42], C. Monini[55], J. Monk[36], E. Monnier[85], J. Montejo Berlingen[12], F. Monticelli[71], S. Monzani[132a,132b], R.W. Moore[3], N. Morange[117], D. Moreno[162], M. Moreno Llácer[54], P. Morettini[50a], M. Morgenstern[44], D. Mori[142], M. Morii[57], M. Morinaga[155], V. Morisbak[119], S. Moritz[83], A.K. Morley[150], G. Mornacchi[30], J.D. Morris[76], S.S. Mortensen[36], A. Morton[53], L. Morvaj[103], M. Mosidze[51b], J. Moss[111], K. Motohashi[157], R. Mount[143], E. Mountricha[25], S.V. Mouraviev[96,*], E.J.W. Moyse[86], S. Muanza[85], R.D. Mudd[18], F. Mueller[101], J. Mueller[125], R.S.P. Mueller[100], T. Mueller[28], D. Muenstermann[49], P. Mullen[53], G.A. Mullier[17], J.A. Murillo Quijada[18], W.J. Murray[170,131], H. Musheghyan[54], E. Musto[152], A.G. Myagkov[130,ab], M. Myska[128], B.P. Nachman[143], O. Nackenhorst[54], J. Nadal[54], K. Nagai[120], R. Nagai[157], Y. Nagai[85], K. Nagano[66], A. Nagarkar[111], Y. Nagasaka[59], K. Nagata[160], M. Nagel[101], E. Nagy[85], A.M. Nairz[30], Y. Nakahama[30], K. Nakamura[66], T. Nakamura[155], I. Nakano[112], H. Namasivayam[41], R.F. Naranjo Garcia[42], R. Narayan[31], T. Naumann[42], G. Navarro[162], R. Nayyar[7], H.A. Neal[89], P.Yu. Nechaeva[96], T.J. Neep[84], P.D. Nef[143], A. Negri[121a,121b], M. Negrini[20a], S. Nektarijevic[106], C. Nellist[117], A. Nelson[163], S. Nemecek[127], P. Nemethy[110], A.A. Nepomuceno[24a], M. Nessi[30,ac], M.S. Neubauer[165], M. Neumann[175], R.M. Neves[110], P. Nevski[25], P.R. Newman[18], D.H. Nguyen[6], R.B. Nickerson[120], R. Nicolaidou[136], B. Nicquevert[30], J. Nielsen[137], N. Nikiforou[35], A. Nikiforov[16], V. Nikolaenko[130,ab], I. Nikolic-Audit[80], K. Nikolopoulos[18], J.K. Nilsen[119], P. Nilsson[25], Y. Ninomiya[155], A. Nisati[132a], R. Nisius[101], T. Nobe[155], M. Nomachi[118], I. Nomidis[29], T. Nooney[76], S. Norberg[113], M. Nordberg[30], O. Novgorodova[44], S. Nowak[101], M. Nozaki[66], L. Nozka[115], K. Ntekas[10], G. Nunes Hanninger[88], T. Nunnemann[100], E. Nurse[78], F. Nuti[88], B.J. O'Brien[46], F. O'grady[7], D.C. O'Neil[142], V. O'Shea[53], F.G. Oakham[29,d], H. Oberlack[101], T. Obermann[21], J. Ocariz[80], A. Ochi[67], I. Ochoa[78], J.P. Ochoa-Ricoux[32a], S. Oda[70], S. Odaka[66], H. Ogren[61], A. Oh[84], S.H. Oh[45], C.C. Ohm[15], H. Ohman[166], H. Oide[30], W. Okamura[118], H. Okawa[160], Y. Okumura[31], T. Okuyama[66], A. Olariu[26a], S.A. Olivares Pino[46], D. Oliveira Damazio[25], E. Oliver Garcia[167], A. Olszewski[39], J. Olszowska[39], A. Onofre[126a,126e], P.U.E. Onyisi[31,r], C.J. Oram[159a], M.J. Oreglia[31], Y. Oren[153], D. Orestano[134a,134b], N. Orlando[154], C. Oropeza Barrera[53], R.S. Orr[158], B. Osculati[50a,50b], R. Ospanov[84], G. Otero y Garzon[27], H. Otono[70], M. Ouchrif[135d], E.A. Ouellette[169], F. Ould-Saada[119], A. Ouraou[136], K.P. Oussoren[107], Q. Ouyang[33a], A. Ovcharova[15], M. Owen[53], R.E. Owen[18], V.E. Ozcan[19a], N. Ozturk[8], K. Pachal[142], A. Pacheco Pages[12], C. Padilla Aranda[12], M. Pagáčová[48], S. Pagan Griso[15], E. Paganis[139], F. Paige[25], P. Pais[86], K. Pajchel[119], G. Palacino[159b], S. Palestini[30], M. Palka[38b], D. Pallin[34], A. Palma[126a,126b], Y.B. Pan[173], E. Panagiotopoulou[10], C.E. Pandini[80], J.G. Panduro Vazquez[77], P. Pani[146a,146b], S. Panitkin[25], D. Pantea[26a], L. Paolozzi[49], Th.D. Papadopoulou[10], K. Papageorgiou[154], A. Paramonov[6], D. Paredes Hernandez[154], M.A. Parker[28], K.A. Parker[139], F. Parodi[50a,50b], J.A. Parsons[35], U. Parzefall[48], E. Pasqualucci[132a], S. Passaggio[50a], F. Pastore[134a,134b,*], Fr. Pastore[77], G. Pásztor[29], S. Pataraia[175], N.D. Patel[150], J.R. Pater[84], T. Pauly[30], J. Pearce[169], B. Pearson[113], L.E. Pedersen[36], M. Pedersen[119], S. Pedraza Lopez[167],

JHEP08(2016)147

R. Pedro[126a,126b], S.V. Peleganchuk[109,c], D. Pelikan[166], O. Penc[127], C. Peng[33a], H. Peng[33b], B. Penning[31], J. Penwell[61], D.V. Perepelitsa[25], E. Perez Codina[159a], M.T. Pérez García-Estañ[167], L. Perini[91a,91b], H. Pernegger[30], S. Perrella[104a,104b], R. Peschke[42], V.D. Peshekhonov[65], K. Peters[30], R.F.Y. Peters[84], B.A. Petersen[30], T.C. Petersen[36], E. Petit[42], A. Petridis[146a,146b], C. Petridou[154], P. Petroff[117], E. Petrolo[132a], F. Petrucci[134a,134b], N.E. Pettersson[157], R. Pezoa[32b], P.W. Phillips[131], G. Piacquadio[143], E. Pianori[170], A. Picazio[49], E. Piccaro[76], M. Piccinini[20a,20b], M.A. Pickering[120], R. Piegaia[27], D.T. Pignotti[111], J.E. Pilcher[31], A.D. Pilkington[84], J. Pina[126a,126b,126d], M. Pinamonti[164a,164c,ad], J.L. Pinfold[3], A. Pingel[36], B. Pinto[126a], S. Pires[80], H. Pirumov[42], M. Pitt[172], C. Pizio[91a,91b], L. Plazak[144a], M.-A. Pleier[25], V. Pleskot[129], E. Plotnikova[65], P. Plucinski[146a,146b], D. Pluth[64], R. Poettgen[146a,146b], L. Poggioli[117], D. Pohl[21], G. Polesello[121a], A. Poley[42], A. Policicchio[37a,37b], R. Polifka[158], A. Polini[20a], C.S. Pollard[53], V. Polychronakos[25], K. Pommès[30], L. Pontecorvo[132a], B.G. Pope[90], G.A. Popeneciu[26b], D.S. Popovic[13], A. Poppleton[30], S. Pospisil[128], K. Potamianos[15], I.N. Potrap[65], C.J. Potter[149], C.T. Potter[116], G. Poulard[30], J. Poveda[30], V. Pozdnyakov[65], P. Pralavorio[85], A. Pranko[15], S. Prasad[30], S. Prell[64], D. Price[84], L.E. Price[6], M. Primavera[73a], S. Prince[87], M. Proissl[46], K. Prokofiev[60c], F. Prokoshin[32b], E. Protopapadaki[136], S. Protopopescu[25], J. Proudfoot[6], M. Przybycien[38a], E. Ptacek[116], D. Puddu[134a,134b], E. Pueschel[86], D. Puldon[148], M. Purohit[25,ae], P. Puzo[117], J. Qian[89], G. Qin[53], Y. Qin[84], A. Quadt[54], D.R. Quarrie[15], W.B. Quayle[164a,164b], M. Queitsch-Maitland[84], D. Quilty[53], S. Raddum[119], V. Radeka[25], V. Radescu[42], S.K. Radhakrishnan[148], P. Radloff[116], P. Rados[88], F. Ragusa[91a,91b], G. Rahal[178], S. Rajagopalan[25], M. Rammensee[30], C. Rangel-Smith[166], F. Rauscher[100], S. Rave[83], T. Ravenscroft[53], M. Raymond[30], A.L. Read[119], N.P. Readioff[74], D.M. Rebuzzi[121a,121b], A. Redelbach[174], G. Redlinger[25], R. Reece[137], K. Reeves[41], L. Rehnisch[16], J. Reichert[122], H. Reisin[27], M. Relich[163], C. Rembser[30], H. Ren[33a], A. Renaud[117], M. Rescigno[132a], S. Resconi[91a], O.L. Rezanova[109,c], P. Reznicek[129], R. Rezvani[95], R. Richter[101], S. Richter[78], E. Richter-Was[38b], O. Ricken[21], M. Ridel[80], P. Rieck[16], C.J. Riegel[175], J. Rieger[54], M. Rijssenbeek[148], A. Rimoldi[121a,121b], L. Rinaldi[20a], B. Ristić[49], E. Ritsch[30], I. Riu[12], F. Rizatdinova[114], E. Rizvi[76], S.H. Robertson[87,k], A. Robichaud-Veronneau[87], D. Robinson[28], J.E.M. Robinson[42], A. Robson[53], C. Roda[124a,124b], S. Roe[30], O. Røhne[119], S. Rolli[161], A. Romaniouk[98], M. Romano[20a,20b], S.M. Romano Saez[34], E. Romero Adam[167], N. Rompotis[138], M. Ronzani[48], L. Roos[80], E. Ros[167], S. Rosati[132a], K. Rosbach[48], P. Rose[137], P.L. Rosendahl[14], O. Rosenthal[141], V. Rossetti[146a,146b], E. Rossi[104a,104b], L.P. Rossi[50a], R. Rosten[138], M. Rotaru[26a], I. Roth[172], J. Rothberg[138], D. Rousseau[117], C.R. Royon[136], A. Rozanov[85], Y. Rozen[152], X. Ruan[145c], F. Rubbo[143], I. Rubinskiy[42], V.I. Rud[99], C. Rudolph[44], M.S. Rudolph[158], F. Rühr[48], A. Ruiz-Martinez[30], Z. Rurikova[48], N.A. Rusakovich[65], A. Ruschke[100], H.L. Russell[138], J.P. Rutherfoord[7], N. Ruthmann[48], Y.F. Ryabov[123], M. Rybar[165], G. Rybkin[117], N.C. Ryder[120], A.F. Saavedra[150], G. Sabato[107], S. Sacerdoti[27], A. Saddique[3], H.F-W. Sadrozinski[137], R. Sadykov[65], F. Safai Tehrani[132a], M. Sahinsoy[19a], M. Saimpert[136], T. Saito[155], H. Sakamoto[155], Y. Sakurai[171], G. Salamanna[134a,134b], A. Salamon[133a], M. Saleem[113], D. Salek[107], P.H. Sales De Bruin[138], D. Salihagic[101], A. Salnikov[143], J. Salt[167], D. Salvatore[37a,37b], F. Salvatore[149], A. Salvucci[106], A. Salzburger[30], D. Sammel[48], D. Sampsonidis[154], A. Sanchez[104a,104b], J. Sánchez[167], V. Sanchez Martinez[167], H. Sandaker[119], R.L. Sandbach[76], H.G. Sander[83], M.P. Sanders[100], M. Sandhoff[175], C. Sandoval[162], R. Sandstroem[101], D.P.C. Sankey[131], M. Sannino[50a,50b], A. Sansoni[47], C. Santoni[34], R. Santonico[133a,133b], H. Santos[126a], I. Santoyo Castillo[149], K. Sapp[125], A. Sapronov[65], J.G. Saraiva[126a,126d], B. Sarrazin[21], O. Sasaki[66], Y. Sasaki[155], K. Sato[160], G. Sauvage[5,*], E. Sauvan[5], G. Savage[77], P. Savard[158,d], C. Sawyer[131], L. Sawyer[79,n], J. Saxon[31], C. Sbarra[20a], A. Sbrizzi[20a,20b], T. Scanlon[78], D.A. Scannicchio[163], M. Scarcella[150], V. Scarfone[37a,37b], J. Schaarschmidt[172], P. Schacht[101], D. Schaefer[30], R. Schaefer[42], J. Schaeffer[83],

JHEP08(2016)147

S. Schaepe[21], S. Schaetzel[58b], U. Schäfer[83], A.C. Schaffer[117], D. Schaile[100], R.D. Schamberger[148], V. Scharf[58a], V.A. Schegelsky[123], D. Scheirich[129], M. Schernau[163], C. Schiavi[50a,50b], C. Schillo[48], M. Schioppa[37a,37b], S. Schlenker[30], E. Schmidt[48], K. Schmieden[30], C. Schmitt[83], S. Schmitt[58b], S. Schmitt[42], B. Schneider[159a], Y.J. Schnellbach[74], U. Schnoor[44], L. Schoeffel[136], A. Schoening[58b], B.D. Schoenrock[90], E. Schopf[21], A.L.S. Schorlemmer[54], M. Schott[83], D. Schouten[159a], J. Schovancova[8], S. Schramm[49], M. Schreyer[174], C. Schroeder[83], N. Schuh[83], M.J. Schultens[21], H.-C. Schultz-Coulon[58a], H. Schulz[16], M. Schumacher[48], B.A. Schumm[137], Ph. Schune[136], C. Schwanenberger[84], A. Schwartzman[143], T.A. Schwarz[89], Ph. Schwegler[101], H. Schweiger[84], Ph. Schwemling[136], R. Schwienhorst[90], J. Schwindling[136], T. Schwindt[21], F.G. Sciacca[17], E. Scifo[117], G. Sciolla[23], F. Scuri[124a,124b], F. Scutti[21], J. Searcy[89], G. Sedov[42], E. Sedykh[123], P. Seema[21], S.C. Seidel[105], A. Seiden[137], F. Seifert[128], J.M. Seixas[24a], G. Sekhniaidze[104a], K. Sekhon[89], S.J. Sekula[40], D.M. Seliverstov[123,*], N. Semprini-Cesari[20a,20b], C. Serfon[30], L. Serin[117], L. Serkin[164a,164b], T. Serre[85], M. Sessa[134a,134b], R. Seuster[159a], H. Severini[113], T. Sfiligoj[75], F. Sforza[30], A. Sfyrla[30], E. Shabalina[54], M. Shamim[116], L.Y. Shan[33a], R. Shang[165], J.T. Shank[22], M. Shapiro[15], P.B. Shatalov[97], K. Shaw[164a,164b], S.M. Shaw[84], A. Shcherbakova[146a,146b], C.Y. Shehu[149], P. Sherwood[78], L. Shi[151,af], S. Shimizu[67], C.O. Shimmin[163], M. Shimojima[102], M. Shiyakova[65], A. Shmeleva[96], D. Shoaleh Saadi[95], M.J. Shochet[31], S. Shojaii[91a,91b], S. Shrestha[111], E. Shulga[98], M.A. Shupe[7], S. Shushkevich[42], P. Sicho[127], P.E. Sidebo[147], O. Sidiropoulou[174], D. Sidorov[114], A. Sidoti[20a,20b], F. Siegert[44], Dj. Sijacki[13], J. Silva[126a,126d], Y. Silver[153], S.B. Silverstein[146a], V. Simak[128], O. Simard[5], Lj. Simic[13], S. Simion[117], E. Simioni[83], B. Simmons[78], D. Simon[34], R. Simoniello[91a,91b], P. Sinervo[158], N.B. Sinev[116], M. Sioli[20a,20b], G. Siragusa[174], A.N. Sisakyan[65,*], S.Yu. Sivoklokov[99], J. Sjölin[146a,146b], T.B. Sjursen[14], M.B. Skinner[72], H.P. Skottowe[57], P. Skubic[113], M. Slater[18], T. Slavicek[128], M. Slawinska[107], K. Sliwa[161], V. Smakhtin[172], B.H. Smart[46], L. Smestad[14], S.Yu. Smirnov[98], Y. Smirnov[98], L.N. Smirnova[99,ag], O. Smirnova[81], M.N.K. Smith[35], R.W. Smith[35], M. Smizanska[72], K. Smolek[128], A.A. Snesarev[96], G. Snidero[76], S. Snyder[25], R. Sobie[169,k], F. Socher[44], A. Soffer[153], D.A. Soh[151,af], C.A. Solans[30], M. Solar[128], J. Solc[128], E.Yu. Soldatov[98], U. Soldevila[167], A.A. Solodkov[130], A. Soloshenko[65], O.V. Solovyanov[130], V. Solovyev[123], P. Sommer[48], H.Y. Song[33b], N. Soni[1], A. Sood[15], A. Sopczak[128], B. Sopko[128], V. Sopko[128], V. Sorin[12], D. Sosa[58b], M. Sosebee[8], C.L. Sotiropoulou[124a,124b], R. Soualah[164a,164c], A.M. Soukharev[109,c], D. South[42], B.C. Sowden[77], S. Spagnolo[73a,73b], M. Spalla[124a,124b], F. Spanò[77], W.R. Spearman[57], D. Sperlich[16], F. Spettel[101], R. Spighi[20a], G. Spigo[30], L.A. Spiller[88], M. Spousta[129], T. Spreitzer[158], R.D. St. Denis[53,*], S. Staerz[44], J. Stahlman[122], R. Stamen[58a], S. Stamm[16], E. Stanecka[39], C. Stanescu[134a], M. Stanescu-Bellu[42], M.M. Stanitzki[42], S. Stapnes[119], E.A. Starchenko[130], J. Stark[55], P. Staroba[127], P. Starovoitov[42], R. Staszewski[39], P. Stavina[144a,*], P. Steinberg[25], B. Stelzer[142], H.J. Stelzer[30], O. Stelzer-Chilton[159a], H. Stenzel[52], G.A. Stewart[53], J.A. Stillings[21], M.C. Stockton[87], M. Stoebe[87], G. Stoicea[26a], P. Stolte[54], S. Stonjek[101], A.R. Stradling[8], A. Straessner[44], M.E. Stramaglia[17], J. Strandberg[147], S. Strandberg[146a,146b], A. Strandlie[119], E. Strauss[143], M. Strauss[113], P. Strizenec[144b], R. Ströhmer[174], D.M. Strom[116], R. Stroynowski[40], A. Strubig[106], S.A. Stucci[17], B. Stugu[14], N.A. Styles[42], D. Su[143], J. Su[125], R. Subramaniam[79], A. Succurro[12], Y. Sugaya[118], C. Suhr[108], M. Suk[128], V.V. Sulin[96], S. Sultansoy[4c], T. Sumida[68], S. Sun[57], X. Sun[33a], J.E. Sundermann[48], K. Suruliz[149], G. Susinno[37a,37b], M.R. Sutton[149], S. Suzuki[66], M. Svatos[127], S. Swedish[168], M. Swiatlowski[143], I. Sykora[144a], T. Sykora[129], D. Ta[90], C. Taccini[134a,134b], K. Tackmann[42], J. Taenzer[158], A. Taffard[163], R. Tafirout[159a], N. Taiblum[153], H. Takai[25], R. Takashima[69], H. Takeda[67], T. Takeshita[140], Y. Takubo[66], M. Talby[85], A.A. Talyshev[109,c], J.Y.C. Tam[174], K.G. Tan[88], J. Tanaka[155], R. Tanaka[117], S. Tanaka[66], B.B. Tannenwald[111], N. Tannoury[21], S. Tapprogge[83], S. Tarem[152], F. Tarrade[29],

JHEP08(2016)147

G.F. Tartarelli[91a], P. Tas[129], M. Tasevsky[127], T. Tashiro[68], E. Tassi[37a,37b], A. Tavares Delgado[126a,126b], Y. Tayalati[135d], F.E. Taylor[94], G.N. Taylor[88], W. Taylor[159b], F.A. Teischinger[30], M. Teixeira Dias Castanheira[76], P. Teixeira-Dias[77], K.K. Temming[48], H. Ten Kate[30], P.K. Teng[151], J.J. Teoh[118], F. Tepel[175], S. Terada[66], K. Terashi[155], J. Terron[82], S. Terzo[101], M. Testa[47], R.J. Teuscher[158,k], T. Theveneaux-Pelzer[34], J.P. Thomas[18], J. Thomas-Wilsker[77], E.N. Thompson[35], P.D. Thompson[18], R.J. Thompson[84], A.S. Thompson[53], L.A. Thomsen[176], E. Thomson[122], M. Thomson[28], R.P. Thun[89,*], M.J. Tibbetts[15], R.E. Ticse Torres[85], V.O. Tikhomirov[96,ah], Yu.A. Tikhonov[109,c], S. Timoshenko[98], E. Tiouchichine[85], P. Tipton[176], S. Tisserant[85], K. Todome[157], T. Todorov[5,*], S. Todorova-Nova[129], J. Tojo[70], S. Tokár[144a], K. Tokushuku[66], K. Tollefson[90], E. Tolley[57], L. Tomlinson[84], M. Tomoto[103], L. Tompkins[143,ai], K. Toms[105], E. Torrence[116], H. Torres[142], E. Torró Pastor[167], J. Toth[85,aj], F. Touchard[85], D.R. Tovey[139], T. Trefzger[174], L. Tremblet[30], A. Tricoli[30], I.M. Trigger[159a], S. Trincaz-Duvoid[80], M.F. Tripiana[12], W. Trischuk[158], B. Trocmé[55], C. Troncon[91a], M. Trottier-McDonald[15], M. Trovatelli[169], P. True[90], L. Truong[164a,164c], M. Trzebinski[39], A. Trzupek[39], C. Tsarouchas[30], J.C-L. Tseng[120], P.V. Tsiareshka[92], D. Tsionou[154], G. Tsipolitis[10], N. Tsirintanis[9], S. Tsiskaridze[12], V. Tsiskaridze[48], E.G. Tskhadadze[51a], I.I. Tsukerman[97], V. Tsulaia[15], S. Tsuno[66], D. Tsybychev[148], A. Tudorache[26a], V. Tudorache[26a], A.N. Tuna[122], S.A. Tupputi[20a,20b], S. Turchikhin[99,ag], D. Turecek[128], R. Turra[91a,91b], A.J. Turvey[40], P.M. Tuts[35], A. Tykhonov[49], M. Tylmad[146a,146b], M. Tyndel[131], I. Ueda[155], R. Ueno[29], M. Ughetto[146a,146b], M. Ugland[14], M. Uhlenbrock[21], F. Ukegawa[160], G. Unal[30], A. Undrus[25], G. Unel[163], F.C. Ungaro[48], Y. Unno[66], C. Unverdorben[100], J. Urban[144b], P. Urquijo[88], P. Urrejola[83], G. Usai[8], A. Usanova[62], L. Vacavant[85], V. Vacek[128], B. Vachon[87], C. Valderanis[83], N. Valencic[107], S. Valentinetti[20a,20b], A. Valero[167], L. Valery[12], S. Valkar[129], E. Valladolid Gallego[167], S. Vallecorsa[49], J.A. Valls Ferrer[167], W. Van Den Wollenberg[107], P.C. Van Der Deijl[107], R. van der Geer[107], H. van der Graaf[107], R. Van Der Leeuw[107], N. van Eldik[152], P. van Gemmeren[6], J. Van Nieuwkoop[142], I. van Vulpen[107], M.C. van Woerden[30], M. Vanadia[132a,132b], W. Vandelli[30], R. Vanguri[122], A. Vaniachine[6], F. Vannucci[80], G. Vardanyan[177], R. Vari[132a], E.W. Varnes[7], T. Varol[40], D. Varouchas[80], A. Vartapetian[8], K.E. Varvell[150], F. Vazeille[34], T. Vazquez Schroeder[87], J. Veatch[7], L.M. Veloce[158], F. Veloso[126a,126c], T. Velz[21], S. Veneziano[132a], A. Ventura[73a,73b], D. Ventura[86], M. Venturi[169], N. Venturi[158], A. Venturini[23], V. Vercesi[121a], M. Verducci[132a,132b], W. Verkerke[107], J.C. Vermeulen[107], A. Vest[44], M.C. Vetterli[142,d], O. Viazlo[81], I. Vichou[165], T. Vickey[139], O.E. Vickey Boeriu[139], G.H.A. Viehhauser[120], S. Viel[15], R. Vigne[62], M. Villa[20a,20b], M. Villaplana Perez[91a,91b], E. Vilucchi[47], M.G. Vincter[29], V.B. Vinogradov[65], I. Vivarelli[149], F. Vives Vaque[3], S. Vlachos[10], D. Vladoiu[100], M. Vlasak[128], M. Vogel[32a], P. Vokac[128], G. Volpi[124a,124b], M. Volpi[88], H. von der Schmitt[101], H. von Radziewski[48], E. von Toerne[21], V. Vorobel[129], K. Vorobev[98], M. Vos[167], R. Voss[30], J.H. Vossebeld[74], N. Vranjes[13], M. Vranjes Milosavljevic[13], V. Vrba[127], M. Vreeswijk[107], R. Vuillermet[30], I. Vukotic[31], Z. Vykydal[128], P. Wagner[21], W. Wagner[175], H. Wahlberg[71], S. Wahrmund[44], J. Wakabayashi[103], J. Walder[72], R. Walker[100], W. Walkowiak[141], C. Wang[151], F. Wang[173], H. Wang[15], H. Wang[40], J. Wang[42], J. Wang[33a], K. Wang[87], R. Wang[6], S.M. Wang[151], T. Wang[21], T. Wang[35], X. Wang[176], C. Wanotayaroj[116], A. Warburton[87], C.P. Ward[28], D.R. Wardrope[78], M. Warsinsky[48], A. Washbrook[46], C. Wasicki[42], P.M. Watkins[18], A.T. Watson[18], I.J. Watson[150], M.F. Watson[18], G. Watts[138], S. Watts[84], B.M. Waugh[78], S. Webb[84], M.S. Weber[17], S.W. Weber[174], J.S. Webster[31], A.R. Weidberg[120], B. Weinert[61], J. Weingarten[54], C. Weiser[48], H. Weits[107], P.S. Wells[30], T. Wenaus[25], T. Wengler[30], S. Wenig[30], N. Wermes[21], M. Werner[48], P. Werner[30], M. Wessels[58a], J. Wetter[161], K. Whalen[116], A.M. Wharton[72], A. White[8], M.J. White[1], R. White[32b], S. White[124a,124b], D. Whiteson[163],

JHEP08(2016)147

F.J. Wickens[131], W. Wiedenmann[173], M. Wielers[131], P. Wienemann[21], C. Wiglesworth[36], L.A.M. Wiik-Fuchs[21], A. Wildauer[101], H.G. Wilkens[30], H.H. Williams[122], S. Williams[107], C. Willis[90], S. Willocq[86], A. Wilson[89], J.A. Wilson[18], I. Wingerter-Seez[5], F. Winklmeier[116], B.T. Winter[21], M. Wittgen[143], J. Wittkowski[100], S.J. Wollstadt[83], M.W. Wolter[39], H. Wolters[126a,126c], B.K. Wosiek[39], J. Wotschack[30], M.J. Woudstra[84], K.W. Wozniak[39], M. Wu[55], M. Wu[31], S.L. Wu[173], X. Wu[49], Y. Wu[89], T.R. Wyatt[84], B.M. Wynne[46], S. Xella[36], D. Xu[33a], L. Xu[33b,ak], B. Yabsley[150], S. Yacoob[145a], R. Yakabe[67], M. Yamada[66], Y. Yamaguchi[118], A. Yamamoto[66], S. Yamamoto[155], T. Yamanaka[155], K. Yamauchi[103], Y. Yamazaki[67], Z. Yan[22], H. Yang[33e], H. Yang[173], Y. Yang[151], W-M. Yao[15], Y. Yasu[66], E. Yatsenko[5], K.H. Yau Wong[21], J. Ye[40], S. Ye[25], I. Yeletskikh[65], A.L. Yen[57], E. Yildirim[42], K. Yorita[171], R. Yoshida[6], K. Yoshihara[122], C. Young[143], C.J.S. Young[30], S. Youssef[22], D.R. Yu[15], J. Yu[8], J.M. Yu[89], J. Yu[114], L. Yuan[67], S.P.Y. Yuen[21], A. Yurkewicz[108], I. Yusuff[28,al], B. Zabinski[39], R. Zaidan[63], A.M. Zaitsev[130,ab], J. Zalieckas[14], A. Zaman[148], S. Zambito[57], L. Zanello[132a,132b], D. Zanzi[88], C. Zeitnitz[175], M. Zeman[128], A. Zemla[38a], K. Zengel[23], O. Zenin[130], T. Ženiš[144a], D. Zerwas[117], D. Zhang[89], F. Zhang[173], H. Zhang[33c], J. Zhang[6], L. Zhang[48], R. Zhang[33b], X. Zhang[33d], Z. Zhang[117], X. Zhao[40], Y. Zhao[33d,117], Z. Zhao[33b], A. Zhemchugov[65], J. Zhong[120], B. Zhou[89], C. Zhou[45], L. Zhou[35], L. Zhou[40], N. Zhou[163], C.G. Zhu[33d], H. Zhu[33a], J. Zhu[89], Y. Zhu[33b], X. Zhuang[33a], K. Zhukov[96], A. Zibell[174], D. Zieminska[61], N.I. Zimine[65], C. Zimmermann[83], S. Zimmermann[48], Z. Zinonos[54], M. Zinser[83], M. Ziolkowski[141], L. Živković[13], G. Zobernig[173], A. Zoccoli[20a,20b], M. zur Nedden[16], G. Zurzolo[104a,104b] and L. Zwalinski[30]

[1] *Department of Physics, University of Adelaide, Adelaide, Australia*
[2] *Physics Department, SUNY Albany, Albany NY, United States of America*
[3] *Department of Physics, University of Alberta, Edmonton AB, Canada*
[4] [(a)] *Department of Physics, Ankara University, Ankara;* [(b)] *Istanbul Aydin University, Istanbul;* [(c)] *Division of Physics, TOBB University of Economics and Technology, Ankara, Turkey*
[5] *LAPP, CNRS/IN2P3 and Université Savoie Mont Blanc, Annecy-le-Vieux, France*
[6] *High Energy Physics Division, Argonne National Laboratory, Argonne IL, United States of America*
[7] *Department of Physics, University of Arizona, Tucson AZ, United States of America*
[8] *Department of Physics, The University of Texas at Arlington, Arlington TX, United States of America*
[9] *Physics Department, University of Athens, Athens, Greece*
[10] *Physics Department, National Technical University of Athens, Zografou, Greece*
[11] *Institute of Physics, Azerbaijan Academy of Sciences, Baku, Azerbaijan*
[12] *Institut de Física d'Altes Energies and Departament de Física de la Universitat Autònoma de Barcelona, Barcelona, Spain*
[13] *Institute of Physics, University of Belgrade, Belgrade, Serbia*
[14] *Department for Physics and Technology, University of Bergen, Bergen, Norway*
[15] *Physics Division, Lawrence Berkeley National Laboratory and University of California, Berkeley CA, United States of America*
[16] *Department of Physics, Humboldt University, Berlin, Germany*
[17] *Albert Einstein Center for Fundamental Physics and Laboratory for High Energy Physics, University of Bern, Bern, Switzerland*
[18] *School of Physics and Astronomy, University of Birmingham, Birmingham, United Kingdom*
[19] [(a)] *Department of Physics, Bogazici University, Istanbul;* [(b)] *Department of Physics Engineering, Gaziantep University, Gaziantep;* [(c)] *Department of Physics, Dogus University, Istanbul, Turkey*
[20] [(a)] *INFN Sezione di Bologna;* [(b)] *Dipartimento di Fisica e Astronomia, Università di Bologna, Bologna, Italy*
[21] *Physikalisches Institut, University of Bonn, Bonn, Germany*
[22] *Department of Physics, Boston University, Boston MA, United States of America*
[23] *Department of Physics, Brandeis University, Waltham MA, United States of America*

JHEP08(2016)147

[24] [(a)] Universidade Federal do Rio De Janeiro COPPE/EE/IF, Rio de Janeiro; [(b)] Electrical Circuits Department, Federal University of Juiz de Fora (UFJF), Juiz de Fora; [(c)] Federal University of Sao Joao del Rei (UFSJ), Sao Joao del Rei; [(d)] Instituto de Fisica, Universidade de Sao Paulo, Sao Paulo, Brazil
[25] Physics Department, Brookhaven National Laboratory, Upton NY, United States of America
[26] [(a)] National Institute of Physics and Nuclear Engineering, Bucharest; [(b)] National Institute for Research and Development of Isotopic and Molecular Technologies, Physics Department, Cluj Napoca; [(c)] University Politehnica Bucharest, Bucharest; [(d)] West University in Timisoara, Timisoara, Romania
[27] Departamento de Física, Universidad de Buenos Aires, Buenos Aires, Argentina
[28] Cavendish Laboratory, University of Cambridge, Cambridge, United Kingdom
[29] Department of Physics, Carleton University, Ottawa ON, Canada
[30] CERN, Geneva, Switzerland
[31] Enrico Fermi Institute, University of Chicago, Chicago IL, United States of America
[32] [(a)] Departamento de Física, Pontificia Universidad Católica de Chile, Santiago; [(b)] Departamento de Física, Universidad Técnica Federico Santa María, Valparaíso, Chile
[33] [(a)] Institute of High Energy Physics, Chinese Academy of Sciences, Beijing; [(b)] Department of Modern Physics, University of Science and Technology of China, Anhui; [(c)] Department of Physics, Nanjing University, Jiangsu; [(d)] School of Physics, Shandong University, Shandong; [(e)] Department of Physics and Astronomy, Shanghai Key Laboratory for Particle Physics and Cosmology, Shanghai Jiao Tong University, Shanghai; [(f)] Physics Department, Tsinghua University, Beijing 100084, China
[34] Laboratoire de Physique Corpusculaire, Clermont Université and Université Blaise Pascal and CNRS/IN2P3, Clermont-Ferrand, France
[35] Nevis Laboratory, Columbia University, Irvington NY, United States of America
[36] Niels Bohr Institute, University of Copenhagen, Kobenhavn, Denmark
[37] [(a)] INFN Gruppo Collegato di Cosenza, Laboratori Nazionali di Frascati; [(b)] Dipartimento di Fisica, Università della Calabria, Rende, Italy
[38] [(a)] AGH University of Science and Technology, Faculty of Physics and Applied Computer Science, Krakow; [(b)] Marian Smoluchowski Institute of Physics, Jagiellonian University, Krakow, Poland
[39] Institute of Nuclear Physics Polish Academy of Sciences, Krakow, Poland
[40] Physics Department, Southern Methodist University, Dallas TX, United States of America
[41] Physics Department, University of Texas at Dallas, Richardson TX, United States of America
[42] DESY, Hamburg and Zeuthen, Germany
[43] Institut für Experimentelle Physik IV, Technische Universität Dortmund, Dortmund, Germany
[44] Institut für Kern- und Teilchenphysik, Technische Universität Dresden, Dresden, Germany
[45] Department of Physics, Duke University, Durham NC, United States of America
[46] SUPA - School of Physics and Astronomy, University of Edinburgh, Edinburgh, United Kingdom
[47] INFN Laboratori Nazionali di Frascati, Frascati, Italy
[48] Fakultät für Mathematik und Physik, Albert-Ludwigs-Universität, Freiburg, Germany
[49] Section de Physique, Université de Genève, Geneva, Switzerland
[50] [(a)] INFN Sezione di Genova; [(b)] Dipartimento di Fisica, Università di Genova, Genova, Italy
[51] [(a)] E. Andronikashvili Institute of Physics, Iv. Javakhishvili Tbilisi State University, Tbilisi; [(b)] High Energy Physics Institute, Tbilisi State University, Tbilisi, Georgia
[52] II Physikalisches Institut, Justus-Liebig-Universität Giessen, Giessen, Germany
[53] SUPA - School of Physics and Astronomy, University of Glasgow, Glasgow, United Kingdom
[54] II Physikalisches Institut, Georg-August-Universität, Göttingen, Germany
[55] Laboratoire de Physique Subatomique et de Cosmologie, Université Grenoble-Alpes, CNRS/IN2P3, Grenoble, France
[56] Department of Physics, Hampton University, Hampton VA, United States of America
[57] Laboratory for Particle Physics and Cosmology, Harvard University, Cambridge MA, United States of America

JHEP08(2016)147

[58] [(a)] Kirchhoff-Institut für Physik, Ruprecht-Karls-Universität Heidelberg, Heidelberg; [(b)] Physikalisches Institut, Ruprecht-Karls-Universität Heidelberg, Heidelberg; [(c)] ZITI Institut für technische Informatik, Ruprecht-Karls-Universität Heidelberg, Mannheim, Germany
[59] Faculty of Applied Information Science, Hiroshima Institute of Technology, Hiroshima, Japan
[60] [(a)] Department of Physics, The Chinese University of Hong Kong, Shatin, N.T., Hong Kong; [(b)] Department of Physics, The University of Hong Kong, Hong Kong; [(c)] Department of Physics, The Hong Kong University of Science and Technology, Clear Water Bay, Kowloon, Hong Kong, China
[61] Department of Physics, Indiana University, Bloomington IN, United States of America
[62] Institut für Astro- und Teilchenphysik, Leopold-Franzens-Universität, Innsbruck, Austria
[63] University of Iowa, Iowa City IA, United States of America
[64] Department of Physics and Astronomy, Iowa State University, Ames IA, United States of America
[65] Joint Institute for Nuclear Research, JINR Dubna, Dubna, Russia
[66] KEK, High Energy Accelerator Research Organization, Tsukuba, Japan
[67] Graduate School of Science, Kobe University, Kobe, Japan
[68] Faculty of Science, Kyoto University, Kyoto, Japan
[69] Kyoto University of Education, Kyoto, Japan
[70] Department of Physics, Kyushu University, Fukuoka, Japan
[71] Instituto de Física La Plata, Universidad Nacional de La Plata and CONICET, La Plata, Argentina
[72] Physics Department, Lancaster University, Lancaster, United Kingdom
[73] [(a)] INFN Sezione di Lecce; [(b)] Dipartimento di Matematica e Fisica, Università del Salento, Lecce, Italy
[74] Oliver Lodge Laboratory, University of Liverpool, Liverpool, United Kingdom
[75] Department of Physics, Jožef Stefan Institute and University of Ljubljana, Ljubljana, Slovenia
[76] School of Physics and Astronomy, Queen Mary University of London, London, United Kingdom
[77] Department of Physics, Royal Holloway University of London, Surrey, United Kingdom
[78] Department of Physics and Astronomy, University College London, London, United Kingdom
[79] Louisiana Tech University, Ruston LA, United States of America
[80] Laboratoire de Physique Nucléaire et de Hautes Energies, UPMC and Université Paris-Diderot and CNRS/IN2P3, Paris, France
[81] Fysiska institutionen, Lunds universitet, Lund, Sweden
[82] Departamento de Fisica Teorica C-15, Universidad Autonoma de Madrid, Madrid, Spain
[83] Institut für Physik, Universität Mainz, Mainz, Germany
[84] School of Physics and Astronomy, University of Manchester, Manchester, United Kingdom
[85] CPPM, Aix-Marseille Université and CNRS/IN2P3, Marseille, France
[86] Department of Physics, University of Massachusetts, Amherst MA, United States of America
[87] Department of Physics, McGill University, Montreal QC, Canada
[88] School of Physics, University of Melbourne, Victoria, Australia
[89] Department of Physics, The University of Michigan, Ann Arbor MI, United States of America
[90] Department of Physics and Astronomy, Michigan State University, East Lansing MI, United States of America
[91] [(a)] INFN Sezione di Milano; [(b)] Dipartimento di Fisica, Università di Milano, Milano, Italy
[92] B.I. Stepanov Institute of Physics, National Academy of Sciences of Belarus, Minsk, Republic of Belarus
[93] National Scientific and Educational Centre for Particle and High Energy Physics, Minsk, Republic of Belarus
[94] Department of Physics, Massachusetts Institute of Technology, Cambridge MA, United States of America
[95] Group of Particle Physics, University of Montreal, Montreal QC, Canada
[96] P.N. Lebedev Institute of Physics, Academy of Sciences, Moscow, Russia
[97] Institute for Theoretical and Experimental Physics (ITEP), Moscow, Russia
[98] National Research Nuclear University MEPhI, Moscow, Russia

JHEP08(2016)147

[99] D.V. Skobeltsyn Institute of Nuclear Physics, M.V. Lomonosov Moscow State University, Moscow, Russia
[100] Fakultät für Physik, Ludwig-Maximilians-Universität München, München, Germany
[101] Max-Planck-Institut für Physik (Werner-Heisenberg-Institut), München, Germany
[102] Nagasaki Institute of Applied Science, Nagasaki, Japan
[103] Graduate School of Science and Kobayashi-Maskawa Institute, Nagoya University, Nagoya, Japan
[104] [(a)] INFN Sezione di Napoli; [(b)] Dipartimento di Fisica, Università di Napoli, Napoli, Italy
[105] Department of Physics and Astronomy, University of New Mexico, Albuquerque NM, United States of America
[106] Institute for Mathematics, Astrophysics and Particle Physics, Radboud University Nijmegen/Nikhef, Nijmegen, Netherlands
[107] Nikhef National Institute for Subatomic Physics and University of Amsterdam, Amsterdam, Netherlands
[108] Department of Physics, Northern Illinois University, DeKalb IL, United States of America
[109] Budker Institute of Nuclear Physics, SB RAS, Novosibirsk, Russia
[110] Department of Physics, New York University, New York NY, United States of America
[111] Ohio State University, Columbus OH, United States of America
[112] Faculty of Science, Okayama University, Okayama, Japan
[113] Homer L. Dodge Department of Physics and Astronomy, University of Oklahoma, Norman OK, United States of America
[114] Department of Physics, Oklahoma State University, Stillwater OK, United States of America
[115] Palacký University, RCPTM, Olomouc, Czech Republic
[116] Center for High Energy Physics, University of Oregon, Eugene OR, United States of America
[117] LAL, Université Paris-Sud and CNRS/IN2P3, Orsay, France
[118] Graduate School of Science, Osaka University, Osaka, Japan
[119] Department of Physics, University of Oslo, Oslo, Norway
[120] Department of Physics, Oxford University, Oxford, United Kingdom
[121] [(a)] INFN Sezione di Pavia; [(b)] Dipartimento di Fisica, Università di Pavia, Pavia, Italy
[122] Department of Physics, University of Pennsylvania, Philadelphia PA, United States of America
[123] National Research Centre "Kurchatov Institute" B.P.Konstantinov Petersburg Nuclear Physics Institute, St. Petersburg, Russia
[124] [(a)] INFN Sezione di Pisa; [(b)] Dipartimento di Fisica E. Fermi, Università di Pisa, Pisa, Italy
[125] Department of Physics and Astronomy, University of Pittsburgh, Pittsburgh PA, United States of America
[126] [(a)] Laboratório de Instrumentação e Física Experimental de Partículas - LIP, Lisboa; [(b)] Faculdade de Ciências, Universidade de Lisboa, Lisboa; [(c)] Department of Physics, University of Coimbra, Coimbra; [(d)] Centro de Física Nuclear da Universidade de Lisboa, Lisboa; [(e)] Departamento de Fisica, Universidade do Minho, Braga; [(f)] Departamento de Fisica Teorica y del Cosmos and CAFPE, Universidad de Granada, Granada (Spain); [(g)] Dep Fisica and CEFITEC of Faculdade de Ciencias e Tecnologia, Universidade Nova de Lisboa, Caparica, Portugal
[127] Institute of Physics, Academy of Sciences of the Czech Republic, Praha, Czech Republic
[128] Czech Technical University in Prague, Praha, Czech Republic
[129] Faculty of Mathematics and Physics, Charles University in Prague, Praha, Czech Republic
[130] State Research Center Institute for High Energy Physics, Protvino, Russia
[131] Particle Physics Department, Rutherford Appleton Laboratory, Didcot, United Kingdom
[132] [(a)] INFN Sezione di Roma; [(b)] Dipartimento di Fisica, Sapienza Università di Roma, Roma, Italy
[133] [(a)] INFN Sezione di Roma Tor Vergata; [(b)] Dipartimento di Fisica, Università di Roma Tor Vergata, Roma, Italy
[134] [(a)] INFN Sezione di Roma Tre; [(b)] Dipartimento di Matematica e Fisica, Università Roma Tre, Roma, Italy
[135] [(a)] Faculté des Sciences Ain Chock, Réseau Universitaire de Physique des Hautes Energies - Université Hassan II, Casablanca; [(b)] Centre National de l'Energie des Sciences Techniques Nucleaires, Rabat; [(c)] Faculté des Sciences Semlalia, Université Cadi Ayyad, LPHEA-Marrakech;

JHEP08(2016)147

[d] Faculté des Sciences, Université Mohamed Premier and LPTPM, Oujda; [e] Faculté des sciences, Université Mohammed V-Agdal, Rabat, Morocco
[136] DSM/IRFU (Institut de Recherches sur les Lois Fondamentales de l'Univers), CEA Saclay (Commissariat à l'Energie Atomique et aux Energies Alternatives), Gif-sur-Yvette, France
[137] Santa Cruz Institute for Particle Physics, University of California Santa Cruz, Santa Cruz CA, United States of America
[138] Department of Physics, University of Washington, Seattle WA, United States of America
[139] Department of Physics and Astronomy, University of Sheffield, Sheffield, United Kingdom
[140] Department of Physics, Shinshu University, Nagano, Japan
[141] Fachbereich Physik, Universität Siegen, Siegen, Germany
[142] Department of Physics, Simon Fraser University, Burnaby BC, Canada
[143] SLAC National Accelerator Laboratory, Stanford CA, United States of America
[144] [a] Faculty of Mathematics, Physics & Informatics, Comenius University, Bratislava; [b] Department of Subnuclear Physics, Institute of Experimental Physics of the Slovak Academy of Sciences, Kosice, Slovak Republic
[145] [a] Department of Physics, University of Cape Town, Cape Town; [b] Department of Physics, University of Johannesburg, Johannesburg; [c] School of Physics, University of the Witwatersrand, Johannesburg, South Africa
[146] [a] Department of Physics, Stockholm University; [b] The Oskar Klein Centre, Stockholm, Sweden
[147] Physics Department, Royal Institute of Technology, Stockholm, Sweden
[148] Departments of Physics & Astronomy and Chemistry, Stony Brook University, Stony Brook NY, United States of America
[149] Department of Physics and Astronomy, University of Sussex, Brighton, United Kingdom
[150] School of Physics, University of Sydney, Sydney, Australia
[151] Institute of Physics, Academia Sinica, Taipei, Taiwan
[152] Department of Physics, Technion: Israel Institute of Technology, Haifa, Israel
[153] Raymond and Beverly Sackler School of Physics and Astronomy, Tel Aviv University, Tel Aviv, Israel
[154] Department of Physics, Aristotle University of Thessaloniki, Thessaloniki, Greece
[155] International Center for Elementary Particle Physics and Department of Physics, The University of Tokyo, Tokyo, Japan
[156] Graduate School of Science and Technology, Tokyo Metropolitan University, Tokyo, Japan
[157] Department of Physics, Tokyo Institute of Technology, Tokyo, Japan
[158] Department of Physics, University of Toronto, Toronto ON, Canada
[159] [a] TRIUMF, Vancouver BC; [b] Department of Physics and Astronomy, York University, Toronto ON, Canada
[160] Faculty of Pure and Applied Sciences, University of Tsukuba, Tsukuba, Japan
[161] Department of Physics and Astronomy, Tufts University, Medford MA, United States of America
[162] Centro de Investigaciones, Universidad Antonio Narino, Bogota, Colombia
[163] Department of Physics and Astronomy, University of California Irvine, Irvine CA, United States of America
[164] [a] INFN Gruppo Collegato di Udine, Sezione di Trieste, Udine; [b] ICTP, Trieste; [c] Dipartimento di Chimica, Fisica e Ambiente, Università di Udine, Udine, Italy
[165] Department of Physics, University of Illinois, Urbana IL, United States of America
[166] Department of Physics and Astronomy, University of Uppsala, Uppsala, Sweden
[167] Instituto de Física Corpuscular (IFIC) and Departamento de Física Atómica, Molecular y Nuclear and Departamento de Ingeniería Electrónica and Instituto de Microelectrónica de Barcelona (IMB-CNM), University of Valencia and CSIC, Valencia, Spain
[168] Department of Physics, University of British Columbia, Vancouver BC, Canada
[169] Department of Physics and Astronomy, University of Victoria, Victoria BC, Canada
[170] Department of Physics, University of Warwick, Coventry, United Kingdom
[171] Waseda University, Tokyo, Japan
[172] Department of Particle Physics, The Weizmann Institute of Science, Rehovot, Israel

JHEP08(2016)147

[173] Department of Physics, University of Wisconsin, Madison WI, United States of America
[174] Fakultät für Physik und Astronomie, Julius-Maximilians-Universität, Würzburg, Germany
[175] Fachbereich C Physik, Bergische Universität Wuppertal, Wuppertal, Germany
[176] Department of Physics, Yale University, New Haven CT, United States of America
[177] Yerevan Physics Institute, Yerevan, Armenia
[178] Centre de Calcul de l'Institut National de Physique Nucléaire et de Physique des Particules (IN2P3), Villeurbanne, France

[a] Also at Department of Physics, King's College London, London, United Kingdom
[b] Also at Institute of Physics, Azerbaijan Academy of Sciences, Baku, Azerbaijan
[c] Also at Novosibirsk State University, Novosibirsk, Russia
[d] Also at TRIUMF, Vancouver BC, Canada
[e] Also at Department of Physics, California State University, Fresno CA, United States of America
[f] Also at Department of Physics, University of Fribourg, Fribourg, Switzerland
[g] Also at Departamento de Fisica e Astronomia, Faculdade de Ciencias, Universidade do Porto, Portugal
[h] Also at Tomsk State University, Tomsk, Russia
[i] Also at CPPM, Aix-Marseille Université and CNRS/IN2P3, Marseille, France
[j] Also at Universita di Napoli Parthenope, Napoli, Italy
[k] Also at Institute of Particle Physics (IPP), Canada
[l] Also at Particle Physics Department, Rutherford Appleton Laboratory, Didcot, United Kingdom
[m] Also at Department of Physics, St. Petersburg State Polytechnical University, St. Petersburg, Russia
[n] Also at Louisiana Tech University, Ruston LA, United States of America
[o] Also at Institucio Catalana de Recerca i Estudis Avancats, ICREA, Barcelona, Spain
[p] Also at Graduate School of Science, Osaka University, Osaka, Japan
[q] Also at Department of Physics, National Tsing Hua University, Taiwan
[r] Also at Department of Physics, The University of Texas at Austin, Austin TX, United States of America
[s] Also at Institute of Theoretical Physics, Ilia State University, Tbilisi, Georgia
[t] Also at CERN, Geneva, Switzerland
[u] Also at Georgian Technical University (GTU),Tbilisi, Georgia
[v] Also at Manhattan College, New York NY, United States of America
[w] Also at Hellenic Open University, Patras, Greece
[x] Also at Institute of Physics, Academia Sinica, Taipei, Taiwan
[y] Also at LAL, Université Paris-Sud and CNRS/IN2P3, Orsay, France
[z] Also at Academia Sinica Grid Computing, Institute of Physics, Academia Sinica, Taipei, Taiwan
[aa] Also at School of Physics, Shandong University, Shandong, China
[ab] Also at Moscow Institute of Physics and Technology State University, Dolgoprudny, Russia
[ac] Also at Section de Physique, Université de Genève, Geneva, Switzerland
[ad] Also at International School for Advanced Studies (SISSA), Trieste, Italy
[ae] Also at Department of Physics and Astronomy, University of South Carolina, Columbia SC, United States of America
[af] Also at School of Physics and Engineering, Sun Yat-sen University, Guangzhou, China
[ag] Also at Faculty of Physics, M.V.Lomonosov Moscow State University, Moscow, Russia
[ah] Also at National Research Nuclear University MEPhI, Moscow, Russia
[ai] Also at Department of Physics, Stanford University, Stanford CA, United States of America
[aj] Also at Institute for Particle and Nuclear Physics, Wigner Research Centre for Physics, Budapest, Hungary
[ak] Also at Department of Physics, The University of Michigan, Ann Arbor MI, United States of America
[al] Also at University of Malaya, Department of Physics, Kuala Lumpur, Malaysia
[*] Deceased

JHEP08(2016)147

PROCEEDINGS OF SCIENCE

Study of Λ_b^0 decay properties with the ATLAS detector

Tatjana Agatonovic Jovin[*†]
Institute of Physics, University of Belgrade
E-mail: tatjana.jovin@ipb.ac.rs

The measurements of the Λ_b^0 baryon decay properties are presented using $4.6-4.9$ fb^{-1} proton-proton collisions data recorded by the ATLAS detector during 2011 LHC operation. The results of the Λ_b^0 mass, lifetime and the lifetime ratio $\tau(\Lambda_b^0)/\tau(B_d^0)$, as well as the parity-violating decay asymmetry parameter, α_b, and the helicity amplitudes of the decay channel $\Lambda_b^0 \to J/\psi(\mu^+\mu^-)\Lambda^0(p\pi^-)$ are reported and compared with those of the LHCb, D0 and CDF experiments, as well as with theoretical models based on heavy-quark effective theory and perturbative QCD.

XXII. International Workshop on Deep-Inelastic Scattering and Related Subjects,
28 April - 2 May 2014
Warsaw, Poland

[*]Speaker.
[†]On behalf of the ATLAS collaboration.

PoS(DIS2014)182

1. Introduction

The lightest baryon with a constituent b-quark, Λ_b^0, with quark composition udb was firstly observed in 1991 by the UA1 experiment at the $p\bar{p}$ collider at CERN in the decay channel $\Lambda_b^0 \to J/\psi\Lambda^0$ [1]. First lifetime measurements are performed by the DELPHI experiment at LEP in 1992 using the semileptonic Λ_b^0 decays [2], while the first lifetime measurement in the fully reconstructed channel is performed by the CDF experiment at Tevatron [3]. Currently the hadron colliders are the only facilities to study properties of b-baryons.

Measurements of the lifetime of hadrons containing b-quarks provide important tests of the significance of strong interactions between the constituent partons in the weak decay of b-hadrons. These interactions produce measurable differences between b-hadron lifetimes that are predicted with good accuracy through the calculation of lifetime ratios such as $\tau(B^-)/\tau(\bar{B}_d^0)$, $\tau(\bar{B}_s^0)/\tau(\bar{B}_d^0)$, and $\tau(\Lambda_b^0)/\tau(\bar{B}_d^0)$ in the heavy-quark effective theory (HQET) [4].

Within the framework of the Standard Model of weak interactions, it has been known that weak decays violate parity. While parity violation in decays of muon and tau leptons is exhibited in its maximal form, parity violation in the hadronic sector is not maximal and depends on the hadron's constituents. Parity violating asymmetry parameter, α_b, for the decay $\Lambda_b^0 \to J/\psi\Lambda^0$, is of particular interest since it can serve as a test for various quark models such as perturbative QCD (pQCD) and factorization models [5]. A measurement of this parameter is of high interest in order to tune the quark models with realistic predictions.

In this report, we present the measurements of the mass and lifetime of the Λ_b^0, the lifetime ratio $\tau(\Lambda_b^0)/\tau(B_d^0)$ [6], as well as the parity-violating decay asymmetry parameter and the helicity amplitudes [7], with the ATLAS detector [8] at LHC, using the decay channel $\Lambda_b^0 \to J/\psi(\mu^+\mu^-)\Lambda^0(p\pi^-)$. The results are compared with those obtained with the LHCb, D0 and CDF experiments, as well as with the theoretical models based on the HQET and pQCD.

The ATLAS detector at the LHC is a general-purpose particle detector designed to be sensitive to a wide range of physics phenomena. It covers almost full solid angle around the pp collision point with layers of tracking detectors, calorimeters and muon chambers. For the measurements presented in this paper, the Inner Detector tracking devices (ID) and the Muon Spectrometer (MS) are of particular importance. The ATLAS ID has acceptance in pseudorapidity $|\eta| < 2.5$, and it is designed to achieve the highest precision in the transverse plane with a relative transverse momentum resolution of $\sigma_{p_T}/p_T = 0.05\% \times p_T(\text{GeV}) \oplus 1\%$ and a transverse impact parameter resolution of 10 μm. The ATLAS MS covers $|\eta| < 2.7$ and has a momentum resolution of $\sim 10\%$ up to 1 TeV. The MS consists of the precision-tracking chambers which are used to determine the coordinate of the muon track in η and the trigger chambers with coarse resolution, but fast response time. Tracks are reconstructed in the ID, and only tracks with p_T above 400 MeV and pseudorapidity $|\eta| < 2.5$ are used in this analysis. Both ID and the MS are used to identify muons.

2. Reconstruction and selection of $\Lambda_b^0 \to J/\psi(\mu^+\mu^-)\Lambda^0(p\pi^-)$ decays

The decay $\Lambda_b^0 \to J/\psi(\mu^+\mu^-)\Lambda^0(p\pi^-)$ has a cascade topology with two vertices and four final state particles, two muons from the J/ψ decay, and proton and pion from the Λ^0 decay. The J/ψ decays instantly at the same point as the Λ_b^0, while Λ^0 lives long enough to form a displaced tertiary

vertex. The di-muon and di-hadron pairs are pre-selected by requiring that their respective tracks are successfully fitted to a common vertex [9]. The di-muon pairs are accepted if the J/ψ vertex-refitted invariant mass lies in the range $2.8 < m_{\mu\mu} < 3.4$ GeV. The di-hadron candidates are accepted if $1.08 < m_{p\pi} < 1.15$ GeV [6].

The preselected muon and hadron track pairs are refitted with a constraint of a $\Lambda_b^0 \to J/\psi(\mu^+\mu^-)\Lambda^0(p\pi^-)$ cascade decay topology. The muons (hadrons) are constrained to intersect in a single vertex while their invariant mass must be equal to the known mass of the J/ψ (Λ^0). The combined momentum of the refitted Λ^0 track pair is constrained to point to the di-muon vertex. The fit is performed on all four final state particles tracks simultaneously taking into account the constraints from cascade topology fit and the full track error matrices [9]. The quality of the fit is characterised by the value of χ^2/N_{dof}, where the number of degrees of freedom $N_{dof} = 6$. The Λ_b^0 candidates are selected if: (i) $\chi^2/N_{dof} < 3$, (ii) $p_{\mathrm{T},\Lambda^0} > 3.5$ GeV, (iii) the transverse decay length of the cascade-refitted Λ^0 vertex measured from the Λ_b^0 vertex, $L_{xy,\Lambda^0} > 10$ mm and (iv) $5380 < m_{J/\psi\Lambda^0} < 5900$ MeV. In order to reject background from $B_d^0 \to J/\psi K_S^0$ decays, a difference of cumulative χ^2 probabilities $\mathscr{P}_{\Lambda_b^0} - \mathscr{P}_{B_d^0} > 0.05$ is required, if the four tracks forming the Λ_b^0 candidate also result in an acceptable B_d^0 fit.

3. Λ_b^0 mass and lifetime measurement

The measurements of the Λ_b^0 mass and lifetime is performed using 4.9 fb^{-1} of data collected with the LHC during 2011 in pp collisions at $\sqrt{s} = 7$ TeV. Events are selected using single-muon, di-muon, and J/ψ triggers. To study systematic effects and to correct for the efficiency and acceptance of the detector a Monte Carlo (MC) sample of 5×10^6 antibaryon $\bar{\Lambda}_b^0$ events is used. The sample is generated using the PYTHIA 6 MC generator [10] with the 2011 ATLAS AUET2B L0** tune [11]. After the selection described in Sec. 2, there are about 2200 Λ_b^0 and $\bar{\Lambda}_b^0$ candidates (including background) in the signal region.

The Λ_b^0 lifetime and mass are determined using a simultaneous unbinned maximum likelihood fit to the reconstructed mass and decay time of the selected candidates. For each reconstructed candidate the proper decay time is calculated as $\tau_{\Lambda_b^0} = L_{xy,\Lambda_b^0} \times m^{PDG}/p_{\mathrm{T}}$, where $m^{PDG} = 5619.4$ MeV [12], p_{T} is the reconstructed Λ_b^0 transverse momentum, and L_{xy,Λ_b^0} is the Λ_b^0 transverse decay distance measured from the primary vertex. Measurement procedure consists of selecting signal events, building probability density function (PDF) for mass and proper decay time for signal and background events. The mass and proper decay time are fitted using a likelihood function defined as [6]:

$$L = \prod_{i=1}^{N} [f_{sig}\mathfrak{M}_s(m_i|\delta_{m_i})\mathfrak{T}_s(\tau_i|\delta_{\tau_i})w_s(\delta_{m_i},\delta_{\tau_i}) + (1-f_{sig})\mathfrak{M}_b(m_i|\delta_{m_i})\mathfrak{T}_b(\tau_i|\delta_{\tau_i})w_b(\delta_{m_i},\delta_{\tau_i})]$$

where f_{sig} is the fraction of reconstructed signal candidates, m_i is the invariant mass of the i^{th} candidate and τ_i is its proper decay time. The corresponding errors, δm_i and $\delta\tau_i$, are estimated on a candidate-by-candidate basis by the cascade topology fit. The $\mathfrak{M}_s$ and $\mathfrak{M}_b$ are PDFs describing the signal and background dependence on mass; $\mathfrak{T}_s$ and $\mathfrak{T}_b$ describe the dependence on the proper decay time. The invariant mass and proper decay time error distributions, $w_{s(b)}(\delta_{m_i},\delta_{\tau_i})$, are extracted from data. The free parameters of the fit are: the Λ_b^0 mass and lifetime, $m_{\Lambda_b^0}$ and $\tau_{\Lambda_b^0}$, the

fraction of signal events, f_{sig}, the error scale factors, S_m and S_τ, and seven parameters describing the background shapes. The other quantities are calculated from the fit parameters. The results from the maximum likelihood fit are listed in Table 1. Projections of the PDF onto the mass and proper decay time axes are shown in Fig. 1.

Table 1: Results from the simultaneous mass and decay time maximum likelihood fit for Λ_b^0 [6].

Parameter	*Value*	*Parameter*	*Value*
$m(\Lambda_b^0)$	5619.7 ± 0.7 MeV	χ^2/N_{dof}	1.09
$\tau(\Lambda_b^0)$	1.449 ± 0.036 ps	N_{sig}	2184 ± 57
f_{sig}	0.268 ± 0.007	N_{bkg}	5970 ± 160
S_m	1.18 ± 0.03	σ_m	31.1 ± 0.8 MeV
S_τ	1.05 ± 0.02	σ_τ	0.117 ± 0.003 ps

The measured values for the Λ_b^0 lifetime and mass are:

$$\tau_{\Lambda_b^0} = 1.449 \pm 0.036(stat) \pm 0.017(syst) \text{ ps};$$
$$m_{\Lambda_b^0} = 5619.7 \pm 0.7(stat) \pm 1.1(syst) \text{ MeV}.$$

In order to cross-check the Λ_b^0 results and to determine the ratio $\tau(\Lambda_b^0)/\tau(B_d^0)$, the B_d^0 lifetime and mass has also been measured using the decay $B_d^0 \to J/\psi(\mu^+\mu^-)K_S^0(\pi^+\pi^-)$. The selection is chosen to be as close as possible to the Λ_b^0 selection in order to reduce the overall systematic error on the lifetime ratio measurement. Using an unbinned maximum likelihood fit, the B_d^0 lifetime and mass are measured to be $\tau_{B_d^0} = 1.509 \pm 0.012(stat) \pm 0.018(syst)$ ps and $m_{B_d^0} = 5279.6 \pm 0.2(stat) \pm 1.0(syst)$ MeV. These values are consistent with the world averages [12]. The value of Λ_b^0 and B_d^0 lifetime ratio is:

$$R = \tau_{\Lambda_b^0}/\tau_{B_d^0} = 0.960 \pm 0.025(stat) \pm 0.016(syst).$$

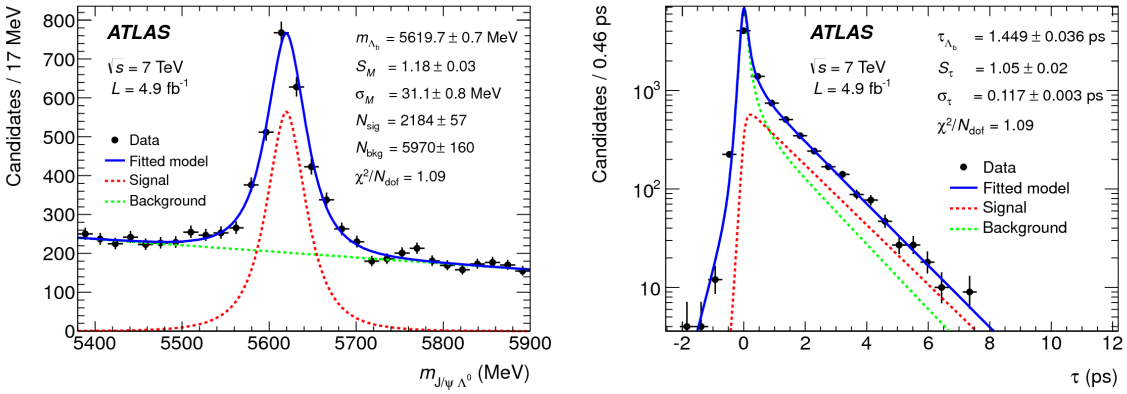

Figure 1: Projections of the fitted PDF onto the mass (left) and the proper decay time (right) axes for Λ_b^0 candidates. The errors are statistical only. The χ^2/N_{dof} value is calculated from the data set binned in mass and decay time with the number of degrees of freedom, $N_{dof} = 61$ [6].

4. Measurement of α_b and helicity amplitudes

The measurement of the parity-violating asymmetry parameter, α_b, and the decay amplitudes is performed by using an angular analysis of $\Lambda_b^0 \to J/\psi(\mu^+\mu^-)\Lambda^0(p\pi^-)$ weak decay. For strongly-produced Λ_b^0 baryons, a large fraction of the transverse b-quark polarisation is predicted by HQET to be retained after hadronisation [13], while the longitudinal polarisation should vanish due to parity conservation in strong interactions. The analysis uses 4.6 fb^{-1} of data collected with the LHC during 2011 in pp collisions at $\sqrt{s} = 7$ TeV. Events are selected using single-muon and J/ψ triggers. To study the efficiency and acceptance of the detector, MC sample of inclusive inelastic events is generated using the PYTHIA 6.4.

The reconstruction and selection of the Λ_b^0 decays is done as described in Sec. 2 with additional requirements: (i) $\mathscr{P}_{\Lambda_b^0} > \mathscr{P}_{B_d^0}$, (ii) $\tau > 0.35$ ps and (iii) 5560 MeV $< m_{J/\psi\Lambda^0} <$ 5680 MeV. After the selection, in total there are 1548 Λ_b^0 and $\bar{\Lambda}_b^0$ candidates (including background) in the signal region.

In the helicity formalism, the process $\Lambda_b^0 \to \Lambda V(1^-)$ can be described by four helicity amplitudes $A(\lambda_1,\lambda_2) : a_+ \equiv A(1/2,0), a_- \equiv A(-1/2,0), b_+ \equiv A(-1/2,-1), b_- \equiv A(1/2,1)$, where $\lambda_{1(2)}$ is the helicity of the $\Lambda(V)$ particle and $|a_+|^2 + |a_-|^2 + |b_+|^2 + |b_-|^2 = 1$. The angular distribution of the decay ($\frac{d\Gamma}{d\Omega_5}$) is reported in [14]. It depends on the five angles shown in Fig. 2: (i) θ, the polar angle of the Λ^0 momentum in the Λ_b^0 rest frame with respect to $\hat{n}$, a unit vector perpendicular to the production plane, (ii) θ_1 and ϕ_1, the polar and azimuthal angles of the proton in the Λ^0 rest frame with respect to the Λ^0 direction in the Λ_b^0 rest frame, (iii) θ_2 and ϕ_2, the polar and azimuthal angles of μ^+ in the J/ψ rest frame with respect to the J/ψ direction in the Λ_b^0 rest frame.

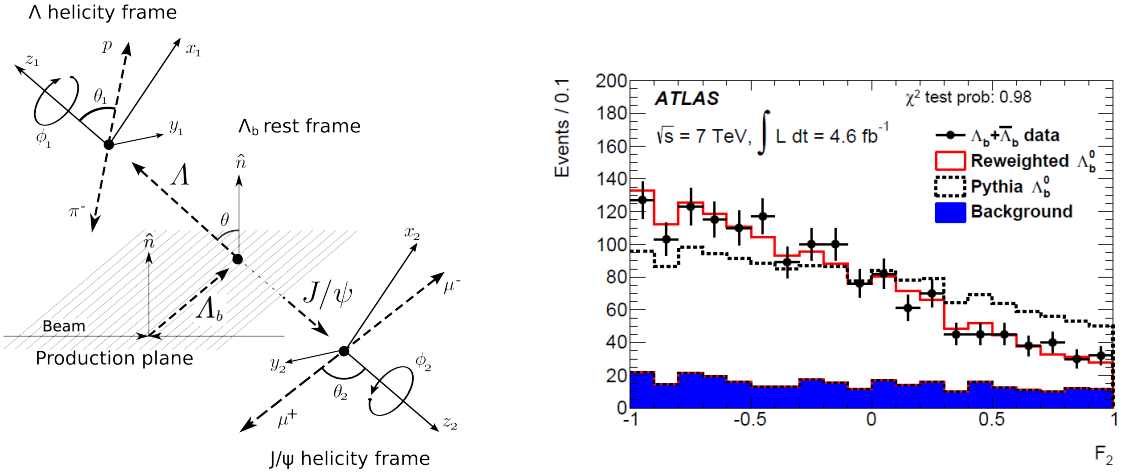

Figure 2: The $\Lambda_b^0 \to J/\psi(\mu^+\mu^-)\Lambda^0$ $(p\pi^-)$ decay angles (left), and distributions of the F_2 variable (right) for the model prediction compared to data (black points). The model prediction is obtained by plotting the weighted MC (red solid histogram) on the top of the background (blue area). The prediction obtained using the un-weighted MC (black dashed histogram) is also shown [7].

The full angular PDF of the decay angles collection $\Omega = (\theta, \phi, \theta_1, \phi_1, \theta_2, \phi_2)$ is [7]:

$$\omega(\Omega, \vec{A}, P) = \frac{1}{(4\pi)^3} \sum_{i=0}^{19} f_{1i}(\vec{A}) f_{2i}(P, \alpha_\Lambda) F_i(\Omega)$$

Table 2: The coefficients f_{1i}, f_{2i} and F_i of the remaining six terms of the PDF for $P = 0$. The f_{1i} functions are expressed using the five free parameters defined in the text [7].

i	f_{1i}	f_{2i}	F_i
0	1	1	1
2	$(k_0^2+k_1^2-1)+\alpha_b(k_0^2-k_1^2)$	α_Λ	$\cos\theta_1$
4	$\frac{1}{4}[(3k_1^2-3k_0^2-1)+3\alpha_b(1-k_1^2-k_0^2)]$	1	$\frac{1}{2}(3\cos^2\theta_2-1)$
6	$-\frac{1}{4}[(k_0^2+k_1^2-1)+\alpha_b(3+k_0^2-k_1^2)]$	α_Λ	$\frac{1}{2}(3\cos^2\theta_2-1)\cos\theta_1$
18	$\frac{3}{\sqrt{2}}[\frac{1-\alpha_b}{2}\sqrt{k_1^2(1-k_1^2)}\cos(-\Delta_-)-\frac{1+\alpha_b}{2}\sqrt{k_0^2(1-k_0^2)}\cos(\Delta_+)]$	α_Λ	$\sin\theta_1\sin\theta_2\cos\theta_2\cos(\phi_1+\phi_2)$
19	$-\frac{3}{\sqrt{2}}[\frac{1-\alpha_b}{2}\sqrt{k_1^2(1-k_1^2)}\sin(-\Delta_-)-\frac{1+\alpha_b}{2}\sqrt{k_0^2(1-k_0^2)}\sin(\Delta_+)]$	α_Λ	$\sin\theta_1\sin\theta_2\cos\theta_2\sin(\phi_1+\phi_2)$

where $f_{1i}(\vec{A})$ are bilinear combinations of the helicity amplitudes, $\vec{A} \equiv (a_+, a_-, b_+, b_-)$, f_{2i} is equal to: $P\alpha_\Lambda$, P, α_Λ or 1, where α_Λ is the decay asymmetry parameter for the decay $\Lambda^0 \to p\pi^-$ and P is the Λ_b^0 polarisation. $F_i(\Omega)$ are orthogonal functions of the decay angles.

There are nine unknown parameters in the given PDF: four complex helicity amplitudes, $a_+ = |a_+|e^{i\rho_+}$, $a_+ = |a_-|e^{i\rho_-}$, $b_+ = |b_+|e^{i\rho_+}$, $b_- = |b_-|e^{i\rho_-}$, and P. Due to a symmetry of the initial state in the beam direction at pp collider (z-axis in the ATLAS coordinate system) and the symmetry of the ATLAS detector in rapidity, the overall polarisation of the collected data-sample will be zero. As a result, the PDF is reduced from twenty to six terms listed in Table 2 and five free parameters: three magnitudes of the helicity amplitudes and two relative phases (from seven parameters). The coefficients f_{1i} are written in terms of the following five parameters chosen to define the model:

$$\alpha_b = |a_+|^2 - |a_-|^2 + |b_+|^2 - |b_-|^2$$
$$k_0 = |a_+|/\sqrt{|a_+|^2+|b_+|^2} \qquad k_1 = |b_-|/\sqrt{|a_-|^2+|b_-|^2}$$
$$\Delta_+ = \rho_+ - \omega_+ \qquad \Delta_- = \rho_- - \omega_-$$

Assuming CP conservation, the PDF of Λ_b^0 and $\bar{\Lambda}_b^0$ decay have the same form, and the samples are combined to measure the asymmetry parameter α_b and the helicity amplitudes with better precision.

The analysis uses the method of moments, by measuring the average values of each of the moments, $\langle F_i \rangle$, to extract the helicity amplitudes and α_b from them. The χ^2 fit is performed to determine the five main parameters of the measurement:

$$\chi^2 = \sum_{i=1}^{5}\sum_{j=1}^{5}(\langle F_i\rangle^{expected} - \langle F_i\rangle)V_{ij}^{-1}(\langle F_j\rangle^{expected} - \langle F_j\rangle)$$

where $\mathbf{V}$ is the covariance matrix of the measured $\langle F_i \rangle$ values and $\langle F_i \rangle^{expected}$ can be calculated from the PDF as: $\langle F_i\rangle^{expected} = \sum f_{1j}(\vec{A}) f_{2j}(\alpha_\Lambda) C_{ij}$. Detector effects are given in the correction matrix $\mathbf{C}$, which is independent of the measured helicity amplitude parameters and is therefore determined from MC simulation with flat angular distributions. The $\langle F_i \rangle$ are measured directly from data after subtraction of the estimated contribution from the combinatorial background and B_d^0 events. Since the combinatorial background[1] depends linearly on the Λ_b mass, its contribution to the measured

[1] *Combinatorial background* consists of real or fake J/ψ and Λ^0 candidates randomly combined to create a Λ_b^0-like topology. It is the main component of the background.

$\langle F_i \rangle$ values is estimated using events from the invariant-mass sidebands. The estimated number of B_d^0 events in the signal region (peaking background) is used to calculate the contribution of the B_d^0 events to the averaged $\langle F_i \rangle$ and the estimated contribution is subtracted. To determine the number of signal, combinatorial and B_d^0 background events, a binned maximum likelihood fit to the Λ_b^0 invariant mass distribution is performed. The observed number of Λ_b^0 is 1243 $\pm$ 44, and the number of B_d^0 events is estimated to be 73 $\pm$ 30. To check the fit results, the MC events were weighted using the signal PDF with the parameters obtained from the fit. This weighted MC and sideband background distributions of F_i are added and compared with data. Figure 2 (right) shows this comparison for the parameter F_2. The values of the asymmetry parameter and helicity amplitudes obtained from the results of the χ^2 fit are:

$$\alpha_b = 0.30 \pm 0.16(stat) \pm 0.06(syst.)$$
$$|a_+| = 0.17^{+0.12}_{-0.17}(stat.) \pm 0.09(syst.) \qquad |a_-| = 0.59^{+0.06}_{-0.07}(stat.) \pm 0.03(syst.)$$
$$|b_+| = 0.79^{+0.04}_{-0.05}(stat.) \pm 0.02(syst.) \qquad |b_-| = 0.08^{+0.13}_{-0.08}(stat.) \pm 0.06(syst.)$$

The large measured values for the helicity amplitudes $|a_-|$ and $|b_+|$ mean that the negative-helicity states for Λ_0 are preferred. The Λ_0 and J/ψ from Λ_b^0 decay are highly polarised. The measured value of the asymmetry parameter is consistent with a recent LHCb measurement [15].

5. Conclusions

The measurements of the Λ_b^0 mass, lifetime and the ratio of the Λ_b^0 and B_d^0 lifetimes, as well as the parity-violating asymmetry parameter and helicity amplitudes are presented. Measured values for the Λ_b^0 mass and lifetime by the ATLAS experiment agree with the world average values [12] and recent measurements by the LHCb [16, 17] and the CMS [18] experiments. The ratio of the Λ_b^0 and B_d^0 lifetimes is consistent with the measurements by the LHCb [17], the D0 [19] and the CDF [20] experiments. The value of the ratio obtained by this measurement is in agreement with the prediction from heavy-quark expansion calculations which predict the value between 0.88 and 0.97 [21] and is compatible with pQCD prediction [22] which is between 0.86 and 0.88 (with an uncertainty of $\pm$ 0.05). The value of the asymmetry parameter, α_b, measured by the ATLAS experiment is consistent with the recent measurement of the LHCb experiment at the level of one standard deviation. Comparing to theoretical models, the ATLAS measurement of α_b differs by about 2.5 standard deviations from the range of $\alpha_b \sim -(0.14 \sim 0.18)$ expected from pQCD [5] and by about 2.9 standard deviations from the HQET expectation [23, 24] of $\alpha_b = 0.78$.

References

[1] UA1 Collaboration, C. Albajar *et al.*, *First observation of the beauty baryon Λ_b in the decay channel $\Lambda_b \to \Lambda J/psi$ at the CERN proton - anti-proton collider*, Phys. Lett. B **273** (1991) 540-548, CERN-PPE-91-202.

[2] DELPHI Collaboration, P. Abreu *et al.*, *Measurement of Λ_b production and lifetime in Z^0 hadronic decays*, Phys. Lett. B **311** (1993) 379-390, CERN-PPE-93-032.

[3] CDF Collaboration, A. Abulencia *et al.*, *Measurement of the Λ_b^0 Lifetime in $\Lambda_b^0 \to J\psi\Lambda^0$ in $p\bar{p}$ Collisions at $\sqrt{s} = 1.96$ TeV*, Phys. Rev. Lett. **98** (2007) 122001.

[4] Heavy Flavor Averaging Group (HFAG), Y. Amhis *et al.*, *Averages of b-hadron, c-hadron, and tau-lepton properties as of early 2012*, arXiv:1207.1158 [hep-ex].

[5] C. H. Chou *et al.*, $\Lambda_b^0 \to \Lambda^0 Jpsi$ *decay in perturbative QCD*, Phys. Rev. D **65** (2002) 074030.

[6] ATLAS Collaboration, *Measurement of the* Λ_b^0 *lifetime and mass in the ATLAS experiment*, Phys. Rev. D **87** (2013) 032002.

[7] ATLAS Collaboration, *Measurement of the parity violating asymmetry parameter* α_b *and the helicity amplitudes for the decay* $\Lambda_b^0 \to J/\psi\Lambda^0$, Phys. Rev. D **89** (2014) 092009.

[8] ATLAS Collaboration, *The ATLAS Experiment at the CERN Large Hadron Collider*, JINST **3** (2008) S08003.

[9] V. Kostyukhin, *VKalVrt - package for vertex reconstruction in ATLAS*, ATL-PHYS-2003-031, https://cds.cern.ch/record/685551.

[10] T. Sjostrand, S. Mrenna, and P. Z. Skands, PYTHIA 6.4 Physics and Manual, JHEP **05** (2006) 026.

[11] ATLAS Collaboration, *ATLAS tunes of PYTHIA 6 and Pythia 8 for MC11*, ATL-PHYS-PUB-2011-009, https://cds.cern.ch/record/1363300.

[12] PDG Collaboration, J. Beringer *et al.*, *Review of Particle Physics*, Phys. Rev. D **86** (2012) 010001.

[13] T. Mannel and G. A. Schuler, *Semileptonic decays of bottom baryons at LEP*, Phys. Lett. B **279** (1992) 194-200.

[14] J. Hrivnac, R. Lednicky, and M. Smizanska, *Feasibility of beauty baryon polarization measurement in the* $\Lambda^0 Jpsi$ *decay channel with the pp collider experiment*, J. Phys. G **21** (1995) 629-638.

[15] LHCb collaboration, R. Aaij *et al.*, *Measurements of the* $\Lambda_b^0 \to \Lambda^0 J/\psi$ *decay amplitudes and the* Λ_b^0 *polarisation in pp collisions at* $\sqrt{s}$ *= 7 TeV*, Phys. Lett. B **724** (2013) 27-35.

[16] LHCb Collaboration, R. Aaij *et al.*, *Measurement of b-hadron masses*, Phys. Lett. B **708** (2012) 241-248.

[17] LHCb Collaboration, R. Aaij *et al.*, *Precision measurement of the* Λ_b^0 *baryon lifetime*, Phys. Rev. Lett. **111** (2013) 102003.

[18] CMS Collaboration, *Measurement of the* Λ_b^0 *lifetime in pp collisions at* $\sqrt{s}$ *= 7 TeV*, JHEP **07** (2013) 163.

[19] D0 Collaboration, V. M. Abazov *et al.*, *Measurement of the* Λ_b^0 *lifetime in the exclusive decay* $\Lambda_b^0 \to J/\psi\Lambda^0$ *in* $p\bar{p}$ *collisions at* $\sqrt{s} = 1.96$ TeV, Phys. Rev. D **85** (2012) 112003.

[20] CDF Collaboration, T. Aaltonen *et al.*, *Measurement of b hadron lifetimes in exclusive decays containing a* J/ψ *in* $p\bar{p}$ *collisions at* $\sqrt{s} = 1.96$ TeV, Phys. Rev. Lett. **106** (2011) 121804.

[21] N. Uraltsev, Phys. Lett. B378 (1996) 303; I. Bigi *et. al.*, Annu.Rev.Nucl.Part.Sci 47 (1997) 591; D. Pirjol and N. Uraltsev, Phys. Rev. D59 (1999) 034012; M. B. Voloshin, Phys. Rev. D **61** (2000) 074026.

[22] C. Tarantino, Eur. Phys. J. C33 (2004) s895 ; F. Gabbiani *et. al.*, Phys. Rev. D **70** (2004) 094031.

[23] Z. Ajaltouni *et. al.*, Λ_b^0 decays into Λ-vector, Phys. Lett. B **614** (2005) 165.

[24] O. Leitner *et. al.*, An angular distribution analysis of Λ_b^0 decays, Nucl. Phys. A **755** (2005) 435.

PoS(DIS2014)182

PROCEEDINGS OF SCIENCE

Flavour Tagging and Systematics for $B_s^0 \to J/\psi\phi$ Measurement in ATLAS

Tatjana Agatonović Jovin[*†]
Vinča Institute of Nuclear Sciences, University of Belgrade
12-14 Mihaila Petrovića Alasa, Belgrade, Serbia
E-mail: Tatjana.Jovin@cern.ch

The ATLAS experiment presents an updated measurement of *CP* violation in the B_s-meson system by studying the asymmetry of $B_s^0 \to J/\psi\phi$ decays into *CP* eigenstates using a *flavour-tagged* time-dependent analysis. Tagging the flavour of the initial-state B_s-meson is of particular importance in removing an ambiguity in the measurement of the weak mixing phase $\phi_s^{J/\psi\phi}$ present in the previous untagged measurement [1].

In this article, the principles and performance of flavour-tagging methods and modelling of systematic effects for $B_s^0 \to J/\psi\phi$ measurement are presented. The analysis presented here uses LHC proton-proton data at $\sqrt{s} = 7$ TeV collected by the ATLAS detector in 2011.

14th International Conference on B-Physics at Hadron Machines
April 8-12, 2013
Bologna, Italy

[*] Speaker.
[†] On behalf of the ATLAS collaboration.

PoS(Beauty 2013)070

1. Introduction

In the Standard Model, *CP* violation occurs through complex phases in the CKM matrix [2]. While the matrix elements, in which large phase occur (V_{ub} , V_{td}) generate large *CP* violation in the B_d^0 system, they do not appear in leading order diagrams contributing to either $B_s^0 \leftrightarrow \overline{B_s^0}$ mixing or to the decay $B_s^0 \to J/\psi\phi$. For this reason, the Standard Model expectation of *CP* violation in $B_s^0 \to J/\psi\phi$ is small (sub-leading penguin contributions are neglected). Experimentally, *CP* violation in $B_s^0 \to J/\psi\phi$ decay occurs *in the interference between mixing and decay*, when the B_s^0 mass eigenstates arising from $B_s^0 \leftrightarrow \overline{B_s^0}$ oscillations, decay into polarization states of the final $J/\psi\phi$ system with different *CP* eigenvalues. It is proportional to the weak mixing phase $\phi_s \sim \phi_M$ that is related to CKM matrix elements using the relation $\phi_s \cong -2\beta_s$ where $\beta_s = arg(-V_{ts}V_{tb}^* / V_{cs}V_{cb}^*)$. The small Standard Model value of $2\beta_s = (0.036 \pm 0.002)$ rad [3] yields a tiny value of *CP* violation. Many *new physics* models predict large ϕ_s values whilst satisfying all existing constraints. Consequently, processes such as $B_s^0 \leftrightarrow \overline{B_s^0}$ mixing play a prominent role in the search for new physics in $b \to s$ *flavour-changing neutral currents* (FCNC's).

In this article, the calibration and performance of the *flavour tagging* algorithms used for the updated measurement of time-dependent asymmetries in $B_s^0 \to J/\psi\phi$ decay in the ATLAS experiment are presented. Furthermore, the modelling of systematic effects for the $B_s^0 \to J/\psi\phi$ measurement is also described.

1.1 Phenomenology of the $B_s^0 \to J/\psi\phi$ decay

The $B_s^0 \leftrightarrow \overline{B_s^0}$ system is characterized by two eigenstates with different masses and decay rates. The states with definite mass and lifetime are physical eigenstates of the whole Hamiltonian $\mathcal{H}$ and they can be written as B_s^L (the lighter) and B_s^H (the heavier) that are linear combinations of the B_s^0 flavour eigenstates, $\left|B_s^L\right\rangle = p\left|B_s^0\right\rangle + q\left|\overline{B_s^0}\right\rangle$ and $\left|B_s^H\right\rangle = p\left|B_s^0\right\rangle - q\left|\overline{B_s^0}\right\rangle$. The *CP*-violating phase is defined as the weak phase difference between the $B_s^0 \leftrightarrow \overline{B_s^0}$ mixing amplitude and the $b \to c\bar{c}s$ decay amplitude. In the absence of *CP* violation, the B_s^H state would correspond exactly to the *CP*-odd state and the B_s^L to the *CP*-even state. The mass and width difference between B_s^H and B_s^L are defined as: $\Delta M_s = M_s^H - M_s^L$, $\Delta\Gamma_s = \Gamma_s^L - \Gamma_s^H$, with a mean decay width of $\Gamma_s = (\Gamma_s^H + \Gamma_s^L)/2$, where $M_s^{H,L}$ and $\Gamma_s^{H,L}$ denote the masses and decay widths of the B_s^H and B_s^L flavour eigenstates.

The $B_s^0 \to J/\psi\phi$ decay proceeds via three final state helicity configurations. Their linear combinations are *CP* eigenstates with different *CP* eigenvalues [4]. The two vector mesons J/ψ and ϕ can have their spins transversely polarized with respect to their momentum and be either parallel or perpendicular to each other. Alternatively, they can both be longitudinally polarized. These polarization states are denoted by $\left|\mathcal{P}_{\|}\right\rangle$, $\left|\mathcal{P}_{\perp}\right\rangle$ and $\left|\mathcal{P}_0\right\rangle$, where final states with orbital angular momentum L = 0 or 2 are *CP*-even, respectively $\left|\mathcal{P}_0\right\rangle$ and $\left|\mathcal{P}_{\|}\right\rangle$, while the state with L = 1 is *CP*-odd, $\left|\mathcal{P}_{\perp}\right\rangle$. Flavour tagging is used to distinguish between the initial B_s^0 and $\overline{B_s^0}$ states. For the extraction of *CP*-violating parameters, the amplitudes describing the decay to *CP*-eigenstates need to be separated statistically through the time-dependence of the decay and angular corellations among the final-state particles [5].

2. Flavour Tagging for $B_s^0 \to J/\psi\phi$ Measurement in ATLAS

To tag the *initial flavour* of neutral *B*-mesons, *opposite-side flavour tagging* (*OST*) algorithms are used [6], where the information from the other *B*-meson (tagging *B*) is exploited that is typically produced from the non-signal *b* quark in the event.

To study and calibrate the *OST* methods, the true dilution is extracted from the self-tagged control channel $B^{\pm} \to J/\psi K^{\pm}$. The flavour of the candidate meson is tagged by the charge of the daughter particle kaon, which predominantly decays into a muon of the same charge [7]. This gives a truth value to compare with the tagging decision, allowing the true dilution to be measured in the sample.

In this analysis, the events satisfy the same data quality, trigger and reconstruction selection criteria as those described in Ref. [8]. Tha data sample corresponds to approximately $\mathcal{L}$ = 4.5 fb^{-1} of integrated luminosity collected by the ATLAS detector from *pp* collisions in 2011.

The two inclusive methods are performed to infer the flavour of the *B*-meson:

- *opposite-side soft-lepton tagging* - by identifying the *muon cone charge* defined as a sum of charges of momentum weighted tracks in the cone around the highest p_T muon on the opposite side of the signal *B* decays.
- *opposite b-jet-charge tagging* - by identifying the charge of the opposite-side *b*-jet.

The discriminating variable *Q* is the muon cone charge or the jet charge defined as:

$$Q_{\mu;\,jet} = \frac{\sum_i^{N\,tracks} q^i \cdot \left(p_T^i\right)^{\kappa}}{\sum_i^{N\,tracks} \left(p_T^i\right)^{\kappa}}$$

where q^i and p_T^i are charge and transverse momentum of the track and κ is a scale parameter that is optimized yielding κ = 1.1. After reconstructing *Q* using the flavour-tagging calibration samples, the probability $P(B|Q)$ that the signal contains a $\bar{b}$ quark at production is calculated for each of the B^+ and B^-, defining $P(Q|B^+)$ and $P(Q|B^-)$, respectively.

The methodology is to search first for high-momentum muons and select all charged tracks with $p_T^i > 0.5$ GeV and $|\eta| < 2.5$ within a cone with radius $\Delta R < 0.5$ around the muon direction. In the absence of a muon, a *b*-flavour tagged jet [9] is required in the event with tracks associated to the same primary interaction vertex as the signal decay, excluding those from the signal candidate. The jet is reconstructed using the anti-k_t algorithm within a cone size $\Delta R = 0.6$. In the case of multiple jets, the jet with a highest value of the *b*-tag weight reference is used. The sum is over all track associated with the jet, using the method described in [6]. Figure 1 shows the distribution of charges for jet-charge and muon cone charge from $B^{\pm}$ signal-side candidates.

The sensitivity for measuring the *CP* asymmetry depends on the *tagging power* $\varepsilon_{eff} = \varepsilon\mathcal{D}^2 = \sum_i \varepsilon_i (2P_i(B|Q)-1)^2$, where ε_i is the *efficiency* of an individual tagger and $P_i(B|Q)$ is the probability that a specific event has a signal decay containing a $\bar{b}$ defined as $P_i(B|Q) = P_i(Q|B^+)/(P_i(Q|B^+) + P_i(Q|B^-))$ and $P_i(\bar{B}|Q) = 1 - P_i(B|Q)$, where the sum is taken over the bins of the probability distribution as a function of the charge variable.

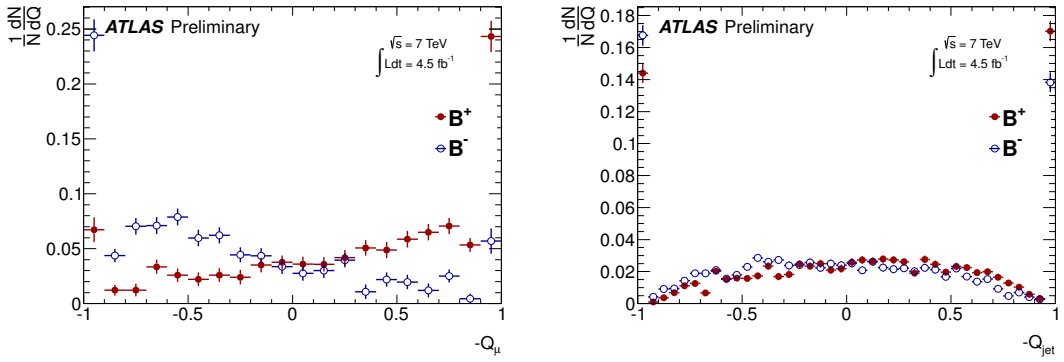

Figure 1: Muon cone charge distribution for $B^{\pm}$ *signal candidates for combined muons (left) and jet-charge distribution for* $B^{\pm}$ *signal candidates (right)* [8]

The efficiency, $\varepsilon = R + W/(R+ W + U)$, represents the fraction of tagged events to the entire sample, where R, W and U are the number of correctly tagged, incorrectly tagged and untagged events, respectively. The *effective dilution*, $\mathcal{D} = \sqrt{\sum_i \varepsilon_i (2P_i(B|Q)-1)^2 / \sum_i \varepsilon_i}$, is calculated for more than one tag and indicates how well the B meson is tagged correctly or incorrectly.

The combination of the tagging methods is applied according to the hierarchy of performance. A single best performing tagging measurement is taken, according to the order: muon, jet.

3. Systematic Uncertainties for $B_s^0 \to J/\psi\phi$

Systematic uncertainties are assigned by considering several effects that are not accounted for in the likelihood fit. These include:

- *Inner Detector Alignment* - the impact of the residual misalignment of the ID effecting the impact parameter (IP) distribution with respect to the primary vertex is estimated using simulated events with and without distorted geometry.
- *Angular acceptance method* - the systematic uncertainty introduced from the choice of binning; different acceptance functions are calculated using different bin width and central values.
- *Trigger efficiency* - to correct for the trigger lifetime bias, the events are re-weighted using the correction parameter ε, and the uncertainty of ε is used to estimate the systematic uncertainty due to the time efficiency correction.
- *Default fit model* - using the bias of the pull-distributions of 1500 pseudo-experiments multiplied by the statistical uncertainty of each parameter, the systematic uncertainty is calculated.
- *Signal and background mass model, resolution model, background lifetime and background angles model* - in order to estimate the size of the systematic uncertainty caused by the assumptions made in the fit, variations of the fit model are tested in pseudo-experiments.
- B_d *contribution* - systematic effects arising from the precision of the B_d fraction estimates are obtained by fitting the data with B_d fractions increased and decreased by 1σ.
- *Tagging* - this is estimated by comparing the default fit with the fits using the alternate tag-probability.

4. Results and Discussion

The tagging performance obtained for different taggers is given in Table 1. The errors are statistical only. The OST method shows comparable results to those of similar measurements, despite the limited number of taggers and relatively simple algorithm for their combination.

Table1: Summary of tagging performance for the different tagging methods [8]

Tagger	*Efficiency* [%]	*Dilution* [%]	*Tagging Power* [%]
Segment Tagged muon	1.08 ± 0.02	36.7 ± 0.7	0.15 ± 0.02
Combined muon	3.37 ± 0.04	50.6 ± 0.5	0.86 ± 0.04
Jet charge	27.7 ± 0.1	12.68 ± 0.06	0.45 ± 0.03
Total	32.1 ± 0.1	21.3 ± 0.08	1.46 ± 0.05

For each event, characterized by a value of discriminating variable Q, one can define the probability $P(Q|B^-)$ ($P(Q|B^+)$) that the decision, that on the opposite signal side b (or $\bar{b}$) quark is produced, is correct. This probability is further used in the likelihood fit, to extract the parameters of interest in $B_s^0 \to J/\psi\phi$ measurement, where each B_s candidate receives a per candidate probability and its statistical uncertainty.

The systematic treatment of the $B_s^0 \to J/\psi\phi$ fit results due to uncertainties in tagging is performed by varying the tag probabilities by the statistical uncertainty in each bin of the distribution, as well as varying the models of parametrizing the probability distributions, as described in Ref. [8].

5. Conclusion

Using data recorded in the 2011 run, the flavour-tagging technique and the treatment of systematic errors in an updated *CP* violation measurement in $B_s^0 \to J/\psi\phi$ decays, have been presented. The use of the opposite-charge muon and the b-jet-charge as the OST methods eliminates the ambiguity in the extraction of the *CP*-violating weak mixing phase ϕ_s and reduces its overall uncertainty, giving the measured value of $\phi_s = 0.12 \pm 0.25(\text{stat}) \pm 0.11(\text{syst})$ rad . This result is consistent with theoretical expectation lying within 1σ of the expected value in the Standard Model.

References

[1] ATLAS Collaboration, G. Aad et al., *Time-dependent angular analysis of the decay $B_s^0 \to J/\psi\phi$ and extraction of $\Delta\Gamma_s$ and the CP-violating weak phase ϕ_s by ATLAS*, *JHEP* **1212** (2012) 072 [arXiv:1208.0572] [hep-ex].

[2] M. Kobayashi and T. Maskawa, *CP-Violation in the Renormalizable Theory of Weak Interaction*, *Prog. Theor. Phys.* **49** (1973) 652.

[3] UTfit Collaboration, M. Bona et al., *Constraints on new physics from the quark mixing unitarity triangle*, *Phys. Rev. Lett.* **97** (2006) 151803, [arXiv:hep-ph/0605213].

[4] A. S. Dighe et al., *Angular distributions and lifetime differences in $B_s^0 \to J/\psi\phi$ decays*, *Phys. Lett.* **B 369** (1996) 144 [arXiv:hep-ph/9511363].

[5] I. Dunietz et al., *How to extract CP-violating asymmetries from angular correlations*, *Phys. Rev.* **D 43** (1991) 2193-2208.

[6] ATLAS Collaboration, G. Aad et al., *Expected Performance of the ATLAS Experiment - Detector, Trigger and Physics*, arXiv:0901.0512 [hep-ex].

[7] PDG Collaboration, K. Nakamura et al., *Review of particle physics,* *J.Phys.G.* **G37** (2010) 075021, and 2011 partical update for the 2012 edition.

[8] ATLAS Collaboration, G. Aad et al., *Flavour tagged time dependent angular analysis of the* $B_s^0 \to J/\psi\phi$ *decay and extraction of* $\Delta\Gamma_s$ *and the weak phase* ϕ_s *in ATLAS*, ATLAS-CONF-2013-039, http://cds.cern.ch/record/1541823.

[9] ATLAS Collaboration, G. Aad et al., *Commissioning of the ATLAS high-performance b-tagging algorithms in the 7 TeV collision data*, ATLAS-CONF-2011-102, http://cds.cern.ch/record/1369219.

PROCEEDINGS OF SCIENCE

CP Violation at ATLAS

Tatjana Jovin[*†]
Vinča Institute of Nuclear Sciences, University of Belgrade,
12-14 Mihaila Petrovića Alasa, Belgrade, Serbia
E-mail: Tatjana.Jovin@cern.ch

The Standard Model predicts a tiny CP-violating effect in the B_s-meson system that can be experimentally determined by the ATLAS experiment at LHC employing a time-dependent analysis of the 'golden' $B_s^0 \to J/\psi\phi$ decay channel to extract the weak mixing phase $\phi_s^{J/\psi\phi}$. Precise measurement of the mass and lifetime of the *B*-hadron is crucial for the measurement of the CP-violating quantities. To validate this, we test the performance of the ATLAS detector by measuring the mass and lifetime of the B_s^0 meson using the $B_s^0 \to J/\psi\phi$ decay. In parallel, the measurement of the mass and lifetime of the B_d^0 meson is performed using the decay channel $B_d^0 \to J/\psi K^{*0}$ as it represents an excellent control channel.
The final state particles from $B_s^0 \to J/\psi\phi$ and $B_d^0 \to J/\psi K^{*0}$ decays are reconstructed in the ATLAS detector using proton-proton collision data at a center-of-mass energy of 7 TeV corresponding to an integrated luminosity of 40 pb^{-1}. Within the statistical uncertainties, the fitted masses and lifetimes of both *B* mesons are consistent with the world average values.

The XIth International Conference on Heavy Quarks and Leptons,
Prague, Czech Republic
June 11-15, 2012

[*] Speaker.
[†] On behalf of the ATLAS collaboration.

PoS(HQL 2012)038

1. Introduction

The Standard Model of particle physics (SM) predicts a violation of the CP symmetry, by including a single irreducible complex phase in the CKM matrix. All measurements of the CP-violating processes, from its discovery in neutral K decays in 1964 through the recent observations in B decays, proof that the CKM phase is different from zero, providing that the matrix of three-generation quark mixing is the dominant source of CP violation within the SM. However, almost all extensions of the SM imply that there are additional sources of CP violation and despite SM phenomenological success it fails to accommodate the observed matter-antimatter asymmetry in the universe by several orders of magnitude. This discrepancy suggests that nature provides additional sources of CP violation beyond the SM.

Thus, the main task of modern day physics is to test the key predictions of the SM, to search for the source of CP violation within it and to search for discrepancies providing evidence for physics beyond the SM that establish a connection between the observed CP violation and the one needed to explain baryon asymmetry.

At present, a promising strategy adopted by the ATLAS experiment at LHC is to study processes where the SM predicts a small CP violation, while SM extensions predict large CP violation effects.

1.1 CP violation in the neutral B_s^0 system

The ATLAS experiment sets its first measurement of CP violation in the B_s-meson system by studying the asymmetry of neutral meson decays into final CP eigenstates, using an untagged time-dependent analysis.

Flavour change via the weak interaction gives rise to $B_s^0 - \overline{B_s^0}$ mixing, and consequently, the B_s^0 meson is found in the quantum superposition states denoted as "heavy" and "light" (B_s^H and B_s^L) which are CP eigenstates, odd and even respectively. Both states have different masses and lifetimes. The oscillation frequency of B_s^0 meson mixing is characterized by the mass difference Δm_s of the B_s^H and B_s^L mass eigenstates and by the CP-violating phase $\phi_s^{J/\psi\phi}$ which arises from the interference between the decay and the mixing. Contrary to any other system, the B_s^0 meson is strongly mixed and thus provides a fruitful domain to search for CP-violating effects. Another physical quantity involved in $B_s^0 - \overline{B_s^0}$ mixing is the decay width difference $\Delta\Gamma_s = \Gamma_L - \Gamma_H$ of B_s^L and B_s^H. Physics beyond the SM is not expected to affect $\Delta\Gamma_s$ as significantly as $\phi_s^{J/\psi\phi}$ [1]. Extracting $\Delta\Gamma_s$ from the data is nevertheless useful as it allows theoretical predictions to be tested.

The decay $B_s^0 \to J/\psi\phi$ is a pseudo-scalar to vector-vector transition. Since J/ψ and ϕ are vector mesons they can have an even or odd relative orbital momentum L in the final state (L = 0, 1, 2). Due to total angular momentum conservation, the final state is therefore an admixture of CP-even (L = 0, 2) and CP-odd (L = 1) states. Consequently, the decay is described by three time-dependent complex amplitudes corresponding to polarisation states of the vector mesons. The resulting admixture tends to dilute (or cancel) the overall CP asymmetry. Using an *angular analysis* method the different CP components could be separated statistically and the CP information can be obtained without dilution [2, 3].

In the absence of CP violation, the B_s^H state would correspond exactly to the CP-odd state and the B_s^L to the CP-even state.

The main reasons why the decay $B_s^0 \to J/\psi\phi$ is considered the 'golden' channel in the study of CP violation with the ATLAS experiment are:

- Theoretically clean sample. This implies that the CP-violating phase $\phi_s^{J/\psi\phi}$ is one of the CP observables with the smallest theoretical uncertainty;
- The phase $\phi_s^{J/\psi\phi}$ is predicted to be small in the SM ~ $O(10^{-2})$ and a precise measurement of $\phi_s^{J/\psi\phi}$ could therefore lead to an indirect discovery of New Physics that would contribute to the $B_s^0 - \overline{B_s^0}$ box diagrams. Measurement of $\phi_s^{J/\psi\phi}$ thus presents a very sensitive probe for New Physics.

In addition, the following topics make the decay channel $B_s^0 \to J/\psi\phi$ interesting as well:

- Experimentally clean sample. This provides clear experimental signature and good separation from background;
- The expected sizeable width difference ($\Delta\Gamma_s$) allows the extraction of CKM phases from untagged B_s^0 data samples, where the rapid oscillations terms ($\Delta m_s t$) cancel out [4];
- This mode has a relatively large branching fraction and with the gigantic B-hadron production rate at LHC (10^{12} $b\bar{b}$ pairs per year/experiment, during the first three years of operation) it will allow large data samples to be accumulated.

The $B_d^0 \to J/\psi K^{*0}$ channel provides a valuable testing ground for measurements of $B_s^0 \to J/\psi\phi$ due to its equivalent topology and similar helicity structure of the final state, with the advantage of higher statistics. The final state of $B_d^0 \to J/\psi K^{*0}$ decay, with a subsequent decay of K^{*0} to charged mesons K and π, allows the flavour of the decaying B_d^0 to be determined. This decay mode will therefore be used to determine the flavour tagging performance in the CP violation studies of $B_s^0 \to J/\psi\phi$ decay.

2. ATLAS detector

2.1 B-physics potential of the ATLAS detector

The ATLAS experiment [5] is a general-purpose particle physics detector with a forward-backward symmetric cylindrical geometry near 4π coverage in the solid angle. New particle searches at the nominal LHC luminosity have defined most of the performance specification of the ATLAS detector. B-physics requirements have been accommodated in the design of the inner detector, the trigger systems and the muon system that are of particular importance of the reconstruction of *B* meson candidates.

The inner tracking detector (ID), surrounded by a superconducting solenoid providing 2T magnetic field, consists of the silicon pixel detector (Pixel), the silicon microstrip detector (SCT) and the transition radiation tracker (TRT). Inner Detector has full coverage in ϕ and covers the pseudorapidity range $|\eta| < 2.5$, with the transverse momentum resolution of $\Delta p_T / p_T = 0.04\% \times p_T \oplus 2\%$ (p_T in GeV) and the resolution of the impact parameter

$\sigma(d_0) = 10\,\mu\text{m}$ ($p_T > 10\,\text{GeV}$). The primary vertex resolution for events with 70 tracks or $\sqrt{\Sigma_{trk}\, p_T^2}$ over 8 GeV has been measured to be ~ 30 μm in the transverse plane and about 50 μm in the longitudinal direction [6]. Typical position resolutions for hits in the Pixel, SCT and TRT are 10, 17 and 130 μm for the *R*-ϕ coordinate, respectively, and in case of the Pixel and SCT, 115 and 580 μm for the *z* coordinate.

The muon spectrometer (MS) surrounds the calorimeters and consists of three large superconducting toroids with eight coils each providing a 0.5 T magnetic field, a system of tracking chambers and detectors for triggering. The MS covers a pseudorapidity region of ± 2.7, with the transverse momentum resolution of $\sigma/p_T < 10\%$ for tracks up to 1 TeV, translating a sagitta along the z-axis of about $500\,\mu\text{m}$ to be measured with a resolution of about $50\,\mu\text{m}$. The muon system is essential for momentum measurements and triggering of muons. For muons with $p_T > 40\,\text{GeV}$ the momentum resolution obtained with the MS is better than the resolution obtained by the ID. For lower p_T muons the ID measurements will determine the momentum resolution but measurements from the MS are still required to identify ID tracks as muons.

The ATLAS B-triggers used to select $B_s^0 \to J/\psi\phi$ and $B_d^0 \to J/\psi K^{*0}$ decays are based on the identification of a $J/\psi \to \mu^+\mu^-$ decay, with either a 4 GeV p_T threshold for both muons or an asymmetric configuration that applies a higher p_T threshold (4-10 GeV) on one of the muons and a looser muon-identification requirement (p_T threshold below 4 GeV) on the other one.

3. Reconstruction and candidate selection

3.1 Selection of B_s^0, B_d^0 and J/ψ candidates

Alongside good quality data coming from the fully operational muon, tracking and trigger systems, events are required to pass the following additional criteria. The event must contain at least one reconstructed primary vertex built with at least four associated ID tracks in order to be considered as a collision candidate. Tracks are required to have at least one hit in the pixel detector and at least four hits in the semiconductor tracker. The event must contain at least one pair of oppositely charged muon candidates that are reconstructed using two algorithms as described in Ref. [7]. The muons are not required to match the object(s) that fired the trigger. No cuts on the p_T of the muons are applied other than the implicit ones in the muon reconstruction.

The muon pair tracks are refitted to a common vertex [8] and accepted for further consideration if the fit results in a $\chi^2/n.d.o.f. < 10$. The invariant mass is calculated from the refitted track parameters. To account for a varying mass resolution the J/ψ candidates are divided into three subsets according to the pseudorapidity η of the muons. A maximum likelihood fit is used to extract the J/ψ mass and the corresponding resolution for these three subsets, using the method described in [9]. When both muons have $|\eta| < 1.05$ the accepted signal candidates are from a region (2959-3229) MeV. When one muon has $1.05 < |\eta| < 2.5$ and the other muon $|\eta| < 1.05$, the corresponding signal region is (2913-3273) MeV. For the third subset, where both muons have $1.05 < |\eta| < 2.5$, the signal region is (2852-3332) MeV. In each case, the signal region is defined to retain 99.8% of the J/ψ signal identified in the fits.

3.2 Selection specific to $B_d^0 \to J/\psi K^{*0}$

The K^{*0} candidates are reconstructed by selecting all pairs of oppositely charged tracks that have not been previously identified as muons, with $p_T > 0.5\,\text{GeV}$ and $|\eta| < 2.5$. Together with the two tracks from the $J/\psi \to \mu^+\mu^-$ decay, these are fitted to a common vertex. In the fit the two muon tracks are constrained to the PDG J/ψ mass value of (3096.916 ± 0.011) MeV [10]. These quadruplets of tracks are accepted for further selections if the fit has a $\chi^2/n.d.o.f. < 2.5$. The new track parameters resulting from the vertex fit are used to calculate the invariant mass of K^{*0} candidates under the assumption that they are $K^+\pi^-$ hadrons. These pairs are assumed to be from K^{*0} decays if the invariant mass falls within the interval (846-946) MeV and the transverse momentum of the K^{*0} candidate is greater than 2.5 GeV. No attempt to use particle identification for the kaon or pion is made in the current study. For each candidate, both $K^{\pm}\pi^{\mp}$ combinations are tested and in cases when both combinations satisfy the mass criterion, the one closest to the K^{*0} is chosen. In cases where more than one candidate per event is found, only the B_d^0 candidate with the lowest $\chi^2/n.d.o.f.$ is retained. The B_d^0 candidates with invariant mass from the interval (5159-5399) MeV are selected for the further analysis.

3.3 Selection specific to $B_s^0 \to J/\psi\phi$

The $\phi \to K^+K^-$ candidates are reconstructed from all pairs of oppositely charged tracks with $p_T > 0.5\,\text{GeV}$ and $|\eta| < 2.5$, which are not identified as muons. $B_s^0 \to J/\psi(\mu^+\mu^-)\phi(K^+K^-)$ candidates are selected by fitting the tracks from each combination of $J/\psi \to \mu^+\mu^-$ and $\phi \to K^+K^-$ to a common vertex. The two muon tracks are constrained to the PDG J/ψ mass. These quadruplets of tracks are assumed to be from $B_s^0 \to J/\psi(\mu^+\mu^-)\phi(K^+K^-)$ decays if the fit results in a $\chi^2/n.d.o.f. < 2$, the fitted p_T of each track from $\phi \to K^+K^-$ is greater than 1 GeV and the invariant mass of the track pairs (under the assumption that they are kaons) falls within the interval $1009\,\text{MeV} < m(K^+K^-) < 1031\,\text{MeV}$. If there is more than one B_s^0 candidate per event then the candidate with the lowest $\chi^2/n.d.o.f.$ is chosen.

4. Method of fit

An unbinned maximum-likelihood fit is performed to extract the B_s^0 (B_d^0) meson mass and lifetime. The likelihood function is defined by:

$$L = \prod_{i=1}^{N} \left(f_{sig}\,\mathcal{M}_{sig}(m_i)\mathcal{T}_{sig}(t_i) + (1 - f_{sig})\,\mathcal{M}_{bkg}(m_i)\mathcal{T}_{bkg}(t_i) \right)$$

where f_{sig} is the fraction of the signal events of the total number of events, N. $\mathcal{M}_{sig}$ and $\mathcal{M}_{bkg}$ are probability density functions (PDF) that model signal and background mass distributions. The terms $\mathcal{T}_{sig}$ and $\mathcal{T}_{bkg}$ describe the decay time distributions of the signal $B_s^0 \to J/\psi\phi$ ($B_d^0 \to J/\psi K^{*0}$) and backgrounds $b\bar{b} \to J/\psi X$ and $pp \to J/\psi X$, respectively. The input variables to the maximum likelihood fit extracted from data are the proper decay time t_i, its

uncertainty δ_{ti}, the mass m_i and its uncertainty δ_{mi} for each B_s^0 (B_d^0) candidate passing the selections.

For the signal, the mass is modelled with a Gaussian distribution and the proper decay time distribution of the *B* candidates is modelled as an exponential function convolved with the proper decay time resolution function.

For the background, the mass distribution is modelled with a linear function, while the proper decay time is modelled depending of the source expected to contribute to the background. For the background containing the promptly produced J/ψ, the proper decay time is described by the resolution function; for the background candidates from non-prompt J/ψ production the proper decay time is described by the sum of the exponential functions, each convolved with the resolution function. Subsequently, all components of the time background PDFs are summed up, relative to their contributions.

The following parameters are left free in the fit: the fraction of the signal events in the mass region of the fit (f_{sig}), the fitted *B* meson mass (m_B) and lifetime (t_B), the slope of the linear background, two scale factors accounting for a difference between measured per-candidate m_i (t_i) errors and the overall mass (proper decay time) resolution and the lifetimes characterising background components of the exponential shape.

The values of the free parameters and a covariance matrix returned by the fit are used to calculate the number of *B* meson signal decays N_{sig}, the mass resolution σ_m and the number of background events N_{bkg} in the mass interval $m_B \pm 3\sigma_m$, where the mass resolution σ_m is defined by FWHM of the *B* mass distribution. The uncertainty on σ_m is calculated using the covariance matrix of the fit. The number of background events N_{bkg} in the mass interval $m_B \pm 3\sigma_m$ and its error are calculated from the fraction of the signal events in the mass region of the fit, the slope of the linear background and the total number of events.

As the available statistics grows it will be possible to add additional terms to the maximum likelihood fit to include decay angles in order to perform an angular analysis, thus allowing extraction of the physics parameters of interest.

5. Results

5.1 Fit results

The likelihood function defined in Section 4. is used in the simultaneous mass and lifetime fit performed on the *B* meson candidates selected by criteria described in Section 3. Figure 1 shows the invariant mass and proper decay time distributions for the selected B_d^0 candidates, overlaid with the fit functions for mass and lifetime obtained by the fit method described in Section 4. Figure 2 shows the invariant mass and proper decay time distributions for the selected B_s^0 candidates. The results of the simultaneous mass and lifetime fit is projected onto the distributions. The results of the key parameters of the mass and lifetime fits for B_d^0 and B_s^0 mesons are summarised in Table 1. The errors given in Table 1 are statistical only. Systematic effects important for this analysis are summarised and evaluated in the next section.

Table 1: Fit parameters determined from the simultaneous mass and lifetime fits of B_d^0 and B_s^0 candidates. Errors are statistical [11].

	t_B [ps]	m_B [MeV]	$\pm_m$ [MeV]	N_{sig}
B_d^0	1.51 ± 0.04	5279.0 ± 0.8	34.3 ± 0.9	2750 ± 90
B_s^0	1.41 ± 0.08	5363.7 ± 1.2	24.8 ± 1.2	463 ± 26

5.2 Systematic uncertainties

The goal of this analysis is to validate the lifetime measurement technique in preparation for CP violation studies and those systematic effects that are believed to be the most important are considered: modelling of signal and background in likelihood fit, fitting procedure, size of the mass window, time uncertainty model, choice of primary vertex and alignment of the Inner Detector. For the data used in this analysis, no systematic uncertainty is assigned due to the fitting procedure and the primary vertex selection method. A summary of all assigned systematic uncertainties is given in Table 2.

Table 2: Systematic uncertainties in the B_d^0 and B_s^0 lifetime measurement [11].

Source of systematics	Systematic uncertainty	
	$\delta_{\text{syst}}(t_{Bd})$ [ps]	$\delta_{\text{syst}}(t_{Bs})$ [ps]
Modelling signal, background	0.01	0.01
Time uncertainty model	0.03	0.03
Mass window	0.01	0.02
Alignment	0.03	0.03
Total, quadratic sum	0.04	0.05

5.3 Discussion of results

The results demonstrate that a simultaneous unbinned maximum likelihood fit to mass and lifetime using per-candidate errors can be used to separate B_s^0 and B_d^0 signals from background. A single exponential fit can be applied to the signal events. The estimated sizes of the systematic errors on the B_s^0 and B_d^0 lifetimes are comparable to their statistical errors.

Measured masses and lifetimes of B mesons agree with the world averages within the precision of the current analysis. Since the $B_s^0 \to J/\psi\phi$ final state is dominated by the shorter-lived component of B_s^0 mesons, the single exponential model applied in the current study is inherently biased. However, within the current precision the fitted value agrees well with the world average $1/\Gamma_s = 1/(\Gamma_L - \Gamma_H)/2$ [10]. The lifetime value returned by the fit is closer to the shorter lifetime, $1/\Gamma_L = 1.408^{+0.033}_{-0.030}\ ps$ [12].

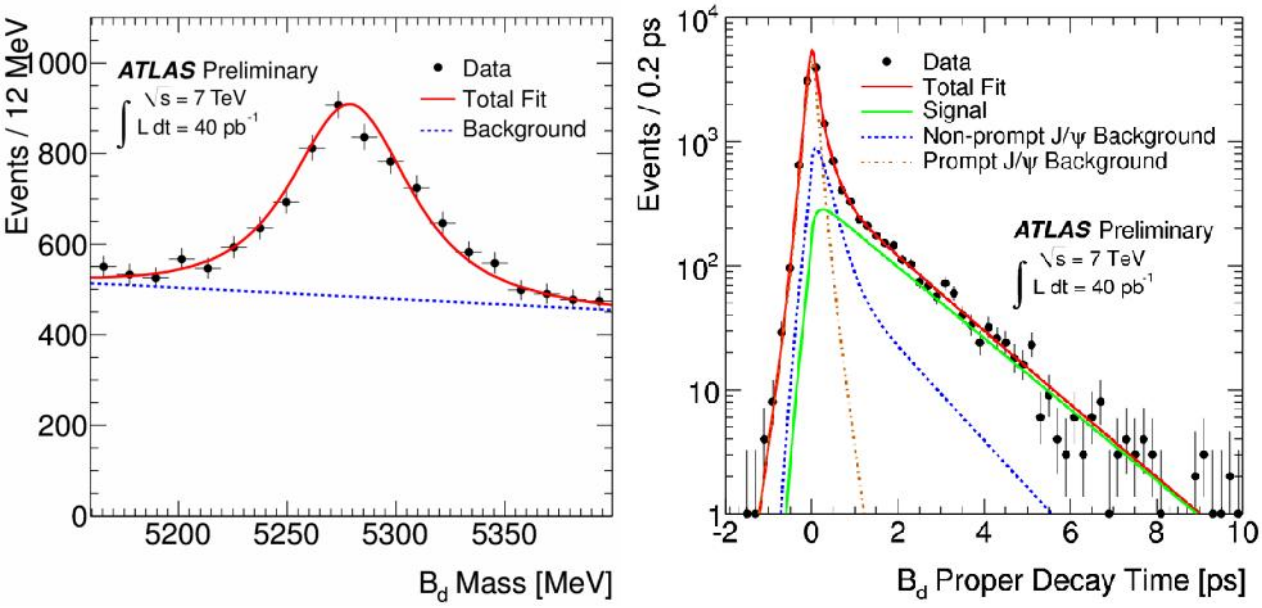

Figure 1: Invariant mass (left) and proper decay time (right) distributions of reconstructed $B_d^0 \to J/\psi K^{*0}$ decay candidates [11].

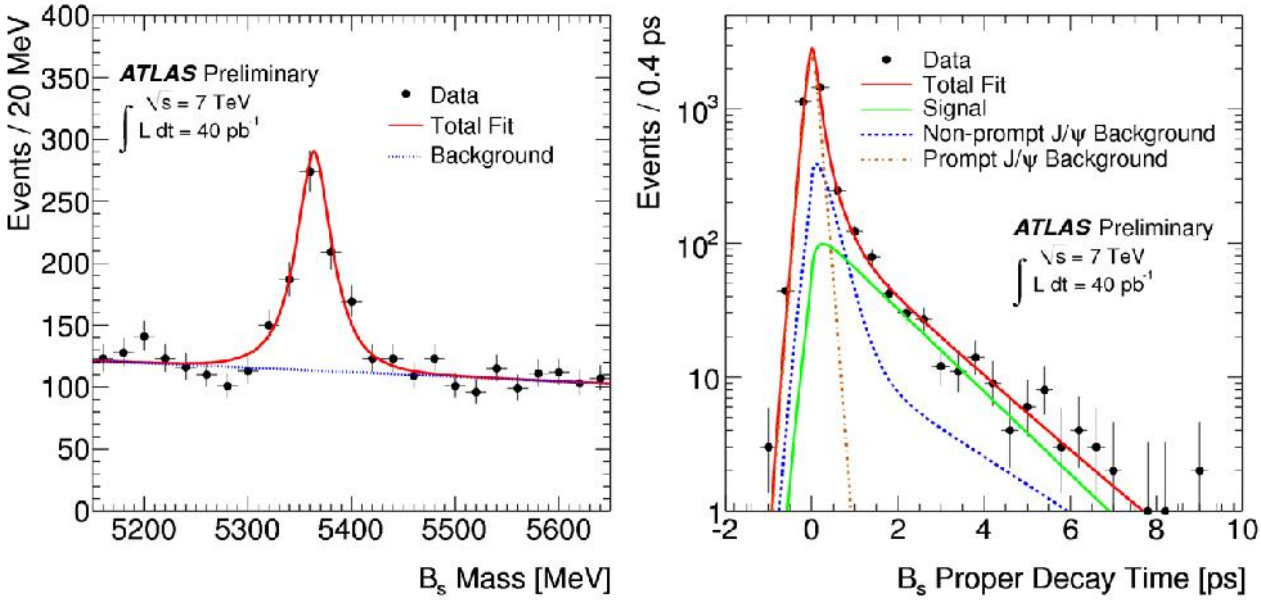

Figure 2: Invariant mass (left) and proper decay time (right) distributions of reconstructed $B_s^0 \to J/\psi\phi$ decay candidates [11].

6. Conclusion

The performance of the ATLAS detector towards CP violation measurements has been tested. Using 40 pb^{-1} of *pp* collision data at 7 TeV the B_s^0 and B_d^0 mesons are reconstructed from their decays $B_s^0 \to J/\psi\phi$ and $B_d^0 \to J/\psi K^{*0}$. The masses and proper decay times of B_s^0 and B_d^0 candidates are measured using a simultaneous unbinned maximum likelihood fit. The results show agreement with the world average values confirming the validity of the methods for reconstructing primary and secondary vertices and measuring the transverse decay length.

This analysis validate the capability of the ATLAS experiment to measure masses and lifetimes of both B_s^0 and B_d^0 mesons with high precision and thus to meet the requirements necessary to perform precision CP violation measurements.

References

[1] A. Lenz and U. Nierste, *Theoretical update of* $B_s^0 - \overline{B_s^0}$ *mixing*, JHEP **06** (2007) 072, arXiv:hep-ph/0612167.

[2] A.S. Dighe, I. Dunietz, H.J. Lipkin and J.L. Rosner, *Angular Distributions and Lifetime Differences in* $B_s^0 \to J/\psi\phi$ *decays*, Phys. Lett. **B369** (1996) 144.

[3] A.S. Dighe, I. Dunietz and R. Fleischer, *Extracting CKM Phases and* $B_S^0 - \overline{B_S^0}$ *Mixing Parameters from Angular Distributions of Non-Leptonic B Decays*, Eur. Phys. J. **C6** (1999) 647.

[4] I. Dunietz, $B_s^0 - \overline{B_s^0}$ *Mixing, CP violation, and extraction of CKM phases from untagged* B_s^0 *data samples*, Phys. Rev. **D52** (1995) 3048.

[5] ATLAS Collaboration, *The ATLAS Experiment at the CERN Large Hadron Collider*, JINST **3** (2008) S08003.

[6] ATLAS Collaboration, *Performance of primary vertex reconstruction in proton-proton collisions at* $\sqrt{s} = 7$ TeV *in the ATLAS experiment*, ATLAS-CONF-2010-069, http://cdsweb.cern.ch/record/1281344.

[7] ATLAS Collaboration, *Observation of the* B_d^0 *and* B_s^0 *mesons in the decays* $B_d^0 \to J/\psi K^{*0}$ *and* $B_s^0 \to J/\psi\phi$ *in ATALS*, ATLAS-CONF-2011-050, http://cdsweb.cern.ch/record/1341815.

[8] ATLAS Collaboration, *VKalVrt - package for vertex reconstruction in ATLAS*, ATL-PHYS-2003-031, http://cdsweb.cern.ch/record/685551.

[9] ATLAS Collaboration, *First observation of the* $J/\psi \to \mu^+\mu^-$ *resonance in ATLAS pp collisions at* $\sqrt{s} = 7$ TeV , ATLAS-CONF-2010-045, http://cdsweb.cern.ch/record/1277685.

[10] K. Nakamura et al., *(Particle Data Group)*, J. Phys. G **37** (2010) 075021.

[11] ATLAS Collaboration, *Measurement of the* B_d^0 *and* B_s^0 *lifetimes in the decay modes* $B_d^0 \to J/\psi K^{*0}$ *and* $B_s^0 \to J/\psi\phi$ *in ATLAS*, ATLAS-CONF-2011-092, http://cdsweb.cern.ch/record/1363779.

[12] O. Schneider et al., $B_s^0 - \overline{B_s^0}$ *Mixing*, J. Phys. G **37** (2010) 075021.

Luminosity Measurement at ILC

I. Bozovic-Jelisavcic[1*] and H. Abramowicz[2], P. Bambade[3], T. Jovin[1], M. Pandurovic[1], B. Pawlik[4], C. Rimbault[3], I. Sadeh,[2] I. Smiljanic[1]

1 – Vinca Institute of Nuclear Sciences, University of Belgrade
Belgrade – Serbia

2 – School of Physics and Astronomy, Tel Aviv University
Tel Aviv – Israel

3 – LAL, University Paris-Sud, IN2P3/CNRS
Orsay – France

4 – Institute of Nuclear Physics PAN
Cracow – Poland

More than twenty institutes join the FCAL Collaboration in study of design of the very forward region of a detector for ILC and CLIC. Of particular importance is an accurate luminosity measurement to the level of 10^{-3}, a requirement driven by the potential for precision physics at a future linear collider. In this paper, the method for luminosity measurement, requirements on luminometer and its integration in the forward region are presented. The impact of several effects contributing to the systematic uncertainty of luminosity measurement is given.

1 Introduction

Physics requirements like production cross-sections measurements, anomalous gauge boson couplings, EW physics and new physics searches impose the high precision of luminosity measurement at a future linear collider. Luminosity will be measured from Bhabha scattering that is dominantly QED process at ILC energies. Achievable precision is limited both by the reconstruction of scattered Bhbha particles as well as by physics effects which have to be experimentally controlled (beam-beam effects, presence of physics background). At the same time, there is an on-going theoretical effort to complete NLO corrections of the Bhabha cross-section.

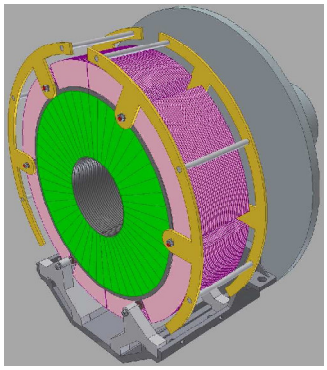

Figure 1: Mechanical structure of the luminosity calorimeter.

2 Luminometer at ILC

Luminosity calorimeter is foreseen as a sampling silicon/tungsten calorimeter consisting of 30 one radiation length thick absorber planes followed by segmented silicon sensor planes. To keep the Moliere radius of 1.5 cm, 1 mm sensor gaps are provided. As illustrated in Figure 1,

* This study has been supported by: Ministry of Science and Technology of the Republic of Serbia through the Project No. 15004B and also by the Commission of the European Communities under the 6th Framework Program "Structuring the European Research Area", contract number RII3-026126.

tungsten disks are precisely positioned using 4 bolts. The system is additionally stabilized by steel rings. Reconstruction of the polar angle of electron is influenced by sensor segmentation that is optimized to 48/64 azimuthal/radial divisions. Luminosity calorimeter is positioned 2.5 m from the IP, with the geometrical aperture between 31 mrad and 78 mrad. Sufficient statistics corresponding to the 2.1 nb of integrated cross-section of the signal is obtained in the detector fiducial volume defined within [41,69] mrad [1]. By restricting the signal for luminosity measurement to the detector fiducial volume, only events with no shower leakage through the edges of luminosity calorimeter are selected. In this volume, a stable sampling term α_{res} (2.1), usually referred to as 'energy resolution', is obtained (Figure 2).

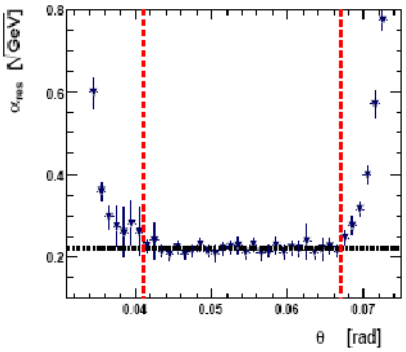

Figure 2: Energy resolution for 250 GeV electrons as a function of the polar angle. Dashed lines mark fiducial volume of the luminosity calorimeter.

In (1.1), the usual parameterization of energy resolution σ_E corresponding to the standard deviation of an energy distribution with a mean E, deposited by electron beam E_{beam} is given:

$$\frac{\sigma_E}{E} = \frac{\alpha_{res}}{\sqrt{E_{beam}[GeV]}} \qquad (2.1)$$

Simulating only electron showers inside the luminometer's fiducial volume, α_{res} is estimated to be: $\alpha_{res} = (0.21 \pm 0.02_{stat})\sqrt{GeV}$. Parameter α_{res} is found to be independent of the shower energy in the range from 50 GeV to 300 GeV. In the same range, the response of luminosity calorimeter is linear with respect to the shower energy [1]. The position of an EM shower in the detector is reconstructed by performing a weighted average over the depositions on individual pads. The weight W_i, of a given detector pad *i*, is determined by logarithmic weighting [2], for which $W_i = max\{0, C + \ln(E_i/E_{tot})\}$. The symbol E_i refers to the individual pad energy, E_{tot} is the total energy in all pads, and C is a constant. In this way, only pads which contain a sufficient fraction of the shower energy contribute to the reconstruction. The polar angle resolution σ_θ, and a polar angle measurement bias $\Delta\theta$, are defined as the Gaussian width and the central value of the distribution of the difference between reconstructed and generated polar angles. They are found to be $(2.2 \pm 0.01)\cdot 10^{-2}$ mrad and $(3.2 \pm 0.1)\cdot 10^{-3}$ mrad, respectively. Uncertainties of α_{res}, σ_θ and $\Delta\theta$ will be considered in Chapters 3.2.3 and 3.2.4 as sources of systematic uncertainty for the luminosity measurement.

3 Luminosity measurement an ILC

3.1 Method

At ILC, the integrated luminosity will be determined from the counted number of Bhbaha

events reconstructed in the detector fiducial volume N_{exp}, corrected for the number of miss-counted events due to various systematic effects. As shown in (3.1), the measured luminosity will also depend on the selection efficiency ε and the theoretical cross-section for Bhabha scattering σ_B.

$$L_{\text{int}} = \frac{N_{\text{exp}} - \sum_i N_i^{cor}}{\varepsilon \cdot \sigma_B} \tag{3.1}$$

In order to exploit the characteristic topology of Bhabha events with two back-to-back showers deposited almost full beam energy in forward and backward arms of the detector and, at the same time, minimize the suppression of the Bhbaha cross-section due to beam-beam effects, the following empirical selection is applied [3]: the polar angle of the reconstructed shower must be within the detector fiducial volume [θ_{min}, θ_{max}] at one side and within [θ_{min}+4 mrad, θ_{max}-7mrad] at the other, and the total energy deposited in the luminometer must be more than 80% of the center-of-mass energy. Polar angle criterion is subsequently applied at the forward and backward side of the detector in order to avoid systematic bias from the longitudinal position of the interaction point.

3.2 Systematic uncertainties

3.2.1 Beam-beam effects

The acceleration of electrons and positrons towards the bunch center when bunches are crossing changes their momentum and, more importantly, electrons and positrons radiate beamstrahlung prior to Bhabha scattering. In addition, final state Bhabha particles get focused by the electromagnetic field of the opposite space charge. The result is an effective reduction of the Bhabha cross-section in the detector fiducial volume, with the dominant contribution stemming from the beamstrahlung. Size of this Bhabha Suppresion Effect (BHSE) is found to depend on selection criteria for the luminosity measurement, amounting to $1.51\%\pm(0.05\%)_{stat}$ [3]. for nominal beam parameters at 500 GeV center of mass energy, for the proposed event selection. BHSE can be understood as an effect one can correct for, once its experimental uncertainty is known. Data-driven method to measure the beamstrahlung component of BHSE has been proposed, based on the reconstruction of the luminosity spectrum [3]. Experimental uncertainty is resulting from the precision to which bunch sizes σ_x and σ_z are measured. In this paper, a BHSE experimental uncertainty is chosen to correspond to the 5% relative error of the bunch size measurement.

3.2.2 Background from physics processes

Four-fermion production via Neutral Current is known to have a large cross-section with maxima at low polar angles. It is dominated by the multiperipheral Feynman diagram where two virtual photons are exchanged between electron spectators. The spectators remain at high energy. Less than 1% of spectators hits the luminosity calorimeter and manifests as a background for Bhabha events. The cross-section amounts to (12.0±0.5) nb at 500 GeV assuming photons with momentum larger than 0.1 GeV/c being exchanged. We used the WHIZARD [4] event generator to obtain sample of events for final states with leptons in the inner legs. Event generator is tuned to reproduce LEP data for charm production in two-

photon processes [5] by adjusting the minimal exchanged momentum of the photon to 10^{-4} GeV/c. A Bhabha sample of 5 pb^{-1} has been generated with the cross-section of (4.70±0.03) nb, at 500 GeV, using the BHLUMI [6] event generator. As mentioned in 3.1, the event selection is optimized to reduce Bhabha suppression from space charge effects. After the selection is applied, the overall impact of four-fermion events on luminosity measurement saturates around background to signal ratio B/S=2.3 10^{-3} at 500 GeV. The Bhabha event selection efficiency is sufficient to maintain statistical error below 10^{-3} for annual running at 500 GeV and at nominal luminosity. Projection of background hits on the front plane of the luminosity calorimeter is shown in Figure 3, before and after event selection is applied.

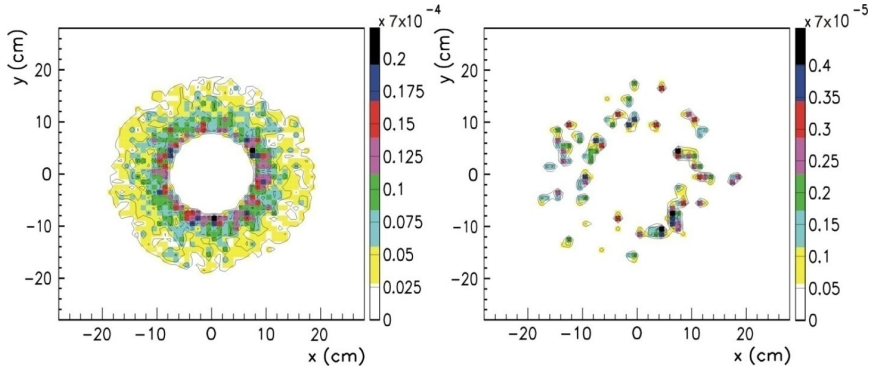

Figure 3: Projections of background hits in the luminometer front plane before *(left)* and after the event selection *(right)*.

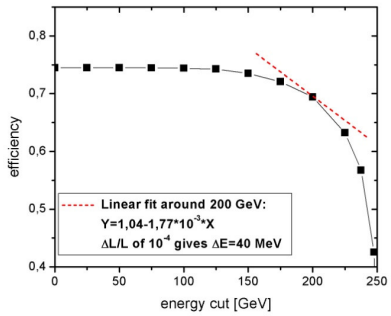

Figure 4: Selection efficiency dependence on the cut-off energy.

3.2.3 Effects from energy resolution and bias of energy scale

Event selection for the luminosity measurement is based on the criterion that the total deposited energy in the fiducial volume of the luminosity calorimeter is more than 80% of the center of mass energy. A possible uncertainty of the Bhabha selection efficiency due to the bias of measured energy, or the uncertainty of the stochastic term α_{res} in (2.1), will result in a corresponding uncertainty of luminosity measurement.

To keep the contribution to the luminosity uncertainty below 10^{-4}, the absolute uncertainty of the measured deposited energy in the luminosity calorimeter (ΔE) would have to be 39 MeV. This results from the linear fit (Figure 4) at the energy cut-off, with the slope of $-1.77 \cdot 10^{-3}$. Detector energy resolution must be understood to $\Delta\alpha_{res}$=2.5% to contribute to the relative

uncertainty in luminosity of 10^{-4}, as shown also in [10]. In the analysis above, photons radiated from the final state are excluded from the simulation. If radiative photons, emitted by Bhabha particle within the cone of one Moliere radius, are taken into account, ΔE and $\Delta\alpha_{res}$ are relaxed to 67 MeV and 4.3%, respectively [11].

3.2.4 Effects from polar angle resolution and bias in polar angle reconstruction

The existence of the bias in polar angle reconstruction may cause a shift in the luminosity measurement, since events may be pushed in or out of the detector fiducial volume. With presently simulated bias of the polar angle reconstruction, a relative uncertainty of the luminosity measurement of $1.6 \cdot 10^{-4}$ is expected as the upper bound. In practice, it is possible to measure the bias of the polar angle reconstruction in a test beam. Only the uncertainty of such a measurement, will than contribute to the luminosity uncertainty. A contribution of similar size to the relative uncertainty of the luminosity measurement can be expected from the resolution of the polar angle reconstruction [11].

Source of uncertainty	**$\Delta L/L$**
Bhabha cross-section σ_B	$5.4\ 10^{-4}$
Polar angle resolution σ_θ	$1.6\ 10^{-4}$
Bias of polar angle $\Delta\theta$	$1.6\ 10^{-4}$
Energy resolution α_{res}	$1.0\ 10^{-4}$
Energy scale	$1.0\ 10^{-4}$
Physics background B/S	$2.3\ 10^{-3}$
BHSE	$1.5\ 10^{-3}$
Beam polarization	$1.9 \cdot 10^{-4}$
Σ	**$3.0\ 10^{-3}$**

Table 1: Summary of systematic errors in the luminosity measurement. Errors are assumed to be uncorrelated. Uncertainty of the theoretical cross-section for Bhabha scattering is taken to be as at LEP energies.

3.2.5 Polarization of beams

If polarization of electron and positron beams is available at ILC as foreseen, this will suppress the Bhabha cross section in the acceptance range of the luminometer by up to a few per cent [8]. In the current design, the maximum values for electron and positron polarization are 0.8 and 0.6, respectively, with an uncertainty of 0.0025 [9], producing a relative reduction of the Bhabha cross section of $2.3 \cdot 10^{-2}$ with an uncertainty of $1.9 \cdot 10^{-4}$ which in turn translates into a relative uncertainty of the luminosity mesurement.

4 Conclusion

At the present level of understanding of the detector performance and physics effects in luminosity measurement it has been shown that it will be possible to measure integrated luminosity at ILC with the total systematic uncertainty of $3 \cdot 10^{-3}$. The largest uncertainty due

to two-photon background can clearly be reduced by correcting for it and using its uncertainty from NLO corrections as a true source of uncertainty of luminosity measurement. As well, effects from the polar angle reconstruction taken at present at full sizes will be replaced by their uncertainties once they are known.

5 Bibliography

References

[1] Report for the ILC Detector R & D Panel Instrumentation of the Very Forward Region [FCAL Collaboration], 2009 , http://www.vinca.rs/hep/pub/prc2009.pdf ;
[2] T. C. Awes et al., A simple method of shower localization and identification in laterally segmented calorimeters, Nucl. Inst. Meth. A311, 130 (1992);
[3] C. Rimbault et al., Impact of beam-beam effects on precision luminosity measurements at the ILC, JINST, 2 P09001, 2007;
[4] W. Kilian. WHIZARD: A generic Monte-Carlo integration and event generation package for multi-particle processes. LC-TOOL-2001-039, 2001;
[5] V.N. Pozdnyakov, Two-photon interactions at LEP, Phys.Part.Nucl.Lett.4:289-303, 2007;
[6] S. Jadach et al.. Monte Carlo program BHLUMI for Bhabha scattering at low polar angle with Yennie-Frautschi-Suura exponentiation. Comp. Phys. Commun., 70 (1992), pp. 305-344;
[7] B. Pawlik. BARBIE V4.3 Easy-to-use-simulation-package of the TESLA LAT Detector , source available from Bogdan.Pawlik@ifj.edu.pl;
[8] H. Abramowicz, I. Bozovic-Jelisavcic, et al. [FCAL Collaboration], Report for the ILC Detector R&D Panel: Instrumentation of the Very Forward Region, editors: Ch. Grah, M. Idzik, R. Ingbir, W. Lange, A. Levy, K. Moenig, W. M. Morse, U. Nauenberg, B. Pawlik, C. Rimbault, W. Wierba, L. Zawiejski, M. Zeller (May 2007) 78 pp, http://www.vinca.rs/hep/pub/FCAL_RD_Report07.pdf ;
[9] S. Boogert et al., Polarimeters and Energy Spectrometers for the ILC Beam Delivery System, 2009 JINST 4 P10015;
[10] A. Stahl, Luminosity Measurement via Bhabha Scattering: Precision Requirements for the Luminosity Calorimeter, LC-DET-2005-004;
[11] H. Abramowicz, I. Bozovic-Jelisavcic, et al. [FCAL Collaboration], R&D for Very Forward Calorimeters at the ILC Detector, (submitted to JINST), 2010.

Forward Region Studies for ILC

Ivanka Bozovic-Jelisavcic[a], Mila Pandurovic[a], Ivan Smiljanic[a], Tatjana Jovin[a] and Iftah Sadeh[b]

[a]*VINCA Institute of Nuclear Sciences, Belgrade, Serbia*
[b]*Tel Aviv University, Tel Aviv, Israel*

Abstract. Systematic effects in precision luminosity measurement at the International Linear Collider are discussed. In particular, beam-beam interaction effects, background from physics processes, and effect of bias and resolution of measured energy in the luminosity calorimeter. Simulation is done at 500 GeV and 1TeV center of mass energy. Some prospects at 3 TeV are also discussed for the CLIC case.

Keywords: Forward Calorimetry, Luminosity measurement
PACS: 13.66.Jn, 29.40.Vj

INTRODUCTION

International Linear Collider is a proposed electron-positron accelerator that will operate at initial center-of-mass energy of 500 GeV with the ability to upgrade to 1 TeV. ILC is foreseen as a complementary machine with the LHC (Large Hadron Collider) dedicated primarily to discover Higgs bosons and SUSY particles, while ILC will provide precise measurements of characteristics of these particles (masses, quantum numbers, couplings) since a collision between an electron and a positron is much simpler than a collision between many quarks, antiquarks and gluons confined in a proton. In 2007 the Reference Design Report of ILC has been delivered [1].

With respect to the LHC physics program, the role of either ILC or CLIC (Compact Linear Collider [2]), another project of possible future particle accelerator, will be to provide better understanding of a new physics discovered at LHC, or if there will not be such discoveries, to restrict the available parameter space through precision measurements. The energy scale of interest for a new physics will be determined by new discoveries at LHC, while both machines are foreseen as lepton colliders to enable precision measurements by minimizing QCD background.

This means that design of detector as well as systematic effects at a future collider have to be well understood. This is particularly true for the luminosity measurement that needs to be controlled at 10^{-3} or 10^{-4} level at ILC, as required for cross-section measurements (i.e. the total hadronic cross-section at Z^0 resonance, 2-fermion production at high energy) or precision EW measurements.

LUMNOSITY MEASUREMENT AT ILC

Integrated luminosity at ILC will be determined from the total number of Bhabha events produced in the fiducial volume of the luminosity calorimeter and the corresponding theoretical cross-section (1).

$$L_{\text{int}} = \frac{N_B}{\sigma_B} \tag{1}$$

Bhabha scattering at small angle is precisely calculable in QED (with theoretical error of the cross-section of 10^{-4}) and has a sufficiently large cross-section to deliver, within one year, statistics for luminosity measurement of

the required precision. However, one has to provide precision particle reconstruction and, in addition, to control numerous systematic effects.

The cross-section is falling steeply with increasing polar angle as $1/\theta^3$, causing luminosity measurement to be sensitive to the detector aperture θ_{min} or corresponding inner radius of the luminosity calorimeter. It should be known within 1 micron tolerance [3]. Two parameters are describing quality of the position reconstruction: bias $\Delta\theta$ and resolution $\sigma(\theta)$ of the polar angle measurement. Suggested sensor design of the luminosity calorimeter has been proven through simulation to provide bias and polar angle resolution better then 10^{-3} mrad and 10^{-2} mrad respectively [3].

Design of luminosity calorimeter as a compact Si-tungsten sandwich calorimeter is illustrated in Figure 1 [4]. Luminosity calorimeter covers geometrical range between 31 mrad and 78mrad with 30 layers of tungsten absorber discs interspersed with silicon sensor planes. Small Moliere radius and the fine sensor segmentation (48x64 pads) enable precise shower position measurement.

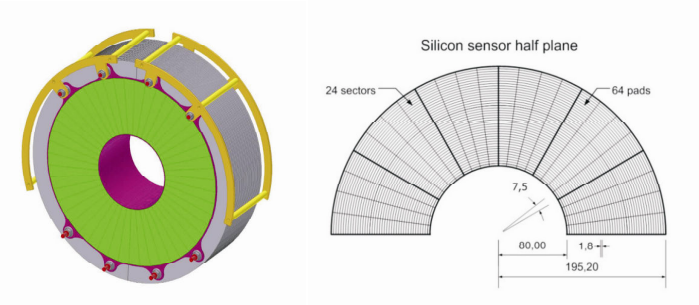

FIGURE 1. Design of the luminosity calorimeter for ILC. Forward electronics and ADC ASICS are positioned at the outer radius in the space between disks. Units are mm and mrad for radii and angles, respectively.

Systematic Effects in Luminosity Measurement

In order to achieve the required precision of luminosity measurement numerous systematic effects have to be well understood and controlled under realistic experimental conditions. Leading effects are beam-beam interaction, background from 2-photon processes and bias and resolution of energy measurement. They all contribute to the systematic error of luminosity measurement as $\alpha\cdot\Delta\alpha$, where α is the size of the effect and $\Delta\alpha$ its uncertainty. Some effects like the suppression of the Bhabha cross-section due to the beam-beam interaction are of the percent order meaning that excellent experimental control of the effect has to be established.

Beam-beam interaction

Experimental selection specified to determine luminosity is affected by beam-beam space charge effects: beamstrahlung radiation and electromagnetic deflection. Interacting particles are likely to be deflected by the space charge of the opposite bunch and their energy reduced due to the emission of beamstrahlung. Both effects are leading to the suppression of Bhabha counting rate (BHSE) in comparison to the theoretically predicted one. The total size of BHSE is -4.41±0.05 % [5] in the luminosity calorimeter acceptance, requiring each of the scattered particles to have more than 80% of the beam energy. Figure 2a [5] illustrates effect of beamstrahlung on spread of Bhabha particles due to modification of initial state four-vector, while Figure 2b [5] gives the change in Bhabha production polar angle due to electromagnetic deflection induced by the space charge of the opposite bunch.

Since the dominating part of the BHSE originates from beamstrahlung radiation by initial-state particles prior to Bhabha scattering, data-driven correction method is suggested from the reconstructed luminosity spectrum [5]. Luminosity spectrum $x_{\exp}$ can be reconstructed by measuring polar angle of Bhabha particles (θ_1, θ_2):

$$x_{\exp} \approx \sqrt{1-2\frac{\sin(\theta_1+\theta_2)}{\sin(\theta_1+\theta_2)-\sin\theta_1-\sin\theta_2}} \qquad (2)$$

and it is almost not modified by the electromagnetic deflection but solely influenced by the beamstrahlung. Thus corresponding part of the BHSE can be determined as a bias of luminosity measurement once $\langle x_{exp} \rangle$ is known. However, contribution to the systematic uncertainty of luminosity measurement comes from the uncertainty of determination of $\langle x_{exp} \rangle$ originating from variations of the bunch width σ_x. It has been proven through simulation that $\Delta\langle x_{exp} \rangle$ should be kept at the level of 10^{-3} in order to keep the uncertainty of BHSE at the 10^{-2} level [5]. Beam parameters σ_x and σ_z should be known within 20% margin [5].

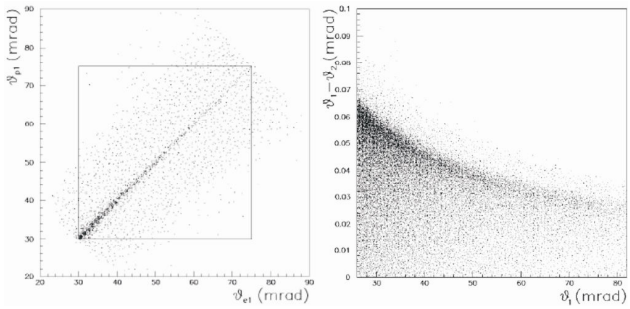

FIGURE 2. a. Polar angle distribution of Bhabha particles (θ_{e1}, θ_{p1}) after accounting for beamstrahlung of the initial state. b. Change in Bhabha production angle (θ_1) due to the electromagnetic deflection.

Background from physics processes

Four-fermion production via Neutral Current mechanism is known as the process peaked forward. It is dominated by multiperipheral diagram (Figure 3a) where two virtual photons are exchanged between electron spectators. Most of the spectators are high energetic particles carrying the most of the beam energy along a beam pipe, as illustrated in Figure 3b and c. Small fraction of them (approximately 0.4%) hits luminosity calorimeter causing the main background for Bhabha signal.

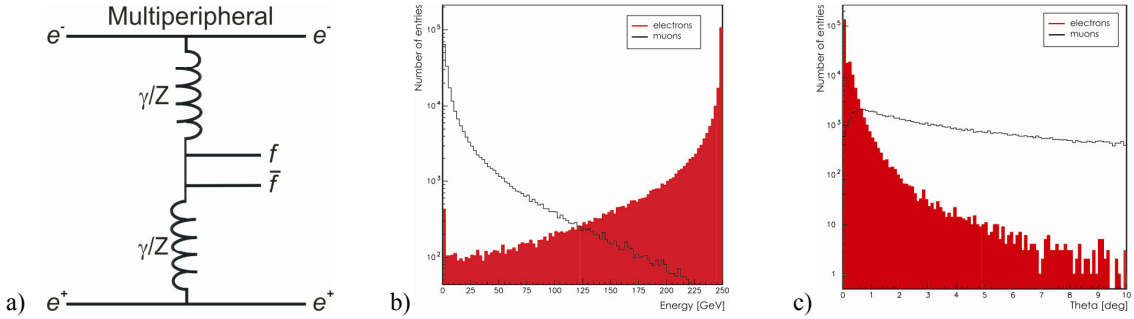

FIGURE 3. a. Dominating Feynman graph for four-fermion production. b. and c. Energy and polar angle distributions of 4-fermion background.

We used BDK [6] and WHIZARD [7] event generators to obtain leptonic samples of 100 kEvt, with cross-sections of 1.16 nb and 9.70 nb respectively, at 500 GeV and 0.45 nb and 12.12nb at 1TeV center-of-mass energy. Cross-sections are generated with statistical error less than percent for both generators. However, there is significant difference in cross-sections for different generators. It has been shown in Table 1 that BDK has smaller fraction of electron spectators with respect to the all particles in the luminosity calorimeter then WHIZARD, so BDK is exhibiting better sensitivity to background rejection for a factor two at all energies. As well, the topology of four-fermion events is somewhat different with BDK, giving more particles closer to the beam-pipe than WHIZARD.

This results in approximately factor 3 larger fraction of quasi-Bhabha pairs in the luminosity calorimeter with WHIZARD than BDK. When combined, these differences between generators compensate, for at least factor 6, initial differences in cross-sections, resulting, as illustrated in Table 2, with the same order of magnitude for background to signal ratio.

Bhabha sample of 5 pb^{-1} has been generated with cross-sections of (4.70±0.03) nb and (1.20±0.03) nb, at 500 GeV and 1TeV respectivly, using BHLUMI [8] event generator. Detector response is simulated using BARBIE V4.3 [9], GEANT3 based simulation. In order to keep BHSE at the percent level the following event selection has been employed: asymmetric cuts on particle polar angle (θ_{min}[mrad]+4mrad, θ_{max}[mrad]-7mrad]) are subsequently applied to forward and backward side of the detector and quasi-Bhabha pair is selected if carrying more than 80% of the center-of-mass. Quasi-Bhabha pair is required to have tracks at opposite detector sides.

TABLE (1). Generator-level fractions of quasi-Bhabha events in luminosity calorimeter (*F* [%]) and background selection efficiency (*Eff* [%]), after energy cut applied, are given for WHIZARD and BDK at ILC energies.

		500 GeV	**1 TeV**
$F \cdot 10^{-2}$ [%]	**WHIZARD**	8.0	4.8
	BDK	2.5	1.7
Eff [%]	**WHIZARD**	17.9	19.0
	BDK	9.9	7.1

TABLE (2). Fraction of quasi-Bhabha pairs (background) to signal (*B/S*), before and after event selection, for WHIZARD and BDK at ILC energies.

		500 GeV	**1 TeV**
B/S before selection	**WHIZARD**	$2.3 \cdot 10^{-3}$	$1.8 \cdot 10^{-3}$
	BDK	$7.9 \cdot 10^{-3}$	$3.6 \cdot 10^{-2}$
B/S after selection	**WHIZARD**	$2.0 \cdot 10^{-4}$	$3.5 \cdot 10^{-4}$
	BDK	$2.5 \cdot 10^{-4}$	$7.4 \cdot 10^{-4}$

As illustrated in Table 2, applied event selection for luminosity measurement is suppressing background for at least factor 10, resulting in comparable results for background to signal ratio for both event generators: $B/S = (2.5 \pm 0.5) \cdot 10^{-4}$ at 500 GeV and $B/S = (7 \pm 4) \cdot 10^{-4}$ at 1 TeV. It is visible that model error is increasing with energy as difference in cross-sections between WHIZARD and BDK is more pronounced. Reduction of background after applied selection is illustrated in Figure 4 where hits projected in the front plane of the luminosity calorimeter are given. Signal selection efficiency is maintained at 68% level, providing statistical error below 10^{-4} for one year of ILC operation at the nominal luminosity of $2 \cdot 10^{34}$ $cm^{-2}s^{-1}$.

Similar analysis has been employed for the CLIC geometry, where fiducial volume of the luminosity calorimeter covers polar angles between 50 mrad and 130 mrad. Sample of 500 fb^{-1} of Bhabha events has been generated with the cross-section of 42.90 pb using BHWIDE [10] event generator. Samples of 10^3 kEvt leptonic and 10^2 kEvt hadronic four-fermion events have been generated with WHIZARD. Events are treated in a way that effective 4-vector is being built of all particles within the fiducial volume of LumiCal, for each arm of the calorimeter. Such an 'effective particle' has average polar angle computed using energy weights, while the effective energy is integrated for all particles. Topological selection is applied requiring colinearity of effective particles in the forward and backward detector better than 1 mrad and balance between energy deposited at opposite detector sides better than 1%. Separation of background to signal of $B/S \approx 2 \cdot 10^{-3}$ [11] can be achieved.

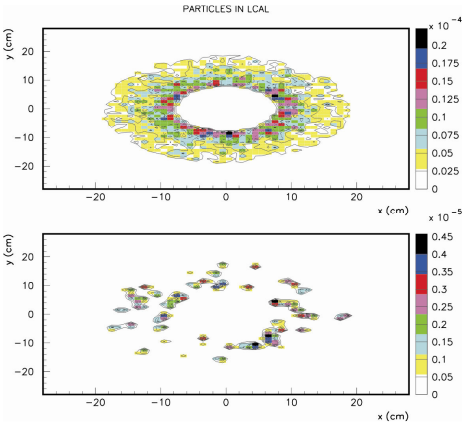

FIGURE 4. Projected hits, normalized per bunch crossing, on the first plane of luminosity calorimeter for background at 500 GeV before (up) and after (down) event selection.

Effects of energy resolution and bias of energy scale

As discussed before, criteria to select Bhabha events in luminosity measurement define requirements on energy resolution of the detector and, more challenging, control of the energy scale. In luminosity calorimeter, energy of particles is measured through calibration procedure assuming that both showers are fully contained in the detector. It has been shown that energy resolution of $\frac{\Delta E}{E} = \frac{\delta(E)}{\sqrt{E}}\sqrt{GeV}$, $\delta(E) \approx 21\%$ [3] is achievable with the current detector design.

In order to keep the luminosity uncertainty at the level of 10^{-4}, cut-off value of Bhabha energy should be known better than 40 MeV. This is illustrated in Figure 5a, showing the linear fit of efficiency slope at 0.8 of the beam energy. In order to estimate how well detector energy resolution has to be known, a random number generator is used to smear particle energy for different $\delta(E)$ values. As shown at Figure 5b, to contribute to uncertainty of luminosity less than 10^{-4}, detector resolution $\delta(E)$ should be controlled at 1.5% level. Since detector will be calibrated under realistic beam conditions, bias of the energy scale can be present. Figure 5c illustrates that bias of energy scale should be less than 70 MeV to keep the luminosity uncertainty below 10^{-4}.

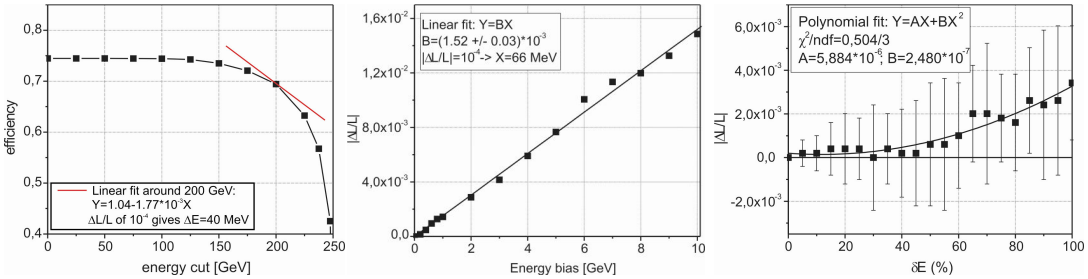

a) b) c)

FIGURE 5. a. Signal selection efficiency dependence on Bhabha energy cut-off value.
b. Contribution to the relative error of luminosity with respect to detector energy resolution.
c. Contribution to the relative error of luminosity with respect to bias of energy scale.

CONCLUSION

Detailed simulations of luminosity measurement at ILC have shown that systematic effects are complex and numerous, requiring experimental control of beam parameters σ_x (σ_z), reconstructed luminosity spectrum, detector energy resolution and energy scale. They have to be known better than: 20%, 10^{-3}, 1.5%, and 10^{-2} MeV, respectively, to maintain contribution to the luminosity relative uncertainty at the 10^{-4} level. Background from 2-photon processes is reducible to 10^{-4} level with respect to the signal, at all ILC energies. Estimations done for the CLIC geometry have also shown that background is reducible to the 10^{-3} level with respect to Bhabha signal, while requirements for precision luminosity determination are looser, at the level of 10^{-2}.

ACKNOWLEDGMENTS

We are grateful to the Ministry of Science and Technology of the Republic of Serbia for supporting this research activity within the project 'Physics and detector studies in HEP Experiments'.

REFERENCES

1. G. Aarons et al., *International Linear Collider Reference Design Report*, ILC-REPORT-2007-001, 2007.
2. CLIC Study Team*, A 3 TeV e+e- Linear Collider based on CLIC Technology,* CERN 2000-08, 2008.
3. H. Abramowicz et al., *Redefinition of the Geometry of the Luminosity Calorimeter*, EUDET-Memo-2008-09, 2008.
4. W. Wierba et al., *Lumical design overview*, Proceedings of the Workshop of the Collaboration on Forward Calorimetry at ILC, Belgrade, Serbia, (September 2008).
5. C. Rimbault et al., *Impact of beam-beam effects on precision luminosity measurements at the ILC,* JINST 2 P09001, 2007.
6. F.A. Berends et al., *Monte Carlo simulation of two-photon processes II: Complete lowest order calculations for four-lepton production processes in electron-positron collisions,* Comp. Phys. Commun. 40 (1986), pp. 285-307.
7. W. Killian, *WHIZARD: A generic Monte-Carlo integration and event generation package for multi-particle processes*, LC-TOOL-2001-039, 2001.
8. S. Jadah et al., *Monte Carlo program BHLUMI for Bhabha scattering at low polar angle with Yennie-Frautschi-Suura exponentiation,* Comp. Phys. Commun. 70 (1992), pp. 305-344.
9. B. Pawlik, *BARBIE V4.3 Easy-to-use-simulation-package of the TESLA LAT Detector, source available from Bogdan.Pawlik@ifj.edu.pl*
10. S. Jadah et al., *BHWIDE: A Monte Carlo Event Generator for Bhabha Scattering at Large (Wide) Angles with O(alpha) YFS Exponentiation*,
11. I. Sadeh, *Proposed design of Lumical for a 3 TeV CLIC,* Workshop of the Collaboration on Forward Calorimetry at ILC, Zeuthen, Germany, (June 2009).

Background reduction at an actively shielded gamma ray spectrometer

I. Bikit, D. Mrđa, N. Todorović, J. Slivka, M. Veskovič, M. Krmar, Lj. Čonkić, S. Forkapić, E. Varga, T. Jovin

Department of Physics, Faculty of Sciences, University of Novi Sad, Serbia and Montenegro

The operational problems of the gamma ray spectrometer shielded passively with 12 cm of lead and actively by five 0.5m x 0.5m x 0.05m plastic veto shields are described. With 1000 V operating voltage the 661 keV ^{137}Cs gamma line gives a fast output pulse with the amplitude of 20 mV. This means that the CFD dynamic range (5 mV - 2.5V) covers the energy range deposited in the scintillator of 150 keV - 75 MeV. With the optimal set up the integral background of 0.31 c/s was achieved for the energy region of 50 - 3000 keV. The detector mass related background was 0.345 c/kgs. The 511 keV annihilation line was reduced by the factor of 7 by the anticoincidence gate.
It is shown that the plastic shields increase the neutron capture gamma line intensities due to neutron thermalisation.

МЕРЕЊЕ ФАЗЕ НАРУШЕЊА CP СИМЕТРИЈЕ У РАСПАДУ $B_s^0 \to J/\psi\phi$ У АТЛАС ЕКСПЕРИМЕНТУ

Т. Агатоновић Јовин, И. Божовић Јелисавчић и П. Ћирковић

Институт за нуклеарне науке „Винча", Универзитет у Београду,
М. Петровића Аласа 12-14, 11001 Винча-Београд
e-mail: tatjana.jovin@cern.ch

Апстракт. У овом раду биће представљено мерење фазе нарушења CP симетрије у распаду $B_s^0 \to J/\Psi\phi$ у ATLAS експерименту на сударачу LHC. Анализа је заснована на измереној маси и времену живота B_s^0 мезона, као и на угловима који описују распад $B_s^0 \to J/\Psi\phi$ у формализму трансверзалитета. Мерење је извршено на узорку који одговара интегралној луминозности од 4.9 fb^{-1} података сакупљених током 2011. године на енергији 7 TeV у систему центра масе.

1. УВОД

Стандардни модел (*eng.abbrev.* SM) предвиђа нарушење CP симетрије, увођењем (јединствене) иредуцибилне фазе, одн. комплексног параметра CKM матрице, као доминантан извор CP симетрије у оквиру SM. Међутим, скоро све екстензије SM укључују додатне изворе нарушења CP симетрије, тако да насупрот феноменолошком успеху SM, који предвиђа малу вредност фазе нарушења CP симетрије, он није у могућности да објасни опажену асиметрију материје и антиматерије у Универзуму за неколико редова величине. Стога, један од главних задатака савремене физике јесте да тестира кључна предвиђања Стандардног модела и да пружи објашњење за опажену барионску асиметрију.

Нови феномени изван Стандардног модела могу да измене нарушење CP симетрије у распаду B мезона. Канал за који се очекује да буде осетљив на доприносе тзв. нове физике (*eng.* New Physics) је распад $B_s^0 \to J/\Psi\phi$. Нарушење CP симетрије у распаду $B_s^0 \to J/\Psi\phi$ (индиректно нарушење) настаје услед чињенице да се својствена CP стања B_s^0 мезона настала услед $B_s^0 - \overline{B_s^0}$ осцилација распадају на поларизациона стања $J/\psi\phi$ система неодговарајуће CP парности. Фреквенцију осциловања мешања B_s^0 мезона описује разлика у маси Δm_s између тешких B_s^H и лаких B_s^L масених својствених стања која су, уједно, и својствена стања CP оператора. У Стандардном моделу фаза $\phi_s^{J/\psi\phi}$ је мала и може се повезати са елементима Кабибо-Кобајаши-Маскава (CKM) матрице мешања кваркова помоћу релације $\phi_s^{J/\psi\phi} = -2\beta_s$ ($\beta s = \arg[-(V_{ts}V^*_{tb})/(V_{cs}V^*_{cb})]$). Вредност $\phi_s^{J/\psi\phi}$ = - (0.0368 +/- 0.0018) *rad* предвиђена је Стандардним моделом.

Друга физичка величина која је у директној вези са $B_s^0 - \overline{B_s^0}$ мешањем је *разлика ширине распада* $\Delta\Gamma_s = \Gamma_L - \Gamma_H$ одговарајућих B_s^L и B_s^H стања. Не очекује се да физика изван SM утиче на $\Delta\Gamma_s$ толико значајно колико на фазу нарушења $\phi_s^{J/\psi\Phi}$. Ипак, мерење $\Delta\Gamma_s$ је значајно јер омогућује тестирање теоријских предвиђања.

Финалном стању векторских мезона $J/\psi\phi$ одговара укупни орбитални угаони момент L = 0, 1 или 2, при чему су стања са орбиталним угаоним моментом L = 0 или 2 CP-парна, док је стање са L = 1 CP-непарно. Метода идентификација наелектрисања валентног b-кварка у почетном стању B_s^0 употребљава се како би се разликовала почетна стања B_s^0 и $\overline{B_s^0}$ мезона. У овом раду ће бити приказани резултати добијени без коришћења информације о знаку наелектрисања валентног b-кварка у B_s^0 мезону. CP стања раздвојена су статистички кроз временску зависност распада и угаоних корелација између честица финалног стања.

У овом раду представљено је мерење фазе нарушења CP симетрије $\phi_s^{J/\psi\phi}$, као и вредности $\Delta\Gamma_s$, реконструкцијом распада $B_s^0 \to J/\Psi\phi$. Резултати представљени у овом раду добијени су анализом података прикупљених у току 2011 године на ATLAS детектору у протон-протон сударима на LHC у систему центра масе од 7 TeV, а који одговарају интегралној луминозности од 4,9 fb^{-1} [1].

2. РЕКОНСТРУКЦИЈА И СЕЛЕКЦИЈА КАНДИДАТА КАНАЛА РАСПАДА $B_s^0 \to J/\psi\phi$

Селекција кандидата на нивоу тригер система базирана је на реконструкцији $J/\psi \to \mu^+\mu^-$ распада, на основу идентификације миона чији је трансверзални импулс изнад неке граничне вредности (нпр. p_T > 4 GeV). У овој анализи реконструисани су трагови миона из Унутрашњег детектора (ID), с обзиром да њихова прецизност у p_T опсегу од интереса у овој анализи доминантно зависи од реконструкције трагова у ID. Фитом максималне веродостојности (*eng.* Maximum Likelihood Fit) одређена је маса J/ψ мезона са ефикасношћу селекције од 99,8%.

Распади $\phi \to K^+K^-$ реконструисани су од свих парова супротно наелектрисаних трагова са $p_T > 0.5$ GeV и $|\eta| < 2.5$ који нису идентификовани као миони. Кандидати $B_s^0 \to J/\psi(\mu^+\mu^-)\phi(K^+K^-)$ реконструисани су методом фитовања трагова за сваку комбинацију $J/\psi \to \mu^+\mu^-$ и $\phi \to K^+K^-$ у заједнички вертекс. Укупно је реконструисано 131k B_s^0 кандидата у опсегу масе (5150 - 5650) MeV.

За сваки реконструсани B_s^0 мезон одрђенео је *сопствено време распада* τ на основу израза:

$$\tau = \frac{L_{xy} M_B}{c p_{T_B}}$$

где је p_T реконструисани трансверзални импулс кандидата B_s^0 мезона, а M_B означава просечну вредност за масу B_s^0 мезона (5.3663 MeV) према PDG [2]. Трансверзална дужина распада L_{xy} је растојање између примарног и секундарног вертекса пројектовано у трансверзалној равни у односу на осу снопа.

3. МЕТОД ФИТОВАЊА

Параметари од значаја, описани у Поглављу 1, за ову анализу одређени су применом фита максималне веродостојности (*eng.* Maximum Likelihood Fit).

Функција вероватноће дефинисана је као:

$$\ln \mathcal{L} = \sum_{i=1}^{N} \{ w_i \cdot \ln(f_{sig} \cdot \mathcal{F}_{sig}(m_i, t_i, \Omega_i) + f_{sig} \cdot f_{B^s} \cdot \mathcal{F}_{B^s}(m_i, t_i, \Omega_i) + (1 - f_{sig} \cdot (1 + f_{B^s})) \mathcal{F}_{bkg}(m_i, t_i, \Omega_i) \}$$

где је N број селектованих кандидата, w је фактор отежињавања који би урачунала ефикасност тригера, f_{sig} је удео догађаја сигнала, $f_B{}^0$ је удео догађаја B^0 мезона фона израчунат као релативна фракција у односу на сигнал. Улазне променљиве у фит функцију добијене су из података које је детектор прикупио током 2011. године, и то су: сопствено време t_i, маса m_i и углови распада финалних продуката/честица распада описани у формализму трансверзалности $\Omega_i = (\theta_T, \psi_T, \varphi_T)$. $\mathcal{F}_{sig}$, $\mathcal{F}_B{}^0$, и $\mathcal{F}_{bkg}$ су расподеле густине вероватноће (PDF) који моделирају дистрибуције сигнала, фона који потиче из B^0 распада и свог осталог фона, респективно.

4. РЕЗУЛТАТИ И ДИСКУСИЈА

Фит описан у Поглављу 3. има 26 слободних параметара, од којих су основни физичког значаја, међу којима и фаза нарушења CP симетрије $\phi_s^{J/\psi\phi}$ и разлика ширине распада $\Delta\Gamma_s$ одговарајућих B_s^L и B_s^H стања, који представљају основни резултат мерења.

Добијен је следећи резултат:

$$\phi_s^{J/\psi\phi} = 0.22 \pm 0.41 \text{ (stat.)} \pm 0.10 \text{ (syst.) rad}$$
$$\Delta\Gamma_s = 0.053 \pm 0.021 \text{ (stat.)} \pm 0.010 \text{ (syst.) ps}^{-1}$$

који је на слици 1 [1] представљен уз контуре које одговарају нивоима поверења од 68%, 90% и 95% и у сагласности су са предвиђањима Стандардног модела. Пошто, као што је речено у Поглављу 1, није коришћена информација о почетном наелектрисања валентног b-кварка у B_s^0 мезону, на основу досадашњих резултата других експеримента ограничена је јака фаза уведена као разлика између трансверзалне и лонгитудиналне амплитуде поларизационих стања векторсих мезона $\delta_\perp = (2.95 \pm 0.39)$ rad [3], док је разлика $\Delta\Gamma_s$ узета позивитивна да би се уклонила неједнозначност резултата $\Delta\Gamma_s$, $-\Delta\Gamma_s$.

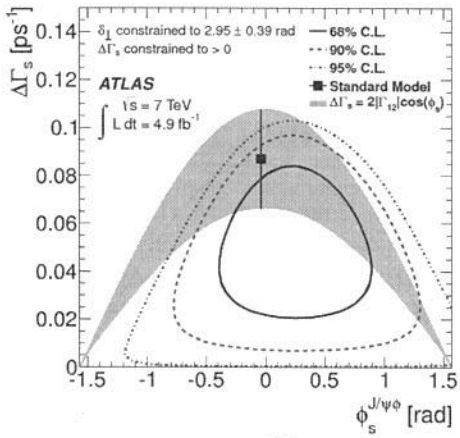

СЛИКА 1. Резултат мерењаосновних праметара $\phi_s^{J/\psi\phi}$ и $\Delta\Gamma_s$ нарушења CP симетрије у ATLAS експерименту приказан контурама које одговарају различитим нивоима поверења.

5. ЗАКЉУЧАК

Мерњем фазе нарушења CP симетрије у ATLAS експерименту у распаду B_s мезона $B_s^0 \to J/\psi\phi$ добијен је резултат који је у складу са предвиђањима Стандардног модела. Такође, добијени резултати су упоредиви са резултатима LHCb експеримента и, посебно, имајући у виду да у овом мерењу није примењена идентификација $b(\bar{b})$ кварка у B_s мезону, показују велики потенцијал ATLAS експеримента када је реч о мерењу нарушења CP симетрије у системима неутралних B мезона.

ЗАХВАЛНИЦА

Овај рад је реализован уз подршку Министарства за просвету, науку и технолошки развој Републике Србије, у оквиру пројекта ОИ171012. Такође, истраживање на ову тему спроводи се уз помоћ и у сарадњи са групом за изучавање B_s мезона у ATLAS експерименту у CERN.

ЛИТЕРАТУРА

[1] ATLAS Collaboration, G.Aad et al., *Time-dependent angular analysis of the decay Bs → J/ψφ and extraction of* ΔΓs *and the CP-violating weak phase* φs *by ATLAS*, *JHEP* **1212** (2012) 072 [arxiv:1208.0572].

[2] PARTICLE DATA GROUP, K. Nakamura et al., *Review of particle physics*, *J. Phys.* **G 37** (2010) 075021, and 2011 partical update for the 2012 edition.

[3] LHCb Collaboration, R. Aaij et al., *Measurement of the CP-violating phase* φs *in the decay Bs → J/ψφ*, *Phys. Rev. Lett.* **108** (2012) 101803 [arXiv:1112.3183].

ИДЕНТИФИКАЦИЈА ЗНАКА НАЕЛЕКТРИСАЊА *b*-КВАРКА У МЕРЕЊУ НАРУШЕЊА CP СИМЕТРИЈЕ У ATLAS ЕКСПЕРИМЕНТУ

П. Ћирковић, И. Божовић-Јелисавчић и Т. Јовин

Институт за нуклеарне науке „Винча", Лабораторија за физику, М. Петровића Аласа 12-14, 11001 Винча – Београд
e-mail: pcirkovic@vinca.rs

Апстракт. У овом раду биће представљен принцип и перформансе алгоритма за идентификацију знака наелектрисања *b*-кварка који је конституент B_s мезона од значаја у мерењу нарушења CP симетрије у ATLAS експерименту на сударачу LHC. Идентификација знака наелектрисања валентног *b*-кварка ($b, \bar{b}$ сепарација) је од посебне важности у уклањању неједнозначности (ϕ_s, $\pi - \phi_s$) у мерењу ϕ_s фазе нарушења CP симетрије у процесу $B_s \to J/\psi\phi$.

1. УВОД

Мерење нарушења CP симетрије у системима *B*-мезона мотивисано је двојаким разлозима: потрагом за неусаглашеностима у односу на Стандардни модел у физици честица, а које би указале на физику изван Стандардног модела, као и успостављањем везе између нарушења CP симетрије измереног у системима неутралних мезона (K^0, B^0) и космолошког нарушења потребног да објасни барионску асиметрију опсервабилну у Универзуму. У ATLAS експерименту на Великом хадронском сударачу (LHC), мерење фазе нарушења (ϕ_s) CP симетрије врши се у распадима $B_s^0 \to J/\psi\phi$ [5], у којима се CP симетрија индиректно нарушава распадом почетног стања које се, услед осцилација $B_s^0 - \overline{B_s^0}$, јавља као квантна суперпозиција стања B_s^0 и $\overline{B_s^0}$ и које се, у малом броју случајева, распада на поларизационо стање векторских мезона ($J/\psi\phi$) супротне CP парности.

Одређивање знака наелектрисања *b*-кварка у B_s мезону уклања неједнозначност (ϕ_s, $\pi - \phi_s$) у мерењу ϕ_s фазе нарушења CP симетрије присутну у претходним мерењима [1]. Узевши у обзир да *B*-мезони настају хадронизацијом из иницијаног пара $b\bar{b}$, довољно је утврдити знак *b*-кварка у мезону на супротној хемисфери од сигнала $B_s^0 \to J/\psi\phi$ и тај метод (*Opposite-Side Tagging* или OST) ће бити представљен у овом раду.

2. РЕКОНСТРУКЦИЈА НАЕЛЕКТРИСАЊА *b*-КВАРКА

У циљу калибрације и утврђивања перформанси OST метода преференцијално се користе распади попут $B^{\pm} \to J/\psi K^{\pm}$, код којих су наелектрисање, односно кварковски састав *B*-мезона једнозначно одређени наелектрисањем каона који се доминантно (у 63.55% случајева) распада на мион истог знака наелектрисања [2]. У анализи је коришћен целокупни узорак од $4.9\,fb^{-1}$ података прикупљених ATLAS детектором током 2011. године, на енергији у систему центра масе $7\,TeV$ и узорак величине $4.5\,fb^{-1}$ добијен *Monte Carlo* симулацијом.

У смислу одређивања ефективног наелектрисања млаза, млаз (или *jet*) може представљати како експериментално реконструисани млаз честица, тако и мион. У принципу, за трагове који се налазе у просторном углу одређеном конусом димензије ΔR, могуће је дефинисати величину Q_{jet} (и аналогно њој Q_{μ}) коју називамо *наелектрисање млаза*, независно од тога да ли је (или није) у конусу реконструисан физички млаз честица, по чијим се траговима врши сумирање:

$$Q_{jet,\mu} = \frac{\sum_i^{N_{tracks}} q_i \cdot {p_T}^{\kappa}}{\sum_i^{N_{tracks}} {p_T}^{\kappa}}.$$

Отежињавање трагова наелектрисаних честица у зависности од њиховог трансверзалног импулса оптимизовано је коефицијентом κ ($\kappa = 1.1$), а величина конуса описаног око осе млаза (вектора импулса миона) износи $\Delta R < 0.5$. Трансверзални импулс (p_T) и псеудорапидитет (η) идентификованих миона задовољавају услове: $p_T > 0.5\,GeV$ и $|\eta| < 2.5$. Уколико је реконструисано више од једног миона или млаза на страни супротној сигналу, узима се мион (или млаз) са највећом вредношћу трансверзалног импулса.

Перформансе метода описују се величинама које се називају *ефикасност*, *разређеност* и *идентификациона моћ* [3]. Ефикасност ε индентификације се дефинише као однос броја исправно (R) или погрешно (W) идентификованих *b*-кваркова (догађаја) према укупном броју кандидата који укључује и неидентификоване догађаје (U). Разређеност (D) показује колико износи ефективно присуство погрешно идентификованих догађаја, узимајући вредности из опсега од -1 (ако нема погрешних идентификација) до 1 (ако су сви догађаји погрешно идентификовани).

$$\varepsilon = \frac{R+W}{R+W+U}, \quad D = \frac{W-R}{W+R}$$

Величина εD^2 представља идентификациону моћ метода. Алгоритам комбиновања тренутно расположивих идентификатора (ефективног наелектрисања миона и ефективног наелектрисања млаза) је хијерархијски: уколико је селектован мион који задовољава услове у погледу трансверзалног импулса и псеудорапидитета, као идентификатор се користи ефективно наелектрисање миона Q_{μ}; у противном користи се наелектрисање

реконструисаног млаза који је идентификован да потиче од b-кварка (*flavour tagging*) Q_{jet}, или се догађај третира као неидентификован. На слици 1. приказане су расподеле ефективног наелектрисања миона за кандидате из распада B^+ и B^- мезона [4].

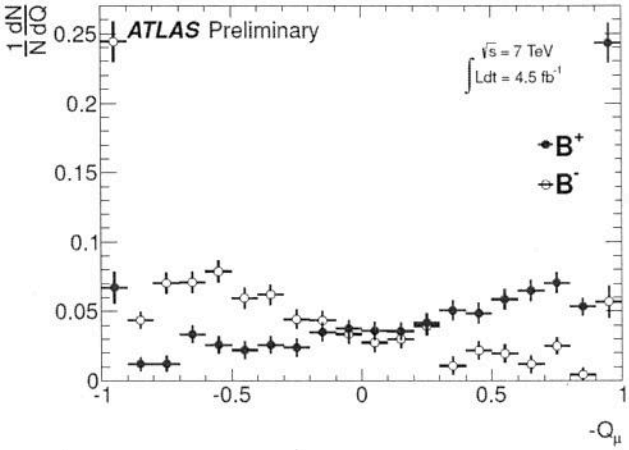

СЛИКА 1. Расподела ефективног наелектрисања миона за кандидате из распада B^+ и B^- мезона добијене *Monte Carlo* симулацијом.

3. РЕЗУЛТАТИ И ДИСКУСИЈА

Перформансе метода за идентификацију знака наелектрисања b-кварка на супротној страни од сигнала, израчунате за различите идентификационе величине, дате су у табели 1 [4]. Наведене грешке су статистичке. Метода ОST показује упоредиве резултате са онима добијеним у сличним мерењима, иако је, услед ограниченог броја идентификатора као и релативно једноставних алгоритма за њихово комбиновање, ефикасност идентификације знака наелектрисања b-кварка мања, а фракција погрешних идентификација већа него у сличним експериментима (нпр. LHCb [3]).

ТАБЕЛА. Преглед перформанси идентификације за различите индентификаторе.

Идентификатор	Ефикасност [%]	Разређеност [%]	Идентификациона моћ [%]
Еф. наелектрисање сегм. идент. миона	1.08±0.02	36.7±0.7	0.15±0.02
Еф. наелектрисање комб. миона	3.37±0.04	50.6±0.5	0.86±0.04
Ефективно наелектрисање млаза	27.7±0.1	12.68±0.06	0.45±0.03
Укупно	32.1±0.1	21.3±0.08	1.45±0.05

За сваки догађај, окарактерисан неком вредношћу идентификатора Q, може се дефинисати вероватноћа $P(Q\,|\,B^-)$ (или $P(Q\,|\,B^+)$) да је одлука – да је на страни супротној сигналу произведен b (или $\bar{b}$) кварк – исправна. Ова вероватноћа се даље користи у математичком опису фита експериментално измерених величина

(масе и времена живота B_s мезона, као и углова који описују распад $B_s^0 \to J/\psi\phi$ у формализму трансверзалитета) у мерењу фазе нарушења CP симетрије. Увођење идентификације знака наелектрисања валентног b-кварка у B_s мезону, као што је већ речено, уклања једну од неједнозначности у мерењу фазе нарушења CP симетрије ϕ_s

ЗАКЉУЧАК

У мерење фазе нарушења CP симетрије у ATLAS експерименту у распаду B_s мезона $B_s^0 \to J/\psi\phi$ уведена је идентификација валентног b-кварка, користећи идентификацију знака наелектрисања b-кварка у хемисфери насупрот сигналу (OST). Иако се тренутно користе само две идентификационе варијабле (ефективно наелектрисање миона и млаза) у хијерархијском алгоритму, увођење OST метода омогућава уклањање неједнозначности у мерењу фазе нарушења CP симетрије ϕ_s и даје у погледу перформанси метода упоредиве резултате са сличним експериментима.

ЗАХВАЛНИЦА

Овај рад је реализован уз подршку Министарства за просвету, науку и технолошки развој Републике Србије, у оквиру пројекта ОИ171012. Такође, истраживање на ову тему спроводи се уз помоћ и у сарадњи са групом за изучавање B_s мезона у ATLAS експерименту у CERN.

ЛИТЕРАТУРА

[1] Aad G., Bozovic-Jelisavcic I., Cirkovic P., Jovin T. et.al. [ATLAS Collaboration], *Time dependent angular analysis of the decay Bs->J/psi phi and extraction of Delta Gamma_s and the CP-violating weak phase phi_s by ATLAS*, JHEP12 (2012) 072, 34 pp, December 2012.

[2] J. Beringer et al. [Particle Data Group], *Review of Particle Physics*, Phys. Rev. D86, 010001 (2012).

[3] R. Aaij et al. [The LHCb Collaboration], *Opposite-side flavour tagging of B mesons at the LHCb experiment*, LHCB-PAPER-2011-027, March 6, 2012.

[4] Aad G., Bozovic-Jelisavcic I., Cirkovic P., Jovin T. et.al. [ATLAS Collaboration], *Flavour tagged time dependent angular analysis of the Bs->J/psi phi and extraction of Delta Gamma_s and the weak phase phi_s in ATLAS*, ATLAS-CONF-2013-039, 18 pp, April 9, 2013.

[5] Jovin T. [On behalf of the ATLAS collaboration], *CP Violation in ATLAS*, The XI International Conference on Heavy Quarks and Leptons, June 2012, Prague, Czech Republic, 11-15 June 2012, PoS (HQL 2012) 038.

SPEKTROSKOPIJA ANTIMIONSKOG PLASTIČNOG DETEKTORA

Nataša Žikić-Todorović, Sofija Forkapić, Tatjana Jovin, Ljiljana Čonkić, Miodrag Krmar
Departman za fiziku, Prirodno-matematički fakultet u Novom Sadu

Sadržaj - *Fonu γ spektrometarskih sistema doprinose sekundarna zračenja proizvedena kosmičkim mionima. Ova komponenta fona ne može se smanjiti povećanjem debljine pasivne zaštite. Zato se za redukciju kosmičkog zračenja koriste se spoljašnji zaštitni detektori velike površine (veto detektori). U ovom radu opisane su spektroskopske osobine plastičnog veto detektora «SCIONIX». Pokazano je da je energetski odgovor detektora linearan i određeni su energija i fluks miona u niskofonskoj laboratoriji departmana za fiziku u IFNS.*

1. UVOD

U mnogim poljima detekcije jonizujućeg zračenja, detektori se primenjuju za probleme vezene za događaje niskih aktivnosti. Tehnika merenja niskih aktivnosti koristi se za rešavanje niza problema, od kontrole kontaminacije prehrambenih proizvoda, pa do proučavanja fundamentalnih procesa u geofizici, astrofizici, nuklearnoj i subnuklearnoj fizici. Za to su neophodni sistemi koji smanjuju *pozadinsko zračenje (fon).* Detaljno poznavanje izvora pozadinskog šuma preduslov je za preduzimanje efektivnih mera za njegovo smanjenje.

Fon niskofonskih γ spektrometarskih sistema potiče delimično od zračenja proizvedenog *mionima* iz kosmičkog zračenja. Upravo nam ta činjenica omogućuje praćenje intenziteta sekundarnog kosmičkog zračenja, kao i njegove varijacije, koje se prepisuju zemaljskim, solarnim i galaktičkim razlozima. Ovakvi eksperimenti zahtevaju specijalnu detektorsku opremu velike osetljivosti, koja nam omogućuje da razlikujemo događaje izazvane kosmičkim zračenjem od događaja indukovanih drugim zračenjem iz okoline. Sekundarno kosmičko zračenje, koje se na nivou mora sastoji pretežno od visokoenergijskih miona, prolazeći kroz detektor gubi deo svoje energije i proizvodi deo kontinuuma u spektru. Niskoenergijski deo ovog kontinuuma ispod oko 3 MeV kombinovan je sa delom proizvedenim sa drugim zračenjima iz okoline, dok visokoenergijski deo praktično sav potiče od kosmičkih zraka, tako da ga uz specijalne detektore u niskofonskim laboratorijama možemo sa velikom tačnošću izdvojiti od ostalog dela spektra, odnosno zračenja koje dolazi iz okoline, ispitujući tako njegove karakteristike kao što su npr. energija i fluks miona na nivou mora, kao i mnoge detalje vezane za interakciju kosmičkog zračenja sa materijalom. Kada materijal detektora ima veliku gustinu, tj. kada je u tečnom ili čvrtom stanju, kao plastični (polistiren, polietilen) i tečni scintilatori (NaI) ili Ge, većina impulsa koji potiču od miona je velika u odnosu na one koji se uobičajeno registruju u γ spektrometriji (ispod 2,6 MeV) [1].

U poglavlju koje sledi biće opisan jedan od specijalnih detektora za tu namenu, plastični scintilacioni detektor «SCIONIX», koji čini aktivnu zaštitu u niskofonskoj laboratiji na površini, čiju spoljašnju zaštitu čine samo tavanice i zidovi zgrade. Takođe će biti opisani i procesi koje mioni indukuju interagujući sa materijalom detektora, kao i teorijska izračunavanja gubitka energije miona na jonizacione procese, pri prolasku kroz aktivni materijal detektora.

2. SPEKTROSKOPIJA MIONA SA PLASTIČNIM DETEKTOROM

2.1. Iinterakcija miona sa materijalom-teorijski uvod

Mioni sa materijom interaguju praktično najviše preko elekromagnetne interakcije. Zbog izuzetno velike energije imaju prodornu moć, tako da mogu prodreti duboko u površinu Zemlje. Procesi koji provlađuju su jonizacija i ekscitacija, ali takođe dolazi i do sudara sa izbijanjem elektrona, i u manjoj meri, do zakočnog zračenja i stvaranja parova. Zaustavljeni negativni mioni upadaju u klopku atomskih orbita, koje su, zbog mnogo veće mase miona, mnogo bliže jezgru nego atomske orbite elektronau materijalima velikog Z. Pri tome se emituje mionsko X zračenje [1]. Radioaktivni raspad miona:

$$\mu^- \rightarrow e^- + \overline{\nu}_e + \nu_\mu$$

$$\mu^+ \rightarrow e^+ + \overline{\nu}_e + \nu_\mu$$

praćen je i zahvatom miona na protonima:

$$\mu^- + p^+ \rightarrow n + \nu$$

Raspad je verovatniji u materijalima malog rednog broja, dok zahvat preovlađuje u jezgrima visokog rednog broja. Pri zahvatu otpušta se masa mirovanja miona i jezgro ostaje u visoko pobuđenom stanju. Ono se deekscituje emitovanjem jednog ili više neutrona. Broj neutrona emitovanih po jednom mionu zavisi od masenog broja jezgra. Ovi brzi neutroni generišu fotone posredstvom neutron-jezgro reakcija u materijalima sa velikim Z. Pri raspadu miona proizvode se pljuskovi elektromagnetnog zračenja [1]. Ovaj proces umnožavanja nastavlja se dok se ne dostigne kritična energija $\mathcal{E}_c$, posle koje elektroni gube više energije jonizacijom nego radijacijom, a fotoni gube više energije Komptonovim rasejanjem nego proizvodnjom parova. Tada umnožavanje u pljusku prestaje. Elektronsko-fotonske kaskade u laboratoriji mogu dolaziti i od spolja i od građevinskih materijala.

Kao što je već pomenuto, mioni, sa $E_\mu < E_c$ u interakciji sa materijom gube svoju energiju, uglavnom putem jonizacije. Srednju vrednost gubitka energije (ili zaustavne moći) miona na jonizaciju daje poznata Betha-Bloch formula [2]:

$$-\frac{dE}{dX} \approx \frac{\rho}{A}\frac{Z}{\beta^2}\left[\ln\left(\frac{2m_e c^2\gamma^2\beta^2 W_{\max}}{I^2}\right) - 2\beta^2 - \frac{\delta}{2}\right]$$

gde je ρ gustina materijala, Z redni broj materijala, A atomski broj materijala, $\beta=v^2/c^2$, v je brzina upadne čestice, $W_{\max}$ maksimalni energetski transfer čestice slobodnom elektronu, I minimalni jonizacioni potencijal, δ funkcija gustine koja opisuje zavisnost polarizacije sredine od gustine.

Pri tačnijim proračunima dodaju se dve korekcij: efekat gustine δ i efekat ljuske C. Srednji jonizacioni potencijal često se procenjuje iz semi empirijskih formula [2]:

$$\frac{I}{Z} = 12 + \frac{7}{Z}eV \qquad Z < 13$$

$$\frac{I}{Z} = 9{,}76 + 58{,}8Z^{-1{,}19}eV \qquad Z \geq 13$$

U oblasti malih brzina dE/dX opada sa porastom brzine kao $1/v^2$ do minimalnog jonizacionog potencijala koji za mione iznosi 2 $MeVcm^2/g$ [3]. Preko minimalne energije dE/dX logaritamski raste.

Na dovoljno visokim energijama, na gubitak energije miona značajnije utiču radijacioni procesi (proizvodnja parova, zakočno zračenje, fotonuklearne reakcije), za razliku od nižih energija gde preovlađuju procesi jonizacuje. Radijacioni procesi počinju da dominiraju pri energijama upadnih miona iznad nekoliko stotina GeV.

Uobičajeno je da se piše za prosečnu vrednost gubitka energije miona piše u obliku [3]:

$$\frac{dE}{dX} = a(E) + b(E)E$$

gde je $a(E)$ gubitak energije čestica na jonizaciju dat Betha-Bloch formulom, a *b(E)* je zbir doprinosa na proizvodnju parova, zakočno zračenje i fotonuklearnu reakciju.

Mionska kritična energija $E_{\mu c}$ može se definisati kao energija gde su radijacioni i jonizacioni gubici jednaki i definiše se kao $E_{\mu c} = a/b$. Ispod kritične energije dominiraju jonizacioni, a iznad radijacioni procesi. Pošto je $a(E) \approx 0.002 GeVg^{-1}cm^2$, *b(E)* dominira kada su energetski gubici iznad nekoliko stotina GeV, gde je *b(E)* približno konstantno [3].

2.2. Opis i karakteristike detektorskog veto sistema ″SCIONIX″

Kao što je već opisano u uvodnom delu, pozadinsko zračenje (fon) γ spektrometara potiče od svojstvene (unutrašnje) radioaktivnosti detektora, okoline detektora i od kosmičkog zračenja. Radijacija koja potiče od prva dva izvora, može se redukovati rigoroznom selekcijom materijala niskih aktivnosti. Fon niskofonskih γ spektrometarskih sistema, tada, potiče uglavnom od sekundarnog zračenja proizvedenog mionima iz kosmičkog zračenje i može se redukovati smeštanjem mernog sistema duboko pod zemlju, gde je intenzitet kosmičkog zračenja smanjen za nekoliko redova veličine. U površinskim i plitko ukopanim laboratorijama, koje su ovde od interesa, kao alternativna tehnika za redukciju fona kosmičkog zračenja koristi se metod aktivne zaštite detektora, kod koje se detektori sem pasivnog sloja materijala (materijali visoke gustine, visokog rednog broja i visoke radiočistoće) okružuju posebnim zaštitnim (guard, veto) detektorima. Veto detektori rade u antikoincidentnom režimu sa glavnim detektorom i elektronski odbacuju istovremene događaje u oba detektora. U laboratoriji na površini u IFNS, čiju spoljašnju zaštitu čine tavanice i zidovi zgrade, postavljen je jedan takav γ spektrometrijski sistem, pod nazivom CRYME (Cosmic Ray Multipurpose Experiment), u kojem aktivna zaštita okružuje pasivno zaštićen detektor (Pb, Fe i Sn). Za razliku od mnogih sličnih sistema koji se eksploatišu u podzemnim laboratorijama, sistem CRYME koristi spektralnu informaciju iz veto detektora i radi u koincidentnom režimu. Na ovaj način, za svaki registrovani događaj u glavnom detektoru znaće se da li je kosmičkog porekla, koja je energija zračenja koja ga je indukovala i iz kog pravca primarnog zračenja dolazi.

Postojeća izvedba, u niskofonskoj laboratoriji IFNS, za redukciju fona od kosmičkog zračenja, koristi plastični veto detektor tipa «SCIONIX», dimenzija 50 cm × 50 cm × 5 cm. Plastika od koje je izrađen ovaj detektorski sistem na bazi je polistirena (C_6H_6). Da bi se postiglo maksimalno smanjenje sekundarnog zračenja i detektovali skoro svi mioni koji ulaze u detektor, u sistemu se koristi 6 velikih pljosnatih, plastičnih detektora; četiri čine zaštitu sa strane, jedan je gornja zaštita, dok je šesti smešten centralno oko sistema na visini od oko 2 m i čini teleskop za kosmičko zračenje. Ovaj zaštitni sistem ima efikasnost detekcije od praktično 100% za mione i protone. Najveći doprinos smanjenju kosmičkog fona, oko 76% [1] , daje veto detektor postavljen odgore.

2.3. Gubici energije miona na jonizaciono zračenje u detektorskom materijalu-teorijski - proračun

Srednja procena gubitka energije miona na jonizaciju, kao što je već napomenuto, izržena je preko Betha-Bloch formule. U ovom radu određene su vrednosti gubitaka kosmičkih miona na jonizaciju, pri prolasku kroz materijal aktivne zaštite detektora «SCIONIX». Detektorski materijal na bazi je plastike-polistiren (C_6H_6).

Kritična energija miona, detektora «SCIONIX», iznosi, prema formuli [3]:

$$E_{\mu c} = \frac{6224 \quad GeV}{(Z + 2.05)^{0.876}}$$

oko 1087 GeV. Iznad ove energije dominiraju radijacioni procesi sudara miona sa detektorskim materijalom. Na Sici 1 prikazan je gubitak energije kosmičkih miona u interakciji sa detektorom u funkciji od energije upadnih miona.

3. EKSPERIMENT

3.1. Energetska kalibracija plastičnog detektora ″SCIONIX″

Da bi odredili energiju kosmičkih miona, neophodno je da izvršimo energetsku kalibraciju spektra kosmičkog

zračenja. Kalibracija je izvršena snimanjem sledećih kalibracionih izvora: Na-22 (pozitronski izvor), Co-60 i Cs-137. U spektrima ovih izvora uočene su karakteristične Komptonove ivice, dok je presek za fotoefekat zanemarljiv, zbog malog rednog broja detektorskog materijala ($Z_{eff} = 5.28$). Jedan takav spektar prikazan je na Slici 2.

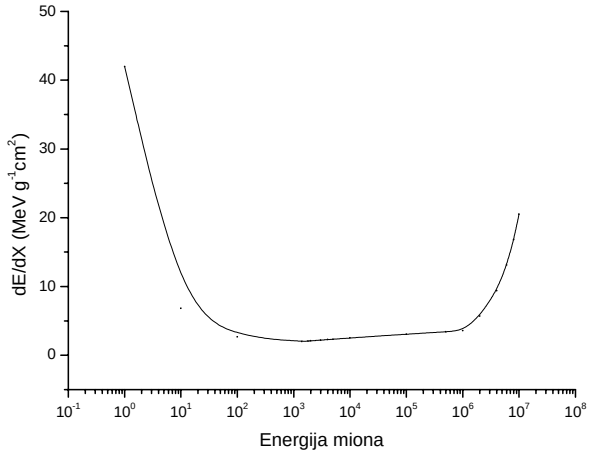

Sl.1. Gubitak energije kosmičkih miona *dE/dX* u funkciji od energije miona

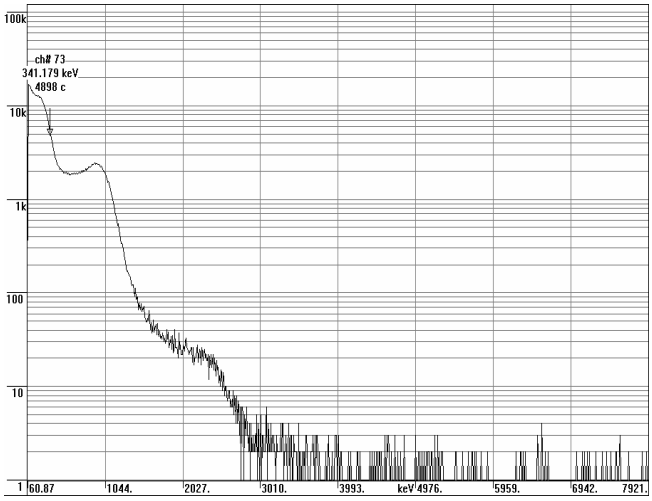

Sl.2. Spektar izvora Na-22 u aktivnoj zaštiti ″SCIONIX″

Teorijski proračunate vrednosti Komptonskih ivica i pozicije ivica očitanih sa kalibracionih spektara, date su u Tabeli I.

Tab.I. Energije i pozicije Komtonovih ivica

Channel	ΔChannel	T^{max}_{compt} [keV]
73	10	341.179
109	10	477.937
272	10	1062.49
327	10	1244.202
580	10	2273.506
665	10	2614.35

Na osnovu podataka datih u Tab.1, energetska kalibraciona kriva, predstavljena je na slici 2.

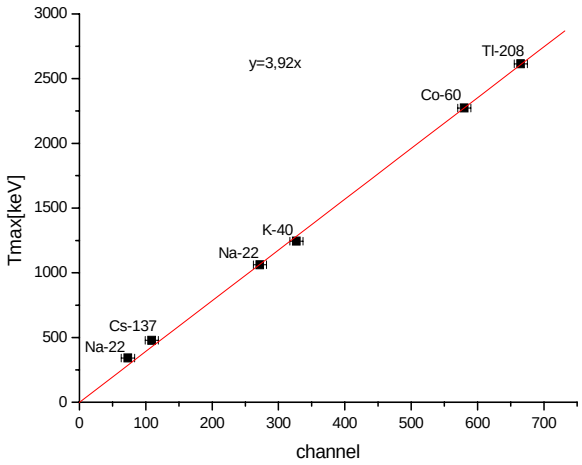

Sl. 3. Energetska kalibracija detektora ″SCIONIX″

Kalibracioni faktor iznosi:

3.92(4)keV/ch.

3.2 Određivanje energije i fluksa miona na nivou mora (iz spektra)

Nakon kalibracije, pristupilo se merenju fonskog spektra u cilju određivanja energije i fluksa kosmičkih miona. U tom cilju koristili smo 5 zaštitnih detektora (4 bočna i teleskop). Vreme sakupljanja iznosilo je t= 4000 s, priključeni napon od U=1000 V i pojačanje 30. Dobijeni spektar prikazan je na Slici 4. Nakon energetske kalibracije, očitana je vrednost energetskog gubitka vertikalne komponente kosmičkih miona i određen fluks integraljenjem ispod krive vertikalne komponente miona.

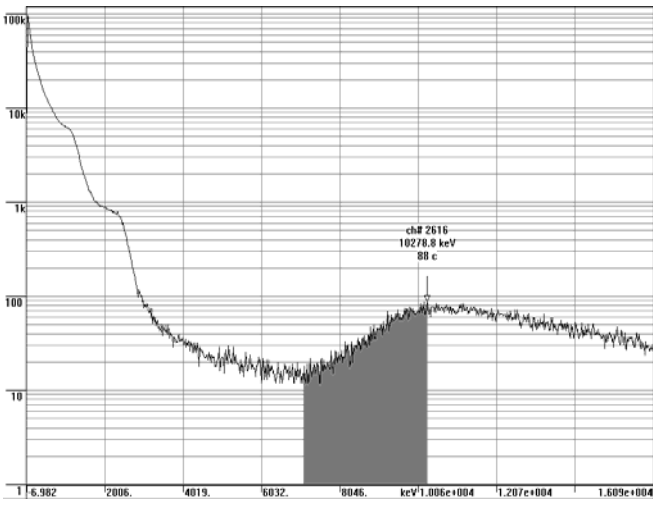

Sl.4. Fonski spektar u aktivnoj zaštiti «SCIONIX»

Kao što se uočava sa slike vrednost deponovane energije upadnih miona u detektorskom materijalu iznosi:

$$E_{\mu d}^{\exp} = 10.278(28)\ \text{MeV}$$

Ovoj vrednosti odgovaraju mioni sa energijama od oko 1.96 GeV. Teorijska izračunavanja pokazuju da ovoj energiji miona odgovara vrednost izgubljene energije od:

$$E_{\mu d}^{teor} = 10.814 \text{ MeV}.$$

Vrednost fluksa vertikalne komponente miona na nivou mora iznosi:

$$\Phi_{\mu}^{\exp} = 54.15(11)\ \text{m}^{-2}\,\text{s}^{-1}$$

4. ZAKLJUČAK

Dobijeni rezultati za energiju i fluks miona na nivou mora, kao i za deponovanu energiju miona u detektorskom materijalu, pokazali su dosta dobru saglasnost između eksperimentalnih rezultata za energiju i fluks miona na nivou mora od, sa rezultatima datim u [3] i [4]. Vrednost energije kosmičkih miona na nivou mora datim prema [3] iznosi oko 2 GeV. Rezultat dobijen na osnovu eksperimenta za vrednost energije iznosi 1,96 GeV. U [4], vrednost fluksa kosmičkih miona na nivou mora iznosi oko 56 $\text{m}^{-2}\,\text{s}^{-1}$, dok vrednost dobijena iz eksperimenta iznosi 54.15 $\text{m}^{-2}\,\text{s}^{-1}$. Takođe je pokazano da je energetski odgovor detektora linearan.

LITERATURA

[1] J. Slivka, I. Bikit, M. Vesković, Lj. Čonkić, "*Gama spektrometrija,"* Univerzitetski udžbenik, Novi Sad, 2000.

[2] William R. Leo, *"Techniques for Nuclear and Particle Physics Experiments, A how to approach*," 2 *th* ed., Springer-Verlag, Berlin Heidelberg New York, 1994

[3] R.M. Barnett et al., *Physical Review D54, 1 th ed.,* AIP Available from LBNL and CERN, 1996

[4] J.F.Ziegler "Terrestrial cosmic ray intensities", *IBM Journal of Research and Development, Vo.42, No.1,* 1998

Abstract – Background in γ spectrometry systems arises mainly from secondary radiation produced by cosmic ray muons. This particular background component can not be reduced by incresing the thickness of the passive protective shielding. Therefore, large surface external protective detectors (i.e. Veto Detectors) are implemented for cosmic radiation reduction. This paper describes the spectroscopic characteristics of a plastic based «SCIONIX» detector aperature. The experiments in the low-level background surface laboratory at IFNS have shown the linear response of the detector and determined the muon flux and energy.

PLASSTIC BASED DETECTOR SPECTROMETRY

Nataša Žikić-Todorović, Sofija Forkapić, Tatjana Jovin, Ljiljana Čonkić, Miodrag Krmar

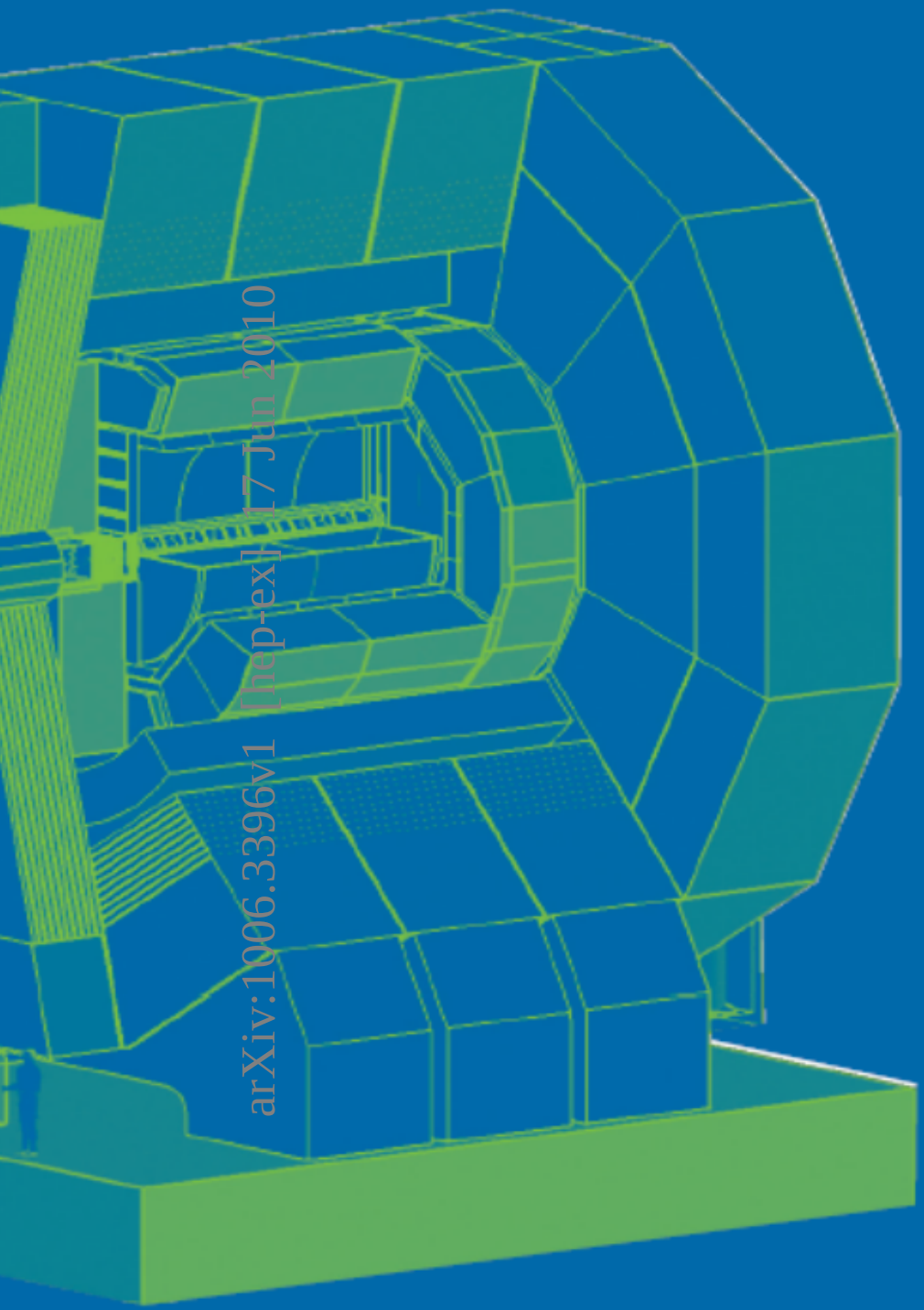

The International Large Detector

Letter of Intent

by the
ILD Concept Group

February 2010

DESY 2009-87
FERMILAB-PUB-09-682-E
KEK Report 2009-6

International Large Detector

Letter Of Intent

The ILD concept group

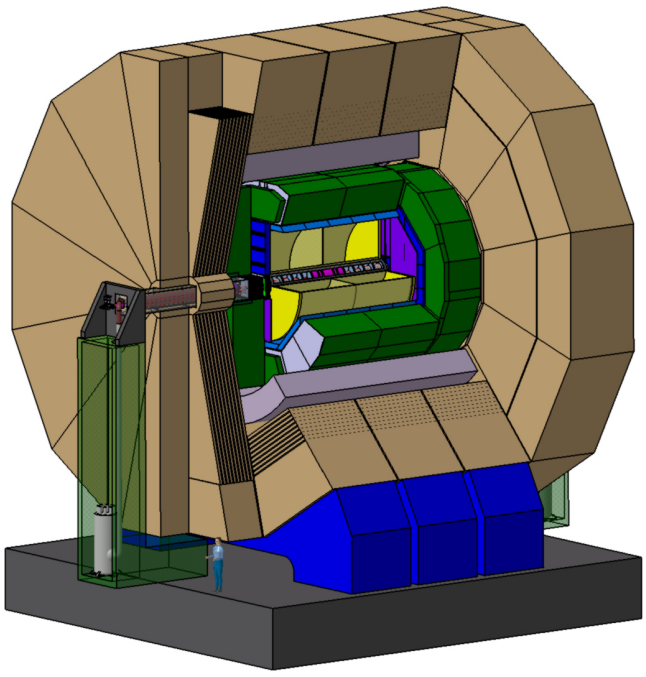

February 2010

International Large Detector - Letter of Intent

DESY / KEK / Fermilab
DESY 2009/87 - Fermilab PUB-09-682-E - KEK Report 2009-6
ISSN 0418-9833
ISBN 978-3-935702-42-3

http://www.ilcild.org and http://www.linearcollider.org

SIGNATORIES

Holger Stoeck
University of Sydney, Falkiner High Energy Physics Group, School of Physics, A28, Sydney, NSW 2006, Australia

Thomas Bergauer, Marko Dragicevic, Helmut Eberl, Sebastian Frank, Elena Ginina, Stephan Haensel, Hana Hlucha, Wolfgang Kiesenhofer, Manfred Krammer, Winfried A. Mitaroff, Fabian Moser, Meinhard Regler, Manfred Valentan, Wolfgang Waltenberger
Österreichische Akademie der Wissenschaften, Institut für Hochenergiephysik, Nikolsdorfergasse 18, A-1050 Vienna, Austria

Konstantin Afanaciev, Vladimir Drugakov, Igor Emeliantchik, Alexandr Ignatenko, Nikolai Shumeiko
National Scientific & Educational Centre of Particle & High Energy Physics (NCPHEP), Belarusian State University, M.Bogdanovich street 153, 220040 Minsk, Belarus

Martin Grunewald
University of Ghent, Department of Subatomic and Radiation Physics, Proeftuinstraat 86, 9000 Gent, Belgium

Alain Bellerive, Madhu S. Dixit[1]
Carleton University, Department of Physics, 1125 Colonel By Drive, Ottawa, Ontario, Canada K1S 5B6

François Corriveau
McGill University, Department of Physics, Ernest Rutherford Physics Bldg., 3600 University Street, Montreal, Quebec, H3A 2T8 Canada

Mauricio Barbi
University of Regina, Department of Physics, Regina, Saskatchewan, S4S 0A2 Canada

Jason M Abernathy, Dean Karlen[1]
University of Victoria, Department of Physics and Astronomy, P.O.Box 3055 Stn Csc, Victoria, BC V8W 3P6, Canada

Jean-Pierre Martin
Université de Montréal, Département de Physique, Groupe de Physique des Particules, C.P. 6128, Succ. Centre-ville, Montréal, Qc H3C 3J7, Canada

Li Bo, Shaomin Chen, Zhi Deng, Yuanning Gao, Fanfan Jing, Yu-Ping Kuang, Yulan Li, Bo Li, Ting Li, Bo Liu, Wenbin Qian, Junping Tian[3], Yi Wang, Zhenwei Yang, Qian Yue, Yanxi Zhang, Baojun Zheng, Liang Zhong, Xianglei Zhu
Center for High Energy Physics (TUHEP), Tsinghua University, Beijing, China 100084

Jin Min Yang
Institute of Theoretical Physics, Chinese Academy of Sciences, P.O.Box 2735, Beijing, China 100080

Chunxu Yu
Nankai University, Department of Physics, Tianjin, China 300071

Cunfeng Feng, Xingtao Huang, Zuotang Liang, Meng Wang, Xueyao Zhang, Chengguang Zhu
Shandong University, 27 Shanda Nanlu, Jinan, China 250100

Hongfang Chen, Liang Han, Ge Jing, Wengan Ma, Ming Shao, Kezhu Song, Qun Wang, Xiaoliang Wang, Zizong Xu, Wenbiao Yan, Renyou Zhang, Ziping Zhang, Jiawei Zhao, Zhengguo Zhao, Yongzhao Zhou
University of Science and Technology of China, Department of Modern Physics (DMP), Jin Zhai Road 96, Hefei, China 230026

Zdenek Dolezal, Zbynek Drasal, Peter Kodys, Peter Kvasnicka, Jan Scheirich, Josef Zacek
Charles University, Institute of Particle & Nuclear Physics, Faculty of Mathematics and Physics, V Holesovickach 2, CZ-18000 Prague 8, Czech Republic

Jaroslav Cvach, Michal Marcisovsky, Stanislav Nemecek, Ivo Polak, Pavel Ruzicka, Petr Sicho, Jan Smolík, Vaclav Vrba, Jaroslav Zalesak
Institute of Physics, ASCR, Academy of Science of the Czech Republic, Division of Elementary Particle Physics, Na Slovance 2, CZ-18221 Prague 8, Czech Republic

Mogens Dam, Peter H Hansen, Stefania Xella
Niels Bohr Institute (NBI), University of Copenhagen, Blegdamsvej 17, DK-2100 Copenhagen, Denmark

Risto Orava[4]
University of Helsinki, Department of Physical Sciences, P.O. Box 64 (Vaino Auerin katu 11), FIN-00014, Helsinki, Finland

David Attie, Marc Besancon, Paul Colas, Eric Delagnes, Nicolas Fourches, Giomataris Ioannis, Francois Kircher, Pierre Lutz[5], Christophe Royon, Maxim Titov
CEA Saclay, IRFU, F-91191 Gif-sur-Yvette, France

Jerome Baudot[6], Auguste Besson[6], Andrea Brogna[6], Gilles Claus[6], Claude Colledani[6], Rita De Masi, Andrei Dorokhov[6], Guy Doziere[6], Abdelkader Himmi[6], Christine Hu-Guo[6], Marc Imhoff[6], Frederic Morel[6], Isabelle Valin[6], Yorgos Voutsinas, Marc Winter
Institut Pluridisciplinaire Hubert Curien, 23 Rue du Loess - BP28, 67037 Strasbourg Cedex 2, France

Helenka Przysiezniak[2]
Laboratoire d'Annecy-le-Vieux de Physique des Particules (LAPP), Chemin du Bellevue, BP 110, F-74941 Annecy-le-Vieux Cedex, France

Bernard Bouquet, Stephane L.C. Callier, Patrick Cornebise, Olivier Dadoun, Christophe De La Taille, Philippe Doublet, Frédéric Dulucq, Michele Faucci Giannelli[22], Julien L Fleury, Matthieu Joré, Hengne Li, Gisele Martin-Chassard, Roman Poeschl, Ludovic Raux, Francois Richard, Nathalie Seguin-Moreau, Dirk Zerwas, Zhiqing Zhang, Fabian Zomer
Laboratoire de l'Accélérateur Linéaire (LAL), Université Paris-Sud 11, Bâtiment 200, 91898 Orsay, France

Cristina Carloganu, Pascal Gay, Philippe Gris
Laboratoire de Physique Corpusculaire de Clermont-Ferrand (LPC), Université Blaise Pascal, I.N.2.P.3./C.N.R.S., 24 avenue des Landais, 63177 Aubière Cedex, France

Alexandre Charpy, Catalin Ciobanu, Wilfrid Da Silva, Guillaume Daubard, Jacques David, Christophe Evrard, Jean-Francois Genat[24], Jean Francois Huppert, Didier Imbault, Frédéric Kapusta, Dhellot Marc, Ghislain Patrick, Thanh Hung Pham, Philippe Repain, Aurore Savoy-Navarro, Rachid Sefri
Laboratoire de Physique Nucléaire et des Hautes Energies (LPNHE), Université Pierre et Marie Curie, IN2P3/CNRS, Tour 43, RdC, 4, Place Jussieu, 75252, Paris-Cedex 05, France

Joël Bouvier, Daniel Dzahini, Laurent Gallin-Martel, Julien Giraud, Denis Grondin, Jean-Yves Hostachy, Sabine Kraml, Kaloyan Krastev, Eric Lagorio, Laurent Morin, Fatah-Ellah Rarbi, Christophe Vescovi, Mahfoud Yamouni
Laboratoire de Physique Subatomique et de Cosmologie (LPSC), Université Joseph Fourier (Grenoble 1), CNRS/IN2P3, Institut Polytechnique de Grenoble, 53 rue des Martyrs, F-38026 Grenoble Cedex, France

Marc Anduze, Khaled Belkadhi, Vincent Boudry, Jean-Claude Brient, Catherine Clerc, Rémi Cornat, David Decotigny, Mickael Frotin, Franck Gastaldi, Daniel T D Jeans, Antoine Mathieu, Paulo Mora De Freitas, Gabriel Musat, Marcel Reinhard, Manqi Ruan, Jean-Charles Vanel, Henri L Videau
Laboratoire Leprince-Ringuet (LLR), École polytechnique – CNRS/IN2P3, Route de Saclay, F-91128 Palaiseau Cedex, France

Jean-Charles Fontaine
Université de Haute Alsace Mulhouse-Colmar, Groupe de Recherche en Physique des Hautes Energies (GRPHE), 61 rue Albert Camus, 68093 Mulhouse Cedex, France

Marc Bedjidian, Christophe Combaret, Gérald Grenier, Robert Kieffer, Imad Laktineh, Patrice Lebrun, Nick Lumb, Hervé Mathez, Kieffer Robert, Muriel Vander Donckt
Université de Lyon, F-69622, Lyon, France ; Université Lyon 1, Villeurbanne ; CNRS/IN2P3, Institut de Physique Nucléaire de Lyon

Uwe Renz, Markus Schumacher
Albert-Ludwigs Universität Freiburg, Physikalisches Institut, Hermann-Herder Str. 3, D-79104 Freiburg, Germany

Ringo Sebastian Schmidt[9]
Brandenburg University of Technology, Postfach 101344, D-03013 Cottbus, Germany

Hartwig Albrecht, Steve J. Aplin, Jochen Bürger, Christoph Bartels[12], Philip Bechtle, Jeannine Beck, Moritz Beckmann[11], Ties Behnke, C. Mikael U. Berggren, Karsten Buesser, Stefano Caiazza[12], Alan J. Campbell, Sandra Christen[12], Dörte David, Klaus Dehmelt, Ralf Diener, Guenter Eckerlin, Wolfgang Ehrenfeld, Eckhard Elsen, Jan Engels, Riccardo Fabbri, Manfred Fleischer, Frank Gaede, Erika Garutti, Andreas Gellrich, Ingrid-Maria Gregor, Tobias Haas, Lea Hallermann[12], Anthony Hartin, Martin Harz, Isa Heinze[12], Christian Helebrant[12], Daniela Käfer, Claus Kleinwort, U. Koetz, Volker Korbel, Dirk Krücker, Bernward Krause, Kirsten Kschioneck, Jan Kuhlmann, Frank Lehner, Diana Linzmaier, Jenny List, Angela Isabela Lucaci-Timoce, Benjamin Lutz[12], Ivan Marchesini[12], Cornelius Martens, Niels Meyer, Norbert Meyners, Joachim Mnich, Sergey Morozov[12], Carsten Niebuhr, Alexander Petrov, Volker Prahl, Alexei Raspereza, Philipp Roloff[12], Christoph Rosemann, K. Peter Schüler, Peter Schade, Joern Schaffran, Sebastian Schmitt, Uwe Schneekloth, Felix Sefkow, Klaus Sinram, Blanka Sobloher[12], Richard Stromhagen, Robert Volkenborn, Nanda Wattimena, Katarzyna Wichmann, Wolfram Zeuner[20]
Deutsches Elektronen-Synchrotron DESY, A Research Centre of the Helmholtz Association, Notkestrasse 85, 22607 Hamburg, Germany (Hamburg site)

Matthias Bergholz[7], Johannes Bluemlein, Maria Elena Castro Carballo, Hans Henschel, Hanna Kluge, Wolfgang Lange, Wolfgang Lohmann, Klaus Moenig, Martin Ohlerich, Sabine Riemann, Tord Riemann, André Sailer, Andreas Schälicke, Heinz Juergen Schreiber, Sergej Schuwalow, Andriy Ushakov
Deutsches Elektronen-Synchrotron DESY, A Research Centre of the Helmholtz Association, Platanenallee 6, 15738 Zeuthen, Germany (Zeuthen site)

Ariane Frey, Carsten Hensel, Arnulf Quadt
Georg-August-Universität Göttingen, II. Physikalisches Institut, Friedrich-Hund-Platz 1, 37077 Göttingen, Germany

Ralph Dollan
Humboldt Universität zu Berlin, Fachbereich Physik, Institut für Elementarteilchenphysik, Newtonstr. 15, D-12489 Berlin, Germany

Wim De Boer[20], Robert Rossmanith
Institut für Experimentelle Kernphysik, KIT,Universität Karlsruhe (TH), Wolfgang-Gaede-Str. 1, Postfach 6980, 76128 Karlsruhe

Stefan Tapprogge
Johannes Gutenberg Universität Mainz, Institut für Physik, 55099 Mainz, Germany

Otmar Biebel, Ralf Hertenberger, Raimund Ströhmer
Ludwig-Maximilians-Universität München, Fakultät für Physik, Am Coulombwall 1, D - 85748 Garching, Germany

Ladislav Andricek, Allen Caldwell, Xun Chen, Christian M Kiesling, Shaojun Lu[10], Andreas Moll[10], Hans-Günther Moser, Bob Olivier, Katja Seidel[10], Ronald Dean Settles, Frank Simon[10], Christian Soldner, Lars Weuste
Max-Planck-Institut für Physik (Werner-Heisenberg-Institut), Föhringer Ring 6, 80805 München, Germany

Werner Bernreuther, Tatsiana Klimkovich, Hans-Ulrich Martyn[8], Stefan Roth
Rheinisch-Westfälische Technische Hochschule (RWTH), Physikalisches Institut, Physikzentrum, Sommerfeldstrasse 14, D-52056 Aachen, Germany

Deepak Kar, Michael Kobel, Wolfgang F. Mader, Xavier Prudent, Rainer Schwierz, Dominik Stockinger, Arno Straessner
Technische Universität Dresden, Institut für Kern- und Teilchenphysik, D-01069 Dresden, Germany

Nils Feege[8], Andreas Imhof, Benno List, Oliver Wendt[8]
University of Hamburg, Physics Department, Institut für Experimentalphysik, Luruper Chaussee 149, 22761 Hamburg, Germany

Alexander Kaplan[8], Hans-Christian Schultz-Coulon
University of Heidelberg, Kirchhoff Institute of Physics, Albert Überle Strasse 3-5, DE-69120 Heidelberg, Germany

Michal Czakon[13], Malgorzata Worek[13], Christian Zeitnitz
University of Wuppertal, Gaußstraße 20, D-42119 Wuppertal, Germany

Ian Brock, Klaus Desch, Jochen Kaminski, Martin Killenberg, Thorsten Krautscheid, Adrian Vogel, Norbert Wermes, Peter Wienemann
Universität Bonn, Physikalisches Institut, Nußallee 12, 53115 Bonn, Germany

Alexander Kaukher, Oliver Schäfer
Universität Rostock, Fachbereich Physik, Universitätsplatz 3, D-18051 Rostock, Germany

Peter Buchholz, Ivor Fleck, Bakul Gaur, Marcus Niechciol
Universität Siegen, Fachbereich für Physik, Emmy Noether Campus, Walter-Flex-Str.3, D-57068 Siegen, Germany

Csaba Hajdu, Dezso Horvath
Hungarian Academy of Sciences, KFKI Research Institute for Particle and Nuclear Physics, P.O. Box 49, H-1525 Budapest, Hungary

Bipul Bhuyan
Indian Institute of Technology, Guwahati, Guwahati, Assam 781039, India

Sudeb Bhattacharya, Nayana Majumdar, Supratik Mukhopadhyay, Sandip Sarkar
Saha Institute of Nuclear Physics, 1/AF Bidhan Nagar, Kolkata 700064, India

Atul Gurtu, Gobinda Majumder
Tata Institute of Fundamental Research, School of Natural Sciences, Homi Bhabha Rd., Mumbai 400005, India

B. C. Choudhary
University of Delhi, Department of Physics and Astrophysics, Delhi 110007, India

Manas Maity
Visva-Bharati University, Department of Physics, Santiniketan 731235, India

Halina Abramowicz, Ronen Ingbir, Aharon Levy, Iftach Sadeh
Tel-Aviv University, School of Physics and Astronomy, Ramat Aviv, Tel Aviv 69978, Israel

Antonio Bulgheroni
Istituto Nazionale di Fisica Nucleare (INFN), Sezione di Milano, Via Celoria 16, I-20133 Milano, Italy

Lodovico Ratti, Valerio Re
Istituto Nazionale di Fisica Nucleare (INFN), Sezione di Pavia, Via Bassi 6, I-27100 Pavia, Italy

Simonetta Gentile
Istituto Nazionale di Fisica Nucleare (INFN), Sezione di Roma, c/o Dipartimento di Fisica - Università degli Studi di Roma "La Sapienza", P.le Aldo Moro 2, I-00185 Roma, Italy

Diego Gamba, Giuseppe Giraudo, Paolo Mereu
Istituto Nazionale di Fisica Nucleare (INFN), Sezione di Torino, c/o Universitá di Torino, facoltá di Fisica, via P Giuria 1, 10125 Torino, Italy

Alessandro Calcaterra, Marcello Piccolo
Laboratori Nazionali di Frascati, via E. Fermi, 40, C.P. 13, I-00044 Frascati, Italy

Massimo Caccia[15], Chiara Cappellini[15]
Università dell'Insubria in Como, Dipartimento di Scienze CC.FF.MM., via Vallegio 11, I-22100 Como, Italy

Takuo Yoshida
Fukui University, Department of Physics, 3-9-1 Bunkyo, Fukui-shi, Fukui 910-8507, Japan

Yasuo Arai, Hirofumi Fujii, Keisuke Fujii, Junpei Fujimoto, Yowichi Fujita, Takanori Hara, Tomiyoshi Haruyama, Takeo Higuchi, Katsumasa Ikematsu, Yukiko Ikemoto, Eiji Inoue, Hideo Itoh, Go Iwai, Nobu Katayama, Masanori Kawai, Makoto Kobayashi, Hideyo Kodama, Takashi Kohriki, Yoshinari Kondou, Akihiro Maki, Yasuhiro Makida, Takeshi Matsuda[8], Satoshi Mihara, Akiya Miyamoto, Takeshi Murakami, Isamu Nakamura, Kazuo Nakayoshi, Shohei Nishida, Mitsuaki Nozaki, Nobuchika Okada, Tsunehiko Omori, Masatoshi Saito, Toshiya Sanami, Hiroshi Sendai, Shoichi Shimazaki, Yusuke Suetsugu, Yasuhiro Sugimoto, Kazutaka Sumisawa, Shuji Tanaka, Manobu Tanaka, Ken-Ichi Tanaka, Toshiaki Tauchi, Kazuya Tauchi, Katsuo Tokushuku, Toru Tsuboyama, Junji Urakawa, Yutaka Ushiroda, Hiroshi Yamaoka, M. Yamauchi, Yoshiji Yasu, Tamaki Yoshioka
High Energy Accelerator Research Organization, KEK, 1-1 Oho, Tsukuba, Ibaraki 305-0801, Japan

Tohru Takahashi
Hiroshima University, Department of Physics, 1-3-1 Kagamiyama, Higashi-Hiroshima, Hiroshima 739-8526, Japan

Masaki Asano
Institute for Cosmic Ray Research, University of Tokyo, 5-1-5 Kashiwa-no-Ha, Kashiwa, Chiba 277-8582, Japan

Toshiyuki Iwamoto, Yoshio Kamiya, Hiroyuki Matsunaga, Toshinori Mori, Wataru Ootani, Taikan Suehara, Tomohiko Tanabe, Satoru Yamashita
International Center for Elementary Particle Physics, University of Tokyo, Hongo 7-3-1, Bunkyo District, Tokyo 113-0033, Japan

Hirokazu Ikeda
Japan Aerospace Exploration Agency, Sagamihara Campus, 3-1-1 Yoshinodai, Sagamihara, Kanagawa 220-8510 , Japan

Yukihiro Kato
Kinki University, Department of Physics, 3-4-1 Kowakae, Higashi-Osaka, Osaka 577-8502, Japan

Akimasa Ishikawa, Kiyotomo Kawagoe, Takashi Matsushita, Hiroshi Takeda, Satoru Uozumi, Yuji Yamazaki
Kobe University, Department of Physics, 1-1 Rokkodai-cho, Nada-ku, Kobe, Hyogo 657-8501, Japan

Takashi Watanabe
Kogakuin University, Department of Physics, Shinjuku Campus, 1-24-2 Nishi-Shinjuku, Shinjuku-ku, Tokyo 163-8677, Japan

Fumiyoshi Kajino
Konan University, Department of Physics, Okamoto 8-9-1, Higashinada, Kobe 658-8501, Japan

Takahiro Fusayasu
Nagasaki Institute of Applied Science, 536 Abamachi, Nagasaki-Shi, Nagasaki 851-0193, Japan

Takashi Mori
Nagoya University, High Energy Physics Lab., Div. of Particle and Astrophysical Sciences, Furo-cho, Chikusa-ku, Nagoya, Aichi 464-8602, Japan

Takeo Kawasaki, Hitoshi Miyata, Minori Watanabe
Niigata University, Department of Physics, Ikarashi, Niigata 950-218, Japan

Hiroaki Ono
Nippon Dental University School of Life Dentistry at Niigata, 1-8 Hamaura-cho, Chuo-ku, Niigata 951-1500, Japan

Eiichi Nakano
Osaka City University, Department of Physics, Faculty of Science, 3-3-138 Sugimoto, Sumiyoshi-ku, Osaka 558-8585, Japan

Hirotoshi Kuroiwa, Kenichi Nakashima, Akira Sugiyama, Shiro Suzuki, Hiroshi Yamaguchi
Saga University, Department of Physics, 1 Honjo-machi, Saga-shi, Saga 840-8502, Japan

Yoji Hasegawa, Yasuhiro Ide, Katsushige Kotera, Miho Nishiyama, Takayuki Sakuma, Tohru Takeshita, Shunsuke Tozuka, Koji Yanagida
Shinshu University, 3-1-1, Asahi, Matsumoto, Nagano 390-8621, Japan

Masaya Iwabuchi, Ryo Yonamine
Sokendai, The Graduate University for Advanced Studies, Shonan Village, Hayama, Kanagawa 240-0193, Japan

Kazurayama Hironori, Yasuyuki Horii, Kennosuke Itagaki, Kazutoshi Ito, Yusuke Kamai, Eriko Kato, Tomonori Kusano, Tadashi Nagamine, Yoshimasa Ono, Yoshiyuki Onuki, Tomoyuki Sanuki, Rei Sasaki, Yutaro Sato, Fumihiko Suekane, Yosuke Takubo, Akira Yamaguchi, Hitoshi Yamamoto, Kohei Yoshida
Tohoku University, Department of Physics, Aoba District, Sendai, Miyagi 980-8578, Japan

Osamu Nitoh
Tokyo University of Agriculture Technology, Department of Applied Physics, Naka-machi, Koganei, Tokyo 183-8488, Japan

Toshinori Abe, Hiroki Kawahara, Sachio Komamiya
University of Tokyo, Department of Physics, 7-3-1 Hongo, Bunkyo District, Tokyo 113-0033, Japan

Toshinori Ikuno, Shinhong Kim, Yuji Sudo
University of Tsukuba, Institute of Physics, 1-1-1 Ten'nodai, Tsukuba, Ibaraki 305-8571, Japan

Donghee Kim, Guinyun Kim, Hyunok Kim, Hong Joo Kim, Hwanbae Park
Center for High Energy Physics (CHEP) / Kyungpook National University, 1370 Sankyuk-dong, Buk-gu, Daegu 702-701, Korea

Eun-Joo Kim
Chonbuk National University, Division of Science Education, Jeonju 561-756, Korea (South)

Jik Lee, Jiwoo Nam, Shinwoo Nam, Il Hung Park, Jongmann Yang
Ewha Womans University, 11-1 Daehyun-Dong, Seodaemun-Gu, Seoul, 120-750, Korea

Byunggu Cheon
Hanyang University, Department of Physics, Seoul 133-791, Korea

Suyong Choi, Intae Yu
Sungkyunkwan University (SKKU), Natural Science Campus 300, Physics Research Division, Chunchun-dong, Jangan-gu, Suwon, Kyunggi-do 440-746, Korea

Choong Sun Kim
Yonsei University, Department of Physics, 134 Sinchon-dong, Sudaemoon-gu, Seoul 120-749, Korea

Nicolo De Groot[16], Sijbrand De Jong[16], Frank Filthaut[16]
Institute for Mathematics, Astrophysics and Particle Physics (IMAPP), P.O. Box 9010, 6500 GL Nijmegen, Netherlands

Stan Bentvelsen, Auke Colijn[16], Paul De Jong, Olga Igonkina, Peter Martin Kluit, Els Koffeman[16], Frank Linde, Marcel Merk[17], Antonio Pellegrino, Jan Timmermans[8], Harry Van Der Graaf, Marcel Vreeswijk
Nikhef, National Institute for Subatomic Physics, P.O. Box 41882, 1009 DB Amsterdam, Netherlands

Gerhard Raven[16]
Vrije Universiteit, Department of Physics, Faculty of Sciences, De Boelelaan 1081, 1081 HV Amsterdam, Netherlands

Gerald Eigen, Per Osland
University of Bergen, Institute of Physics, Allegaten 55, N-5007 Bergen, Norway

Sameen Ahmed Khan
Salalah College of Technology (SCOT), Engineering Department, Post Box No. 608, Postal Code 211, Salalah, Sultanate of Oman

Editha P. Jacosalem
MSU-Iligan Institute of Technology, Department of Physics, Andres Bonifacio Avenue, 9200 Iligan City, Phillipines

Marek Idzik, Danuta Kisielewska, Krzysztof Swientek
AGH University of Science and Technology, Akademia Gorniczo-Hutnicza im. Stanislawa Staszica w Krakowie, Al. Mickiewicza 30 PL-30-059 Cracow, Poland

Marek Adamus
Andrzej Soltan Institute for Nuclear Studies, High Energy Physics Department, P-6, Ul. Hoza 69, PL-00 681 Warsaw, Poland

Witold Daniluk, Eryk Kielar, Tadeusz Lesiak, Krzysztof Oliwa, Bogdan Pawlik, Wojciech Wierba, Leszek Zawiejski
The Henryk Niewodniczanski Institute of Nuclear Physics, Polish Academy of Sciences (IFJ PAN), ul. Radzikowskiego 152, PL-31342 Cracow, Poland

Pawel Luzniak
University of Lodz, Faculty of Physics and Applied Informatics, Pomorska 149/153, PL-90-236 Lodz, Poland

Jacek Ciborowski[18], Grzegorz Grzelak, Lukasz Maczewski[18], Piotr Niezurawski, Aleksander Filip Zarnecki
University of Warsaw, Institute of Experimental Physics, Ul. Hoza 69, PL-00 681 Warsaw, Poland

Janusz Rosiek
University of Warsaw, Institute of Theoretical Physics, Ul. Hoza 69, PL-00 681 Warsaw, Poland

Cornelia Coca, Mihai-Octavian Dima, Laurentiu Alexandru Dumitru, Marius Ciprian Orlandea, Eliza Teodorescu
National Institute of Physics and Nuclear Engineering "Horia Hulubei" (IFIN-HH), Str. Atomistilor no. 407, P.O. Box MG-6, R-76900 Bucharest - Magurele, Romania

Aura Rosca[19]
West University of Timisoara, Faculty of Physics, Bd. V. Parvan 4, 300223 Timisoara, Romania

A. Bondar, A.F. Buzulutskov, L.I. Shechtman, Valery I. Telnov
Budker Institute for Nuclear Physics (BINP), 630090 Novosibirsk, Russia

Marina Chadeeva, Mikhail Danilov, Vasily Morgunov[8], Vladimir Rusinov, Evgueny I. Tarkovsky
Institute of Theoretical and Experimetal Physics, B. Cheremushkinskawa, 25, RU-117259, Moscow, Russia

Alexander Olchevski
Joint Institute for Nuclear Research (JINR), Joliot-Curie 6, 141980, Dubna, Moscow Region, Russia

Eduard Boos, Leonid Gladilin, Mikhail M. Merkin
Lomonosov Moscow State University, Skobeltsyn Institute of Nuclear Physics (MSU SINP), 1(2), Leninskie gory, GSP-1, Moscow 119991, Russia

Boris A. Dolgoshein, Elena Popova
Moscow Engineering Physics Institute (MEPhI), Dept. of Physics, 31, Kashirskoye shosse, 115409 Moscow, Russia

Nicola D'Ascenzo[8], Valery Galkin, Alexei Galkin, Dmitri Ossetski, Dmitri Ryzhikov, Valeri Saveliev
Obninsk State Technical University for Nuclear Engineering (IATE), Obninsk, Russia

Ivanka Bozovic-Jelisavcic, Stevan Jokic, Tatjana Jovin, Judita Mamuzic, Mihajlo Mudrinic, Mila Pandurovic, Ivan Smiljanic
VINCA Institute of Nuclear Sciences, Laboratory of Physics, PO Box 522, YU-11001 Belgrade, Serbia and Montenegro

Jozef Ferencei
Institute of Experimental Physics, Slovak Academy of Sciences, Watsonova 47, SK-04001 Kosice, Slovakia

Enrique Calvo Alamillo, Mary-Cruz Fouz, Jesus Puerta-Pelayo
Centro de Investigaciones Energéticas, Medioambientales y Tecnológicas, CIEMAT, Avenida Complutense 22, E-28040 Madrid, Spain

Juan Pablo Balbuena, Daniela Bassignana, Celeste Fleta, Manuel Lozano, Giulio Pellegrini, Miguel Ullán
Centro Nacional de Microelectrónica (CNM), Instituto de Microelectrónica de Barcelona (IMB), Campus UAB, 08193 Cerdanyola del Vallès (Bellaterra), Barcelona, Spain

Carmen Alabau Pons, Markus Ball, Angeles Faus-Golfe, Juan Fuster, Carlos Lacasta Llácer, Carlos Mariñas, Marcel Vos
Instituto de Fisica Corpuscular (IFIC), Centro Mixto CSIC-UVEG, Edificio Investigacion Paterna, Apartado 22085, 46071 Valencia, Spain

Jordi Duarte Campderrós, Marcos Fernandez Garcia, Francisco Javier González Sánchez, Richard Jaramillo Echeverría, Amparo Lopez Virto, Celso Martinez Rivero, David Moya, Alberto Ruiz-Jimeno, Ivan Vila
Instituto de Fisica de Cantabria, (IFCA, CSIC-UC), Facultad de Ciencias, Avda. Los Castros s/n, 39005 Santander, Spain

Bernardo Adeva, Abraham Gallas, Carmen Iglesias Escudero, Juan J. Saborido, Pablo Vazquez Regueiro
Instituto Galego de Fisica de Altas Enerxias (IGFAE,USC) Facultad de Fisica, Campus Sur E-15782 Santiago de Compostela, Spain

Juan Antonio Aguilar-Saavedra, Nuno Castro
Universidad de Granada, Departamento de Física Teórica y del Cosmos, Campus de Fuentenueva, E-18071 Granada, Spain

Thorsten Lux, Cristobal Padilla, Imma Riu
Universitat Autònoma de Barcelona, Institut de Fisica d'Altes Energies (IFAE), Campus UAB, Edifici Cn, E-08193 Bellaterra, Barcelona, Spain

Jordi Riera-Babures, Xavier Vilasis-Cardona
Universitat Ramon Llull, La Salle, C/ Quatre Camins 2, 08022 Barcelona, Spain

Angel Dieguez, Lluis Garrido Beltran
University de Barcelona, Facultat de Física, Av. Diagonal, 647, Barcelona 08028, Spain

Vincent Hedberg, Leif Jonsson, Bjorn Lundberg, Ulf Mjornmark, Anders Oskarsson, Lennart Osterman, Evert Stenlund
Lunds Universitet, Fysiska Institutionen, Avdelningen för Experimentell Högenergifysik, Box 118, 221 00 Lund, Sweden

Michael Campbell, Albert De Roeck, Konrad Elsener, Andrea Gaddi, Hubert Gerwig, Christian Grefe[14], Michael Hauschild, Lucie Linssen, Xavier Llopart Cudie, Luciano Musa, Dieter Schlatter, Peter Speckmayer
CERN, CH-1211 Genève 23, Switzerland

Günther Dissertori, Gerard Faber, Alain Hervé, Nebojsa Smiljkovic
ETH Zürich, Institute for Particle Physics (IPP), Schafmattstrasse 20, CH-8093 Zürich, Switzerland

Hideyuki Nakazawa
National Central University, High Energy Group, Department of Physics, Chung-li, Taiwan 32001

Paoti Chang, Wei-Shu Hou, Koji Ueno, Min-Zu Wang
National Taiwan University, Physics Department, Taipei, Taiwan 106

Gudrid A. Moortgat-Pick[21]
Durham University, Department of Physics, Ogen Center for Fundamental Physics, South Rd., Durham DH1 3LE, UK

James Ballin
Imperial College, Blackett Laboratory, Department of Physics, Prince Consort Road, London, SW7 2BW, UK

Andre Sopczak
Lancaster University, Physics Department, Lancaster LA1 4YB, UK

Grahame Blair, Veronique Boisvert
Royal Holloway, University of London (RHUL), Department of Physics, Egham, Surrey TW20 0EX, UK

Chris Damerell, Kristian Harder
STFC Rutherford Appleton Laboratory, Chilton, Didcot, Oxon OX11 0QX, UK

Derek J. Attree, Valeria Bartsch, Filimon Gournaris, Alexey Lyapin, David J. Miller, Martin Postranecky, Matthew Warren, Matthew Wing
University College of London (UCL), High Energy Physics Group, Physics and Astronomy Department, Gower Street, London WC1E 6BT, UK

Owen Miller, Nigel K. Watson, John A. Wilson
University of Birmingham, School of Physics and Astronomy, Particle Physics Group, Edgbaston, Birmingham B15 2TT, UK

Joel Goldstein
University of Bristol, H. H. Wills Physics Lab, Tyndall Ave., Bristol BS8 1TL, UK

Bart Hommels, John Marshall, Georgios Mavromanolakis[25], Mark Thomson, David R Ward

University of Cambridge, Cavendish Laboratory, J J Thomson Avenue, Cambridge CB3 0HE, UK

Victoria J Martin, Hajrah Tabassam, Roberval Walsh
University of Edinburgh, School of Physics, James Clerk Maxwell Building, The King's Buildings, Mayfield Road, Edinburgh EH9 3JZ, UK

Richard Bates, Craig Buttar, Tony Doyle, Lars Eklund, Val O'Shea, Chris Parkes, Aidan Robson
University of Glasgow, Department of Physics & Astronomy, University Avenue, Glasgow G12 8QQ, Scotland, UK

Tim Greenshaw
University of Liverpool, Department of Physics, Oliver Lodge Lab, Oxford St., Liverpool L69 7ZE, UK

David Bailey, Roger Barlow[21]
University of Manchester, School of Physics and Astronomy, Schuster Lab, Manchester M13 9PL, UK

Brian Foster
University of Oxford, Particle Physics Department, Denys Wilkinson Bldg., Keble Road, Oxford OX1 3RH England, UK

Stefano Moretti[23]
University of Southampton, School of Physics and Astronomy, Highfield, Southampton S017 1BJ, England, UK

Jose Repond
Argonne National Laboratory (ANL), 9700 S. Cass Avenue, Argonne, IL 60439, USA

John Butler
Boston University, Department of Physics, 590 Commonwealth Avenue, Boston, MA 02215, USA

Lawrence Gibbons, J. Ritchie Patterson, Daniel Peterson
Cornell University, Laboratory for Elementary-Particle Physics (LEPP), Ithaca, NY 14853, USA

Marco Verzocchi
Fermi National Accelerator Laboratory (FNAL), P.O.Box 500, Batavia, IL 60510-0500, USA

Rick J. Van Kooten
Indiana University, Department of Physics, Swain Hall West 117, 727 E. 3rd St., Bloomington, IN 47405-7105, USA

Z.D. Greenwood, Lee Sawyer, Markus Wobisch
Louisiana Tech University, Department of Physics, Ruston, LA 71272, USA

Dhiman Chakraborty, David Hedin, Guilherme Lima, Vishnu Zutshi
Northern Illinois University, Department of Physics, DeKalb, Illinois 60115-2825, USA

Qing He, Kirk T Mcdonald
Princeton University, Department of Physics, P.O. Box 708, Princeton, NJ 08542-0708, USA

Bruce A. Schumm
University of California Santa Cruz, Institute for Particle Physics, 1156 High Street, Santa Cruz, CA 95064, USA

Burak Bilki, Ed Norbeck, Yasar Onel
University of Iowa, Department of Physics and Astronomy, 203 Van Allen Hall, Iowa City, IA 52242-1479, USA

Jadranka Sekaric, Brian Van Doren, Graham W. Wilson
University of Kansas, Department of Physics and Astronomy, Malott Hall, 1251 Wescoe Hall Drive, Room 1082, Lawrence, KS 66045-7582, USA

Haijun Yang
University of Michigan, Department of Physics, 500 E. University Ave., Ann Arbor, MI 48109-1120, USA

Giovanni Bonvicini
Wayne State University, Department of Physics, Detroit, MI 48202, USA

[1] also at TRIUMF, 4004 Wesbrook Mall, Vancouver, BC V6T 2A3, Canada

[2] also at Université de Montréal, Département de Physique, Groupe de Physique des Particules, C.P. 6128, Succ. Centre-ville, Montréal, Qc H3C 3J7, Canada

[3] also at Institute of High Energy Physics - IHEP, Chinese Academy of Sciences, P.O. Box 918, Beijing, China 100049

[4] also at Helsinki Institute of Physics (HIP), P.O. Box 64, FIN-00014 University of Helsinki, Finland

[5] also at Laboratoire de l'Accélérateur Linéaire (LAL), Université Paris-Sud 11, Bâtiment 200, 91898 Orsay, France

[6] also at Université de Strasbourg, UFR de Sciences Physiques, 3-5 Rue de l'Université, F-67084 Strasbourg Cedex, France

[7] also at Brandenburg University of Technology, Postfach 101344, D-03013 Cottbus, Germany

[8] also at Deutsches Elektronen-Synchrotron DESY, A Research Centre of the Helmholtz Association, Notkestrasse 85, 22607 Hamburg, Germany (Hamburg site)

[9] also at Deutsches Elektronen-Synchrotron DESY, A Research Centre of the Helmholtz Association, Platanenallee 6, 15738 Zeuthen, Germany (Zeuthen site)

[10] also at Excellence Cluster Universe, Technische Universität München, Boltzmannstr. 2, 85748 Garching, Germany

[11] also at Gottfried Wilhelm Leibniz Universität Hannover, Fakultät für Mathematik und Physik, Appelstraße 2, 30167 Hannover, Germany

[12] also at University of Hamburg, Physics Department, Institut für Experimentalphysik, Luruper Chaussee 149, 22761 Hamburg, Germany

[13] also at University of Wuppertal, Gaußstraße 20, D-42119 Wuppertal, Germany

[14] also at Universität Bonn, Physikalisches Institut, Nußallee 12, 53115 Bonn, Germany

[15] also at Istituto Nazionale di Fisica Nucleare (INFN), Sezione di Milano, Via Celoria 16, I-20133 Milano, Italy

[16] also at Nikhef, National Institute for Subatomic Physics, P.O. Box 41882, 1009 DB Amsterdam, Netherlands

[17] also at Vrije Universiteit, Department of Physics, Faculty of Sciences, De Boelelaan 1081, 1081 HV Amsterdam, Netherlands

[18] also at University of Lodz, Faculty of Physics and Applied Informatics, Pomorska 149/153, PL-90-236 Lodz, Poland

[19] also at National Institute of Physics and Nuclear Engineering "Horia Hulubei" (IFIN-HH), Str. Atomistilor no. 407, P.O. Box MG-6, R-76900 Bucharest - Magurele, Romania

[20] also at CERN, CH-1211 Genève 23, Switzerland

[21] also at Cockcroft Institute, Daresbury, Warrington WA4 4AD, UK

[22] also at Royal Holloway, University of London (RHUL), Department of Physics, Egham, Surrey TW20 0EX, UK

[23] also at STFC Rutherford Appleton Laboratory, Chilton, Didcot, Oxon OX11 0QX, UK

[24] also at Enrico Fermi Institute, University of Chicago, 5640 S. Ellis Avenue, RI-183, Chicago, IL 60637, USA

[25] also at Fermi National Accelerator Laboratory (FNAL), P.O.Box 500, Batavia, IL 60510-0500, USA

CONTENTS

LIST of FIGURES

LIST of TABLES

LIST OF TABLES

CHAPTER 1

Introduction

1.1 ILD PHILOSOPHY

The **I**nternational **L**arge **D**etector (ILD) is a concept for a detector at the International Linear Collider, ILC. The ILC will collide electrons and positrons at energies of initially 500 GeV, upgradeable to 1 TeV. The ILC has an ambitious physics program, which will extend and complement that of the Large Hadron Collider (LHC). The ILC physics case has been well documented, most recently in the ILC Reference Design Report, RDR [1]. A hallmark of physics at the ILC is precision. The clean initial state and the comparatively benign environment of a lepton collider are ideally suited to high precision measurements. To take full advantage of the physics potential of ILC places great demands on the detector performance. The design of ILD, which is based on the GLD [2] and the LDC [3] detector concepts, is driven by these requirements. Excellent calorimetry and tracking are combined to obtain the best possible overall event reconstruction, including the capability to reconstruct individual particles within jets for particle flow calorimetry. This requires excellent spatial resolution for all detector systems. A highly granular calorimeter system is combined with a central tracker which stresses redundancy and efficiency. In addition, efficient reconstruction of secondary vertices and excellent momentum resolution for charged particles are essential for an ILC detector. The interaction region of the ILC is designed to host two detectors, which can be moved into the beam position with a "push-pull" scheme. The mechanical design of ILD and the overall integration of subdetectors takes these operational conditions into account. The main features of ILD are outlined below.

The central component of the ILD tracker is a Time Projection Chamber (TPC) which provides up to 224 precise measurements along the track of a charged particle. This is supplemented by a system of Silicon (Si) based tracking detectors, which provide additional measurement points inside and outside of the TPC, and extend the angular coverage down to very small angles. A Si-pixel based vertex detector (VTX) enables long lived particles such as b- and c-hadrons to be reconstructed. This combination of tracking devices, which has a large degree of redundancy, results in high track reconstruction efficiencies, and unprecedented momentum resolution and vertex reconstruction capabilities. One of the most direct measures of detector performance at the ILC is the jet-energy resolution. Precise di-jet mass reconstruction and separation of hadronically decaying W and Z bosons are essential for many physics channels. The ultimate jet energy resolution is achieved when every particle in the event, charged and neutral, is measured with the best possible precision. Within the

paradigm of particle flow calorimetry, this goal is achieved by reconstructing charged particles in the tracker, photons in the electromagnetic calorimeter (ECAL), and neutral hadrons in the ECAL and hadronic calorimeter (HCAL). The ultimate performance is reached for perfect separation of charged-particle clusters from neutral particle clusters in the calorimeters. Thus, a highly granular calorimeter outside the tracker is the second key component of ILD. Sampling calorimeters with dense absorber material and fine grained readout are used. A tungsten absorber based electromagnetic calorimeter (ECAL) covers the first interaction length, followed by a somewhat coarser steel based sampling hadronic calorimeter (HCAL). Several ECAL and HCAL readout technologies are being pursued.

1.2 BASIC LAYOUT OF ILD

The proposed ILD concept is designed as a multi-purpose detector, which provides excellent precision in spatial and energy measurement over a large solid angle. It has the following components:

- A multi-layer pixel-vertex detector (VTX), with three super-layers each comprising two layers. To minimise the occupancy from background hits, the first super-layer is only half as long as the outer two. Whilst the underlying detector technology has not yet been decided, the VTX is optimised for excellent point resolution and minimum material thickness. A five layer geometry, VTX-SL, with the layers spaced at equal distances to the IP is investigated as an alternative. In either case the vertex detector has a purely barrel geometry.
- A system of strip and pixel detectors surrounding the VTX detector. In the barrel, two layers of Si strip detectors (SIT) are arranged to bridge the gap between the VTX and the TPC. In the forward region, a system of Si-pixel and Si-strip disks (FTD) provides low angle tracking coverage.
- A large volume time projection chamber (TPC) with up to 224 points per track. The TPC is optimised for excellent 3-dimensional point resolution and minimum material in the field cage and in the end-plate. It also provides $\mathrm{d}E/\mathrm{d}x$ based particle identification capabilities.
- A system of Si-strip detectors, one behind the end-plate of the TPC (ETD) and one in between the TPC and the ECAL (SET). These provide additional high precision space points which improve the tracking measurements and provide additional redundancy in the regions between the main tracking volume and the calorimeters.
- A highly segmented ECAL providing up to 30 samples in depth and small transverse cell size. Two technology options are considered; Si-W and scintillator-W.
- A highly segmented HCAL with up to 48 longitudinal samples and small transverse cell size. Two options are considered, both based on a Steel-absorber structure. One option uses scintillator tiles of $3 \times 3\,\mathrm{cm}^2$, which are read out with an analogue system. The second uses a gas-based readout which allows a $1 \times 1\,\mathrm{cm}^2$ cell geometry with a binary or semi-digital readout of each cell.
- A system of high precision, radiation hard, calorimetric detectors in the very forward region (LumiCAL, BCAL, LHCAL). These extend the calorimetric coverage to almost 4π, measure the luminosity, and monitor the quality of the colliding beams.
- A large volume superconducting coil surrounds the calorimeters, creating an axial B-field of nominally 3.5 Tesla.

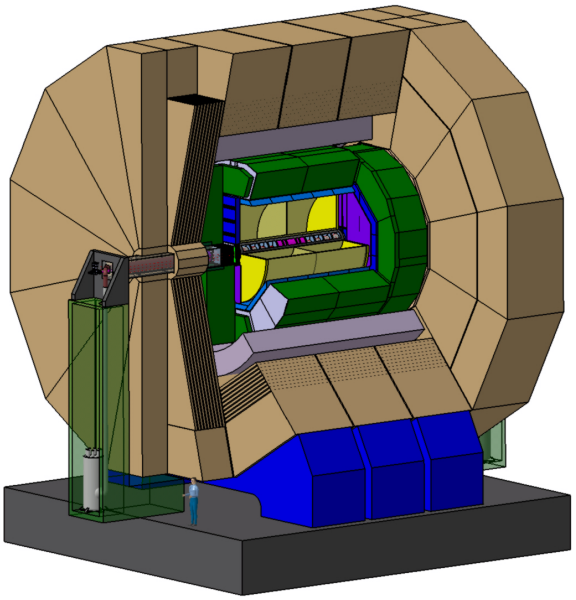

FIGURE 1.2-1. View of the ILD detector concept.

- An iron yoke, instrumented with scintillator strips or RPCs, returns the magnetic flux of the solenoid, and at the same time, serves as a muon filter, muon detector and tail catcher.
- A sophisticated data acquisition (DAQ) system which operates without an external trigger, to maximise the physics sensitivity.

Precision physics at the ILC requires that the beam parameters are known with great accuracy. The beam energy and the beam polarization will be measured in small dedicated experiments, which are shared by the two detectors present in the interaction region. These detectors will only be covered briefly in this document, more details may be found in a dedicated document. The luminosity of the interaction will be measured by the luminometers integrated in ILD. To enable the operation of the detector in a "push-pul" scenario, the complete detector is mounted on a movable platform, which can move sideways out of the beam to make space for the second detector in the interaction region. The platform ensures that the integrity and calibration of the detector is minimally disturbed during the moving process, making the re-commissioning of the detector after the "push-pull" operation easier. The ILD detector concept is shown graphically in Figure 1.2-1.

1.3 PERFORMANCE REQUIREMENTS

The requirements and resulting challenges for detectors at the ILC are described in the ILC RDR [4]. The ILC is designed to investigate in detail the mechanism of the electroweak symmetry breaking, and to search for and study new physics at energy scales up to 1 TeV. In addition, the collider will provide a wealth of information on Standard Model (SM) physics, for example top physics, heavy flavour physics, and physics of the Z and W bosons. The requirements for a detector are, therefore, that multi-jet final states, typical for many physics channels, can be reconstructed with high accuracy. The jet energy resolution should be sufficiently good that the hadronic decays of the W and Z can be separated. This translates

into a jet energy resolution of $\sigma_E/E \sim 3-4\%$ (equivalent to $30\%/\sqrt{E}$ at energies below 100 GeV). This requirement is one of the most challenging for ILD and has a large impact on the design of the calorimeters. It also impacts the way the tracking system is optimised. Nevertheless, the reconstruction of events with high precision benefits the ILD physics programme in several ways. A more precise detector will result in smaller systematic errors for many measurements, and thus will extend the ultimate physics reach of the ILC. In addition, a more precise detector implies that the luminosity delivered by the collider is used more efficiently, making it possible to reduce the overall running costs of the facility to reach a particular accuracy.

It is difficult to anticipate the full physics programme at a new facility before the physics of the energy regime where it will operate is known. A detector for the ILC therefore needs to be designed and optimised not only in view of a limited set of benchmark reactions, but also to be as versatile and as flexible as possible. Nevertheless the ILC community has defined a number of challenging benchmark physics reactions, which, to the best of our current knowledge, will form an important part of the physics programme at the ILC. The benchmark reactions stress the study of the Higgs boson and Supersymmetry (SUSY) as a model for a possible new physics scenario at the ILC. They also rely on excellent lepton and flavour tagging and probe the missing energy measurement capability of the detector. These reactions give only a flavour of the physics reach of the ILC.

1.4 OVERVIEW OF THE ILD LETTER OF INTENT

The signatories of this Letter of Intent are an international group of physicists with strong participation from Asia, Europe and the Americas. With this letter of intent the undersigned express their intention to develop further the ILD concept to a point where a concrete proposal can be made. However, at this stage, this does not represent a firm commitment either in terms of manpower or resources.

This document is organised as follows: Chapter 2 describes the studies used to optimise and define the main parameters of the ILD concept; Chapter 3 presents the performance of the ILD concept in terms of the low level detector response, such as momentum resolution, jet energy resolution, and flavour-tagging performance. It also describes a number of physics studies which demonstrate that the ILC concept is well optimised for physics at the ILC operating in the centre-of-mass energy range 200 GeV to 1 TeV; Chapter 4 describes the ILD subdetector systems in the context of the ongoing R&D programme; Chapter 6 describes the interface between ILD and the ILC; Chapter 7 discusses the current understanding of the likely cost of ILD; and finally, Chapters 8 and 9 describe the structure of the ILD group and the necessary R&D needed to realise this project.

CHAPTER 2

Detector Optimisation

The choice of the main parameters of the ILD, such as the magnetic field, B, and overall size, is motivated by extensive simulation studies based on variants of the GLD [2] and LDC [3] detector concepts. The main studies, described in the following sections, are of: i) the performance of particle flow calorimetry in terms of jet energy resolution; ii) the tracking performance for momentum resolution and impact parameter resolution; iii) the beam-related backgrounds and the impact of the choice of B; iv) the efficiency and purity of heavy flavour tagging; v) and the impact on physics performance in three benchmark processes.

Ideally the overall detector cost would feed directly into the optimisation of the ILD detector. However, because of the large uncertainties in the cost of raw materials and detector sensors, it is felt that the approach of optimising the detector performance for a fixed cost is not reliable at this stage. Hence, whilst cost is a consideration in defining the parameters of the ILD concept, the main criterion is to develop a detector concept optimised for physics at the ILC.

2.1 SIMULATION TOOLS AND DETECTOR PARAMETERS

The optimisation of the ILD concept was performed in parallel using the software tools developed by the GLD and the LDC groups. The detector models were simulated using a fairly detailed GEANT4 [5] simulation. A significant effort has been made to use a reasonable geometry for the subdetectors, including a description of dead regions and support structures, as described in in Section 3.1. The studies presented are based on full reconstruction of the simulated events without reference to the Monte Carlo (MC) truth information.

Six detector models were defined; three based on the GLD simulation (GLD, GLDPrime and GLD4LDC) and three based on the LDC simulation (LDC, LDCPrime, and LDC4GLD). The main parameters of the models are summarised in Table 2.1-1. The models represent different compromises between magnetic field and TPC outer radius. The software frameworks (JSF/Jupiter/Satellites and Mokka/Marlin) used to simulate and reconstruct the detector models are summarised below. The detector simulation was performed using GEANT4 (version 9.1 patch01) with the `LCPhysics` physics list [6].

Model Name		GLD	GLD′	GLD4LDC	LDC4GLD	LDC′	LDC	ILD
Simulator		Jupiter			Mokka			Mokka
B field (T)		3.0	3.5	4.0	3.0	3.5	4.0	3.5
Beampipe R_{min}		15.0	14.0	13.0	15.5	14.0	13.0	14.5
Vertex	Geometry	cylindrical			ladders			ladders
Detector	Layers	3 doublets			5			3 doublets
	R_{min}	17.5	16.0	15.0	16.5	15.0	14.0	16.0
Barrel	Layers	4 cylinders			2 cylinders			2 cylinders
SIT	Radii	90, 160, 230, 300			161.4, 270.1			165, 309
TPC	R_{min}	437	435	371	371			395
drift	R_{max}	1978	1740	1520	1931	1733	1511	1739
region	z_{max}	2600	2350	2160	2498	2248	2186	2247.5
TPC pad rows		256	217	196	260	227	190	224
ECAL	R_{min}	2100	1850	1600	2020	1825	1610	1847.4
barrel	Layers	33			20(thin)+9(thick)			20+9
	Total X_0	28.4			22.9			23.6
ECAL endcap z_{min}		2800	2250	2100	2700	2300	2550	2450
HCAL	Layers	46	42	37	48			48
barrel	R_{max}	3617	3260	2857	3554	3359	3144	3330
λ_I (ECAL+HCAL)		6.79	6.29	5.67	6.86			6.86

TABLE 2.1-1
Geometrical parameters of the baseline detector models used for the optimisation studies (GLD, GLDPrime, GLD4LDC, LDC4GLD, LDCPrime and LDC). Also shown are the corresponding parameters for the ILD baseline detector. Unless otherwise specified, values are shown in units of mm.

2.1.1 GLD Software: JSF

JSF [7] is a ROOT [8] based software framework for modular applications, such as event generation, fast and full simulation, event reconstruction and data analysis. The two main components are Jupiter [9] and Satellites [9]. Jupiter is a GEANT4 based detector simulation, designed to enable easy installation and modification of subdetector components. Satellites is a collection of event reconstruction modules in the JSF framework. Satellites includes smearing of hit points simulated by Jupiter, a "cheated" track finder using MC information to associate hits to tracks, a Kalman Filter based track fitter, and a cheated particle flow algorithm (PFA).

Jupiter reads a set of detector parameters at run time from a text file, which makes it easy to study different detector configurations. The geometry information is saved in an output ROOT file for use by event reconstruction. In the Jupiter detector simulation the vertex detector and intermediate silicon trackers are modelled as cylinders. The calorimeters have a 12-fold symmetry. The electromagnetic calorimeter consists of a sandwich structure comprising layers of 3 mm of tungsten absorber, 2 mm of scintillator, and a 1 mm air gap. The hadron calorimeter consists of layers comprising of 20 mm of iron absorber, 5 mm of

plastic scintillator, and a 1 mm air gap. For the purpose of simulation, the scintillator in both the ECAL and HCAL is segmented into $1 \times 1\,\mathrm{cm}^2$ readout tiles. Signals in these tiles can be combined at the time of reconstruction to simulate the strip readout structure of proposed system. In the version of the simulation used for the studies presented here, there is no gap between the ECAL and HCAL. Jupiter was executed as a module of the JSF and GEANT4 hits in each sensitive detector are saved in a ROOT file for subsequent study with the Satellites package or as an LCIO [10] file for reconstruction with MarlinReco [11].

The point resolution of the tracking chambers was implemented in the Satellites reconstruction. The GEANT4 hit points in the vertex detector (VTX) and intermediate silicon tracker (IT) were smeared with a Gaussian with the following resolutions. For the VTX, $\sigma_{r\phi}$ and σ_z were taken to be 2.8μm. For the barrel silicon tracker, a resolution of $10\,\mu$m was used for both $\sigma_{r\phi}$ and σ_z. The TPC space points were smeared by Gaussian resolutions, $\sigma_{r\phi}$ and σ_z, given by the following physically motivated form:

$$\begin{aligned} \sigma^2_{r\phi}/\mu\mathrm{m}^2 &= 50^2 + 900^2 \sin^2\phi + \left((25^2/22) \times (4/B)^2 \sin\theta\right) z; \\ \sigma^2_{z}/\mu\mathrm{m}^2 &= 400^2 + 80^2 \times z; \end{aligned}$$

where z is the drift length in cm, B is the magnetic field strength in Tesla, and θ and ϕ are the track angles with respect to the axes perpendicular to the readout plane and perpendicular to the pad rows, and the resolutions are given in μm. For the calorimeter hits, no additional smearing is applied at reconstruction time; the simulated energy deposits in the scintillator tiles are used directly.

The optimisation studies in the GLD framework use the Satellites reconstruction to investigate tracking performance and MarlinReco for other studies. The interoperability between the two software frameworks is provided by the LCIO data format, *e.g.* after simulating the detector response with the Jupiter program, MarlinReco and PandoraPFA [12] were used for the event reconstruction.

2.1.2 LDC Software: Mokka and Marlin

The software framework developed by the LDC concept is based on the LCIO persistency format and event data model. The detailed simulation of the detector response is performed by the GEANT4 based Mokka [13] application. The detailed subdetector geometries and component materials are stored in a MySQL database. The overall detector is then built from individual subdetectors, making it relatively straightforward to compare different technology choices. The corresponding `C++` code instantiating the subdetector geometry in memory is written such that the whole detector model can be scaled in length and radius; this feature proved invaluable in optimising the detector geometry. The GEAR [14] package provides access to these geometrical detector properties at the reconstruction and analysis level. The Mokka simulation of the different subdetectors is described in more detail in Section 3.1.

The Mokka generated events are processed in Marlin [15]. Marlin is a modular `C++` application framework which supports plug-in modules (called processors) which can be loaded at runtime. This plug-in-based design supports the distributed development of reconstruction algorithms and also allows comparison of different algorithms at runtime, *e.g.* it is possible to run two tracking algorithms producing parallel collections of reconstructed tracks.

Event reconstruction is performed with the MarlinReco [16] package. This consists of a set of modules for digitisation, track finding, track fitting, particle flow reconstruction, and flavour tagging. The hit smearing for the tracking detectors is implemented at the digitisation

stage using the same parameterisation as used for Satellites, except that resolutions for the intermediate silicon tracker (SIT) are taken to be $4\,\mu$m for $\sigma_{r\phi}$ and $50\,\mu$m for σ_z. The pattern recognition processors use Kalman Filter techniques and code developed for the LEP experiments. Tracks from standalone pattern recognition in the silicon trackers and in the TPC are combined and refitted, The resulting momentum resolution is discussed in Section 3.2.1. Reconstruction of the individual particles in the event is performed with the particle flow algorithm in the PandoraPFA [12] package, currently the best algorithm available. The LCFIVertex [17] package provides sophisticated code for vertex finding/fitting and for the identification of heavy flavour jets using a neural network approach. It also provides jet charge estimation. In addition to reconstruction algorithms, MarlinReco includes a set of analysis tools such as algorithms for jet finding and kinematic fitting. The RAVE toolkit [18], also available within Marlin, provides an alternative set of vertex reconstruction based on linear and non-linear estimators.

2.2 DETECTOR OPTIMISATION FOR PARTICLE FLOW

One of the main design considerations for a detector at the ILC is the ability to efficiently identify and distinguish $\mathrm{Z} \to \mathrm{q\bar{q}}$ and $\mathrm{W} \to \mathrm{q\bar{q}}$ decays. This imposes the requirement that the di-jet mass resolution should be comparable to the natural widths of the electroweak gauge bosons, $\sigma_m/m < 2.7\,\% \approx \Gamma_\mathrm{Z}/m_\mathrm{Z} \approx \Gamma_\mathrm{W}/m_\mathrm{W}$. In terms of jet energy resolution this requirement approximately corresponds to $\sigma_E/E < 3.8\,\%$. After accounting for the gauge boson widths, this results in a ~ 2.75 standard deviation separation of the W and Z mass peaks for di-jet events. Most of the interesting physics at the ILC, operating in the centre-of-mass range $\sqrt{s} = 0.5 - 1.0\,\mathrm{TeV}$, will consist of final states with four or more fermions and for processes near threshold, the gauge bosons will decay almost at rest. Hence the typical di-jet energies of interest will be in the range $80 - 350\,\mathrm{GeV}$. This sets the requirement on calorimetric performance of $\sigma_E/E \sim 30\,\%/\sqrt{E}$. It has been demonstrated that one way of reaching this goal is particle flow calorimetry[19]. Whilst, the separation of W and Z bosons defines the *minimum* requirement for the jet energy resolution, it should be remembered that di-jet invariant masses will be an important part of the event selection for many physics analyses; the jet energy resolution will affect the signal-to-background ratio in many analyses.

The ILD concept is based on the belief that particle flow calorimetry provides the best way of achieving the ILC jet energy goals. Particle flow reconstruction places strong requirements on the subdetector technologies and the overall detector design. Particle flow calorimetry requires efficient separation of photons and showers produced by neutral hadrons from showers produced by the interactions of charged hadrons. This implies high granularity calorimetry and that both the ECAL and HCAL lie inside the detector solenoid. For high energy jets, failures in the ability to efficiently separate energy deposits from different particles, the *confusion* term, will dominate the jet energy resolution. The physical separation of calorimetric energy deposits from different particles will be greater in a large detector, scaling as the inner radius of the ECAL, R, in the barrel region and the detector length, L, in the endcap region. There are also arguments favouring a high magnetic field, as this will tend to deflect charged particles away from the core of a jet. The scaling law here is less clear. The separation between a charged particle and an initially collinear neutral particle will scale as BR^2. However, there is no reason to believe that this will hold for a jet of (non-collinear) neutral and charged particles. The true dependence of particle flow on the overall detector parameters (B and R) has to be evaluated empirically.

2.2.1 Particle Flow Optimisation Methodology

The particle flow optimisation studies for ILD use the PandoraPFA algorithm[12] to reconstruct events for both the LDC and the GLD detector models. All studies are based on full reconstruction of the tracking and the calorimetric information. The starting point for the optimisation studies is the LDCPrime model with a 3.5 T magnetic field, an ECAL inner radius of 1825 mm and a 48 layer ($6\lambda_I$) HCAL. The ECAL and HCAL transverse segmentations are $5 \times 5\,\mathrm{mm}^2$ and $3 \times 3\,\mathrm{cm}^2$ respectively. The studies use variations of this model where (usually) a single parameter is changed and the dependence of jet energy resolution is determined as a function of this parameter. For each model variation, particle flow performance was evaluated using samples of approximately 10000 $\mathrm{Z} \to \mathrm{q\overline{q}}$ events (only light quarks, *i.e.* $q = u, d, s$) generated with the Z decaying at rest (no ISR or beamstrahlung) with $E_{\mathrm{Z}} = 91.2$, 200, 360, and 500 GeV. These jet energies are typical of those expected at the ILC for $\sqrt{s} = 0.5 - 1.0\,\mathrm{TeV}$. For each set of events, the rms_{90} of the total reconstructed energy distribution was determined, where rms_{90} is the root-mean-squared deviation from the mean in the smallest energy range containing 90 % of the reconstructed events.

2.2.2 HCAL Depth

Good particle flow calorimetry requires that both the ECAL and HCAL are within the detector solenoid. Consequently, in addition to the cost of the HCAL, the HCAL thickness impacts the cost of the overall detector through the radius of the superconducting solenoid. The thickness of the HCAL determines the average fraction of jet energy contained within the calorimeter system. The impact of the HCAL thickness on the particle flow performance is assessed by changing the number of HCAL layers in the LDCPrime model from 32 to 63. This corresponds to a variation of $4.0 - 7.9\,\lambda_I$ ($4.8 - 8.7\,\lambda_I$) in the HCAL (ECAL+HCAL).

The study of the optimal HCAL thickness depends on the possible use of the instrumented return yoke (the muon system) to correct for leakage of high energy showers out of the rear of the HCAL. The effectiveness of this approach is limited by the fact that, for much of the polar angle, the muon system is behind the relatively thick solenoid ($2\lambda_I$ in the Mokka simulation of the detector). Nevertheless, to assess the possible impact of using the muon detector as a "tail-catcher", the energy depositions in the muon detectors were included in the PandoraPFA reconstruction. Whilst the treatment could be improved upon, it provides an estimate of how much of the degradation in jet energy resolution due to leakage can be recovered in this way. The results are summarised in Figure 2.2-1 which shows the jet energy resolution obtained from PandoraPFA as a function of HCAL thickness. The effect of leakage is clearly visible, with about half of the degradation in resolution being recovered when including the muon detector information. For jet energies of 100 GeV or less, leakage is not a major contributor to the jet energy resolution provided the HCAL is approximately $4.7\lambda_I$ thick (38 layers). However, for $180 - 250$ GeV jets this is not sufficient; for leakage not to contribute significantly to the jet energy resolution at $\sqrt{s} = 1\,\mathrm{TeV}$, the results in Figure 2.2-1 suggest that the HCAL thickness should be between $5.5 - 6.0\lambda_I$ ($43 - 48$ layers). To allow for uncertainties in the simulation of the longitudinal development of hadronic showers, and to ensure the detector is appropriate for collisions at 1 TeV, a 48 layer HCAL was chosen for ILD. This was also used for the LDC-based models discussed below.

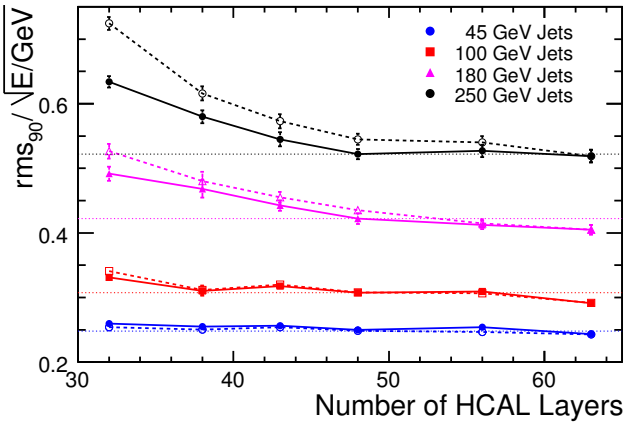

FIGURE 2.2-1. Jet energy resolutions (rms_{90}) for the LDCPrime detector model with different numbers of HCAL layers. Results are shown with (solid markers) and without (open markers) taking into account energy depositions in the muon detectors. All results are based on $\mathrm{Z} \to \mathrm{u\bar{u}}, \mathrm{d\bar{d}}, \mathrm{s\bar{s}}$ with generated polar angle in the barrel region of the detector, $|\cos\theta_{\mathrm{q\bar{q}}}| < 0.7$.

2.2.3 Magnetic Field versus Detector Radius

The dependence of particle flow performance on B and R is studied in the region of parameter space close to the LDCPrime model. The LDCPrime model assumes a magnetic field of 3.5 T and an ECAL inner radius of 1820 mm. A number of variations on these parameters were studied: i) variations of both B and R with four sets of parameters considered, "LDC-like" (B=4.0 T, R = 1600 mm), "GLD-like" (B=3.0 T, R = 2020 mm), "Small" (B=4.5 T, R = 1420 mm), and "SiD-like" (B=5.0 T, R = 1280 mm); i) variations in the ECAL inner radius from $1280 - 2020$ mm with $B = 3.5$ T; and iii) variations in B from $2.5 - 4.5$ T with $R = 1825$ mm. In total thirteen sets of parameters were considered spanning a wide range of B and R. In each case particle flow performance was evaluated for 45, 100, 180, and 250 GeV jets. Table 2.2-2 compares the jet energy resolutions for LDC, LDCPrime and LDC4GLD models. The differences between these models is small, $\sim 5\,\%$,. This is not surprising; the parameters of the LDC and GLD concepts on which these models are based were chosen such

Model			σ_E/E [%] versus E_{jet}			
Name	B/T	R/m	45 GeV	100 GeV	180 GeV	250 GeV
SiD-like	5.0	1.25	4.19 ± 0.06	3.72 ± 0.06	3.70 ± 0.07	3.94 ± 0.10
Small	4.5	1.42	3.90 ± 0.08	3.34 ± 0.07	3.54 ± 0.06	3.75 ± 0.08
LDC	4.0	1.60	3.82 ± 0.06	3.14 ± 0.06	3.26 ± 0.08	3.37 ± 0.07
LDCPrime	3.5	1.82	3.70 ± 0.06	3.07 ± 0.05	3.15 ± 0.07	3.30 ± 0.06
LDC4GLD	3.0	2.02	3.60 ± 0.05	2.97 ± 0.05	3.16 ± 0.06	3.32 ± 0.06

TABLE 2.2-2
Jet energy resolutions (rms_{90}) for different detector parameters. All results are based on $\mathrm{Z} \to \mathrm{u\bar{u}}, \mathrm{d\bar{d}}, \mathrm{s\bar{s}}$ events using scaled versions of the Mokka LDCPrime detector model. The results are quoted for the barrel region of the detector $|\cos\theta_{\mathrm{q\bar{q}}}| < 0.7$.

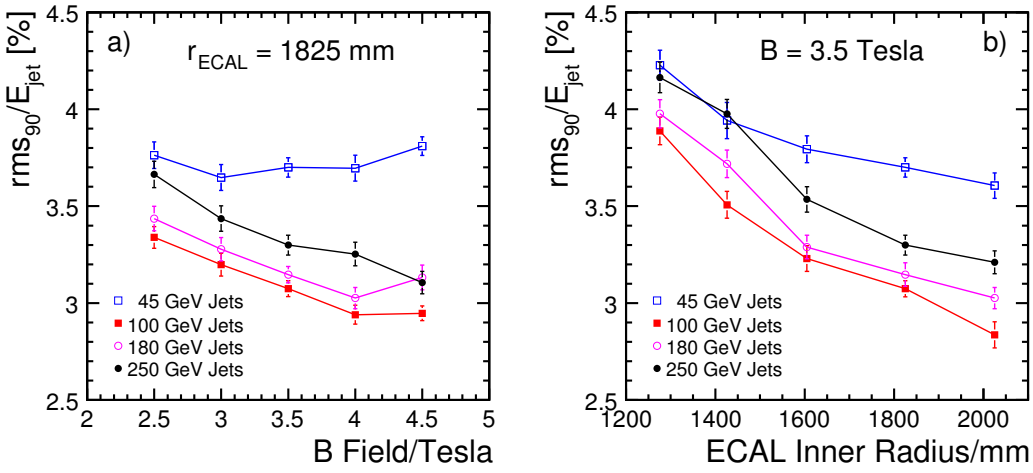

FIGURE 2.2-2. a) the dependence of the jet energy resolution (rms_{90}) on the magnetic field for a fixed ECAL inner radius (B=3.5 T corresponds to the LDCPrime model). b) the dependence of the jet energy resolution (rms_{90}) on the ECAL inner radius a fixed value of the magnetic field (R=1825 mm corresponds to the LDCPrime model).

that the smaller detector radius is compensated by a higher B. For the two smaller, higher B models listed in Table 2.2-2 degradations in performance are observed.

Figure 2.2-2 shows the dependence of the jet energy resolution ($\mathrm{rms}_{90}/\mathrm{E}_{\mathrm{jet}}$) on: a) magnetic field (fixed R) and b) ECAL inner radius (fixed B) for four different jet energies. For 45 GeV jets, the dependence of the jet energy resolution on B and R is weak; for these energies the intrinsic calorimetric energy resolutions, rather than the confusion term dominates. For higher jet energies, where the confusion term dominates, the jet energy resolution shows a stronger dependence on R than B.

The jet energy resolutions listed in Table 2.2-2 and those shown in Figure 2.2-2 are reasonably well described by the function:

$$\frac{\sigma_E}{E} = \frac{21}{\sqrt{E/\mathrm{GeV}}} \oplus 0.7 \oplus 0.004E \oplus 2.1 \left(\frac{R}{1825\,\mathrm{mm}}\right)^{-1.0} \left(\frac{B}{3.5\,\mathrm{T}}\right)^{-0.3} \left(\frac{E}{100\,\mathrm{GeV}}\right)^{0.3} \%.$$

This is the quadrature sum of four terms: i) the estimated contribution to the jet energy resolution from the intrinsic calorimetric resolution; ii) the contribution from imperfect track reconstruction, estimated by comparing the jet energy resolutions with those using tracks obtained from the MC information; iii) leakage, estimated by comparing the jet energy resolutions with those for an $8\,\lambda_I$ HCAL; and iv) the contribution from confusion obtained empirically from a fit to the data of Table 2.2-2 and Figure 2.2-2. In fitting the confusion term, a power-law $\kappa B^{\alpha} R^{\beta} E^{\gamma}$ provides a reasonable parameterisation of the data [1]. From the perspective of the optimisation of the detector, these studies show that for the particle flow calorimetry using the PandoraPFA algorithm, that the confusion term scales as approximately $B^{-0.3}R^{-1}$. For particle flow performance (with the PandoraPFA algorithm) the detector radius is more important than the magnetic field. This forms part of the motivation for the choice of a large detector radius for the ILD conceptual design. Table 2.2-3 lists the

[1] The majority of the data points lie within 2.5σ of the parameterisation, the only exception being the 45 GeV and 100 GeV jet energy resolutions for the "SiD-like" detector where the fit underestimates the resolution.

relative values of $B^{0.3}R$ and relative jet energy resolutions from the parameterisation above for the LDC, LDCPrime and LDC4GLD detector models. The main conclusion of this study is that, in terms of particle flow performance, the differences between the LDC, LDCPrime, and LDC4GLD detector models are at the level of $\pm 5\,\%$, with the larger models being slightly prefered.

Model			$B^{-0.3}R^{-1}$	Relative σ_E/E versus E_{jet}			
Name	B/T	R/m	(relative)	45 GeV	100 GeV	180 GeV	250 GeV
LDC	4.0	1.60	1.08	1.02	1.04	1.05	1.06
LDC4GLD	3.0	2.02	0.95	0.99	0.97	0.96	0.96

TABLE 2.2-3
Expected jet energy resolutions (rms_{90}) of the LDC and LDC4GLD detector models relative to the LDCPrime resolution.

2.2.4 Detector Aspect Ratio

Although the cost of ILD will depend less strongly on length than on radius, it is, nevertheless, an important parameter in the detector optimisation. From the perspective of particle flow, the main effect will be on the performance of forward jets. For forward tracks, the importance of the B-field will be further diminished, and one might expect the confusion term to scale as L^{-1}, where L is the z-position of the endcap ECAL. Figure 2.2-3a shows the particle flow performance for jets in the endcap region ($0.80 < |\cos\theta_{\mathrm{q\bar{q}}}| < 0.95$). For particle flow reconstruction of forward jets it is beneficial to have the ECAL endcaps further from the interaction region. To maintain good jet energy resolution in the forward region of the detector the TPC drift length needs to be $\gtrsim 2000\,\mathrm{mm}$.

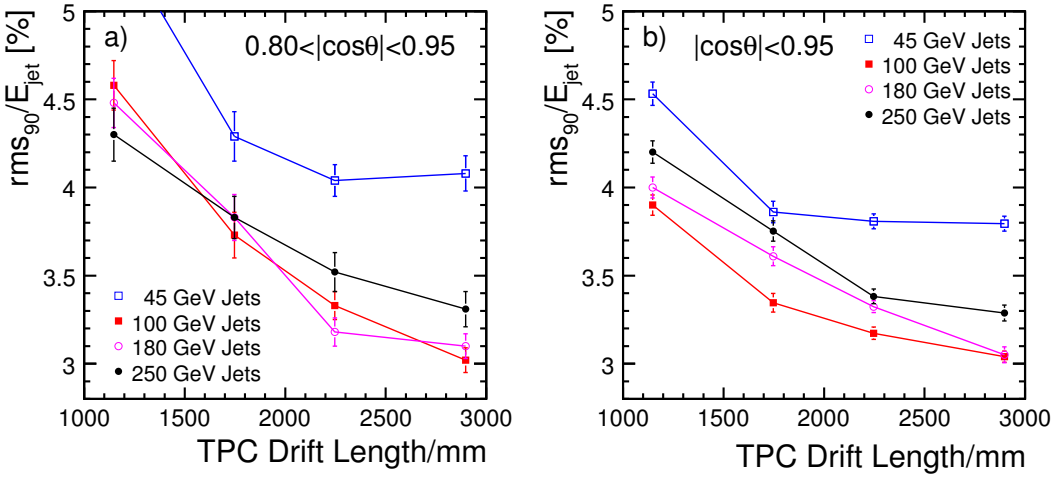

FIGURE 2.2-3. a) the dependence of the jet energy resolution in the "endcap" region ($0.80 < |\cos\theta_{\mathrm{q\bar{q}}}| < 0.95$) as a function of the TPC drift length in the LDCPrime model. b) the dependence of the jet energy resolution in the region ($|\cos\theta_{\mathrm{q\bar{q}}}| < 0.95$) as a function of the TPC drift length in the LDCPrime model.

Figure 2.2-3b shows the length dependence of the average jet energy resolution for jets with $|\cos\theta_{q\bar{q}}| < 0.95$. When considering all jets, the benefits to particle flow performance in going beyond a TPC drift length of 2200 mm are relatively small. From this study a TPC drift length of 2200 mm looks reasonable; the benefits of increasing the detector length are unlikely to justify the additional costs.

2.2.5 ECAL and HCAL Granularity

The dependence of particle flow performance on the transverse segmentation of the ECAL was studied using versions of the LDCPrime model with silicon pixel sizes of $5 \times 5\,\mathrm{mm}^2$, $10 \times 10\,\mathrm{mm}^2$, $20 \times 20\,\mathrm{mm}^2$, and $30 \times 30\,\mathrm{mm}^2$. The two main clustering parameters in the PandoraPFA algorithm were re-optimised for each ECAL granularity. The particle flow performance results are summarised in Figure 2.2-4a. For 45 GeV jets the dependence is relatively weak since the confusion term is not the dominant contribution to the resolution. For higher energy jets, a significant degradation in performance is observed with increasing pixel size. Within the context of the current reconstruction, the ECAL transverse segmentation has to be at least as fine as $10 \times 10\,\mathrm{mm}^2$ to meet the ILC jet energy requirement, $\sigma_E/E < 3.8\,\%$, for the jet energies relevant at $\sqrt{s} = 1\,\mathrm{TeV}$, with $5 \times 5\,\mathrm{mm}^2$ being preferred.

A similar study was performed for the HCAL using scintillator tile sizes of $1 \times 1\,\mathrm{cm}^2$, $3 \times 3\,\mathrm{cm}^2$, $5 \times 5\,\mathrm{cm}^2$, and $10 \times 10\,\mathrm{cm}^2$. The particle flow performance results are summarised in Figure 2.2-4b. From this study, it is concluded that the ILC jet energy resolution goals can be achieved with an HCAL transverse segmentation of $5 \times 5\,\mathrm{cm}^2$, although for higher energy jets there is a significant gain in going to $3 \times 3\,\mathrm{cm}^2$. There appears to be little motivation for $1 \times 1\,\mathrm{cm}^2$ over $3 \times 3\,\mathrm{cm}^2$ tiles.

2.2.6 ECAL and HCAL detector technology

The ILD concept incorporates two different technology options for both the ECAL and HCAL. The two ECAL technologies are: i) a Silicon-Tungsten (SiW) calorimeter where the baseline

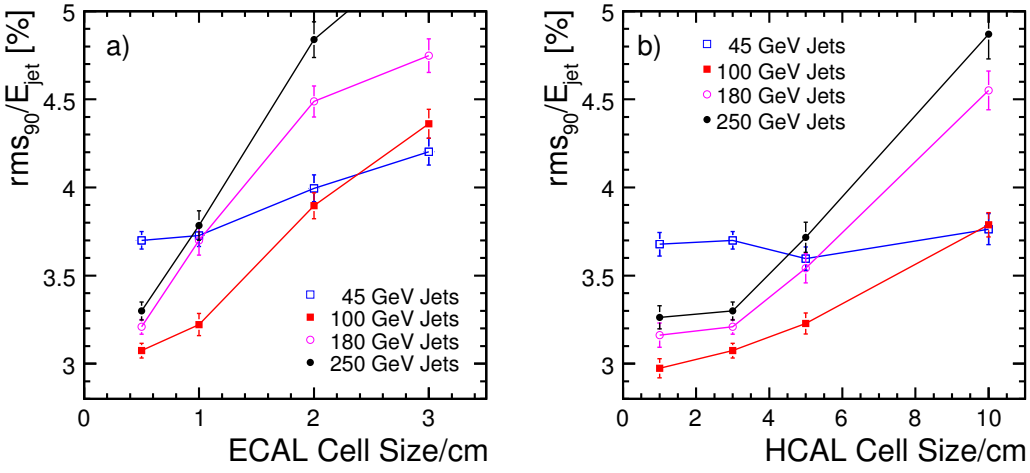

FIGURE 2.2-4. a) the dependence of the jet energy resolution (rms_{90}) on the ECAL transverse segmentation (Silicon pixel size) in the LDCPrime model. b) the dependence of the jet energy resolution (rms_{90}) on the HCAL transverse segmentation (scintillator tile size) in the LDCPrime model.

pixel size of $5 \times 5\,\mathrm{mm}^2$; and ii) a scintillator-Tungsten calorimeter where the $1 \times 4\,\mathrm{cm}^2$ scintillator strips in successive layers are perpendicular to each other with the aim of achieving a $1 \times 1\,\mathrm{cm}^2$ effective transverse granularity. The particle flow studies described above were obtained using the simulation of the SiW calorimeter. To extend these studies to the scintillator strip option requires additional step in the reconstruction, namely strip-based clustering. First studies[20] indicate that for 100 GeV jets the performance of the scintillator option with $1 \times 4\,\mathrm{cm}^2$ strips may approach that which would be obtained with a scintillator segmentation of $1 \times 1\,\mathrm{cm}^2$. However, at this stage, further work is needed to understand the limitations of the strip based ECAL for higher energy jets and whether it is possible to extend the approach to narrower strips to achieve an effective $5 \times 5\,\mathrm{mm}^2$ segmentation. The potential advantages of even finer segmentation, *e.g.* as provided by the MAPs-based ECAL, has yet to be studied in detail.

The two HCAL technologies under consideration are: i) an analogue steel-scintillator hadron calorimeter (AHCAL) with a tile size of $\sim 3 \times 3\,\mathrm{cm}^2$; and ii) a semi-digital calorimeter (DHCAL), *e.g.* using RPCs, with a readout pixel size of $1 \times 1\,\mathrm{cm}^2$ and a three level (2 bit per cell) readout. The particle flow studies described above used the AHCAL option. The particle flow performance of the semi-digital option is currently being studied in the context of the current PandoraPFA algorithm. Earlier studies (with the LDC detector model and a previous version of the PandoraPFA algorithm) found that the jet energy resolution for 100 GeV jets with a digital (single bit) readout was similar to that obtained with the AHCAL option. Further study is needed to establish the particle flow performance of the DHCAL option.

2.3 BACKGROUND CONSIDERATIONS

Beam-related backgrounds, and in particular e^+e^- pairs created by beam-beam interactions, are an essential input to the ILD design and optimisation. The e^+e^- pairs are produced at relatively low angles to the beam direction and spiral along the magnetic field lines parallel to the beam axis. As shown in Figure 2.3-5, the resulting pair-background tracks form a dense core with an approximately quadratic envelope. The radius of the dense core for a given value of z is roughly proportional to $\sqrt{B}$ [21]. The pair background determines the minimum radius of the beam pipe needed to avoid a large source of secondary background from electrons and positrons hitting the beam pipe. In turn, the radius of the beam pipe determines the radius of the innermost layer of the vertex detector, and consequently influences the impact parameter resolution for relatively low-momentum charged tracks. However, it has been shown [2], that if the magnetic field is $\gtrsim 3\,\mathrm{T}$, the required impact parameter resolution of $5\,\mu\mathrm{m} \oplus 10\,\mu\mathrm{m}/p(\mathrm{GeV})\sin^{3/2}\theta$ is achievable with a vertex detector layer thickness of $0.1 - 0.2\,\% X_0$/layer.

In terms of optimisation of ILD, the main effect of the pair background is to determine the inner radius of the vertex detector, which affects the impact parameter resolution and thus the flavour tagging performance. However, the difference between the radius of the core of the pair background between a 3T and a 4T magnetic field is only 15 %. In practice, the impact of the magnetic field on the inner radius of the vertex detector is less than this, as it is necessary to leave gaps between the dense core of the pair background and the beam pipe and between the beam pipe and the first layer of the vertex detector. These gaps are independent of the magnetic field, and when this is taken into account, the difference of inner radius of the vertex detector between a B-field of 3 T and 4 T is only $\sim 10\,\%$. The impact on the detector performance is discussed in the next two sections.

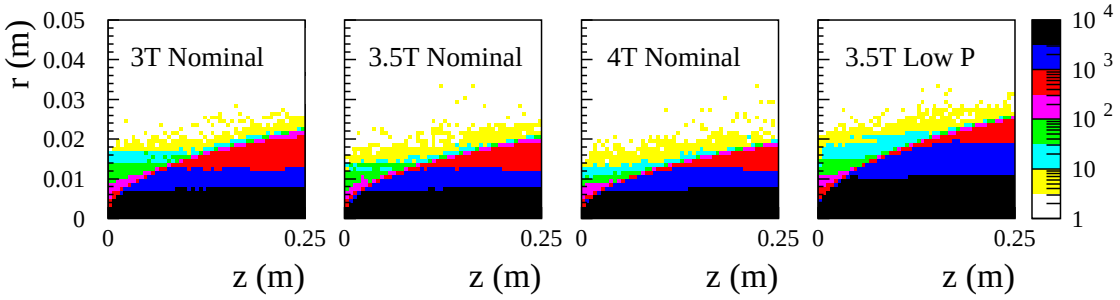

FIGURE 2.3-5. Track density of the e^+e^- pair background ($/cm^{-2}/BX$) with the nominal ILC beam parameters at $\sqrt{s} = 500\,\text{GeV}$ for the detector magnetic field of 3 T, 3.5 T, and 4 T. Also shown is the background with the lowP option for the ILC beam parameters at $\sqrt{s} = 500\,\text{GeV}$ with $B = 3.5\,\text{T}$.

Finally, it is worth noting that the inner radius of the vertex detector for the lowP option of the ILC machine parameters is about 20% larger than that for the nominal option. Therefore, it can be concluded that the machine parameters have a larger impact on the inner radius of the vertex detector than the magnetic field of the detector.

2.4 DETECTOR OPTIMISATION FOR TRACKING

The tracking system of the ILD detector concept consists of a vertex detector (VTX) and a large volume TPC, complemented by additional Silicon tracking layers (FTD/SIT). In addition, in the LDC-based models, silicon tracking layers immediately outside the TPC are considered (ETD and SET). The dependence of the performance of the tracking system on the magnetic field and detector size was an important consideration in optimising the ILD. Considerations of momentum resolution favour a larger detector and higher magnetic field. As discussed above, a higher magnetic field also allows the first layer of the vertex detector to be closer to the interaction point (IP). The optimisation of the tracking system is, again, a balance between the magnetic field and detector radius. The parameter space spanning the LDC (smaller R, higher B-field) and GLD (larger R, lower B) concepts is investigated using the six detector models summarised in Table 2.1-1.

2.4.1 Momentum Resolution

Figure 2.4-6(a) shows the $1/p_T$ resolution, as a function of p_T, for single muons in the GLD, GLDPrime and GLD4LDC models. The results were obtained using the Satellites Kalman Filter (Section 2.1.1). Figure 2.4-6(b) shows the relative $1/p_T$ resolution compared to the average of three detector models at a particular value of p_T, plotted as a function of p_T. Above approximately 50 GeV, the resolution obtained with the GLD4LDC model is $\sim$5 % worse than the larger detector models due to the shorter lever arm of the TPC. For lower energy tracks the situation is reversed with the higher magnetic field resulting in the resolution for 4 T being $\sim$10 % better than for 3 T. Similar results were obtained with the LDC-based models using Mokka and MarlinReco (Section 2.1.2). The relative performance does not depend strongly on the angle. The differences in resolution for the range of B and R considered are small ($\lesssim 10\,\%$) compared to those arising from different layouts for the tracking system and the point resolutions of the components. For example, the use of hits in the silicon external

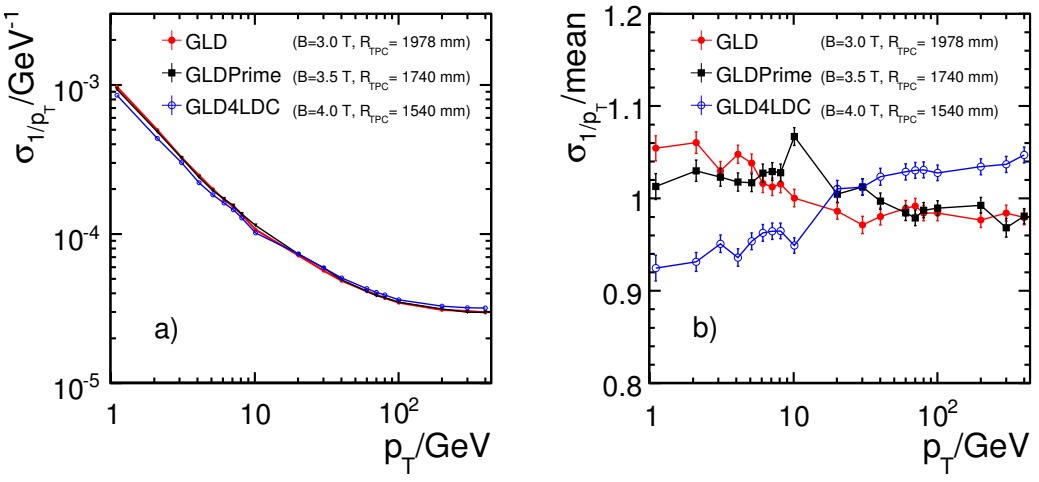

FIGURE 2.4-6. (a) $\sigma_{1/p_{\mathrm{T}}}$ for single muon tracks at 90° to the beam axis, as a function of transverse momentum, for the GLD, GLDPrime, and GLD4LDC models; and (b) the ratio of $\sigma_{1/p_{\mathrm{T}}}$ to the average of the three detector models as a function of transverse momentum. To avoid the TPC central membrane the generated muons were displaced from the IP by a few centimetres.

tracker (SET) outside the TPC in the LDCPrime model improves the momentum resolution by 15 % assuming an SET $r\phi$ hit resolution of 4 μm.

2.4.2 Impact Parameter Resolution

The impact parameter resolution, $\sigma_{r\phi}$, of the tracking system is an important input to the heavy flavour tagging capability of the detector. The most important detector considerations are the vertex detector design (point resolution and material budget) and the magnetic field which, as discussed in Section 2.3 affects the minimum distance of the first layer of the vertex detector from the interaction region, R_{min}. Figure 2.4-7a shows $\sigma_{r\phi}$ as a function of p_{T} for the GDC-based detector models. The GLD4LDC model has the best resolution, because the higher B-field allows the innermost layer of the vertex detector to be closer to the interaction point (IP). However the differences between the detector models considered, Figure 2.4-7b, are relatively small $\lesssim 5-10\,\%$.

Figure 2.4-7c shows the $\sigma_{r\phi}$ resolution for 1 GeV muons for the GLD-based detector models, plotted as a function of the track angle. Whilst the higher magnetic fields are favoured, the differences between the detector models are $\lesssim 15\,\%$. For higher energy tracks, where the effect of multiple Coulomb scattering is negligible, the differences between the models are even smaller. Although the variations in magnetic field and the corresponding inner radii of the vertex detector lead to relatively small differences in impact parameter resolution, different detector layouts have a more significant impact. Figure 2.4-7d compares the impact parameter resolution for the GLDPrime and LDCPrime detector models. The GLDPrime detector assumes a vertex detector consisting of six layers arranged in three closely spaced doublets (see Section 4.1.4), whereas the LDCPrime model assumes five equally spaced layers. The three double layer layout results in a significantly better impact parameter resolution for high momentum tracks because it gives two, rather than one, high precision measurements close to the IP.

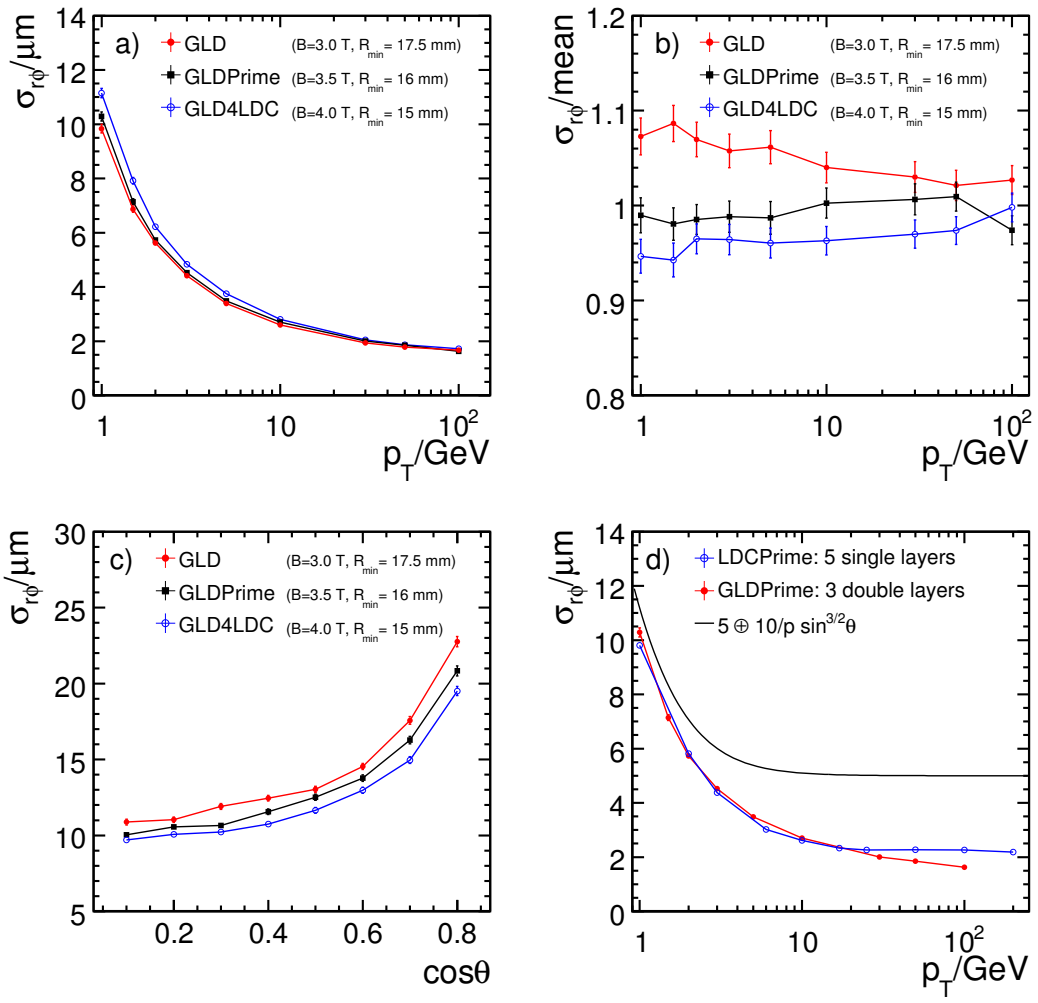

FIGURE 2.4-7. (a) $\sigma_{r\phi}$ as a function of p_{T} for GLD, GLDPrime, and GLD4LDC, and (b) the ratio of $\sigma_{r\phi}$ to the average of the three detector models. c) $\sigma_{r\phi}$ as a function of the track angle at the track energy of 1 GeV for GLD, GLDPrime, and GLD4LDC. d) the impact parameter resolution as a function of p_{T} for GLDPrime and LDCPrime. Also shown is the nominal ILC goal for impact parameter resolution.

2.4.3 Conclusions

For the range of B and R considered here, the differences in momentum resolution are $\lesssim 10\,\%$, with higher B-field preferred for low p_{T} tracks and a larger R preferred for high p_{T} tracks. The impact parameter resolution, $\sigma_{r\phi}$, is better for models with higher B as the first layer of the vertex detector can be placed closer to the IP. However, the differences in impact parameter resolution obtained with a 3 T and 4 T magnetic field are small, at most 15 % for low momentum tracks and $\lesssim 5\,\%$ for tracks above 2 GeV. It can be concluded that for the range of B and R spanned by the LDC and GLD detector concepts, the differences in impact parameter and momentum resolution are relatively small. It is also concluded that the tracking resolutions depend much more strongly on the subdetector technologies and tracking system layout than on the global parameters (B and R) of the detector.

2.5 FLAVOUR TAGGING

Heavy flavour tagging will be an essential tool in many physics analyses at the ILC. The flavour tagging performance depends primarily on the design of the vertex detector and, in particular, the impact parameter resolution. The flavour tagging performance is studied using MarlinReco for the full reconstruction of the simulated events and the sophisticated LCFIVertex package for heavy flavour tagging [22]. The LCFIVertex [17] flavour tagging uses three artificial neural networks (ANNs): i) a b-tag to discriminate b-quark jets from jets from charm and light quarks; ii) a c-tag to discriminate c-quark jets from b and light quark jets; and iii) a c/b-tag to discriminate between c-quark jets and b-quark jets. The ANNs use different sets of discriminant variables depending on whether either one, two, or more than two vertices are found in the jet. The ANN architecture is a multi-layer perceptron with $N = 8$ inputs, one hidden layer with $2N - 2$ nodes, and sigmoid activation functions. The weights were calculated using the back propagation conjugate gradient algorithm. Two of the most powerful inputs to the flavour tag are the joint likelihoods (in $r-\phi$ and in $r-z$) for all tracks in the jet to have originated from the primary vertex. The joint likelihoods depend on the respective $r-\phi$ and $r-z$ impact parameter significances of all the tracks in the jet. Consequently the impact parameter resolution of the vertex detector plays a central role in determining the flavour tagging performance. It was demonstrated in the previous section that the difference in $\sigma_{r\phi}$ in going from 3 T to 4 T is rather small. Consequently, one might expect the same to be true for flavour tagging performance.

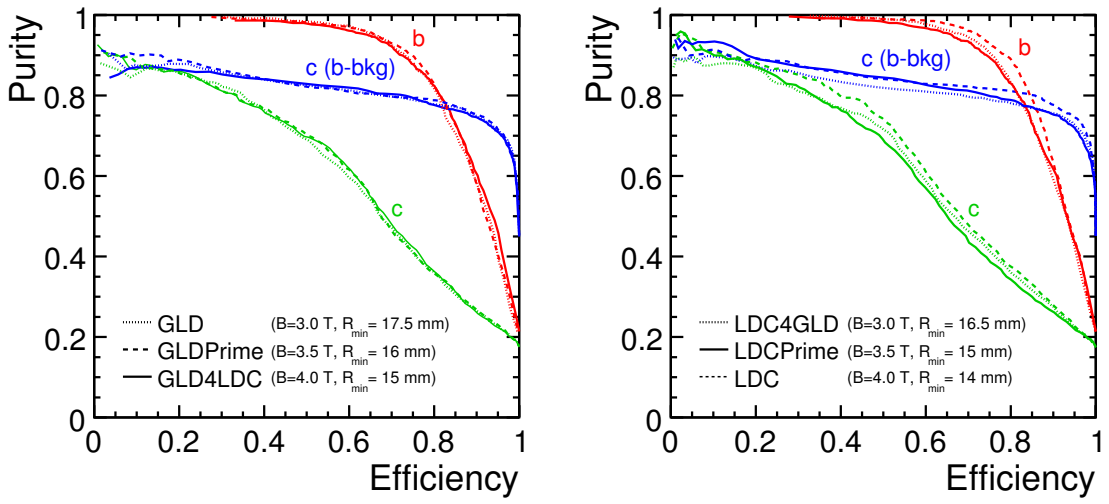

FIGURE 2.5-8. Flavour tagging performance for the (left) GLD-based and (right) LDC-based detector models.

The dependence of flavour tagging performance on the global detector parameters was investigated using the GLD- and LDC-based detector models. Separate ANNs were trained for each of the models. The samples used to evaluate the flavour tagging performance, which were generated with SM Z boson branching ratios, were independent of those used for the training. All the samples were generated at $\sqrt{s} = m_Z$. The results are shown in Figure 2.5-8. The observed differences in the flavour tagging performances between the GLD (LDC) models are $\lesssim 1\,\%$ ($\lesssim 4\,\%$). There is a preference for the 4.0 T configuration, in particular for

the b-tag at high efficiencies. However, the uncertainties on the efficiencies due to statistics and the ANN training procedure are $\sim 2\,\%$, and hence statistical significance of the observed differences are $\lesssim 2\sigma$. From this study it is concluded that the increased inner radius of the vertex detector when going from B=4 T to B=3 T, does not have a large impact on the flavour tagging performance of the detector.

2.6 PHYSICS PERFORMANCE

The previous sections of this chapter discuss the impact of the detector design on the low level measurements of jet energies, track momenta, impact parameters and flavour identification. Here the performance of the different detector models in Table 2.1-1 are compared for three physics analyses: the measurement of the Higgs mass, τ pair production and polarisation, and chargino/neutralino pair production.

2.6.1 Higgs Recoil Mass

One of the prime motivations for the unprecedented track momentum resolution at the ILC is the determination of the Higgs mass from the recoil mass distribution in $ZH \to \mu^+\mu^- X$ and $ZH \to \mathrm{e}^+\mathrm{e}^- X$ events. This sensitivities to this process if the LDC, LDCPrime and LDC4GLD detector models were compared. For this study only $\mathrm{e}^+\mathrm{e}^- \to ZZ \to \mathrm{e}^+\mathrm{e}^-/\mu^+\mu^- Z$ background was included. Figure 2.6-9 shows, for the LDCPrime model, the Higgs recoil mass distribution for selected events. To determine the Higgs mass and production cross section, the recoil mass distributions were fitted using a Gaussian for the peak region with an exponential component for the tails [23].

The results for the different detector models are summarised in Table 2.6-4. These numbers should not be compared with the physics sensitivity studies presented in Section 3.3.1 as only $\mathrm{e}^+\mathrm{e}^- \to ZZ \to \mathrm{e}^+\mathrm{e}^-/\mu^+\mu^- Z$ background is included and the events were generated with a different luminosity spectrum.

When interpreting the above results it is necessary to consider the relative importance of momentum resolution and the beam energy spread. For the assumed beam energy spread (a

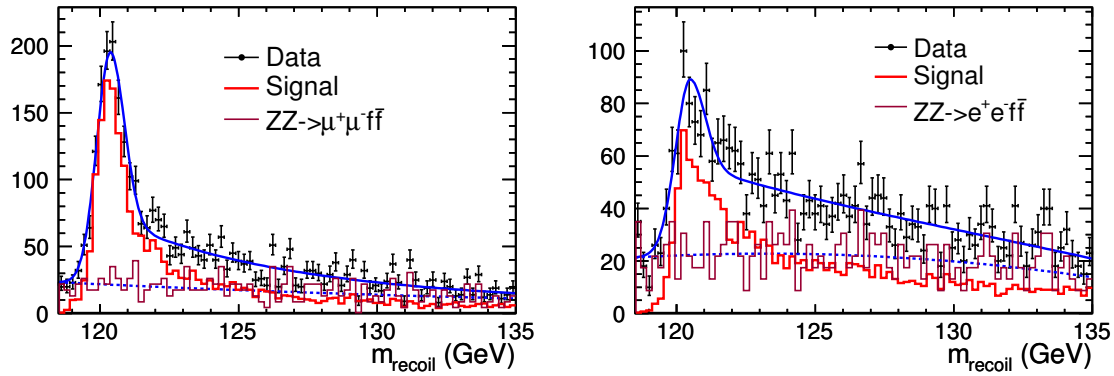

FIGURE 2.6-9. Distributions of the reconstructed Higgs recoil mass obtained with the LDCPrime model for (a) ZH $\to \mu^+\mu^- X$ and (b) ZH $\to \mathrm{e}^+\mathrm{e}^- X$. The events were generated with a top-hat beam energy distribution with a half width of 0.28% for the electron beam and 0.18% for the positron beam.

	$ZH \to \mu^+\mu^- X$		$ZH \to e^+e^- X$	
	$\Delta m_{\mathrm{recoil}}$	$\Delta\sigma$	$\Delta m_{\mathrm{recoil}}$	$\Delta\sigma$
LDCPrime	23 ± 0.4 MeV	0.28 fb	47±0.9 MeV	0.49 fb
LDC	23 ± 0.4 MeV	0.27 fb	47±0.9 MeV	0.52 fb

TABLE 2.6-4
The measurement precision of the Higgs recoil mass ($\Delta m_{\mathrm{recoil}}$) and cross section ($\Delta\sigma$) for ZH $\to$ $\mu^+\mu^- X$/e$^+$e^-X. The events were generated with a top-hat beam energy distribution with a half width of 0.28% for the electron beam and 0.18% for the positron beam.

top-hat distribution with half-widths 0.28 % and 0.18 % for the electron and positron beams respectively), the event-by-event recoil mass resolution in the peak region is ~ 400 MeV, which this includes contributions from the beam energy spread and from beamstrahlung. From MC studies, the other major contribution to the event-by-event recoil mass resolution arises, as expected, from the track momentum resolution. This is found to contribute ~ 350 MeV to the recoil mass resolution. For the detector models considered in this study, the differences in momentum resolution are $\lesssim 5$ %, for the relevant momentum range. Even these small differences are diluted by the contribution from the beam energy spread and, as verified in this study, significant differences in the m_{H} mass resolution are not expected.

2.6.2 Tau pairs

The reconstruction of tau pair events at $\sqrt{s} = 500$ GeV provides a powerful test of a number of aspects of the detector performance, *e.g.* π^0 reconstruction and the tracking efficiency for nearby tracks in three-prong tau decays. The performances of the GLD, GLDPrime, GLD4LDC and LDCPrime models are compared for the measurement of the τ polarisation, P_τ which is primarily sensitive to the ability to resolve photons from π^0 decay from the charged hadron in $\tau \to \rho\nu$ decays. Figure 2.6-10 shows the reconstructed π^0 and $\rho^\pm$ invariant mass distributions used in the tau decay selections. The numbers of events in the π^0 mass peak reflect the efficiency for reconstructing both photons from $\pi^0 \to \gamma\gamma$ decays. The LDCPrime detector model gives the highest $\pi^0 \to \gamma\gamma$ reconstruction efficiency, demonstrating the advantages of smaller ECAL pixel size ($5 \times 5\,\mathrm{mm}^2$). For the GLD models, all with an ECAL pixel size of $10 \times 10\,\mathrm{mm}^2$, the π^0 reconstruction efficiency increases with detector radius due to the increased spatial separation of the two photons.

Table 2.6-5 summarises the impact of the different detector models on the P_τ measurement from $\tau \to \pi\nu$ decays. The $\tau \to \pi\nu$ selection requires that a tau jet consists of a single track and at most 1 GeV of energy not assigned to the track. Cuts to remove $\tau \to e\nu\overline{\nu}$ and $\tau \to \mu\nu\overline{\nu}$ decays are also applied. The P_τ is determined from the cosine of the $\pi^\pm$ decay angle in the τ rest-frame (which is determined by the charged pion energy). The differences in the different detector models are most evident in the purities of the $\tau \to \pi\nu$ selection. The advantages of smaller ECAL pixels (LDCPrime compared to GLDPrime) are clear and it can be seen that higher purities are obtained for larger detector radii. However, similar sensitivities to P_τ are obtained from the $\tau \to \pi\nu$ channel. One should not draw too strong a conclusion from this as the measurement of P_τ from $\tau \to \rho\nu$ and $\tau \to a_1\nu$ decays could show a stronger dependence on the detector model.

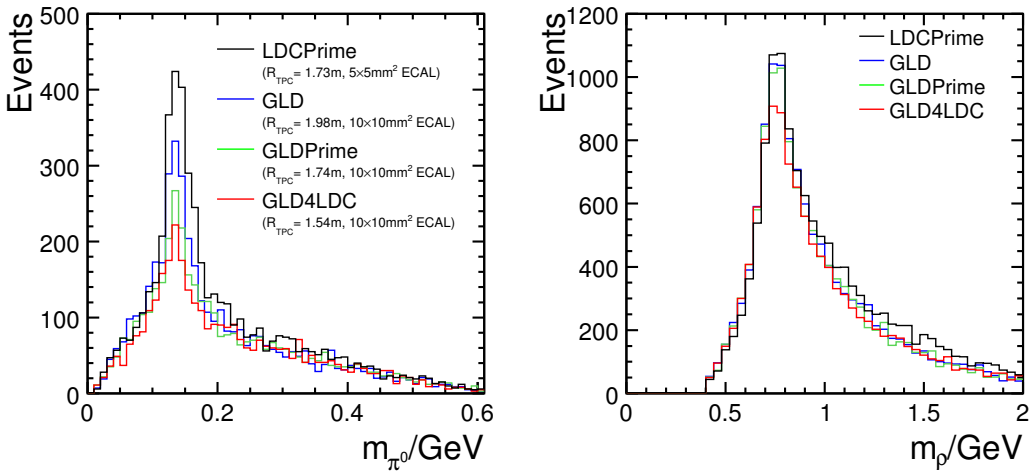

FIGURE 2.6-10. a) The reconstructed π^0 invariant mass distribution in the selected $\tau^+\tau^-$ events at $\sqrt{s} = 500\,\text{GeV}$. Only events where more than one photon is reconstructed are shown. b) The corresponding reconstructed $\rho^\pm \to \pi^\pm\pi^0$ mass distribution for decays where ≥ 1 photon cluster is reconstructed. For both plots the distributions include all tau decay modes.

Detector	ECAL/mm^2	R_{TPC}/m	Eff	Purity	σ_{P_τ}
GLD	10×10	1.98	84.5 %	85.7 %	0.0454 ± 0.0005
GLDPrime	10×10	1.74	85.2 %	83.6 %	0.0452 ± 0.0005
GLD4LDC	10×10	1.54	84.9 %	80.8 %	0.0460 ± 0.0006
LDCPrime	5×5	1.73	84.1 %	88.5 %	0.0430 ± 0.0005

TABLE 2.6-5
Summary of $\tau^\pm \to \pi^\pm\nu$ selection efficiencies and purities for events generated with the GLD, GLDPrime, GLD4LDC, and LDCPrime detector models. The efficiencies are calculated with with respect to the $\tau^+\tau^-$ selection and the purities only include the background from the different tau decay modes. The statistical uncertainties on the efficiencies and purities are all $\pm 0.5\,\%$. The uncertainty on the tau polarisation measurement assumes an electron-positron polarisation of $(-80\,\%, +30\,\%)$ and corresponds to $80\,\text{fb}^{-1}$ of data.

2.6.3 Chargino and neutralino production

Chargino and neutralino pair production at $\sqrt{s}$ =500 GeV is studied in the context of SUSY point-5 benchmark scenario. The main signal is jets plus missing energy from $\chi_1^+\chi_1^- \to \text{W}^+\text{W}^-\chi_1^0\chi_1^0$ and $\chi_2^0\chi_2^0 \to \text{ZZ}\chi_1^0\chi_1^0$. The process $\chi_2^0\chi_2^0 \to \text{ZZ}\chi_1^0\chi_1^0$ is the main background to study $\chi_1^+\chi_1^- \to \text{W}^+\text{W}^-\chi_1^0\chi_1^0$ and *vice versa*. The identification of the separate chargino and neutralino final states relies on the ability to distinguish W^+W^- from ZZ and thus is sensitive to the jet energy resolution of the detector. Figure 2.6-11a shows the reconstructed invariant masses of hadronically decaying $W^\pm$ and Z bosons from decays of $\chi_1^\pm$ and χ_2^0, respectively. Neutralino and chargino event samples were separated based on the consistency of the reconstructed di-jet masses with the Z and W boson hypotheses. The selection efficiencies for $\chi_1^\pm$ and χ_2^0 events for the GLD-based detector models are summarised in Table 2.6-6. The different detector models give statistically compatible selection efficiencies. This is consistent with the fact that the differences in the jet energy resolutions for the three detector models

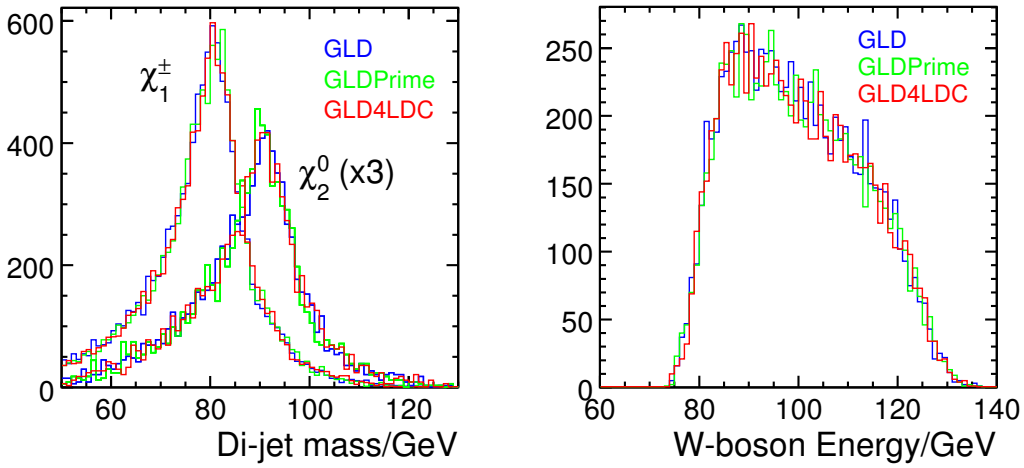

FIGURE 2.6-11. (a) The reconstructed masses of W and Z bosons from the decays of $\chi_1^\pm$ and χ_2^0. (b) The energy distribution of the reconstructed W bosons from $\chi_1^\pm$ decays.

	Chargino selection		Neutralino selection	
	Efficiency ($\chi_1^\pm$)	Efficiency (χ_2^0)	Efficiency ($\chi_1^\pm$)	Efficiency (χ_2^0)
GLD	$47.9 \pm 0.3\,\%$	$1.0 \pm 0.1\,\%$	$11.2 \pm 0.5\,\%$	$33.8 \pm 0.6\,\%$
GLDPrime	$48.4 \pm 0.3\,\%$	$1.0 \pm 0.1\,\%$	$11.4 \pm 0.5\,\%$	$33.3 \pm 0.6\,\%$
GLD4LDC	$48.8 \pm 0.3\,\%$	$1.1 \pm 0.1\,\%$	$11.4 \pm 0.5\,\%$	$34.1 \pm 0.6\,\%$

TABLE 2.6-6
The efficiency for $\chi_1^\pm$ and χ_2^0 selection.

considered are at the level of $3-4\,\%$ for the jet energy range $50-100\,\mathrm{GeV}$ (Table 2.2-2).

Because $\chi_1^\pm \to W^\pm\chi_1^0$ and $\chi_2^0 \to Z\chi_1^0$ are two body decays, the masses of $\chi_1^\pm$, χ_2^0, and lightest SUSY particle (LSP), χ_1^0, can be derived by using the energy distributions of the W and Z bosons. The energy distributions of the reconstructed W bosons are shown in Figure 2.6-11b. The different detector models result in very similar distributions and, consequently, have the same sensitivity to the $\chi_1^\pm$, χ_2^0 and LSP masses.

2.7 CONCLUSIONS

The studies described above informed the choice of parameters for the baseline ILD concept. The conclusions of these studies are:

- **B-field (vertex reconstruction):** The radius of the beam background envelope scales as $B^{-0.5}$. This determines that the minimum acceptable inner radius of the vertex detector goes from $\sim 14\,\mathrm{mm} \to 16\,\mathrm{mm}$ for $B = 4\,\mathrm{T} \to 3\,\mathrm{T}$. The effect on impact parameter resolution is $\lesssim 10\,\%$ and the resulting differences in flavour tagging efficiency are small ($\sim 2\,\%$).
- **B-field versus Radius (particle flow):** The confusion term in particle flow reconstruction scales as R^{-1}. This can be partially compensated by the magnetic field,

although the dependence is weak, $B^{-0.3}$. For the entire range of detector parameters spanning the GLD and LDC concepts, the ILC jet energy resolution requirements can be met. The differences in particle flow performance between the LDC and GLD parameters are small, $\lesssim 6\,\%$, with the larger radius/lower field option being preferred.

- **B-field versus Radius (momentum resolution):** In terms of momentum resolution, the differences between the models considered are small $\lesssim 10\,\%$. For high p_{T} tracks, larger radius/lower field detector is preferred. For low p_{T} tracks the opposite is true. All detector models considered here meet the ILC momentum resolution goals.
- **TPC aspect ratio (particle flow):** the aspect ratio of the TPC ($R : z = 1 : 1.3$) used in the studies is close to optimum for particle flow; there is no significant advantage in a longer TPC and a shorter TPC would significantly degrade the performance in the forward region.
- **ECAL Segmentation (particle flow):** The ECAL pixel size should be no greater than $10 \times 10\,\mathrm{mm}^2$ in order to meet the ILC jet energy resolution goals for the jets relevant at $\sqrt{s} = 500\,\mathrm{GeV}$. Within the context of the current reconstruction, $5 \times 5\,\mathrm{mm}^2$ gives significant advantages over $10 \times 10\,\mathrm{mm}^2$, particularly for higher energy jets.
- **ECAL Segmentation (physics):** For the reconstruction of tau decays, a $5 \times 5\,\mathrm{mm}^2$ ECAL pixel size is favoured over $10 \times 10\,\mathrm{mm}^2$.
- **Physics Performance:** The models considered give comparable physics performance. This is not surprising; the differences in the underlying detector performance measures are small because the models trade-off R against B in such a way that *each* represents a reasonable detector choice.
- **HCAL Segmentation/Depth (particle flow):** For sufficient containment of jets at $\sqrt{s} = 500\,\mathrm{GeV}$, the HCAL should be between $5 - 6\lambda_I$. The baseline for the ILD was chosen to be $6\lambda_I$ to ensure good jet containment for the highest energy jets and to allow for possible differences between the simulation of hadronic showers and reality. For the current reconstruction, there appears to be no significant advantage in going below $3 \times 3\,\mathrm{cm}^2$.
- **Vertex Detector:** two detector layouts were considered: five single layers and six layers arranged in three doublets. Both conceptual designs meet the ILC goals for impact parameter resolution, with the doublet structure giving an impact parameter resolution which is better, particularly for high momentum tracks.
- **SiW versus Scintillator-W ECAL:** results from studies of the strip reconstruction and the resulting jet energy resolution of the Scintillator/Tungsten option, whilst promising, have yet to reach the level of sophistication where the performance of the strip based ECAL option can be fully evaluated. For this reason, the SiW ECAL is used in the simulation of the ILD for the physics studies in the next section.
- **AHCAL versus DHCAL:** results from studies of the digital HCAL option are not yet at the level where its performance has been demonstrated. For this reason the AHCAL option with $3 \times 3\,\mathrm{cm}^2$ tiles is used in the simulation of ILD.
- **Cost:** From the studies presented in this section it is clear any of the detector models listed in Table 2.1-1 are viable detectors for the ILC. For the same subdetector technologies, the differences in the costs for the detector parameters considered are estimated to be $\sim 10 - 20\,\%$; a large $B = 3\,\mathrm{T}$ detector is disfavoured on grounds of cost. However, given the large fluctuations in raw material costs (as seen in the last year) and the difficulty extrapolating detector sensor costs to the future, it is not yet possible to choose between the models on this basis.

2.8 CHOICE OF ILD PARAMETERS

On the basis of the considerations above, the ILD detector parameters (listed Table 2.1-1) are chosen to be close to those of the LDCPrime/GLDPrime models. The main arguments for the choices are as follows:

- **Choice of B-field:** The operational magnetic field is chosen to be 3.5 T, although it is assumed that the solenoid would be designed for 4.0 T to allow a safety margin in the mechanical design. This can be achieved without extrapolating significantly beyond the current CMS design. The arguments for a higher field are relatively weak: the benefits are marginal, and it would increase the cost of the detector. Whilst a lower B-field is not excluded, it is felt that until the likely ILC backgrounds and their impact on the ILD concept are better understood, it would be unwise to go to 3 T.
- **Choice of Radius:** The ECAL inner radius is chosen to be 1.85 m. The ILD concept is designed for particle flow calorimetry and the jet energy performance is the main motivation for this choice. For B=3.5 T the gain in going to an ECAL radius of 2.0 m is modest and may not justify the increase in cost. For a B=3.5 T, the ILC jet energy goals suggest that the radius should be greater than $1.5 - 1.6$ m. However, the studies presented above rely on the simulation of hadronic showers. By selecting a detector radius of 1.85 m, it is likely that the ILD concept will meet the ILC jet energy goals, even if the current performance estimates are on the optimistic side.
- **Choice of Sub-detector Technologies:** At this stage we are not in a position to choose the ECAL, HCAL and vertex detector technologies. All options are considered on an equal basis. Nevertheless, for the physics studies that follow it is necessary to define a baseline for the simulation. The six layer (three doublets) vertex detector layout is used on the basis that it gives the best impact parameter resolution. For the calorimetry, the SiW ECAL and the AHCAL are used in the simulation as they have been well studied and we are confident that they give the desired jet energy resolution. The strip-based ECAL and DHCAL will be actively supported in simulation and software with the intention of evaluating their ultimate performance.

The optimisation of the ILD parameters was performed in a rigorous manner using information from a number of detailed studies. On this basis, we are confident that the ILD concept is well optimised for physics at the ILC operating in the energy range 200 GeV−1 TeV.

CHAPTER 3

Physics Performance

The performance of ILD is established using a detailed GEANT4 model and full reconstruction of the simulated events. Both detector performance measures and physics analyses are studied. Whilst the simulation and reconstruction are not perfect, they are at least as sophisticated as those used in the majority of studies for previous large collider detector TDRs.

3.1 SOFTWARE FOR ILD PERFORMANCE STUDIES

To demonstrate the physics capabilities of ILD, more than 30 million Monte Carlo (MC) events have been fully simulated and reconstructed for the benchmark reactions [24] and other physics channels of interest at the ILC. Signal samples typically correspond to an integrated luminosity of 500 fb^{-1} or more. These are combined with sufficiently large sets of SM events for background estimation. The "simulation reference ILD detector model", ILD_00, is implemented in Mokka. The silicon based tracking detectors are modelled with the appropriate material thicknesses and support structures without specifying the exact readout technology. Instead, in the digitisation stage, simulated hits are smeared by the effective point resolutions listed in Table 3.1-1. These represent the most realistic estimates from the relevant subdetector R&D groups. The SiW option with 5×5 mm^2 transverse cell size and the Steel-Scintillator option with $3 \times 3\,\mathrm{cm}^2$ tiles are used for the ECAL and HCAL respectively. As discussed in Section 2.2.6, these are the most mature of the technology options in terms of simulation and reconstruction; this does not imply any pre-decision on the ultimate technology choice. The main parameters of the ILD_00 model are listed in Table 2.1-1 and a drawing of this model is shown in Figure 3.1. Further details of the geometrical parameters can be found in [25].

	$\sigma_{r-\phi}/\mu\mathrm{m}$	$\sigma_z/\mu\mathrm{m}$		$\sigma_{r-\phi}/\mu\mathrm{m}$	$\sigma_z/\mu\mathrm{m}$
VTX	2.8	2.8	FTD	5.8	5.8
SIT/SET	7.0	50.0	ETD	7.0	7.0
TPC	$\sigma^2_{r\phi} = 50^2 + 900^2 \sin^2\phi + \left((25^2/22) \times (4/B)^2 \sin\theta\right) (z/\mathrm{cm})\,\mu\mathrm{m}^2$ $\sigma^2_z = 400^2 + 80^2 \times (z/\mathrm{cm})\,\mu\mathrm{m}^2$				

TABLE 3.1-1
Effective point resolutions used in the digitisation of the MC samples.

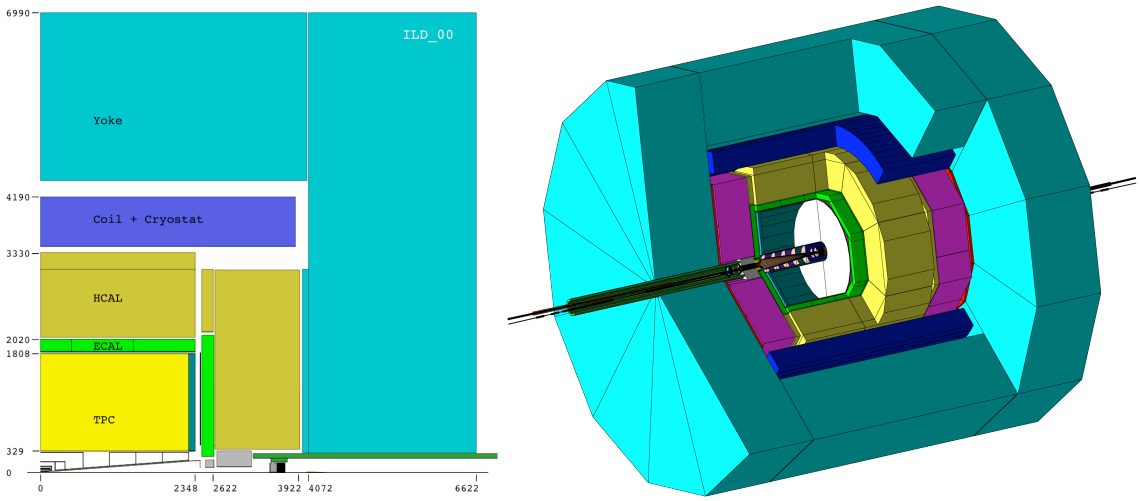

FIGURE 3.1-1. The ILD_00 detector model as implemented in Mokka. From the inside to the outside, the detector components are the: VTX, SIT, TPC, SET, ECAL, HCAL and Yoke. In the forward region the FTD, ETD, LCAL, LHCAL and BCAL are shown.

Most of the subdetectors in the ILD_00 model have been implemented including a significant amount of engineering detail such as mechanical support structures, electronics and cabling as well as dead material and cracks. This provides a reasonable estimate of the material budget and thus the effect of multiple scattering in the tracking detectors; it is also crucial for a realistic demonstration of particle flow performance. In the simulation, the vertex detector has a staggered layout of six 50 μm thick silicon ladders and corresponding support structures. The additional silicon tracking detectors, FTD/ETD (forward Si tracking) and SIT/SET (inner and outer Si tracking), are modelled as disks and cylinders respectively. The material thicknesses for these detectors give the effective radiation lengths listed in Table 4.2-3. The TPC model includes the material in the inner and outer field cage, this corresponds to a total of 4.5 % X_0 including the drift gas mixture. The hits from charged particles were simulated according to an end-plate layout with 224 rows of pads, 1 mm wide and 6 mm high. The ECAL simulation includes the alveolar structure and also the dead regions around the silicon pixels and between the modules. The HCAL simulation includes steel and aluminium support structures which result in dead regions. The energy response of the scintillator tiles was corrected according to Birks' law. The simulation of the forward region includes realistic support structures and the shielding masks. All subdetectors are enclosed by a dodecagonal iron yoke, instrumented in the simulation with ten layers of RPCs. The superconducting coil and cryostat are simulated as a 750 mm thick aluminium cylinder, corresponding to 1.9 λ_I.

All events are reconstructed using the Kalman-Filter based track reconstruction in MarlinReco, the PandoraPFA particle flow algorithm and the LCFIVertex flavour tagging. The flavour tagging artificial neural networks (ANNs) have been trained using fully simulated and reconstructed ILD_00 MC events. The boost resulting from the 14 mrad crossing angle is taken into account in the analyses that use BCAL hit distributions as an electron veto.

3.2 ILD DETECTOR PERFORMANCE

3.2.1 ILD Tracking Performance

The tracking system envisaged for ILD consists of three subsystems each capable of standalone tracking VTX, FTD and the TPC. These are augmented by three auxiliary tracking systems the SIT, SET and ETD, which provide additional high resolution measurement points. The momentum resolution goal [26] is

$$\sigma_{1/p_T} \approx 2 \times 10^{-5}\,\mathrm{GeV}^{-1},$$

and that for impact parameter resolution is

$$\sigma_{r\phi} = 5\,\mu\mathrm{m} \oplus \frac{10}{\mathrm{p(GeV)}\sin^{3/2}\theta}\,\mu\mathrm{m}.$$

3.2.1.1 Coverage and Material Budget

Figure 3.2-2a shows, as a function of polar angle, θ, the average number of reconstructed hits associated with simulated 100 GeV muons. The TPC provides full coverage down to $\theta = 37°$. Beyond this the number of measurement points decreases. The last measurement point provided by the TPC corresponds to $\theta \approx 10°$. The central inner tracking system, consisting of the six layer VTX and the two layer SIT, provides eight precise measurements down to $\theta = 26°$. The innermost and middle double layer of the VTX extend the coverage down to $\theta \sim 16°$. The FTD provides up to a maximum of five measurement points for tracks at small polar angles. The SET and ETD provide a single high precision measurement point with large lever arm outside of the TPC volume down to a $\theta \sim 10°$. The different tracking system contributions to the detector material budget, including support structures, is shown in Figure 3.2-2b.

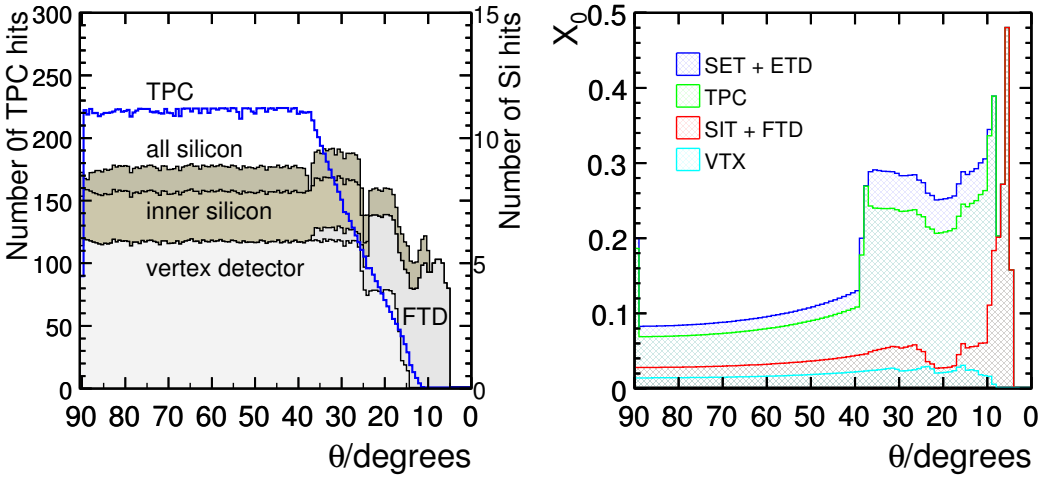

FIGURE 3.2-2. a) Average number of hits for simulated charged particle tracks as a function of polar angle. b) Average total radiation length of the material in the tracking detectors as a function of polar angle.

3.2.1.2 Momentum Resolution for the Overall Tracking System

The momentum resolution achieved with the ILD simulation and full reconstruction is shown in Figure 3.2-3a. The study was performed using muons generated at fixed polar angles of $\theta = 7°, 20°, 30°$ and $85°$, and the momentum was varied over the range $1 - 200\,\mathrm{GeV}$. For two polar angles, this is compared to the expected parametric form of, $\sigma_{1/p_T} = a \oplus b/(p_T \sin\theta)$, with $a = 2 \times 10^{-5}\,\mathrm{GeV}^{-1}$ and $b = 1 \times 10^{-3}$. As can be seen, at a polar angle of 85°, the required momentum resolution is attainable over the full momentum range from 1 GeV upwards, this remains true over the full length of the barrel region of the detector, where the TPC in conjunction with the SET is able to provide the longest possible radial lever arm for the track fit. For high momentum tracks, the asymptotic value of the momentum resolution is $\sigma_{1/p_T} = 2 \times 10^{-5}\,\mathrm{GeV}^{-1}$. At $\theta = 30°$, the SET no longer contributes, the effective lever-arm of the tracking system is reduced by 25 %. Nevertheless, the momentum resolution is still within the required level of performance. In the very forward region, the momentum resolution is inevitably worse due to the relatively small angle between the B-field and the track momentum.

3.2.1.3 Impact Parameter Resolution

Figure 3.2-3b shows $r\phi$ impact parameter resolution as a function of the track momentum. The required performance is achieved down to a track momentum of 1 GeV, whilst it is exceeded for high momentum tracks where the asymptotic resolution is 2 μm. The rz impact parameter resolution (not shown) is better than $\sim 10\,\mu$m down to momenta of 3 GeV and reaches an asymptotic value of $< 5\,\mu$m for the whole barrel region. Because of the relatively large distance of the innermost FTD disk to the interaction point, the impact parameter resolution degrades for very shallow tracks, $\theta < 15°$. It should be noted that these studies do not account for the possible mis-alignment of the tracking systems.

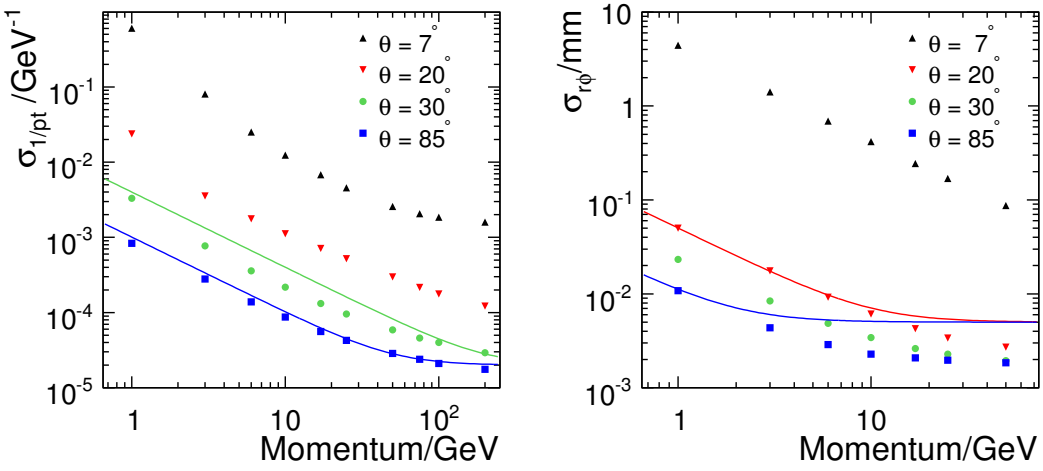

FIGURE 3.2-3. a) Transverse momentum resolution for muons plotted versus polar angle for four different simulated muon momenta. The lines show $\sigma_{1/p_T} = 2 \times 10^{-5} \oplus 1 \times 10^{-3}/(p_T \sin\theta)$ for $\theta = 30°$ (green) and $\theta = 85°$ (blue). b) Impact parameter resolution for muons versus polar angle for four different simulated muon momenta.

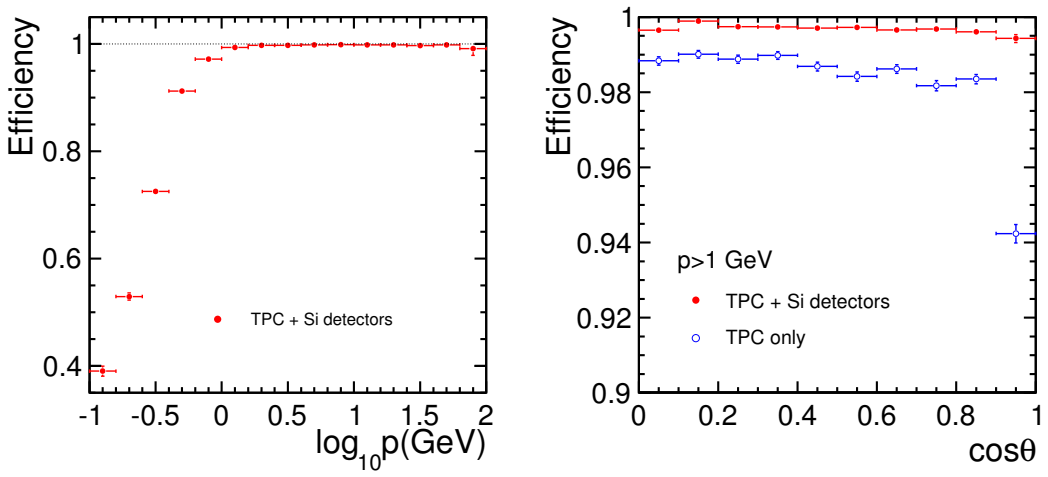

FIGURE 3.2-4. Tracking Efficiency as a function for $t\bar{t} \rightarrow$ 6 jets at 500GeV plotted against a) momentum and b) $\cos\theta$. Efficiencies are plotted with respect to MC tracks which leave at least 4 hits in the tracking detectors including decays and V^0s.

3.2.1.4 Tracking Efficiency

With over 200 contiguous readout layers, pattern recognition and track reconstruction in a TPC is relatively straightforward, even in an environment with a large number of background hits. In addition, the standalone tracking capability of the VTX enables the reconstruction of low transverse momentum tracks which do not reach the TPC. Hermetic tracking down to low angles is important at the ILC [27] and the FTD coverage enables tracks to be reconstructed to polar angles below $\theta = 7°$.

Figure 3.2-4 shows, as a function of momentum and polar angle, the track reconstruction efficiency in simulated (high multiplicity) $t\bar{t} \rightarrow$ 6 jet events at $\sqrt{s}$ =500 GeV. For the combined tracking system, the track reconstruction efficiency is approximately 99.5 % for tracks with momenta greater than 1 GeV across almost the entire polar angle range. The effects of background from the machine and from multi-peripheral $\gamma\gamma \rightarrow$ hadrons events are not yet taken into account; dedicated studies form part of the ongoing simulation R&D effort. Nevertheless, a study of the TPC reconstruction efficiency as a function of the noise occupancy is described in Section 4.3.3. This demonstrates that there is no loss of efficiency for 1 % noise occupancy.

3.2.2 Background Studies

The studies presented above do not include the effects of background from the machine and from multi-peripheral $\gamma\gamma \rightarrow$ hadrons events. The impact of machine background has been studied in the context of the ILD concept. These studies are based on the expected simulated detector hits from approximately 2000 bunch crossings (BXs). The hits are super-imposed on simulated physics events taking into account the 369 ns bunch structure of the ILC and conservative estimates of the readout rates of the tracking detector components.

3.2.2.1 Background in the TPC

For a conservative value for the TPC gas drift velocity, $4\,\mathrm{cm}\,\mu\mathrm{s}^{-1}$, the maximum TPC drift length of 2.25 m corresponds to 150 BXs. Nominal background in the TPC is thus simulated as 150 BXs appropriately shifted in z. Prior to the reconstruction, nearby hits are merged taking into account the expected $r\phi$ and z extent of the charge cloud. For the TPC readout assumed for ILD, 150 BXs of beam-related background correspond to a voxel occupancy of approximately 0.05 % (the TPC voxel size is taken to be 1 mm in the ϕ direction, 6 mm in r and 5 mm in z).

Figure 3.2-5 shows the TPC hits for a single $\mathrm{t\bar{t}}$ event at $\sqrt{s} = 500\,\mathrm{GeV}$ overlayed with 150 BXs of pair-background hits. On average there are 265,000 background hits in the TPC, compared to the average number of signal hits of 23100 (8630 from charged particles with $p_T > 1\,\mathrm{GeV}$). Even with this level of background, the tracks from the $\mathrm{t\bar{t}}$ event are clearly visible in the $r\phi$ view. A significant fraction of the background hits in the TPC arise from low energy electrons/positrons from photon conversions. These low energy particles form small radius helices parallel to the z axis, clearly visible as lines in the rz view. These "micro-curlers" deposit charge on a small number of TPC pads over a large number of BXs. Specific pattern recognition software has been written to identify and remove these hits prior to track reconstruction. (Whilst not explicitly studied, similar cuts are expected to remove a significant fraction of hits from beam halo muons.) Figure 3.2-6 shows the TPC hits after removing hits from micro-curlers. Whilst not perfect, the cuts remove approximately 99 % of the background hits and only 3 % of hits from the primary interation and the majority of these are from low p_T tracks. Less than 1 % of hits from tracks with $p_T > 1\,\mathrm{GeV}$ originating from the $\mathrm{t\bar{t}}$ event are removed.

This level of background hits proves no problem for the track-finding pattern recognition software, as can be seen from Figure 3.2-7. Even when the background level is increased by a factor of three over the nominal background no degradation of TPC track finding efficiency is observed for the 100 events simulated. This study demonstrates the robustness of TPC tracking in the ILC background environment.

These conclusions are supported by an earlier study based on a detector concept with

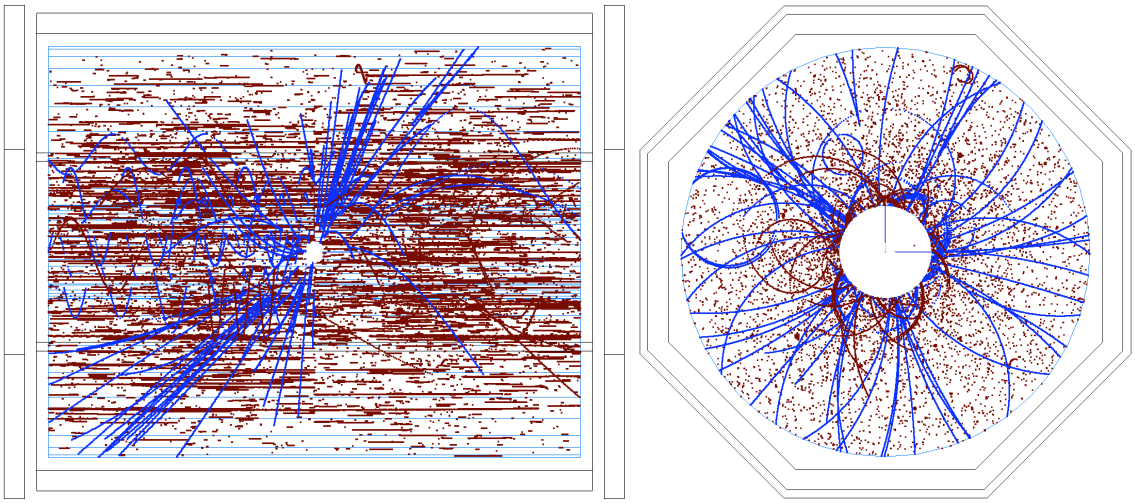

FIGURE 3.2-5. The rz and $r\phi$ views of the TPC hits from a 500 GeV $\mathrm{t\bar{t}}$ event (blue) with 150 BXs of beam background (red) overlayed.

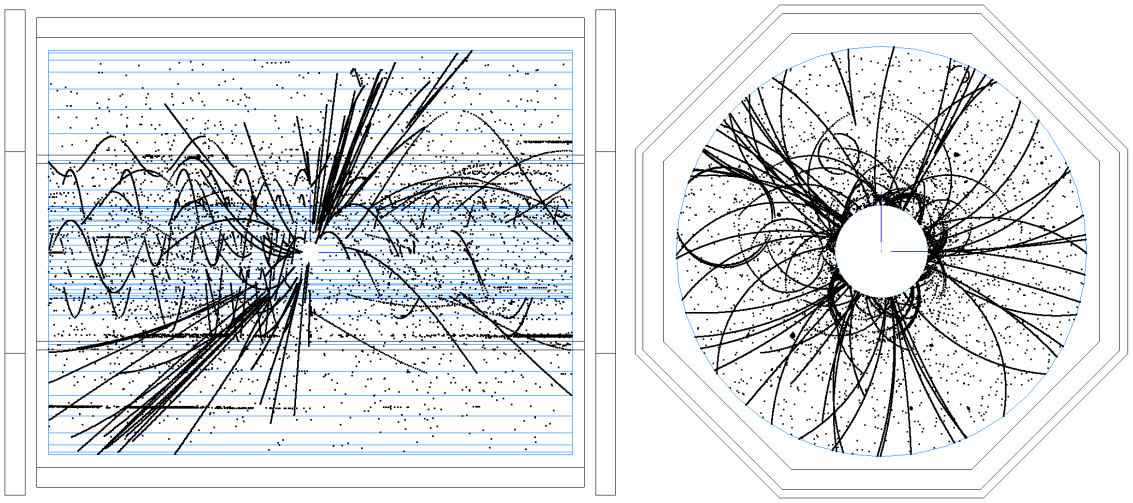

FIGURE 3.2-6. The same event as the previous figure, with the micro-curler removal algorithm applied. This is the input to the TPC track finding algorithm.

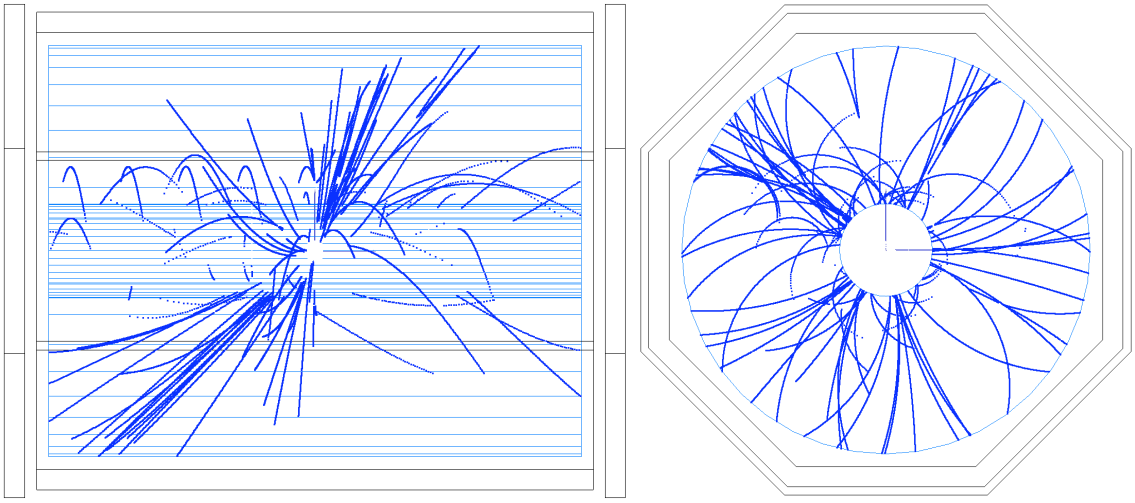

FIGURE 3.2-7. The same event as the previous plot, now showing the reconstructed TPC tracks.

$B = 3.0\,\mathrm{T}$, a TPC radius of 1.9 m and TPC readout cells of $3\times10\,\mathrm{mm}^2$. This earlier study used a uniform distribution of background hits in the TPC volume, but included a very detailed simulation of the digitised detector response and full pattern recognition is performed in both time and space. The TPC reconstruction efficiency as a function of the noise occupancy remains essentially unaffected for 1 % occupancy (uniformly distributed through the TPC). It should be noted that this level of occupancy is twice the nominal occupancy at the TPC inner radius and about fifty times the typical total occupancy in the TPC. This earlier study is presented in more detail in Section 4.3.2.

3.2.2.2 Background in the Vertex Detector

The impact of background in the vertex detector (VTX) depends on the assumptions made for the Silicon read-out time. If one were to assume single BX time-stamping capability in the vertex detector, the anticipated background level is negligible. However, it is anticipated

that the readout of the Silicon pixel ladders will integrate over many BXs. For the studies presented here, it is assumed that vertex detector readout integrates over 83 and 333 BXs for the inner two and outer four layers respectively. For the silicon strip-based SIT detector, single BX time-stamping is assumed. Hence the background hits which are superimposed on the physics event correspond to 1 BX in the SIT, 150 BXs in the TPC and 83/333 BXs in the VTX. It should be noted that the background studies have not yet been extended to the FTD.

With the above assumptions, the background in the vertex detector corresponds to approximately 2×10^5 hits per event, with the corresponding layer occupancies listed in Table 3.2-2. The hit occupancies account for the finite cluster size reflecting the fact that a single charged particle crossing a layer of the VTX will deposit hits in multiple pixels. The distribution of cluster sizes, taken to be the product of the z and $r\phi$ extent of the energy deposition in the Silicon, are determined from the full simulation of the beam related background. The mean background cluster size is found to be 10 pixels, where a pixel is taken to be $25 \times 25\,\mu$m.

Layer	radius/mm	BXs	Pixel Occupancy
0	16.0	83	3.33 %
1	17.9	83	1.90 %
2	37.0	333	0.40 %
3	38.9	333	0.33 %
4	58.0	333	0.08 %
5	59.9	333	0.06 %

TABLE 3.2-2
Vertex detector occupancies for the readout times assumed in the background studies. The occupancies account for the finite cluster size.

Pattern recognition in the environment of 10^5 background hits is non-trivial and required modifications to the existing Silicon track finding code. Specifically, tracks in the Silicon detectors are now seeded using only layers $2-5$ of the vertex detector and the two layers of the SIT. Seeded tracks are then projected inwards to pick up hits in the inner two silicon layers (layers 0 and 1). Tracks with transverse momentum of $p_T < 200\,$MeV are rejected. There are a number of questions which can be asked: i) Can the number of "ghost" tracks, *i.e.* those formed from random combinations of hits be reduced to an acceptable level; ii) how many genuine tracks from the pair background remain; iii) how do any additional cuts used to reduce the beam background affect the signal; and iv) what is the loss of efficiency due to hits from the primary interaction being merged with the clusters of pixels from background hits. These four questions are addressed below.

Figure 3.2-8a) shows the p_T distribution of reconstructed tracks in the Silicon detectors with the background overlayed. Due to the conservative assumptions for the VTX readout times, an average of 34 low-p_T silicon tracks are reconstructed per physics event, reflecting the integration over 83/333 BXs. The number of background tracks would be dramatically reduced by the requirement the reconstructed track is in the same BX as the underlying physics interaction. Tracks are thus required to have at least one SIT hit (which provides unambiguous BX identification) or to be associated with at least 10 TPC hits (where the

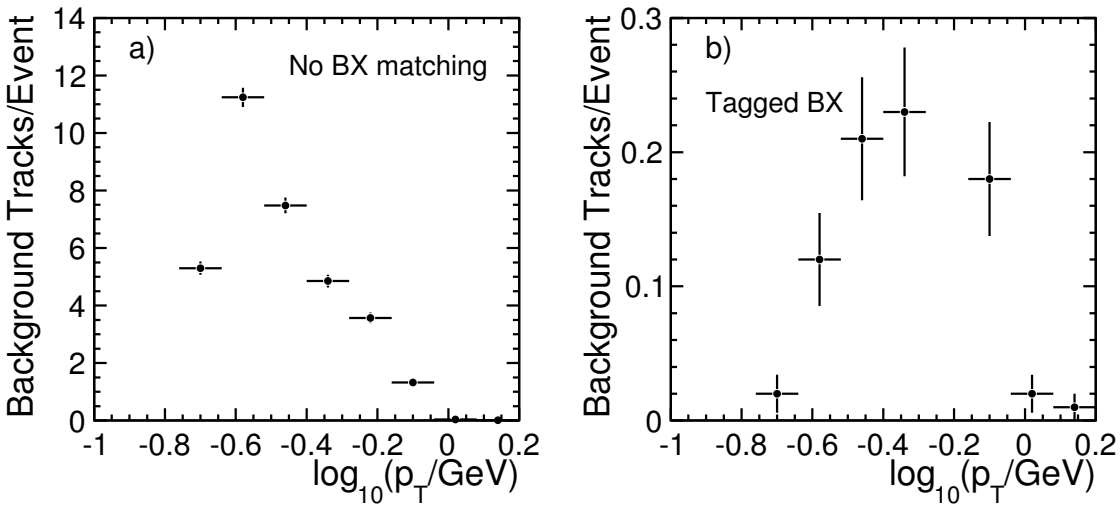

FIGURE 3.2-8. The p_T distribution of reconstructed background tracks in the Silicon detectors (VTX+SIT) a) before requiring the track to be in time with the physics interaction beam crossing (BX) and b) after requiring at least 1 SIT hit or a match to at least 10 TPC hits. A track is considered to be from background if more than 20 % of the associated hits come from the overlayed background events.

matching in z can be used to identify the BX). Figure 3.2-8 shows the resulting p_T distribution of the remaining background tracks. On average 1.2 background tracks per event remain with a mean p_T of 500 MeV. The majority of the remaining background tracks are either from relatively high p_T electrons/positrons or from combinations of signal and background hits. Firstly, there may be a loss of efficiency due to the additional requirements of associated SIT or TPC hits. For tracks from the primary physics interaction (*i.e.* the $t\bar{t}$ event), the SIT/TPC requirements remove approximately 1 % of tracks with $p_T < 1$ GeV, whilst for $p_T > 1$ GeV there is no observed loss of efficiency.

The presence of a large number background hits not only results in a small number of background tracks, it may also lead to a degradation of the pattern recognition performance. In addition, if a charged particle from the interaction passes close to a cluster of pixels from the pair background, a single larger cluster will be formed. It is assumed such an extended cluster will not be included in the track-finding algorithm, and hence hits close to background clusters effectively will be lost. In addition to overlaying 83/333 BXs of background, the pixel occupancies in Table 3.2-2 are used to remove the appropriate number of hits from the primary interaction. The effect of the overlayed background and the resulting hit inefficiencies is studied for simulated $t\bar{t} \rightarrow 6$ jets events at $\sqrt{s} = 500$ GeV. Figure 3.2-9a) shows the overall track reconstruction efficiency with and without background. The main effect of the background is to reduce the efficiency for tracks with $p_T < 300$ MeV. For tracks $p_T > 1$ GeV, the presence of background reduces the track finding efficiency by less than 0.1 %. In the presence of background the efficiency for tracks with $p_T > 1$ GeV is 98.8 %. Care has to be taken in interpreting this number; the efficiencies depend on how the denominator is defined. For example, the inefficiency for high p_T tracks arises almost entirely from tracks which decay or interact within the volume of the VTX/SIT. Figure 3.2-9b) shows the track finding efficiency for tracks which (in simulation) deposit energy in the TPC gas volume. For this sample, the efficiency is greater than 99.9 % for tracks with $p_T > 1$ GeV, with or without background. It is concluded that the ILD tracking efficiency is not significantly degraded by

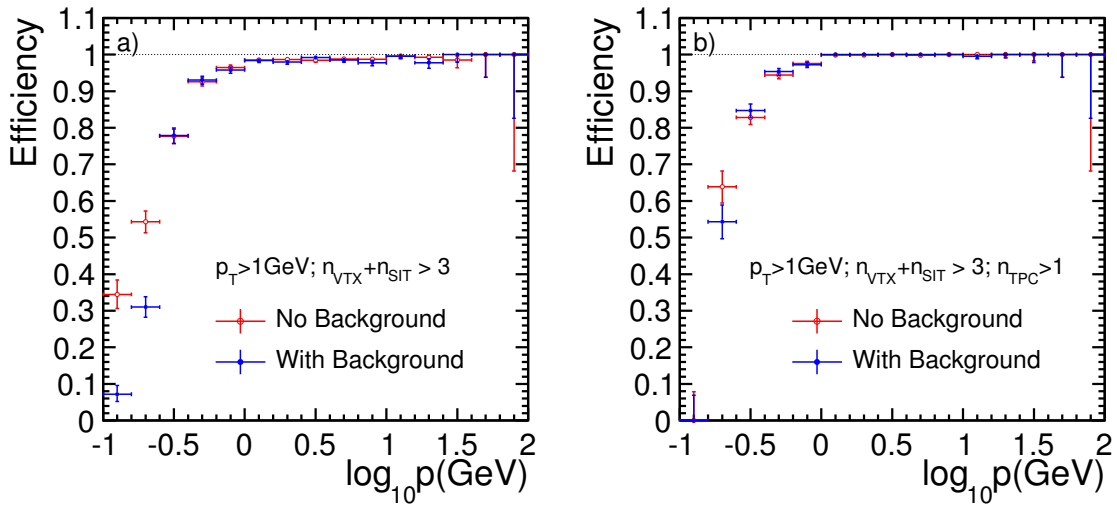

FIGURE 3.2-9. Tracking efficiency with overlayed background in the vertex detector vs transverse momentum for $t\bar{t} \rightarrow$ 6 jets at 500GeV ($|\cos\theta| < 0.8$) a) for all charged particles and b) for charged particles which deposit at least one hit in the TPC. The tracking efficiency is shown for tracks with $p_T > 1$ GeV with a total of at least 4 hits in the VTX and SIT. Tracks are considered to be well reconstructed if there is at least one associated SIT hit or more than 10 TPC hits and if at least 70 % of the hits on the track are from the original Monte Carlo Particle.

the nominal level of background expected at the ILC.

3.2.2.3 Impact of background on physics analyses

To fully simulate the effect of background on a particular physics channel would require overlaying 1 BX in the SIT, 150 BXs in the TPC and 83/333 BXs in the VTX on each simulated physics event and would require vast CPU resources. From the studies above it is expected that the track finding inefficiencies for the high momentum muons in the $ZH \rightarrow \mu^+\mu^- X$ channel will be negligibly small. In addition, the presence of the relatively few low p_T background tracks will not affect the recoil mass distribution. The possibility that the loss of hits in the vertex detector due to background occupancy might distort the recoil mass distribution has been investigated (see Figure 3.2-10). The observed differences are negligibly small.

3.2.3 ILD Flavour Tagging Performance

Identification of b-quark and c-quark jets plays an important role within the ILC physics programme. The vertex detector design and the impact parameter resolution are of particular importance for flavour tagging. The LCFIVertex flavour tagging (see Section 2.5) uses ANNs to discriminate b-quark jets from c and light-quark jets (b-tag), c-quark jets from b and light-quark jets (c-tag), and c-quark jets from b-quark jets (bc-tag).

The flavour tagging performance [22] of ILD is studied for the two vertex detector geometries considered, three double-sided ladders (VTX-DL) and five single-sided (VTX-SL) ladders. No significant differences in the input variables for the ANNs are seen for two geometries, and therefore the ANNs trained for the VTX-DL option were used for both VTX configurations. The samples used in the training consisted of 150000 $Z \rightarrow q\bar{q}$, at the Z pole

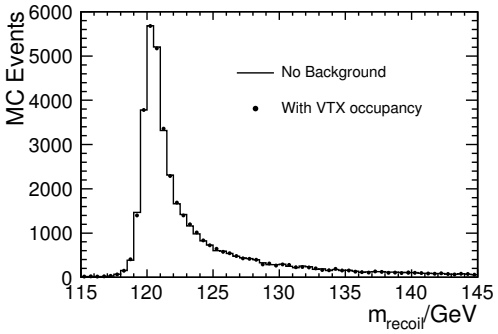

FIGURE 3.2-10. The Higgs recoil mass distribution in the $\mu^+\mu^- X$ channel from 50000 generated MC events after selection for the case of no background and with inefficiencies in the vertex detector due to the occupancy level expected from the pair background.

energy, equally distributed among the three decay modes $q = b, c$ and light quarks. The test samples used to evaluate the flavour tagging performance were generated independently and consist of 10000 events of $Z \to \mathrm{q\bar{q}}$ generated at both $\sqrt{s} = 91\,\mathrm{GeV}$ and $\sqrt{s} = 500\,\mathrm{GeV}$, with the SM flavour mix of hadronic final states. The ILD flavour tagging performances at 91 GeV for the two vertex detector options are shown in Figure 3.2-11a). The performance differences between the two VTX geometries are small ($\lesssim 1\%$). Uncertainites due to the statistical fluctuations of the test sample and in those introduced in the ANN training are estimated to be $\lesssim 2\%$. The performance for $Z \to \mathrm{q\bar{q}}$ at $\sqrt{s} = 500\,\mathrm{GeV}$ is shown in Figure 3.2-11b). It should be noted that for the 500 GeV results the ANNs were not retrained, *i.e.* those obtained for $\sqrt{s} = 91\,\mathrm{GeV}$ were used. Consequently, improvements in the performance are expected.

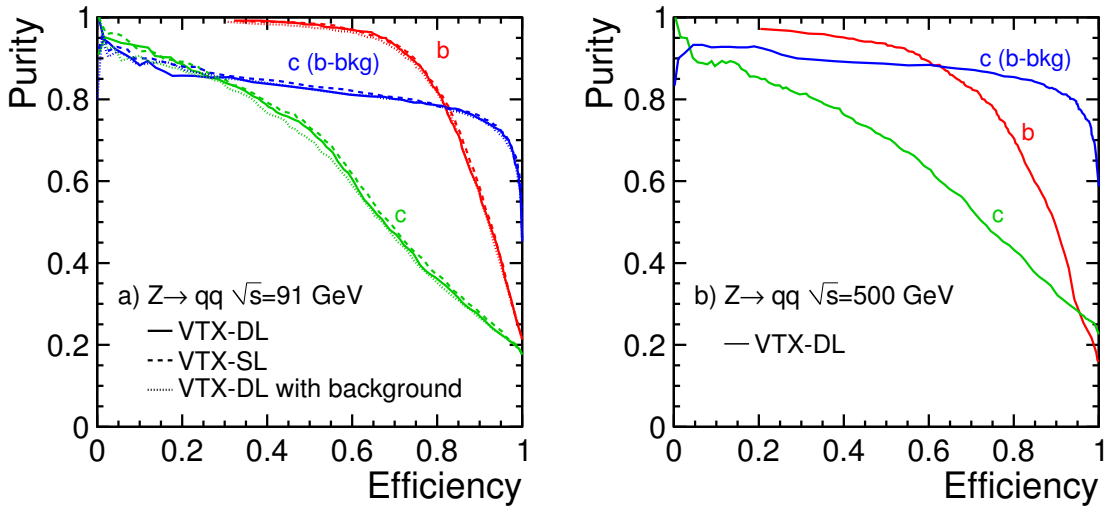

FIGURE 3.2-11. a) Flavour tagging performance of the ILD detector for 91 GeV $Z \to \mathrm{q\bar{q}}$ events for both the three double-sided ladders (VTX-DL) layout and with five single-sided ladder layout (VTX-SL). Also shown for the VTX-DL is the impact of background on the flavour tagging performance. b) Flavour tagging performance of the ILD detector for 500 GeV $Z \to \mathrm{q\bar{q}}$ events for the VTX-DL layout. In all cases the acceptance corresponds to $|\cos\theta_{\mathrm{jet}}| < 0.95$.

3.2.3.1 Impact of Background

Do to the large computational requirements in overlaying background hits from many BXs a parametric approach is taken to assess the impact of background on the flavour tagging performance. In Section 3.2.2.2 is was demonstrated that hits from pair background integrated over 83 (333) BXs for layers 0 and 1 ($2-5$) of the VTX-DL doublet layout of six ladders does not result in a significant number of background tracks and that the overall tracking efficiency is not significantly reduced. The main impact on flavour tagging is likely to be from the resulting hit inefficiencies particularly in the inner layers. To simulate the effect of background the pixel occupancies of Table 3.2-2 are used to randomly remove Silicon hits from the events before track finding and flavour tagging. This results in a slight degradation in tracking performance in the Silicon detectors; the number of TPC tracks associated with a complete track in the vertex detector (6 hits) decreases by 2 %. The resulting flavour tagging performance is shown in Figure 3.2-11a). Although there is a suggestion of a small degradation in the performance of the c-tag in the low efficiencies/high purity region, the presence of pair background does not significantly degrade the flavour tagging performance.

3.2.4 ILD Particle Flow Performance

Many important physics channels at the ILC will consist of final states with at least six fermions, setting a "typical" energy scale for ILC jets as approximately 85 GeV and 170 GeV at $\sqrt{s} = 500\,\text{GeV}$ and $\sqrt{s}$ =1 TeV respectively. The current performance of the PandoraPFA algorithm applied to ILD Monte Carlo simulated data is summarised in Table 3.2-3. The observed jet energy resolution (rms_{90}) is not described by the expression $\sigma_E/E = \alpha/\sqrt{E/\text{GeV}}$. This is not surprising, as the particle density increases it becomes harder to correctly associate the calorimetric energy deposits to the particles and the confusion term increases. The single jet energy resolution is also listed. The jet energy resolution (rms_{90}) is better than 3.8 % for the jet energy range of approximately $40-400\,\text{GeV}$. The resolutions quoted in terms of rms_{90} should be multiplied by a factor of approximately 1.1 to obtain an equivalent Gaussian analysing power[12].

Jet Energy	raw rms	rms_{90}	$\text{rms}_{90}/\sqrt{E_{jj}/\text{GeV}}$	σ_{E_j}/E_j
45 GeV	3.3 GeV	2.4 GeV	25.0 %	(3.71 ± 0.05) %
100 GeV	5.8 GeV	4.1 GeV	29.5 %	(2.95 ± 0.04) %
180 GeV	11.2 GeV	7.5 GeV	40.1 %	(2.99 ± 0.04) %
250 GeV	16.9 GeV	11.1 GeV	50.1 %	(3.17 ± 0.05) %

TABLE 3.2-3
Jet energy resolution for Z →uds events with $|\cos\theta_{\text{q}\bar{\text{q}}}| < 0.7$, expressed as, rms_{90} for the di-jet energy distribution, the effective constant α in $\text{rms}_{90}/E = \alpha(E_{jj})/\sqrt{E_{jj}/\text{GeV}}$, and the fractional jet energy resolution for a single jets, σ_{E_j}/E_j. The jet energy resolution is calculated from rms_{90}.

Figure 3.2-12 shows the jet energy resolution for Z →uds events plotted against the cosine of the polar angle of the generated $\text{q}\bar{\text{q}}$ pair, $\cos\theta_{\text{q}\bar{\text{q}}}$, for four different values of $\sqrt{s}$. Due to the calorimetric coverage in the forward region, the jet energy resolution remains good down to $\theta = 13^\circ$ ($\cos\theta = 0.975$).

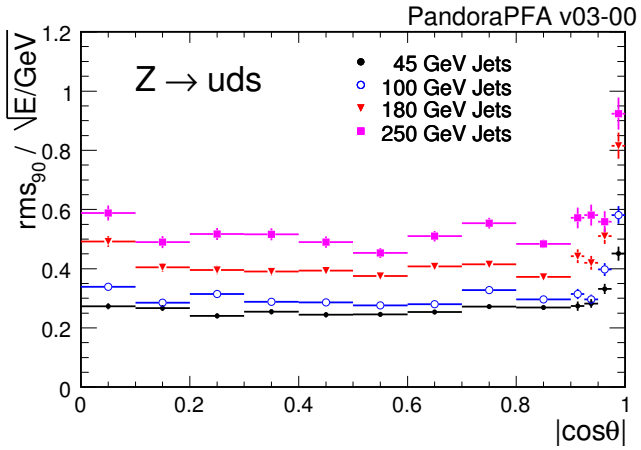

FIGURE 3.2-12. The jet energy resolution, defined as the α in $\sigma_E/E = \alpha\sqrt{E/\mathrm{GeV}}$, plotted versus $\cos\theta_{\mathrm{q\bar{q}}}$ for four different jet energies.

3.3 PHYSICS PERFORMANCE

The ILD detector performance has been evaluated for a number of physics processes. The analyses, described below, all use the full simulation of ILD and full event reconstruction. Jet finding is performed using the Durham algorithm[28] with the hadronic system being forced into the appropriate number of jets for the event topology. The benchmark physics analyses[24] are studied at $\sqrt{s} = 250\,\mathrm{GeV}$ and $\sqrt{s} = 500\,\mathrm{GeV}$. Unless otherwise stated, the results for $\sqrt{s} = 250\,\mathrm{GeV}$ ($\sqrt{s} = 500\,\mathrm{GeV}$) correspond to an integrated luminosity of $250\,\mathrm{fb}^{-1}$ ($500\,\mathrm{fb}^{-1}$) and a beam polarisation of $P(\mathrm{e}^+,\mathrm{e}^-) = (+30\,\%, -80\,\%)$.

3.3.1 Higgs Boson mass

The precise determination of the properties of the Higgs boson is one of the main goals of the ILC. Of particular importance are its mass, m_{H}, the total production cross section, $\sigma(\mathrm{e}^+\mathrm{e}^- \to \mathrm{HZ})$, and the Higgs branching ratios. Fits to current electroweak data[29] and direct limits from searches at LEP and at the Tevatron favour a relatively low value for m_{H}. Studies of these measurements with ILD are described below. A data sample of $250\,\mathrm{fb}^{-1}$ at $\sqrt{s} = 250\,\mathrm{GeV}$ is assumed and m_{H} is taken to be 120 GeV. For these values, the dominant Higgs production process is Higgs-strahlung, $e^+e^- \to \mathrm{ZH}$.

The Higgs boson mass can be determined precisely from the distribution of the recoil mass, m_{recoil}, in $\mathrm{ZH} \to \mathrm{e}^+\mathrm{e}^- X$ and $\mathrm{ZH} \to \mu^+\mu^- X$ events, where X represents the Higgs decay products. The recoil mass is calculated from the reconstructed four-momentum of the system recoiling against the Z. The $\mu^+\mu^- X$-channel yields the most precise measurement as the $\mathrm{e}^+\mathrm{e}^- X$-channel suffers from larger experimental uncertainties due to bremsstrahlung from the electrons and the larger background from Bhabha scattering events. The study[30, 31] is performed for two electron/positron beam polarisations: $P(e^+, e^-) = (-30\,\%, +80\,\%)$ and $P(e^+, e^-) = (+30\,\%, -80\,\%)$. In the simulation, Gaussian beam energy spreads of 0.28 % and 0.18 % are assumed for the incoming electron and positron beams respectively.

The first stage in the event selection is the identification of leptonically decaying Z bosons. Candidate lepton tracks are required to be well-measured, removing tracks with large uncertainties on the reconstructed momentum. Lepton identification is performed using the

associated calorimetric information resulting in an event efficiency of 95.4 % for identifying both in $\mu^+\mu^- X$ events and 98.8 % for both electrons in $\mathrm{e^+e^-}X$ events. Candidate Z decays are identified from oppositely charged pairs of identified leptons within a mass window around m_{Z}. Background from $\mathrm{Z} \to \ell^+\ell^-$ is rejected using cuts on the transverse momentum of the di-lepton system and the acollinearity of the two lepton tracks. Additional cuts reject $\mathrm{Z} \to \ell^+\ell^-$ events with initial and final state radiation. The backgrounds from $e^+e^- \to \mathrm{ZZ}$ and $e^+e^- \to \mathrm{W^+W^-}$ are reduced using a multi-variate likelihood analysis based on the acoplanarity, polar angle, transverse momentum and the invariant mass of the di-lepton system.

The reconstructed m_{recoil} distributions are shown in Figure 3.3-13. The combination of signal and background is fitted using a function which assumes a Gaussian-like signal and that the background can be approximated by a polynomial function. The results of the fit for m_{H} and $\sigma(\mathrm{e^+e^-} \to \mathrm{ZH})$ are listed in Table 3.3-4. Also shown are the results obtained when assuming the SM decay modes and branching fractions. In this case, labelled "Model Dependent", the background is further reduced by requiring charged particle tracks in addition to those generated by the Z boson decay products.

3.3.1.1 Influence of Bremsstrahlung

From figure 3.3-13 it is clear that Bremsstrahlung from final state electrons and positrons significantly degrades the recoil mass resolution in the $\mathrm{e^+e^-}X$ channel. One possible strategy to mitigate this effect is to identify the final state photons and include these in the recoil mass calculation. A dedicated algorithm to identify Bremsstrahlung photons is used [32] and the four momenta of the $\mathrm{e^+e^-}X + n\gamma$ system is used in the event selection and recoil mass calculation. Figure 3.3-14a) compares the recoil mass distribution with and without including identified Bremsstrahlung photons. Figure 3.3-14b) shows the recoil mass distribution for the model independent impact analysis including Bremsstrahlung photons. To extract the mass and cross section a modified fitting function is used. The results of the fits ($\mathrm{e^+e^-}X n\gamma$) for m_{H} and $\sigma(\mathrm{e^+e^-} \to \mathrm{ZH})$ are listed in Table 3.3-4. Including Bremsstrahlung photons improves

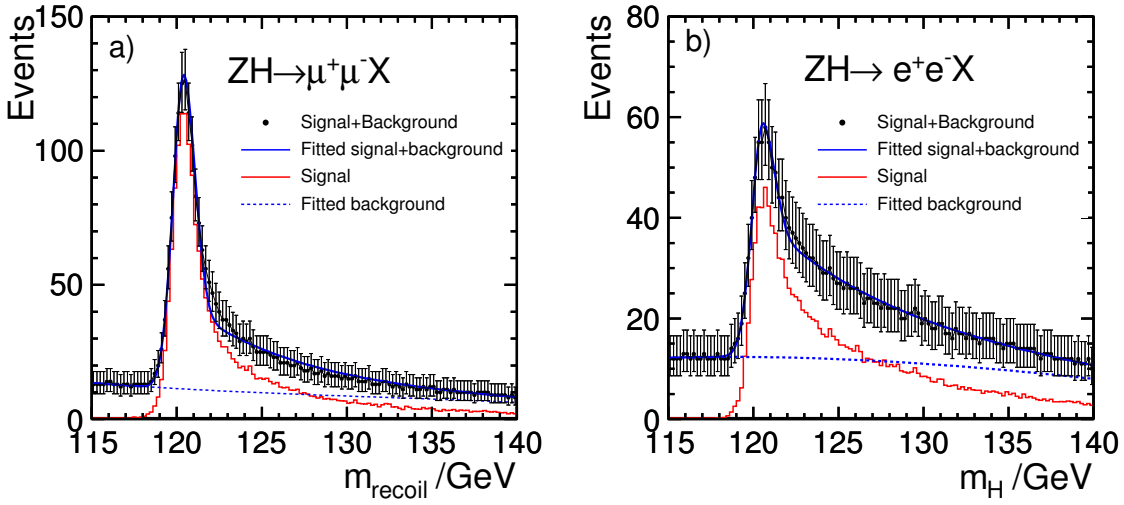

FIGURE 3.3-13. Results of the model independent analysis of the Higgs-strahlung process $\mathrm{e^+e^-} \to \mathrm{HZ}$ in which a) $\mathrm{Z} \to \mu^+\mu^-$ and b) $\mathrm{Z} \to \mathrm{e^+e^-}$. The results are shown for a beam polarisation of $P(e^+, e^-) = (+30\,\%, -80\,\%)$.

Analysis	Polarisation (e^-, e^+)	Channel	$\sigma_{m_{\mathrm{H}}}$	Cross section	
Model Independent	$(+80\,\%,\ -30\,\%)$	$\mu^+\mu^- X$	40 MeV	± 0.28 fb	$(3.6\,\%)$
		$\mathrm{e^+e^-}X$	88 MeV	± 0.43 fb	$(5.1\,\%)$
		$\mathrm{e^+e^-}(n\gamma)X$	81 MeV	± 0.36 fb	$(4.3\,\%)$
	$(-80\,\%,\ +30\,\%)$	$\mu^+\mu^- X$	36 MeV	± 0.39 fb	$(3.3\,\%)$
		$\mathrm{e^+e^-}X$	72 MeV	± 0.61 fb	$(4.8\,\%)$
		$\mathrm{e^+e^-}(n\gamma)X$	74 MeV	± 0.47 fb	$(4.0\,\%)$
Model Dependent	$(+80\,\%,\ -30\,\%)$	$\mu^+\mu^- X$	36 MeV	± 0.26 fb	$(3.3\,\%)$
		$\mathrm{e^+e^-}X$	77 MeV	± 0.38 fb	$(4.5\,\%)$
		$\mathrm{e^+e^-}(n\gamma)X$	73 MeV	± 0.31 fb	$(3.8\,\%)$
	$(-80\,\%,\ +30\,\%)$	$\mu^+\mu^- X$	31 MeV	± 0.32 fb	$(2.7\,\%)$
		$\mathrm{e^+e^-}X$	64 MeV	± 0.47 fb	$(3.7\,\%)$
		$\mathrm{e^+e^-}(n\gamma)X$	59 MeV	± 0.37 fb	$(3.1\,\%)$

TABLE 3.3-4
Expected statistical uncertainties on m_{H} from the recoil mass distribution in Higgs-strahlung events where the Z decays into either $\mathrm{e^+e^-}$ or $\mu^+\mu^-$. Results are listed for both the model independent and model dependent analyses. Also listed are the experimental uncertainties on the Higgs-strahlung cross section. The results are given for two different beam polarisations. In the case of the $\mathrm{e^+e^-}X$-channel results are given without ($\mathrm{e^+e^-}X$) and with ($\mathrm{e^+e^-}(n\gamma)X$) the inclusion of identified Bremsstrahlung photons.

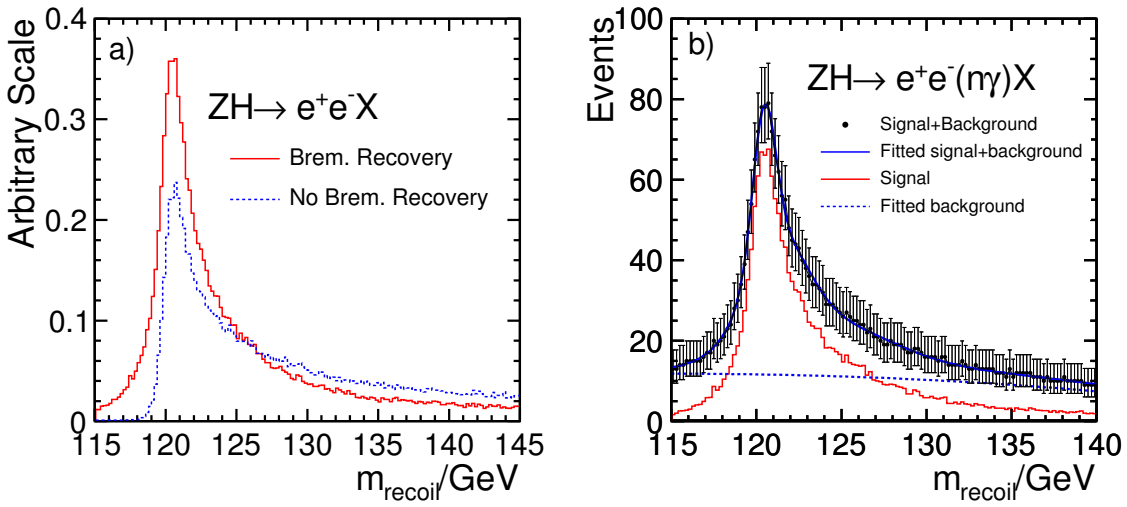

FIGURE 3.3-14. The effect of including identified Bremsstrahlung photons in the $\mathrm{e^+e^-}X$ channel: a) comparison of the recoil mass distribution with and without inclusion of Bremsstrahlung photons and b) the fitted recoil mass distribution for the model independent analysis with Bremsstrahlung recovery. The plots are shown for a beam polarisation of $P(e^+, e^-) = (+30\,\%, -80\,\%)$.

the mass resolution by 10 % and the cross section resolution by 20 %. The improvement to the mass resolution is limited by the degradation in the sharpness of the leading edge of the recoil mass distribution. It should be noted that a more complete treatment would involve a refit of the track taking into account the candidate Bremsstrahlung photons; at this stage no strong conclusions should be drawn.

3.3.1.2 Influence of Beam Energy Uncertainties

The width of the peak of the recoil mass distribution is a convolution of the detector response and the luminosity spectrum of the centre-of-mass energy from the intrinsic beam energy spread and beamstrahlung. For the $\mu^+\mu^- X$ channel, the contribution from the detector response is primarily due to the momentum resolution, whereas for the $e^+e^- X$ channel bremsstrahlung dominates. Figure 3.3-15 shows the recoil mass spectrum for the $\mu^+\mu^- X$ channel obtained from the generated four momenta of the muon pair compared to that obtained from the reconstructed momenta. The detector response leads to the broadening of the recoil mass peak; an increase from 560 MeV to 650 MeV. The contribution from momentum resolution is therefore estimated to be 330 MeV. For the beam energy spectrum used in the simulation, the effect of detector resolution is not negligible, however, the dominant contribution to the observed width of the $\mu^+\mu^- X$ recoil mass distribution arises from the incoming beams rather than the response of ILD.

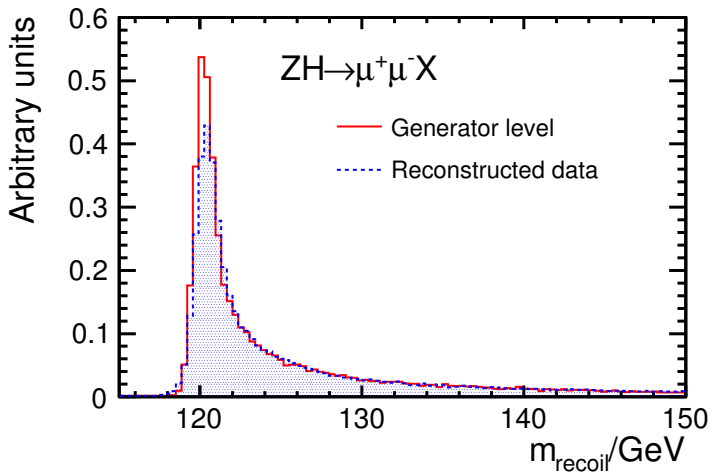

FIGURE 3.3-15. The Higgs recoil mass distribution in the $\mu^+\mu^- X$ channel obtained from the generator level and reconstructed muon pair momenta.

3.3.1.3 Conclusions

From Figure 3.3-13 and Table 3.3-4 the following conclusions can be drawn: i) using the recoil mass distributions in the $e^+e^- X$ and $\mu^+\mu^- X$ final states and 250 fb^{-1} of data with $P(e^+, e^-) = (+30\,\%, -80\,\%)$ beam polarisation, m_H can be determined with a statistical uncertainty of 32 MeV independent of its decay modes and the Higgs-strahlung cross section can be measured with a precision of 2.5 %; ii) the precision on m_H obtained in the $e^+e^- X$ channel is approximately a factor two worse than that obtained from the $\mu^+\mu^- X$ channel; iii) with the current algorithm, the inclusion of Beamstrahlung photons in the recoil mass distribution in the $e^+e^- X$ channel improves the Higgs mass resolution by approximately 10 %. iv) the ILD track resolution does not significantly degrade the m_H resolution obtained from the $\mu^+\mu^- X$ recoil mass distribution.

3.3.2 Higgs Boson Branching Fractions

The determination of the Higgs boson branching fractions is central to the ILC physics programme. In the context of the SM, this allows a test of the hypothesis that the strength of the Higgs coupling depends linearly on the particle masses. The statistical uncertainties on the branching ratios are estimated, for an integrated luminosity of $250\,\mathrm{fb}^{-1}$ at $\sqrt{s} = 250\,\mathrm{GeV}$, based on the analysis of the Higgs-strahlung process $\mathrm{e^+e^-} \to \mathrm{ZH}$ for the three possible Z decay topologies: $\mathrm{Z} \to \mathrm{q\bar{q}}$, $\mathrm{Z} \to \nu\bar{\nu}$, and $\mathrm{Z} \to \ell^+\ell^-$. Heavy flavour tagging is essential to the analysis; cuts on the c-tag and b-tag for the two jets from the candidate Higgs decay are employed. In addition, the c-tag information from two jets is combined into a single variable, c-likeness. For each topology, the uncertainty on the exclusive cross sections are determined, *e.g.* $\sigma(\mathrm{e^+e^-} \to \mathrm{ZH} \to \mathrm{q\bar{q}c\bar{c}})$. This is combined with the 2.5 % uncertainty on the total cross section, $\sigma(\mathrm{e^+e^-} \to \mathrm{ZH})$, obtained from the model Independent analysis described in the previous section, to give the uncertainty on the branching ratios.

3.3.2.1 $ZH \to \ell^+\ell^-\mathrm{q\bar{q}}$

Although statistically limited compared to the other Z decay channels, $\mathrm{Z} \to \mathrm{e^+e^-}$ and $\mathrm{Z} \to \mu^+\mu^-$ provide a clean signal which can be identified with high efficiency, independent of whether the Higgs decays to $\mathrm{b\bar{b}}$, $\mathrm{c\bar{c}}$ or gg [33]. The dominant background is ZZ production. The event selection requires a pair of oppositely-charged electrons or muons with an invariant mass consistent with m_Z. The recoil mass is required to be consistent with m_H as is the invariant mass of the recoiling hadronic system. Events in which the Z candidate is close to the beam axis are rejected to suppress background from ZZ. The final selection is performed by cutting on the value of a likelihood function formed from variables related to the thrust, di-jet and di-lepton masses and angular distributions. The hadronic system is reconstructed as two jets. To extract the Higgs branching ratios it is not sufficient to simply apply cuts to select, for example, $\mathrm{H} \to \mathrm{c\bar{c}}$ events since one of the main background is from $\mathrm{H} \to \mathrm{b\bar{b}}$ for which the branching ratio also needs to be determined. Instead, the fractions of $\mathrm{H} \to \mathrm{b\bar{b}}$, $\mathrm{H} \to \mathrm{c\bar{c}}$, $\mathrm{H} \to gg$ and background present are determined from the distribution of b-likeness and c-likeness which is fitted using templates made from exclusive samples of each type as shown in Figure 3.3-16. The measurement accuracy obtained is $(2.7 \oplus 2.5)\,\%$ for $BR(\mathrm{H} \to \mathrm{b\bar{b}})$, $(28 \oplus 2.5)\,\%$ for $BR(H \to \mathrm{c\bar{c}})$ and $(29 \oplus 2.5)\,\%$ for $BR(\mathrm{H} \to gg)$.

3.3.2.2 $\mathrm{ZH} \to \nu\bar{\nu}\mathrm{H}$

The signal topology comprises two jets plus missing energy. Events are selected based on missing mass, net transverse momentum, and net longitudinal momentum. Background containing high momentum leptons is rejected using lepton identification cuts and by requiring that the maximum track momentum in the event is less than 30 GeV. The dominant remaining backgrounds are $\nu\bar{\nu}\mathrm{q\bar{q}}$ and $\tau\nu_\tau\mathrm{q\bar{q}}$ from ZZ and $\mathrm{W^+W^-}$ respectively. These backgrounds are suppressed using y_{12} and y_{23}, the y-cut values in the Durham jet-finding algorithm for the transitions between one or two and two or three reconstructed jets. The selection efficiencies for $\mathrm{ZH} \to \nu\bar{\nu}\mathrm{c\bar{c}}$ and $\mathrm{ZH} \to \nu\bar{\nu}\mathrm{b\bar{b}}$ are both approximately 44 %. The branching ratios $BR(\mathrm{H} \to \mathrm{b\bar{b}})$ and $BR(\mathrm{H} \to \mathrm{c\bar{c}})$ are determined using the b-, c-, and bc- flavour tags. The reconstructed di-jet mass distribution after applying a cut on the c-tag is shown in Figure 3.3-17b. To extract the Higgs branching ratios the template fit of Section 3.3.2.1 is extended to three dimensions by including the bc-tag information. It is assumed that the non-Higgs background is well understood. By fitting the signal contributions to this distribution, the

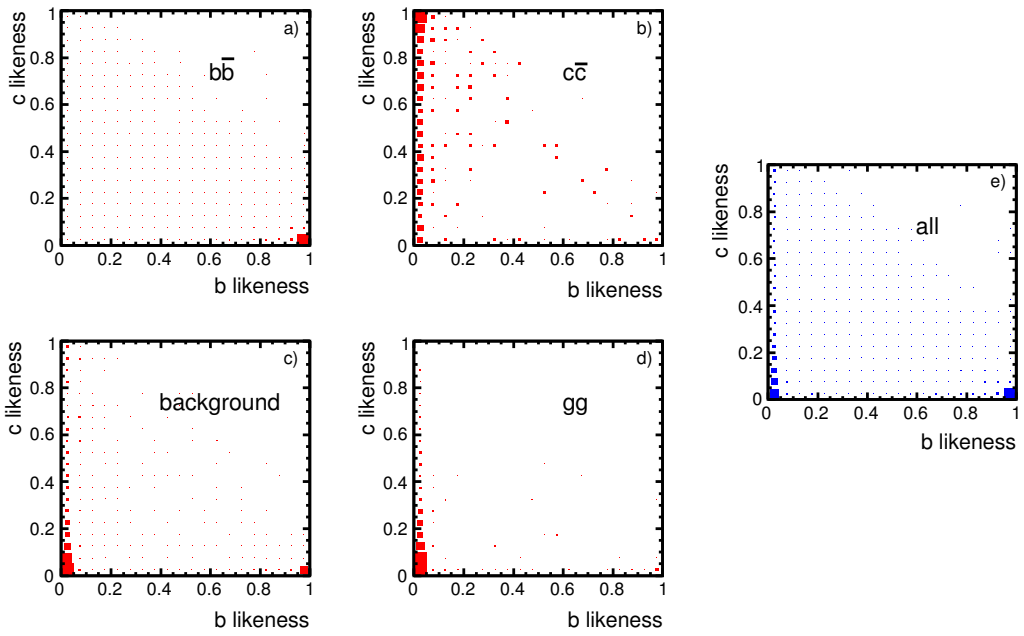

FIGURE 3.3-16. Distributions of b- and c-likeness for exclusive samples of $H \to b\bar{b}$, $H \to c\bar{c}$, $H \to gg$, background and an independent combined "data" sample.

$H \to c\bar{c}$ and $H \to b\bar{b}$ cross sections can be determined. The measurement accuracies for $BR(H \to c\bar{c})$ and $BR(H \to b\bar{b})$ are $(13.8 \oplus 2.5)$ and $(1.1 \oplus 2.5)\,\%$ repectively.

3.3.2.3 $ZH \to q\bar{q}c\bar{c}$

The decay topology for $ZH \to q\bar{q}c\bar{c}$ consists of four jets, two compatible with m_Z and two compatible with m_H. The main backgrounds are $e^+e^- \to W^+W^-/ZZ \to q\bar{q}q\bar{q}$ and four-jet events from the fragmentation of $e^+e^- \to Z/\gamma^\star \to q\bar{q}$. For the $Z/\gamma^\star \to q\bar{q}$ background, four-jet events arise mainly from the $q\bar{q}gg$ final state in which the gluon jets are generally less energetic and are produced at relatively small angles to the quark jets. Consequently, cuts on event shape variables, such as the smallest jet-jet angle, are used to reject the $Z/\gamma^\star$ background. Background from $q\bar{q}q\bar{q}$ production are suppressed using kinematic fits. A second fit, which imposes energy-momentum conservation and constrains one di-jet mass to equal m_Z, is used to reconstruct the Higgs mass, m_H^{fit}. The $ZH \to q\bar{q}c\bar{c}$ sample is selected by requiring $115 < m_H^{fit} < 125\,\text{GeV}$ and using cuts on the c-likeness and the $c-$tags of the two jets from the Higgs decay, shown in Figure 3.3-17. For an integrated luminosity of $250\,\text{fb}^{-1}$, the expected numbers of signal and background events after all cuts are 37.2 and 121.2 respectively. This leads to a $(30 \oplus 2.5)\,\%$ uncertainty on $BR(H \to c\bar{c})$ [1] .

3.3.2.4 Combined Result

The results for the Higgs branching ratios are summarised in Table 3.3-5. The statistical uncertainties are from the exclusive measurements and the 2.5 % uncertainty on the total cross section. After taking into account the different integrated luminosity and different

[1] Ongoing studies show that the expected statistical uncertainty from a more optimal analysis is more than a factor two smaller than the value quoted here.

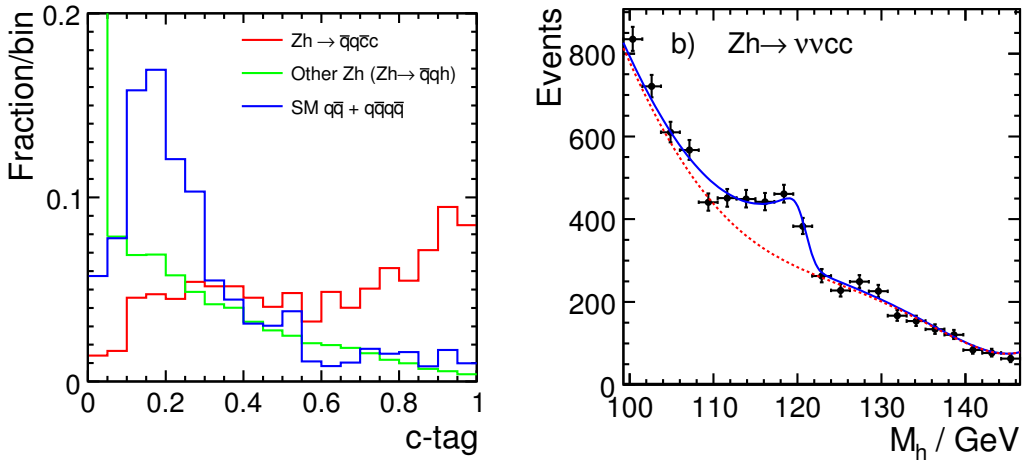

FIGURE 3.3-17. a) The c-tag of the two jets in candidate $\mathrm{ZH} \to \mathrm{q\bar{q}c\bar{c}}$ events after all other cuts apart from the c-tag and c-likeness cut. b) Distribution of the reconstructed di-jet mass for the $\mathrm{ZH} \to \nu\bar{\nu}c\bar{c}$ sample prepared by bc-tagging.

centre-of-mass energy, the combined results shown in Table 3.3-5 are broadly in agreement with those obtained with a fast simulation analysis performed in the context of the TESLA TDR [34].

Channel	$Br(\mathrm{H} \to \mathrm{b\bar{b}})$	$Br(\mathrm{H} \to \mathrm{c\bar{c}})$	$Br(\mathrm{H} \to gg)$
$\mathrm{ZH} \to \ell^+\ell^-\mathrm{q\bar{q}}$	$(2.7 \oplus 2.5)\,\%$	$(28 \oplus 2.5)\,\%$	$(29 \oplus 2.5)\,\%$
$\mathrm{ZH} \to \nu\bar{\nu}H$	$(1.1 \oplus 2.5)\,\%$	$(13.8 \oplus 2.5)\,\%$	–
$\mathrm{ZH} \to \mathrm{q\bar{q}c\bar{c}}$	–	$(30 \oplus 2.5)\,\%$	–
Combined	2.7 %	12 %	29 %

TABLE 3.3-5
Expected precision for the Higgs boson branching fraction measurements ($\sqrt{s} = 250\,\mathrm{GeV}$) for the individual Z decay channels and for the combined result. The expected 2.5 % uncertainty on the total Higgs production cross section is added in quadrature. The results are based on full simulation/reconstruction and assume an integrated luminosity of $250\,\mathrm{fb}^{-1}$. Entries marked – indicate that results are not yet available.

3.3.3 Tau-pairs

The reconstruction of $\tau^+\tau^-$ events at $\sqrt{s} = 500$ GeV provides a challenging test of the detector performance in terms of separating nearby tracks and photons. The expected statistical sensitivities for the $\tau^+\tau^-$ cross section, the $\tau^+\tau^-$ forward-backward asymmetry, A_{FB}, and the mean tau polarisation, P_τ, are determined for and integrated luminosity of $500\,\mathrm{fb}^{-1}$ with beam polarisation, $P(e^+, e^-) = (+30\,\%, -80\,\%)$.

Simulated events with less than seven tracks are clustered into candidate tau jets each of which contains at least one charged particle. Tau-pair events are selected by requiring exactly two candidate tau jets with opposite charge. The opening angle between the two tau candidates is required to be $> 178^\circ$ to reject events with significant ISR (including radiative

return to the Z). After cuts on visible energy, the polar angles of the tau jets, and lepton identification, the purity of the $\tau^+\tau^-$ event sample is 92.4 %. For 500 fb^{-1} the statistical error of the cross section measurement, $|\cos\theta| < 0.95$, corresponds to 0.29%. The uncertainty on A_{FB}, determined from the numbers of τ^- in the forward and backward hemispheres, is ± 0.0025.

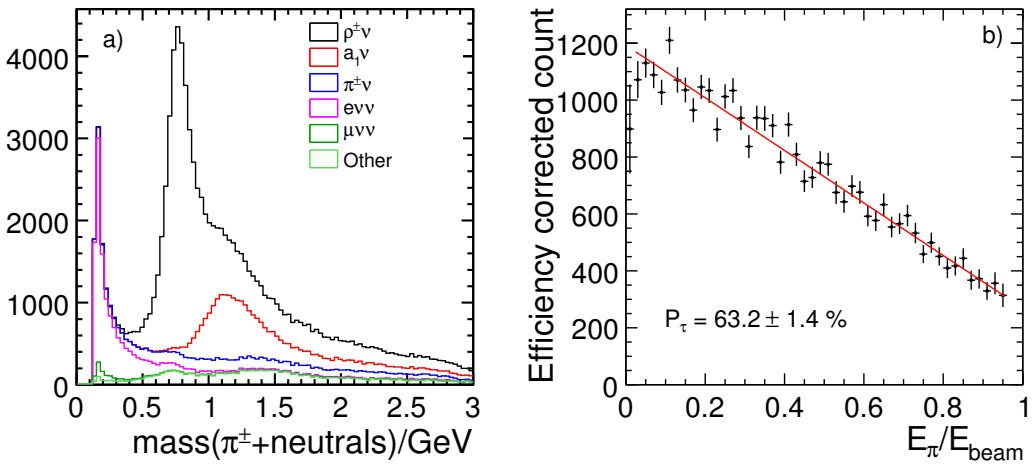

FIGURE 3.3-18. a) The invariant mass distribution for selected 1-prong tau-candidates and b) The efficiency corrected reconstructed pion energy distribution for selected $\tau \to \pi\nu$ candidates.

The $\tau \to \pi\nu$ and $\tau \to \rho\nu$ decays have the highest sensitivity to P_τ. The separation of the 1-prong decay modes relies on lepton identification and the ability to separate the neutral energy deposits from π^0 decays from the hadronic shower. The invariant mass distribution for 1-prong events is shown in Figure 3.3-18a. A neutral network approach based on nine input variables is used to identify the tau decays modes for each tau cone. The variables include: the total energy of the identified photons, the invariant mass of the track and all identified photons (Figure 3.3-18a); and electron and muon particle identification variables based on calorimetric information and track momentum. Table 3.3-6 shows the efficiency and purity achieved for the six main tau decay modes. The high granularity and the large detector radius of ILD results in excellent separation.

For the beam polarisations of $P(e^+, e^-) = (+30\,\%, -80\,\%)$ and $P(e^+, e^-) = (-30\,\%, +80\,\%)$ the mean tau polarisations are -0.625 and $+0.528$ respectively. For the measurement of P_τ, only the $e^\pm\nu\nu$, $\mu^\pm\nu\nu$, $\pi^\pm\nu$, and $\rho^\pm\nu$ decay modes are used. The optimal variable approach [35] is used to obtain the best sensitivity to the tau polarisation. In the case of the $\pi^\pm\nu$ decay mode, the optimal observable is the simply reconstructed $\pi^\pm$ energy divided by the beam energy, shown in Figure 3.3-18b. For the selected event sample and decay mode identification the resulting statistical uncertainties on the measured mean tau polarisations are ± 0.007 and ± 0.008 for $P(e^+, e^-) = (+30\,\%, -80\,\%)$ and $P(e^+, e^-) = (-30\,\%, +80\,\%)$ respectively.

3.3.4 Chargino and Neutralino Production

In the SUSY "point 5" scenario with non-universal soft SUSY-breaking contributions to the Higgs masses, $\tilde{\chi}_1^\pm$ and $\tilde{\chi}_2^0$ are not only nearly mass degenerate but decay predominantly into $W^\pm\tilde{\chi}_1^0$ and $Z\tilde{\chi}_1^0$, respectively. This benchmark point has the following parameters: $M_0 =$

Mode	Efficiency	Purity
$e\nu\nu$	98.9 %	98.9 %
$\mu\nu\nu$	98.8 %	99.3 %
$\pi\nu$	96.0 %	89.5 %
$\rho\nu$	91.6 %	88.6 %
$a_1\nu$ (1-prong)	67.5 %	73.4 %
$a_1\nu$ (3-prong)	91.1 %	88.9 %

TABLE 3.3-6
Purity and efficiency of the main tau decay mode selections. The selection efficiency is calculated with respect to the sample of $\tau^+\tau^-$ after the requirement that the two tau candidates are almost back-to-back. The purity only includes the contamination from other $\tau^+\tau^-$ decays.

206 GeV, $M_{1/2} = 293\,\text{GeV}$, $\tan\beta = 10$, $A_0 = 0$, and $\mu = 375\,\text{GeV}$ and the gaugino masses are: $m(\tilde{\chi}_1^0) = 115.7\,\text{GeV}$, $m(\tilde{\chi}_1^\pm) = 216.5\,\text{GeV}$, $m(\tilde{\chi}_2^0 = 216.7\,\text{GeV}$, and $m(\tilde{\chi}_3^0) = 380\,\text{GeV}$.

Both $e^+e^- \to \tilde{\chi}_1^+\tilde{\chi}_1^- \to qq\tilde{\chi}_1^0 qq\tilde{\chi}_1^0$ and $e^+e^- \to \tilde{\chi}_2^0\tilde{\chi}_2^0 \to qq\tilde{\chi}_1^0 qq\tilde{\chi}_1^0$ result in four jets and missing energy, where the di-jet masses are characteristic of the decays of W^+W^- or ZZ. Separating W and Z decays in the fully-hadronic decay mode relies on good jet energy resolution. It thus provides a benchmark for particle flow based jet reconstruction. The analysis is complicated by the fact that the $\tilde{\chi}_2^0\tilde{\chi}_2^0$ cross section is only 10 % of that for $\tilde{\chi}_1^+\tilde{\chi}_1^-$.

The event selection starts by forcing events into four jets. A cut based preselection retains events consistent with a four-jet plus missing energy topology. All three possible di-jet associations to two bosons are considered. A kinematic fit which constrains the two boson masses to be equal is applied; in terms of mass resolution this is essentially equivalent to taking the average mass of the two di-jet systems. Two analysis strategies are used to assess the expected uncertainty on the measured cross sections: **i)** The first method aims to reduce the SM background as far as possible. Cuts on the number of particle flow objects in each jet, the direction of the missing momentum, and the missing mass are applied. The kinematic fit is required to converge for at least one jet pairing. The jet pairing yielding the highest χ^2 probability is used. Figure 3.3-19a shows the resulting di-jet mass distribution. The Chargino signal has a small shoulder from the Neutralino contribution. The cross sections are obtained from a fit to the mass spectrum using a function with three components: a Breit-Wigner $(m_\text{W}, \Gamma_\text{W})$ convolved with a Gaussian for the W-peak; a Breit-Wigner $(m_\text{Z}, \Gamma_\text{Z})$ convolved with the same Gaussian for the Z peak; and a second order polynomial. The width of the Gaussian is fixed to 3.4 GeV reflecting the mass resolution. The two free parameters of the fit are the normalisations of the W and Z peaks. Figure 3.3-19b shows the result of the fit. The statistical errors on the cross sections are 0.95 % for the Chargino signal and 2.9 % for the Neutralino signal. **ii)** The second approach, which does not use kinematic fitting, is to fit the two-dimensional distribution of the two di-jet masses in each event with MC templates, leaving only the normalisations of the two signal contributions free. The fit is performed after the preselection cuts. All three possible jet pairings are included. This method yields smaller statistical errors of 0.64 % for the Chargino and 2.1 % for the Neutralino production rates.

To determine the $\tilde{\chi}_1^\pm$ and $\tilde{\chi}_2^0$ masses, $\tilde{\chi}_1^+\tilde{\chi}_1^-$ and $\tilde{\chi}_2^0\tilde{\chi}_2^0$ samples are defined on the basis of the di-jet mass distributions (without the kinematic fit). The resulting energy spectra of the W and Z candidates from the kinematic fit are shown in Figure 3.3-19c/d. The masses

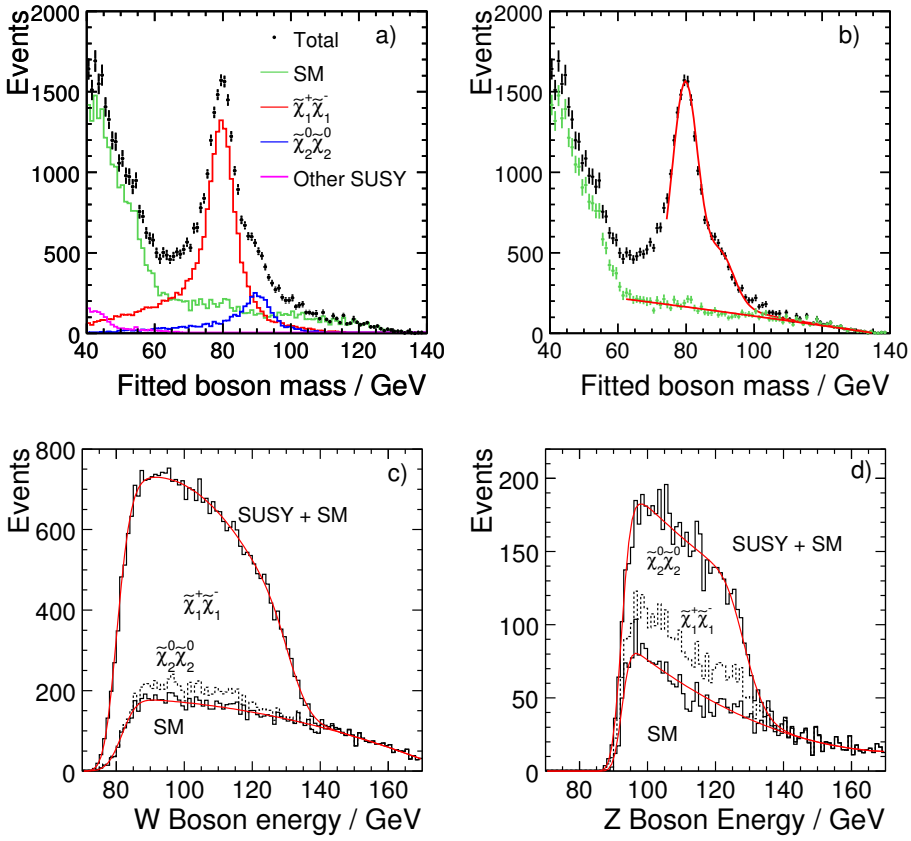

FIGURE 3.3-19. a) Di-jet mass from the 5C kinematic fit after all selection cuts. b) Fit of the background and Chargino and Neutralino contributions. The fit parameters are the normalisations of the W and Z peaks. c) Energy spectra of W and Z boson candidates after the Chargino and d) Neutralino event selections, shown including fits to signal and background contributions.

of the gauginos are determined from the kinematic edges of the distributions located using an empirically determined fitting function for the signal and a parameterisation of the SM background. From the fit results the upper and lower kinematic edges of the $\tilde{\chi}_1^\pm$ sample are determined to ± 0.2 GeV and ± 0.7 GeV respectively. The corresponding numbers for the $\tilde{\chi}_2^0$ sample are: ± 0.4 GeV and ± 0.8 GeV. For the SUSY point 5 parameters, the $\tilde{\chi}_1^\pm$ lower edge is close to m_W and, thus, does not significantly constrain the gaugino masses. The other three kinematic edges can be used to determine the gaugino masses with a statistical precision of 2.9 GeV, 1.7 GeV and 1.0 GeV for the $\tilde{\chi}_1^\pm$, $\tilde{\chi}_2^0$, and $\tilde{\chi}_1^0$ respectively. The errors on the masses are larger than the errors on the positions of the edges themselves. This reflects the large correlations between the extracted gaugino masses; the differences in masses are better determined than the sum. If the LSP mass were known from other measurements, *e.g.* from the slepton sector, the errors on the $\tilde{\chi}_1^\pm$ and $\tilde{\chi}_2^0$ masses would be significantly reduced. Furthermore, the resolutions can be improved by about a factor of two using a kinematic fit which constrains the boson masses for chargino (neutralino) candidates not only to be equal to each other, but also to be equal to the nominal W (Z) mass. In this case, statistical precisions of 2.4 GeV, 0.9 GeV, and 0.8 GeV are obtained for the $\tilde{\chi}_1^\pm$, $\tilde{\chi}_2^0$, and $\tilde{\chi}_1^0$ respectively.

3.3.5 Top production

Top physics will be an important part of the scientific programme at the ILC. In particular, the top mass, m_t, and top width, Γ_t, can be determined with high precision. The measurement of m_t and Γ_t from the direct reconstruction of $e^+e^- \to t\bar{t}$ events is studied with the full ILD detector simulation and reconstruction. Two main decay topologies are considered: fully-hadronic, $t\bar{t} \to (bq\bar{q})(\bar{b}q\bar{q})$, and semi-leptonic, $t\bar{t} \to (bq\bar{q})(\bar{b}\ell\nu)$. Results are obtained for an integrated luminosity of 100fb^{-1} at $\sqrt{s} = 500\,\text{GeV}$, assuming unpolarised beams.

Events with an isolated lepton are considered to be candidates for the semi-leptonic analysis, otherwise they are assumed to be candidates for the fully-hadronic analysis branch. In the fully hadronic branch, the event is reconstructed as six jets which are combined to form Ws and top quarks. The two b-jets originating directly from the top quark decays are identified using the flavour-tagging information. The four remaining jets are considered as the decay products of the two Ws. The combination of the four jets into two di-jets which gives the smallest value of $|m_{ij} - m_W| + |m_{kl} - m_W|$ is chosen to form the two Ws (where m_{ij} and m_{kl} are the di-jet masses for a given jet pairing). Out of two possible combinations to pair the Ws with the b-jets, the one which yields the smallest mass difference is chosen. The first step in the semi-leptonic branch is to remove the identified lepton and to force the remainder of the event into four jets. The two b-jets are identified using flavour-tagging information. The two remaining jets are assigned to the hadronically decaying W. The identified lepton and the neutrino are assigned to the leptonically decaying W, with the three-momentum of the neutrino defined as the missing momentum. The pairing of the Ws with the b-jets which yields the smallest reconstructed top mass difference is chosen. For each analysis branch, background events are rejected using a multi-variate likelihood technique [36]. Finally, a kinematic fit [37] is applied in order to improve the final m_t resolution. Events with a poor fit χ^2 are rejected. The reconstructed mass distributions are shown in Figure 3.3-20.

For an integrated luminosity of $500\,\text{fb}^{-1}$, $\sigma(e^+e^- \to t\bar{t})$ can be determined with a statistical uncertainty of 0.4 % using the fully-hadronic decays only. The invariant mass spectra are fitted with the convolution of a Breit-Wigner function and an asymmetric double Gaussian,

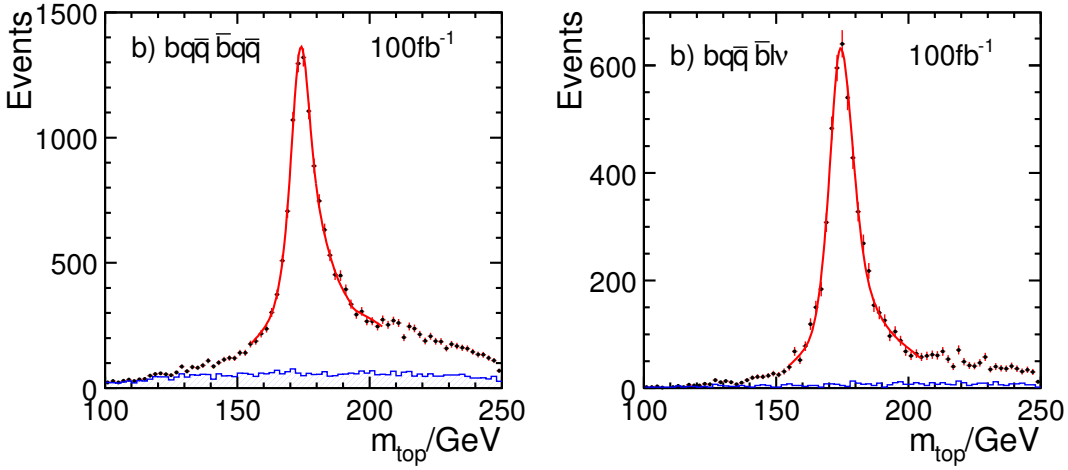

FIGURE 3.3-20. Distribution of the reconstructed top quark mass for a) the fully-hadronic $t\bar{t} \to (bq\bar{q})(\bar{b}q\bar{q})$ signal sample and b) the semi-leptonic $t\bar{t} \to (bq\bar{q})(\bar{b}\ell\nu)$ signal sample. The contribution from the non-$t\bar{t}$ background is indicated by the hashed distribution. The fits to the distributions are also shown.

the latter representing the detector resolution. The combinatoric background and the background from other process is described by a 2$^{\text{nd}}$ order polynomial. The fully-hadronic (semi-leptonic) analysis branch results in statistical uncertainties of 90 MeV (120 MeV) and 60 MeV (100 MeV) for m_{t} and Γ_{t} respectively. Scaling the combined results to an integrated luminosity of 500 fb^{-1} leads to uncertainties of 30 MeV on m_{t} and 22 MeV on Γ_{t}. The relatively small gain in statistical precision from a beam polarisation of $P(e^+, e^-) = (+30\,\%, -80\,\%)$ has not been accounted for.

3.3.5.1 Top Quark Forward-Backward Asymmetry

The top quark forward-backward asymmetry, A^t_{FB}, provides a potentially interesting test of the SM. For the semi-leptonic the analysis is relatively straightforward as the charge of the lepton tags the charge of the W-boson and, thus, enables the t and $\bar{t}$ to be identified. In the fully-hadronic channel the t and $\bar{t}$ can be identified by tagging the $b/\bar{b}$ from the charge of the secondary vertex from charged B-hadron decays. This measurement provides a test of the vertex reconstruction capability of ILD. This study is performed for 500 fb^{-1} with $P(e^+, e^-) = (+30\,\%, -80\,\%)$. Secondary vertices identified by the LCFIVertex algorithm for the two identified b-jets are used. For each of the two identified b-jets, the jet charge is reconstructed. Events with like sign combinations are rejected as are events with two neutral secondary vertices. In addition, the acollinearity between the two top quark jets is required to be $< 8^\circ$ to reject events with $\sqrt{s'}$ significantly less than 500 GeV. Of the 20 % of fully hadronic $\text{t}\bar{\text{t}}$ events which pass these cuts, 79 % have the correctly identified top quark charge. Figure 3.3-21 shows the distribution of the cosine of the reconstructed polar angle of the tagged top-quark, showing a clear forward-backward asymmetry. The relative numbers of events in the forward and backward hemispheres, accounting for the charge identification/mis-identification probabilities, are used to determine

$$A^t_{\text{FB}} = 0.334 \pm 0.0079.$$

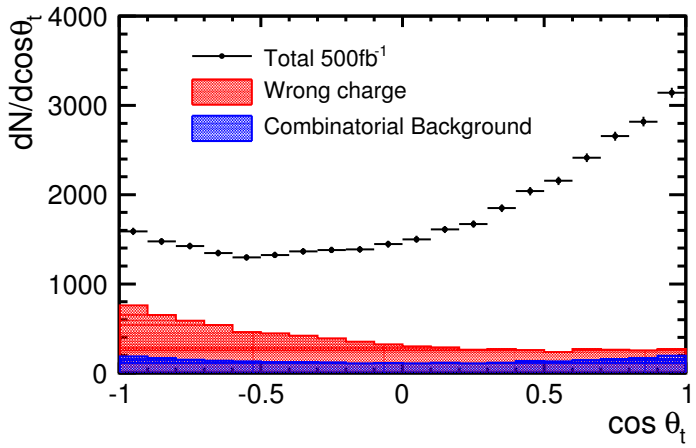

FIGURE 3.3-21. Distribution of the reconstructed polar angle of the identified top quark in fully-hadronic $\text{t}\bar{\text{t}}$ events. The contributions from events with the wrong charge (red) and the case where the b-quark is misidentified are shown (blue).

3.3.6 Strong EWSB

If strong electroweak symmetry breaking (EWSB) is realised in nature, the study of the WW-scattering processes is particularly important. At the ILC, the $W^+W^- \to W^+W^-$ and $W^+W^- \to ZZ$ vertices can be probed via the processes $e^+e^- \to \nu_e\bar{\nu}_e q\bar{q}q\bar{q}$ where the final state di-jet masses are from the decays of two W-bosons or two Z-bosons. Separating the two processes through the reconstruction of the di-jet masses provides a test of the jet energy resolution of the ILD detector.

Strong EWSB can be described by an effective Lagrangian approach in which there are two anomalous quartic gauge couplings, α_4 and α_5 [38] which are identically zero in the SM. The WW scattering events are generated at $\sqrt{s} = 1\,\text{TeV}$ with WHiZard [39] assuming $\alpha_4 = \alpha_5 = 0$. Results are obtained for an integrated luminosity of $1\,\text{ab}^{-1}$ with $P(e^+, e^-) = (+0.3, -0.8)$. Event selection cuts, similar to those of [38, 40, 41, 42], reduce the backgrounds from processes other than the quartic coupling diagrams to $\sim 20\,\%$ of the signal. Of the three possible jet-pairings, the one which minimises $|m_{ij} - m_{W/Z}| \times |m_{kl} - m_{W/Z}|$ is chosen. Figure 3.3-22 shows, for $\nu_e\bar{\nu}_e$WW and $\nu_e\bar{\nu}_e$ZZ events, a) the reconstructed di-jet mass distribution, and b) the distribution of average reconstructed mass, $(m_{ij} + m_{kl})/2.0$. Clear separation between the W and Z peaks is obtained.

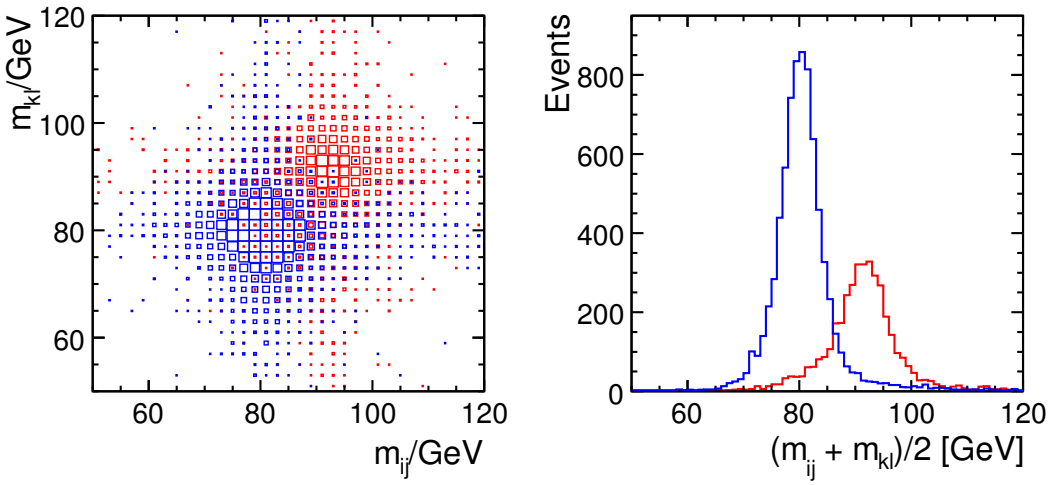

FIGURE 3.3-22. a) The reconstructed di-jet mass distributions for the best jet-pairing in selected $\nu_e\bar{\nu}_e$WW (blue) and $\nu_e\bar{\nu}_e$ZZ (red) events at $\sqrt{s} = 1\,TeV$. b) Distributions of the average reconstructed di-jet mass, $(m_{ij} + m^B_{kl})/2.0$, for the best jet-pairing for $\nu_e\bar{\nu}_e$WW (blue) and $\nu_e\bar{\nu}_e$ZZ (red) events.

The parameters α_4 and α_5 are obtained from a binned maximum likelihood fit to the two-dimensional distribution (10×10 bins) of the boson polar angle in the reference frame of boson pair and the jet polar angle in the reference frame of each boson, giving $-1.38 < \alpha_4 < +1.10$ and $-0.92 < \alpha_5 < +0.77$. These sensitivities are slightly tighter than those from a previous fast simulation study with the TESLA detector concept [41, 42].

3.3.7 Lepton production in SPS1a'

SUSY may provide a rich spectrum of kinematically accessible particles at the ILC operating at $\sqrt{s} = 500\,\text{GeV}$, for example the production of gauginos and sleptons with masses below 250 GeV. The signals for new physics consist of a complex mixture of dominant and

sub-dominant processes, often with identical visible final states [43]. Here we consider final states consisting of missing energy and either two muons or two taus in mSUGRA SUSY with the SPS1a' parameter set: $M_0 = 70\,\text{GeV}$, $M_{1/2} = 250\,\text{GeV}$, $A_0 = -300\,\text{GeV}$, $\text{sign}(\mu) = +1$, and $\tan\beta = 10$. For these parameters the relevant gaugino and slepton masses are: $m(\tilde{\chi}_1^0) = 97.7\,\text{GeV}$, $m(\tilde{\chi}_2^0) = 183.9\,\text{GeV}$, $\text{m}(\tilde{\mu}_R) = 125.3\,\text{GeV}$, $\text{m}(\tilde{\mu}_L) = 189.9\,\text{GeV}$ and $\text{m}(\tilde{\tau}_1) = 107.9\,\text{GeV}$.

3.3.7.1 Muons and Missing Energy

The ILC sensitivity to pair production of the lightest scalar muon, $\tilde{\mu}_R^+\tilde{\mu}_R^-$, leading to a final state of two muons and missing energy has been extensively studied[44]. The study presented here concentrates on sub-dominant di-muon plus missing energy processes which have to compete with the large SUSY background and in particular, the challenging scenario where the di-muon decay modes are suppressed. For these sub-dominant processes, the $\tilde{\chi}_1^0$, $\tilde{\chi}_2^0$, and $\tilde{\mu}_L$ masses can be measured from $\tilde{\chi}_2^0\tilde{\chi}_1^0 \to \mu\mu\tilde{\chi}_1^0\tilde{\chi}_1^0$ ($\sigma = 4.1\,\text{fb}$) and $\tilde{\mu}_L\tilde{\mu}_L \to \mu\mu\tilde{\chi}_1^0\tilde{\chi}_1^0$ ($\sigma = 54\,\text{fb}$). In both cases the signal is characterised by two energetic muons and missing energy. Muons are identified with 95 % efficiency using track, HCAL and muon chamber information. Background is rejected using: missing energy, di-muon invariant mass, recoil mass, transverse momentum, and the direction and speed of the di-muon system. Cuts on these variables are used to define $\tilde{\mu}_L\tilde{\mu}_L \to \mu\mu\tilde{\chi}_1^0\tilde{\chi}_1^0$ and $\tilde{\chi}_2^0\tilde{\chi}_1^0 \to \mu\mu\tilde{\chi}_1^0\tilde{\chi}_1^0$ event samples.

The masses of the $\tilde{\chi}_1^0$ and $\tilde{\mu}_L$ are measured from the kinematic edges of the momentum distribution of the muons in the $\tilde{\mu}_L\tilde{\mu}_L \to \mu\mu\tilde{\chi}_1^0\tilde{\chi}_1^0$ [45] event selection, shown in Figure 3.3-23a. The kinematic edges of the signal, at 32 GeV and 151 GeV, are fitted with a step function giving measurements of the $\tilde{\chi}_1^0$ and $\tilde{\mu}_L$ masses with statistical uncertainties of 1.40 % and 0.27 % repectively. The signal cross section is determined with an uncertainty of 2.5 % from the number of selected events. The sharpness of the kinematic edges, and consequently the mass measurements, are limited by beamstrahlung rather than the track momentum resolution and it is estimated that the uncertainty in the $\tilde{\chi}_1^0$ mass would be a factor two worse for the lowP option for the ILC with the same integrated luminosity. The $\tilde{\chi}_2^0$ mass is determined from the kinematic edge of the di-muon mass distribution in the decay chain $\tilde{\chi}_2^0\tilde{\chi}_1^0 \to \mu\mu\tilde{\chi}_1^0\tilde{\chi}_1^0$ [45]. The distribution of $m_{\mu\mu}$ after selection is shown in Figure 3.3-23b. The kinematic edge of the signal is visible below the Z peak. A fit to the region $40\,\text{GeV} < \text{m}_{\mu\mu} < 85\,\text{GeV}$ is used to determine the mass of the $\tilde{\chi}_2^0$. In this region the statistical significance of the excess corresponds to 9 standard deviations and the $\tilde{\chi}_2^0$ mass resolution obtained is 1.41 %. It should be noted that a higher positron polarisation yields significantly improved precision, particularly for $\tilde{\chi}_2^0\tilde{\chi}_1^0$ production where a positron polarisation of 60 % rather than 30 % results in 50 % more signal events for a relatively small increase in background.

3.3.7.2 Stau Production and Decay

For the SUSY SPS1a' parameters, $e^+e^- \to \tilde{\tau}\tilde{\tau} \to \tilde{\chi}_1^0\tau\tilde{\chi}_1^0\tau$, results in a signal of missing energy and the relatively low energy visible decay products of the tau leptons ($E_\tau \lesssim 43\,\text{GeV}$). Measurements of $\tilde{\tau}\tilde{\tau}$ production requires precision tracking of relatively low momentum particles, good particle identification, a highly hermetic detector, and low machine background.

The stau pair event selection requires two low multiplicity tau-jets and at least 400 GeV of missing energy. The tau jets are required to have $|\cos\theta| < 0.9$ and to have an acoplanarity of greater than 85°. Background is further reduced by cutting on the transverse momentum with respect to the transverse event thrust axis. Given that the tau-jets are relatively low

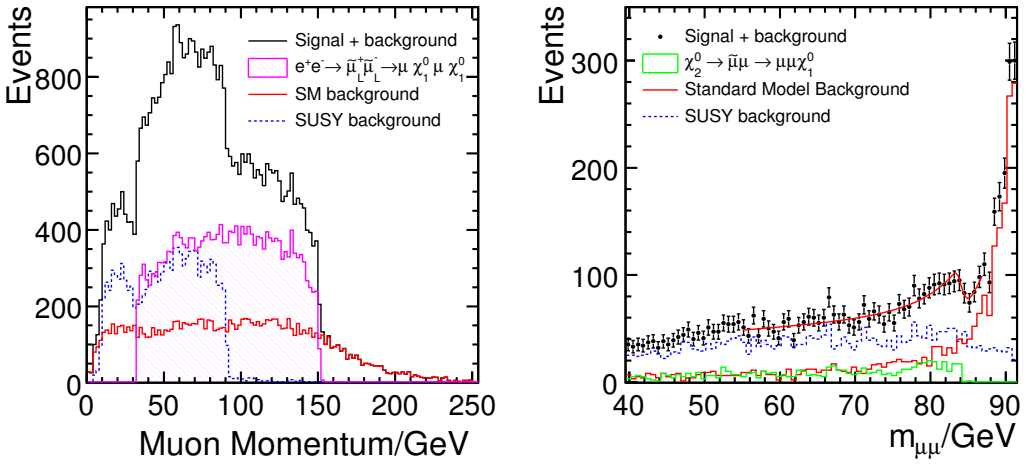

FIGURE 3.3-23. (a) Distribution of the momentum of the μ^+ in the laboratory frame after the selection of the $\tilde{\mu}_L\tilde{\mu}_L$ pair candidates. The total observed signal and the backgrounds (SUSY and SM) are reported. The mass of the $\tilde{\chi}_1^0$ is measured from the kinematic edges of the distribution of the momentum of the di-muons. There are two entries for each event. (b) Fitted $m_{\mu\mu}$ spectrum. The kinematic edge corresponding to the $\tilde{\chi}_2^0 \to \tilde{\mu}_R\mu$ can be extracted from the fit on top of the left tail of the Z peak. Both plots are shown for a beam polarisation of -80 %, 60 % and correspond to an integrated luminosity of 500 fb^{-1}.

momentum, background from multi-peripheral two photon processes, $e^+e^- \to e^+e^-X$, is particularly important due to the very high cross section. This background is reduced using the beam calorimeter (BCAL) to veto the forward going electrons/positrons. Due to the holes in the BCAL acceptance around the incoming and outgoing beam pipes, the regions $\phi \leq 110°$ or $\phi \geq 250°$ are not used (for details see [46]).

The $\tilde{\tau}$ mass can be extracted from the end-point of the tau-jet energy spectrum and knowledge of the $\tilde{\chi}_1^0$ mass, *e.g.* from the study of smuon production. For the stau mass determination, the stau pair selection is augmented by additional cuts on tau-jet masses and the polar angle of the missing momentum vector. Figure 3.3-24a shows the distribution of the tau jet energy after these cuts. The selection efficiency is 12 % and the sample purity is 80 %. The end-point tau energy is determined from a fit to the spectrum of Figure 3.3-24a in the region $30 < E < 41.5$ GeV. The signal, which in this region is dominated by $\tau \to \pi\nu$ decays, is described by a linear function. The resulting statistical uncertainty on the end-point is 0.1 GeV. When accounting for the uncertainty on the $\tilde{\chi}_1^0$ mass, σ_{LSP}, this leads to a measurement precision on $M_{\tilde{\tau}_1}$ of $0.1\,\text{GeV} \oplus 1.3\sigma_{\text{LSP}}$. Systematic uncertainties are not included.

The measurement of tau polarisation, P_τ, in $\tilde{\tau}_1$ decays gives direct access to the mixing of mass and interaction eigenstates in the stau sector, and thus provides sensitivity to a number of SUSY parameters. For SPS1a' $P_\tau = 97\,\%$. P_τ can be measured most cleanly in $\tau \to \pi\nu$ decays where the slope of the $\pi^\pm$ energy spectrum depends on P_τ. The potential signal is large, for 500 fb^{-1}, ~17500 $\pi\nu$ decays are expected. In addition to the stau pair selection, calorimeter and $\text{d}E/\text{d}x$ information are used to identify $\tau \to \pi\nu$ decays. The selection efficiency is 13.8 % and the remaining background fraction is 21 %. The underlying pion spectrum is reconstructed by subtracting the background in a parametrised form and applying an energy dependent efficiency correction. The shape of the spectrum is influenced by the luminosity spectrum of the machine, and this effect is folded into the fit function.

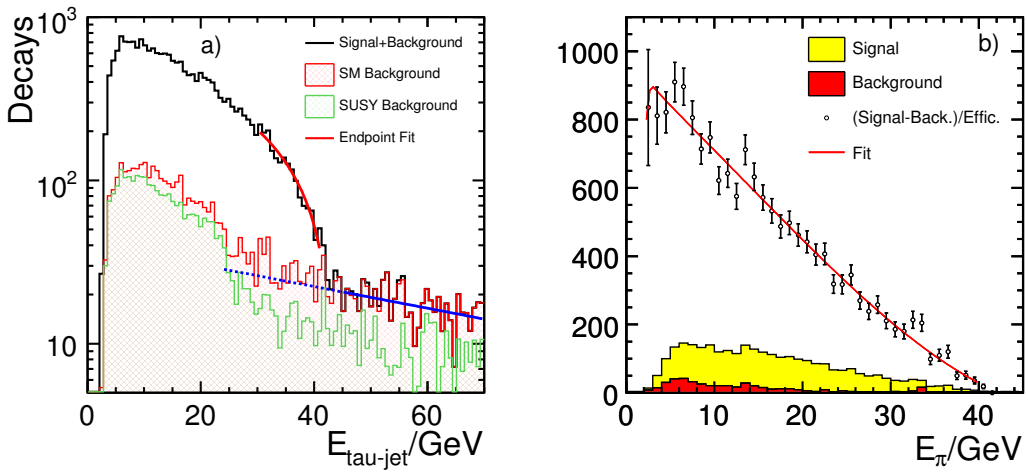

FIGURE 3.3-24. a) Tau-jet energy spectrum, showing the fit to determine the endpoint (two entries per event). b) Energy spectrum of selected tau decays and the fit to determine P_τ.

Figure 3.3-24 shows the reconstructed data together with the fit. This study shows that a measurement of P_τ with an accuracy of 0.15 is realistic.

3.3.8 Photon Final States

Physics beyond the standard model can manifest itself in final states consisting of two (or more) photons and missing momentum. The high granularity and good photon reconstruction capability of the ILD detector is well suited to these measurements.

3.3.8.1 Model-independent WIMP search

Weakly Interacting Massive Particles (WIMPs) are possible candidates for dark matter. If they can pair annihilate into e^+e^-, then the reverse process can be detected at the ILC. In this case the two neutral (undetected) WIMPs are accompanied by photon radiation from the incoming e^+e^-. In these $e^+e^- \to \chi\chi\gamma$ events, the photon recoil mass distribution has a characteristic onset. The location of the onset and shape of the recoil mass distribution depends on the WIMP mass and spin. Experimentally, the WIMP signal has to be resolved from the large irreducible ISR background from $e^+e^- \to \nu\bar{\nu} + n\gamma$. Good photon energy and angular resolution are required in order to detect a clear edge in the photon energy spectrum above this large background. Assuming that the total cross-section for WIMP pair annihilation into SM fermion pairs, $\tilde{\chi}\tilde{\chi} \to f\bar{f}$, is known from cosmological observations, the ILC sensitivity can be expressed in terms of the WIMP pair branching fraction into e^+e^-, κ_e. The ILD detector has been used to study this process [47]. In general, κ_e values of 0.1 are accessible for WIMP masses between 150 GeV and 200 GeV.

3.3.8.2 Long-lived Neutralinos in GMSB

In the Gauge-Mediated SUSY Breaking (GMSB) scenario, $\tilde{\chi}_1^0$ decays into a Gravitino $\tilde{G}$ (the LSP) and a photon. Depending on the SUSY parameters, the lifetime of the $\tilde{\chi}_1^0$ may be such that it decays inside the detector tracking volume. In this case the signal for GMSB neutralino

production is a pair of photons with production point displaced from the origin. The signal is thus two non-pointing photons. The excellent angular resolution for reconstructed photons in the ECAL allows the $\tilde{\chi}_1^0$ lifetime to be determined from photon impact parameter distribution. This process has been studied in detail [48] with the full ILD simulation. For neutralino lifetimes in the range $0.2 - 2.0\,\text{ns}$ a signal to background ratio of approximately unity is achieved. This allows the neutralino mass to be determined with a precision of $\pm 2\,\text{GeV}$ and the lifetime can be measured to 1 %. Decay lengths of 100 cm can be well measured, while a decay length of 10 cm can not be reconstructed with the ECAL only.

3.4 OTHER STUDIES

The previous section described a number of physics studies related to specific aspects of the detector performance, based on full simulation and reconstruction. In addition, a number of other studies have been performed which demonstrate the general purpose nature of the ILD concept. Three of these are described briefly below.

3.4.1 Measurement of Beam Polarisation from WW production

One of the unique features of the ILC is the possibility of both electron and positron beam polarisation [49]. The baseline design foresees a longitudinal electron polarisation of 80 % and a positron polarisation of 30 % with an option of 60 %. This provides a tool for improving the sensitivity to new physics [50]. For many of these applications, the final goal of an ultimate relative precision of 0.2 % of the measurement of the beam polarisations is desirable to bring the systematics from the uncertainty of the beam polarisation to a negligible level.

While polarimeters [51] will be used to measure the polarisation on a bunch-by-bunch basis, the absolute calibration of the average luminosity-weighted polarisation at the interaction point can be achieved using $\mathrm{W^+W^-}$ production. Two methods are considered: i) the modified Blondel scheme [52, 53] which uses the measured $\mathrm{W^+W^-}$ production cross-sections for different beam polarisations; and ii) the angular fit method which uses the distribution of the production angle $\cos\theta_W$ of the W^- with respect to the e^- beam axis [54].

A comparison of these two methods is performed using the full simulation of events in ILD. Semi-leptonic decays of W-pair events ($\mathrm{q\bar{q}}\ell\nu$) are selected with an efficiency of 68.7 % and 93 % purity. The charge of the lepton tags the charges of two W bosons so that the $\mathrm{W^-}$ angular distribution can be determined. In the modified Blondel scheme, the total luminosity necessary to reach the desired relative precision of 0.2 % is around $500\,\text{fb}^{-1}$. Using the angular fit method the same level of precision can be achieved with an integrated luminosity of $250\,\text{fb}^{-1}$. The lower luminosity demand reduces the time spent on the $++$ and $--$ helicity combinations, which are less interesting from the physics point of view. To reach the desired precision for the measurement of the beam polarisation, $\mathcal{L} = 250\,\text{fb}^{-1}$ is required for the case of 60 % positron polarisation, while $\mathcal{L} = 1200\,\text{fb}^{-1}$ is required if only the baseline 30 % positron polarization is available.

3.4.2 Heavy Gauge Boson Production in Littlest Higgs Model

The Littlest Higgs model with T-parity (LHT) has been proposed as a solution to the little hierarchy problem. Since heavy gauge bosons acquire mass terms through the breaking of the global symmetry, precise measurements of their masses allow a determination of the

vacuum expectation value of the breaking (f). Furthermore, since the heavy photon, $A_{\rm H}$, is a candidate for dark matter, the determination of its properties is important for both particle physics and cosmology. However, at the LHC it is difficult to determine the properties of heavy gauge bosons because they have no colour charge.

The potential of an ILD-like detector concept, studied using the fast simulation of the GLD concept, is described in detail in [55]. Here the processes $e^+e^- \to A_{\rm H}Z_{\rm H} \to A_{\rm H}A_{\rm H}H$ at $\sqrt{s} = 500\,\text{GeV}$ and $e^+e^- \to W^+_{\rm H}W^-_{\rm H} \to A_{\rm H}W^+A_{\rm H}W^-$ at $\sqrt{s} = 1\,\text{TeV}$, where $A_{\rm H}$, $Z_{\rm H}$, and $W^\pm_{\rm H}$ are the heavy gauge bosons, are studied. The experimental signatures considered for each process are b-jets with missing energy and four-jets with missing energy. The masses and the vacuum expectation value, f, were set to $(M_{A_{\rm H}}, M_{Z_{\rm H}}, M^\pm_{W_{\rm H}}) = (81.9\ \text{GeV}, 369\ \text{GeV}, 368\ \text{GeV})$, $m_{\rm H} = 134\,\text{GeV}$ and $f = 580$ GeV. It is found that the masses of $A_{\rm H}$ and $Z_{\rm H}$ can be measured with an accuracy of 16.2 % and 4.3 % respectively at $\sqrt{s} = 500$ GeV, and those of $A_{\rm H}$ and $W_{\rm H}$ can be determined with an accuracy of 0.2 % and 0.8 % respectively at $\sqrt{s} = 1\,\text{TeV}$ [55]. In addition f can be with measured to 4.3 % at $\sqrt{s} = 500\,\text{GeV}$ and 0.1 % at $\sqrt{s} = 1\,\text{TeV}$. Finally it is shown that the abundance of dark matter relics can be determined to the 10% and 1% levels at $\sqrt{s} = 500\,\text{GeV}$ and $\sqrt{s} = 1\,\text{TeV}$, respectively. These accuracies are comparable to those of the current and future cosmological observations of the cosmic microwave background.

3.4.3 ZHH Production

The Higgs boson tri-linear coupling can be studied at the ILC through the processes $\text{e}^+\text{e}^- \to \nu_e\overline{\nu}_e\text{HH}$ and $\text{e}^+\text{e}^- \to \text{ZHH}$. For $m_{\rm H} = 120\,\text{GeV}$, the cross section for the latter process is 0.18 fb at $\sqrt{s} = 500\,\text{GeV}$. The $\text{q}\overline{\text{q}}\text{b}\overline{\text{b}}\text{b}\overline{\text{b}}$ decay mode (34 % of the ZHH decays) has been studied using the ILD simulation and reconstruction [56]. A multi-variate selection including the invariant masses of jet combinations and flavour tagging information is used. For an integrated luminosity of $500\,\text{fb}^{-1}$, a precision of 90 % on $\sigma(\text{e}^+\text{e}^- \to \text{ZHH})$ is achieved. It should be noted that the sensitivity does not yet approach that of earlier fast simulation studies [44]. Whilst significant improvements are expected, this study demonstrates the difficulty of this analysis; excellent particle flow and flavour tagging performance are likely to prove essential for this important measurement.

3.5 CONCLUSIONS

3.5.1 Detector Performance

It has been demonstrated in Section 3.2 that ILD meets the requirements for an ILC detector:

- **Track reconstruction:** The ILD tracking system provides highly efficiency track reconstruction ($\sim 99.5\,\%$), even in a dense multi-jet environment.
- **Momentum resolution:** When hits in the TPC are combined with those in Si tracking detectors, the asymptotic value of the momentum resolution is $\sigma_{1/p_T} \approx 2\times10^{-5}\,\text{GeV}^{-1}$, as required.
- **Impact parameter resolution:** For either option for the VTX layout, the required impact parameter resolution is achieved, with asymptotic values of $\sigma_{r\phi} = 2\,\mu$m and $\sigma_{rz} = 5\,\mu$m.
- **Particle flow performance:** A jet energy resolution of $< 3.8\,\%$ is achieved for jets in the energy range $40 - 400\,\text{GeV}$. For the range of energies typical of much of the ILC

physics, $80 - 200\,\mathrm{GeV}$ the jet energy resolutions is $\approx 3\,\%$. The performance does not depend strongly on the polar angle of the jet, except in the very forward region.

3.5.2 Physics Performance

The physics benchmark studies presented above are summarised in Table 3.5-7. However, care is needed in interpreting the results shown. They do not represent the ultimate ILD performance as significant improvements in the analyses are possible. However, the range of different measurements studied and precision achieved demonstrate the general purpose nature of ILD.

Analysis	$\sqrt{s}$	Observable	Precision	Comments
Higgs recoil mass	250 GeV	$\sigma(\mathrm{e^+e^-} \to \mathrm{ZH})$	$\pm 0.30\,\mathrm{fb}$ (2.5 %)	Model Independent
		m_{H}	32 MeV	Model Independent
		m_{H}	27 MeV	Model Dependent
Higgs Decay	250 GeV	$Br(\mathrm{H} \to \mathrm{b\bar{b}})$	2.7 %	includes 2.5 %
		$Br(\mathrm{H} \to \mathrm{c\bar{c}})$	12 %	from
		$Br(\mathrm{H} \to gg)$	29 %	$\sigma(\mathrm{e^+e^-} \to \mathrm{ZH})$
$\tau^+\tau^-$	500 GeV	$\sigma(\mathrm{e^+e^-} \to \tau^+\tau^-)$	0.29 %	$\theta_{\tau^+\tau^-} > 178^\circ$
		A_{FB}	± 0.0025	$\theta_{\tau^+\tau^-} > 178^\circ$
		P_τ	± 0.007	exclucing $\tau \to a_1\nu$
Gaugino Production	500 GeV	$\sigma(\mathrm{e^+e^-} \to \tilde{\chi}_1^+\tilde{\chi}_1^-)$	0.6 %	
		$\sigma(\mathrm{e^+e^-} \to \tilde{\chi}_2^0\tilde{\chi}_2^0)$	2.1 %	
		$m(\tilde{\chi}_1^\pm)$	2.4 GeV	from kin. edges
		$m(\tilde{\chi}_2^0)$	0.9 GeV	from kin. edges
		$m(\tilde{\chi}_1^0)$	0.8 GeV	from kin. edges
$\mathrm{e^+e^-} \to \mathrm{t\bar{t}}$	500 GeV	$\sigma(\mathrm{e^+e^-} \to \mathrm{t\bar{t}})$	0.4 %	$(\mathrm{bq\bar{q}})$ $(\mathrm{\bar{b}q\bar{q}})$ only
		m_t	40 MeV	fully-hadronic only
		m_t	30 MeV	+ semi-leptonic
		Γ_t	27 MeV	fully-hadronic only
		Γ_t	22 MeV	+ semi-leptonic
		A_{FB}^t	± 0.0079	fully-hadronic only
Smuons in SPS1a'	500 GeV	$\sigma(\mathrm{e^+e^-} \to \tilde{\mu}_L^+\tilde{\mu}_L^-)$	2.5 %	
		$m(\tilde{\mu}_L)$	0.5 GeV	
Staus in SPS1a'	500 GeV	$m(\tilde{\tau}_1)$	$0.1\,\mathrm{GeV} \oplus 1.3\sigma_{\mathrm{LSP}}$	
WW Scattering	1 TeV	α_4	$-1.4 < \alpha_4 < 1.1$	
		α_5	$-0.9 < \alpha_5 < +0.8$	

TABLE 3.5-7
A summary of the main observables presented in Section 3.3.

CHAPTER 4

The ILD Sub-Detector Systems

The ILD detector is strongly influenced by two basic assumptions about experimentation at a linear collider: particle flow as a way to reconstruct the overall event properties, and high resolution vertexing. Particle flow calorimetry requires a reliable and redundant tracking system which enables charge particle momenta to be reconstructed with high precision, and in particular, with very high efficiency. ILD is built around a calorimeter system with very good granularity both in the transverse and in the longitudinal direction, and a combination of Silicon and gaseous tracking systems. Vertexing, the other great challenge, is addressed by a high precision pixelated detector very close to the interaction point.

In this section the different sub-detectors are described in more detail, proposed technological solutions are outlined, and necessary development work is highlighted, particularly where it is essential to advance the concept to a point where this detector could be built.

Development of technologies for a detector at a linear collider is an active field, with many ideas being pursued, and great advances in technology are being made. ILD therefore does not at this moment exclude any promising technology from its consideration. Wherever possible, ILD supports that more than one avenue is followed to eventually identify the best solution possible. Therefore, at this stage, all promising technologies are considered as possible candidates for the ILD detector. Consequently for a number of subdetectors more than one option are described.

4.1 VERTEX DETECTOR

The Vertex Detector (VTX) is the key to achieving very high performance flavour tagging by reconstructing displaced vertices. It also plays an important role in the track reconstruction, especially for low momentum particles which don't reach the main tracker or barely penetrate its sensitive volume because of the strong magnetic field of the experiment, or due to their shallow production angle.

The flavour tagging performance needed for physics implies that the first measured point on a track should be as close as possible to the IP. This creates a major technical challenge because of the rapidly increasing beam-related background when approaching the IP. The sensor technology best adapted to the high background environment is not yet defined. It is however clear that existing technologies are not able to satisfy all of the requirements defined by the physics goals (granularity, material budget) and those imposed by the running conditions near the IP (*e.g.* occupancy and radiation dose). Several alternative, innovative, pixel

technologies are being considered and actively developed to satisfy the VTX requirements.

The VTX flavour tagging performance relies on a low material budget for the detector sensors and the support structures. The VTX is also necessary in some physics studies to measure the vertex charge (the net charge of all tracks from the decay chain) which implies distinguishing between the tracks from the primary vertex and the decay chain. This is particularly challenging for low momentum tracks in the jet. Finally, secondary particle production and trajectory kinks due to secondary interactions with the detector material need to be mitigated because of their impact on the particle flow reconstruction. Minimising the VTX material budget therefore motivates an ambitious R&D programme.

4.1.1 Physics Driven Requirements and Running Constraints

To identify the flavor (b or charm) of heavy-flavor jets, to measure the associated vertex charge, and to recognize tau-lepton decays, the VTX design needs to be optimised in terms of single point resolution and distance between the first measured point of tracks and the IP. The high granularity necessary to achieve the single point resolution needs to be complemented with a particularly low material budget allowing high precision pointing with low momentum tracks. A high granularity is also required to separate neighboring tracks in a jet, a constraint which applies predominantly to the detector elements closest to the IP.

Following the usual convention, the performances of the VTX in terms of impact parameter resolution are summarised in a compact way by its well known gaussian expression:

$$\sigma_{ip} = a \oplus b/p \cdot \sin^{3/2}\theta \qquad \text{(i)}$$

The parameters a and b are required to be below 5 μm and 10 μm·GeV/c, respectively. Monte-Carlo studies show that these specifications are met with the following inputs:

- a single point accuracy of $\lesssim 3\ \mu m$,
- a vertex detector geometry providing a first measured point of tracks at ~ 15 mm from the IP.
- a material budget between the IP and the first measured point restricted to a few per mill of radiation length.

The values of a and b significantly exceed those achieved so far, as illustrated by the comparison made in table 4.1-1, which provides values of a and b obtained with vertex detectors operated at LEP, SLC and LHC as well as planned at RHIC.

To achieve this new tagging performance standard, a beam pipe radius of 14 mm is envisaged, which is still compatible with the need to contain the core of the beam-related pair background within the vacuum pipe. The pipe is assumed to be made of machined beryllium, 250 μm thick, potentially covered with a 25 μm thin foil of titanium against background from synchrotron radiation. Beam-related background, which ultimately sets the performance limits for the VTX, is expected to be dominated by beamstrahlung e^+e^- pairs. Most of these have low transverse momentum and remain trapped inside the vacuum pipe by the 3.5 T solenoid field. Extensive Monte-Carlo simulations, based on the GuineaPig [57] and CAIN generators [58], were performed to estimate the rate of $e^\pm$ reaching the vertex detector. The predicted rates amount to $5.3/4.4 \pm 0.5$ hits/cm^2 per bunch crossing (BX) at 15/16 mm radii, including $e^\pm$ backscattered from elements located near the outgoing beam lines [59]. Since most of these $e^\pm$ have a transverse momentum close to the cut-off value of $\lesssim 10$ MeV/c,

Accelerator	a (μm)	b (μm·GeV/c)
LEP	25	70
SLC	8	33
LHC	12	70
RHIC-II	13	19
ILD	< 5	< 10

TABLE 4.1-1
Values of the parameters a and b entering the expression of σ_{ip} foreseen for the ILD, compared to those achieved with past, present or upcoming experiments at existing colliders.

they tend to penetrate the sensitive volume of the VTX sensors at rather shallow angle, and tend to tend to generate pixel clusters which are elongated in the beam direction. This feature may be used offline to reject a substantial fraction of the beamstrahlung clusters. It also impacts the radiation dose. The annual dose was calculated to be in the order of 500 Gy ionising dose per year, with a corresponding fluence of $\lesssim 10^{11}$ n_{eq}/cm^2 at 15 mm radius. To account for the limited accuracy of the simulated beamstrahlung $e^{\pm}$ rate, the latter was multiplied by a safety factor of 3 to derive the sensor specifications. Other backgrounds, such as photon and neutron gas, are expected to add marginal contributions. Overall, the annual radiation levels the sensors have to comply with are in excess of 1 kGy and of 10^{11} n_{eq}/cm^2.

Another environmental concern entering the specifications of the VTX is related to the electrical interference associated with leakage of the beam-related RF from ports used for beam position monitors and other equipment in the interaction region. Their potential effect is motivating specific (delayed) signal processing read-out architectures of the sensors, taking advantage of the ILC beam time structure.

4.1.2 Global Design Aspects

The VTX design is still evolving, but its prominent aspects are well defined. It is made of 5 or 6 cylindrical layers, all equipped with $\lesssim 50$ μm thin pixel sensors providing a single point resolution of 2.8 μm all over the sensitive VTX area (see sub-section 4.1.3.1). The innermost layer has a radius of 15-16 mm, a value for which the beam-related background rate is expected to still be acceptable. As a consequence, the innermost layer intercepts all particles produced with a polar angle (θ) such that $|\cos\theta| \lesssim 0.97$.

Two alternative geometries are being considered, one (called VTX-SL) featuring 5 equidistant single layers (i.e. equipped with one layer of sensors only), and an alternative option (called VTX-DL) featuring 3 double layers (i.e. each layer being equipped with two, $\lesssim 2$ mm apart, arrays of sensors). They are not associated with a specific sensor technology. The double layer option allows spatial correlations between hits generated by the same particle in the two sensor layers equipping a ladder, even if the occupancy is high. It is therefore more robust against (low momentum) beamstrahlung background. It is also expected to provide additional pointing accuracy. Moreover, it should facilitate the internal alignment, allowing the use of a large fraction of tracks traversing the overlapping bands of neighbouring ladders. Finally, it is expected to improve the modeling with tracks reconstructed at shallow angle in the very forward region. This geometry may however be less efficient in reconstructing long lived B mesons decaying outside of the beam pipe. It is also technically more challenging

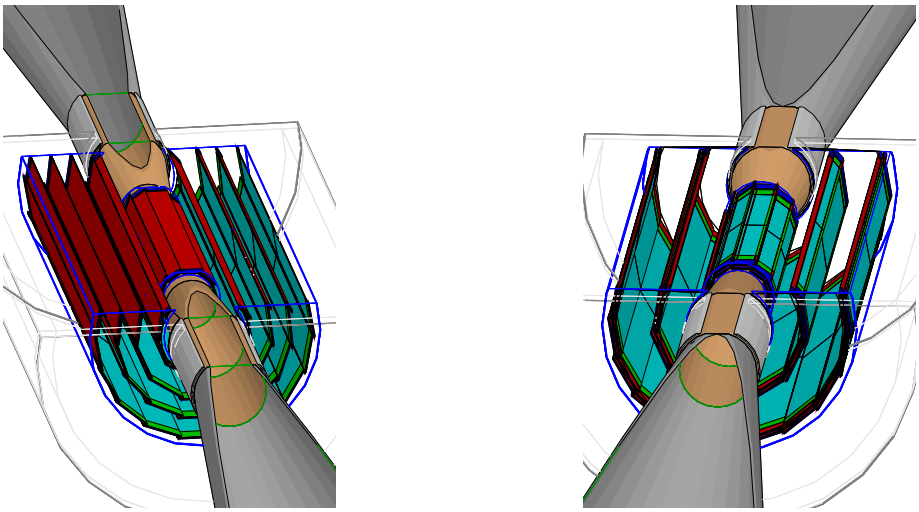

FIGURE 4.1-1. Vertex detector geometries of the two design options. Left: 5 single ladders (VTX-SL). Right: 3 double ladders (VTX-DL).

because of the additional difficulty to realise double ladders as compared to single ones. It may however be robust against mechanical distortions resulting from power pulsing the sensors inside the solenoid field. The two VTX geometries are displayed on figure 4.1-1. Some of their main geometrical parameters are listed in table 4.1-2.

	radius [mm]		ladder length [mm]		read-out time [μs]	
geometry	VTX-SL	VTX-DL	VTX-SL	VTX-DL	VTX-SL	VTX-DL
layer 1	15.0	16.0/18.0	125.0	125.0	25–50	25–50
layer 2	26.0	37.0/39.0	250.0	250.0	50–100	100-200
layer 3	37.0	58.0/60.0	250.0	250.0	100-200	100-200
layer 4	48.0		250.0		100-200	
layer 5	60.0		250.0		100-200	

TABLE 4.1-2
Radius and ladder length for each layer of the two vertex detector geometries. For the double layer option (VTX-DL), the radii are provided for each of both pixel arrays equipping a ladder.The read-out times are provided for each layer in the specific case of a continuous sensor read-out (see subsection 4.1.3).

The complete VTX-SL ladder thickness is equivalent to 0.11 % X_0, while the double ladders of VTX-DL represent 0.16 % X_0. These values assume 50 μm thin silicon pixel sensors. The length of the innermost ladder (125 mm) is limited due to the radial expansion of the pair background envelope as it diverges from the IP. It would shrink significantly when considering the so-called "low-P" option of the machine parameter. In this case, the innermost ladders should be shortened to $<$ 100 mm and/or the inner radius should be increased in ordre to accommodate the increased beam-beam disruption. The loss in physics performance consecutive to the geometrical acceptance shrinkage and to the potential impact parameter resolution degradation is still being evaluated.

Both device options are enclosed in a $\sim$ 500 μm thick (0.14 % X_0), 65 mm radius, cylindrical beryllium support. The latter is surrounded by a light foam cryostat (0.05 % X_0), complemented with a 0.5 mm aluminum foil (0.55 % X_0) which acts as a Faraday cage. The whole system, including support, cryostat and cage adds up to 0.74 % X_0. While the ladders of the three (resp. two) external layers of VTX-SL (resp. VTX-DL) are mounted on the beryllium support, the ladders composing the inner layers are supported by straight sections of the vacuum pipe.

The detector alignment is expected to proceed through two main steps. The ladders will first be aligned inside their layer. An overlap of $\lesssim$ 500 μm between the sensitive areas of neighbouring ladders is foreseen for this purpose. Tracks with momentum in excess of a couple of GeV/c traversing these overlapping bands will be used. Next the layers will be aligned with respect to the rest of the detector using straight tracks such as those of $\mu^+\mu^-$ final states.

The pros and cons of each design option are still being assessed. Moreover, the concept itself, which assumes extended cylinders, rather than shorter ones complemented with disks at small polar angle, is based on the present understanding of the minimal material budget which would separate the barrel from the disks. Depending on the evolution of technologies and materials, the choice between both alternatives may be reconsidered.

4.1.3 Pixel Technology and System Integration Studies

4.1.3.1 R&D on Pixels and Read-out Architectures

Intensive R&D has been under way for several years, addressing the numerous challenging issues underlying the vertex detector specifications. Because of the scale of the challenge and of its complexity, several alternative sensor technologies are being developed in parallel, aiming for the best suited ones. The goal of the development is to optimise the charge sensing system and the charge to electrical signal conversion, as well as the read-out, steering and control micro-circuits. The technologies presently concentrating most of the R&D effort within the ILD group are CMOS sensors [60, 61, 62, 63], DEPFETs [64, 65], FPCCDs [66, 67], and ISIS [64]. Since recently, CMOS sensors exploiting vertical integration technology [68] are also developed. Alternative technological approaches mentioned in [64] may also be considered, though not currently developed inside the ILD group. The R&D achieved so far has already demonstrated that the goals of a single point resolution of ($\lesssim$ 3 μm), double hit separation of ($\lesssim$ 40 μm) and sensor thickness of ($\lesssim$ 50 μm) are achievable.

The most demanding requirement for all technologies is to comply with the occupancy generated by the beam related background in the innermost layers. Two alternative approaches are being investigated, one where the sensors are read out continuously, and one where the signal is stored during the whole train duration and read out during the beamless period separating two consecutive trains.

In the continuous read-out approach, most of the R&D effort is invested in achieving the low noise high read-out frequency required for the inner layers, while keeping the power consumption at an affordable level. Typical read-out time target values are summarised in table 4.1-2 for each layer. Present R&D achievements indicate that the upper bounds of each time interval can already be considered as within reach.

Power dissipation estimates, based on fabricated sensors and accounting for power cycling, were performed. It was assumed that the beam time structure can be used to suppress the power during a large fraction of the inter-train time by about two orders of magnitude,

estimating to about $1-2$ milliseconds before and after the train the transient time needed to switch on and off all sensors in a well controlled way. In this case, Lorentz forces applied to the ladders are expected to remain acceptable. With a rather conservative duty cycle of 2% (while the machine duty cycle is 0.5%), the average power dissipation would amount to a few tens of watts only (e.g. 30 W for CMOS sensors [60]). Such values are compatible with modest cooling, based on air flow, which does not require introducing additional material in the VTX fiducial volume.

Power consumption may even be mitigated more with the delayed read-out approach because of the very low read-out clock frequency it allows for, a feature which also translates into reduced Lorentz forces on the ladders. Moreover, if the signal charge is converted into an electrical signal only after the end of the train (e.g. like in FPCCD or ISIS devices), immunity against EMI can be reinforced.

Most pixel technologies and read-out architectures still need at least a couple of years until all main VTX specifications have been addressed. The recently considered vertical integration approach, which may have the highest potential, is likely to need more time to reach maturity. It may be a technological solution for a second generation VTX, to be used a couple of years after the start of the ILC programme. It is in particular a promising solution for the machine operation near 1 TeV, where the beam-related background may call for sensors substantially faster than those needed at 500 GeV.

4.1.3.2 System Integration Studies

The R&D on the sensors and their read-out circuits is complemented with studies addressing their main system integration issues. One of the main aims of these studies is to tackle the design goal of $\lesssim 0.1$ % X_0 thickness per layer over their active area. Attempts are made to find materials which combine low density and high rigidity against potential vibrations generated by the air cooling system and by power cycling (temperature gradient, Lorentz forces). The latter also requires good thermal expansion compatibility between the support and the sensors. Low density materials were tested [64], such as silicon carbide foam, which have a thermal expansion coefficient close to silicon, and feature a density of a few per-cent only. They may actually also be used for the structural material of the entire VTX assembly.

Trials to use silicon as a support material are also made [65]. They consist in using the silicon substrate of the sensors, excavating the silicon bulk wherever it is not essential for the ladder stability. The latter is provided by "window frames" left after the bulk excavation. This approach is currently followed for the upgrade of the SuperBELLE vertex detector [69].

Finally, a third approach consists in extrapolating from the current state-of-the-art. It relies on the ladders equipping the upcoming PIXEL vertex detector of the STAR experiment at RHIC [70]. With a total material budget of ~ 0.3 % X_0, its concept may be extended to the ILD with an ultimate budget of $\lesssim 0.2$ % X_0.

4.1.4 Outlook

Definite choices concerning the sensor technology, the read-out architecture and the ladder design still have to wait until full-scale fully-serviced ladders, as well as still more realistic simulation studies are available. For instance, a detailed understanding of the handling of the beam-related background will impact the maximal background rate acceptable, with direct consequences on the read-out architecture and the sensor technology. The validation

of the VTX concept will follow, including the outcome of current studies of servicing issues, presumably around 2012.

4.2 SILICON TRACKING

The tracking system of the ILD has been optimised to deliver outstanding resolution together with excellent efficiency and redundancy. The choice of ILD is a combination of gaseous tracking, giving a large number of hits, and the redundancy this gives, with a sophisticated system of silicon based tracking disks and barrels. Together the system achieves excellent resolution, and covers the solid angle down to the very forward region.

An important consideration is the ability of the system to be calibrated to the desired precision. Here the combination of gaseous and silicon based tracking offers some unique advantages due to the very different nature of possible systematic distortions, and due to the possibility to cross-calibrate the different systems. For example, the Silicon tracker will help in monitoring possible field distortions in the TPC, as well as contributing to alignment and time stamping (bunch tagging). Silicon tracking is relatively easy to calibrate and as such it is expected to provide robustness, redundancy, and ease in the calibration of the overall tracking system.

The silicon tracking system of the ILD has been developed by the SiLC collaboration. Detailed descriptions of the wide ranging R&D activities conducted within the SiLC collaboration can be found in the latest documents and presentations issued by the SiLC Collaboration, and references therein [71, 72, 73, 74, 75, 76].

4.2.1 Baseline Design of the Silicon Trackers

Combined with the Silicon vertex detector and the central gaseous tracker TPC, a Silicon Tracking system is proposed for the ILD. It is based on modern Silicon detector technology, deep sub micron CMOS technology for the front-end (FE) electronics with a new on-detector electronics connection and new material technology for the support architecture. Special challenges for the ILD are a significant reduction in material compared to the most recent examples of large scale silicon detectors (*e.g.* LHC detectors), operating at very low power, and reaching excellent point resolution and calibration. The Silicon tracker is made of two sets of detectors:

- The first set is located in the central barrel and is made of the SIT (Silicon Internal Tracker), and the SET (Silicon External Tracker). Both devices have false double-sided Silicon strip detectors, together providing three precision space points.
- The second set is located in the forward region and is constituted of the FTD (Forward Tracking Detector) in the very forward region, and the ETD (end cap Tracking Detector), providing a space point between the TPC endplate and the calorimeter in the endcap region.

The complete silicon tracking system is implemented in the MOKKA simulation of the ILD, including estimates of support structures.

4.2.1.1 The Silicon Tracker in the Barrel: SET and SIT

The SIT is positioned in the radial gap between the vertex detector and the TPC. The role of the SIT is to improve the linking efficiency between the vertex detector and the TPC; it

improves the momentum resolution and the reconstruction of low p_T charged particles and improves the reconstruction of long lived stable particles.

The SET is located in the barrel part between the TPC and the central barrel electromagnetic calorimeter (ECAL). The SET gives an entry point to the ECAL after the TPC end wall (3% X_0). It acts as the third Silicon layer in the central barrel and also improves the overall momentum resolution. The SIT and SET, in addition to improving momentum resolution (Fig. 4.2-3), provide time-stamping information for separation between the bunches and thus allowing the bunch-tagging of each event. These two central Silicon components may serve in monitoring the distortion of the TPC and for the alignment of the overall tracking.

4.2.1.2 The Endcap and Forward Silicon Tracking: ETD and FTD

The FTD is positioned in the innermost part of the tracking region, and covers the very forward region down to about 0.15 radians. In total seven disks are foreseen in this region.

The ETD is positioned between the TPC end cap and the end cap calorimeter system. The role of the ETD is to serve as entry point for the calorimeter and to improve the momentum resolution for the charged tracks with a reduced path in the TPC. Moreover it helps reducing the effect of the material of the TPC End Plates (currently estimated to be 15% X_0). It thus might improves the matching efficiency between the TPC tracks and the shower clusters in the EM calorimeter. It also contributes to extending the lever arm and angular coverage of the overall tracking system at large angle. Both the ETD and the FTD ensure the full tracking hermeticity.

4.2.2 Performances of the Silicon tracking system

The main detector performances of the Silicon tracking ILD system are summarized in terms of its contribution to i) full angular coverage, ii) momentum and impact parameter resolution, iii) calibration of distortions, iv) alignment, v) time stamping (bunch tagging), and vi) redundancy and robustness of the overall tracking system. Full simulation studies are being performed in order to best understand the performances of the Silicon tracking system in terms of momentum and spatial reconstruction and pattern reconstruction. These detailed simulations are completing the already available performance studies based on fast simulation (LiC Detector Toy Monte Carlo "LDT" and SGV) [71].

4.2.2.1 Angular Coverage

Combining the Silicon components with the vertex detector and the TPC ensures efficient tracking over the full angular coverage down to very small angles close to the beam. It helps in crucial regions such as: i) the transition from the central barrel to the End Cap region, ii) the end cap regions and iii) the very forward regions (Fig. 4.2-2).

4.2.2.2 Momentum and Impact Parameters Performances

To demonstrate the contribution of the various Si tracking components to the improvement of the overall tracking performances in terms of momentum and impact parameter resolution, a number of studies have been performed based on both fast simulation and the MOKKA-Marlin and GEANT 4 simulation. Some of the most relevant results (evaluation using fast Monte Carlo, muon tracking) are shown in Figure 4.2-3.

SIT characteristics (current baseline = false double-sided Si microstrips)					
Geometry			Characteristics		Material
R[mm]	Z[mm]	cosθ	Resolution R-ϕ[μm]	Time [ns]	RL[%]
165	371	0.910	R: σ=7.0,	307.7 (153.8)	0.65
309	645	0.902	z: σ=50.0	σ=80.0	0.65
SET characteristics (current baseline = false double-sided Si microstrips)					
Geometry			Characteristics		Material
R[mm]	Z[mm]	cosθ	Resolution R-ϕ[μm]	Time [ns]	RL[%]
1833	2350	0.789	R: σ=7.0,	307.7 (153.8)	0.65
1835	2350	0.789	z: σ=50.0	σ=80.0	0.65
FTD characteristics (current baseline = pixels for first 3 disks, microstrips for the other 4))					
Geometry			Characteristics		Material
R[mm]	Z[mm]	cosθ	Resolution R-ϕ[μm]		RL[%]
39-164	220	0.985-0.802			0.25
49.6-164	371.3	0.991-0.914			0.25
70.1-308	644.9	0.994-0.902			0.25
100.3-309	1046.1	0.994-0.959	σ=7.0		0.65
130.4-309	1447.3	0.995-0.998			0.65
160.5-309	1848.5	0.996-0.986			0.65
190.5-309	2250	0.996-0.990			0.65
ETD characteristics (current baseline = single-sided Si micro-strips, same as SET ones)					
Geometry			Characteristics		Material
R[mm]	Z[mm]	cosθ	Resolution R-ϕ[μm]		RL[%]
419.3-1822.7	2426	0.985-0.799	x:σ=7.0		0.65
419.3-1822.7	2428	0.985-0.799	y:σ=7.0		0.65
419.3-1822.7	2430	0.985-0.799	z:σ=7.0		0.65

TABLE 4.2-3
The projected values of basic SIT, SET, FTD, and ETD characteristics.

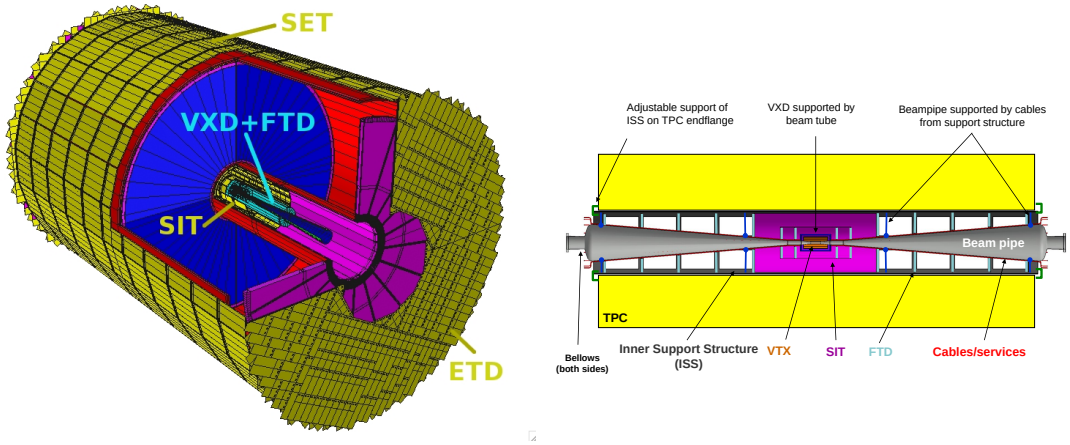

FIGURE 4.2-2. Silicon tracking components as described in the Table 4.2-3 (GEANT 4-based simulation). The plot on the right shows a side-view of the inner silicon tracking system, including the support structure.

For tracks in the barrel region the present combined Silicon and TPC tracking system delivers an outstanding momentum resolution of $\sigma(\Delta p_T/p_T^2) < 2 \cdot 10^{-5}$ GeV as shown in Fig. 4.2-3(left). The plots compare four different arrangements: the ILD setup as described above (blue), a setup without the inner tracker SIT (red), a setup without the external tracker

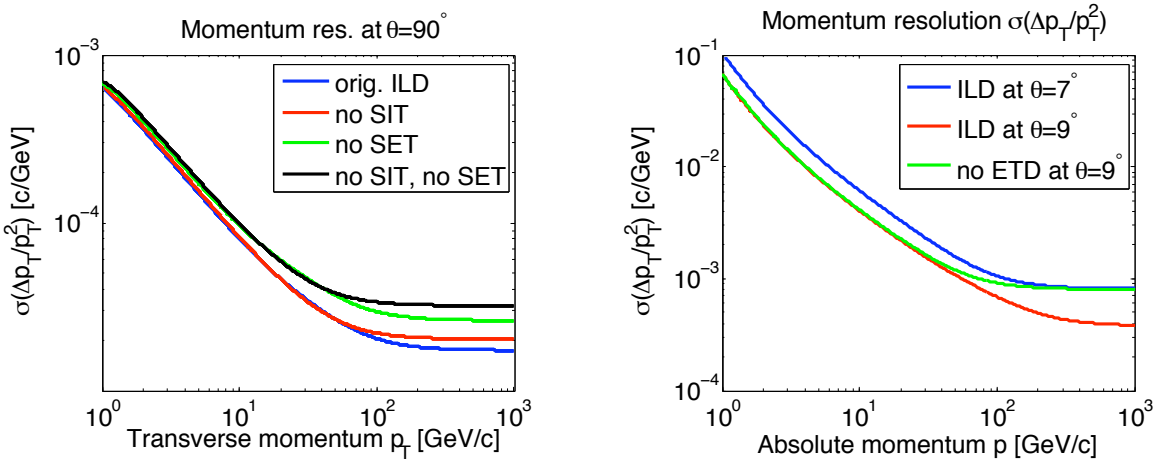

FIGURE 4.2-3. Left plot: barrel region, transverse momentum reduced resolution as function of p_T. Right plot: forward region, transverse momentum reduced resolution as function of absolute momentum p. The different scenarios are described in the text.

	VTX ($3 \times 3\mu m^2$)	VTX ($5 \times 5\mu m^2$)	VTX ($3 \times 3\mu m^2$) + SIT ($5 \times 10\mu m^2$)	VTX ($3 \times 3\mu m^2$) + SET ($5 \times 50\mu m^2$)
σ(R-ϕ)@ R = 150cm	1.3 cm	2.2 cm	0.6 mm	78 μm
σ(z)@ R = 50cm	35 μm	60 μm	16 μm	28 μm
σ(z)@ R = 100cm	77 μm	126 μm	39 μm	30 μm
σ(z)@ R = 118cm	118 μm	192 μm	50 μm	39 μm

TABLE 4.2-4
The precision of the extrapolated R-ϕ and z-coordinates for a 100 GeV track at $\theta = 90°$, at three radii in the TPC volume.

SET (green), and a setup without SIT and SET (black).

Figure 4.2-3(right) shows the momentum resolution for very forward going tracks, for three different angular ranges. While the addition of the silicon tracking system improves the momentum resolution, the impact parameter resolution remains virtually unchanged.

Table 4.2-4 offers an alternative illustration to the improvement generated by both SIT and SET on spatial resolution.

4.2.2.3 Distortion Monitoring and Handling

The Silicon trackers are mechanically stable devices which will help improve the absolute alignment of the overall tracking system, and of the ILD as a whole. This alignment is sensitive in particular to temperature fluctuations, which will need to be understood to the 2 μm level. These alignment systematics will be very different from the TPC ones. The TPC is sensitive to ambient temperature and to atmospheric pressure variations, to non-homogeneities in E and B fields, etc. In particular the E drift field in the TPC may depend on space charge transient effects due to variations in the machine backgrounds. The SIT and SET give an independent and effective means to monitor accurately such effects on real data. Experience at LEP has shown that this capability gives an invaluable redundancy during data analysis, and a unique mean to disentangle and understand anomalous behaviours. It is a necessary complement to the unique pattern recognition capabilities of the TPC.

4.2.2.4 Electronic Time Stamping

Based on the performances of the front end (FE) chip currently developed, currently a bunch crossing tagging with a precision of 160 ns can be obtained corresponding to a shaping time around 0.5-0.7 μs and 8 sampling cells. This precision depends on the sampling frequency. A more refined estimate based on the Cleland and Stern algorithm [77], and function of the signal to noise, the number of samples, and the shaping time, indicates that the currently developed framework could allow identifying the bunch crossing with a resolution of order of 20 to 40 ns.

4.2.3 Calibration Procedures

The Front End Electronics as currently available in the current 130nm CMOS technology includes a full readout electronic chain with a high level digital control of the functionality of the overall chip. In particular a fully programmable test pulse system is included. It will allow calibrating and monitoring of this signal processing device and play a crucial role in the silicon DAQ.

Environmental conditions around the detector due to local temperature gradients, humidity changes, etc. will induce some instability of the support structures comparable in size to the precision of the detectors. Consequently, independent alignment systems monitoring these changes will be needed. For the case of silicon trackers one can profit from the weak (but non-zero) absorption of infrared light in Silicon and use laser beams as pseudo-tracks that traverse consecutive sensors.

For the SIT and FTD subdetectors, which have several Silicon layers, the alignment procedure is based on the use of their own tracking detectors as photo-sensors; the transmittance of Silicon to infrared beams compared to the existing AMS and CMS tracker systems can be improved by a further 20-30%, leading to a transmittance value between 70 to 80%. Resolutions on the order of 2 microns can be obtained with this procedure [78].

The SET and ETD are single layer detectors; the SET can be aligned with respect to fiducial marks on the outer cage of the TPC at the level of 100 microns by standard procedures. The monitoring of the SIT position could be done one order of magnitude better [79]. Similar procedures can be done for the ETD. Finally, tracks will be used for internal alignment at the precision level of few microns, by using adequate χ^2 minimisation algorithms already employed in the LHC and other experiments.

4.2.4 Silicon Tracker Material Budget

A crucial concern of the design of the silicon tracking system has been to minimise the material budget. New silicon sensors and modern material technology based on carbon fibre composite materials (CFC) provide optimal solutions for the silicon tracking components. New front end electronics based on DSM CMOS feature less power dissipation (see already achieved performance of the newly developed FE chip) and allow a direct connection onto the detector, thus removing the need for cooling. All these facts allow a reduction of the sensitive thickness of the sensors to at least 250 μm, or 0.25% X_0. Engineering studies have shown that a support structure for the envisioned silicon detectors equivalent to a 1 mm thick CFC layer are possible, corresponding to a contribution of 0.4%X_0 per layer. Together with services etc a thickness of 0.65% X_0 per layer seems in reach (see table 4.2-3). The final goal

is 0.5% RL per layer in the innermost part of the detector, which will need further R&D. A further reduction might be possible if new sensor and support technologies become available.

4.2.5 Baseline construction and Integration of Silicon components

The baseline design to construct the ILD Silicon system is an unified design for all the components apart from the very small FTD disks. The SIT, SET and ETD components will be made of Silicon strip sensors with a unique sensor type. The current baseline are sensors of square shape from a 6″ wafer, 200μm thick, 50μm readout pitch (true pitch of 25μm). The modules will be made of one up to a few sensors depending on the location of the module in the detector. The readout chip will be directly connected onto the sensor. The chip will be made in deep sub-micron technology (current prototypes are in 130nm technology), most probably in 90 nm. It is a mixed analogue-digital FE and readout chip with a full processing of the analogue signal, long shaping time (1μs), sparsification, digitisation and a high level of digital processing allowing full programmability of the chip. A full prototype is presently developed [80]. The power dissipation of at most 1m W per channel is achieved and power cycling is included. The goal is to avoid a dedicated liquid cooling system, but instead to rely on a forced gas cooling as is also considered for the VTX and the TPC systems. Details of this however are not yet worked out.

The integration of the silicon tracking components depends critically on the neigbbouring detectors. The SET will be made of 24×2 identical super-modules, each covering 2.35×0.5 m^2 supported by a light structure made from composite material. The support structure will be supported from the TPC end-flange, and might also rest at intermediate z-positions on the TPC field cage. The two SIT layers will be made in the same way as the SET, namely 18 and 12 super-modules for the external and the innermost layers, respectively. Together with the outer four FTD disks the SIT layers will be supported by a CFC support structure, fixed to the TPC end-flange at their inner radius. The ETD, thanks to its XUV geometry is built in the same way as the barrel components and will be fixed to the electromagnetic end cap calorimeter.

The support architecture of SIT, SET and ETD will be designed in the same way focusing on robust, very light and easy to mount structures. The design for the FTD disks is currently based on pixels (same type as the vertex detector) for the first three disks and false double sided strips for the other four disks. These four disks will be made of trapezoidal sensors and altogether 16 petals as in the present ATLAS forward detector.

4.2.6 R&D needs and prospects for Silicon tracking

The Silicon technology for large-area tracking systems will continue to evolve over the next years because of the stringent needs of the Large Collider experiments (LHC upgrades, ILC and CLIC). The SiLC R&D collaboration takes an active part in these worldwide efforts dedicated to novel and high technology. The group will continue to develop novel sensors. Options include, as a first step, the edgeless planar micro-strip sensors followed by the 3D planar micro-strips sensors. The goal is to have thinner, lower voltage biased strip sensors and larger wafer size (8″). In addition, the application of pixel technology to at least dedicated regions of the Silicon tracking, including 3D based pixel technology is part of this R&D objective. The ongoing development of Front End and readout electronics based on ASICs in very deep sub micron CMOS technology, with a high degree of processing of digital information on the detector, low noise, low power consumption, robustness (redundancy

and fault tolerance), will be further pursued. New interconnection technologies of the ASIC directly onto the sensors by bump bonding and then by 3D vertical interconnect as well as new cabling techniques will be addressed. Challenging aspects on mechanics in order to build light, robust, and large area mechanical structures, with stringent mechanical constraints on alignment, stability (ex: push pull) and quality control will impact the final design and construction of these devices. A reduced material budget resulting in improved tracking performance, robustness, reliability, easy to build (and not expensive) are the main goals of this ambitious R&D program [71].

4.3 THE TIME PROJECTION CHAMBER

4.3.1 Motivation

The subdetectors for the linear collider detector must be designed coherently to cover all possible physics channels because their roles in reconstructing these channels are highly interconnected. Two important aspects for tracking are, (a) precision-physics measurements require that the momentum of charged tracks be measured an order of magnitude more precisely than in previous experiments, and (b) high resolution measurements of the jet-energy using the particle-flow technique require efficient reconstruction of individual particles within dense jets. Aspects (a) and (b) for the ILD detector are demonstrated in Section 3.2.1 and 3.2.4. of this document.

A TPC as the main tracker in a linear collider experiment offers several advantages. Tracks can be measured with a large number of three-dimensional $r\phi$,z space points. The point resolution, σ_{point}, and double-hit resolution, which are moderate when compared to silicon detectors, are compensated by continuous tracking. The TPC presents a minimum amount of material X_0 as required for the best calorimeter performance. A low material budget also minimizes the effect due to the $\sim 10^3$ beamstrahlung photons per bunch-crossing which traverse the barrel region. Topological time-stamping in conjunction with inner silicon detectors is precise to $\sim$2 ns so that tracks from interactions at different bunch-crossings or from cosmics can readily be distinguished. To obtain good momentum resolution and to suppress backgrounds, the detector will be situated in a strong magnetic field of several Tesla, for which the TPC is well suited since the electrons drift parallel to $\vec{\mathrm{B}}$. The strong B-field improves σ_{point} and the two-hit resolution by compressing the transverse diffusion of the drifting electrons to $\mathcal{O}(1$ mm) [81].

Continuous tracking facilitates reconstruction of non-pointing tracks, e.g. from V^0s or certain Susy (GMSB) channels, which are significant for the particle-flow measurement and in the reconstruction of physics signatures in many standard-model-and-beyond scenarios. The TPC gives good particle identification via the specific energy loss dE/dx which is valuable for the majority of physics analyses and for electron identification. The TPC will be designed to be robust while easy to maintain so that an endcap readout module can readily be accessed if repair is needed.

A Time Projection Chamber (TPC) is chosen for the central tracker because of its demonstrated performance in past collider experiments [82]. The main design issues at the linear collider are covered in Section 4.3.2. In Section 4.3.3, the R&D by the LCTPC groups[83, 84] to determine the best state-of-the-art technology for the TPC is described.

4.3.2 Design

There are important, and interconnected, design issues related to the performance, endcap, electronics, fieldcage, robustness in backgrounds, corrections and alignment. Since methods of investigating these issues have been established from past operational experience, the LCTPC groups have been actively investigating all aspects since 2001.

4.3.2.1 Performance

Main goals for the TPC performance at the linear collider are given in Table 4.3-5. Understanding the properties and achieving the best possible point resolution have been the object of R&D studies of Micro-Pattern Gas Detectors (MPGD), MicroMegas[85] and GEM[86] (Section 4.3.3), and results from this work are reflected in Table 4.3-5. More details about the issues are explained in the following paragraphs.

TABLE 4.3-5
Goals for performance and design parameters for an LCTPC with standard electronics.

Size	$\phi = 3.6$m, L = 4.3m outside dimensions
Momentum resolution (3.5T)	$\delta(1/p_t) \sim 9 \times 10^{-5}$/GeV/c TPC only ($\times$ 0.4 if IP incl.)
Momentum resolution (3.5T)	$\delta(1/p_t) \sim 2 \times 10^{-5}$/GeV/c (SET+TPC+SIT+VTX)
Solid angle coverage	Up to $\cos\theta \simeq 0.98$ (10 pad rows)
TPC material budget	$\sim 0.04 X_0$ to outer fieldcage in r
	$\sim 0.15 X_0$ for readout endcaps in z
Number of pads/timebuckets	$\sim 1{\times}10^6/1000$ per endcap
Pad size/no.padrows	$\sim$ 1mm$\times$4–6mm/$\sim$200 (standard readout)
σ_{point} in $r\phi$	$< 100\mu$m (average over $L_{sensitive}$, modulo track ϕ angle)
σ_{point} in rz	$\sim$ 0.5 mm (modulo track θ angle)
2-hit resolution in $r\phi$	$\sim$ 2 mm (modulo track angles)
2-hit resolution in rz	$\sim$ 6 mm (modulo track angles)
dE/dx resolution	$\sim$ 5 %
Performance	$>$ 97% efficiency for TPC only ($p_t >$ 1GeV/c), and
	$>$ 99% all tracking ($p_t >$ 1GeV/c) [87]
Background robustness	Full efficiency with 1% occupancy,
	simulated for example in Fig. 4.3-4(right)
Background safety factor	Chamber will be prepared for 10 $\times$ worse backgrounds
	at the linear collider start-up

4.3.2.2 Endcap

The two TPC endcaps will have an area of 10 m^2 each. The readout pads, their size, geometry and connection to the electronics and the cooling of the electronics, are all highly

correlated design tasks. The material of the endcap and its effect on ECAL for the particle-flow measurement in the forward direction must be minimized, and the goal is to keep it below 15%X_0. Designing for the finest possible granularity will minimize the occupancy arising from the TPC drifttime integrating over about 100 bunch-crossings[88]. The sensitive volume will consist of several$\times 10^9$ 3D-electronic standard-readout voxels (two orders of magnitude more than at LEP) or 10^{12} voxels in case of pixel readout. Development of the layout of the endcaps, i.e. conceptual design, stiffness, division into sectors and dead space, has started, and first ideas are shown below (Section 4.3.3).

4.3.2.3 Electronics

For the readout electronics, one of the important questions is the density of pads that can be accommodated while maintaining a stiff, thin, coolable endcap. The options being studied are (A) standard readout of several million pads or (B) pixel readout of a thousand times more pads using CMOS techniques. Table 4.3-5 assumes standard readout electronics; a similar table for pixel electronics will be made when the R&D is further advanced [83] [84]. A basic ingredient for the front-end electronics will be the use of power-pulsing which is possible due to the bunch-train time structure and is assumed to give a power reduction of order 100; what can be achieved in practice is an important R&D issue (Section 4.3.3).
(A) Standard readout:
Small pads, $\sim$ 1mm$\times$5mm, have been found to provide good resolution from the R&D work and to guarantee the low occupancy in Table 4.3-5. Studies have started to establish the realistic density of pads that can be achieved on the endcap. A preliminary look at the FADC approach (à la Alice[89][90]) using 130 nm technology indicates that even smaller sizes might be feasible. An alternative to the FADC-type is the TDC approach (see [84][90]) in which time of arrival and charge per pulse by time-to-charge conversion are measured. In preparation for the possibility that the material budget requires larger pads, the resistive-anode charge-dispersion readout technique[91] is being studied as an option to maintain the good point resolution. Since this technique could compromise the two-track resolution, more R&D is required.
(B) CMOS pixel readout:
A new concept for the combined gas amplification and readout is under development [84][92]. In this concept the "standard" MPGD is produced in wafer post-processing technology on top of a CMOS pixel readout chip, thus forming a thin integrated device of an amplifying grid and a very high granularity endcap with all necessary readout electronics incorporated. For a readout chip with $\sim 50\mu$m pixel size, this would result in $\sim 2 \cdot 10^9$ pads ($\sim 4 \cdot 10^4$ chips) per endcap. This concept offers the possibility of pad sizes small enough to observe the individual primary electrons formed in the gas and to count the number of ionisation clusters per unit track length, instead of measuring the integrated charge collected. The R&D program (Section 4.3.3) will determine on what time scale this technology will become feasible for a large TPC[83].

4.3.2.4 Fieldcage

The design of the inner and outer fieldcages involves the geometry of the potential rings, the resistor chains, the central HV-membrane, the gas container and a laser system. These must be laid out to sustain at least 100kV at the HV-membrane with a minimum of material. The goals for the inner and outer fieldcage thicknesses are about 1%X_0 and 3%X_0, respectively,

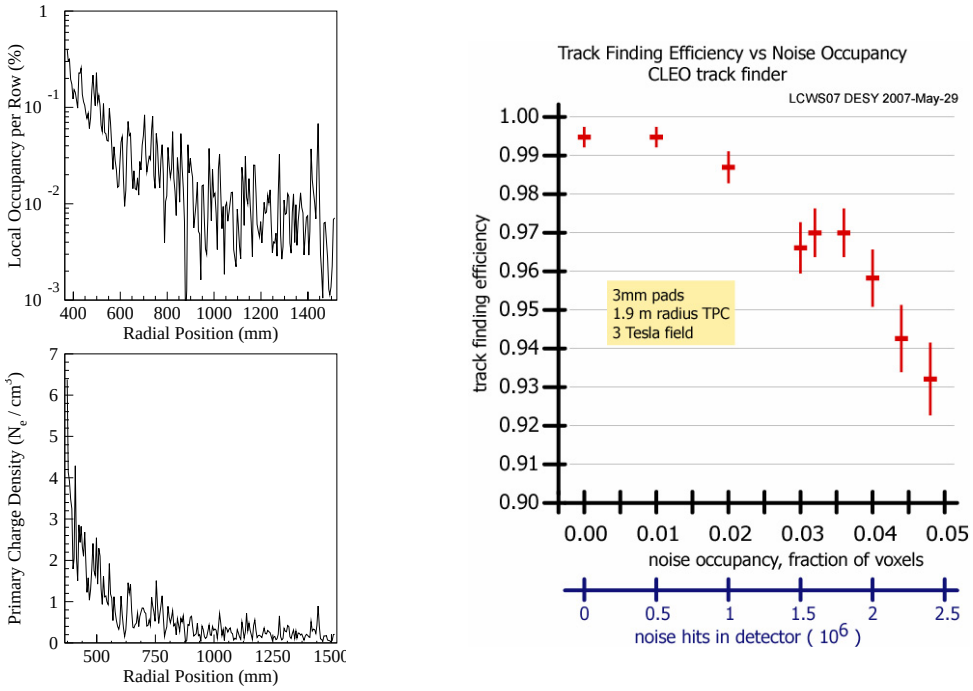

FIGURE 4.3-4. Occupancy for xyz $= 1 \times 5 \times 5\text{mm}^3$ voxels (left, top) and space charge(left, bottom) due to the major beam-beam effects (beamstrahlung photons, electron-positron pairs and neutrons) as simulated in [88]. Study of the tracking efficiency in the presence of backgrounds (right); this study [94] assumed a conservative voxel size of $3 \times 10 \times 40\text{mm}^3$.

while the chamber gas adds another $1\%X_0$. For alignment purposes the laser system is foreseen and may be integrated into the fieldcage [89][93]. The non-uniformities due to the fieldcage design and fabrication can be minimized using the experience gained in past TPCs.

4.3.2.5 Backgrounds and robustness

The issues are the space-charge, covered in the next item below, and the track-finding efficiency in the presence of backgrounds which will be discussed here. There are backgrounds from the collider, from cosmics or other sources and from physics events. The main source is the collider, which gives rise to gammas, neutrons and charged particles due to $\gamma\gamma$ interactions and beam-halo muons being deposited in the TPC at each bunch-crossing [83]. Simulations of the main sources [88] arising from beam-beam effects–gammas, pairs and neutrons–under nominal conditions indicate an average occupancy of the TPC of less than 0.1%, Fig. 4.3-4 (left). The TPC track finding remains robust at these occupancies; the continuous 3D-granularity tracking is inherently simple and suffers no loss in efficiency even with a uniform 1% noise occupancy as demonstrated by the study in Figure 4.3-4(right). Note that the latter study was performed for a slightly different TPC design than the one adopted by ILD. The study was based on a TPC with a radius of 1.9m, readout cells of $3 \times 10\text{mm}^2$ immersed in a 3T magnetic field. A uniform distribution of hits was assumed, and a very detailed simulation of the signal development and digitisation was performed. The 1% uniform noise occupancy mentioned above is about twice the beam-related occupancy in Figure 4.3-4(left) at the TPC inner radius and about fifty times the total occupancy in the TPC.

Since the backgrounds at the beginning of operation could be much larger until the linear collider machine is well understood, the LCTPC is preparing for an occupancy of 10%.

4.3.2.6 Corrections for non-uniform fields

Both fields, (A) magnetic and (B) electric, can have non-uniformities which must be corrected. The (C) chamber gas will play a crucial role in minimizing corrections.

(A) Magnetic field

Non-uniformity of the magnetic field of the solenoid will be by design within the tolerance of $\int_{\ell_{\rm drift}} \frac{B_r}{B_z} dz < 2-10$mm as used for previous TPCs. This homogeneity is achieved by corrector windings at the ends of the solenoid. At the ILC, larger gradients will arise from the fields of the DID (Detector Integrated Dipole) or anti-DID, which are options for handling the beams inside the detector at an IR with ±7 mrad crossing-angle. This issue was studied intensively and summarized in [95], where it is concluded that the TPC performance will not be degraded if the B-field is mapped to around 10^{-4} relative accuracy and the procedures outlined below (under **Alignment**) are followed. These procedures will lead to an overall systematic error due to the field components of ~ 30 μm over the whole chamber which has been shown to be sufficient [95] and was already achieved by the Aleph TPC. Based on past experience, the field-mapping gear and methods will be able to accomplish the goal of 10^{-4} for the relative accuracy. The B-field should also be monitored during running since the currents in the DID or corrector windings may differ from the configurations mapped.

(B) Electric field

Three sources of space charge are (*i*) primary ion build-up in the drift volume, (*ii*) ion build-up at the readout plane and (*iii*) ion backdrift, where ions created at the readout plane could drift back into the TPC volume.

(*i*) Primary ion build-up in the drift volume. An irreducible positive-ion density due to the primary ionisation collected during about 1s (the time it takes for an ion to drift the full length of the TPC) will be present in the drift volume. The positive-ion density will be higher near the cathode, where the local volume integrates over backgrounds from up-to-five bunch trains, and using Fig. 4.3-4(middle)[1], the charge will reach ∼1 fC/cm^3 at the inner fieldcage and ∼0.02 fC/cm^3 at the outer fieldcage. The effect of the charge density will be established by the R&D program, but the experience of the STAR TPC [93] indicates that 100 fC/cm^3 is tolerable[83] and is two orders of magnitude larger than expected for the LCTPC.

(*ii*) Ion build-up at the readout plane. At the surface of the gas-amplification plane during an ILC bunch train of about 3000 bunch crossings spanning 1 ms, there will be few-mm sheet layer of positive ions built up due to the gas amplification of the incoming charge followed by ion backflow. An important property of MPGDs is that they suppress naturally the backflow of ions produced in the amplification stage; studies show that this backflow can be reduced to about 0.25% [83]. Using the results from Fig. 4.3-4 (middle), this layer of readout-plane ions will attain a density of $\mathcal{O}(80)$ fC/cm^3 at the inner radius and $\mathcal{O}(2)$ fC/cm^3 at the outer radius of the TPC. Its effect will be simulated, but it should affect coordinate measurement only by a small amount since the incoming drift electrons experience this environment during only the last few mm of drift. The TPC must plan to run with the lowest possible gas gain, meaning of order $\sim 2 \times 10^3$ or less, in order to minimize this effect.

[1]The numbers in the text derived from this figure have been multiplied by a safety factor of two to account for other sources of backgrounds.

(*iii*) Ion backdrift and gating. The ion buildup described in (*ii*) will drift as an "ion sheet" back through the TPC volume unless eliminated by a gating plane. In the drift volume, an ion sheet would be followed by sufficient drift distance to result in track distortions. Thus an intra-train gate is foreseen to guarantee a stable and robust chamber operation. The ILC bunch train structure requires an open-gate operation, without intra-train gating between bunch crossings, to optimally utilize the delivered luminosity. The gate will remain open throughout one full train and be closed between bunch trains. As the ion drift velocity is much less than that of the electrons, the gate timing allows collection of all of the ions. The added amount of material for a gating plane will be small (e.g., $< 0.5\%\mathrm{X}_0$ was the average thickness for the Aleph TPC gate).

(C) Chamber gas
The choice of the gas for the LCTPC is crucial for efficient and stable operation at the linear collider[81]. The σ_{point} resolution achievable in $r\phi$ is dominated by the transverse diffusion, which should be as small as possible; this implies that $\omega\tau$ for the gas should be large so that the transverse diffusion is compressed by the B-field. Large $\omega\tau$ means that the drifting electrons follow the B-field, for which there is a program to measure well[95], and has the added advantage of making the chamber less sensitive to space-charge effects and other sources of electric field non-uniformities. Simultaneously a sufficient number of ionisation electrons should be created for the position and dE/dx measurements. The drift velocity at a drift field of at most a few times 100 V/cm should be around 5–10 cm/μs to limit the central cathode voltage and the event overlap. The choice of operating voltage must also take into account the stability of the drift velocity due to fluctuations in temperature and pressure.

4.3.2.7 Alignment

Achieving a momentum resolution an order of magnitude better than any of the collider detectors to date will be a challenge. The systematics of alignment of tracking subdetectors must be well thought through from the beginning to guarantee the integrity of tracking over a radius of two meters. Redundant tools for solving this issue are Z-peak running, the laser system, the B-field map as described in [95] and monitored by a matrix of Hall-plates/NMR-probes outside the TPC, and Si-layers inside the inner fieldcage and outside the outer fieldcage. In general based on experience at LEP[96], about 10 pb^{-1} of data at the Z peak are requested during commissioning for the alignment of the different subdetectors, and typically 1 pb^{-1} during the year may be needed depending on the backgound and operation of the linear collider machine (e.g., after push-pull or beam loss).

The strategy learned at LEP for aligning the tracking subdetectors is also applicable for the ILD. Needed to start with are: a common alignment software package for all subdetectors, the fabrication tolerances for each subdetector $\simeq$ 10–20μm internal and $\simeq$ 0.1–0.2mm external (with respect to the other subdetectors) and the B-field mapped to the requirements outlined in [95]. Then the steps are: first pass through a subset of data (hadronic tracks or μ pairs from Z-peak or from $\sqrt{s}$ running), each tracking detector is aligned internally; second pass, the tracking subdetectors are lined up with respect to one another using a subset of data; finally the preceeding two steps are iterated until the correct momentum for $Z \to \mu\mu$ events

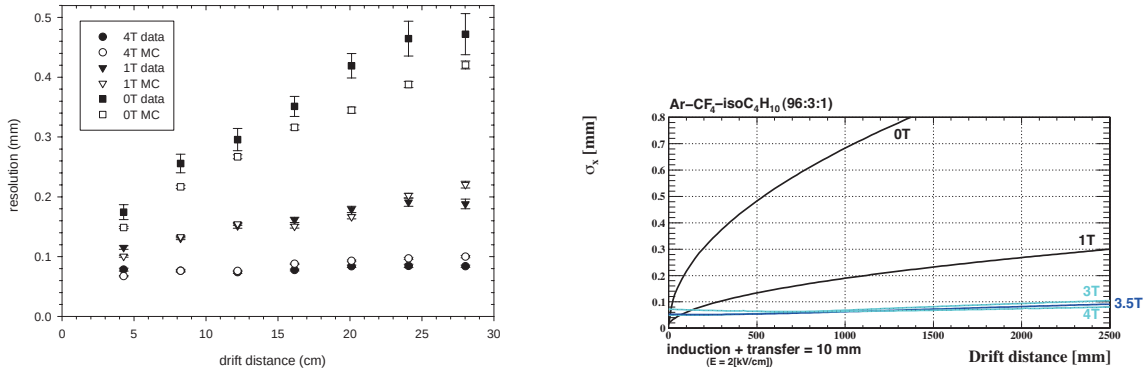

FIGURE 4.3-5. (left): Example of resolution results from a small prototype [97] measurements with TDR gas, $ArCH_4CO_2$ (95-3-2); other candidate gases are e.g. P5 and $ArCF_4$Isobutane. (Right): Theoretical resolution for $ArCF_4$Isobutane (96-3-1) gas (right), based on an algorithm [84] verified during SP studies.

is achieved.

4.3.3 R&D Effort for the LCTPC

All of the issues affecting the TPC performance are being addressed by the R&D program; a recent status report with extensive references to past and on-going work is contained in [84]. As described in the LCTPC-Collaboration MoA, the R&D is proceeding in three phases: (1) Small Prototypes (SP), (2) Large Prototypes (LP), and (3) Design.

Up to now during Phase(1), about 6 years of MPGD experience has been gathered, gas properties have been well measured, the best achievable point resolution is understood, the resistive-anode charge-dispersion technique has been demonstrated, CMOS pixel RO technology has been demonstrated, the proof of principle of TDC-based electronics has been shown and commissioning has started for the LP.

The Phase(2) LP and SP work is expected to take another two–three years. Regular bi-weekly WP phone meetings started in May 2006 where details for the LP design were worked out and next R&D steps developed. The LP commissioning is well advanced as evidenced by Fig. 4.3-5(left), while the fruits of the SP work resulting in the expected resolution are shown in Fig. 4.3-5(center) and Fig. 4.3-5(right).

The following list gives an overview of the currently envisioned timeline for completing the studies and the construction of the ILD TPC.

• 2009-12: Continue R&D on technologies at LP, SP, pursue simulations, verify performance goals (details are available in [84]).

• 2009-11: Plan and do R&D on advanced endcap; power-pulsing, electronics and mechanics are critical issues.

• 2011-12: Test advanced-endcap prototype at high energy and power-pulsing in high B-field.

• 2012-18: Design and build the LCTPC.

Construction of endplates that satisfy the material requirements of the ILD, as well as the structural requirements of the TPC, will require extensive R&D.

This work has started with first ideas having been developed in a series of "advanced-endcap" meetings during the past year. Examples are presented in Fig. 4.3-6, and the groups agree that there will be an evolution of endcaps towards a true prototype for the LCTPC.

During the R&D period 2009-2011, engineering studies of detailed computer models of advanced endplate designs will be performed. The models will be evaluated relative to the requirements of material limits and distribution, space limits, rigidity in response to applied

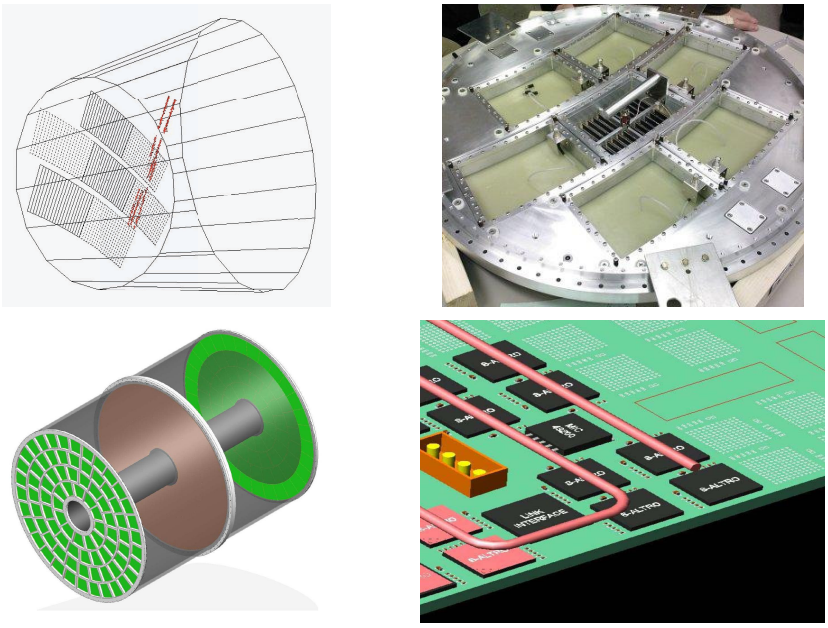

FIGURE 4.3-6. (Top left): Event display from the LP beam tests. (Top right) View of the Endcap subdivision as used for the Large Prototype. (Bottom left)Conceptual design of enplate for LCTPC. (Bottom right) Possible layout of PCB, electronics and cooling for the LCTPC.

forces, manufacturing complexity and manufacturing precision. Possible endcap designs fall into two general groups. The first group is the evolution of a traditional machined endplate, as used in the first endcap of the LP, Fig. 4.3-6 (left), but with significant use of lighter materials; in addition, unnecessary material must be removed from the machined structure. The second group is the simulation of true space-frame designs which can be constructed utilizing various techniques, e.g., fully machined, bonded composites and assembly of individual components.

During the period 2011-2012, further study of designs that were successful as computer models will follow. Several prototypes of the advanced endplate will be manufactured; both scale-models (20-50% full size) and sections of the full size endplate will be used to evaluate the manufacturing integrity and uncover sources of loss of precision or rigidity in the design. Finite element analysis will be used to predict the strength of the full size endplate; this analysis will be calibrated by comparison with measurements on the prototypes.

At the beginning of the period 2012-18, the selection must be made from the different technological options – GEM, MicroMegas, resistive anode, pixel, electronics, endcap structure – to establish a working model for the design of the LCTPC. This design will be used for the ILD proposal in 2012 and include pad segmentation, electronics, mechanics, cooling and integration, so that performance, timeline and cost can be estimated reliably.

For the technology selection, a scenario could be that questions must be answered as to which options give the best performance based on R&D results from LP, SP, electronics and endcap studies. Main performance criteria could be endcap thickness and σ_{point}, double-hit and momentum resolution for single tracks and for tracks in a jet environment. Choice of criteria to use will be decided over the next two years.

Finally, as to the $\sqrt{s}$ coverage, simulations in Chapter 2 of this LOI have shown that, with the performance goals in Table 4.3-5, the LCTPC will give good performance up to and well beyond 1 TeV.

4.4 THE CALORIMETER SYSTEM

4.4.1 Introduction to calorimeters

Tagging of electroweak gauge bosons at the ILC, based on di-jet mass reconstruction, makes the reconstruction of multijet events a major goal for detectors at the ILC. The particle flow approach (see e.g. [98]), which consists of individual particle reconstruction dictates many fundamental aspects of the calorimeter design, most notably the requirement for very fine transverse and longitudinal segmentation of the calorimeters, as studied in Section 2.2. It has to be noted that a highly granular calorimeter, optimised for PFA, leads also to a way to have a very efficient software compensation, as it is shown in 4.4.4.2. The choice of technology for the ECAL and HCAL are driven by the requirements of pattern recognition more than the intrinsic single particle energy resolution, although the latter is still an important consideration.

Several technologies for electromagnetic and hadronic calorimeters are being pursued, with a number of prototypes in test beams. Next generation prototypes are being constructed with dimensions and integration issues very close to those of final ILD detector modules. The research and development work is carried out in the context of the CALICE collaboration [99].

4.4.2 General Layout

The calorimeter system is divided in depth into an electromagnetic section, optimised for the measurement of photons and electrons, and a hadronic section dealing with the bulk of hadronic showers. The two parts are installed within the coil to minimise the inactive material in front of the calorimeters. To follow the symmetry imposed by the beams and the coil, the calorimeter is divided into a cylindrical barrel and two end-caps.

The electromagnetic calorimeter consists of tungsten absorber plates interleaved with layers of Silicon (pads or pixels), or Scintillator detectors with very fine segmentation of the readout. The hadronic calorimeter is planned as a sampling calorimeter with steel absorber plates and fine grained readout. Two options are currently proposed. The first uses scintillator cells with fine granularity and multi-bit (analogue) readout. The second is based on gaseous detectors and uses even finer granularity. Due to the large number of cells, in the second case one- or two-bit (semi-digital) readout is sufficient.

4.4.3 The Electromagnetic Calorimeter

For the electromagnetic calorimeter the requirements on granularity, compactness and particle separation lead to the choice of a sampling calorimeter with tungsten (radiation length $X_0 = 3.5\,\mathrm{mm}$, Molière Radius $R_M = 9\,\mathrm{mm}$ and interaction length $\lambda_I = 99\,\mathrm{mm}$) as absorber material. This allows for a compact design with a depth of roughly $24\,X_0$ within 20 cm and, compared to e.g. lead, a better separation of EM showers generated by near-by particles.

To achieve an adequate energy resolution, the ECAL is longitudinally segmented into around 30 layers, possibly with varying tungsten thicknesses. The active layers (either silicon diodes or scintillator) are segmented into cells with a lateral size of $5 - 10\,\mathrm{mm}$ to reach the required pattern recognition performance.

4.4.3.1 Geometry and Mechanical Design

One of the requirements for the calorimeter is to ensure the best possible hermeticity. Three regions are of particular concern for this question: the boundaries between mechanical modules, the overlap between barrel and end-cap, and the small angle region with the connection to the luminosity monitor. To minimise the number and effect of cracks in the barrel, a design with large modules is preferred, with inter-module boundaries not pointing back to the IP. The cylindrical symmetry of the coil has been approximated by an eight-fold symmetry and the modules are designed in a such a way (c.f. fig. 4.4-7 that the cracks are at very large angle with respect to the radial direction. This octagonal shape optimises the barrel module sizes and their mechanical properties without diverging too far from a circle. One eighth of the barrel calorimeter is called a stave. Each stave is fastened to the HCAL front face with a precise system of rails. Some space is left between the ECAL and the HCAL to accommodate different services such as cooling, electrical power and signal distribution. Along the beam axis, a stave is subdivided into five modules. The ECAL end-caps are attached to the front face of the hadronic end cap calorimeters using a similar rail system.

A detailed mechanical design of the modules has been prepared, and is tested under real conditions in several test beam experiments. More details can be found in [100].

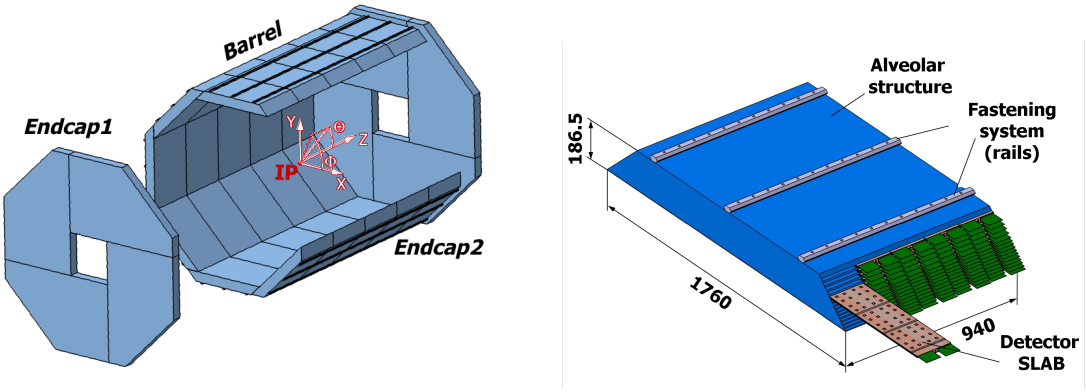

FIGURE 4.4-7. Global layout of the ECAL (left) and layout of one module (right).

4.4.3.2 Optimisation

For the final detector, a global optimisation study of the longitudinal profile has to be performed, by varying the thickness of the Silicon and Tungsten layers as a function of the depth, in order to minimise cost, lateral spread and energy resolution.

The dependence of the ECAL energy resolution as a function of the longitudinal sampling scheme has been studied in simulation [101]. For a given number of sampling layers, the energy resolution improves if the first part of the calorimeter is more finely segmented than the latter part. The effect of the silicon cell size on ECAL performance has been studied in simulation, focusing on the photon reconstruction capability in di-jet events and hadronic τ decays. Three different cell-sizes ($5 \times 5\,\mathrm{mm}^2$, $10 \times 10\,\mathrm{mm}^2$ and $20 \times 20\,\mathrm{mm}^2$) have been investigated. In both cases a specialised photon reconstruction algorithm (GARLIC [102]) has been applied. The algorithm was separately tuned for each cell-size.

Figure 4.4-8 shows the mean ratio of calorimetric energy reconstructed as photons to the true photon energy, in simulated di-jet events at $E_{\mathrm{CM}} = 400\,\mathrm{GeV}$ for a variety of cell sizes. A

	$5 \times 5\,\mathrm{mm}^2$			$10 \times 10\,\mathrm{mm}^2$			$20 \times 20\,\mathrm{mm}^2$		
	π_{sim}	ρ_{sim}	$a1_{\mathrm{sim}}$	π_{sim}	ρ_{sim}	$a1_{\mathrm{sim}}$	π_{sim}	ρ_{sim}	$a1_{\mathrm{sim}}$
π_{rec}	98.8	2.8	1.9	98.7	5.9	1.6	98.6	27.1	7.0
ρ_{rec}	1.2	96.5	9.2	1.3	93.4	15.0	1.4	72.3	54.4
$a1_{\mathrm{rec}}$	0	0.7	88.9	0	0.7	83.4	0	0.6	38.6

TABLE 4.4-6
Reconstruction efficiencies and purities of hadronic τ decays in $ZH \to \mu\mu\tau\tau$ events with various ECAL cell-sizes

cell-size of $5 \times 5\,\mathrm{mm}^2$ is clearly to reconstruct the correct fraction of photon energy inside jets. The interpretation of these result, which is based on a dedicated photon finding algorithm, requires care. It can not be applied directly to full particle flow reconstruction, which in general shows a weaker dependence.

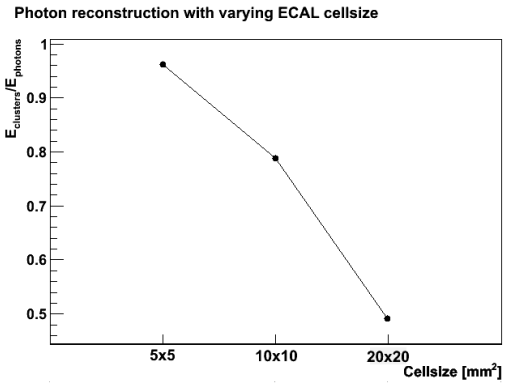

FIGURE 4.4-8. Fraction of energy identified as photon induced to true photon energy (Monte Carlo truth) in di-jet events at $E_{\mathrm{CM}} = 400\,\mathrm{GeV}$.

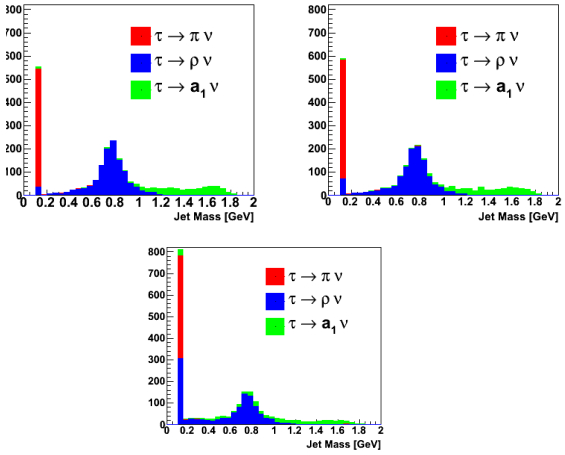

FIGURE 4.4-9.]
Reconstructed invariant mass of hadronic τ decay products in ZH $\to \mu\mu\tau\tau$ events for different ECAL cell sizes (starting at top left: $5 \times 5\mathrm{mm}^2$, $10 \times 10\mathrm{mm}^2$, and $20 \times 20\mathrm{mm}^2$.

Studies of τ reconstruction have been performed in ZH (H $\to \tau\tau$) events at $E_{\mathrm{CM}} = 230\,\mathrm{GeV}$ with $m_{\mathrm{H}} = 120\,\mathrm{GeV}$. The three decay modes $\tau \to \nu\pi$, $\tau \to \nu\rho$ and $\tau \to \nu a_1$ have been considered. The reconstructed invariant mass of the visible τ decay products is shown in Fig. 4.4-9 for the three different cell sizes. A simple selection based on particle flow (reconstructed photons) and jet mass (cut at 200 MeV) allows one to reach good efficiency and purity, without the need for the more sophisticated analysis. The efficiencies and purities of the reconstruction of the various decay channels are given in Table 4.4-6. Again a cell size of $5 \times 5\,\mathrm{mm}^2$ is favoured although the performance loss with respect to $10 \times 10\,\mathrm{mm}^2$ cells is smaller than in high-energy jets.

To study the effect of material in front of the ECAL on the particle flow performance, 4 GeV single charged pion events have been simulated. The π^0's produced in interactions

in the tracker region may give rise to additional reconstructed photons in the ECAL. The GARLIC photon identification algorithm [102] has been applied to the single pion events. For the approximately six percent of pions which interact in the tracking volume, Fig. 4.4-10 shows the position of the pion interaction point inside the detector for events in which photon clusters are (red points, 55%) or are not (black points, 45%) found. The TPC end-plates and gas give the largest contribution to the total number of pion interactions in front of the ECAL. When only those interactions which give rise to identified photon clusters are considered, the detector components at the centre of the detector, that is, the vertex detector, SIT, beam tube and FTD support, also give significant contributions. Even though ILD has been designed with with minimum material in the tracker in mind, there is still about one pion per event which interacts in the tracker volume. This underlines the need for continued R&D and continued care toward further material reduction in the tracker.

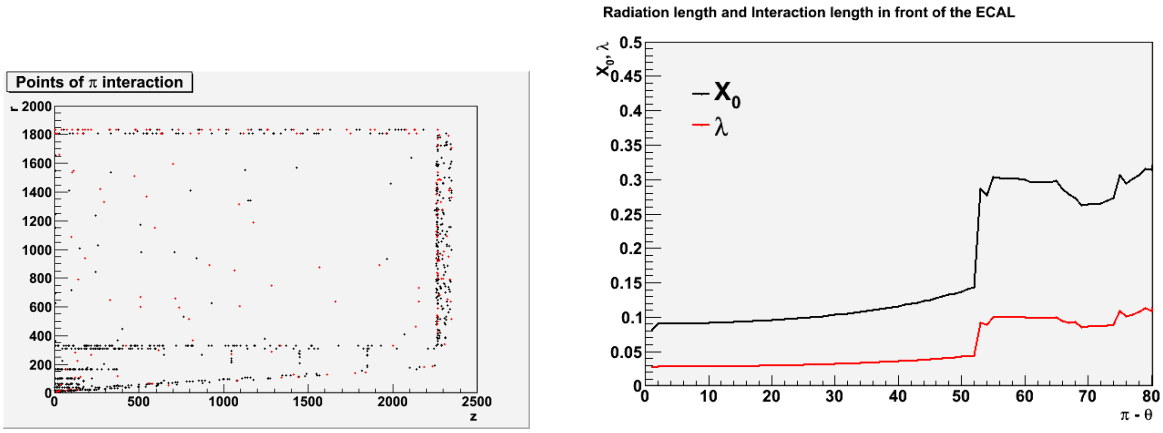

FIGURE 4.4-10. Left: Interactions points of single photons in the tracker region of ILD. The black points correspond to interactions that lead to the creation of clusters in the calorimeter found with the GARLIC photon reconstruction while the red points correspond to interactions that did not create any clusters. Right: Number of radiation and interaction length in front of the ECAL as a function of the polar angle.

4.4.3.3 Silicon - Tungsten Electromagnetic Calorimeter

The general requirement about compactness (small Molière radius) has led to a sandwich calorimeter with a tungsten radiator and silicon for the sensitive medium. To reach an adequate energy resolution the first 12 radiation lengths are filled with 20 layers of $0.6\,X_0$ thick tungsten absorbers (2.1 mm), followed by another 11 radiation lengths made from 9 layers of tungsten $1.2\,X_0$ thick. The calorimeter starts with an active layer. For the chosen geometry the Molière radius is 19 mm. The choice of silicon technology for the readout layer permits a very high transverse granularity, now fixed at $5 \times 5\,\mathrm{mm}^2$.

The final calorimeter will contain around 10^8 readout cells in total. To keep the final system as compact as possible, and reduce dead areas, the very front end electronics will be embedded into the detector layers.

The challenging construction of the SiW ECAL is currently tested by a large scale R&D program pursued by the CALICE Collaboration. Results from test beam measurements demonstrating the feasibility to realise the detector have been published in [100, 103]. The energy resolution has been determined to be $(16.6 \pm 0.1)/\sqrt{E(\mathrm{GeV})} \oplus (1.1 \pm 0.1)\,\%$ with a MIP signal over noise ratio $S/N \approx 7.5$.

	% of total interactions	% with clusters	% of total events with clusters
VTX	11.9	64.5	13.9
SIT	11.8	68.7	14.6
Beam pipe	10.4	62.9	11.8
FTD	8.9	66.1	10.6
TPC inner field cage	5.4	63.8	6.2
TPC gas	17.1	23.0	7.1
TPC outer field cage	6.5	50.6	5.9
TPC endplate	22.3	61.4	24.8
SET	3.1	58.0	3.3
ETD	2.8	35.1	1.8

TABLE 4.4-7
Interaction of pions in the different parts of the tracker region.

At present, the CALICE collaboration is preparing the construction of a prototype module with a size and shape close to the modules envisaged for the final calorimeter.

The detector slabs are built around an H-shaped supporting structure incorporating a layer of tungsten absorber. An active layer is placed on each side of this structure. This active layer is a chain of identical Active Sensor Units (ASUs), which consist of a printed circuit board (PCB) integrating the Silicon sensors, Front-End electronics and electrical infrastructure. Each ASU can run as a standalone unit, allowing testing of each piece before, during and after slab assembly, resulting in a high detector yield, and thus a reduced cost.

Since the electronics are deeply embedded in the detector volume, and no space is available for active cooling, their power consumption must be kept to a minimum to prevent overheating. By power-pulsing the electronics according to the duty-cycle of the ILC machine, the consumption can be kept below $25\,\mu W$ per channel.

The sensors are based on high resistivity silicon ($5\,k\Omega/cm$) with individual pin-diodes of $5 \times 5mm^2$ size. This size is also feasible for the readout electronics. A test batch of sensors based on 6" wafers has been used by Hamamatsu to produce $9 \times 9\,cm^2$ matrices. The bonding of the sensors onto the PCB is performed using a well controlled gluing technique.

The silicon sensors are built and integrated using well known, widely used and well controlled technologies. The matrix of PIN diodes is burned onto 330 μm thick raw silicon wafers using standard manufacturing processes from the microelectronics industry such as acceptor/donator ion implantation, oxide growth or metal deposit. The bonding of the sensors onto the PCB is performed using a well controlled gluing technique: standard glue (EPOTEK 410) applied by a robotic gluing machine. Prototypes of sensors have been ordered to various companies and academic centres with two different sizes of PIN diodes. No problems due to the gluing technique have been observed over a time span of several years.

The total surface of sensors for the whole ECAL is about $2500\,m^2$. The sensors and their integration are kept as simple as possible to avoid any dependence on a proprietary technique owned by a single manufacturer; allowing for a variety of suppliers and manufacturers to share the production will decrease the inherent financial risks and enable a competitive downscaling of the costs.

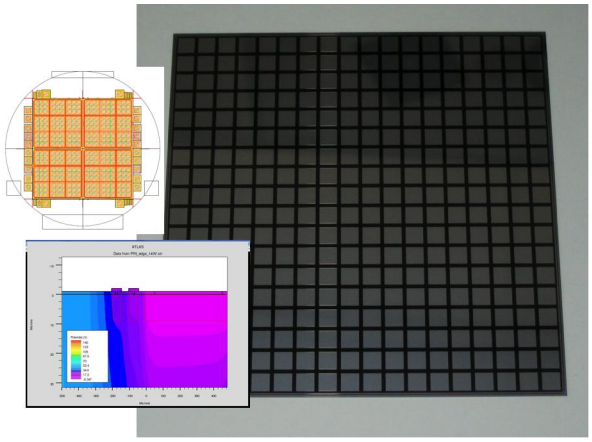

FIGURE 4.4-11. $5 \times 5\,\mathrm{mm}^2$ pad Hamamatsu sensor (right). Layout of prototype sensors with optimised edges (upper left). In depth simulation of the potential near a guard ring (lower left).

4.4.3.3.1 Calibration The charge produced by a MIP in the silicon depends only on the silicon thickness, and is therefore expected to be stable with time. A single calibration before detector assembly will therefore be sufficient. The ASUs will be calibrated in a muon beam before the assembly of detector slabs and their integration into detector modules.

The VFE electronics will be calibrated by means of the VFE chips' charge injection calibration system.

Since the tracks of muons and non-interacting charged pions in the ECAL can easily be identified due to the ECAL's high granularity, they can be used to monitor the calibration during the lifetime of the detector.

4.4.3.4 Scintillator - Tungsten Electromagnetic Calorimeter

The scintillator-tungsten sandwich ECAL (ScECAL) is proposed to realise a fine-segmented calorimetry in a stable, robust and cost effective way. The fine grained readout is realised by planes of 1 cm wide and 4.5 cm long strips, arranged in orthogonally in adjacent layers. Thanks to the strip structure, the number of necessary readout channels is significantly reduced ($\sim 10^7$ channels) relative to the Si-W option. Scintillator strips can be cheaply produced by the extrusion method. Compact photo-sensors (MPPC) and highly integrated readout electronics make dead area in the ScECAL almost negligible. Keeping the required granularity and these merits, the ScECAL has good energy resolution and linearity.

The ScECAL consists of 24 super-layers. A schematic view of a few super-layers of the ScECAL is shown in Figure 4.4-12. They will be mounted in an alveolar structure similar to the case of the SiW ECAL. A super-layer is made of a tungsten plate (3 mm thick), scintillator strips (2 mm thick), and a readout/service layer (2 mm thick). Scintillator strips in adjacent super-layers are arranged to be orthogonal aiming for better effective granularity. The thickness of a super-layer is 7 mm. The total ScECAL thickness is 172 mm, or $20.6\,\mathrm{X}_0$ in radiation length.

4.4.3.4.1 The active layers The dimension of an individual scintillator strip (see Fig. 4.4-12) is $1 \times 4.5 \times 0.2\,\mathrm{cm}^3$. Although a strip width of 5 mm, to realise an effective granularity of $5 \times 5\,\mathrm{mm}^2$, is thought to be feasible, further R&D is necessary. Each strip is covered by a mirror reflector film to improve collection efficiency and uniformity of the scintillation light. Photons from each scintillator strip are read out via an 1 mm diameter wavelength shift-

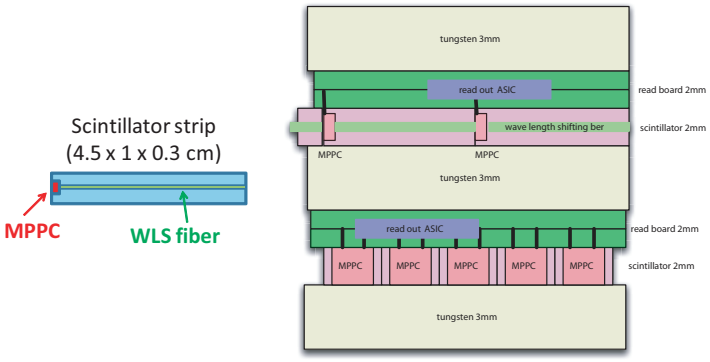

FIGURE 4.4-12. Dimension of the scintillator-strip (left, view from top) and side view of the ScECAL layer structure (right).

ing fibre (WLSF) embedded in a straight groove by a very compact photon sensor, MPPC, attached at the end of the strip.

The MPPC is a version of a novel semiconductor photo-sensors consisting of a matrix of micro APD pixels operated in Geiger mode. Photo-detection performance and amplification power is comparable with conventional photomultiplier tubes. The dynamic range of an MPPC is limited by the number of APD pixels. A MPPC with 1600 APD pixels in an area of $1\,\mathrm{mm}^2$ is already commercially available. However MPPC with ~ 3000 pixels should be developed to precisely measure up to $\sim 100\,\mathrm{GeV}$ electromagnetic clusters.

Signals from about 80 MPPC are fed into a readout chip through micro-strip lines. They are arranged on one identical flexible readout board (FPC) (c.f. Fig. 4.4-13). After shaping, digitisation and zero-suppression of the analog signals on the chip, signals are taken out serially from the detector and brought to a digitisation board by a thin FPC cable ($\sim 200\,\mu\mathrm{m}$) through detector gap.

4.4.3.4.2 Calibration systems A light distribution system has been designed to monitor possible gain drifts of MPPCs by monitoring photo-electron peaks. The system consists of a pulse generator, a chip LED, and a notched fibre. A schematic structure of the system is shown in Figure 4.4-14. The pulse generator circuit and the chip LED are arranged on a thin ($\sim 200\,\mu\mathrm{m}$) FPC board. The chip LED is directly connected to the notched fibre to distribute lights to ~ 80 strips through its notches.

Each scintillator strip can be calibrated with data by monitoring the MIP peak using multi-hadron events at the ILC. Monte Carlo simulation shows that more than 100 MIP hits per strip will be obtained if running at the Z^0. With this method the strips can be calibrated to better than $5\,\%$ with $1\,\mathrm{fb}^{-1}$ of $\mathrm{Z}^0 \to jj$ events).

4.4.3.4.3 Status and Future R&D plans The feasibility of the ScECAL has been proven by a test of a small prototype using $1-32\,\mathrm{GeV}$ electron beams. At the test clean MIP signal and electron energy spectra are observed with negligible contamination from electrical noise. The energy resolution is measured to be $\sigma_E/E = 14/\sqrt{E} \oplus 2\,\%$ which is consistent with expectation from simulation.

In order to fully establish the feasibility of the ScECAL, further extensive R&D efforts are necessary to clarify the remaining technical issues as follows:

- Photon sensors: properties of the MPPC have to be further studied and improved. The

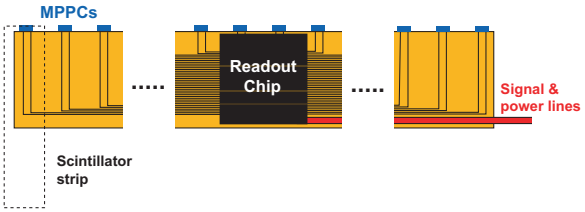

FIGURE 4.4-13. Layout of the MPPC, micro-strip line and readout chip on the FPC board.

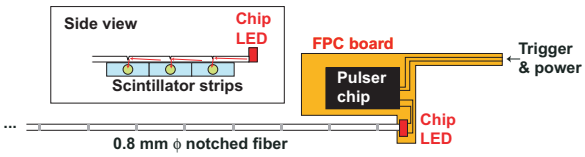

FIGURE 4.4-14. Schematics of the MPPC gain monitoring system with LED and notched fibre. Light pulses from the LED are scattered and distributed into each strip.

increase of the dynamic range is especially important.

- Development of readout electronics: A highly integrated readout chip is needed due to the limited space in the detector.
- Strip clustering: The strip structure is chosen in order to improve the effective granularity of the calorimeter. A clustering algorithm has been developed which can cope with the strip structure as well as the usual square-tile structure. The algorithm is being further improved, and performance of the strip structure must be demonstrated.

4.4.3.5 Digital (MAPS) Silicon-Tungsten Electromagnetic Calorimeter

The silicon-tungsten digital ECAL (DECAL) is an alternative to the analogue silicon design described in Section 4.4.3.3. The basic principle is to replace the high resistivity pad diodes with CMOS based binary readout pixels sufficiently small in size that, even in the core of high energy electromagnetic showers where the density is typically equivalent to $\sim 100\,\mathrm{MIPs/mm^2}$, the probability of a pixel being hit by more than a single particle will be low. This allows the shower energy to be measured by the number of binary pixels above threshold. To ensure that linearity of response is preserved even at higher energies, pixels are required to be $O(50 \times 50\,\mu\mathrm{m}^2)$, leading to $O(10^{12})$ pixels in the complete ECAL. A very high level of integration of the readout in the pixel is therefore mandatory.

The active layers are based on CMOS Monolithic Active Pixel Sensors (MAPS) which allow data reduction and processing logic to be contained within each pixel. The target noise level is 10^{-6}. A new process ("INMAPS" [104], developed by the CALICE UK groups) ensures efficient charge collection by using deep p-wells and charge collection by diffusion in the sensor. Signals (time stamp and pixel address) are stored on the sensor during a bunch train and read out in the interval between bunch trains. By using industry standard CMOS processes available from a large number of foundries, costs are potentially lower per unit area than analogue silicon diodes, with reduced risk to production schedules.

The performance of the DECAL has been studied using Mokka in the context of LDC [105, 106, 107], including effects of dead area, digitisation and clustering. A preliminary study of the energy resolution of the DECAL to single photons, implemented by adapting only the ECAL sensitive region in the ILD00 silicon-tungsten model in Mokka, gives $\sigma_E/E = 19.7\,\%/\sqrt{E}$. A first prototype sensor (TPAC1.0) was designed in 0.18 µm process, having 28224 ($50\times50\,\mu\mathrm{m}^2$) pixels [104]. This $9 \times 9\,\mathrm{mm}^2$ sensor was fabricated and characterised, e.g. [108, 109, 110] during 2007–8. A second revision of the sensor is expected for 2009. A proof-of-principle R&D project is in progress to develop and test a 16 layer DECAL prototype large enough to contain electromagnetic showers [111] by 2012.

The DECAL option is designed to work with the same mechanical structure as the Si-W ECAL, thus profiting from the large R&D done in this area. A topic for future R&D is the reduction and control of the power consumption, which at the moment is expected to be larger though uniformly distributed across the sensor unlike the analogue SiW sensor.

4.4.4 The Hadronic Calorimeter

In a particle flow calorimeter the HCAL plays a crucial role in separating and measuring the energy deposits of charged and neutral hadrons. Since the energy deposited by neutral hadrons fluctuates widely, its precise measurement is a key component of a well performing particle flow calorimeter. Consequently, the imaging capabilities of the HCAL are of prime importance and demand high transverse and longitudinal segmentation and a design with a minimum of uninstrumented ("dead") regions. However, a very good hadronic energy resolution is also mandatory, both to assist the topological assignment of clusters and tracks, and to optimise the precision of the hadronic energy part characterised as neutral. The high granularity allows the application of weighting techniques to compensate for differences between hadronic and electromagnetic response and for "invisible" energy depositions ("software compensation") and improves the hadronic energy resolution further.

4.4.4.1 Geometry and Mechanical Design

The HCAL is conceived as a sampling calorimeter with steel as absorber and scintillator tiles (analogue HCAL) or gaseous devices (digital HCAL) as active medium. As the HCAL must be located within the coil, the absorber has to be non-magnetic. Stainless Steel has been chosen both for mechanical and calorimetric reasons. Due to its rigidity, a self-supporting structure without auxiliary supports (and thus dead regions) can be realised. Moreover, in contrast to heavier materials, iron with its moderate ratio of hadronic interaction length ($\lambda_\mathrm{I} = 17\,\mathrm{cm}$) to electromagnetic radiation length ($\mathrm{X}_0 = 1.8\,\mathrm{cm}$) allows a fine longitudinal sampling in terms of X_0 with a reasonable number of layers in a given total hadronic absorption length, thus keeping the detector volume and readout channel count small. This fine sampling is beneficial both for the measurement of the sizable electromagnetic energy part in hadronic showers as for the topological resolution of shower substructure, needed for particle separation and weighting.

4.4.4.1.1 Overall architecture The overall structure follows the "short barrel" concept, with two large endcaps with about the same outer radius as the barrel. The total hadronic absorption length corresponds to a minimum of $5.5\,\lambda_\mathrm{I}$ in addition to the ECAL. The endcaps are subdivided into four quadrants, their absorber plates are oriented perpendicular to the beam line. The mechanical engineering of the absorber structure has so far concentrated on the barrel. It is assumed that the solutions can be transferred to the endcaps later-on. Compared with existing hadron calorimeters, the ILD HCAL has a rather fine longitudinal sampling, with a correspondingly high pressure on the thickness of the active layer gaps, but also on mechanical tolerances. This, together with the requirement of minimum dead zones represents a challenge to the large scale engineering which is presently being addressed with prototypes within the EUDET/CALICE framework.

For the barrel, two design approaches are being followed: one with long barrel modules, subdivided only once in z, and with electronics and service connections at the end faces, and a second, with 5 rings and interfaces situated at the outer barrel perimeter. The main

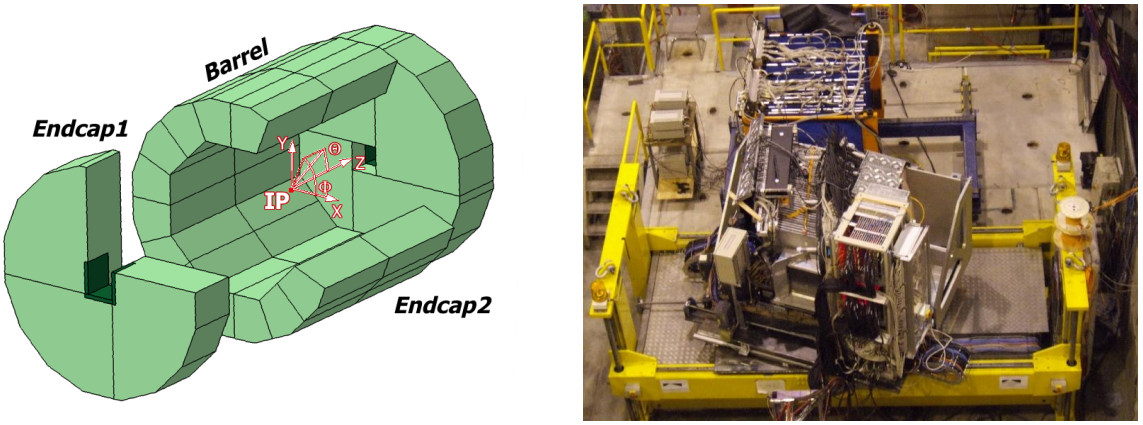

FIGURE 4.4-15. Layout 1 of the HCAL (left), and view of the integrated ECAL and HCAL beam test setup (right).

advantages of the first are the accessibility of the electronics and a maximum filling of the detector volume limited by the coil radius, whereas the second provides better rigidity in the transverse plane, eliminates pointing cracks and allows for a tighter barrel end-cap transition. In principle, each concept can be instrumented with both scintillator and gaseous devices. In practice, the detailed engineering is presently being worked out for scintillator in the first, and for gaseous readout in the second approach.

4.4.4.1.2 Design 1 In the first version of the HCAL design, the barrel is subdivided into two sections in z and eight octants in φ, each octant has two halves which constitute the basic modules, 32 in total. Each module has a weight of almost 20 tons, which is manageable with standard installation techniques. The modules are constructed independently of the active layers, which can be inserted before or after installation of the modules. There are 48 absorber plates, 16 mm thick each, held together by 3 mm thick side panels in the rz planes; no additional spacers are foreseen. The active layers will contribute 4 mm of steel to each absorption layer, and require 5.5 mm for instrumentation (3 mm thick scintillator plus readout and calibration devices). A drawing of the structure is shown in figure 4.4-15(left). The HCAL structure has been extensively simulated using finite element methods, including the integration of the heavy ECAL structure. Maximum deformations are found to be less than 3 mm, if the barrel structure is supported by two rails in the cryostat.

Presently the boundaries between modules are pointing in φ and in z. Variants with non-pointing boundaries have been validated in finite element calculations as well, but are disfavoured to ease the mechanical construction. The pointing geometry does not degrade the performance as long as the cracks are filled with absorber material, and if the active instrumentation extends up to the boundary within tolerances, which is the case in the present scintillator layer design.

4.4.4.1.3 Design 2 This design intends to reduce cracks both in φ and θ and to reduce the distance between the barrel and the endcaps. The barrel part is made of 5 independent and self supporting wheels along the beam axis which eliminates the θ=90 degree crack. The segmentation of each wheel in 8 identical modules is directly linked with the segmentation of the ECAL barrel. A module is made of 48 stainless steel absorber plates (welded with 2 transverse 10 mm stainless steel plates) with independent readout cassettes inserted between

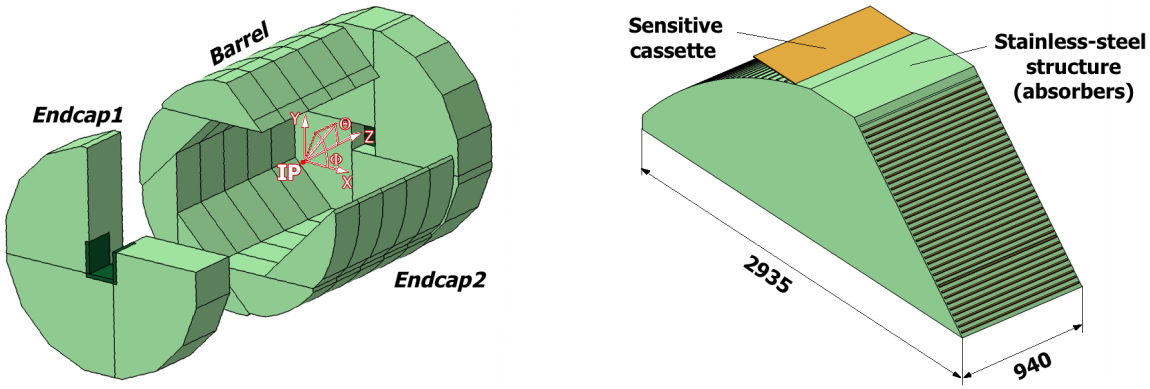

FIGURE 4.4-16. Design 2 layout of the HCAL (left) and layout of one module (right).

the plates. They define the rigid structure on to which the corresponding ECAL modules are mounted. A drawing of the structure is shown in figure 4.4-16(right). The absorber plates consist of a total of 20 mm stainless steel: 16 mm absorber from the welded structure and 4 mm from the mechanical support of the detector layer.

Each wheel is independently supported by two rails on the inner wall of the cryostat of the magnet coil. The cables as well the cooling pipes will be routed outside the HCAL in the space left between the outer side of the barrel HCAL and the inner side of the cryostat. The HCAL endcaps the same geometrical structure proposed in design 1. The distance between the barrel and the endcaps, which have the same structure as in design 1, is thus reduced, as only space to ensure inner detector cabling is required.

4.4.4.2 Analogue Hadronic Calorimeter

With the advent of novel, multi-pixel Geiger mode silicon photo-diodes, so-called SiPMs, high granularities as required for a particle flow detector can be realised with the well-established and robust scintillator technology at reasonable cost. The scintillator tiles provide both energy and position measurement and thus allow to trade amplitude versus spatial resolution. The transverse segmentation suggested by simulations is about $3\times3\,\mathrm{cm}^2$ and leads to a number of read-out channels an order of magnitude smaller than in the digital case with $1 \times 1\,\mathrm{cm}^2$ cells.

4.4.4.2.1 The Active Layers The arrangement of the active layers with internal and external electronics components is sketched in Figure 4.4-17. The layer consists, from bottom to top, of a 2 mm thick steel support plate covered with reflector foil, the scintillator tiles (3 mm), the printed circuit board with electronics components (2 mm), covered with reflector foil from underneath, and a polymide foil for insulation. The PCB carries the SPIROC readout ASICs (described in section 4.4.5.1)and auxiliary components as well as an LED based optical calibration system, whilst interfaces for data acquisition, clock and control, for power distribution and for calibration system steering are accessible at the end face. Since the ASICs are operated in power-pulsed mode, no cooling is needed inside the detector volume. The PCB is subdivided into units (HCAL base units, HBUs) of smaller size, manageable for automated mounting and soldering techniques. The standard unit is 12 by 12 tiles, $36 \times 36\,\mathrm{cm}^2$, so six units are aligned along z to fill a half barrel. In order to accommodate

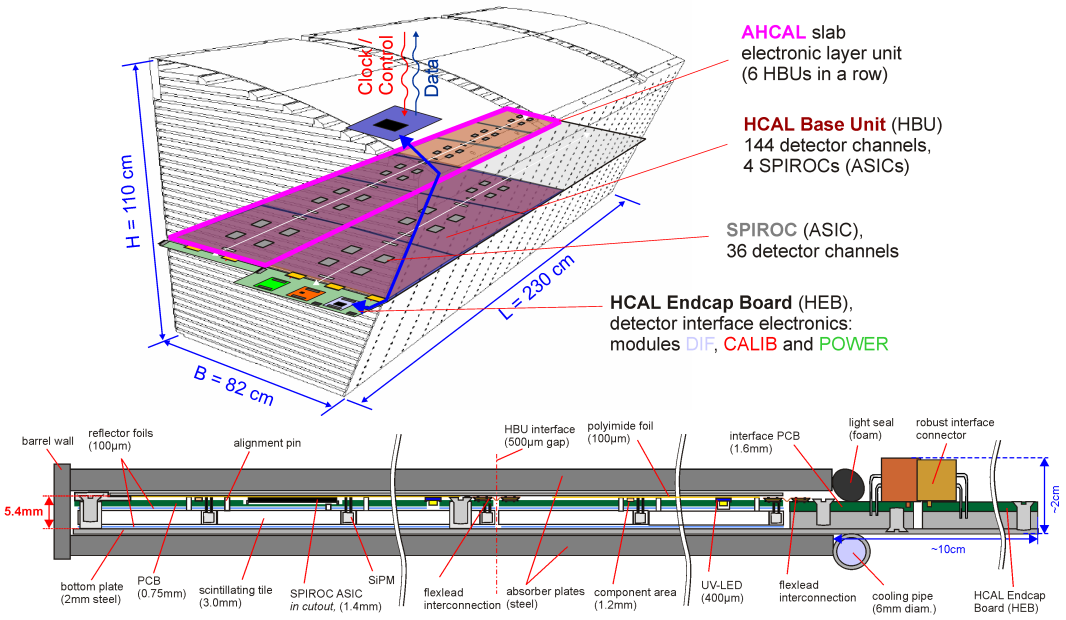

FIGURE 4.4-17. Arrangement of AHCAL layers with electronic components (top), cross section of an active layer (bottom).

the variation in layer width with increasing radius, 4 different HBUs, 8 to 12 tiles wide, are needed. At the layer edges, tiles with smaller size, e.g. $2 \times 3\,\mathrm{cm}^2$, are placed such that the uninstrumented region near the sector boundary is never larger than 5 mm and 2.5 mm on average.

The electronics at the end face will require cooling, mainly due to the use of FPGAs in the DIF (Detector InterFace board described in 4.4.5.2). The boards will extend 5 to 10 cm in z, but occupy only a fraction of the full width in φ, thus leaving space for ECAL and main tracker services as well as for the TPC support along radial directions. The required extra separation between barrel and endcap is therefore much smaller.

4.4.4.2.2 Scintillators and Photo-Sensors, R&D The successful operation of the 8000 channel CALICE HCAL test beam prototype over several years has proven that the new sensor and scintillator technology is robust and reliable. Less than one per-mil of the SiPMs showed signs of aging in form of increasing noise levels. In the meantime, progress was made by various manufacturers, e.g. in Russia or Japan, to provide sensors with lower dark count rate and / or smaller inter-pixel cross-talk which allow to decrease the noise occupancy above threshold of 10^{-3} in the present prototype by an order of magnitude and thus fulfill the requirements from both physics (for neutron hit identification) and DAQ band width. The demands on dynamic range are less critical than for the ECAL.

For the coupling of sensors to scintillator and PCB different approaches are being followed, based on either wavelength-shifting WLS fibre mediated or direct read-out with blue-sensitive photo-diodes. The WLS option was successfully operated in the HCAL (and ECAL) testbeam prototypes. The production, test and integration of sensors has been industrialised further, e.g. the grove for the fibre can be included in the injection moulding process (or the hole in the extrusion process). The positioning of the tiles must match the precision of the PCBs, for example with alignment pins. Alternatively, so-called mega-tiles (plastic modules comprising several cells, separated by groves) are also being discussed.

In the direct coupling case, the sensor is mounted in SMD style with its sensitive surface in the PCB plane, and collects the scintillation light directly from the tile. The tile has to be shaped in a dedicated way to compensate for the otherwise prohibitive light collection non-uniformities. Verification of both concepts in beam tests are important; besides uniformity also the stability of the light collection must be ensured.

Machine-related backgrounds are not a concern for the AHCAL. Simulations have shown that only in the innermost regions of the end-caps, the neutron fluence reaches levels which may degrade the visibility of single photo-electron signals for SiPM monitoring, but not the MIP detection capability. One may have to revert to alternative monitoring strategies here, or use more robust sensors which are under development.

4.4.4.2.3 Calibration The calibration procedure has to relate the electronic readout signal to the energy deposition in the cell. For the pre-amplifiers and discriminators, charge injection is used as in the ECAL or DHCAL case. The gain of the photo-diodes is monitored by means of an optical calibration system, and adjusted via the bias voltage, by observing the spacing between single photo-electron peaks in LED-induced pulse-height spectra. Using test bench measurements this cares also for sensor efficiency variations, correlated with the gain.

We follow two approaches for the technical realisation of the LED system, one based on a central driver located at the end faces of the modules and optical light distribution via fibres, and one with electrical signal distribution and surface-mounted LEDs for each tile. To check for long-term effects, track segments in hadronic showers can be used for a large fraction of the calorimeter volume. This has been shown with test beam data and simulated for ILD multi-jet events. Also systems based on radio-active sources might need to be considered.

4.4.4.2.4 Optimisation and Performance The main cost- and performance driving parameters of the AHCAL are the depth and the longitudinal and transverse segmentation. These parameters have been varied, and their current settings have been found, using detailed simulations and particle flow reconstruction as described in the overall detector optimisation section 2.2. The simulations include a modeling of inactive regions at module boundaries which is more conservative than the present engineering design.

The performance of a scintillator-tile HCAL with SiPM read-out and the proposed segmentation has been demonstrated with test beam data taken with the CALICE physics prototype. The detector showed very good imaging capabilities which reveal the substructure in hadronic showers, see Fig. 4.4-18.

Using test bench data and in-situ measurements, temperature induced variations and SiPM saturation effects could be corrected, and a linearity of better than 2 % for electron induced showers up to 50 GeV was achieved. The calorimeter is non-compensating, but the e/π ratio is not large and the observed linearity is also good for hadronic showers, see Fig. 4.4-19. A hadronic energy resolution of $61\,\%/\sqrt{E}$ is obtained on the electromagnetic scale, which can be reduced to $49\,\%/\sqrt{E}$, preserving linearity, with a simple weighting algorithm, which takes only the energy per tile, but not yet any shower substructure into account.

Based on experimental results from the CALICE prototype a reasonable agreement of the shower profiles with GEANT 4 based simulations has been found, as shown in figure 4.4-20. We found that it is essential to model details of the detector response, such as saturation effects in the scintillator according to Birks' law and the shaping time of the readout electronics, in order to reach this good agreement. These primarily affect the response to neutrons

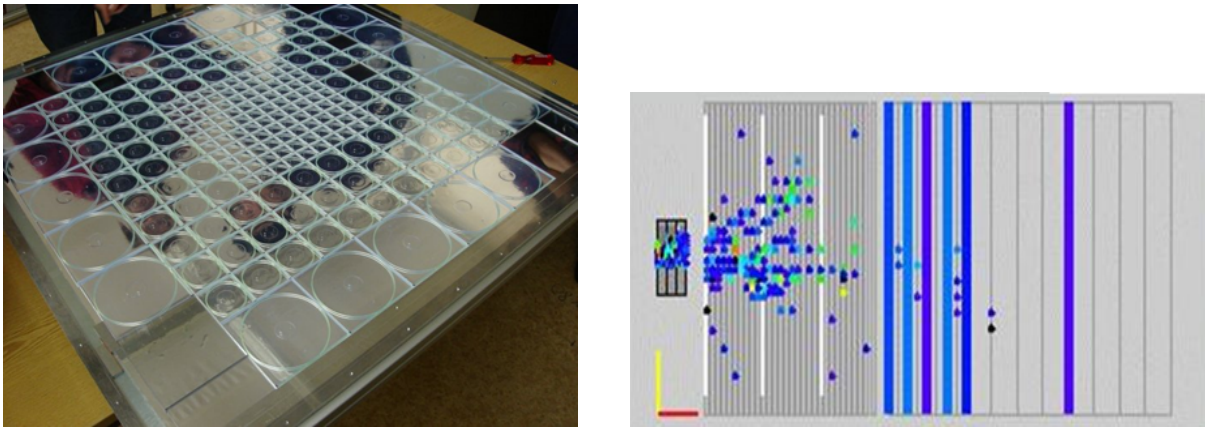

FIGURE 4.4-18. AHCAL physics prototype layer (left), event display (right).

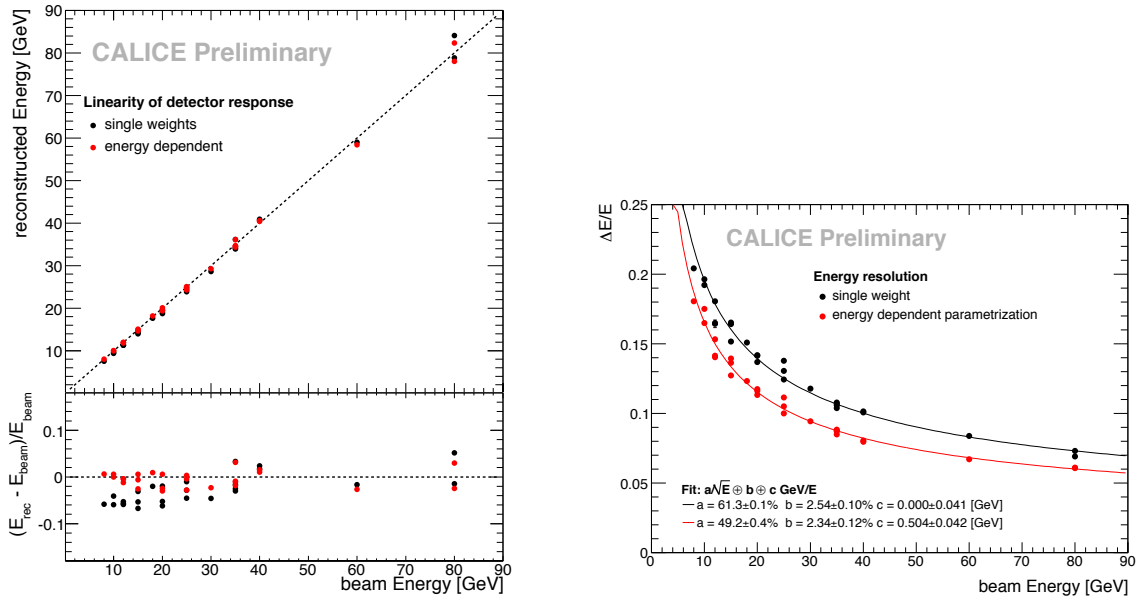

FIGURE 4.4-19. Linearity (left) and resolution (right), on electromagnetic scale and after weighting.

which would otherwise be overestimated.

4.4.4.3 Semi-Digital Hadronic Gas Calorimeter

The capacity to apply successfully the particle flow algorithms can be enhanced by increasing the granularity of the different ILD sub-detectors. In the hadronic calorimeter this will doubtlessly help reduce the confusion between charged and neutral hadronic particles by providing a better separation of the associated showers. However, the cost related to such an increase in detector segmentation should be minimised. To satisfy both, a gas hadronic calorimeter with a semi-digital readout is proposed. The study of such an HCAL has been going on for few years in order to validate this option.

The choice of gaseous detectors as the sensitive medium in the HCAL offers the possibility to have very fine segmentation while providing high detection efficiency. The glass resistive plate chamber (GRPC) is one of these detectors which can be built in large quantities at

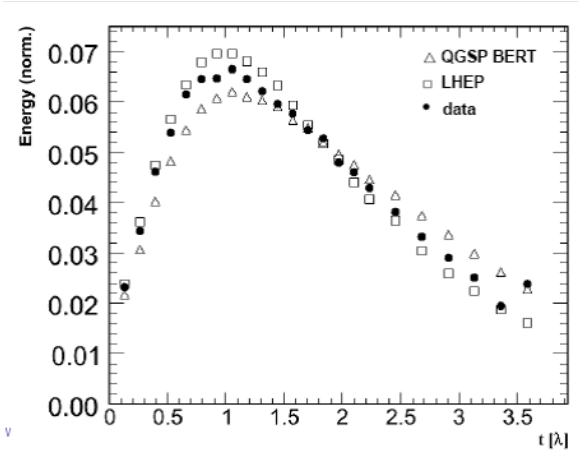

FIGURE 4.4-20. Longitudinal shower profile, test beam data and simulations.

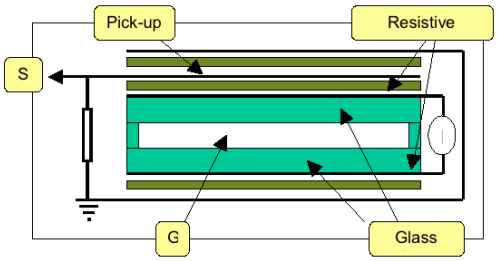

FIGURE 4.4-21. Single gap GRPC scheme

low cost. Large GRPCs as the ones required for the ILD HCAL can be easily produced. This is an important advantage with respect to other detectors since it guarantees very good homogeneity. Several experiments like BELLE have been using such large detectors with success for years. However, the GRPCs to be used in the ILD HCAL need to be more elaborate. As the HCAL is situated inside the magnet coil, the sensitive medium thickness is an important issue. Very thin GRPCs are requested and 3.3 mm thick GRPCs were indeed produced and successfully tested. In figure 4.4-21 a scheme of such a single gap GRPC is shown. Some key properties of these detectors are:

- GRPC operated in avalanche mode and have been shown to show no ageing for the accumulated charge expected over the ILC running period.
- Test beam performed at DESY have shown that a strong magnetic field has negligible effect on GRPC performance.
- GRPC detectors are insensitive to slow neutrons preventing thus an additional confusion.

Increasing the granularity will lead to a large number of channels. To limit the amount of data we propose a semi-digital readout solution. This simplifies the data treatment while minimising the consequences on the energy resolution performance. Indeed, based on several independent simulation studies, a two-bit readout would provide better energy resolution in the low-energy jet range (1–20 GeV) and a comparable one at higher energies when compared to an analogue readout [112].

Similiar to the case of the analogue HCAL the readout electronics will be integrated into the sensitive layer of the system, thus minimising dead areas. Large electronics boards

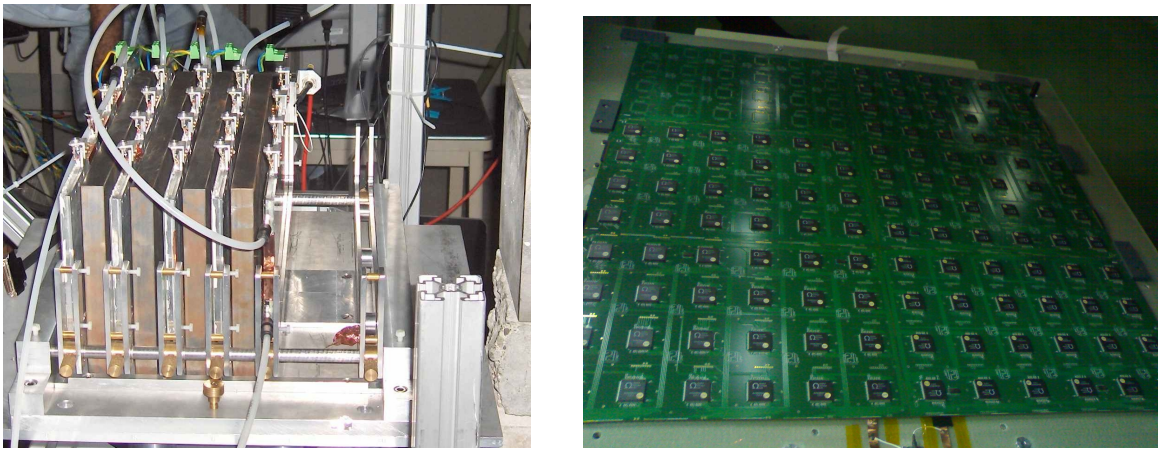

FIGURE 4.4-22. Mini-DHCAL prototype (left); Prototype of a large instrumented GRPC (right).

are assembled together to form extra large boards before they are attached to the GRPCs. The board assembly will be made possible thanks to a mechanical structure made of 4 mm stainless steel plate. In addition, to keep the HCAL as compact as possible, the fully equipped electronic boards are designed to have less than 3 mm thickness in all. A mini hadronic calorimeter using this concept was built and successfully tested in beam conditions at CERN in 2008 (see figure 4.4-22).

4.4.4.3.1 The Active Layers R&D activities on large GRPC detectors are being followed. Different kinds of spacers are tested to reduce detector noise and inefficiency while increasing the detector robustness. New gas distribution schemes as well as gas recycling systems are worked out to lower gas consumption and pollution. Although the present GRPC detection rate of 100 Hz/cm^2 obtained with efficiencies greater than 90 % is enough for the needs of ILC, a new development based on using semi-conductive glass will lead to increase this rate. Multi-gap GRPCs are also investigated. This allows reducing the spread of the MIP charge spectrum leading to a better exploitation of the semi-digital information.

Few large GRPCs with different options were built and are currently tested using a 1 m^2 fully equipped electronics board (see figure 4.4-22(right)). This will allow to build the most appropriate GRPC detector to be used in the ILD DHCAL.

In addition to the GRPCs activities, development on other thin and large gaseous detectors like GEM and MICROMEGAS are also followed.

The GRPCs produces strong electric currents (a few 10 pC in 10-20 ns) in the DHCAL pads. In order to reduce cross-talk effects between the pads below the percent level the very front end electronics is located on the other side of the PCBs, (semi-)buried vias are used.

4.4.4.3.2 Energy Reconstruction & Calibration The semi-digital HCAL cell energy reconstruction can, to first order, be estimated as $E_{\text{cell}} = 1$, 5 and 10 MIP if the charge is above the thresholds typically placed at 0.1, 2 and 8 MIPs (for the envisaged GRPC about 0.26, 5.2 and 20.8 pC). Preliminary results on simulation, without algorithm optimisation, show PFA performances comparable to the AHCAL reconstruction.

An interesting aspect of the gaseous semi-digital HCAL is the simplicity with which the detector calibration is performed, if one is needed at all. The sDHCAL energy calibration requires 3 independent steps:

- *An intercalibration of the ASIC thresholds in charge*: All ASICs will have to be tested and calibrated by injecting a precisely controlled charge, adapted for each of the threshold, at the entrance of their final ASU/PCB pad. The variations can be compensated channel by channel in the ASIC by adjusting the channel gains (over a range of 0–2 coded on 8 bits in the current version of HaRDROC, described in sec 4.4.5.1);
- *A calibration of the multiplicity of the RPC*: The multiplicity response curve of the RPC to muons as a function of high voltage applied, thresholds, position and gas flow and atmospheric pressure can be measured on a cosmic test bench or muon beam and parametrised for each type of RPC.
- *A calibration with physics*: The two first steps bring an absolute calibration at the level of the MIP, which can be cross-checked with cosmic muons or $Z \to \mu\mu$ events; the final energy scale will be a complex interplay in the scope of the PFA analysis between the clustering algorithms, jet and particle energies and types.

The definition of the calibration procedure, and an estimation of the achievable precision, is a part of the DHCAL $1\,\mathrm{m}^3$ programme.

4.4.4.3.3 Status and Future R&D Plans A technological prototype of $1\,\mathrm{m}^3$ HCAL based on the same principle is currently under study. It aims to validate at large scale the semi-digital HCAL concept. Questions related to the mechanical structure mentioned in the previous section as well as the management of the limited space for services will be addressed. The prototype is to be built by 2010. Combined test beams with the different ECAL prototypes developed within the CALICE collaboration will then be organised at FERMILAB and CERN.

4.4.5 Calorimeter Readout System

A considerable effort has been made in the framework of the CALICE collaboration to standardise the read-out of different type of calorimeter with embedded Very Front-End (VFE) electronics while minimising the space needed for the configuration distribution and the data readout.

4.4.5.1 Very Front End (VFE) ASIC description

The front-end ASICs should ensure a data format uniformity in all the calorimeters, thus having identical back-ends to allow a standardised detector interface board (DIF) for all detectors.

Ensuring such a compatibility between all electronics components involves a unique read-out system based on token ring that allows a number of ASICs to be read out by one output line, using the same protocol. That protocol will help reducing the number of data lines outputted from the calorimeters where the front-end ASICs are now embedded.

All the VFE will feature three operating mode : Acquisition (1 ms), A/D conversion (1 ms), and data outputting during inter-bunch (199 ms) using an ultra low power protocol. When a FE ASIC is in neither of the above modes, it is turned to an idle mode to save up to 99.5 % of power, bringing the power down to 10 to 25 μW per channel.

Three ASICs differing mostly on their analog front-end have been developed to fit the different detectors.

- SKIROC ("Silicon Kalorimeter Integrated Read-Out Chip"): 64 channels charge preamplifier for charge measurement down to the MIP (3.84 fC) to a maximum around 2500 MIP. Dual gain shaping, analog memory, 12 bit-digitisation, self-trigger capability on single MIP. 25 μW/ per channel to run without any active cooling ensuring therefore an extreme compactness of the calorimeter.
- SPIROC ("Si-Pm Integrated Read-Out Chip"): auto-triggered, dual-gain voltage preamp, 36-channel ASIC which allows to measure for each channel the charge from 1 to 2000 photo-electrons with a 12 bit internal ADC and the time with a 1 ns accurate TDC. One 8-bit 5 V input DAC per channel ensures operation of the SiPM at its optimum bias.
- HARDROC("HArdronic RPC Detector ReadOut Chip"): 24 channels semi-digital readout for RPCs or MicroMegas pads, allowing both good tracking and coarse energy measurement. Each channel made of a variable gain low input impedance current preamp followed by 3 variable gain shapers and 3 low offset discriminators to auto-trig down to 10 fC up to 10 pC. A 128 deep digital memory to store the encoded outputs of the discriminators as well as the bunch crossing identification.

Prototypes of each type have been produced in the years 2007-2008. Boards equipped with 4 HARDROC(v1) ASICs have been designed for the DHCAL. The electronics readout under beam conditions has been validated. Some key points such as the digital daisy chaining for configuration and readout, the stability, the efficiency, and the capability of the chip to be used without any external components have been checked. A small production is foreseen in Fall 2009 to equip a technological prototype (called EUDET prototype) in 2010.

4.4.5.2 Detector Interface

The ASICs are managed by specifically designed DIF (Detector InterFace) cards; one DIF handles a full slab, whose maximum size are of $260 \times 141\,\mathrm{cm}^2$ for the AHCAL structure, and $90 \times 273\,\mathrm{cm}^2$ for the DHCAL structures. The corresponding maximum number of ASIC per slab are respectively 576 and 420. For an estimated occupancy per ASIC of the HCAL of 5 events / train of 2600 BC, the expected data volume to be read in the inter-train is of 336000 bits; readout at a speed of 5 MHz this takes 67 ms. During the readout phase the ASICs will be on standby except when explicitly addressed.

4.4.5.3 DAQ system

The data acquisition (DAQ) system is defined to start with the detector interface boards (DIF) which service the detector slabs from the ends and which are specific to the VFE of the subsystem. The DIF provides a generic interface, independent of the calorimeter type, to the DAQ system. Because of the limited space available for cabling and services, data are concentrated onto a single optical communication channel with the off-detector electronics, by a link-data aggregator (LDA) inside the detector. The resulting data volume is mainly determined by the zero-suppression scheme incorporated in the self-triggering Front-End electronics. But as the calorimeter has over 100 million readout channels, significant demands are put on the scalability and on an attractive price/performance ratio of the readout electronics and the associated data-acquisition systems. Therefore the design should minimise the number of LDAs and maximise the data rates on the link which are expected to be 10 GB Ethernet links.

With the data delivered over optical high-speed links, an optical switch is used to dynamically redirect the data streams coming from the detector towards available data receivers of the off-detector system. The off-detector is currently realised as a PCIexpress card hosted in a commodity PC but can be easily implemented in a μTCA crate for the future detector.

For the event building the machine clock will be fed into the off-detector system to the data concentrators and the detector interfaces. The requirements on the clock are a low jitter and fixed latency between the machine clock and the clock in the detector interfaces. This part of the system needs to be custom built to guarantee delivery times and latencies.

For all of the introduced systems (detector interface, data concentrator, off detector system and the clock) prototypes already exist which have been built within the EUDET [113] project. The prototypes perform the same tasks as in the final detector, however the prototypes are build for a proof of principle and need to be optimised for the final detector design.

4.4.6 Status and future R&D plans

The technology-specific R&D will continue in CALICE. However, in order to study the system performance of the proposed solutions, to validate the accuracy of simulations, and to develop the reconstruction techniques further, large test beam experiments are indispensable. The particle flow approach demands integrated set-ups with ECAL and HCAL together. This programme is pursued for the calorimeters in the framework of the CALICE collaboration, in a cooperative way maximising the use of scarce resources with common mechanical structures, electronics components, DAQ systems and software frameworks.

CALICE has completed a series of full-size proof-of-principle tests with so-called physics prototypes of both ECAL technologies and the scintillator HCAL. The programme is to be completed by tests with a RPC-based DHCAL at Fermilab in 2009-10, and by a test of a MAPS-based DECAL prototype until 2012. Large data sets have been and will be collected and form the basis for test and refinement of hadron shower simulations. The emphasis in the more realistic second generation "technological prototypes" is shifted more toward a demonstration of the feasibility of a compact integrated detector design fulfilling the ambitious demands of compactness and hermeticity. Operational challenges not yet addressed with physics prototypes are the power-pulsed front end electronics and the on-detector zero-suppression in auto-triggered mode, which requires continuous and precise on-line control of thresholds. Therefore also technological prototypes need to undergo full-size beam tests. While the focus is rather on calibration and stability than on shower physics, beam campaigns of several weeks in combined set-ups are foreseen to start in 2010.

4.5 FORWARD DETECTORS

Special calorimeters are foreseen in the very forward region of the ILD near the interaction point - LumiCal for the precise measurement of the luminosity and BeamCal for the fast estimate of the luminosity [114]. The LHCal will extend the coverage of the HCAL endcap to smaller polar angles. Together they will improve the hermeticity of the detector.

A third calorimeter, GamCal, about 100 m downstream of the detector, will assist in beam-tuning. Also for beam-tuning a pair monitor is foreseen, positioned just in front of BeamCal.

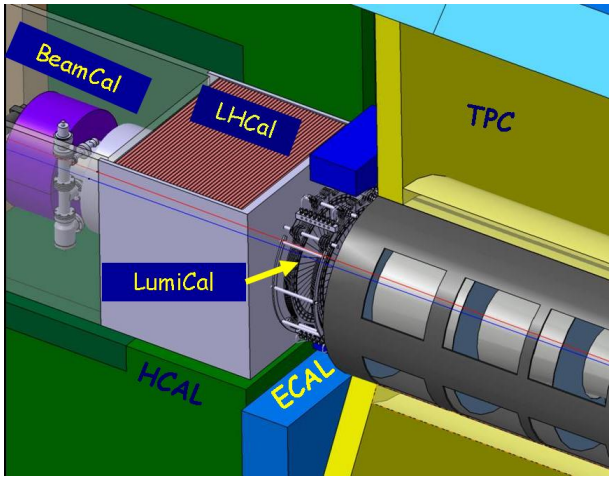

FIGURE 4.5-23. The very forward region of the ILD detector. LumiCal, BeamCal and LHCAL are carried by the support structure of the QD0 magnet.

LumiCal will measure the luminosity using Bhabha scattering, $e^+e^- \to e^+e^-(\gamma)$ as gauge process . To match the physics benchmarks, an accuracy of better than 10^{-3} is needed[2]. Hence, LumiCal is a precision device with challenging requirements on the mechanics and position control.

BeamCal is positioned just outside the beam pipe, in front of the final focussing quadupoles. A large amount of low energy electron-positron pairs originating from beamstrahlung will deposit their energy in BeamCal. These deposits, useful for a bunch-by-bunch luminosity estimate and the determination of beam parameters [116], will lead, however, to a radiation dose of several MGy per year in the sensors at lower polar angles. Hence extremely radiation hard sensors are needed to instrument BeamCal.

A pair monitor, consisting of a layer of pixel sensors positioned just in front of BeamCal, will measure the distribution of beamstrahlung pairs and give additional information for beam parameter determination.

These detectors in the very forward region have to tackle relatively high occupancies, requiring special FE electronics and data transfer equipment. A small Molière radius is of invaluable importance for BeamCal and LumiCal. It ensures an excellent electron veto capability for BeamCal even at small polar angles, being essential to suppress background in new particle searches where the signatures are large missing energy and momentum. In LumiCal, the precise reconstruction of electron and positron showers of Bhabha events is facilitated and background processes will be rejected efficiently.

LHCal will be a hadron calorimeter extending the coverage of the HCAL endcaps to small polar angles. It will allow a fair hadron shower measurement in the polar angle range of LumiCal and enhance the particle identification capabilities.

4.5.1 The Design of the Very Forward Region

A sketch of the very forward region of the ILD detector is shown in Figure 4.5-23. The design of these devices is complicated by the small crossing angle of the two beams. LumiCal and BeamCal are cylindrical electromagnetic calorimeters, centered around the outgoing beam. LumiCal is positioned inside and aligned with the forward electromagnetic calorimeter.

[2]For the GigaZ option an accuracy of 10^{-4} is the goal [115].

BeamCal is placed just in front of the final focus quadrupole. The pair monitor will be positioned just in front of BeamCal.

The structure of the ECAL end cap leaves a square hole at its centre. LumiCal needs to be positioned very precisely with a well defined fiducial zone around the outgoing beam and is therefore restricted to a minimal size to facility mechanical stability and position control. The "ECAL ring" fills the gap between the LumiCal and the ECAL. This device could be realised in the same technology as the ECAL, i.e. a 30 layer tungsten-silicon sandwich providing 24 radiation lengths.

The 30 mm gap between the ring and the end cap is partly filled by the electronics concentrating cards. This gap is covered in the back by the HCAL which ensures hermeticity in that region. The gap between the ring and the LumiCal contains the electronics of the latter and provides space for the tie-rods which suspend the magnet support structure from the coil cryostat. This gap is covered on the back by the LHCAL.A laser position monitoring system is foreseen to monitor the position of LumiCal and BeamCal with respect to the beam-pipe and the distance between them [117]. More details on the integration of the forward region are given in [118].

4.5.2 LumiCal

Monte Carlo studies have shown that a compact silicon-tungsten sandwich calorimeter is a proper technology for LumiCal [119]. In the current design [120], as sketched in Figure 4.5-24, LumiCal covers the polar angular range between 32 and 74 mrad. The 30 layers of tungsten absorbers are interspersed with silicon sensor planes. The FE and ADC ASICS are positioned at the outer radius in the space between the tungsten disks. The small Molière radius and finely radially segmented silicon pad sensors ensure an efficient selection of Bhabha events and a precise shower position measurement. The luminosity, $\mathcal{L}$, is obtained from $\mathcal{L} = \mathcal{N}/\sigma$, where $\mathcal{N}$ is the number of Bhabha events counted in a certain polar angle range and σ is the Bhabha scattering cross section in the same angular range calculated from theory. The most critical quantity to control when counting Bhabha scattering events is the inner acceptance radius of the calorimeter, defined as the lower cut in the polar angle. The precise determination of luminosity requires an excellent knowledge of the lower acceptance of the calorimeter. From Monte Carlo studies of the present design a tolerance of a few μm has been estimated [121]. Since there is bremsstrahlung radiation in Bhabha scattering, cuts on the shower energy will also be applied. The criteria to select good Bhabha events hence define requirements on the energy resolution and, more challenging, on the control of the energy scale of the calorimeter. The latter quantity must be known to about a few per mille [122]. Monte Carlo simulations are also used to optimise the radial and azimuthal segmentation of silicon pad sensors for LumiCal [119] to match the requirements on the shower measurement performance.

A first batch of prototype sensors [123], as shown in Figure 4.5-25, has been delivered from Hamamatsu Corp.. At the first stage these sensors will be characterised and qualified, in a later stage, they will be instrumented with Front-End (FE) electronics for investigations in the test-beam and eventually the construction of a calorimeter prototype.

Front-end and ADC ASICS are designed with a shaping and conversion time less than 300 ns, being potentially able to readout the calorimeter after each bunch crossing. The range of sensor pad capacitance and the expected signal range in electromagnetic showers originating from Bhabha events are taken from Monte-Carlo simulations [124]. Prototypes of the FE ASICS and pipeline ADC ASICS, manufactured in 0.35 μm AMS technology, are

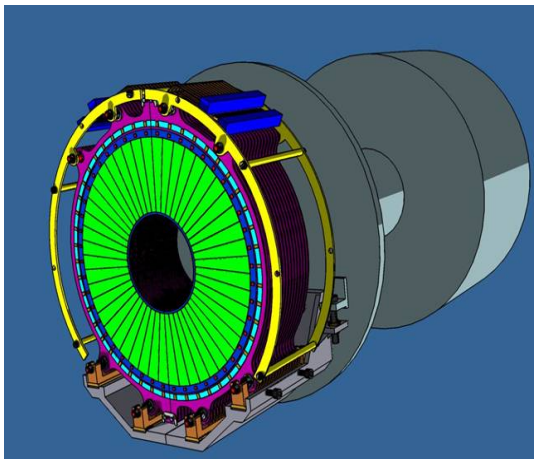

FIGURE 4.5-24. LumiCal designed as a silicon-tungsten sandwich calorimeter. In green the silicon sensor segments are shown and in yellow the mechanical frame which ensures the necessary mechanical stability.

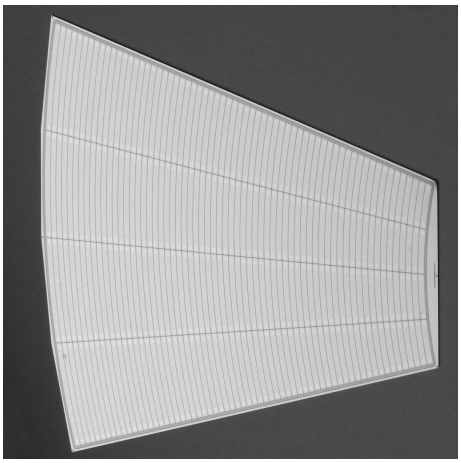

FIGURE 4.5-25. A prototype of a silicon sensor for LumiCal. The sensor in manufactured using 6 inch wafer of n-type silicon, the strip pitch is 1.8 mm.

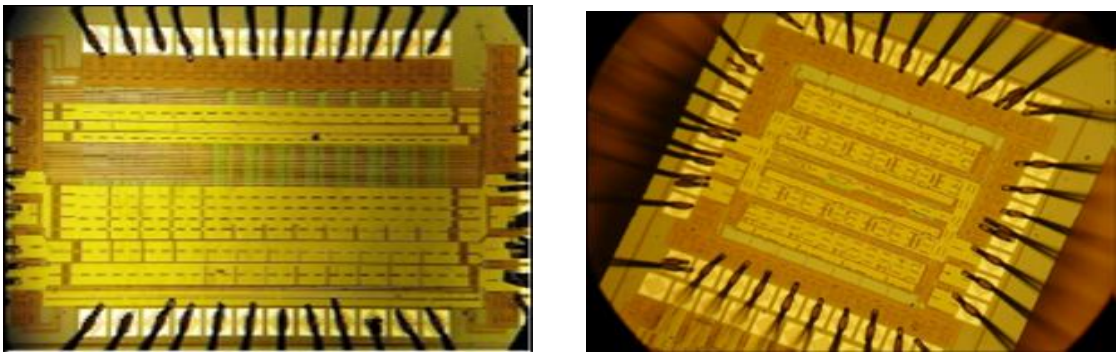

FIGURE 4.5-26. Prototypes of the FE (left) and ADC ASICS (right) prepared for systematic tests in the laboratory.

shown in Figure 4.5-26. The FE ASIC can be operated in low and high amplification mode. The high amplification mode allows to measure the depositions of minimum ionising particles. Hence muons can be used from the beam halo or from annihilations for the calibration and sensor alignment studies. The low amplification mode will be used for the measurement of electromagnetic showers. Tests of these ASICS prototype are ongoing [125]. Results on linearity, noise and cross talk measured are matching the requirements for the performance derived from Monte-Carlo simulations. For 2010 multi-channel prototypes of the ASICS are planned, allowing to instrument prototypes of sensor planes to investigate the performance of the full system in the test-beam.

4.5.3 BeamCal

BeamCal is designed as a solid state sensor-tungsten sandwich calorimeter, as shown in Figure 4.5-27, covering the polar angle range between 5 and 40 mrad. The tungsten absorber disks will be of one radiation length thickness and interspersed with thin sensor layers

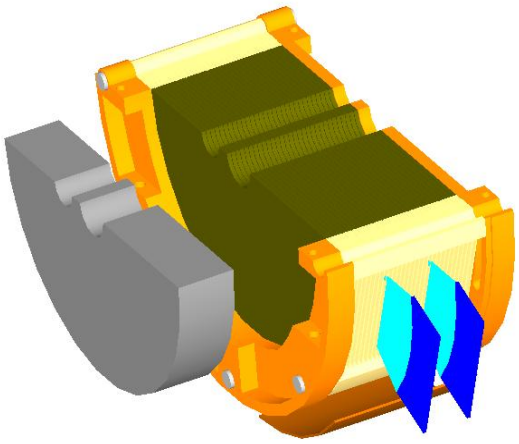

FIGURE 4.5-27. One half of BeamCal designed as a sensor-tungsten sandwich calorimeter. The graphite block is shown in gray, the tungsten absorber and the sensors in green and the FE electronics in blue.

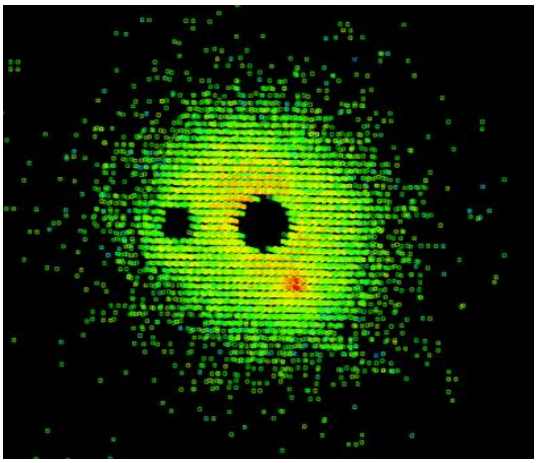

FIGURE 4.5-28. The distribution of depositions of beamstrahlung pairs after one bunch crossing on BeamCal. Superimposed is the deposition of a single high energy electron (red spot in the bottom part). The black holes correspond to the beam-pipes.

equipped with FE electronics positioned at the outer radius. In front of BeamCal a 5 cm thick graphite block is placed to absorb low energy back-scattered particles.

BeamCal will be hit after each bunch crossing by a large number of beamstrahlung pairs, as shown in Figure 4.5-28. The energy, up to several TeV per bunch crossing, and shape of these deposition allow a bunch-by-bunch luminosity estimate and the determination of beam parameters [116]. However, depositions of single high energy electrons must be detected on top of the wider spread beamstrahlung. Superimposed on the pair depositions in Figure 4.5-28 is the local deposition of one high energy electron, seen as the red spot at the bottom. Using an appropriate subtraction of the pair deposits and a shower finding algorithm which takes into account the longitudinal shower profile, the deposition of the high energy electron can be detected with high efficiency and modest energy resolution, sufficient to suppress the background from two-photon processes in a search e.g. for supersymmetric tau-leptons [126] in certain scenarios.

The challenge of BeamCal is the development of radiation hard sensors, surviving up to 10 MGy of dose per year. Polycrystalline CVD diamond sensors of 1 cm^2 size, and larger sectors of GaAs pad sensors as shown in Figure 4.5-29 have been studied. Polycrystalline CVD diamond sensors have been irradiated up to 7 MGy and were found to be still operational [127]. GaAs sensors are found to tolerate nearly 2 MGy [128]. Since large area CVD diamond sensors are still very expensive, they might be used only at the innermost part of BeamCal. At larger radii GaAs sensors seem to be a promising option. These studies will be continued in the future for a better understanding of the damage mechanisms and possible improvements of the sensor materials.

The FE ASIC development for BeamCal, including a fast analog summation for the beam feedback system and an on-chip digital memory for readout in between two bunch trains [129] is ongoing, first prototypes are expected in 2009.

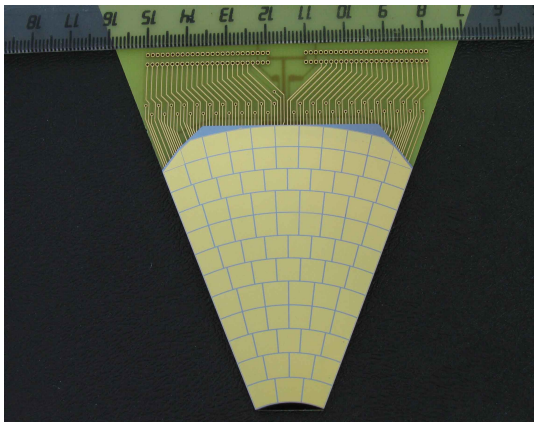

FIGURE 4.5-29. A prototype of a GaAs sensor sector for BeamCal with pads of about 1 cm2 area.

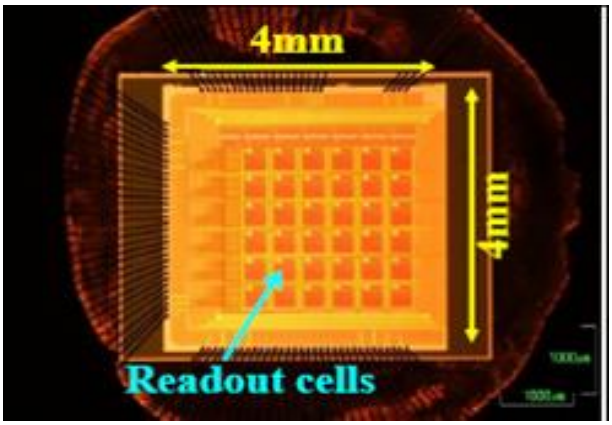

FIGURE 4.5-30. A prototype ASIC for the Pair Monitor Pixel layer. The pixel size is 400x400 μm^2.

4.5.4 The Pair Monitor

The pair monitor consists of one layer of silicon pixel sensors just in front of BeamCal to measure the distribution of the number of beamstrahlung pairs. Monte Carlo simulation have shown that the pair monitor will give essential additional information for beam tuning. For example, averaging over several bunch crossings, the beam sizes at the interaction point can be reconstructed with per cent precision [130]. A special ASIC, shown in Figure 4.5-30, is developed for the pair monitor. Prototypes manufactured in 0.25 μm TSMC technology are under study. At a later stage, the pixel sensor and the ASIC are foreseen to be embedded in the same wafer. The latter development will be done in SoI technology [131].

4.5.5 GamCal

GamCal is supposed to exploit the photons from beamstrahlung for fast beam diagnostics. Near the nominal luminosity the energy of beamstrahlung photons supplements the data from BeamCal and Pair Monitor improving the precision of beam parameter measurements and reducing substantially the correlations between several parameters [116]. At low luminosity the amount of depositions on BeamCal will drop dramatically, however, GamCal will still give robust information for beam tuning.

To measure the beamstrahlung spectrum a small fraction of photons will be converted by a thin diamond foil or a gas-jet target about 100 m downstream of the interaction point. The created electrons or positrons will be measured by an electromagnetic calorimeter. A conceptual design of GamCal exists, more detailed Monte Carlo studies are necessary to fully understand the potential of GamCal for beam tuning and beam parameter determination.

4.5.6 LHCal

The LHCal fits in the square hole of the HCAL and embraces the beam tube which is centred on the outgoing beam. It has a thickness of four interaction lengths comprised by 40 layers of tungsten of 1 cm thickness. The sensitive medium could be silicon sensors similar to the ECAL ones. LHCAL is supported by two vertical plates which are part of the forward structure. It would be made of two halves separated vertically, making it easy to dismantle.

The electonics concentrating cards would be on the top and the bottom.

4.5.7 Priority R&D topics

The current research work covers several fields of high priority to demonstrate that the designed devices match the requirements from physics. These are:

- Development of radiation hard sensors for BeamCal. The feasibility of BeamCal depends essentially on the availability large area radiation hard sensors.
- Development of high quality sensors for LumiCal, integration of the FE electronics in a miniaturised version and tuning of the full system to the required performance.
- Prototyping of a laser position monitoring system for LumiCal. In particular the control of the inner acceptance radius with μm accuracy is a challenge and must be demonstrated.
- Development and prototyping of FE ASICs for BeamCal and the pair monitor. There are challenging requirements on the readout speed, the dynamic range, the buffering depth and the power dissipation. In addition, a system for the data transfer to the back-end electronics has to be developed.

Also of high priority, but not covered for the moment, is the design of GamCal and an estimate of its potential for a fast feedback beam-tuning system.

4.6 COIL AND RETURN YOKE

The basic layout of the ILD detector has always followed the strategy of tracking in a magnetic field. The ILD detector design therefore asks for a 4 T field in a large volume, with a high field homogeneity within the TPC volume and with a reduced fringe field outside the detector.

The parameters of the ILD magnet being very similar to the CMS ones (c.f. [132], [133]), basic designs of both magnets are similar. An anti DiD (Dipole in Detector) is also added in the design, which allows to compensate the effect of the crossing angle for the outgoing beam (and pairs) behind the I.P.

4.6.1 Physics Requirements

The main requests from the physics for the ILD magnet are a solenoidal central field of nominal 3.5 T and maximum 4 T, in a volume of 6.9 m in diameter and a length of 7.35 m with the following requests:

- A high integral field homogeneity:

$$\left| \int_0^{2.25m} (B_r/B_z)\, dz \right| \leq 10\ mm; B_r = B_x(x/r) + B_y(y/r)$$

  within the TPC volume, which is a cylinder 3.6 m in diameter and 4.5 m long. This high homogeneity requests incorporating compensation windings.

- A fringe field in the radial direction less than 50 G at R = 15 m to not magnetically perturb the second detector when in operation on the beam line.

- A yoke instrumented for the detection of muons and for tail catching (see section 4.7).

4.6.2 Magnet Design

The magnet consists of the superconducting solenoid, including the correction coils, and of the iron yoke, one barrel yoke in three pieces and two end-cap yokes, also in two pieces each. The anti DiD is located outside the solenoid.

Concerning the correction coils, it seemed practically simpler and less space consuming to incorporate them into the main winding, by adding extra currents in appropriate locations of the winding.

The cross section of the ILD detector magnet is shown on Figure 4.6-31. Its main geometrical and electrical parameters are given in Table 4.6-8.

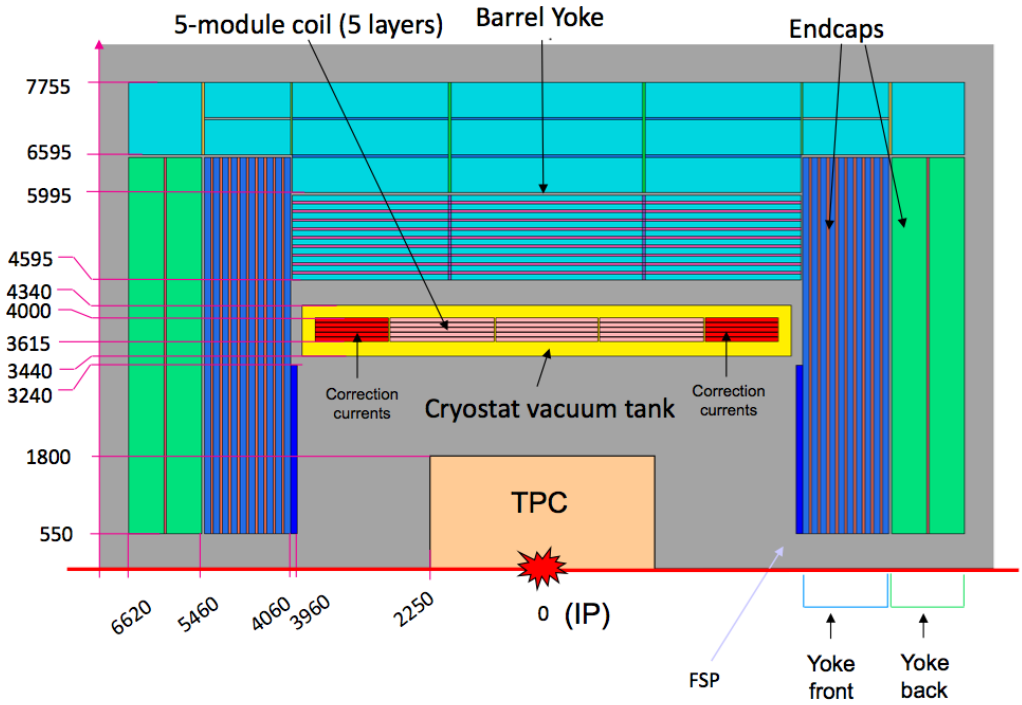

FIGURE 4.6-31. Cross section of the ILD magnet.

The coil is divided into five modules, electrically and mechanically connected: there are three central modules, 1.65 m long each, and two external modules, 1.2 m long each. All modules consist of a four-layer winding.

The nominal main current, 18.2 kA for a central field of 4.0 T, runs through all the turns of the solenoid. An extra correction current of about 15.8 kA is added in the turns of the four layers of the two external modules to get the integral field homogeneity.

The barrel yoke has a dodecagonal shape. It is longitudinally split into three parts. In the radial direction, the inner part of the yoke is made from 10 iron plates of 100 mm thickness, with a space of 40 mm between each to house detectors for tail catching and muon detection. Three thicker iron plates of 560 mm each with 40 mm spaces for muon detectors form the outer part of the barrel yoke. The weight of the barrel yoke is around 7000 t.

The end-cap yokes, also of dodecagonal shape, have a similar split structure, with 10 iron plates of 100 mm thickness in the inner part, with a space of 40 mm between each to house the tail catcher and muon detectors, and two external thick plates, each 560 mm thick, to

Cryostat inner radius (mm)	3440	Maximum central field (T)	4.0
Coil inner radius (mm)	3615	Maximum field on conductor (T)	5.35
Coil outer radius (mm)	4065	Stored energy (GJ)	2.0
Cryostat outer radius (mm)	4340	Stored energy/ cold mass (kJ/kg)	12.2
Barrel yoke inner radius (mm)	4595	Nominal main current (kA)	18.2
Barrel yoke outer radius (mm)	7755	Nominal correction current (kA)	15.8
Coil length (mm)	7350	Ampere-turns main coil (MAt)	1.52
Cryostat length (mm)	7810	Ampere-turns correction coils (MAt)	1.36
Yoke overall length (mm)	$6620 * 2$		

TABLE 4.6-8
Main geometrical and electrical parameters

make up the total iron thickness. A 100 mm thick field shaping plate (FSP) will be added inside each end-cap to improve the field homogeneity. The weight of each end cap yoke is around 3250 t and thus the total weight of the yoke is around 13400 t.

The main design challenge of the yoke endcaps is to contain the magnetic forces themselves. A weight equivalent of ≈18000 t pulls at each endcap. A FEM analysis shows that if the endcaps are constructed in radially fixed segments (c.f. figure 4.6-32) the deformation of the endcaps due to the magnetic force could be less than 3 mm; alternative designs which lead to comparable small deformations are also under study. These deformations are far smaller than e.g. at CMS where the endcaps are deformed by ≈16 mm during the powering of the magnet.

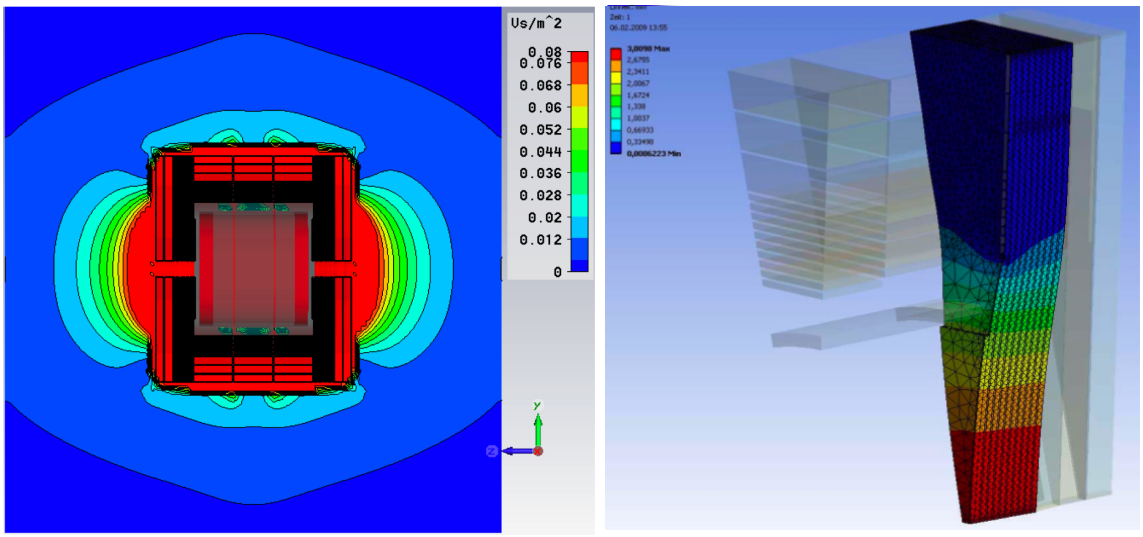

FIGURE 4.6-32. Stray fields outside the yoke (left). Deformation of an endcap segment (right).

4.6.3 Magnetic Field

The calculated integral field homogeneity, with the nominal values of the main and correction currents given in table 4.6-8 meets the requirement (maximum value of 7 mm at 4 T). Note that the effect of the anti DiD is not taken into account in this calculation.

With the yoke structure described, the calculated fringing field is ≈40 Gauss at 15 m in the radial direction and therefore fulfils the requirements (c.f. figure 4.6-32).

4.6.4 Technical Aspects

As several technical aspects are quite similar for the ILD and CMS magnets, the experience gained during the construction of the CMS magnet will be of great help for ILD.

The conductor will consist of a superconducting cable coextruded inside a low electrical resistivity stabiliser and mechanically reinforced by adding high-strength aluminum alloy. Two different conductors will be necessary, using different superconducting cables and different ratio of mechanical reinforcement, but with the same overall dimensions.

The winding will be done using an inner winding technique. The magnetic forces will be contained both by the local reinforcement of the conductor and by an external cylinder. The coil will be indirectly cooled by saturated liquid helium at 4.5 K, circulating in a thermo-siphon mode.

The central barrel yoke ring will support the vacuum tank. Internal sub-detectors will be supported on rails inside the vacuum tank.

4.7 MUON DETECTOR

The identification of leptons is an important part of the physics programme at the ILC. For muons above a few GeV, the instrumented iron return yoke is used as a high efficiency muon identifier. The clean environment of an electron-positron Linear Collider allows for a muon system design that is much simpler compared to the ones that have been developed for the hadron colliders. There is no need to trigger on muon tracks; instead the clean nature of the events at the ILC allows the linking of track candidates from the inner detectors with tracks in the muon system.

In addition to its muon tagging ability the system will be instrumented to allow for a limited calorimetric performance. In this way it can act as a tail catcher, tagging late developing showers and thus improving the energy measurement.

A muon is most easily identified by a track in a muon detector behind significant material. At the ILD, the muon system is reached by muons with a momentum above about 3 GeV. The strong central magnetic field will keep lower energy particles from reaching the muon system. The main challenge then for these type of muons is the joining of a signal in the calorimeter with a track segment outside the coil. Multiple scattering in the calorimeters and the coil will have a large impact on this, and the efficiency of association will increase with momentum. At lower momenta, the signal in the calorimeter will be used to identify muons. In particular inside jets this is difficult, and more in - depth studies are needed within ILD to reach strong conclusions.

4.7.1 Conceptual Design

The muon system in ILD will cover a large area of several thousand square meters. The detectors therefore need to be reliable, easy to build, and economical. Signals from the detectors should be large so that simple readout systems and cable routings can be used to the readout modules. The detectors should have a reasonable temporal and spatial resolution. Searches for long-lived particles and tagging of cosmics and beam halo muons requires that a few nsec time resolution be achievable. Since multiple scattering is significant, spatial resolutions in the range of cm are sufficient. Occupancies are low, so that both strip and pixel devices can be considered. The efficiency and reliability of muon identification somewhat depends on the iron longitudinal segmentation as do calorimetric performances. Mechanical construction and practical considerations indicate that plate thickness cannot be below 10 cm. For the ILD design, the total thickness needed to close the magnetic flux is ≈ 275 cm (see 4.6). It is instrumented with 10 layers of detector with 10 cm thick absorber plates in between, and a few layers at larger distance in the remainder of the yoke.

Both gas detector and extruded scintillator strips can in principle fulfill the requirements. Plastic Streamer Tubes (PST) or Resistive Plate Chambers (RPC) are candidates for the gas detector. However, RPCs tend to be preferred over PSTs due to their reduced cost and greater flexibility in the segmentation achievable. For the RPC option one could use strips $3 - 4$ cm wide to obtain the desired resolution. Each gap could provide two orthogonal coordinates, with orthogonal strips on the two sides of the gas gap, while energy would be measured for non muon-hits just by hit counting. The electronics would consist of single bit information per strip; the front-end would include a variable threshold discriminator. The channel count would range around 100K.

An alternative solution relies on extruded plastic scintillator strips. Wavelength shifting fibres are embedded into the strips, and are read out at either end of the strips with silicon photomultipliers (SiPMs). The small size, low operating voltages and magnetic field immunity of the SiPMs implies that they can be placed inside the detector, thus obviating the need for routing fragile fibres. Orthogonal placement of strips can provide space-points with the required resolution. A prototype based on this technology, the tail-catcher/muon tracker (TCMT), has been built and exposed to a test beam by the CALICE collaboration at CERN and Fermilab during the 2006-2008 period. The extended operation of the TCMT has clearly demonstrated its excellent reliability and performance (see Fig. 4.7-33). It should be noted that useful synergies may exist between the muon system and the hadron calorimeter since RPCs and scintillator are both potential technology options for the HCAL.

4.7.2 Performance

Performances of the muon identification system described in the previous paragraph have been evaluated both with single particles and high multiplicity final states. In order to assess the linking capabilities of the proposed detector, single particle efficiency has been evaluated as shown in Figure 4.7-34(left top). In the same figure (left bottom) the efficiency is shown for muons identified in $b\overline{b}$ events. The plots in Figure 4.7-34 show that the performance remains excellent also in complex high multiplicity events .

The muon system also does have a limited calorimetric capability. On average the energy leakage into the muon system is small but with large event-to-event fluctuations. For K^0_L the average energy leakage is 3% for a range of energies, but energy leakage four or five times the average is not uncommon. The use of the muon system to estimate and correct for the leakage

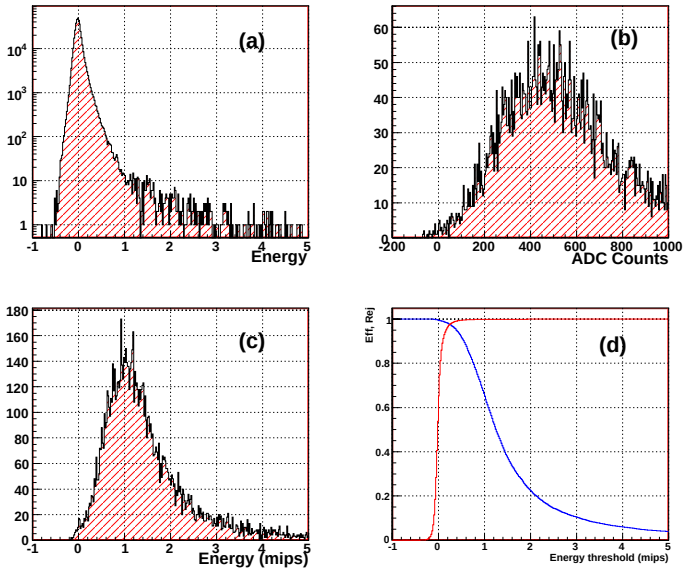

FIGURE 4.7-33. For a typical TCMT strip:(a) pedestal distribution (b) pedestal subtracted MIP signal from muons (c) MIP calibrated signal (d) efficiency (blue) and noise rejection (red) as a function of the energy threshold.

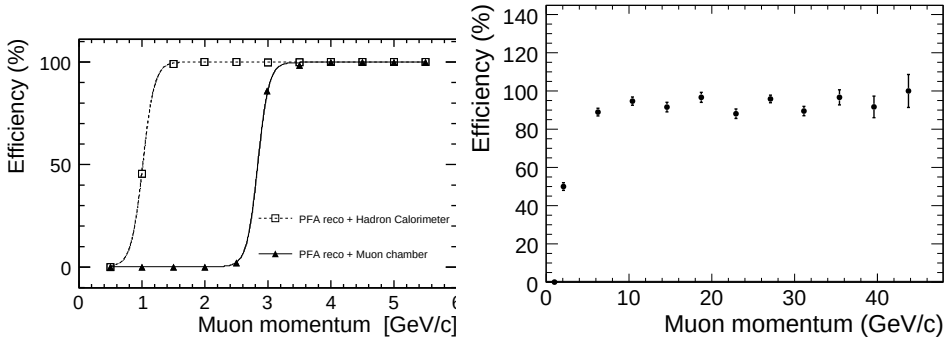

FIGURE 4.7-34. (top): Muon identification efficiency vs. momentum for single muon. The right curve represent muon found only in the muon system, the left curves muons which were found by a combination of HCAL and muon system. (bottom): Muon finding efficiency in $b\bar{b}$ events.

is hampered by the presence of the coil, which introduces close to two interaction lengths of dead material between the last calorimeter layer and the first muon layer. Nevertheless a correlation between the energy of hadrons and the leakage signal recorded in the muon system can be observed and used to improve resolution in simulation and test beam data (see Fig. 4.7-35).

4.7.3 Outlook

The proposed muon system for the ILD concept is well matched to the requirements as laid down in this document. Two alternative technological implementations are discussed, one based on gaseous detectors and the other based on plastic scintillator strips. The system will

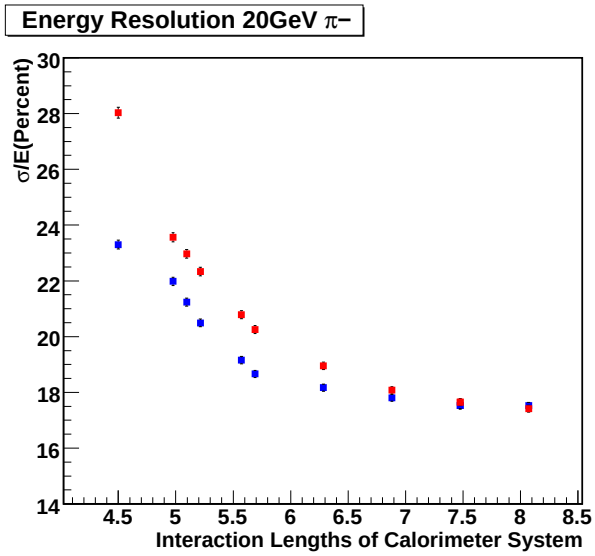

FIGURE 4.7-35. Resolution improvement for 20 GeV pions by including energy beyond the coil using CALICE testbeam data. The red points correspond to the resolution obtained for a given thickness of the calorimeter system while the black points supplement the energy in the calorimeter system with that from beyond the coil. The change in length of the calorimeter system, the material contained in the coil and energy beyond the coil are simulated by rejecting or accepting layers in the TCMT.

serve primarily as a muon identifier, but will also play an important role as a tail catcher to compensate for leakage from the calorimeter system. Continued R&D is required to establish a detailed, realistic design and make an informed technology choice.

4.8 CALIBRATION AND ALIGNMENT

The ILD detector is a sophisticated precision instrument. It consists of a high precision tracking detector, surrounding the interaction point, followed by a granular calorimeter system covering nearly the entire solid angle.

To reach the anticipated performance calibration and alignment of the sub-detectors and of the overall detector system are a central part of the detector design and is important for the complete life cycle of the experiment, from the design over the construction to the operation of the device.

For the rest of this section we define calibration to be all tasks which deal with the internal description of the detectors. Alignment is the relative positioning of internal parts of the subdetectors or of sub-detectors relative to each other.

Calibration and alignment of all sub-systems will be based on a mixture of data from dedicated calibration systems and from particles recorded during physics running.

During construction tolerances must be carefully controlled, during commissioning systematic metrology of the different detector parts is needed. This will provide an initial alignment of the modules internally, and of the different systems relative to each other. The need for a high precision metrology has consequences for the mechanical design of the differ-

ent sub-systems, which from the beginning need tolerances determined to allow the necessary level of mechanical precision. In particular in the tracking system care has to be taken to ensure that the mechanical systems are stable enough to allow an alignment at the level of 10μm or better.

After installation, and throughout the lifetime of the detector, constant measurements will be taken using dedicated hardware to monitor the position of the different detector components, improving the alignment from the initial situation.

The final calibration of the detector will be done using particles. Tracks from the decay of the Z - boson will play an important role here, as they are of well known high momentum. The best source of such tracks are from short and dedicated runs of the collider on the peak of the Z resonance, at 91 GeV. For the discussions in the following sections we assume that around $1pb^{-1}$ of data can be collected within a few hours of running at 91 GeV. This will result in some 30000 Z bosons, of which around 1000 will decay as $Z \rightarrow \mu^+\mu^-$.

The final high precision calibration will be derived from tracks in the data sample taken at high energies. Stiff tracks e.g. from W decays or from $q\bar{q}$ pair events will provide a large sample of tracks. The design of the detector has been optimised in a way to allow a calibration heavily relying on such data.

The detector alignment at the ILC is a particular challenge because of the intended push-pull mechanism to switch between two detectors. This implies that each detector will move out and back in into the interaction region frequently, and that the overall alignment of the system should be re-established rapidly after a push-pull operation. As discussed in 6.4 the switchover times between the two detectors should be of order of a few days with consequently the need to do a rapid re-establishment of calibration constants within a day or so. Both the detector design and the alignment concept need to take these requirements into account.

Another challenge will be the need to power-pulse the detectors inside the magnetic coil to limit the total power consumption. Most detectors will be switched off or switched to reduced power in between trains of the collider. This procedure of power pulsing will potentially apply significant forces to the detector structure, during the ramp up or ramp down of the power, and stress the components with significant swings in temperature. Special care must be exercised during the design of the mechanical system to ensure that the structure does not move during these cycles, and that the alignment does not suffer from train to train.

In this section the calibration and alignment strategies of the overall detector are discussed. Calibration strategies for individual sub-detectors have been discussed in the relevant sections describing the sub-detector technologies.

4.8.1 Tracking System Calibration and Alignment

A main purpose of the tracking system is the efficient finding of charged particles, the reconstruction of their momenta and their impact parameters. The anticipated precision for the momentum and the impact parameter are significantly above anything ever achieved before in a detector of this size and complexity. Using a simple model of the track parameters dependence on alignment tolerances, the following limits for the alignment of each of the tracking sub-systems have been derived:

- coherent displacement of the VTX, 2.8 μm;
- coherent displacement of the SIT, 3.5 μm;
- coherent displacement of the SET, 6 μm; and
- coherent displacement of the TPC, 3.6 μm.

These values must be confirmed by further studies.

An important aspect of the overall alignment of the tracking system is the knowledge of the central magnetic field. Uncertainties on the size and direction of the field within the tracking volume will directly impact the momentum resolution. Using sophisticated magnetic field probes the field will be measured to a precision of $dB/B < 10^{-4}$. This level of precision has been reached in previous experiments using large volume magnetic fields [95].

The above distortion limit defines the precision required for the magnetic field calibration. In a TPC, the drifting electrons follow the magnetic field lines; field components perpendicular to B_z result in deflections of the track as measured at the readout plane. The magnet is designed to have a field uniformity of $\int B_r(constructed)/B_z dz = 2$ mm $-$ 10 mm. These deflections are largely corrected with the application of the magnetic field map. However, residual misunderstanding of the magnetic field will result in track distortions. Thus, the mapping of the magnetic field must be significantly improved beyond the initial probe precision stated above, $dB/B < 10^{-4}$. Based on the limit of the internal fit sagitta above, the magnetic field map must have a precision of $\int B_r(correction)/B_z dz < 20 - 30\mu$m. For the case that magnetic field distortions that are coherent along the drift length of about 2 meters, the integral is equivalent to the requirement that $dB/B < 10^{-5}$. It is envisioned that stiff tracks as observed in either Z decays of in high energy collisions will provide the necessary information.

4.8.1.1 Silicon Tracking Alignment

Calibration and alignment of the detectors are an important consideration already during the design and construction phase of the different silicon based sub-detectors. These aspects are discussed in detail in section 4.2.6. The alignment among different sub-detectors, and relative to the rest of the ILD detector, will be based on a three-fold approach: two laser based alignment systems will be combined with a sophisticated alignment strategy based on tracks.

The extent of the challenge for alignment becomes clear if one considers the number of degrees of freedom which need to be determined. For the ILD silicon tracker this number is of the order of 100.000 (calculated as six times the number of sensors). If the relative sensor positions in the module are known to the required precision (from survey data or from other hardware alignment systems) the number of degrees of freedom is reduced by a large factor (a factor five in SET that dominates the NDOF count, a factor two or three in ETD). The contribution of the outer tracking system is larger than that of the inner tracker by a factor 10.

If we can assume that the different support structures are basically rigid, and do not change dimensions internally, within the precision anticipated, we only need to worry about the overall alignment of the different sub-detectors relative to the rest of the detector. The goal of ILD is that this situation is reached for a re-alignment after a push-pull operation. In this case the number of degrees of freedom is greatly reduced:

- The outer Silicon tracker, SET, is fixed to the TPC. It is supported by a rigid carbon fibre structure. It probably needs to be split in the middle. In this case 12 degrees of freedom are needed to determine the position of the overall SET.
- The ETD is attached to the endcap calorimeter in one piece. In total 8 degrees of freedom need to be considered.
- The SIT and the FTD are connected to a common support structure. The movement of this structure has 6 degrees of freedom.

Component	number of		# of sensors/	# of channels	area
	layers	modules	module		m^2
SIT1	layer 1	33	3	66000	0.9
	layer 2	99	1	198000	0.9
SIT2	layer 1	90	3	180000	2.7
	layer 2	270	1	540000	2.7
SET	layer 1	1260	5	2520000	55.2
	layer 2	1260	5	2520000	55.2
ETD_F	X,U,V	984		2000000	30
ETD_B	X,U,V	984		2000000	30
FTD	7	350		5000000	

TABLE 4.8-9
Number of modules, channel count, and sensitive area for the different Silicon based detectors.

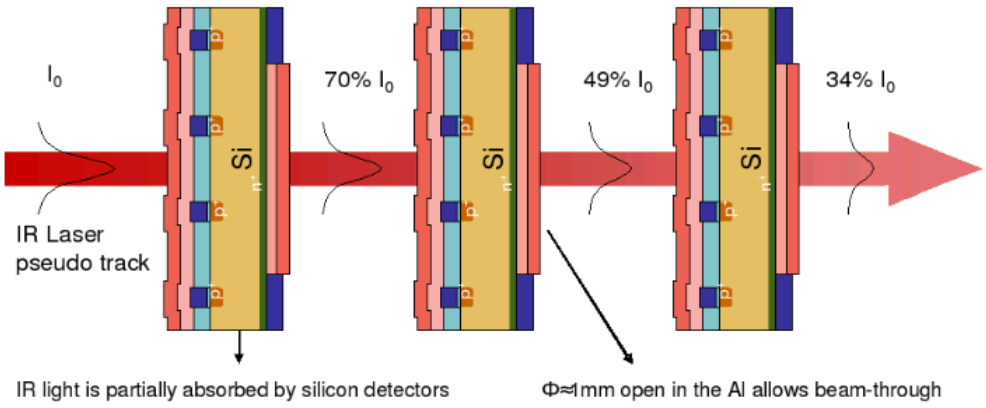

FIGURE 4.8-36. Schematic view of the infra-red laser beam traversing several micro-strip sensors.

In total 26 degrees of freedom are present in this case. This reduces the initial problem to one which can be solved in fairly short amount of time.

Details about the module and channel count in the silicon system are given in Table 4.8-9.

4.8.1.2 A laser based alignment system

A hardware position monitor system based on infra-red laser beams mimicking straight tracks will be installed in the ILD detector. The laser beams traverse several sensors optimized for IR laser transmittance (see Fig. 4.8-36). The signals from the laser are readout using the module sensor and front end electronics. Therefore, there is no added contribution to the error budget associated to the mechanical transfer between monitored fiducial marks and strips. The resolution expected on sensor transversal movements will depend on the number

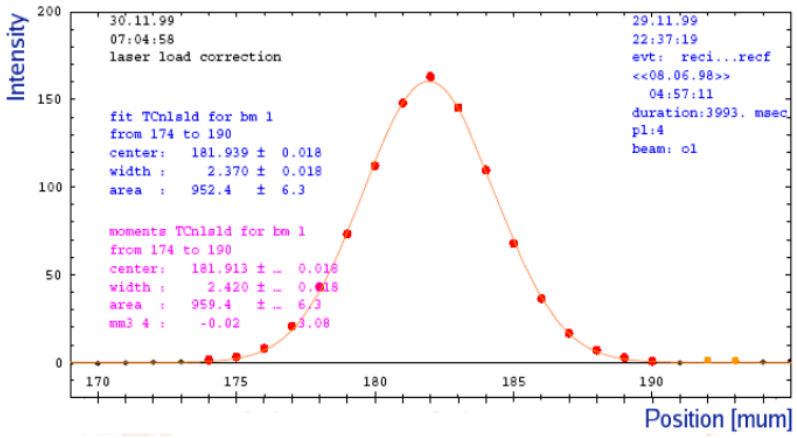

FIGURE 4.8-37. AMS results on the reconstruction of the laser signal on the third sensors in the stack. The data points are the result of averaging 480 readings. The position of the laser pulse can be reconstructed with a resolution of 1 micron.

of strips illuminated by the beam and the sensor pitch. For a pitch value of 50 μm with a gaussian width of the laser beam of $\sigma = 300\mu$m, resolutions below 1μm are achievable. A similar system is in use im the AMS experiment where a silicon tracker with a geometry similar to the FTD (comparable tracking volume, number of layers and cylindrical symmetry) has reached an accuracy of 2μm [134] (see Fig. 4.8-37). The laser alignment system provides the possibility to precisely monitor relativly fast movements. The current design of the ILD forward tracking disks incorporates this system. The system is able to constrain several degrees of freedom of a large fraction of the installed micro-strip sensors in the FTD and the other strip detector, and of the third tracking disk based on pixel technology. The extension to other sub-detectors is being investigated.

Particularly challenging is the connection between the inner and the outer silicon detectors, because of the large distance between them, and the connection between the silicon tracker and other detector elements. Here a pixel based monitoring system (PMD), excited by an IR laser through optical fibres is under consideration. In this system special pixel detectors are attached to the sensors to be aligned. The pixel devices will be installed in several strategic places of the tracking system

The IR laser systems will be complemented by a network of fiber optic sensors (Fiber Bragg System or FBS) that will monitor structural changes like deformations or relative displacements among structures, and environmental parameters as humidity and temperature. These sensors are based on Bragg gratings built into mono-mode optical fibers. In this technology, the carrier fiber is also the readout line. Compared to other traditional sensing techniques they are immune to electromagnetic interference and temperature effects.

4.8.1.3 Alignment of the Time Projection Chamber

The large volume time projection chamber is a central piece of the ILD tracking system. The TPC will provide more than 200 space points along a track. The longest drift distance possible is around 2.3 m. The anticipated spatial resolution in the device is around 60-100 μm.

In addition to the calibration issues discussed in the previous chapters, the TPC is particularly sensitive to the magnetic field in the detector. The survey and calibration of the magnetic field will be a major part of the TPC calibration.

Mechanically the Silicon tracking detectors will all be mounted relative to the TPC. Most probably - though a detailed engineering design has not yet been done - the inner Silicon tracking system will be suspended from the end - plate of the TPC on either side. The external Silicon tracking in the barrel will be supported by the field cage, the external Silicon tracking behind the TPC endplate will be supported by the endplate itself, or possibly by the endcap electromagnetic calorimeter. The TPC as a whole will be suspended from the coil of the ILD detector.

The PMD laser system will possibly be used to reference the TPC relative to the Silicon detectors, and transfer the location of the TPC to the coil. With this system the main degrees of rotation and shift between the TPC and the rest of the Silicon can be determined, and serve as starting point for the overall determination of alignment constants.

4.8.1.3.1 Internal TPC Alignment

The internal alignment of the TPC will be based on a well understood and measured field cage of the system. A construction of the field cage at the 0.1 mm level seems possible, and a survey of the finished field cage at the level of 30μm might be not unrealistic.

The B-field, which is as important to the ultimate measurement precision as the mechanical components, will be mapped using probes to a level of $dB/B < 10^{-4}$ as described in [95]. Starting from a well understood magnetic field, unambiguous preliminary tracks can be defined in the TPC. These will be used to iterativly improve the calibration of the TPC, and will eventually serve as starting points for tracks spanning the full tracking system.

In the TPC, the internal components, i.e. the detector readout modules, will be manufactured to tolerances of 20μm, while tolerances for placing the modules on the end-plate will be about 60μm. The internal TPC alignment process must provide the final required precision for both the mechanical alignment and the magnetic field measurement. Achieving these goals will require iteration. As mechanical distortions and magnetic field distortions can lead to similar track distortions, supplementary alignment systems will be used to resolve the ambiguities.

The internal alignment in the TPC will be helped by laser systems installed on the TPC in two ways: using a system of mirrors straight tracks created by a laser are created inside the drift volume, and can be used to determine many calibration constants. In addition diffuse light will be shone on the cathode surface, on which an appropriate coating creates a pattern of charge, which can e.g. be used to calibrate field distortions and the drift velocity.

4.8.1.4 Maintaining the alignment

Probes mounted on the fieldcage of the TPC will be used to monitor the B-field during running. Pressure and temperature will be measured continuously and will be corrected for on the fly. Cosmic-ray tracks and laser systems will be used to check for changes of the internal alignment in the TPC. Tracks from Z running will be used to extend coverage to the whole detector because lasers can only monitor a limited number of reference points, and cosmic rays give reasonable coverage of the vertical direction only.

The PMD laser system will provide a constant stream of alignment data and monitor in real-time the position of the TPC relative to the rest of the detector.

4.8.1.5 Track Based Alignment

While the hardware based systems are invaluable to do a fast re-calibration of the tracking system for the most relevant degrees of freedom, they are not suited for the final high precision alignment. This will need to be based on data from particle tracks. Previous experiments have developed a sophisticated machinery and have shown that the alignment transform can be determined to a precision well below the intrinsic resolution of their detectors, assuming that a large enough sample of high quality alignment tracks can be collected. The most important consideration in selecting the track sample is to tightly constrain all degrees of freedom of the detector geometry, including those that leave the track residual distributions (nearly) unchanged. Typically, the alignment sample is composed of a mixture of collision data and tracks from other sources. High p_T tracks are particularly valuable as they minimize the influence of multiple scattering. A strong constraint on the detector geometry derives from tracks that traverse overlapping detector modules (in the vertex detector and silicon tracking systems). Tracks from cosmic rays and beam halo are useful as they allow to relate different parts of the detector (upper and lower half, both end-caps). Tracks with known momentum are extremely valuable, both as a means to determine some of the weakly constrained alignment parameters and as a monitoring tool to validate the alignment. This role has traditionally been played by tracks from resonances with a well-known mass (the Z-resonance is the most popular as it provides stiff tracks, but J/Ψ and Upsilon have been used as well).

One of the main limitations of the track based system is that it will not be able to follow fast changes in the detector. Given the rather small production rate for $Z- > \mu^+\mu^-$ events in the ILC at 500 GeV the typical time constant to align all degrees of freedom of the detector is likely to be of the order of months . However, reduced sets of degrees of freedom, corresponding to higher-level mechanical units like ladders and rings, or even complete cylinders and disks, can be aligned with much less statistics and, hence, at a much greater frequency. In how far tracks from high energy running can be used is a matter of discussion, and will need further in-depth investigation.

4.8.2 Calorimeter Calibration and Alignment

A central part of the ILD detector is a highly granular calorimeter. At the moment a number of different technology options for the different parts are under consideration. In general though they all display a large number of channels, to obtain the excellent spatial resolution needed for particle flow. For any sort of stochastic calibration or alignment uncertainly this is an asset rather than a burden, since the precision with which these effects need to be known scale with $1/\sqrt{N}$, where N is the number of channels. Nevertheless the detailed procedures and the way calibration is implemented differ significantly from technology to technology, and will be discussed separately below.

4.8.2.1 Si-W electromagnetic calorimeter

The information used for defining the alignment and calibration procedures of the ILD electromagnetic calorimeter comes from two sources: a very detailed simulation of the calorimeter and the results from a prototype exposed to beam for now four years. Alignment: The requirements on alignment come from the precision we can reach in measuring the position of a shower. This is of the order of $1\text{mm}/\sqrt{E}$. Therefore an alignment precision of 100μm is

the goal. The main uncertainty comes from the play of the slabs inside the alveoli. With a survey of the module and a careful positioning we can reach 250μm, we need then an alignment with tracks in situ. A small number of electrons, thousands, should be enough to align the calorimeter with respect to the tracking system at the required precision.

4.8.2.1.1 Energy calibration An early study had shown that the energy measurement in our calorimeter is robust against dead channels. Provided they are quite randomly distributed, a fraction up to 5% dead channels does not harm the resolution. The mean response is restored by estimating the dead channels response from their neighbours and the resolution is very marginally touched. The measurement of the channel noise provides the identification of the dead ones.

A good energy calibration is the result of a suite of dedicated actions. First the design of the detector is chosen to provide an intrinsic stability with variables like temperature, humidity, radiation, voltages, etc. Second a monitoring of these variables and of the detector response evolution with them is ensured. Third the cells are, at construction time, intercalibrated at an adequate level of precision. Finally the absolute calibration is determined in test beams for few modules and globally at running time. The large number of cells is an asset, as teh calibration fluctuations decrease with $\sqrt{N}$ os the number of cells. The estimation of energy uses a combination of two estimators, the deposited energy and the counting of cells. The fully depleted silicon diodes offer a very stable behaviour. The tungsten plates can be checked. A complete cosmic ray testing produces the accuracy needed by measuring the minimum ionising particle peak. This has been done in the prototype with success. It is estimated to be a work of 200 days. The electronics is monitored accurately by injecting charges calibrated by a band gap device. It can be noted that the two estimators of energy are sensitive to very different systematic effects providing a powerful global test. After the inter-calibration, the absolute calibration is done by comparison with the tracker or using electrons and photons kinematically constrained like Bhabha's or return to the Z. This does not require any running at the Z peak

4.8.2.2 Scintillator Tungsten Electromagnetic Calorimeter

The scintillator ECAL consists of 1 cm $\times$ 4.5 cm scintilator strips, readout with Multi Pixel Photon Counters (MPPC). The calibration of these devices, similar to the analogue HCAL, needs to be done for the energy scale and limearity, and should be monitored against changes of environmental conditions such as temperatur etc.. The calibration will be based on a mixture of built-in calibration systems and the use of particle, either from cosmic-ray muons, or from test beams, before installation.

A further calibration of the strips may be done using tracks during operation of the device. To reach an accuray of 5% per channel, about 100 calibration quality tracks are needed. An ideal data sample for this would be an extended run at the Z-pole; to collect enough tracks about $100pb^{-1}$ would be sufficient. This amount of data will only be available at rather infrequent intervals, since it corresponds to a few weeks of running on the Z pole. However once calibrated the system is intrinsically stable if monitored well, and no frequent channel-by-channel recalibration is needed.

The photon sensor MPPC has a powerful built-in calibration capability, which is also used in the AHCAL. By identifying the response to single, two, three etc photons, a precise response and energy dependence can be established from data, for every single MPPC channel. THe single photon signals will be produced by a system of light fibres and blue LEDs, which

illuminate each channel with a well defined intensity. This system will be used to monitor the time dependence of the calibration constants as well.

4.8.2.3 Hadron calorimeter alignment

Depending on the choice of technology the hadronic calorimeter has cell sizes as small as $10 \times 10\text{mm}^2$, thus requiring a mechanical precision at the mm level for the absorber and sensor structures. This precision will be somewhat less stringent for the analogue hadronic calorimeter, which has larger cells. From the construction and survey the location of the cells to this accuracy will be known for the installed detector. The alignment required between different parts of the calorimeter system are also at a level of mm and will be established with data, based on muons from different sources.

4.8.2.3.1 Scintillator analogue hadronic calorimeter energy calibration The scintillator tile HCAL, segmented in 48 layers and 32 barrel, 32 end-cap modules, has 8 million read out channels. While electromagnetic and hadronic energy scales can be established with sample structures of the HCAL alone or in conjunction with the ECAL exposed to beams of muons, electrons and hadrons, the inter-calibration of the detector cells must be established with muon beams for all active layers of the detector. Based on test beam experience, we estimate that this can be accomplished in about two months. The calibration accuracy is maintained using LED monitoring of the photo-sensor gain, in-situ MIP calibration based on track segments in hadron showers and classical slow-control recording of the relevant operation parameters, temperature and bias voltage. These methods have been successfully applied to test beam data.

Simulating ILC events and using algorithms bench-marked with test beam data, we have determined the required luminosity for in-situ MIP calibration of individual cells and of average values for sub-sections of the detector, like module layers. A cell-by-cell in-situ calibration is not possible with realistic running times, but it is also not necessary. Average values for individual module layers can be obtained with a comfortable accuracy of 3% from a data set corresponding to $10pb^{-1}$ at the Z resonance or $20fb^{-1}$ at 500 GeV. For the innermost 20 layers, this accuracy is achieved with $1pb^{-1}$ or $2fb^{-1}$, respectively (see Fig. 4.8-38 for more details).

Using detailed simulations of the ILD detector and reconstruction based on the Pandora PFA, we have modeled different scenarios of statistically independent as well as coherent miscalibration effects, affecting the entire HCAL or parts of it. Purely statistical variations, like those arising from calibration errors or random aging effects, do not affect the resolution at all. However, they may degrade the in-situ MIP calibration capability. From this, a moderate requirement of the inter-calibration stability of 10% is derived. Coherent effects which could for example arise from uncorrected temperature variation induced changes of the response are potentially more harmful, as they directly show up in the constant term, if they affect the entire detector. However, these are easy to detect, and even a 5% variation only mildly propagates into the jet energy resolution. Systematic effects in sub-sections like layers are unnoticeable unless they exceed about 15%, comfortably in range of the in-situ calibration method accuracies.

The concept was experimentally verified by using data from two independent test beam experiments, performed with the same module, at two different locations CERN and Fermilab. The module which had some 9000 channels was calibrated based on data in one location, and

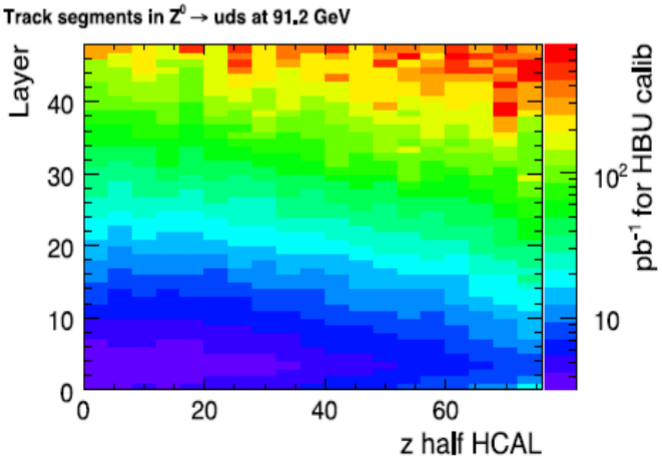

FIGURE 4.8-38. Required luminosity for an in-situ calibration of the AHCAL, as af function of position of the cell to be calibrated. The scale on the right gives the amount of integrated luminosity needed for one HCAL base unit (HBU).

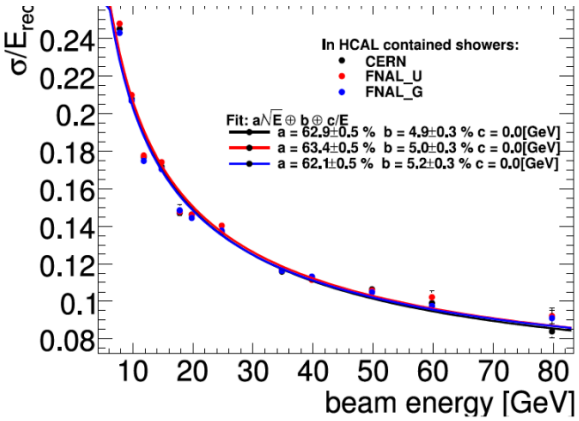

FIGURE 4.8-39. Comparison of measured energy resolution from three independent test beam experiments. The calibration constants were obtained in one experiment, and transported to the other ones. Excellent agreement is achieved, demonstrating the intrinsic stability of the system.

the calibration constants were then applied to the data recorded at the second location. The resulting comparison of the energy resolution of the detector is shown in Fig. 4.8-39.

We convinced ourselves of the validity of these simulation based estimates by treating our test beam experiment like a collider detector, using cell-by-cell inter-calibrations only from data taking at a different site, under different conditions. Applying only in-situ monitoring techniques, we re-established the scale and reproduced the resolution. Imperfections absent in the simulation showed up, but were successfully compensated. All in all, we conclude that the high granularity and channel count is a blessing rather than a curse. On one hand, thanks to the law-of-large-numbers suppression of statistical effects, the requirements on individual cell precision are very relaxed. Coherent effects, on the other hand, can be studied with any desired combination of channels, be it layers, longitudinal sections, electronics units or

according to any other supposed hypothesis of systematic effects. This has been proven to work with data taken at CERN and at FNAL.

4.8.2.3.2 Semi-Digital hadronic calorimeter energy calibration The most important features of the semi-digital HCAL option which have an impact on the calibration strategy are the large number of ≈ 70 million electronic channels, their semi-digital readout which means that efficiency is the meaningful quantity rather than energy, and the stable and homogeneous nature of the sensitive medium made of resistive plate chambers. The electronics calibration includes a gain correction procedure, a noise level measurement and a linearity measurement. The gain correction intends to reduce the dispersion of the electronic channels response to a given charge. A dispersion of a few percent for the threshold levels of the semi-digital electronics readout is currently obtained. The procedure is to inject charges corresponding to the lowest threshold level with different gains. The procedure is completely automated and will be applied to all the electronics boards before installation.

We foresee to apply the same procedure in situ. Based on our experience with a fully equipped $1m^3$ detector (9216 channels) we estimate that 200 minutes are needed to calibrate all the detector channels in parallel. The frequency of the calibration is under study. Preliminary results based on procedures applied one year apart on the same electronics board showed small variation ($< 2\%$).

To perform the detector calibration, a procedure will be used at construction time to qualify every piece, and a global control will be made at running time. The homogeneity of each GRPC detector will be tested by exposing all the HCAL detectors to cosmic rays before installation. To estimate the effort involved we can say that in order to achieve an efficiency measurement resolution better than 1% for each square cm of all the detectors using benches hosting five detectors, 5000 hours will be needed.

After installation, thanks to the detectors homogeneity only global efficiency of each detector needs to be controlled. This will be done using:

- Cosmic rays: Their number will depend on the detector depth. At sea level and taking into account the ILC duty cycle of 5% only a few hours are needed to calibrate the horizontal detectors. More time is needed for the inclined ones.
- Beam halo muons: At the ILC with the best currently proposed shielding scheme, 660 halo beam muons are expected per second to traverse the detector. Only a few seconds of running will be sufficient to calibrate the end-cap detectors based on these muons.
- Tracks produced in hadronic showers: There are few of them in each hadronic shower.
- Muons produced in data: Those produced from direct decay of $Z \rightarrow \mu^+\mu^-$ and those resulting from decays in the tau tau and $b\bar{b}$ channels become an essential source in case the GigaZ scenario is approved. With $10^{33} cm^{-2} s^{-1}$ of instantaneous luminosity less than five hours are needed to calibrate all the detectors.

In addition different procedures will be used to monitor the behaviour of the calorimeter, like following the leakage current, following the ratio of pads above the different thresholds. If necessary, we can consider injecting radioactive gas to check the response homogeneity.

4.8.3 Conclusions

In this section we have discussed the current state of thinking about aligning the different detectors in ILD. We propose to base the alignment on a mixture of harware alignment

systems, and a sophisticated use of tracks taken from data. Even though many details of the alignment systems still have to be finalised, and a lot of technical developments are still needed, we have established a number of key components central to the proposed procedures in test beam experiments. We are therefore confident that the system is adequate and that we realistically can expect to reach the anticipated precision required for physics at the ILC.

We consider the ability of the collider to deliver some luminosity on the peak of the Z resonance to be important and very beneficial for a fast calibration, and in particular a fast re-calibration after a push pull operation.

CHAPTER 5

Data Acquisition and Computing

As outlined in the detector outline documents [2, 3, 135] the data acquisition (DAQ) system of a detector at the ILC has to fulfill the needs of a high luminosity, high precision experiment without compromising on rare or yet unknown physics processes. Although the average collision rate of the order of a few kHz is small compared to the LHC, peak rates within a bunch train will reach several MHz due to the bunched operation. In addition the ILC physics goals require higher precision in many measurements than has ever been achieved in a colliding beam experiment. This improved accuracy can only be achieved by a substantially bigger number of readout channels than in previous detectors. Taking advantage of the bunched operations mode at the ILC, event building without a hardware trigger, followed by a software based event selection was proposed in [34] and has been adopted for the ILD. This will assure the needed flexibility as well as scalability and will be able to cope with the expected complexity of the physics and detector data without compromising on efficiency or performance.

The very large number of readout channels for the ILD will require signal processing and data compression already at the detector electronics level as well as high bandwidth for the event building network to cope with the data flow. The recently commissioned LHC experiments have up to 10^8 front-end readout channels and a maximum event building rate of 100 kHz, moving data with up to 100 GB/s [136]. The proposed ILD DAQ system will be less demanding in terms of data throughput but the number of readout channels is likely to be a factor of 10 or more larger. The computing requirements for the ILC event processing in terms of storage and CPU are also going to be less demanding than those of the LHC experiments. The details of the DAQ and computing system depend to a large extent on the developments in microprocessors and electronics and the final design of the different sub detector electronic components. Therefore the DAQ and computing system presented here will have to be rather conceptual, highlighting some key points to be addressed in the coming years.

5.1 DAQ CONCEPT

In contrast to past and recent colliders, such as HERA, Tevatron or LHC, which have a continuous rate of equidistant bunch crossings the ILC has a pulsed operation mode. The nominal parameter set [137] of the ILC with

- 2625 bunch crossings in a train about 1ms long,

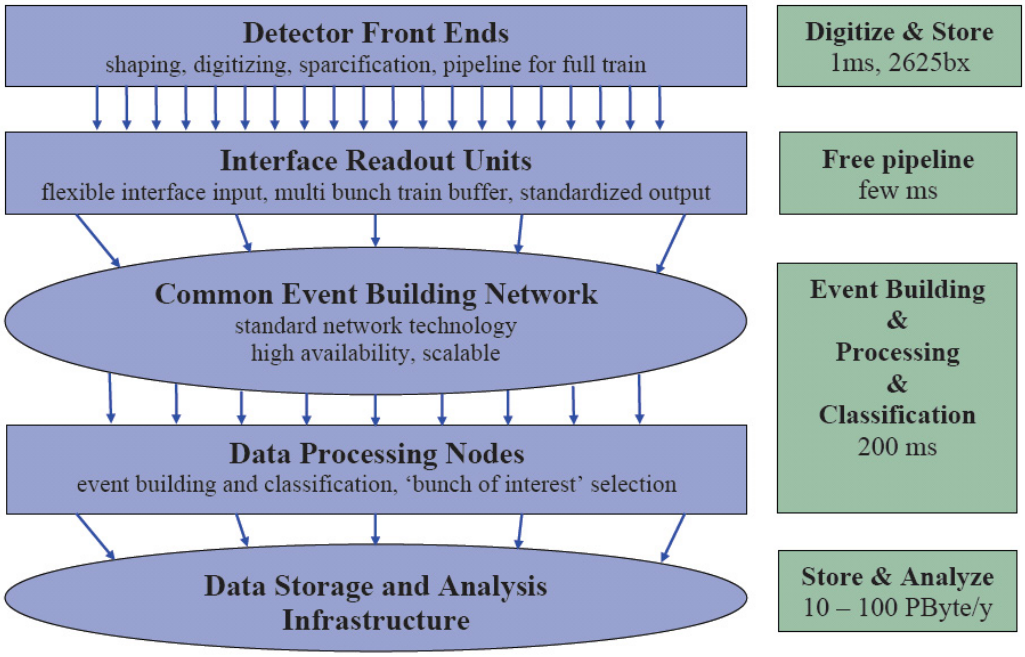

FIGURE 5.1-1. General layout of the DAQ system

- 369 ns between bunch crossings inside a bunch train and
- a bunch train repetition rate of 5 Hz

results in a burst of collisions at a rate of 2.6MHz over 1ms followed by 200ms without any interaction. The overall collision rate of 13kHz is significantly smaller then the expected event building rate for the LHC experiments.

The burst structure of the collisions at the ILC immediately leads to the suggested DAQ system with

- dead time free pipeline of 1 ms,
- no hardware trigger,
- front-end pipeline readout within 200 ms and
- event selection by software.

Rapidly developing fast network infrastructures and high performance computing technologies, as well as the higher integration and lower power consumption of electronic components are essential ingredients for the proposed data acquisition system. Furthermore for such large systems a restriction to standardised components is vital to achieve maintainability at an affordable effort, requiring commodity hardware and industry standards to be used wherever possible.

The general layout of the proposed DAQ system is shown in figure 5.1 The front end electronics on the detector or sensor level has to be detector specific and will digitize and store the data of ≈2600 bunch crossings. But already on or near the detector a standardized interface with additional buffering and processing capability will assure a common protocol for the subsequent event building which is currently estimated to be done by a standard switched network technology like 10G Ethernet. Event building of all data from the bunch train will be done in a single processing unit. Hence all data of the complete train will be available

Subdetector	Channels [10^6]	Occupancy [%]	Data volume [MB]
VTX	800	1.0	50
TPC	2	< 0.1	12
FTD	1	9	2
SIT	1	30	6
SET	5	1	1
ETD	4	10	7
ECAL	100	< 0.1	3
HCAL	8	1	130
MUON	0.1	< 0.1	≤ 1
LCAL	0.2	70	4
BEAMCAL	0.04	100	126
TOTAL	$\approx$920		$\approx$340

TABLE 5.1-1
Data Volume in MB per bunch train for the major ILD detector components

for the event processing without further data transfer which is essential since many detectors will integrate over several bunch crossings. The purpose of this online event processing will be mainly event classification, calibration, alignment and data quality monitoring. Although no event rejection is foreseen a scheme of event finders may be used to identify 'bunches of interest' which could then be used for the physics analysis or for fast analysis streams.

The data volume will be dominated by machine background which in turn is mainly pair production from beam-beam interaction(see section 6.7). For the nominal ILC parameter set it is expected that this background produces per bunch crossing $\approx$ 8000 hits in the HCAL, $\approx$ 150 hits in the ECAL, $\approx$ 400 hits in the TPC and $\approx$ 3 hits/cm^2 in the inner layer of the Vertex detector. Physics events which are less then 0.1 per bunch train will hence contribute less then 1% of the data recorded. Details of the simulated background are described in Section 6.7.

Table 5.1-1 lists the expected data volume per train for the major ILD detector components. Only values for the configuration used in the ILD detector simulation (see table 2.1-1) are shown as an example. For different technologies and options numbers may vary (DHCAL for instance $<$ 20MB). The occupancies are quoted for the detector-spcific time intervals. Some detectors digitise individual bunches, others like the TPC integrate over several bunches or the full bunch train.

The total data volume per trains is estimated to be $\approx$ 340MByte, hence the event building network has to cope with 1.7 GB/s. Assuming a safety factor of 10 on the background estimation and further contributions from electronic noise hits the maximum bandwidth anticipated is less than 20 GB/s. For the ILC Low-P parameter set backgrounds will increase by a factor 5 to 10 for the different subdetectors, with a resulting higher bandwidth demand.

Since machine parameters and beam conditions like beam energy or polarisation will be a vital input for the high precision physics analyses they should be stored alongside with the data. The time structure and data volume are similar, hence a common DAQ and data

storage model is envisaged.

5.2 FRONT END ELECTRONICS

In contrast to the central DAQ system the front end readout electronics for the different subdetector prototypes has to be designed now to allow for a realistic engineering and detector performance tests. Several approaches are underway for the calorimeters, TPC, silicon trackers and vertex detectors. Common to all the designs is a highly integrated front end electronics with signal shaping, amplifying, digitizing, hit detection, data storage and highly multiplexed data transfer to reduce the number of cables. Some designs foresee data processing like noise detection or cluster finding already at this stage to further reduce cables. For a detailed description see for example Section 4.4.5.3 on the calorimeter readout which had been developed for the EUDET project with a unified test beam DAQ system for various ILC Calorimeters.

For a highly granular detector like the ILD with the resulting large channel counts both the material budget as well as the power consumption are areas of concern. Minimizing the number of cables by data processing and multiplexing already on the sensor level is required as well as high density electronics with low power consumption. A common approach to reduce the power consumption is to turn the front end electronics off in the train gaps. First systems have been designed and build with this power pulsing capability.

5.3 DETECTOR CONTROL AND MONITORING

Modern data acquisition, detector control and monitoring systems are closely coupled to ensure good efficiency and data quality. An overall experiment control system will keep DAQ, detector control and monitoring synchronised, and assure proper timing, conditions and error handling. The systems should be designed such that subdetectors can be treated independently for commissioning or calibration runs in parallel to collision data taking.

In addition the ILD will be operated in a truly worldwide collaboration with partners all over the world. Similar to the global accelerator network (GAN) a global detector network (GDN) is proposed to operate the ILD detector remotely from the participating institutes. First experience was gained with the CALICE remote control room at DESY during test beams at CERN and FNAL. In addition the experience from the CMS remote operation centers at CERN, FNAL and DESY will be taken into account. The design of the DAQ and control system should have remote operation features built in from the start.

5.4 DATA PROCESSING

5.4.1 Event Building and Prompt Reconstruction

Event building and prompt reconstruction will be performed on the *Online Filter Farm* – a sufficiently large farm of processing units near the detector, connected to the front end electronics via the Common Event Building Network as shown in figure 5.1. Every data processing unit of the Online Filter Farm will process the data of one complete bunch train at a time. The raw data of a complete bunch train is kept in the raw data file after compression. This is essential as many detectors will integrate over several bunch crossings or even the

full bunch train. The event reconstruction will be an iterative procedure where in a first step a preliminary reconstruction will be done on the data from every subdetector. Bunches of interest are then identified by exploiting correlations in time and space between the data from all subdetectors. After calibration and alignment finally a full event reconstruction is performed on the event data. The reconstructed events are then written to the storage systems in an object oriented data format that is suited for further analysis with appropriate pointers into the raw data file containing the bunch train data. A first version of such an event data model has been developed and is in used for several test beam efforts and for the offline analyses within ILD [10]. An event filter mechanism run at prompt reconstruction will provide the necessary meta data for fast event selection at the physics analysis level.

5.4.2 Offline computing

The further offline data processing will exploit the existing Grid infrastructure for distributed computing using a multi-tier like approach similar to what is done for the LHC-experiments [138, 139]. The offline computing tasks such as the production of more condensed files with derived physics quantities (DST/AOD), Monte Carlo simulations and re-processing of the data will be distributed to the various tiers of the ILC-computing Grid. Setting up a data Grid and suitable data catalogues will allow the physicists to efficiently access the data needed for their analyses.

5.5 SOFTWARE

As is fairly standard with current HEP experiments, ILD will have a modular software framework based on object oriented programming languages such as C++. A component based plugin system together with well defined abstract interfaces will allow the flexible combination and exchange of algorithms with minimal configuration overhead. Using the same software components in the online and offline computing as much as possible will facilitate frequent data re-processing with improved calibrations and algorithms. A common object oriented persistency format that is used from the prompt reconstruction to the final analysis will allow transparent access to lower level data objects at later stages of the data processing chain. The actual raw data format containing the data read out per bunch train will essentially be defined by the front end electronics. Using abstract interfaces for the object oriented event data model will provide the flexibility to change the underlying persistency format in case the need might arise at some point in the lifetime of the experiment. The long term archiving of the data even beyond the experiments lifetime should be taken into account when choosing the persistency format. Data for calibration, slow control and alignment will be stored in a conditions database system that provides a suitable timestamp mechanism and versioning capabilities.

ILD already has two fully functional software frameworks (Sections 2.1.1, 2.1.2) which have been used for the massive Monte Carlo production for detector optimisation. One of the frameworks is also used by a number of ILC testbeam experiments for detector R&D [16] providing important feedback on the usability of the software in real world experimental conditions.

5.6 OUTLOOK AND R&D

Due to the timescales involved and the rapid changing computing and network market a decision on the DAQ hardware will be done as late as possible to profit from the developments in this area.

Nevertheless key elements of the DAQ systems have to be defined to guide the R&D of the subdetectors front end electronics especially when entering the technical prototype stage. This includes standardized interfaces to the central DAQ, online calibration and alignment strategies as well as detector control and monitoring concepts with remote operation build in. To gain experience and prepare for the decision on how to build the central DAQ system new developments and evolving standards, like ATCA [140] for example, should be evaluated in the next years.

In addition efficient event processing and event classification strategies taking realistic background simulations into account have to be developed. The ongoing test beam and simulation efforts will be a first step to learn how to treat the data but a more dedicated effort toward online processing and bunch tagging in a multi bunch environment will be needed to ensure efficient processing.

GRID resources currently available for post-LOI studies are limited. Especially, the inter-regional bandwidth (between Europe and Asia), CPU and storage resources especially in Asia, and the connectivity to OSG-GRID are the area which need more improvement.

A continues effort on improving the software framework according to needs and adapting to new computing hardware, introducing multi-threading capabilities for multi core processors for example, is needed to keep up with the activities both in the subdetector R&D as well as the computing infrastructure

CHAPTER 6

Detector Integration Machine Detector Interface

6.1 MECHANICAL CONCEPT

The mechanical design of the ILD detector is shown in figures 1.2-1 and 6.1-1. The major components are the five parts of the iron return yoke: three barrel rings and two endcaps. The central barrel ring carries the cryostat with the solenoid coil in which the barrel calorimeters are installed. The TPC and the outer silicon envelope detectors are also suspended from the cryostat using tie rods. The endcap calorimeters are supported by the endcap yoke sections which can be moved independently from the barrel sections to allow an opening of the detector at the beam line. The beam pipe, the vertex detector and the other inner silicon detectors are supported from a structure of carbon fibre reinforced plastic (CFRP), which hangs at the flanges of the TPC field cage. The whole structure can be aligned with respect to the beam axis using actuators and a laser alignment system. The QD0 magnets are mounted independent of the yoke endcaps in a support structure that carries the magnets and the forward calorimeters. This structure is supported from a pillar outside of the detector and is suspended from the solenoid cryostat using tie rods. The QD0 magnets are also monitored

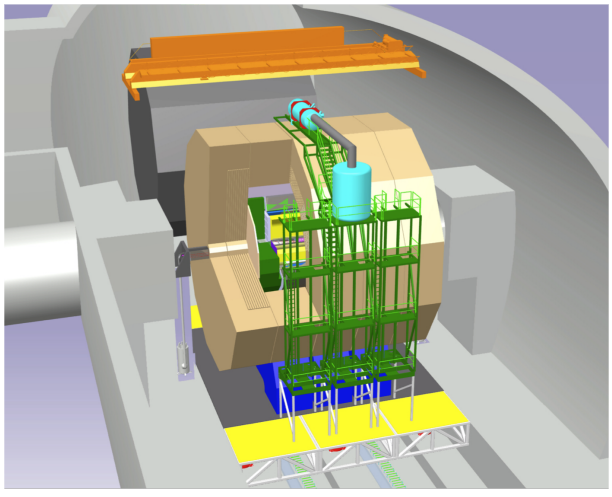

FIGURE 6.1-1. The ILD detector and its services.

by a laser alignment system and can be moved using actuators.

A full 3D CAD model of the ILD detector exists and is the baseline for all engineering and technical studies presented in this LoI. The actual dimensions and masses of the ILD subcomponents can be found in [141]. The engineering model of ILD has been synchronised to the detector model used in the full detector MC studies. A detailed description of the integration of the ILD detector including a conceptual scheme for the cabling is given in [118].

6.2 DETECTOR ASSEMBLY AND OPENING

The ILD detector will be assembled in large parts in a surface building above the underground experimental hall. The pre-assembled sections will then be lowered into the underground cavern using a temporary portal crane. The largest and heaviest (≈3500t) part will be the central barrel ring with the solenoid coil and the barrel calorimeters installed. The underground assembly sequence comprises the following steps:

1. The first pillar for the support of the QD0 magnet is installed. This pillar needs to be movable in the garage position but will not move on the beam line. The service helium cryostat is also carried by the pillar.
2. The QD0 magnet is suspended from the pillar together with its support structure.
3. The endcap yoke with the pre-mounted endcap calorimeters are installed.
4. The first part of the barrel yoke is installed.
5. The central part of the barrel yoke carrying the coil and the barrel calorimeters is installed; the cables are routed through the slits between the central yoke ring and the other rings.
6. The TPC is inserted, the cables follow the same routes as the cables of the barrel calorimeters.
7. The inner part of the detector including the beam pipe and the inner silicon detectors is inserted into the TPC, cables are routed to the outside following the same routes as the cables of the barrel calorimeters.
8. The third part of the barrel is lowered.
9. The second pillar, QD0 (with support) and the second yoke endcap are installed.

The detector can be opened and maintained in the garage position using the above described procedures. The space required is available in a garage zone with side access tunnels (c.f. figure 6.2-2). It is planned to allow the opening of the detector endcaps also at the beam line. As space is limited there due to the machine elements, only limited access can be reached. The QF1 magnets including their ancillaries extend to ≈9 m from the IP. Preliminary studies show that access space of ≈1 m can be gained between the endcap and the barrel yoke. This would allow limited access to the inner detector for short maintenance and connection/deconnection actions at the beam line (c.f. figure 6.2-2). Major interventions would be done in the garage position taking advantage of the push-pull system.

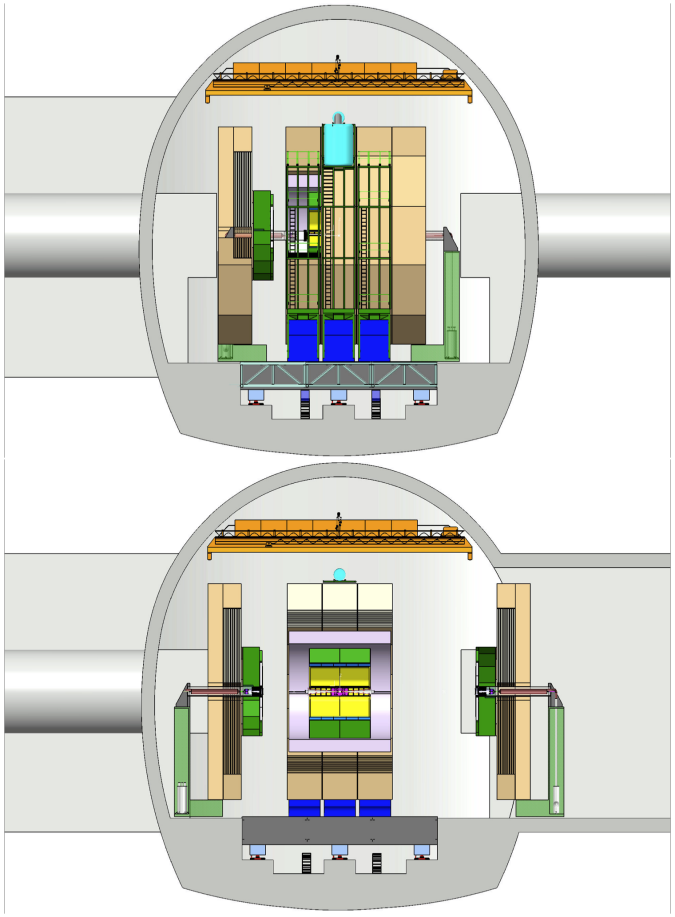

FIGURE 6.2-2. Detector opening on the beamline (top) and in the garage position (bottom).

6.3 CIVIL FACILITIES AND SERVICES

6.3.1 Detector Services

A number of services are needed for the operation of the ILD detector. The concept of push-pull puts stringent requirements on the design, as the services need to be designed for a moving detector. Therefore they must be integrated in the design of the detector and the civil facilities from the beginning.

6.3.1.1 Primary Services

Primary services are usually provided by installations that are located on surface due to their dimensions, possible impact on the detectors (vibrations, etc.) and related risks. Examples are water chillers that provide cooling water, high to medium voltage power transformers (e.g. 18 kV/ 400 V AC tri-phase), UPS facility (Diesel generator), helium storage and compressor plant for the solenoid coil and gas and compressed air plants.

6.3.1.2 Secondary Services

Secondary service plants often need to be close to the detector and should be located in the underground areas. Typical secondary services are temperature stabilised cooling water,

voltage supplies for front-end electronics, AC/DC converters for the super-conducting coil and cryogenics and vacuum services. Data connections for the transmission of the detector readout also need to be included. Due to the push-pull design, these services are permanently connected and run in cable-chains towards the detector. As the flexible pipes and cables in the chains need to be kept within reasonable lengths, it would be very convenient to locate a small service cavern for the secondary services at the end of the main underground cavern with independent ventilation and limited crane access. Electrical noise and vibrations are kept away from the vicinity of the detector, and people working in the main underground cavern would also be protected from physical noise coming from various equipment. The main benefit of the usage of cable chains is the permanent connection of the detector to all its services and readout cables. The chains can be equipped when the detector is still being assembled on the surface, and this would greatly speed up the connection and commissioning time in the underground cavern once the detector parts are lowered. The hall floor can be kept clean and without obstructions by the use of cable chains.

6.3.1.3 On-Board Services

Some secondary services need to be carried on board with the detector if the connection through cable chains are found to be technically difficult or too expensive. As this increases the risks for the detector operation in the push-pull scenario, these on-board services should be kept to a minimum. Examples are the service cryostats for the helium supply for the solenoid and the QD0 magnets.

6.3.1.4 Cryogenics

Figure 6.3-3 shows the block diagram of the cryogenics needed for the operation of the detector solenoid coil and the QD0 magnets. While the primary facilities like the helium storage and compressors are on the surface, the helium liquefier (4K) and the re-heater are in the underground hall. Directly on-board of the detector are the valve box, which distributes the helium to the coil, and the liquid helium tank. Also the 2K sub-cooler and the service cryostat for the QD0 magnet are moving with the detector.

6.3.2 Surface Assembly Hall

The detector will be assembled in a surface hall. The RDR baseline design of the surface hall (100 × 25m, 25 m high, 400 t crane capacity) is well suited for the assembly of the ILD detector. A portal crane with a capacity of 3500 t needs to be installed temporarily at the main shaft to lower the pre-assembled detector elements into the underground cavern.

6.3.3 Underground Experiment Hall

The underground experiment hall needs to accommodate both push-pull detectors. The design of the hall presented in the ILC RDR [137] has not been optimised taking into account realistic assumptions for the services of the detector in the push-pull environment. Figure 6.3-4 shows a design study of the underground hall which has been optimised for ILD taking into account the following criteria:

- minimum impact on civil engineering cost with respect to the RDR baseline (reduced main cavern diameter and length),

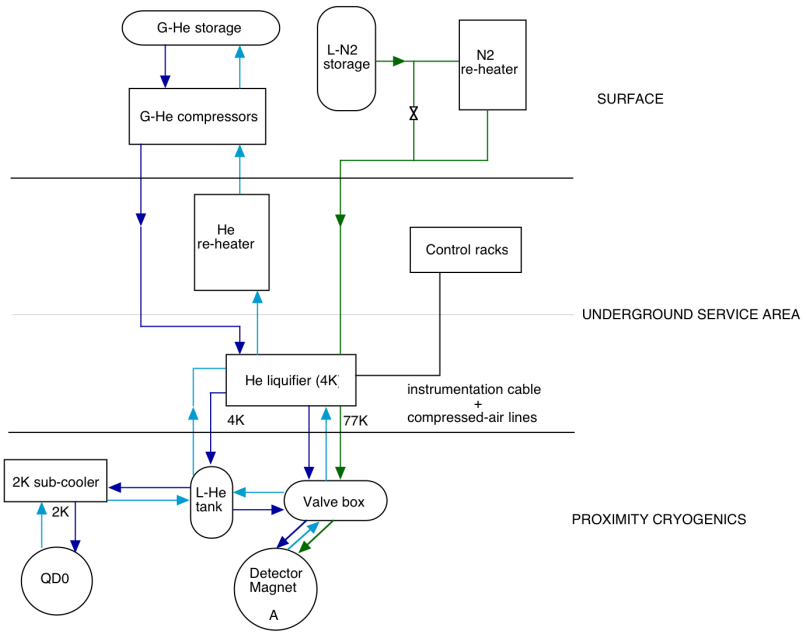

FIGURE 6.3-3. Diagram of the cryogenic services for the detector.

- enhanced safety and reduced time losses by moving the shaft from the cavern ceiling to a side alcove providing also the necessary space for the full opening of the detector,
- small service cavern at the end of the hall for the secondary services (6.3.1.2),
- optimised for push-pull.

A hall width of 25 m is sufficient for the detector assembly and maintenance procedures as the side alcove for the vertical shaft increases the parking positions substantially. The beam height has been assumed to be 12 m from the floor of the hall. This allows for the detector to rest on a 2-m-high platform. It must be noted that if the experimental area is a deep construction in a terrain requesting a cylindrical or semi-cylindrical hall for question of rock stability the space situated below the floor level has to be filled with concrete up to the proper level. The platform and the cave-like structures containing the supporting mechanism and the cable are thus just a special part of this filling. As the heavy parts of the detector will be moved on air pads and on the platform, the crane capacity in the underground hall is modest. Two 40t cranes, which can be connected to form an 80t crane are largely sufficient.

6.4 PUSH-PULL OPERATIONS

The present ILC baseline design foresees one interaction beamline that needs to be shared by two detectors in a push-pull configuration. While one detector is taking data on the beamline, the other one is parked in its garage position in the same underground hall. Following a still-to-be-defined time schedule, the detector on the beam line is moved away to its own garage position to make space for the waiting detector to collect data. This push-pull scenario has never been tested at existing accelerators and poses unprecedented engineering challenges to the detector designs.

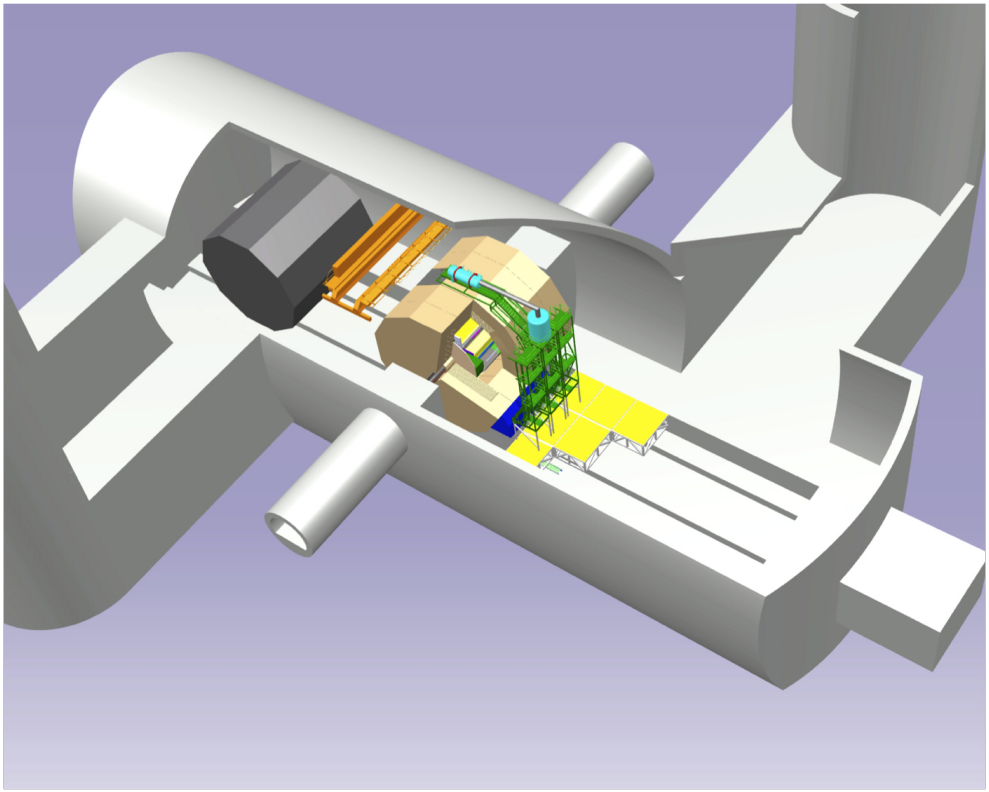

FIGURE 6.3-4. Design study of the underground experiment hall with ILD (left) and the second detector in push-pull configuration.

The LoI concept groups and the ILC Beam Delivery System group have agreed on a set of minimum functional requirements [142] which define the boundary conditions for the push-pull operations. Most of these requirements comprise geometrical boundaries, like the size of the underground hall or the limits of the garage position of the detectors. But also physical limits for ionising radiation and magnetic fields need to be defined to allow a friendly co-existence of two detectors in one hall. In addition direct requirements come from the machine itself. As the QD0 final focus magnets will move with the detectors, requirements on alignment tolerances and vibration limits have been defined.

The timescale for the push-pull operation needs still to be defined, but it is clear that the time for the exchange of both detectors needs to be minimised to maximise the integrated luminosity. The full push-pull procedure comprises for the outgoing detector:

- securing the beams,
- powering down of the detector solenoid,
- removing the radiation shield between detector and hall,
- disconnecting all local supplies (in principle only the main bus-bars),
- disconnecting the beam pipe between the QD0 and the QF1 magnets,
- moving the detector out towards its garage position,
- connecting back the main bus-bars in the garage position.

For the incoming detector the procedure is reversed, but additionally needs to include time for alignment and eventually calibration of the detector system at the beam line. It is

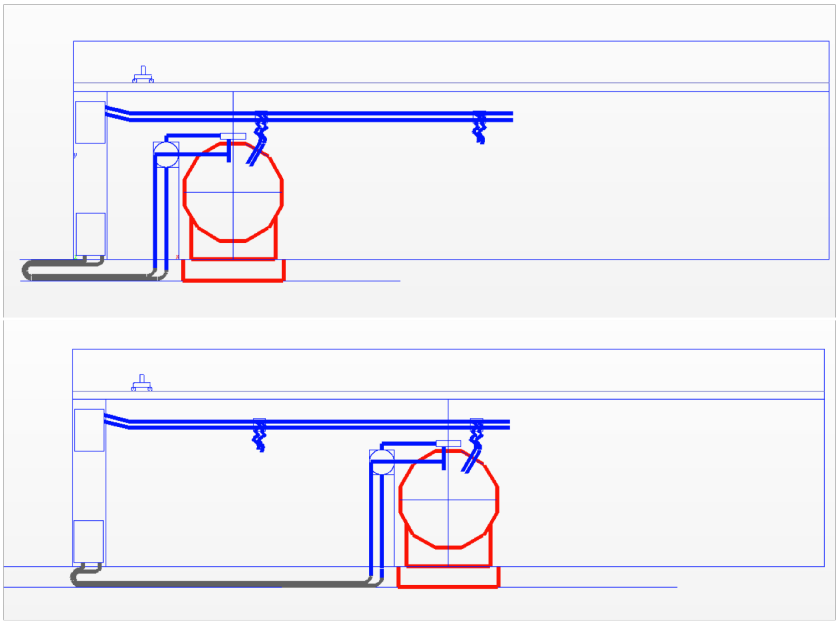

FIGURE 6.4-5. ILD detector in the garage position and on the beam line. The detector will be disconnected from the power bus bars (top, blue) during movement, while the cables and cryogenic service lines run in cable chains (bottom, grey).

envisaged to complete the full push-pull operations on a timescale of about two days after procedures have been optimised based on experience. However, as the full understanding of the challenges requires a detailed engineering design of the hall and the definition of the procedures, a final evaluation of the push-pull operation for ILD is beyond the scope of this LoI and needs to be studied in the following Technical Design Phase. Nevertheless this section describes our conceptual understanding of the ILD operations.

6.4.1 Moving the ILD Detector

The ILD detector will be placed on a concrete platform to avoid possible damages due to non-synchronised movements or from vibrations during push-pull and also to ease internal alignment challenges. The concrete platform will have a size of approximately 15 $\times$ 20m and needs to be $\approx$ 2m thick. Figure 6.3-4 shows the ILD detector on its platform on the beam line. The platform will move on the hall floor using a system of rollers suitable solution for this one-dimensional movement or air pads that may provide more easily a millimetric positioning tolerance.

All supplies for the detector will be provided by using flexible supply lines that move with the platform. This includes the cryogenic lines that supply the detector solenoid and QD0 systems with 4K helium. As the development of flexible cryo lines for 2K helium is challenging, the QD0 magnet will be connected permanently to a service cryostat that moves together with the detector on the platform. As the detector solenoid does not need to be powered during the movement, the detector can be disconnected from the power bus bars and re-connected in the parking position. Figure 6.4-5 shows a schematic drawing of the movement of the detector with the cable chains and the power bus bars. The detector elements can be moved on the platform by using either a roller system, or by using air pads similar to the solution CMS has adopted. As the axial space at the beam line is limited, only the opening

of the detector endcaps is foreseen to allow a limited access to the inner detectors. In the garage position more space is needed to allow major maintenance work, e.g. the removal of the TPC. More details of the opening procedures are described in section 6.2.

6.4.2 Shielding

The ILD detector will be self-shielding with respect to maximum credible accident beam loss scenarios. Detailed simulations show [143] that a proper design of the detector provides shielding which is sufficient to still allow access to the detector hall for professional workers. This is important to fulfil the minimum requirements which are needed to allow access to the other detector in its garage position during beam operations.

A movable concrete shield needs to fill the gap between the detector and the walls of the underground hall. As this shielding needs to fit both detectors, no engineering effort has been pursued so far to find a detailed design. This has been referred to the Technical Design Phase where it will be studied in collaboration with the second detector concept group. Nevertheless, these kind of shieldings have been used in other accelerator experiments (e.g. at HERA) and pose no conceptual design challenge.

6.4.3 Alignment and Calibration

The ILD detector will be moved on a platform that will be repositioned very precisely on the IP. Nevertheless, the alignment of the detector after being brought to the beam position is not trivial. The functional requirements ask for an alignment accuracy of the detector axis $\pm$1mm and 100μrad after push-pull. The requirements for the QD0 magnet are even tighter: $\pm$ 200 μm and 5 μrad. ILD will be equipped with a laser-interferometric alignment system like MONALISA [144]. This system allows for alignment of both QD0 magnets which are carried by the detector to the ILC beam lines on each side of the hall. In addition, the detector itself can be positioned within the required tolerances using this system. The QD0 magnets will be placed on actuators that allow for an independent alignment of the magnets with respect to the detector.

After the alignment of the detector described above and the commissioning of the beam, some calibration data taken at the energy of the Z resonance would allow to check the alignment of the subdetectors. The internal alignment of the subdetectors can then be done most precisely in offline analysis. This technique was used at LEP where experience shows that about 1 pb^{-1} of calibration data on the Z peak will be sufficienct after the push-pull procedure at ILC [96]. If the ILC machine cannot easily switch between Z-peak and $\sqrt{s}$ running, then other techniques than used at LEP will be developed.

6.5 R&D PLANS: DETECTOR INTEGRATION

This Letter of Intent describes a conceptual design of the integration efforts for the ILD detector. Though no show-stoppers have been identified, a challenging engineering programme needs to be set up to transform this conceptual design into a technical design based on engineering studies. Main points of work will be among others:

- Integration of the subdetectors in close collaboration with the subdetector R&D groups.
- Engineering design of the yoke.

- Opening and assembly procedures including a study on the tooling needed for it.
- Development of an engineering solution for push-pull. This includes the very important issue of cryogenic supplies for a moving detector.
- Find an optimised underground hall design in close collaboration with the ILC machine CF&S group and the other detector concept groups. This includes a common shielding strategy.
- Elaborate the alignment strategy and find technical solutions for interferometric systems la MONALISA.

6.6 THE INTERACTION REGION

The interaction region of the ILD detector comprises the beampipe, the surrounding silicon detectors, the forward calorimeters with the masking system and the QD0 magnet with its ancillaries and the support structure. Figure 6.6-6 shows a blow-up of this region.

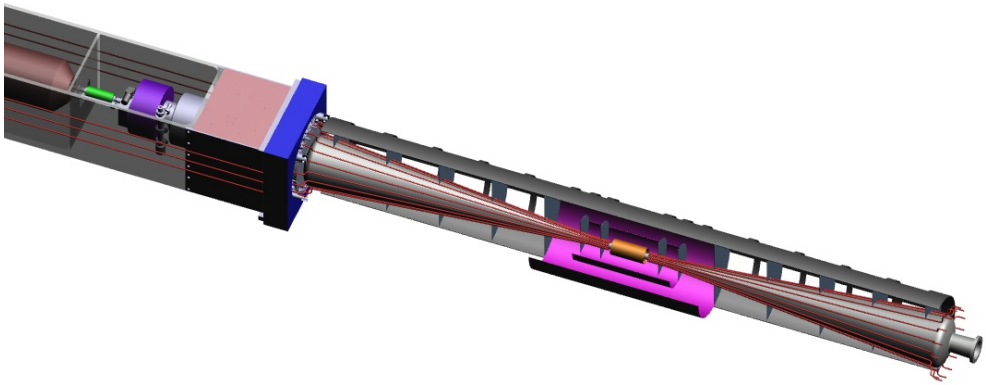

FIGURE 6.6-6. Interaction region of the ILD detector. Shown are the vertex detector (yellow), the SIT (pink), the ECAL plug (blue) with the LumiCal, the LHCAL (light red) and the BeamCal (violet). The routing of the cables is also shown.

6.6.1 The Beampipe

The design of the beam tube has to obey several constraints:

1. It must not interfere with the luminosity.
2. Its central part must be small enough to optimise the measurement of the impact parameter and large enough not to interfere with the background.
3. It must comply with a crossing angle of 7 mrad.
4. It must be as light as possible to reduce photon conversions and hadron interactions, withstanding nevertheless the atmospheric pressure.
5. It must not induce electromagnetic perturbations generating heat.
6. It has to be pumped down to an agreed level.

6.6.1.1 Mechanics

The current mechanical design is shown on figure 6.6-7. The tube is conical, offering very little matter in front of the luminosity monitor LumiCal (LCAL). The tube is made of beryllium with some ring reinforcements at the level of the forward detectors. The part inside the vertex detector is a cylinder, the connection with the large cone is such that background does not interfere. This very thin tube (8 kg total) has to be supported from the inner detector structure. The mechanical behaviour has been studied in detail [145]. The most important constraint is related to the buckling where a safety coefficient of 6 is being considered, see figure 6.6-8. To go beyond this first approach, one would need to work with manufacturers because the technology becomes very important. The example of LHCb tube shows that such a tube results from a strong R&D by the manufacturer on the way to realise cones and to perform the weldings. Figure 6.6-7 shows the dimensions, figure 6.6-8 shows the buckling behaviour.

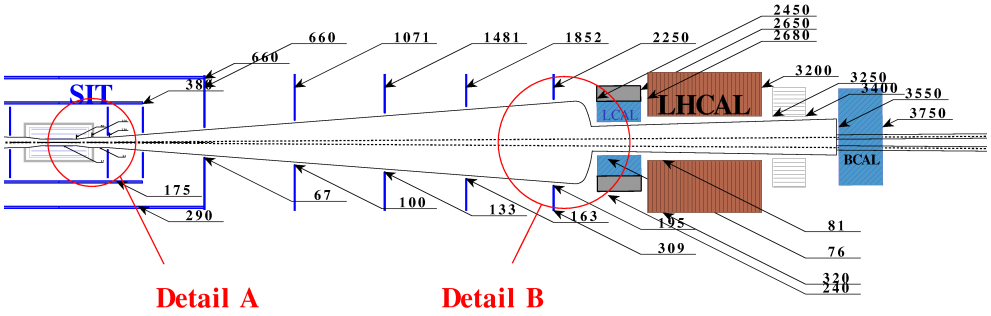

FIGURE 6.6-7. Beam pipe geometry.

6.6.1.2 Vacuum

The vacuum situation in the beam pipe has been studied in detail [146]. It is assumed that the whole beam pipe would be pumped by vacuum pumps which are located in the space between the LHCAL and the BeamCal, about 3.3 m from the IP. Assuming effective pumping speeds of 0.72 (0.12) $m^3 s^{-1}$ for H_2 (CO) yields in pressures of approximately 1×10^{-6} (6×10^{-7}) Pa. The limit on the effective pumping speed is given by the conductance of the small pipe at the back side of the conical part. The vacuum profile for H_2 is shown in figure 6.6-8.

6.6.1.3 Wakefield Losses

The wakefields generated by the passing beam in the beam pipe result in parasitic losses which have been studied taking into account the ILC Low-P beam parameters [146]. The parasitic losses are in the range of 20-24 W so that air cooling will be sufficient to remove this additional power. Higher order modes can be excited in the beam pipe, the resulting parasitic losses are small and will be dissipated in the surface region of the beam pipe.

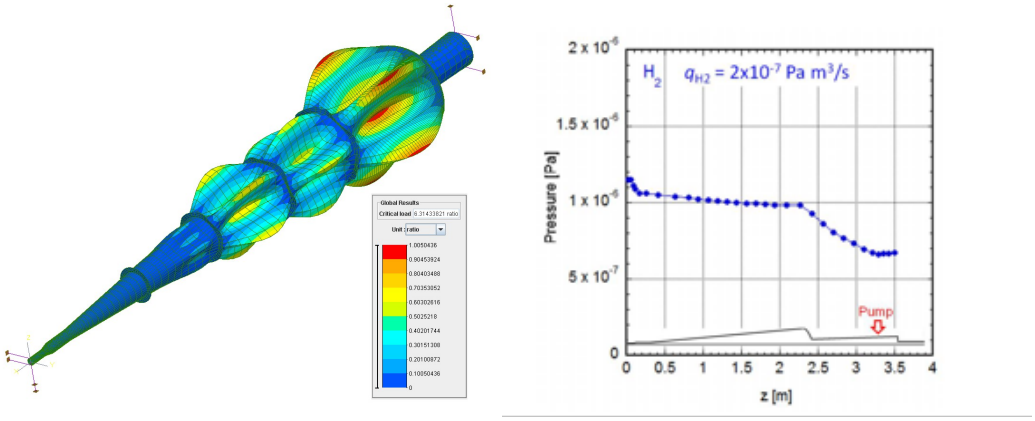

FIGURE 6.6-8. Beampipe buckling (left) and vacuum profile for H_2 (right).

6.6.2 Support of the Final Focus Magnets

While the QF1 magnets of the final doublet will stay fixed in their positions, the QD0 magnets need to move with the detector during push-pull operation. The magnets are installed in a support structure which is supported from pillars residing on the push-pull platform. The support structure has a square cross section and is suspended from the solenoid cryostat using carbon-fibre tie rods (c.f. figure 6.6-9. This assembly allows the opening of the yoke end caps without interference with the alignment of the QD0 magnets. The inner silicon

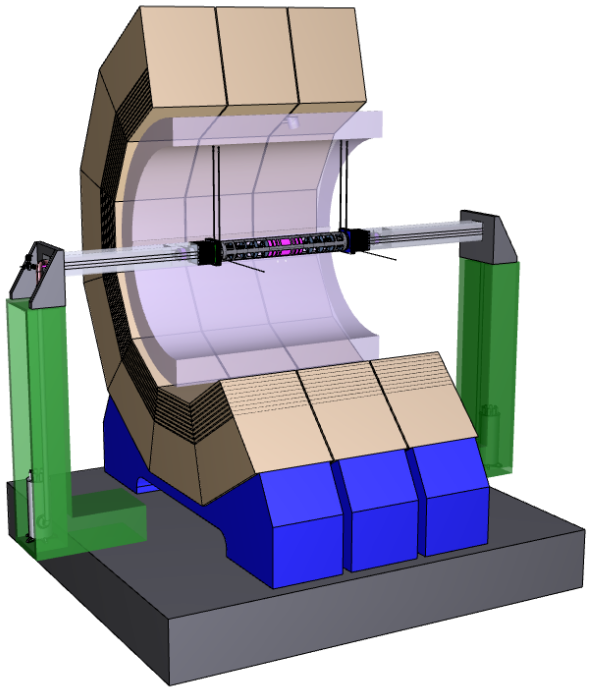

FIGURE 6.6-9. Support of the magnets in the detector. The inner detector part and the beam pipe are suspended from the TPC end flanges, not shown in this figure.

detectors (SIT, vertex detector) and the beam pipe are supported by a CFRP structure

which is suspended from the TPC end flanges. The QD0 magnets reside on actuators in their support structure and are monitored using an interferometric laser alignment system like MONALISA [144]. The service cryostat for the supply of the QD0 magnets on the beam line, in the garage position and during the push-pull operations are located at the bases of the pillars and move with the platform.

The stability of the QD0 support structure has been studied. The vibrations induced by ground motions are at most 2.2 nm at 8.3 Hz which is below the limits of 50 nm defined in the minimum requirements document [142].

6.7 MACHINE-INDUCED BACKGROUNDS

Machine-induced backgrounds have been studied in detail for the ILD detector and its predecessors GLD and LDC [2, 3]. The main relevant background are pairs from beamstrahlung which are produced in the highly charged environment of the beam-beam interaction. The background levels found are well below the critical limit for most sub-detectors. The subdetector most sensitive to beam-related backgrounds is the vertex detector, which features an inner radius value dictated by the maximum affordable beamstrahlung hit rate.

Table 6.7-1 summarises the expected background levels in the ILD subdetectors for several beam parameter sets: the nominal ILC beam parameters for 500 and 1000 GeV cms energy and the Low-P parameter set[1]. The numbers are the result of a study using the same full ILD detector Monte Carlo that has been used for the physics studies described in this LoI (c.f. sections 2 and 3), i.e. with the nominal detector geometries and 3.5 T magnetic field. In these background simulations, the double-layer option of the vertex detector has been chosen. It should be noted that the background numbers for the single-layer option are 15% larger for the inner layer due to the smaller radius. The ILC parameter sets used are the ones described in the ILC Reference Design Report [137]. It should be kept in mind that the numbers given are per bunch crossing (BX). As in the different ILC parameter sets the bunch crossing distance varies, the number of hits per subdetector readout must be scaled accordingly, if the corresponding subdetector integrates over several bunch crossings.

Figure 6.7-10 shows the distribution of the background hit densities on the inner silicon detectors (VTX-DL, SIT, FTD). The correlation of the hit densities with the distance from the interaction point can clearly be seen. The most critical point is the innermost layer of the vertex detector.

6.7.1 Background Uncertainties

As the vertex detector is most critical with respect to beam induced backgrounds, detailed studies have been performed to understand the influence of different detector geometries and simulation parameters like the choice of range cut parameters in Geant4. The number of hits on the vertex detector change up to 30% which gives an order of magnitude of the uncertainties for these simulation results [59]. Another study of the uncertainties of the background simulations has been done in [88] where a general safety factor of 5-10 has been suggested.

[1]The Low-P parameter sets might require modifications to the baseline detector design which are discussed in section 6.7.2. The numbers in the table are valid for the baseline detector design only.

Subdetector	Units	Layer	Nom-500	Low-P-500	Nom-1000
VTX-DL	hits/cm^2/BX	1	3.214±0.601	7.065±0.818	7.124±1.162
		2	1.988±0.464	4.314±0.604	4.516±0.780
		3	0.144±0.080	0.332±0.107	0.340±0.152
		4	0.118±0.074	0.255±0.095	0.248±0.101
		5	0.027±0.026	0.055±0.037	0.046±0.036
		6	0.024±0.022	0.046±0.030	0.049±0.044
SIT	hits/cm^2/BX	1	0.017±0.001	0.031±0.007	0.032±0.012
		2	0.004±0.003	0.016±0.005	0.008±0.002
FTD	hits/cm^2/BX	1	0.013±0.005	0.031±0.007	0.019±0.006
		2	0.008±0.003	0.023±0.007	0.013±0.005
		3	0.002±0.001	0.005±0.002	0.003±0.001
		4	0.002±0.001	0.007±0.002	0.004±0.001
		5	0.001±0.001	0.006±0.002	0.002±0.001
		6	0.001±0.001	0.005±0.002	0.002±0.001
		7	0.001±0.001	0.007±0.002	0.001±0.001
SET	hits/BX	1	5.642±2.480	57.507±10.686	13.022±7.338
		2	5.978±2.360	59.775±8.479	13.711±7.606
TPC	hits/BX	-	408±292	3621±709	803±356
ECAL	hits/BX	-	155±50	1176±105	274±76
HCAL	hits/BX	-	8419±649	24222±744	19905±650

TABLE 6.7-1
Pair induced backgrounds in the subdetectors for nominal (500 GeV and 1 TeV) and Low-P (500 GeV) beam parameters. The numbers for the ECAL and the HCAL are summed over barrel and endcaps. For the vertex detecor, the double-layer option has been chosen for this simulation, the numbers for the single-layer option differ. The errors represent the RMS of the hit distributions of the simulation of ≈ 100 bunch crossings (BX).

6.7.2 Provisions for the Low-P Beam Parameters

The Low-P beam parameter set assumes an ILC machine with less RF-power available. The number of bunches in a train is reduced while the loss in luminosity is compensated by squeezing the bunches to smaller sizes during the collisions. This results in larger losses due to beamstrahlung photons and therefore in a diluted luminosity spectrum. On the other hand the number of pairs produced in beamstrahlung gamma collisions is enhanced significantly.

Table 6.7-1 shows how the increased pair production results in an increase of background hits in the subdetectors. Especially the inner vertex detector layer suffers from the enhanced backgrounds[2]. Matters to remedy the situation are still under study a possible solutions is an increased radius of the inner vertex detector layer. Also the ladder of the inner layers might need to be shortened to keep their read-out electronics out of the hot cone of the beamstrahlung pairs.

[2]It should be remembered, however, that the numbers in the table are given per bunch crossing. As the bunch spacing in the RDR Low-P option is increased to 480.0 ns as compared to the 369.2 ns in the nominal case, the background numbers per readout need to be scaled down by ≈25% for Low-P to make them comparable to the nominal case.

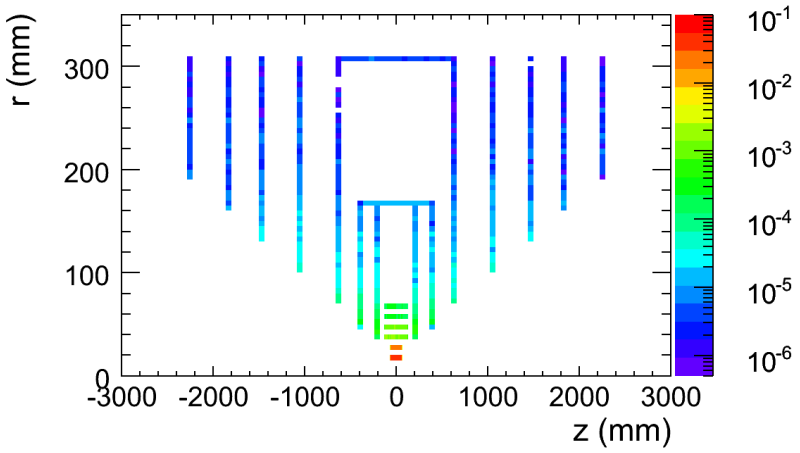

FIGURE 6.7-10. Distribution of the background hit densities on the inner silicon detectors (VTX, SIT, FTD) in units of [hits/mm^2/BX].

6.8 MEASUREMENT OF ENERGY AND POLARISATION

Traditionally the methods of measuring the beam energy and the beam polarisation are also parts of the Machine Detector Interface. As the polarimeters and the energy spectrometers are not a part of the detectors at the ILC but are common facilities in the machine, we will refer here only to the common design efforts [51].

6.9 R&D PLANS: MACHINE DETECTOR INTERFACE

As in the area of detector integration 6.5, also in the integration with the accelerator many topics need to be studied in engineering detail level before the construction of the detector could be envisaged. Important R&D topics are e.g.:

- Engineeering study of the beam pipe including its vacuum behaviour in close collaboration with possible manufacturers.
- Support and monitoring of the QD0 magnets. Adaptions to new BDS schemes which would allow larger L* optics.
- Detailed study of the beam induced backgrounds.

CHAPTER 7

Costing

The cost of the ILD detector as presented in this section has been evaluated based on a common methodology of costing, and a detailed work breakdown structure for each of the sub-detectors. Costing a detector as complex as ILD at this early stage of the project is difficult at best, and certainly not precise. For this document, a rather crude evaluation has therefore been done focusing on the cost driving items. Another important aspect was as well to understand the scaling of the cost of the different sub-systems with the main design parameters, to realize the impact of the sub-system on the overall cost, and to evaluate possible cost savings versus performance.

7.1 METHODOLOGY OF COSTING

The method used here follows the prescriptions from the GDE at the time of the RDR. For each important item a work breakdown structure (WBS) has been developed, and each part has been costed to the best of our knowledge up to a level equivalent to about 1% of the total cost. The bases of the cost have been experience when constructing the LHC detectors and ILD prototypes, and, in some cases, quotes from manufacturers. An attempt has been made to use consistent cost numbers across different sub-detectors. The prices are expressed in ILC units (ILCU) which correspond in 2006 values to 1 US dollars, 117 Yen or 0.83 EUR.

No attempt was made to guess the impact of future escalation. Contingencies are currently not taken into account. No R&D costs are included, except in some cases costs for industrialisation. No maintenance and operation has been estimated. In some instances, prices for the same item vary widely between different countries and regions. In this case the price used is the one proposed by the group in charge of this component. Different options have been costed independently, but the tables and numbers correspond to the detector which has been simulated for physics studies.

It should be noted that the level of detail and even of understanding for the different sub-detectors and options may be different. This may reflect in the cost estimates as well as in the performances. The manpower has been estimated roughly from past experiences for the different items and is added globally. Some options have no estimate yet.

7.2 ILD WORK BREAKDOWN STRUCTURE

The actual WBS for the different sub-systems can be found in [147] . The list of sub-systems under consideration is given in table 7.3.

As a guide we tried to estimate for the different systems the following items:

- the amount of material and a unit price, the manufacturing,
- the sensors,
- the front-end electronics including printed circuit boards,
- the local acquisition, testing and calibration,
- the transportation (not knowing where it is made and where is the experimental site),
- the assembly on site, tooling,
- the spares and miscellaneous.

7.3 ILD CURRENT COST EVALUATION

The following material costs have been used in the estimate:

- Tungsten at 120 ILCU/kg (from a quotation for 40t of pure tungsten plates with tolerances),
- Stainless steel for the Hcal at 18 ILCU/kg (from Atlas), and for the cryostat 15 ILCU/kg for SS304,
- Yoke steel (low carbon) at 4.1 ILCU/kg,
- Silicon strips for tracking at 7 ILCU/cm^2,
- Silicon sensors for ECal at 3 ILCU/cm^2,
- SiPM(MPPC) at 1.2 ILCU per piece from industrial quotation.

The cost estimates for the different sub-systems in ILD are listed in table 7.3. In addition we estimate the cost for other options to be 41 MILCU for the DHCal and 35.7 for the SC-ECal.

The cost driving items are the yoke, and the calorimeters. The price for the yoke is as large as it is as a direct consequence of the push-pull operation. The restriction on the stray-field outside the detector can only be met with a rather thick iron yoke, inflating the price significantly. The cost for the integration is an estimate of the scenario described in section 6, and might vary significantly with different scenarios. It includes the extra cost for the large platform on which the detectors moves, as well as the extra costs of the cryogenics needed to allow a cold move of the detector. In the absence of platform and cable chain, the lower part of the experimental hall would have to be filled with concrete. The cost for this is subtracted. Some integration tooling has been added. The offline computing represents a significant cost. Owing to the continued large advances in computing technology, we have estimated this at 20% of the equivalent cost for the LHC detectors.

A first estimate of the manpower needed has been done for each sub-system (see table 7.3, last column). Detailed estimates are available only for the major components, the rest is estimated to be around 100 MY in total. The average cost per MY has been taken to be 93 kILCU including overheads. This value is typical for the mix of qualifications needed for a sophisticated project like the ILD. The estimate only includes the manpower needed to build

Item	cost	fraction in %	man-years
Magnet yoke	68.4	16.8	
Muon system	8.4	2.1	100
Magnet coil	47.6	11.7	200
Magnet ancillaries	11.0	2.7	
AHCal	48.3	11.9	300
Si-ECal	112.0	27.5	300
Silicon tracking	21.6	5.3	200
Vertex	2.9	0.7	100
TPC	34.3	8.4	100
Forward calorimeter	5.3	1.3	
Beam tube	1.6	0.4	
Integration	1.7	0.4	
Global DAQ	1.2	0.3	
Offline computing	30.0	7.4	
Transport	13.0	3.2	
Total	407.0	100.00	

TABLE 7.3-1
Costs in MILCU and estimate of the manpower in man-years for the technologies retained in the simulation for physics studies. Options for two major sub-systems are included, but not used in the sum.

the detector, and does not include needs to finish the R&D or work out a detailed design of the detector. The manpower is then estimated to be in total 1400 MY, or 130 MILCU.

The overall ILD cost could then be 530 MILCU + 100 / - 50 MILCU.

The study has been carried out assuming that the detector is in a push-pull configuration. Most of the sub-system costs are only marginally affected by this assumption, with the exception of the integration costs, as discussed above. It has been estimated that without these requirements the total cost of the detector might be reduced by some $5 - 10\%$.

7.4 COST SCALING LAWS WITH DETECTOR PARAMETERS

The parameters which have been considered for possible scalings are the following:

- the magnetic field;
- a characteristic transverse size chosen as the inner radius of the ECAL barrel;
- a characteristic longitudinal size chosen as the length of the ECAL barrel or TPC;
- the number of samples for the ECAL (for a given number of radiation lengths);
- the number of samples for the HCAL (for a given layer interaction length or a given total interaction length);
- the calorimeter cell sizes.

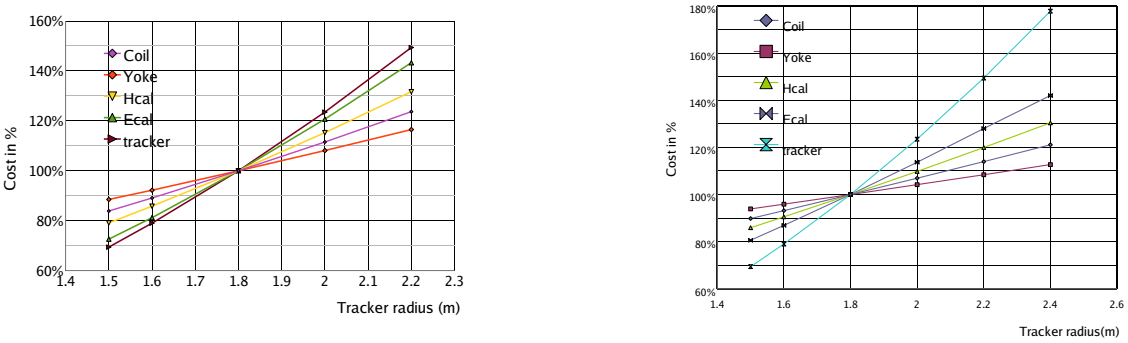

FIGURE 7.4-1. Dependence of the cost of the main items with the size, on the left for a constant angle, on the right changing only the transverse size

The study was done under the assumption that the technologies remain the same. This implies that the range for scaling is rather small, basically at the level of 25%. To go further would in most cases require reassessing the technology choices.

The nominal field is 3.5 T, but the magnet is designed to withstand 4T. Reducing the field below 3.5T might offer cost savings, but also result in a large loss of the physics potential of the detector. ILD therefore does not consider this option of de-scoping. There is a clear impact on the overall cost of the coil from the correction coils. Reducing the requirements on the field quality would result in cost savings. Whether or not this might be acceptable is currently unknown.

The dimensions of the detector parts inside the TPC are dictated by considerations of background and assembly. They are not very relevant for costing. Therefore a characteristic transverse scaling parameter is the radius of the transition from the tracker into the calorimeter, a characteristic longitudinal scaling parameter is the length of the TPC. Moving these parameters impacts calorimetry, coil and yoke. There are two ways we can envisage to scale down the size of the detector, either by keeping the aspect ratio constant, or by reducing only the radius. The estimate of the cost variation with a constant aspect ratio from the reference design is shown in figure 7.4-1 on the left. The figure on the right shows the impact of changing solely the TPC radius. The figure 7.4-2 illustrates the total cost scaling of ILD in the same conditions.

The scaling of the ECal sampling has been done under the assumption that the total number of radiation lengths in the ECAL is kept constant. The area of sensitive medium and the number of readout channels then scale proportional to the number of samplings. On the other hand, as the total amount of radiator does not change, the thickness of the absorber plates changes and the manufacturing of the plates varies in a non negligible way. Reducing the number of samples will reduce the overall thickness of the ECAL even when the total amount of absorber material stays constant. For example, going from 30 to 20 samples will reduce the radial thickness by 20 mm. In the cost scaling we do not consider the impact on the surrounding detectors (see figure 7.4-3).

In the case of the HCAL we investigate two different scenarios for reducing the sampling: either we keep the depth in radiation length constant by increasing the layer thickness, or we keep the layer thickness the same, changing the total number of interaction lengths. The same approach can be taken for the analogue and the digital HCAL option. This impacts the radiator, sensors and all the surrounding subsystems. The global impact on the ILD cost

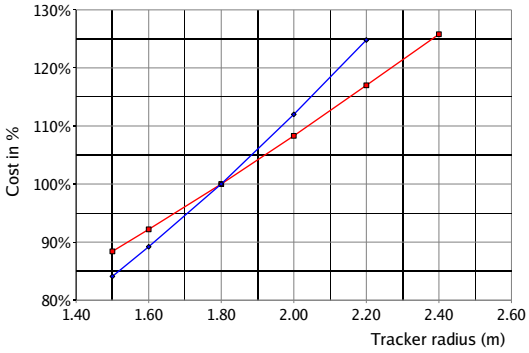

FIGURE 7.4-2. Dependence of the total cost with the size of the detector, in blue when the aspect ratio is kept, in red when the radius only changes.

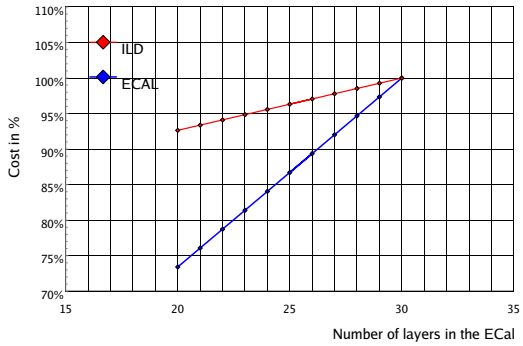

FIGURE 7.4-3. Dependence of the cost with the number of layers in the ECal.

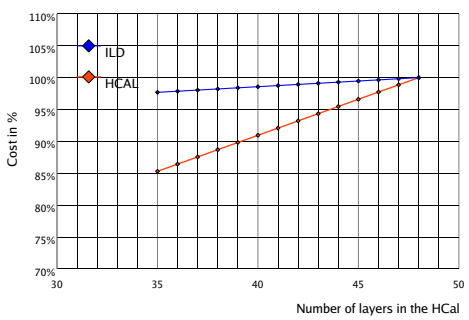

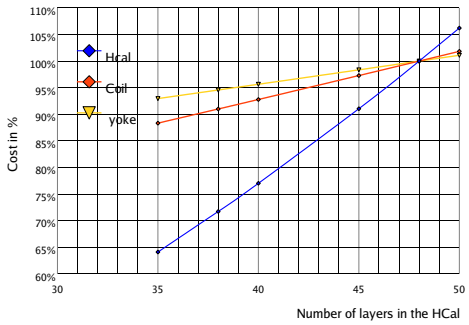

FIGURE 7.4-4. Dependence of the cost with the number of layers in the HCal, on the left if you keep the total number of interaction lengths, on the right if you keep the thickness of the layers.

is about 7% when changing from 48 to 40 layers in the HCAL as can be seen in figure 7.4-4.

The cell sizes of the electromagnetic calorimeter are already quite at a lower limit, as long as the design currently under development is used. To go below, a new design, may be a different approach will be needed. The MAPS ECAL which cost has not been estimated may be one of the possibilities. Increasing the cell sizes within the same technology will have only a minor impact on the cost, as the cost roughly scales with the area of silicon, not the number of readout channels. There is of course some effect due to a different cost of the printed circuit boards and other ancilliary equipment. We estimate that reducing the number of cells by an order of magnitude reduces the cost of the ECAL by less than 10%, or 3% of the total detector cost. The impact on the cost for the scintillator version may be larger but it is unlikely that scaling up the size in this version would be considered.

For the hadronic calorimeter changing the cell sizes will result in a changed number of FE chips, calibration devices etc. We estimate that a reduction of the number of readout channels by an order of magnitude reduces the cost of the digital HCAL by about 20%, of the analogue HCAL by about 10%. This has to be balanced with a large performance loss.

7.5 CONCLUSION

The cost of the ILD detector has been estimated to be about 500 MILCU. It includes the material and labour to build the detector, but does not include cost escalation and contingencies. The dependence of the cost on the main detector parameters has been studied, and effects of order 10% or less per item on the total detector cost have been found. To illustrate the possibilities, a cost reduction of 20% can be reached by reducing the number of HCAL layers from 48 to 40, the number of ECAL layers to 20, the inner radius of the ECAL to 160 cm, and the length accordingly. This reduces clearly the performances of the detector (See section 2). It should be noted that in many instances, a reduced performance of the detector translates into a longer running time of the accelerator until the desired physics measurements can be made.

The quoted cost of the ILD detector is comparable to the total cost of the recently completed large LHC detectors.

Although costs quoted in many instances are based on actual costs of prototypes, together with educated guesses toward mass production etc, there are still large uncertainties. A more reliable cost estimate will only be possible when a more complete and detailed engineering of the ILD detector will have been done.

CHAPTER 8

The ILD group

The ILD concept group was formed in 2007 by the merger of the GLD and the LDC groups. The ILD group has members from all three regions of the world, but is particularly well anchored in Europe and in Asia. More than 650 signatories from about 170 institutions support this Letter of Intent for ILD. Since the ILD group is not yet a collaboration, the membership of the ILD group has not been very clearly defined. The signatories of the Letter of Intent is the first set of names that comes close to the membership of the ILD group. They are, however, in a state of flux. Anybody who has contributed or intends to contribute to the ILD detector concept study is welcome to sign the LoI and can do so without any formal evaluation. On the other hand, the management of the ILD group has been defined clearly and is in operation with well defined membership and distribution of responsibilities.

The combined leadership of the two former groups GLD and LDC elected a joint steering board charged to produce a single letter of intent. The newly formed detector concept was named 'ILD' which stands for 'International Large Detector'. The joint steering board consists of two representatives from each of the three regions - Asia, Europe, and North America. The joint steering board then elected working group leaders, subdetector contacts, and representatives for the research directorate.

There are four working groups - optimisation, MDI/integration, costing, and software - and each has two conveners. The optimisation working group is charged with optimising the detector parameters based on simulations and to evaluate physics performance of the resulting detector. This working group played a key role in unifying the detector parameters of the GLD and LDC detector concepts, and continues to be the main framework for physics analyses. The MDI/integration working group was formed to fill the immediate need to liaise with the accelerator activities on such issues as dimension and shape of the experimental hall, design of push-pull operation, support of the final quads, etc. As the name suggests, the MDI/integration working group handles the issues of overall integration of the detector. There are three technical coordinators which belong to the MDI/integration working group. We believe that system engineers with strong authority are not needed at this stage of the detector development. The costing working group essentially consists of two conveners only, and is charged with estimating the cost of the whole detector and to represent the ILD group in discussions to define common costing rules with other LoI groups in the framework of the ILC research directorate. The responsibility of the software working group is to unify the softwares of the two former concept groups, and manage the development of the resulting software system.

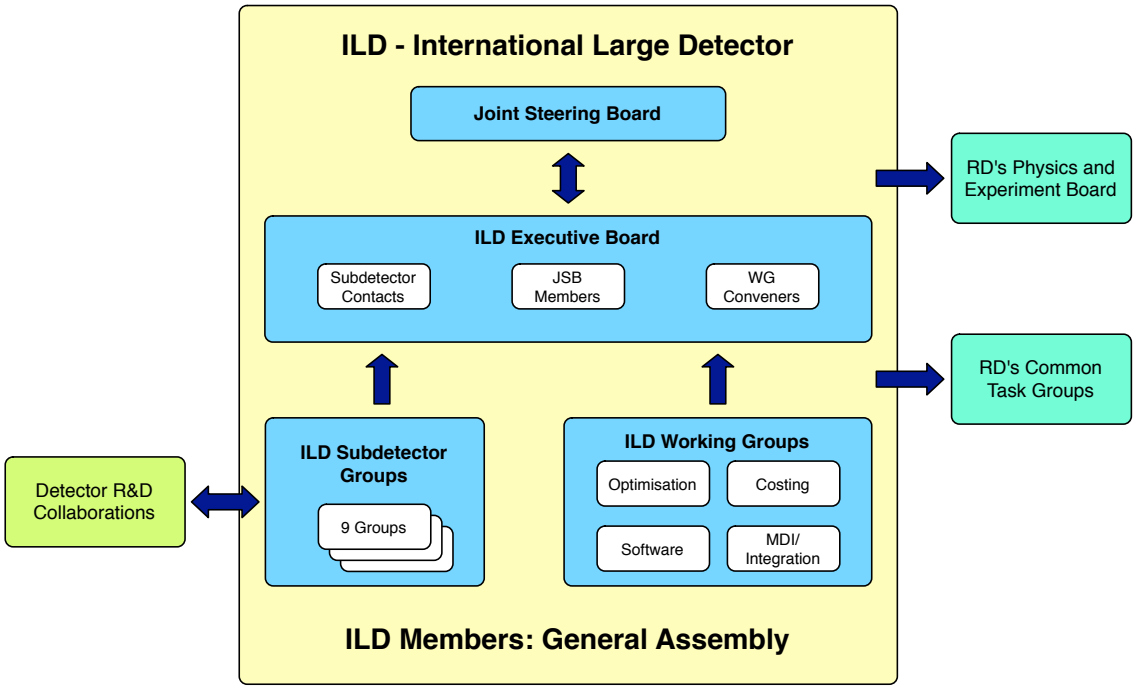

FIGURE 8.0-1. Structure of the ILD group.

The ILC detector R&D groups play a critical role in the ILD detector development. They are sometimes called 'horizontal' collaborations as opposed to LoI groups which are viewed as vertical organisations. Examples are the CALICE collaboration for calorimeters, the SiLC collaboration for silicon trackers, the LCTPC collaboration for TPC, and the FCAL collaboration for the calorimeters and instrumentation in the forward region. These groups are in principle independent of LoI groups and often bound by a "Memorandum of Understanding" to form more formal collaborations. Subdetector contact persons have been selected for vertexing, silicon trackers, TPC, ECAL, HCAL, FCAL, Muon system, DAQ, and solenoid. The number of contact persons is two per subdetector except for FCAL and muon system for which number is one. When relevant detector R&D collaborations exists for a given subdetector, a person appropriate as a liaison for that group was chosen. The subdetector contacts are charged to act as contact points to R&D groups and to make sure that the relevant detector technology is applied to the ILD environment.

In addition, the ILD group nominates members of the common task groups which serve under the ILC research director. There are two representatives of the ILD LoI group, two for MDI, one for engineering tools, three for the R&D common task group, two for the physics group, and two for the software group. They are often the same persons as the corresponding working group conveners or subdetector contacts, and act as a link to the research directorate.

In figure 8.0-1 the organisational structure of the ILD group is shown.

The joint steering board, working group conveners, subdetector contacts, and representatives for the research directorate form an entity called the executive board. The ILD executive board forms the core of the ILD-related activities, and meets roughly biweekly over internet or in person. General ILD meetings lasting a half day to a full day are usually attached to each ILC workshop. Separately we have a few dedicated ILD workshops per year of a few days each. At these meetings and dedicated workshops we have general ILD assembly meetings which take in opinions and comments from the wider community.

CHAPTER 9

R&D Plan

The ILD detector has been developed under the assumptions that particle flow is the most best method for event reconstruction and that an excellent vertex reconstruction is needed for many physics channels. To reach the proposed performance of ILD, significant advances in detector technology are needed, compared to existing detectors. Over the past years R&D collaborations have formed to address the main issues in technological development. ILD is closely cooperating with these R&D collaborations and is discussing and coordinating the needed work with these groups.

Particle flow has consequences in many parts of the detector: it is essential that a calorimeter is built that is capable of imaging the shower, and that it is complemented by a very powerful and efficient tracking system.

ILD has chosen a solution where a highly granular calorimeter is combined with a powerful and highly redundant tracking system, which contains both a large volume gaseous tracker (time projection chamber) and a high precision Si tracker with excellent tracking and vertexing capabilities. The main technological innovation relevant for ILD is the granularity in particular of the calorimeter, and the overall very low material budget projected for the tracking system while reaching excellent spatial resolution for charged particles.

Over the past years significant R&D has taken place to establish the basic feasibility of the main technologies which have been proposed. Major projects have been started to study granular calorimeters, both electromagnets and hadronic, which are organised in the context of the CALICE collaboration. A novel type of time projection chamber is under development, based on micro-pattern gas detectors, organised by the LC-TPC collaboration. New low-mass systems have been developed for all parts of the Si tracking system, in the context of the SiLC, LCFI, the MAPS, the DEPFET collaboration and other groups. Instrumentation in the very forward direction, which is special in that it is the only place in the ILC detector where radiation hardness is required, is studied in the context of the FCAL collaboration. Large area muon chambers, which can also serve as tail catchers, are being developed, also in the context of the CALICE collaboration, and by independent efforts.

The first round of R&D established for most subdetectors the basic feasibility of these systems. Test experiments with highly granular calorimeters were successfully completed at both CERN and Fermilab. The concept of a micro-pattern TPC could be established with small prototypes. First prototypes of extremely low-mass Silicon-based detectors have been developed and tested.

Internationally the linear collider experimental community wants to be able to make a reliable and well understood proposal for experiments at the ILC by 2012. This requires

that a fundamental understanding of the major detector components needs to be achieved by this time, and that a first version of an engineering solution is available. The work needs to advance to a different level than described in this document, and goes beyond the feasibility tests of the last years. It has to address system integration aspects within the sub-detector - integrated mechnical design, realistic integration of readout electronics, power management, cooling etc - but also address questions of integrating different sub-detectors.

Based on this, ILD considers that the experimental investigation of particle flow has the highest priority of R&D. This has a number of different aspects:

- Develop technological solutions for a granular electromagnetic and hadronic calorimeter.
- Develop the alternatives of Si-based and scintillator-based electromagnetic calorimeter to a point that both can be proposed, and that a future ILD collaboration can take a rapid decision after approval.
- Develop the alternatives of analogue and digital hadronic calorimetry to a point where a rapid decision between the options can be taken by a future ILD collaboration after approval. Ensure that both the analogue and the digital hadronic calorimetry are tested at the same level of sophistication in large scale setups.
- Continue to develop the simulation and software tools needed to study particle flow in detail, and continue to refine the particle flow reconstruction tools.
- Develop an experimental program, which can convincingly demonstrate the feasibility of the concept of particle flow.

The very forward detector systems in ILD are small but very different from the rest of the detector. They are the only devices where significant radiation hardness is needed. The flux of electromagnetic radiation seen by these devices is even larger than what is anticipated at the LHC. Dedicated R&D is therefore needed to develop adequate technologies for the precision calorimeters needed at very forward angles.

Particle Flow relies on a very powerful tracking system. ILD is special in all the ILC concept groups that it is proposing a TPC as central tracker. This is central to the overall performance and robustness of the system. The experimental proof that a TPC can be built and operated with the required precision and stability has very high priority for ILD.

ILD includes in its tracker a very powerful Si tracking system. The main challenge here is the development of a technology which is powerful enough and which meets the requirements in terms of material, power consumption and speed. Solutions seem to be in reach for the strip tracking system, many different options are being studied for the pixel-based vertex detector part of the system. ILD considers powerful Si tracking systems to be an essential part of the or detector concept. ILD stresses the need to pursue a broad range of different Silicon detector technologies, in particular for the vertex detector, so that an optimal solution can be chosen as close in time as possible to the construction of the detector. In particular in the rapidly and quickly evolving field of Si detectors which are dominated by commercial developments a final choice of technology should be delayed to the latest possible moment. ILD considers it essential to follow the technological developments, to develop as many alternative solutions as possible to be in a position to pick the optimal one quickly, once needed.

Testing sophisticated hardware components requires adequate testing facilities. The next generation of test beam experiments should address the interplay of different sub-detectors, in addition to novel technologies of the sub-detectors. The experiments should comprise vertexing, tracking and calorimetric components together, in an interchangeable way, in a sufficient magnetic field, at a hadron beam. A beam with an ILC-like particle bunch structure

would be a big bonus. It would test integration aspects, aspects of a common data acquisition, and the data from such an experiment would be very useful in the continuing improvement of the understanding of the different reconstruction techniques needed for ILD. ILD considers the creation of such an integrated test facility of high importance for the eventual success of the programme.

Even though most of the work currently done is on technologies for sub-detectors, the overall detector integration has to be considered as well. The concept of push - pull, which is currently favored to save one beam line, will require dedicated designs for many of the sub-detectors. These points need to be known early on, and may require some significant R&D on their own. Points of concern are sensitivity to vibrations, reproducibility of alignments, and the external monitoring of inter- detector alignments.

The ILD group intends to continue its work toward a full technical design of the detector at the end of the technical design phase 2 (around 2012), in step with the plans of the GDE for the machine. The different R&D plans of the sub-detector components are detailed in the individual sections. For the large components calorimetry and time projection chamber, large second generation prototypes should be running and delivering results by the end of 2012, such that - if the ILD group is transformed into a collaboration, and if the ILC project gets approval - a selection of technologies is possible. The steps needed to advance all options to this point are described in the individual sections. For sub-detectors like the vertex detector, intense R&D into sensor technologies will continue. A decision on the technology can be taken at a later stage, but the integration aspect of the VTX detector will need to advanced enough in 2012, that a realistic design can be proposed. The same is true for the other smaller sub-systems discussed in the context of ILD.

CHAPTER 10

Conclusions

In the summer of 2007, the GLD concept study group, whose membership was largely based in Asia, and the LDC concept study group, which was mostly based in Europe with a strong north american membership, joined forces to produce a single Letter of Intent for a detector at the International Linear Collider, and formed the ILD concept group. Both the GLD and LDC concepts used the particle flow algorithm for jet reconstruction and a TPC for the central tracker. The basic parameters of the two concepts such as the size of the detector and the strength of the solenoid field, however, were quite different and had to be unified in order to write this letter of intent for ILD. Also, other critical details such as the interaction region design had to be unified. This was a non-trivial task, neither politically nor sociologically.

The newly-formed concept study group, the ILD group, created a management team and engaged in intense studies to define the ILD detector concept by scientifically optimising the detector designs. The process has worked remarkably well, and we present here the outcome of this study as well as the large amount of studies that preceded separately by the two older concept groups. The ILD detector concept is now well defined, even though some technology choices are still open. One of the merits of unifying the detector concepts was that it revitalised the studies on physics performance and detector designs. We believe that the level of sophistication of the simulation and physics analyses has reached a high degree of sophistication for a detector group at this stage. This was achieved through collaboration and competition, and is the result of a productive learning process.

The unification had also positive effects on the subdetector R&D efforts. Most R&D on detector technologies relevant to the GLD and LDC groups is being performed within the framework of detector R&D collaborations such as LCTPC, SiLC, CALICE, and FCAL which pursue their own goals of detector technology development. Members of the detector concept groups participate in the R&D collaborations and make sure that the detector technologies are successfully applied to the detector concept designs. By the creation of the ILD concept group, the application efforts became more focused. Currently, the ILD management includes subdetector contacts who are also key members of the detector R&D collaborations. This scheme is working efficiently such that we can finish basic R&D in time for the Technical Design Report which is envisaged around 2012.

Overall, the ILD group structure is efficient while keeping flexibility and openness. Even though we are still short on person power and funding at this time, we believe that we are well positioned to successfully complete a technical design for a detector at the International Linear Collider. The ILD group is firmly committed to the ILD project.

CONCLUSIONS

BIBLIOGRAPHY

[1] **ILC Project**, A. Djouadi *et al.*, eds., *International Linear Collider Reference Design Report Volume 2: Physics at the ILC*. 2007. arXiv:0709.1893 [hep-ph]. ILC-REPORT-2007-001.

[2] **GLD Concept Study Group**, K. Abe *et al.*, "GLD detector outline document" arXiv:physics/0607154.

[3] **LDC Working Group**, D. Kisielewska *et al.*, "Detector Outline Document for the Large Detector Concept". http://www.ilcldc.org/documents/dod/.

[4] **ILC Project**, T. Behnke *et al.*, eds., *International Linear Collider Reference Design Report Volume 4: Detectors*. 2007. arXiv:0712.2356 [physics.ins-det]. ILC-REPORT-2007-001.

[5] **GEANT4 Collaboration**, S. Agostinelli *et al.*, "GEANT4: A simulation toolkit" *Nucl. Instrum. Meth.* **A506** (2003) 250–303.

[6] "Linear Collider Physics List Description". http://www.slac.stanford.edu/comp/physics/geant4/slac_physics_lists/ilc/physlistdoc.html.

[7] A. Miyamoto, "JLC Study Framework". Prepared for International Workshop on Linear Colliders (LCWS 2002), Jeju Island, Korea, 715-717 Aug 2002.

[8] R. Brun and F. Rademakers, "ROOT: An object oriented data analysis framework" *Nucl. Instrum. Meth.* **A389** (1997) 81–86.

[9] K. Hoshina, "Simulator Status of Jupiter and Satellites". Prepared for APPI Winter Institute, International (APPI2002), APPI, Japan, KEK Proceedings 2002-08, July 2002.

[10] F. Gaede, T. Behnke, N. Graf, and T. Johnson, "LCIO: A persistency framework for linear collider simulation studies" *Proceedings of CHEP 03, La Jolla, California, 24-28 Mar 2003, TUKT001* (2003) , arXiv:physics/0306114.

[11] F. Gaede *et al.*, "MarlinReco webpage". http://ilcsoft.desy.de/portal/software_packages/marlinreco.

[12] M. A. Thomson, "Particle Flow Calorimetry and the PandoraPFA Algorithm" *Nucl. Instrum. Meth.* **A611** (2009) 25–46.

[13] P. Mora de Freitas and H. Videau, "Detector simulation with MOKKA / GEANT4: Present and future". Prepared for International Workshop on Linear Colliders (LCWS 2002), Jeju Island, Korea, 26-30 Aug 2002.

[14] "GEAR - a geometry description toolkit for ILC reconstruction software". http://ilcsoft.desy.de/portal/software_packages/gear.

[15] F. Gaede, "Marlin and LCCD: Software tools for the ILC" *Nucl. Instrum. Meth.* **A559** (2006) 177–180.

[16] F. Gaede and J. Engels, "Marlin et al - A software Framework for ILC detector R&D". http://www.eudet.org/e26/e27/e584/eudet-report-2007-11.pdf. EUDET-Report-2007-11.

[17] **LCFI**, . D. Bailey *et al.*, "The LCFIVertex package: vertexing, flavour tagging and vertex charge reconstruction with an ILC vertex detector" *Nucl. Instrum. Meth.* **A610** (2009) 573–589, arXiv:0908.3019 [physics.ins-det].

[18] R. Fruhwirth, W. Waltenberger, and P. Vanlaer, "Adaptive vertex fitting" *J. Phys.* **G34** (2007) N343.

[19] M. A. Thomson, "Progress with Particle Flow Calorimetry" arXiv:0709.1360 [physics.ins-det].

[20] D. Jeans, "Particle Flow in a strip calorimeter". http://www.awa.tohoku.ac.jp/TILC08/. Presented at the TILC08 workshop.

[21] M. Battaglia, "The vertex tracker at future e+ e- linear colliders" *Nucl. Instrum. Meth.* **A530** (2004) 33–37, arXiv:physics/0312039.

[22] R. Walsh *et al.*, "Flavour tagging optimisation studies at ILD". http://www.ilcild.org/documents/ild-loi-material/flavour_tagging.pdf/at_download/file.

[23] H. Li *et al.*, "Precision Measurements of SM Higgs Recoil Mass and Cross Section for $\sqrt{s}$ of 230 GeV and 250 GeV at the ILC" arXiv:0901.4893 [physics.hep-ex]. proceedings of LCWS08 and ILC08, Chicago, Illinois, Nov 2008.

[24] **WWS Software Panel**, T. Behnke *et al.*, "Benchmark reactions for the ILC LoI". http://ilcdoc.linearcollider.org/record/14681/files/Benchmark_Reactions_for_the_ILC_LOI.pdf.

[25] "ILD reference detector model". http://www.ilcild.org/documents/ild-loi-material/ILDreferencedetector.pdf/at_download/file.

[26] T. Barklow, "Physics Impact of Detector Performance". http://www-conf.slac.stanford.edu/lcws05/program/talks/18mar2005.ppt. Presented at 2005 International Linear Collider Workshop.

[27] J. Fuster *et al.*, "Forward tracking at the next e^+e^- collider - part I: the physics case" *JINST* **4** (2009) P08002.

[28] S. Bethke, Z. Kunszt, D. E. Soper, and W. J. Stirling, "New jet cluster algorithms: Next-to-leading order QCD and hadronisation corrections" *Nucl. Phys.* **B370** (1992) 310–334.

[29] **The ALEPH, CDF, D0, DELPHI, L3, OPAL, SLD Collaborations, the LEP Electroweak Working Group, the Tevatron Electroweak Working Group, and the SLD electroweak and heavy flavour groups**, "Precision Electroweak Measurements and Constraints on the Standard Model" arXiv:0811.4682 [hep-ex].

[30] H. Li *et al.*, "HZ Recoil Mass and Cross-Section Analysis in ILD". LAL-09-121, LC-PHSM-2009-006.

[31] H. Li, "Ph.D Thesis, LAL/Universite Paris-SUD XI". LAL-09-118.

[32] M. A. Thomson, "ZFinder".

[33] J. Goldstein *et al.*, "Analysis of the higgs hadronic branching ratios in the ZH $\to \ell\ell$qq channel". http://www.ilcild.org/documents/ild-loi-material/higgs_branching_ratios.pdf/at_download/file.

[34] T. Behnke, S. Bertolucci, R. D. Heuer, and R. Settles, eds., *TESLA: The superconducting electron positron linear collider with an integrated X-ray laser laboratory. Technical design report. Pt. 4: A detector for TESLA*. DESY, 2001. http://tesla.desy.de/new_pages/TDR_CD/PartIV/detect.html. DESY-01-011.

[35] M. Davier, L. Duflot, F. Le Diberder, and A. Rouge, "The Optimal method for the measurement of tau polarization" *Phys. Lett.* **B306** (1993) 411–417.

[36] **OPAL Collaboration**, K. Ackerstaff *et al.*, "Search for the standard model Higgs boson in e+ e- collisions at s**(1/2) = 161-GeV to 172-GeV" *Eur. Phys. J.* **C1** (1998) 425–438, arXiv:hep-ex/9709003.

[37] List, B. and List, J., "MarlinKinFit: Kinematic Fitting for the ILC". talk given at ILD optimisation meeting 20/02/2008. http://ilcagenda.linearcollider.org/getFile.py/access?contribId=0&resId=0&materialId=slides&confId=2538.

[38] R. Chierici, S. Rosati, and M. Kobel, "Strong electroweak symmetry breaking signals in WW scattering at TESLA". http://www-flc.desy.de/lcnotes/notes/LC-PHSM-2001-038.ps.gz. Prepared for 5th International Linear Collider Workshop (LCWS 2000), Fermilab, Batavia, Illinois, 24-28 Oct 2000, LC-PHSM-2001-038.

[39] W. Kilian, T. Ohl, and J. Reuter, "WHIZARD: Simulating Multi-Particle Processes at LHC and ILC" arXiv:0708.4233 [hep-ph].

[40] A. F. Osorio, *WW scattering studies for a future linear collider*. PhD thesis, University of Manchester, 2006.

[41] M. Beyer *et al.*, "Determination of new electroweak parameters at the ILC: Sensitivity to new physics" *Eur. Phys. J.* **C48** (2006) 353–388, arXiv:hep-ph/0604048.

[42] P. Krstonosic, K. Monig, M. Beyer, E. Schmidt, and H. Schroder, "Experimental studies of strong electroweak symmetry breaking in gauge boson scattering and three gauge boson production" arXiv:hep-ph/0508179.

[43] P. Bechtle, K. Desch, W. Porod, and P. Wienemann, "Determination of MSSM parameters from LHC and ILC observables in a global fit" *Eur. Phys. J.* **C46** (2006) 533–544, arXiv:hep-ph/0511006.

[44] R. Heuer, D. Miller, F. Richard, and P. Zerwas, eds., *TESLA Technical Design Report Part III: Physics at an e^+e^- Linear Collider*. 2001. arXiv:hep-ph/0106315. http://tesla.desy.de/new_pages/TDR_CD/PartIII/physic.html. DESY-01-011.

[45] N. D'Ascenzo, "Study of the neutralino sector and analysis of the muon response of a highly granular hadron calorimeter at the International Linear Collider". http://www-library.desy.de/preparch/desy/thesis/desy-thesis-09-004.pdf. DESY-THESIS-2009-004.

[46] P. Bechtle, M. Berggren, J. List, P. Schade, and O. Stempel, "Prospects for the study of the $\tilde{\tau}$-system in SPS1a' at the ILC" arXiv:0908.0876 [hep-ex].

[47] C. Bartels and J. List, "Model Independent WIMP Search at 500 GeV". http://www.ilcild.org/documents/ild-loi-material/WIMPs.pdf/at_download/file.

[48] N. Wattimena and J. List, "Long-lived χ_1^0 in Gauge Mediated SUSY Breaking" tech. rep., 2009. http://www-flc.desy.de/lcnotes/notes/PREL-LC-DET-2009-001.pdf. LC-DET-2009-002.

[49] **ILC Project**, J. Brau, Y. Okada, and N. Walker, eds., *ILC Reference Design Report Volume 1: Executive Summary*. 2007. arXiv:0712.1950 [physics.acc-ph]. ILC-REPORT-2007-001.

[50] G. A. Moortgat-Pick *et al.*, "The role of polarized positrons and electrons in revealing fundamental interactions at the linear collider" *Phys. Rept.* **460** (2008) 131–243, arXiv:hep-ph/0507011.

[51] S. Boogert *et al.*, "Polarimeters and energy spectrometers for the ILC beam delivery system". http://ilcdoc.linearcollider.org/record/19682/files/loi-PolEnergy.pdf?version=1. ILC-NOTE-2009-049.

[52] A. Blondel, "A scheme to measure the polarisation asymmetry at the Z pole in LEP" *Phys. Lett.* **B202** (1988) 145.

[53] K. Monig, "The use of positron polarization for precision measurements". http://www-flc.desy.de/lcnotes/notes/LC-PHSM-2000-059.ps.gz. LC-PHSM-2000-059.

[54] P. Bechtle, W. Ehrenfeld, and I. Marchesini, "Measurement of the beam polarization at the ILC using the W^+W^- production". http://www.ilcild.org/documents/ild-loi-material/ww_pol.pdf/at_download/file. LC-PHSM-2009-XXX (in preparation).

[55] E. Asakawa *et al.*, "Precision Measurements of Little Higgs Parameters at the International Linear Collider" arXiv:0901.1081 [hep-ph].

[56] M. Giannelli, "Sensitivity to the Higgs Self-coupling Using the ZHH Channel". http://www.ilcild.org/documents/ild-loi-material/Proceedings%20LCWS09.pdf/at_download/file. Prepared for LCWS08.

[57] D. Schulte, "Study of electromagnetic and hadronic background in the interaction region of the TESLA Collider". DESY-TESLA-97-08.

[58] "User's manual of CAIN, Version 2.35". http://lcdev.kek.jp/~yokoya/CAIN/cain235/CainMan235.pdf.

[59] R. D. Masi *et al.*, "Estimate of the background on the vertex detector of ILD from beamstrahlung". http://www.ilcild.org/documents/ild-loi-material/BKGStudies.pdf/at_download/file. LC-Note in preparation.

[60] M. Winter *et al.*, "Development of Swift and Slim CMOS Sensors for a Vertex Detector at the International Linear Collider" 2007. http://iphc.in2p3.fr/Others,116.html. Internal Note.

[61] M. Winter *et al.*, "M.i.p. detection performances of a 100 us read-out CMOS pixel sensor with digitised outputs" arXiv:0902.2717 [physics.ins-det].

[62] G. Rizzo *et al.*, "Development of deep N-well MAPS in a 130 nm CMOS technology and beam test results on a 4k-pixel matrix with digital sparsified readout" in *Nuclear Science Symposium Conference Record. NSS'08*, pp. 3242–3247, IEEE. 2008.

[63] G. Traversi *et al.*, "Performance of a DNW CMOS active pixel sensor designed for the ILC Vertex Detector Development of deep N-well MAPS in a 130 nm CMOS" in *Nuclear Science Symposium Conference Record. NSS'08*, pp. 1361–1368, IEEE. 2008.

[64] C. Damerell *et al.*, "ILC Vertex Detector R&D - Report of Review Committee". http://ilcdoc.linearcollider.org/record/17962/files/Vertex_Detector_Review-final.pdf?version=1. ILC-Report-2008-016.

[65] **DEPFET collaboration**, L. Feld *et al.*, "DEPFET Pixel Vertex Detector for the ILC". http://www.hll.mpg.de/~lca/ilc/DEPFET-VTX-ILC.pdf. Internal Note.

[66] Y. Sugimoto *et al.*, "FPCCD vertex detector R&D for ILC" 2007. http://www-jlc.kek.jp/subg/vtx/pub/FPCCD_Rev.pdf. Internal Note.

[67] Y. Sugimoto *et al.*, "R&D status of FPCCD VTX" arXiv:0902.2067 [physics.ins-det].

[68] FNAL and IPHC-Strasbourg and IRFU-Saclay and Bergamo University, "Consortium for Developing 3D/vertically Integrated Readout Electronics and Sensors". http://3dic.fnal.gov/.

[69] L. Andricek *et al.*, "The DEPFET active pixel sensor for vertexing at ILC and SuperKEKB" in *Proceedings of the TIPP-09 workshop*. Tsukuba (Japan), March 11-17 , 2009. to be published.

[70] M. Szelezniak, "Small-Scale Readout System Prototype for the STAR PIXEL Detector". http://repositories.cdlib.org/lbnl/LBNL-1086E-1. Lawrence Berkeley National Laboratory. Paper LBNL-1086E-1.

[71] **SiLC R&D Collaboration**, A. Savoy-Navarro, ed., *Proposal to the ILCSC R&D Panel on Tracking for the ILC*. submitted January 29, 2007. http://lpnhe-lc.in2p3.fr/DOCS/beijing.pdf.

[72] **SiLC R&D Collaboration**, A. Savoy-Navarro, ed., *Status report to the PRC-DESY*. 2008. http://prc.desy.de/e38/e60/e126/infoboxContent129/PRC65-SiLC_report.pdf.

[73] **SiLC R&D Collaboration**, "Eudet memos". see the references in the Website address of the PRC-DESY status report [72] above.

[74] V. Saveliev and M. Vos, "Presentations at the first ILD meeting". http://ilcagenda.linearcollider.org/conferenceDisplay.py?confId=2389.

[75] A. Ruiz, A. Savoy-Navarro, and M.Vos, "Presentations at TILC08". http://www.awa.tohoku.ac.jp/TILC08/.

[76] V. Saveliev, Z. Drasal, M.Fernandez-Garcia, W. Mitaroff, and A. Savoy-Navarro, "Presentations at ECFA Workshop in Warsaw". http://ilcagenda.linearcollider.org/conferenceDisplay.py?confId=2642.

[77] W. Cleland and E. Stern, "Signal processing considerations for liquid ionization calorimeters in a high rate environment" *Nucl. Instrum. Meth.* **A 338** (1994) 467.

[78] A. R. Jimeno, "Alignment of Silicon tracking systems R&D and First Prototype". http://ilcagenda.linearcollider.org/getFile.py/access?contribId=484&sessionId=21&resId=1&materialId=slides&confId=2628.

[79] A. Charpy *et al.*, "Integration of a Silicon tracking system combined with a TPC for the ILD project". ILC Internal Note under submission.

[80] T. H. Pham, "An 88-channel mixed mode chip in 130nm for Silicon strips readout at the ILC". http://kds.kek.jp/getFile.py/access?contribId=101&sessionId=57&resId=0&materialId=slides&confId=2376.

[81] M. Gruwe, "Gas studies for the TPC of a detector for the future Linear Collider". http://www-flc.desy.de/lcnotes/notes/LC-DET-1999-003-TESLA.ps.gz. LC-DET-1999-003.

[82] M. Ronan, "Time-projection chambers" *PDG Particle Physics Booklet* (2006) 264. http://instrumentationcolloquium.lbl.gov/Time_Projection_Chamber_R&D.pdf.

[83] LCTPC Groups, "TPC R&D for an ILC Detector". http://www-flc.desy.de/lcnotes/notes/LC-DET-2007-005.pdf. LC-DET-2007-005.

[84] **LCTPC Collaboration**, "TPC R&D for a Linear Collider Detector". http://prc.desy.de/sites/site_prc/content/e38/e60/e126/infoboxContent130/PRC65-TPC_report_31March2008.pdf. Status report April 2008 to the DESY PRC65 meeting.

[85] Y. Giomataris, P. Rebourgeard, J. P. Robert, and G. Charpak, "MICROMEGAS: A high-granularity position-sensitive gaseous detector for high particle-flux environments" *Nucl. Instrum. Meth.* **A376** (1996) 29–35.

[86] F. Sauli, "GEM: A new concept for electron amplification in gas detectors" *Nucl. Instrum. Meth.* **A386** (1997) 531–534.

[87] A. Raspiereza, "LDC Tracking Package" (2007) . http://www-zeuthen.desy.de/ILC/lcws07/pdf/Sim_Reco/raspereza_alexei.pdf. Contribution to the Sim/Reco sesstion at LCWS2007, DESY Hamburg 29 May - 4 June 2007.

[88] A. Vogel, *Beam-Induced Backgrounds in Detectors at the ILC*. PhD thesis, Department Physik der Universität Hamburg, 2008. http://www-library.desy.de/preparch/desy/thesis/desy-thesis-08-036.pdf. DESY-THESIS-2008-036.

[89] **ALICE Collaboration**, G. Dellacasa *et al.*, "ALICE technical design report of the time projection chamber". CERN-OPEN-2000-183.

[90] **EUDET Consortium**, "The EUDET facility at DESY". http://www.eudet.org/.

[91] M. S. Dixit, J. Dubeau, J. P. Martin, and K. Sachs, "Position sensing from charge dispersion in micro-pattern gas detectors with a resistive anode" *Nucl. Instrum. Meth.* **A518** (2004) 721–727, arXiv:physics/0307152.

[92] **LCTPC Collaboration**, "A TPC for a future linear collider". http://www-flc.desy.de/lcnotes/notes/LC-DET-2002-008.ps.gz. LC-DET-2002-008.

[93] **STAR Collaboration**, "STAR TPC". http://www.star.bnl.gov/.

[94] D. Peterson, "Presentations at LCWS07 tracking session". http://www.lepp.cornell.edu/~dpp/linear_collider/ILC_Presentations.html.

[95] R. Settles and W. Wiedenmann, "The Linear Collider TPC: Revised Magnetic-field Requirements". http://www-flc.desy.de/lcnotes/notes/LC-DET-2008-002.pdf. LC-DET-2008-002.

[96] R. Settles and M. Thomson, "Suggestion for Amount of Alignment-Data Needed". http://acfahep.kek.jp/subg/ir/bds/ilc-bds.html. See replies linked therein at 4. MDI.

[97] D. Karlen *et al.*, "Tpc performance in magnetic fields with gem and pad readout" *Nucl. Instrum. Meth.* **A555** (2005) 80.

[98] J.-C. Brient and H. Videau, "The calorimetry at the future e+ e- linear collider" arXiv:hep-ex/0202004.

[99] **CALICE Collaboration**. http://polywww.in2p3.fr/flc/calice.html.

[100] **CALICE Collaboration**, J. Repond *et al.*, "Design and Electronics Commissioning of the Physics Prototype of a Si-W Electromagnetic Calorimeter for the International Linear Collider" *JINST* **3** (2008) P08001, arXiv:0805.4833 [physics.ins-det].

[101] H. Videau, "Few considerations on the design of the electromagnetic calorimeter". http://ilcagenda.linearcollider.org/getFile.py/access?contribId=108&sessionId=6&resId=0&materialId=slides&confId=1049. presentation at ECFA meeting, Valencia, Nov. 2006.

[102] M. Reinhard and J.-C. Brient, "GARLIC - GAmma Reconstruciton for the LInear Collider" arXiv:0902.3042 [hep-ex].

[103] **CALICE Collaboration**, J. Repond *et al.*, "Response of the CALICE Si-W Electromagnetic Calorimeter Physics Prototype to Electrons" arXiv:0811.2354 [physics.ins-det]. Submitted to NIMA.

[104] J. A. Ballin *et al.*, "Monolithic Active Pixel Sensors (MAPS) in a quadruple well technology for nearly 100% fill factor and full CMOS pixels" *Sensors* **8** (2008) 5336, arXiv:0807.2920 [Unknown].

[105] J. A. Ballin *et al.*, "A MAPS-based Digital Electromagnetic Calorimeter for the ILC" arXiv:0709.1346 [physics.ins-det].

[106] N. K. Watson *et al.*, "A MAPS-based readout of an electromagnetic calorimeter for the ILC" *J. Phys. Conf. Ser.* **110** (2008) 092035.

[107] **CALICE Collaboration**, C. Adloff *et al.*, "CALICE Report to the Calorimeter R&D Review Panel" arXiv:0707.1245 [physics.ins-det].

[108] M. Stanitzki *et al.*, "A Tera-Pixel Calorimeter for the ILC" in *Nuclear Science Symposium Conference Record. NSS'07*, vol. 1, p. 254, IEEE. 2007.

[109] J. P. Crooks *et al.*, "A Novel CMOS Monolithic Active Pixel Sensor with Analog Signal Processing and 100% Fill Factor" in *Nuclear Science Symposium Conference Record. NSS'07*, vol. 2, p. 931, IEEE. 2007.

[110] J. A. Ballin *et al.*, "TPAC: A 0.18 Micron MAPS for Digital Electromagnetic Calorimetry at the ILC" in *Nuclear Science Symposium Conference Record. NSS '08.*, pp. 2224–2227, IEEE. 2008.

[111] T. S. Group, "Silicon pixel detector r&d". http://ilcagenda.linearcollider.org/categoryDisplay.py?categId=171.

[112] H. Matsunaga, "Software studies of GLD calorimeter" *Pramana* **69** (2007) 1057–1061. http://www.ias.ac.in/pramana/v69/p1057/fulltext.pdf.

[113] V. Bartsch *et al.*, "Status of the DAQ system for the EUDET Calorimetry". http://www.eudet.org/e26/e28/e615/e800/EUDET-Memo-2008-19.pdf. EUDET-Memo-2008-19.

[114] H. Abramowicz *et al.*, "Instrumentation of the very forward region of a linear collider detector" *IEEE Trans. Nucl. Sci.* **51** (2004) 2983–2989.

[115] K. Mönig, "Physics needs for the Forward Region" *V. Workshop: Instrumentation of the Forward Region of a Linear Collider Detector* (2004) . http://www-zeuthen.desy.de/lcdet/Aug_04_WS/talks/moenig_lum04.pdf.

[116] C. Grah and A. Sapronov, "Beam parameter determination using beamstrahlung photons and incoherent pairs" *JINST* **3** (2008) P10004.

[117] W. Daniluk *et al.*, "Laser Alignment System for LumiCal". http://www.eudet.org/e26/e26/e27/e826/EUDET_report_05.pdf. EUDET-Report-2008-05.

[118] C. Clerc and M. Joré, "Note on the integration of the ILD detector". http://www.ilcild.org/documents/ild-loi-material/ILD_integration_note.pdf/at_download/file.

[119] H. Abramowicz *et al.*, "A Luminosity Detetor for the International Linear Collider". http://www-flc.desy.de/lcnotes/notes/LC-DET-2007-006.pdf. LC-DET-2007-006.

[120] W. Wierba *et al.*, "LumiCal mechanical design proposal and integration with ILD". http://www.eudet.org/e26/e28/e615/e762/EUDET-Memo-2008-13.doc. EUDET-Memo-2008-13.

[121] A. Stahl, "Luminosity Measurement via Bhabha Scattering: Precision Requirements for the Luminosity Calorimeter". http://www-flc.desy.de/lcnotes/notes/LC-DET-2005-004.ps.gz. LC-DET-2005-004.

[122] I. Smiljanic, "Towards a final selection for luminosity measurement" *Proceedings of the Workshop of the Collaboration on Forward Calorimetry at ILC* (Belgrade 2008) . http://www.vinca.rs/hep/pub/FCAL_Belgrade.pdf.

[123] W. Wierba *et al.*, "Silicon Sensors for LumiCal Status Report". http://www.eudet.org/e26/e28/e615/e761/EUDET-Memo-2008-12.doc. EUDET-Memo-2008-12.

[124] H. Abramowicz *et al.*, "GEANT4 Simulation of the Electronic Readout Constraints for the Luminosity Detector of the ILC". http://www.eudet.org/e26/e28/e182/e308/eudet-memo-2007-17.pdf. EUDET-Memo-2007-17.

[125] M. Idzik *et al.*, "Status of LumiCal Readout Electronics". http://www.eudet.org/e26/e26/e27/e823/eudet_08.pdf. EUDET-Report-2008-08.

[126] P. Bambade, V. Drugakov, and W. Lohmann, "The impact of BeamCal performance at different ILC beam parameters and crossing angles on stau searches" *Pramana* **69** (2007) 1123–1128, arXiv:physics/0610145.

[127] C. Grah *et al.*, "Polycrystalline CVD Diamond Sensors for the Beam Calorimeter of the ILC" *IEEE Trans.Nucl.Sci., accepted for publication* (2009) .

[128] C. Grah *et al.*, "Radiation hard sensor for the BeamCal of the ILC detector" in *Nuclear Science Symposium Conference Record. NSS'07*, vol. 3, pp. 2281–2284, IEEE. 2007.

[129] A. Abusleme *et al.*, "BeamCal front-end electronics: Design and Simulation" *Proceedings of the Workshop of the Collaboration on Forward Calorimetry at ILC* (2008) . http://www.vinca.rs/hep/pub/FCAL_Belgrade.pdf.

[130] Y. Sato, "Study of Pair-Monitor for ILD" *Proceedings of the Workshop of the Collaboration on Forward Calorimetry at ILC* (2008) . http://www.vinca.rs/hep/pub/FCAL_Belgrade.pdf.

[131] Y. Takubo, "Development of Pair Monitor" *Proceedings of the Workshop of the Collaboration on Forward Calorimetry at ILC* (2008) . http://www.vinca.rs/hep/pub/FCAL_Belgrade.pdf.

[132] **CMS Collaboration**, G. Acquistapace *et al.*, "CMS, the magnet project: Technical design report". http://cmsdoc.cern.ch/ftp/TDR/MAGNET/magnet.html. CERN-LHCC-97-10.

[133] A. Hervé, F. Kircher, *et al.*, "Experience Gained from the Construction, Test and Operation of the Large 4-T CMS Coil" in *IEEE Trans. on Appl. Superc.*, vol. 18-2, pp. 346–351. 2008.

[134] M. Fernandez *et al.*, "Experimental validation of optical simulations for microstrip detectors". http://www.eudet.org/. EUDET-memo-2008-37.

[135] **The SiD Concept Group**, "The SiD detector outline document". http://hep.uchicago.edu/~oreglia/siddod.pdf.

[136] **CMS Collaboration**, P. Sphicas, ed., *CMS: The TriDAS project. Technical design report, Vol. 2: Data acquisition and high-level trigger*. http://cdsweb.cern.ch/record/578006/files/cer-2336481.pdf. CERN-LHCC-2002-026.

[137] **ILC Project**, N. Phinney, N. Toge, and N. Walker, eds., *ILC Reference Design Report Volume 3: Accelerator*. 2007. arXiv:0712.2361 [physics.acc-ph]. ILC-REPORT-2007-001.

[138] **ATLAS Collaboration**, G. Duckeck *et al.*, eds., *ATLAS computing: Technical design report*. http://cdsweb.cern.ch/record/837738/files/lhcc-2005-022.pdf. CERN-LHCC-2005-022.

[139] **CMS Collaboration**, "CMS: The computing project. Technical design report". http://cdsweb.cern.ch/record/838359/files/lhcc-2005-023.pdf. CERN-LHCC-2005-023.

[140] "ATCA Short Form Spec.". http://www.picmg.org/pdf/PICMG_3_0_Shortform.pdf.

[141] C. Clerc, "Dimensions and weights of the ILD components". http://www.ilcild.org/documents/ild-loi-material/ILD00_dimensions-weights.pdf/at_download/file.

[142] B. Parker *et al.*, "Functional requirements on the design of the detectors and the interaction region of an e^+e^- linear collider with a push-pull arrangement of detectors". ILC-Note in preparation.

[143] T. Sanami, "IR hall dose rate estimates for a self-shielding detector". http://ilcagenda.linearcollider.org/getFile.py/access?contribId=49&sessionId=44&resId=0&materialId=0&confId=3159. Presented at the ILD workshop, Seoul, Korea.

[144] M. Warden *et al.*, "Nanometre precision interferometric stability monitoring system for key accelerator components". http://www.eurotev.org/reports_presentations/eurotev_reports/2008/e1109/EUROTeV-Report-2008-032.pdf. EUROTeV-Report-2008-032.

[145] M. Anduze, H. Videau, and M. Jore, "Note on the beam tube for ILD" (2009) . http://www.ilcild.org/documents/ild-loi-material/Beam_tube_note.pdf/at_download/file.

[146] Y. Suetsugu, "Technical note for ILD beam pipe". http://www.ilcild.org/documents/ild-loi-material/Suetsugu_beam_pipe.pdf/at_download/file.

[147] C. Clerc, "ILD work breakdown structure". http://www.ilcild.org/documents/ild-loi-material/ILD%20WBS%202009.xlsx/at_download/file.

ATLAS NOTE

ATLAS-CONF-2013-039

April 9, 2013

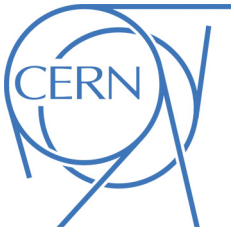

Flavour tagged time dependent angular analysis of the $B_s^0 \to J/\psi\phi$ decay and extraction of $\Delta\Gamma_s$ and the weak phase ϕ_s in ATLAS

The ATLAS Collaboration

Abstract

A measurement of the $B_s^0 \to J/\psi\phi$ decay parameters, updated to include flavour tagging is reported using 4.9 fb^{-1} of integrated luminosity collected by the ATLAS detector from pp collisions recorded in 2011. The values measured for the physical parameters are:

$$\begin{aligned}
\phi_s &= 0.12 \pm 0.25\ (\text{stat.}) \pm 0.11\ (\text{syst.})\ \text{rad} \\
\Delta\Gamma_s &= 0.053 \pm 0.021\ (\text{stat.}) \pm 0.009\ (\text{syst.})\ \text{ps}^{-1} \\
\Gamma_s &= 0.677 \pm 0.007\ (\text{stat.}) \pm 0.003\ (\text{syst.})\ \text{ps}^{-1} \\
|A_0(0)|^2 &= 0.529 \pm 0.006(\text{stat.}) \pm 0.011\ (\text{syst.}) \\
|A_{\|}(0)|^2 &= 0.220 \pm 0.008(\text{stat.}) \pm 0.009\ (\text{syst.}) \\
\delta_{\perp} &= 3.89 \pm 0.46\ (\text{stat.}) \pm\ 0.13\ (\text{syst.})\ \text{rad}
\end{aligned}$$

where the parameter $\Delta\Gamma_s$ is constrained to be positive. The fraction $|A_S(0)|^2$, of S-wave KK or f_0 contamination through the decays $B_s^0 \to J/\psi K^+K^-(f_0)$ is also measured and is found to be compatible with zero. Results for ϕ_s and $\Delta\Gamma_s$ are also presented as 68% and 95% likelihood contours, which show agreement with the Standard Model expectations.

ATLAS-CONF-2013-039
12 April 2013

1 Introduction

New phenomena beyond the predictions of the Standard Model (SM) may alter *CP* violation in B-decays. A channel that is expected to be sensitive to new physics contributions is the decay $B_s^0 \to J/\psi\phi$. *CP* violation in the $B_s^0 \to J/\psi\phi$ decay occurs due to interference between direct decays and decays occurring through $B_s^0 - \overline{B_s^0}$ mixing. The oscillation frequency of B_s^0 meson mixing is characterized by the mass difference Δm_s of the heavy (B_H) and light (B_L) mass eigenstates. The *CP*-violating phase ϕ_s is defined as the weak phase difference between the $B_s^0 - \overline{B_s^0}$ mixing amplitude and the $b \to c\bar{c}s$ decay amplitude. In the absence of *CP* violation, the B_H state would correspond exactly to the *CP*-odd state and the B_L to the *CP*-even state. In the SM the phase ϕ_s is small and can be related to CKM quark mixing matrix elements via the relation $\phi_s \simeq -2\beta_s$, with $\beta_s = \arg[-(V_{ts}V_{tb}^*)/(V_{cs}V_{cb}^*)]$; a value of $\phi_s \simeq -2\beta_s = -0.0368 \pm 0.0018$ rad [1] is predicted in the SM. Many new physics models predict large ϕ_s values whilst satisfying all existing constraints, including the precisely measured value of Δm_s [2, 3].

Another physical quantity involved in $B_s^0 - \overline{B_s^0}$ mixing is the width difference $\Delta\Gamma_s = \Gamma_L - \Gamma_H$ of B_L and $B_H$which is predicted to be $\Delta\Gamma_s = 0.087 \pm 0.021$ ps^{-1}[4]. Physics beyond the SM is not expected to affect $\Delta\Gamma_s$ as significantly as ϕ_s [5]. Extracting $\Delta\Gamma_s$ from data is nevertheless useful as it allows theoretical predictions to be tested [5].

The decay of the pseudoscalar B_s^0 to the vector-vector final-state $J/\psi\phi$ results in an admixture of *CP*-odd and *CP*-even states, with orbital angular momentum $L = 0$, 1 or 2. The final states with orbital angular momentum $L = 0$ or 2 are *CP*-even while the state with $L = 1$ is *CP*-odd. Flavour tagging is used to distinguish between the initial B_s^0 and $\overline{B_s^0}$ states. The *CP* states are separated statistically through the time-dependence of the decay and angular correlations amongst the final-state particles.

In this paper, an update to the previous measurement [6] of ϕ_s, the average decay width $\Gamma_s = (\Gamma_L + \Gamma_H)/2$ and the value of $\Delta\Gamma_s$, using flavour tagging, is presented. Previous measurements of these quantities have been reported by the CDF and DØ collaborations [7, 8] and recently by the LHCb collaboration [9]. The analysis presented here uses LHC pp data at $\sqrt{s} = 7$ TeV collected by the ATLAS detector in 2011.

2 ATLAS detector and Monte Carlo simulation

The ATLAS experiment [10] is a multipurpose particle physics detector with a forward-backward symmetric cylindrical geometry and near 4π coverage in solid angle. The inner tracking detector (ID) consists of a silicon pixel detector, a silicon microstrip detector and a transition radiation tracker. The ID is surrounded by a thin superconducting solenoid providing a 2 T axial magnetic field, and by an high-granularity liquid-argon (LAr) sampling electromagnetic calorimeter. An iron/scintillator tile calorimeter provides hadronic coverage in the central rapidity range. The end-cap and forward regions are instrumented with LAr calorimeters for both electromagnetic and hadronic measurements. The muon spectrometer (MS) surrounds the calorimeters and consists of three large superconducting toroids with eight coils each, a system of tracking chambers, and detectors for triggering.

The muon and tracking systems are of particular importance in the reconstruction of B meson candidates. Only data where both systems were operating correctly and where the LHC beams were declared to be stable are used. A muon identified using a reconstruction relying on a statistical combination of MS and ID track parameters is referred to as *combined*. A muon formed by segments which are not associated with an MS track, but which are matched to ID tracks extrapolated to the MS is referred to as *segment tagged*.

The data were collected during a period of rising instantaneous luminosity at the LHC, and the trigger conditions varied over this time. The triggers used to select events for this analysis are based on

identification of a $J/\psi \to \mu^+\mu^-$ decay, with either a 4 GeV transverse momentum* (p_{T}) threshold for each muon or an asymmetric configuration that applies a p_{T} threshold beyond 4 GeV p_{T} to one of the muons and accepting the second muon with p_{T} as low as 2 GeV.

Monte Carlo (MC) simulation is used to study the detector response, estimate backgrounds and model systematic effects. For this study, 12 million MC-simulated $B_s^0 \to J/\psi\phi$ events were generated using PYTHIA [11] tuned with recent ATLAS data [12]. No p_{T} cuts were applied at the generator level. Detector responses for these events were simulated using the ATLAS simulation package based on GEANT4 [13]. In order to take into account the varying trigger configurations during data-taking, the MC events were weighted to have the same trigger composition as the collected collision data. Additional samples of the background decay $B_d^0 \to J/\psi K^{0*}$ as well as the more general $bb \to J/\psi X$ and $pp \to J/\psi X$ backgrounds were also simulated using PYTHIA.

3 Reconstruction and candidate selection

Events passing the trigger and the data quality selections described in Section 2 are required to pass the following additional criteria: the event must contain at least one reconstructed primary vertex built from at least four ID tracks and at least one pair of oppositely charged muon candidates that are reconstructed using one of the two algorithms that combine the information from the MS and the ID [14]. In this analysis the muon track parameters are taken from the ID measurement alone, since the precision of the measured track parameters for muons in the p_{T} range of interest for this analysis is dominated by the ID track reconstruction. The pairs of muon tracks are refitted to a common vertex and accepted for further consideration if the fit results in χ^2/d.o.f. < 10. The invariant mass of the muon pair is calculated from the refitted track parameters. To account for varying mass resolution, the J/ψ candidates are divided into three subsets according to the pseudorapidity η of the muons. A maximum likelihood fit is used to extract the J/ψ mass and the corresponding resolution for these three subsets. When both muons have $|\eta| < 1.05$, the di-muon invariant mass must fall in the range $(2.959 - 3.229)$ GeV to be accepted as a J/ψ candidate. When one muon has $1.05 < |\eta| < 2.5$ and the other muon $|\eta| < 1.05$, the corresponding signal region is $(2.913 - 3.273)$ GeV. For the third subset, where both muons have $1.05 < |\eta| < 2.5$, the signal region is $(2.852 - 3.332)$ GeV. In each case the signal region is defined so as to retain 99.8% of the J/ψ candidates identified in the fits.

The candidates for $\phi \to K^+K^-$ are reconstructed from all pairs of oppositely charged particles with $p_{\mathrm{T}} > 0.5$ GeV and $|\eta| < 2.5$ that are not identified as muons. Candidates for $B_s^0 \to J/\psi(\mu^+\mu^-)\phi(K^+K^-)$ are sought by fitting the tracks for each combination of $J/\psi \to \mu^+\mu^-$ and $\phi \to K^+K^-$ to a common vertex. Each of the four tracks are required to have at least one hit in the pixel detector and at least four hits in the silicon strip detector. The fit is further constrained by fixing the invariant mass calculated from the two muon tracks to the world average J/ψ mass [15]. These quadruplets of tracks are accepted for further analysis if the vertex fit has a χ^2/d.o.f. < 3, the fitted p_{T} of each track from $\phi \to K^+K^-$ is greater than 1 GeV and the invariant mass of the track pairs (under the assumption that they are kaons) falls within the interval $1.0085\ \mathrm{GeV} < m(K^+K^-) < 1.0305\ \mathrm{GeV}$. In total 131k B_s^0 candidates are collected within a mass range of $5.15 < m(B_s^0) < 5.65$ GeV used in the fit.

For each B_s^0 meson candidate the proper decay time t is determined by the expression:

$$t = \frac{L_{xy}\, M_B}{c\, p_{\mathrm{T}_B}},$$

where p_{T_B} is the reconstructed transverse momentum of the B_s^0 meson candidate and M_B denotes the world average mass value [15] of the B_s^0 meson (5.3663 GeV). The transverse decay length, L_{xy}, is the

*The ATLAS coordinate system and the definition of transverse momentum are described in reference [10]

displacement in the transverse plane of the B_s^0 meson decay vertex with respect to the primary vertex, projected onto the direction of the B_s^0 transverse momentum. The position of the primary vertex used to calculate this quantity is refitted following the removal of the tracks used to reconstruct the B_s^0 meson candidate.

For the selected events the average number of pileup interactions is 5.6, necessitating a choice of the best candidate for the primary vertex at which the B_s^0 meson is produced. The variable used is a three-dimensional impact parameter d_0, which is calculated as the distance between the line extrapolated from the reconstructed B_s^0 meson vertex in the direction of the B_s^0 momentum, and each primary vertex candidate. The chosen primary vertex is the one with the smallest d_0. Using MC simulation it is shown that the fraction of B_s^0 candidates which are assigned the wrong primary vertex is less than 1% and that the corresponding effect on the final results is negligible. No B_s^0 meson lifetime cut is applied in the analysis.

4 Flavour tagging

The determination of the initial flavour of neutral B-mesons can be inferred using information from the other B-meson that is typically produced from the other b quark in the event, referred to as the Opposite-Side Tagging (OST).

To study and calibrate the OST methods, the decays of $B^{\pm} \to J/\psi K^{\pm}$ can be used, where flavour of the charge of the B-meson at production is provided by the kaon charge. Events from the entire 2011 run period satisfying the same data quality selections as described in section 2 are used.

4.1 $B^{\pm} \to J/\psi K^{\pm}$ event selection

To be selected for use in the calibration analysis, events must satisfy a trigger condition requiring two oppositely-charged muons within an invariant mass range around the nominal J/ψ mass. Candidate $B^{\pm} \to J/\psi K^{\pm}$ decays are identified using two oppositely-charged combined muons forming a good vertex using information supplied by the inner detector. Each muon is required to have a transverse momentum of at least 4 GeV and pseudo-rapidity within $|\eta| < 2.5$. The invariant mass of the di-muon candidate is required to satisfy $2.8 < m(\mu\mu) < 3.4$ GeV. To form the B candidate an additional track with $p_{\mathrm{T}} > 1$ GeV , $|\eta| < 2.5$ is combined with the di-muon candidate and a vertex fit performed applying a mass-constraint for the di-muons to the known value of the J/ψ mass. To reduce the majority of the prompt component of the combinatorial background the requirement $L_{xy} > 0.1$ mm is made on the B candidate.

In order to study the distributions corresponding to the signal processes with the background component removed, a sideband subtraction method is defined. Events are separated into five regions of B candidate rapidity and three mass regions. The mass regions are defined as a signal region around the fitted peak signal mass position $\mu \pm 2\sigma$ and the sidebands are $[\mu - 5\sigma, \mu - 3\sigma]$ and $[\mu + 3\sigma, \mu + 5\sigma]$, where μ and σ are the peak and widths of the Gaussian model of the B signal mass respectively. Individual binned extended likelihood fits are performed to the invariant mass distribution in each region of rapidity.

The background is modelled by an exponential to describe combinatorial background and a hyperbolic tangent function to parameterise the low-mass contribution from mis- and partially-reconstructed B decays. This component has negligible contribution to either the signal or sideband regions. Figure 1 shows the invariant mass distribution of B candidates for all rapidity regions overlaid with the fit result for the combined data.

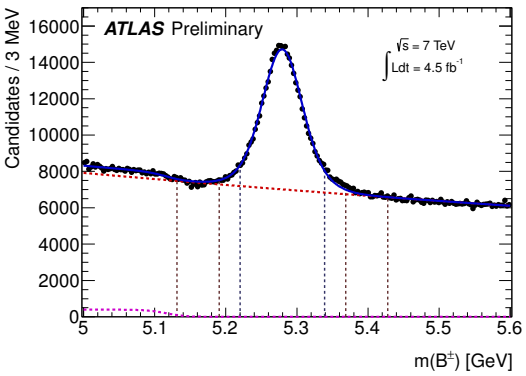

Figure 1: The invariant mass distribution for $B^{\pm} \to J/\psi K^{\pm}$ candidates. Included in this plot are all events passing the selection criteria. The data are shown by points, the overall result of the fit is given by the blue curve. The combinatorial background component is given by the dashed line, and the contribution of the background from partially reconstructed decays is shown in the dotted curve. The red vertical dashed lines indicate the left and right sidebands while the blue vertical dashed lines indicate the signal region.

4.2 Tagging methods

Several methods are available to infer the flavour of the opposite-side meson, with varying efficiencies and discriminating powers. Identifying the charge of a muon through the semi-leptonic decay of the B meson provides strong power of separation, however the $b \to \mu$ transitions are diluted through neutral B meson oscillations, as well as by cascade decays $b \to c \to \mu$ which can alter the sign of the muon relative to the one coming from direct semi-leptonic decays $b \to \mu$. The separation power of tag muons can be enhanced by considering a weighted sum of the charge of the tracks in a cone around the muon. If no muon is present, a weighted sum of the charge of tracks associated to the opposite side B meson decay will also provide some separation. The tagging methods are described in detail below.

An additional muon is searched for in the event, having originated near the original interaction point. Muons are separated into their two reconstruction classes: *combined* and *segment tagged*. In the case of multiple muons, the one with the highest transverse momentum is selected. A muon *cone charge* variable is constructed, defined as

$$Q_{\mu} = \frac{\sum_i^{N\,\text{tracks}} q^i \cdot (p_T^i)^{\kappa}}{\sum_i^{N\,\text{tracks}} (p_T^i)^{\kappa}}, \tag{1}$$

where the value of the parameter $\kappa = 1.1$, which was tuned to optimise the tagging power, and the sum is performed over the reconstructed ID tracks within a cone of $\Delta R < 0.5$ around the muon momentum axis, with $p_{\mathrm{T}} > 0.5$ GeV and $|\eta| < 2.5$. The value of parameter κ has been determined in the process of optimisation of the tagging performance. Tracks associated to the signal-side of the decay are explicitly excluded from the sum. In Fig. 2 the distribution of muon cone charge is shown for candidates from $B^{\pm}$ signal decays, for each class of muon.

In the absence of a muon, a b-tagged jet [16] is required in the event, with tracks associated to the same primary interaction vertex as the signal decay, excluding those from the signal candidate. The jet is reconstucted using the Anti-k_t algorithm with a cone size of 0.6. In the case of multiple jets, the jet with the highest value of the b-tag weight reference is used.

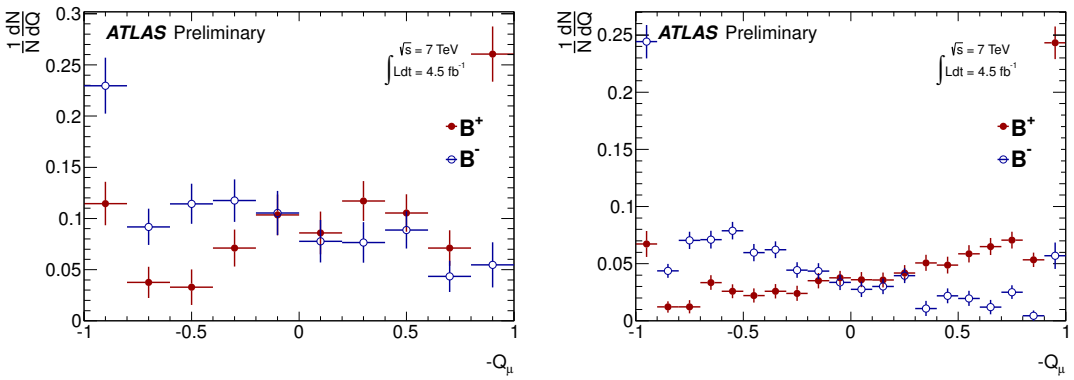

Figure 2: Muon cone charge distribution for $B^{\pm}$ signal candidates for *segment tagged* (left) and *combined* (right) muons.

A *jet charge* is defined

$$Q_{\text{jet}} = \frac{\sum_i^{N\text{ tracks}} q^i \cdot (p_T^i)^\kappa}{\sum_i^{N\text{ tracks}} (p_T^i)^\kappa}, \tag{2}$$

where $\kappa = 1.1$, and the sum is over the tracks associated to the jet, using the method described in [17]. Figure 3 shows the distribution of charges for jet-charge from $B^{\pm}$ signal-side candidates.

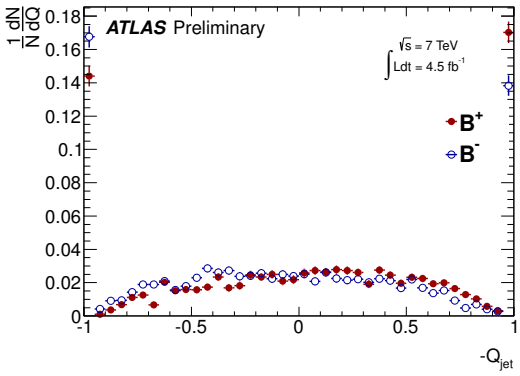

Figure 3: Jet-charge distribution for $B^{\pm}$ signal candidates.

The efficiency ε of an individual tagger is defined as the ratio of the number of tagged events to the total number of candidates. A probability that a specific event has a signal decay containing a $\bar{b}$ given the value of the discriminating variable $P(B|Q)$ is constructed from the calibration samples for each of the B^+ and B^- samples, defining $P(Q|B^+)$ and $P(Q|B^-)$ respectively. The probability to tag a signal event as a $\bar{b}$ is therefore $P(B|Q) = P(Q|B^+)/(P(Q|B^+) + P(Q|B^-))$ and $P(\bar{B}|Q) = 1 - P(B|Q)$. The tagging power is defined as $\varepsilon\mathscr{D}^2 = \sum_i \varepsilon_i \cdot (2P_i(B|Q_i) - 1)^2$, where the sum is over the bins of the probability distribution as a function of the charge variable. An effective dilution $\mathscr{D}$ is calculated from the tagging power and the efficiency.

The combination of the tagging methods is applied according to the hierarchy of performance. The single best performing tagging measurement is taken, according to the order: *combined* muon cone charge, *segment tagged* muon cone charge, jet charge. If it is not possible to provide a tagging response

for the event, then the probability of 0.5 is assigned. A summary of the tagging performance is given in Table 1.

Table 1: Summary of tagging performance for the different tagging methods described in the text. Uncertainties shown are statistical only. The efficiency and tagging power are each determined by summing over the individual bins of the charge distribution. The effective dilution is obtained from the measured efficiency and tagging power, as shown in the table. For the efficiency, dilution, and tagging power, the corresponding uncertainty is each determined by combining the appropriate uncertainties on the individual bins of each charge distribution.

Tagger	Efficiency [%]	Dilution [%]	Tagging Power [%]
Segment Tagged muon	1.08 ± 0.02	36.7 ± 0.7	0.15 ± 0.02
Combined muon	3.37 ± 0.04	50.6 ± 0.5	0.86 ± 0.04
Jet charge	27.7 ± 0.1	12.68 ± 0.06	0.45 ± 0.03
Total	32.1 ± 0.1	21.3 ± 0.08	1.45 ± 0.05

5 Maximum Likelihood Fit

An unbinned maximum likelihood fit is performed on the selected events to extract the parameters of the $B_s^0 \to J/\psi(\mu^+\mu^-)\phi(K^+K^-)$ decay. The fit uses information about the reconstructed mass m, the measured proper decay time t, the measured mass and proper decay time uncertainties σ_m and σ_t, the tag probability, and the transversity angles Ω of each $B_s^0 \to J/\psi\phi$ decay candidate. There are three transversity angles; $\Omega = (\theta_T, \psi_T, \phi_T)$ and these are defined in section 5.1.

The likelihood function is defined as a combination of the signal and background probability density functions as follows:

$$\ln \mathscr{L} = \sum_{i=1}^{N} \{ w_i \cdot \ln(f_{\rm s} \cdot \mathscr{F}_{\rm s}(m_i, t_i, \Omega_i) + f_{\rm s} \cdot f_{B^0} \cdot \mathscr{F}_{B^0}(m_i, t_i, \Omega_i) + (1 - f_{\rm s} \cdot (1 + f_{B^0})) \mathscr{F}_{\rm bkg}(m_i, t_i, \Omega_i)) \} \tag{3}$$

where N is the number of selected candidates, w_i is a weighting factor to account for the trigger efficiency, $f_{\rm s}$ is the fraction of signal candidates, f_{B^0} is the fraction of peaking B^0 meson background events calculated relative to the number of signal events; this parameter is fixed in the likelihood fit. The mass m_i, the proper decay time t_i and the decay angles Ω_i are the values measured from the data for each event i. $\mathscr{F}_{\rm s}$, $\mathscr{F}_{B^0}$ and $\mathscr{F}_{\rm bkg}$ are the probability density functions (PDF) modelling the signal, the specific B^0 background and the other background distributions, respectively. A detailed description of the signal PDF terms in equation 3 is given in sections 5.1. The terms describing the background PDFs are described in the previous analysis [6] and are unchanged.

5.1 Signal PDF

The PDF describing the signal events, $\mathscr{F}_{\rm s}$, has the form of a product of PDFs for each quantity measured from the data:

$$\mathscr{F}_{\rm s}(m_i, t_i, \Omega_i, P(B|Q)) = P_{\rm s}(m_i|\sigma_{m_i}) \cdot P_{\rm s}(\sigma_{m_i}) \cdot P_{\rm s}(\Omega_i, t_i, P(B|Q)|\sigma_{t_i}) \cdot P_{\rm s}(\sigma_{t_i}) \cdot P_{\rm s}(P(B|Q)) \cdot A(\Omega_i, p_{{\rm T}i}) \cdot P_{\rm s}(p_{{\rm T}i}) \tag{4}$$

The terms $P_{\rm s}(m_i|\sigma_{m_i})$, $P_{\rm s}(\Omega_i,t_i,P(B|Q)|\sigma_{t_i})$ and $A(\Omega_i,p_{{\rm T}i})$ are explained in the current section. The tagging probability term $P_{\rm s}(P(B|Q))$ is described in section 5.2 and the remaining probability terms $P_{\rm s}(\sigma_{m_i})$, $P_{\rm s}(\sigma_{t_i})$ and $P_{\rm s}(p_{{\rm T}i})$ are unchanged from the previous analysis and described there [6]. Ignoring detector effects, the joint distribution for the decay time t and the transversity angles Ω for the $B_s^0 \to J/\psi(\mu^+\mu^-)\phi(K^+K^-)$ decay is given by the differential decay rate [18]:

$$\frac{d^4\Gamma}{dt\, d\Omega} = \sum_{k=1}^{10} \mathscr{O}^{(k)}(t) g^{(k)}(\theta_T, \psi_T, \phi_T), \tag{5}$$

where $\mathscr{O}^{(k)}(t)$ are the time-dependent amplitudes and $g^{(k)}(\theta_T, \psi_T, \phi_T)$ are the angular functions, given in table 2. The formulae for the time-dependent amplitudes have the same structure for B_s^0 and $\overline{B_s^0}$ but with a sign reversal in the terms containing Δm_s. $A_\perp(t)$ describes a CP-odd final-state configuration while both $A_0(t)$ and $A_\parallel(t)$ correspond to CP-even final-state configurations. A_S describes the contribution of CP-odd $B_s \to J/\psi K^+K^-(f_0)$, where the non-resonant KK or f_0 meson is an S-wave state. The corresponding amplitudes are given in the last four lines of Table 2 (k=7-10) and follow the convention used in the previous analysis [9]. The likelihood is independent of the invariant KK mass distribution.

The equations are normalised such that the squares of the amplitudes sum to unity; three of the four amplitudes are fit parameters and $|A_\perp(0)|^2$ is determined according to this constraint.

The angles $(\theta_T, \psi_T, \phi_T)$, are defined in the rest frames of the final-state particles. The x-axis is determined by the direction of the ϕ meson in the J/ψ rest frame, the K^+K^- system defines the xy plane, where $p_y(K^+) > 0$. The three angles are defined:

- θ_T, the angle between $p(\mu^+)$ and the xy plane, in the J/ψ meson rest frame
- ϕ_T, the angle between the x-axis and $p_{xy}(\mu^+)$, the projection of the μ^+ momentum in the xy plane, in the J/ψ meson rest frame
- ψ_T, the angle between $p(K^+)$ and $-p(J/\psi)$ in the ϕ meson rest frame

The signal PDF, $P_s(\Omega,t|\sigma_t)$ needs to take into account lifetime resolution so each time element in Table 2 is smeared with a Gaussian function. This smearing is done numerically on an event-by-event basis where the width of the Gaussian is the proper decay time uncertainty, measured for each event, multiplied by a scale factor to account for any mis-measurements.

The angular sculpting of the detector and kinematic cuts on the angular distributions is included in the likelihood function through $A(\Omega_i,p_{Ti})$. This is calculated using a 4-D binned acceptance method, applying an event-by-event efficiency according to the transversity angles $(\theta_T, \psi_T, \phi_T)$ and the $p_{\rm T}$ of the event. The p_T binning is necessary because the angular sculpting is influenced by the p_T of the B_s^0. The acceptance was calculated from the $B_s^0 \to J/\psi\phi$ MC events. In the likelihood function, the acceptance is treated as an angular sculpting PDF, which is multiplied with the the time and angular dependent PDF describing the $B_s^0 \to J/\psi(\mu^+\mu^-)\phi(K^+K^-)$ decays, thus the complete angular function must be normalised simultaneously as both the acceptance and time-angular decay PDFs depend on the transversity angles. This normalisation is done numerically during the likelihood fit.

The signal mass function, $P_s(m)$, is modelled using a single Gaussian function smeared with an event-by-event mass resolution. The PDF is normalised over the range $5150 < M(B_s^0) < 5650$ MeV.

5.2 Using tag information in the fit

The tag-probability for each B_s^0 candidate is determined from the calibrations of $B^\pm \to J/\psi K^\pm$ candidates, as described in Section 4. The distributions of tag probabilities for the signal and background are different and since the background cannot be factorized out, extra PDF terms are included to account for

Table 2: Table showing the ten time-dependent amplitudes, $\mathscr{O}^{(k)}(t)$ and the functions of the transversity angles $g^{(k)}(\theta_T, \psi_T, \phi_T)$. The amplitudes $|A_0(0)|^2$ and $|A\|(0)|^2$ are for the CP even components of the $B_s^0 \to J/\psi\phi$ decay, $|A(0)_\perp|^2$ is the CP odd amplitude, they have corresponding strong phases δ_0, $\delta_\|$ and $\delta_\perp$, by convention δ_0 is set to be zero. The $S-$wave amplitude $|A_S(0)|^2$ gives the fraction of $B_s^0 \to J/\psi K^+K^-(f_0)$ and has a related strong phase δ_S. The $\pm$ and $\mp$ terms denote two cases: the upper sign describes the decay of a meson that was initially a B_s^0, while the lower sign describes the decays of a meson that was initially $\overline{B_s^0}$.

k	$\mathscr{O}^{(k)}(t)$	$g^{(k)}(\theta_T, \psi_T, \phi_T)$
1	$\frac{1}{2}\lvert A_0(0)\rvert^2 \left[(1+\cos\phi_s)\,e^{-\Gamma_{\rm L}^{(s)}t} + (1-\cos\phi_s)\,e^{-\Gamma_{\rm H}^{(s)}t} \pm 2e^{-\Gamma_s t}\sin(\Delta m_s t)\sin\phi_s\right]$	$2\cos^2\psi_T(1-\sin^2\theta_T\cos^2\phi_T)$
2	$\frac{1}{2}\lvert A_\|(0)\rvert^2 \left[(1+\cos\phi_s)\,e^{-\Gamma_{\rm L}^{(s)}t} + (1-\cos\phi_s)\,e^{-\Gamma_{\rm H}^{(s)}t} \pm 2e^{-\Gamma_s t}\sin(\Delta m_s t)\sin\phi_s\right]$	$\sin^2\psi_T(1-\sin^2\theta_T\sin^2\phi_T)$
3	$\frac{1}{2}\lvert A_\perp(0)\rvert^2 \left[(1-\cos\phi_s)\,e^{-\Gamma_{\rm L}^{(s)}t} + (1+\cos\phi_s)\,e^{-\Gamma_{\rm H}^{(s)}t} \mp 2e^{-\Gamma_s t}\sin(\Delta m_s t)\sin\phi_s\right]$	$\sin^2\psi_T\sin^2\theta_T$
4	$\frac{1}{2}\lvert A_0(0)\rvert\lvert A_\|(0)\rvert\cos\delta_\| \left[(1+\cos\phi_s)\,e^{-\Gamma_{\rm L}^{(s)}t} + (1-\cos\phi_s)\,e^{-\Gamma_{\rm H}^{(s)}t} \pm 2e^{-\Gamma_s t}\sin(\Delta m_s t)\sin\phi_s\right]$	$-\frac{1}{\sqrt{2}}\sin 2\psi_T\sin^2\theta_T\sin 2\phi_T$
5	$\lvert A_\|(0)\rvert\lvert A_\perp(0)\rvert[\frac{1}{2}(e^{-\Gamma_{\rm L}^{(s)}t} - e^{-\Gamma_{\rm H}^{(s)}t})\cos(\delta_\perp-\delta_\|)\sin\phi_s \pm e^{-\Gamma_s t}(\sin(\delta_\perp-\delta_\|)\cos(\Delta m_s t) - \cos(\delta_\perp-\delta_\|)\cos\phi_s\sin(\Delta m_s t))]$	$\sin^2\psi_T\sin 2\theta_T\sin\phi_T$
6	$\lvert A_0(0)\rvert\lvert A_\perp(0)\rvert[\frac{1}{2}(e^{-\Gamma_{\rm L}^{(s)}t} - e^{-\Gamma_{\rm H}^{(s)}t})\cos\delta_\perp\sin\phi_s \pm e^{-\Gamma_s t}(\sin\delta_\perp\cos(\Delta m_s t) - \cos\delta_\perp\cos\phi_s\sin(\Delta m_s t))]$	$\frac{1}{\sqrt{2}}\sin 2\psi_T\sin 2\theta_T\cos\phi_T$
7	$\frac{1}{2}\lvert A_S(0)\rvert^2 \left[(1-\cos\phi_s)\,e^{-\Gamma_{\rm L}^{(s)}t} + (1+\cos\phi_s)\,e^{-\Gamma_{\rm H}^{(s)}t} \mp 2e^{-\Gamma_s t}\sin(\Delta m_s t)\sin\phi_s\right]$	$\frac{2}{3}\left(1-\sin\theta_T\cos^2\phi_T\right)$
8	$\lvert A_S\rvert\lvert A_\|(0)\rvert[\frac{1}{2}(e^{-\Gamma_{\rm L}^{(s)}t} - e^{-\Gamma_{\rm H}^{(s)}t})\sin(\delta_\|-\delta_S)\sin\phi_s \pm e^{-\Gamma_s t}(\cos(\delta_\|-\delta_S)\cos(\Delta m_s t) - \sin(\delta_\|-\delta_S)\cos\phi_s\sin(\Delta m_s t))]$	$\frac{1}{3}\sqrt{6}\sin\psi_T\sin^2\theta_T\sin 2\phi_T$
9	$\frac{1}{2}\lvert A_S\rvert\lvert A_\perp(0)\rvert\sin(\delta_\perp-\delta_S) \left[(1+\cos\phi_s)\,e^{-\Gamma_{\rm L}^{(s)}t} + (1+\cos\phi_s)\,e^{-\Gamma_{\rm H}^{(s)}t} \mp 2e^{-\Gamma_s t}\sin(\Delta m_s t)\sin\phi_s\right]$	$\frac{1}{3}\sqrt{6}\sin\psi_T\sin 2\theta_T\cos\phi_T$
10	$\lvert A_0(0)\rvert\lvert A_S(0)\rvert[\frac{1}{2}(e^{-\Gamma_{\rm H}^{(s)}t} - e^{-\Gamma_{\rm L}^{(s)}t})\sin\delta_S\sin\phi_s \pm e^{-\Gamma_s t}(\cos\delta_S\cos(\Delta m_s t) + \sin\delta_S\cos\phi_s\sin(\Delta m_s t))]$	$\frac{4}{3}\sqrt{3}\cos\psi_T\left(1-\sin^2\theta_T\cos^2\phi_T\right)$

this difference. The distributions of the B_s candidates tag-probabilities consist of continuous and discrete parts (spikes). These are described separately.

To describe the continuous parts, the sidebands are parametrized first. Sidebands are selected according to B_s mass, i.e. $m(B_s) < 5317$ MeV or $m(B_s) > 5417$ MeV. In the next step, the same function as for the sidebands is used to describe events in the signal region: background parameters are fixed to the values obtained in sidebands while signal parameters are free in this step. The ratio of background and signal (obtained from simultaneous mass-lifetime fit) is fixed as well. The function describing tagging using combined muons has the form of a fourth-order Chebychev polynomial:

$$f_1(x) = 1 + \sum_{i=1,4} a_i T_i(x) \tag{6}$$

for the tagging method using segment tagged muons a third order polynomial is used:

$$f_2(x) = 1 + \sum_{i=1,3} a_i x^i \tag{7}$$

In both of the above formulas x represents the tag probability. A fourth-order Chebychev polynomial is also applied for the jet-charge tagging algorithm. In all three cases unbinned maximum likelihood fits are used. Results of fits projected on histograms are shown in Fig. 4.

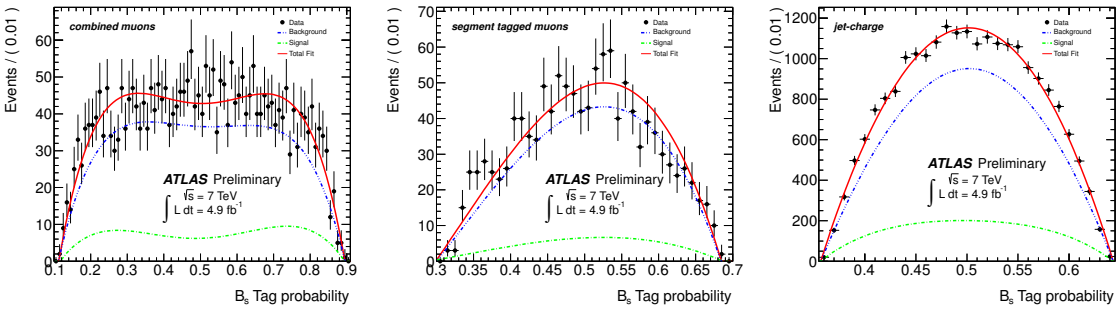

Figure 4: The tag probability for tagging using combined muons (left), segment tagged muons (middle) and jet-charge (right). Black dots are data after removing spikes, blue is a fit to the sidebands, green to the signal and red is a sum of both fits.

The spikes have their origin in tagging objects formed from a single track, providing a tag charge of exactly +1 or -1. When a background candidate is formed from a random combination of a J/ψ and a pair of tracks, the positive and negative charges are equally probable. However some of the background events are formed of partially reconstructed B-hadrons in these cases tag charges +1 or -1 are not equally probable. For signal events obviously tag charges are not symmetric. For the fit it is important to derive fractions f_{+1}, f_{-1} of events tagged with charges +1 and -1, respectively and separately for signal and background. The remaining 1- f_{+1} -f_{-1} is the fraction of events in continuous region. The fractions f_{+1} and f_{-1} are determined using the same B_s^0 mass sidebands and signals regions as in case of continuous parts. Table 3 summarises the obtained relative probabilities between tag charges +1 and -1 for signal and background events and for all tag-methods. Similarly the sidebands subtraction method is also used to determine the relative population of the tag-methods in the background and signal events which also have to be included in the PDF. The results are summarised in Table 4.

If the tag-probability PDFs were ignored from the likelihood fit, equivalent to assuming identical signal and background behaviour, the impact on the fit result would be small, affecting the results by less then 10% of the statistical uncertainty.

Table 3: Table summarising the obtained relative probabilities between tag charges +1 and -1 for signal and background events and for all tag-methods. Only statistical errors are quoted. The asymmetry in the signal combined-muon tagging method has no impact on the results as it affects only 1% of the signal events (in addition to the negligible effect of the tag-probability distributions themselves).

Tag method	Signal		Background	
	f_{+1}	f_{-1}	f_{+1}	f_{-1}
combined μ	0.106 ± 0.019	0.187 ± 0.022	0.098 ± 0.006	0.108 ± 0.006
segment tag μ	0.152 ± 0.043	0.153 ± 0.043	0.098 ± 0.009	0.095 ± 0.008
jet-charge	0.167 ± 0.010	0.164 ± 0.010	0.176 ± 0.003	0.180 ± 0.003

Table 4: Table summarising the relative population of the tag-methods in the background and signal events. Only statistical errors are quoted.

Tag method	Signal	Background
combined μ	0.0372 ± 0.0023	0.0272 ± 0.0005
segment tag μ	0.0111 ± 0.0014	0.0121 ± 0.0003
jet-charge	0.277 ± 0.007	0.254 ± 0.002
Untagged	0.675 ± 0.011	0.707 ± 0.003

6 Results

The full simultaneous maximum likelihood fit contains 25 free parameters. This includes the nine physics parameters: $\Delta\Gamma_s$, ϕ_s, Γ_s, $|A_0(0)|^2$, $|A_{\|}(0)|^2$, $\delta_{\|}$, $\delta_{\perp}$, $|A_S|^2$ and δ_S. The other parameters in the likelihood function are the B_s^0 signal fraction f_s, the parameters describing the $J/\psi\phi$ mass distribution, the parameters describing the B_s^0 meson decay time plus angular distributions of background events, the parameters used to describe the estimated decay time uncertainty distributions for signal and background events, and scale factors between the estimated decay time and mass uncertainties and their true uncertainties. In addition to this there are also 82 nuisance parameters describing the background and acceptance functions that are fixed at the time of the fit.

The number of signal B_s^0 meson candidates extracted from the fits is 22670 ± 150. The results and correlations for the measured physics parameters of the simultaneous unbinned maximum likelihood fit are given in Table 5 and 6. Fit projections of the mass, proper decay time and angles are given in Figures 5 and 6 respectively.

7 Systematic uncertainties

Systematic uncertainties are assigned by considering several effects that are not accounted for in the likelihood fit. These are described below.

- **Inner Detector Alignment:** Residual misalignments of the Inner Detector will affect the impact parameter distribution with respect to the primary vertex. The impact of the residual misalignment is estimated using simulated events with and without distorted geometry. For this the impact parameter distribution with respect to the primary vertex is measured with data as a function of η and ϕ with the maximum deviation from zero being less than 10 μm. The measurement is used to distort the geometry for simulated events in order to reproduce the impact parameter distribution

Table 5: Fitted values for the physical parameters along with their statistical and systematic uncertainties.

Parameter	Value	Statistical uncertainty	Systematic uncertainty
ϕ_s(rad)	0.12	0.25	0.11
$\Delta\Gamma_s(\mathrm{ps}^{-1})$	0.053	0.021	0.009
$\Gamma_s(\mathrm{ps}^{-1})$	0.677	0.007	0.003
$\lvert A_{\parallel}(0)\rvert^2$	0.220	0.008	0.009
$\lvert A_0(0)\rvert^2$	0.529	0.006	0.011
$\lvert A_S\rvert^2$	0.024	0.014	0.028
$\delta_\perp$	3.89	0.46	0.13
$\delta_{\parallel}$	[3.04-3.23]		0.09
$\delta_\perp - \delta_S$	[3.02-3.25]		0.04

Table 6: Correlations between the physics parameters.

	ϕ_s	$\Delta\Gamma$	Γ_s	$\lvert A_{\lvert\rvert}(0)\rvert^2$	$\lvert A_0(0)\rvert^2$	$\lvert A_S(0)\rvert^2$	$\delta_{\parallel}$	$\delta_\perp$	$\delta_\perp - \delta_S$
ϕ_s	1.000	0.107	0.026	0.010	0.002	0.029	0.021	-0.043	-0.003
$\Delta\Gamma$		1.000	-0.617	0.105	0.103	0.069	0.006	-0.017	0.001
Γ_s			1.000	-0.093	-0.063	0.034	-0.003	0.001	-0.009
$\lvert A_{\lvert\rvert}(0)\rvert^2$				1.000	-0.316	0.077	0.008	0.005	-0.010
$\lvert A_0(0)\rvert^2$					1.000	0.283	- 0.003	-0.016	-0.025
$\lvert A_S(0)\rvert^2$						1.000	-0.011	-0.054	-0.098
$\delta_{\parallel}$							1.000	0.038	0.007
$\delta_\perp$								1.000	0.081
$\delta_\perp - \delta_S$									1.000

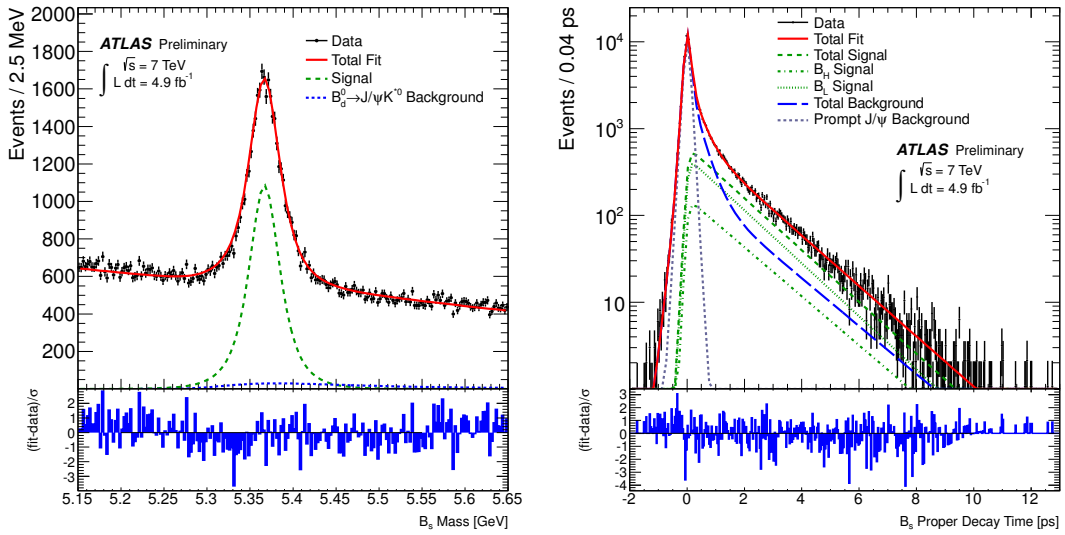

Figure 5: (Left) Mass fit projection for the B_s^0. The pull distributions at the bottom show the difference between data and fit value normalized to the data uncertainty. (Right) Proper decay time fit projection for the B_s^0. The pull distributions at the bottom show the difference between data and fit value normalized to the data uncertainty.

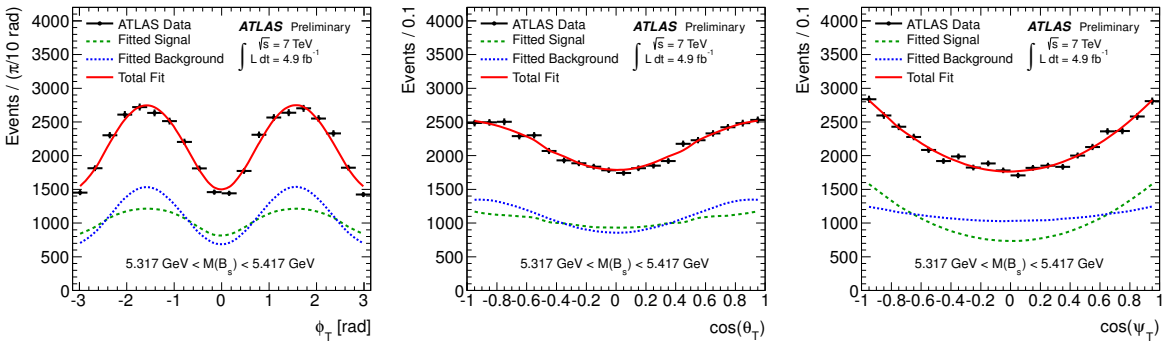

Figure 6: Fit projections for transversity angles. (Left): ϕ_T, (Centre): $\cos\theta_T$, (Right): $\cos\psi_T$.

measured as a function of η and ϕ. The difference between the measurement using simulated events with and without the distorted geometry is used as the systematic uncertainty.

- **Angular acceptance method:** The angular acceptance is calculated from a binned fit to Monte Carlo data. In order to estimate the size of the systematic uncertainty introduced from the choice of binning, different acceptance functions are calculated using different bin widths and central values.

- **Trigger efficiency:** To correct for the trigger lifetime bias the events are re-weighted according to

$$w = e^{-|t|/(\tau_{sin}+\varepsilon)} / e^{-|t|/\tau_{sin}}.$$

  Details of this correction has been given in previous publication [6]. The uncertainty of the parameter ε is used to estimate the systematic uncertainty due to the time efficiency correction.

- **Default fit model:** The systematic uncertainty of the default fit model is calculated using the bias of the pull-distribution, see figure 10 in Appendix A, of 1500 pseudo-experiments, multiplied by the statistical uncertainty of each parameter.

- **Signal and background mass model, resolution model, background lifetime and background angles model:** In order to estimate the size of systematic uncertainties caused by the assumptions made in the fit model, variations of the model are tested in pseudo-experiments. A set of 1500 pseudo-experiments is generated for each variation considered, and fitted with the default model. The systematic error quoted for each effect is the difference between the mean shift of the fitted value of each parameter from its input value for the pseudo-experiments with the systematic alteration included. The variations are: two different scale factors are used to generate the signal mass. The background mass is generated from an exponential function. Two different scale factors are used to generate the lifetime uncertainty. The background lifetimes are generated by sampling data from the mass sidebands. Pseudo-experiments are generated with background angles taken from histograms from sideband data and are fitted with the default fit model to assess the systematic uncertainty to the parametrisation of the background angles in the fit.

- B_d **contribution:** Contaminations from $B_d \to J/\psi K^{0*}$ and $B_d \to J/\psi K\pi$ events mis-reconstructed as $B_s^0 \to J/\psi\phi$ is accounted for in the default fit, the fractions of these contributions are fixed to values estimated from selection efficiencies in MC and production and branching fractions from [15]. To estimate the systematic uncertainty arising from the precision of the fraction estimates, the data is fitted with these fractions increase and decreased by 1σ. The largest shift in the fitted values from the default case is taken as the systematic uncertainty for each parameter of interest.

- **Tagging:** Systematic errors of the fit parameters due to uncertainty in tagging are estimated by comparing the default fit with the fits using alternate tag probabilities. The tag probabilities are altered in two ways: firstly, the tag probabilities are varied coherently up and down by the statistical uncertainty on each bin of the distribution; secondly, by varying the models of the parameterisation of the probability distributions, as described in Section 4, and altering the tag probabilities by the maximal deviations from the central value. Additional uncertainties are included by varying the PDF terms accounting for differences between signal and background tag probabilities. Due to small differences between the kinematics of the signal decays B_S and $B^{\pm}$, the difference in the OST response is estimated to be small compared to the other uncertainties and has not been considered as an additional systematic within this analysis.

The systematic uncertainties are provided in Table 7. For each variable, the total systematic error is obtained adding in quadrature the different contributions.

Table 7: Summary of systematic uncertainties assigned to parameters of interest.

	ϕ_s (rad)	$\Delta\Gamma_s$ (ps^{-1})	Γ_s (ps^{-1})	$\lvert A_\parallel(0)\rvert^2$	$\lvert A_0(0)\rvert^2$	$\lvert A_S(0)\rvert^2$	$\delta_\perp$ (rad)	$\delta_\parallel$ (rad)	$\delta_\perp - \delta_S$ (rad)
ID alignment	$<10^{-2}$	$<10^{-3}$	$<10^{-3}$	$<10^{-3}$	$<10^{-3}$	-	$<10^{-2}$	$<10^{-2}$	-
Trigger efficiency	$<10^{-2}$	$<10^{-3}$	0.002	$<10^{-3}$	$<10^{-3}$	$< 10^{-3}$	$<10^{-2}$	$<10^{-2}$	$<10^{-2}$
B_d^0 contribution	0.03	0.001	$<10^{-3}$	$<10^{-3}$	0.005	0.001	0.02	$<10^{-2}$	$<10^{-2}$
Tagging	0.10	0.001	$<10^{-3}$	$<10^{-3}$	$<10^{-3}$	0.002	0.05	$<10^{-2}$	$<10^{-2}$
Models:									
default fit	$<10^{-2}$	0.002	$<10^{-3}$	0.003	0.002	0.006	0.07	0.01	0.01
signal mass	$<10^{-2}$	0.001	$<10^{-3}$	$<10^{-3}$	0.001	$<10^{-3}$	0.03	0.04	0.01
background mass	$<10^{-2}$	0.001	0.001	$<10^{-3}$	$<10^{-3}$	0.002	0.06	0.02	0.02
resolution	0.02	$<10^{-3}$	0.001	0.001	$<10^{-3}$	0.002	0.04	0.02	0.01
background time	0.01	0.001	$<10^{-3}$	0.001	$<10^{-3}$	0.002	0.01	0.02	0.02
background angles	0.02	0.008	0.002	0.008	0.009	0.027	0.06	0.07	0.03
Total	0.11	0.009	0.003	0.009	0.011	0.028	0.13	0.09	0.04

8 Discussion

The PDF describing the $B_s^0 \to J/\psi\phi$ decay is invariant under the following simultaneous transformations:

$$\{\phi_s, \Delta\Gamma, \delta_\perp, \delta_\parallel\} \to (\pi - \phi_s, -\Delta\Gamma, \pi - \delta_\perp, 2\pi - \delta_\parallel)$$

$\Delta\Gamma_s$ has been determined to be positive [19]. Therefore there is a unique solution. Uncertainties on individual parameters have been studied in details in likelihood scans. Figure 7 shows the 1D likelihood scans for ϕ_s and $\Delta\Gamma_s$. Figure 8 shows the likelihood contours in ϕ_s - $\Delta\Gamma_s$ plane.

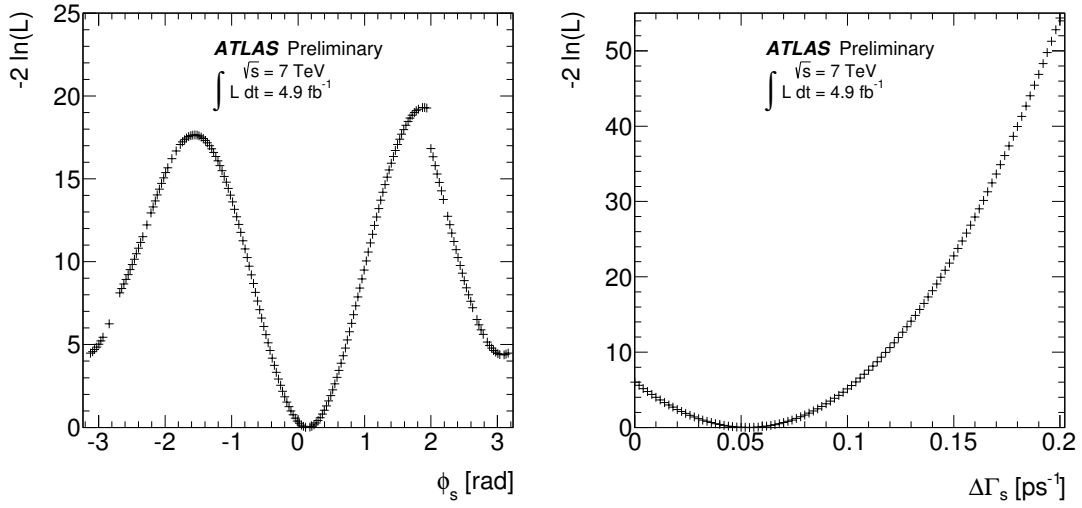

Figure 7: 1D likelihood scans for ϕ_s (left) and $\Delta\Gamma_s$ (right)

The behaviour of the amplitudes around their fitted values is as expected, however the strong phases are more complicated. Figure 9 shows the 1D likelihood scans for the three measured strong phases.

The behaviour of $\delta_\perp$ appears gaussian and therefore it is reasonable to quote $\delta_\perp = 3.89 \pm 0.47(stat)$ rad. For $\delta_\perp - \delta_S$ the the likelihood scan shows a minimum close to π, however it is insensitive over

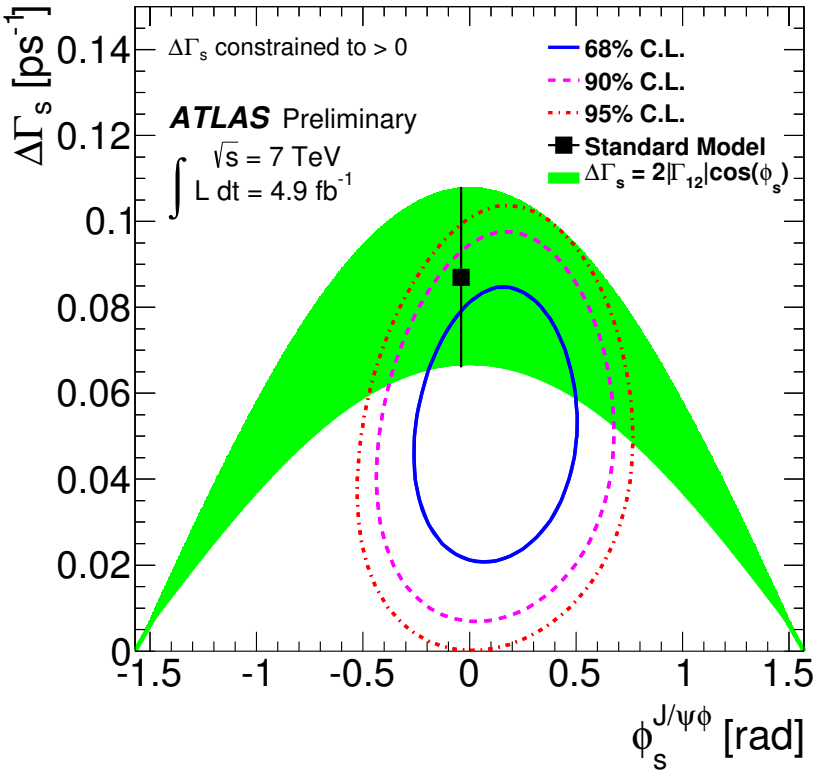

Figure 8: Likelihood contours in ϕ_s - $\Delta\Gamma_s$ plane. The blue and red contours show the 68% and 95% likelihood contours, respectively (statistical errors only). The green band is the theoretical prediction of mixing- induced CP violation.

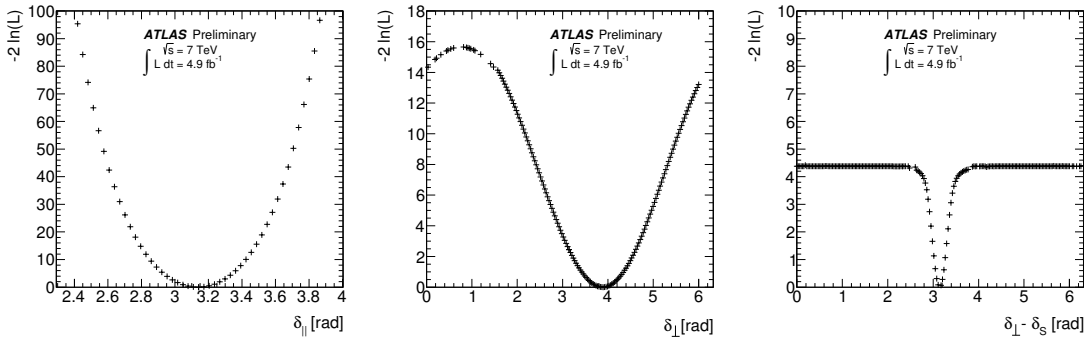

Figure 9: 1D likelihood scans for $\delta_{||}$ (left), $\delta_\perp$ and $\delta_\perp - \delta_S$ (right)

the rest of the scan at the level of 4.3σ. Therefore the measured value of the difference $\delta_\perp - \delta_S$ is only given as 1σ confidence interval [3.02-3.25] rad. $\delta_{||}$ shows normal gaussian behaviour around the minimum however the systematic pull plots show unusual behaviour so it is also given in the form of a 1σ confidence interval [3.04-3.23] rad.

9 Conclusion

A measurement of CP violation in $B_s^0 \to J/\psi(\mu^+\mu^-)\phi(K^+K^-)$ decays from a data sample of $4.9\,\text{fb}^{-1}$ pp collisions collected with the ATLAS detector during the 2011 $\sqrt{s} = 7$ TeV run has been presented. Several parameters describing the B_s^0 meson system are measured. These include the mean B_s^0 lifetime Γ_s the decay width difference $\Delta\Gamma_s$ between the heavy and light mass eigenstates, the transversity amplitudes, $|A_0(0)|$ and $|A_{||}(0)|$. These are consistent with the world average. We also provide a likelihood contour in the ϕ_s - $\Delta\Gamma_s$ plane. The fraction of S-wave KK or f_0 contamination is measured to be consistent with zero, at 0.024 ± 0.014 .

The measured values are:

$$\begin{aligned}
\phi_s &= 0.12 \pm 0.25\ (\text{stat.}) \pm 0.11\ (\text{syst.})\ \text{rad} \\
\Delta\Gamma_s &= 0.053 \pm 0.021\ (\text{stat.}) \pm 0.009\ (\text{syst.})\ \text{ps}^{-1} \\
\Gamma_s &= 0.677 \pm 0.007\ (\text{stat.}) \pm 0.003\ (\text{syst.})\ \text{ps}^{-1} \\
|A_0(0)|^2 &= 0.529 \pm 0.006\ (\text{stat.}) \pm 0.011\ (\text{syst.}) \\
|A_{||}(0)|^2 &= 0.220 \pm 0.008\ (\text{stat.}) \pm 0.009\ (\text{syst.}) \\
\delta_\perp &= 3.89 \pm 0.46\ (\text{stat.}) \pm 0.13\ (\text{syst.})\ \text{rad}
\end{aligned}$$

The values are consistent with those obtained in our untagged analysis [6], and as expected improving significantly on the overall uncertainty on ϕ_s. These results are also consistent with theoretical expectations, in particular ϕ_s and $\Delta\Gamma_s$ are in good agreement, within their uncertainties and with the values predicted in the Standard Model.

References

[1] UTfit Collaboration, M. Bona et al., *Constraints on new physics from the quark mixing unitarity triangle*, Phys.Rev.Lett. **97** (2006) 151803, arXiv:hep-ph/0605213 [hep-ph].

[2] CDF Collaboration, A. Abulencia et al., *Observation of $B_s^0 - \bar{B}_s^0$ Oscillations*, Phys.Rev.Lett. **97** (2006) 242003, arXiv:hep-ex/0609040 [hep-ex].

[3] LHCb Collaboration, R. Aaij et al., *Measurement of the $B_s^0 - \bar{B}_s^0$ oscillation frequency Δm_s in $B_s^0 \to D_s^-(3)\pi$ decays*, Phys.Lett. **B709** (2012) 177–184, arXiv:1112.4311 [hep-ex].

[4] A. Lenz and U. Nierste, *Numerical Updates of Lifetimes and Mixing Parameters of B Mesons*, arXiv:1102.4274 [hep-ph].

[5] A. Lenz and U. Nierste, *Theoretical update of $B_s^0 - \bar{B}_s^0$ mixing*, JHEP **0706** (2007) 072, arXiv:hep-ph/0612167 [hep-ph].

[6] ATLAS Collaboration, G. Aad et al., *Time-dependent angular analysis of the decay $B_s \to J/\psi\phi$ and extraction of $\Delta\Gamma_s$ and the CP-violating weak phase ϕ_s by ATLAS*, JHEP **1212** (2012) 072, arXiv:1208.0572 [hep-ex].

[7] CDF Collaboration, T. Aaltonen et al., *Measurement of the CP-Violating Phase $\beta_s^{J/\psi\phi}$ in $B_s^0 \to J/\psi\phi$ Decays with the CDF II Detector*, Phys.Rev. **D85** (2012) 072002, arXiv:1112.1726 [hep-ex].

[8] D0 Collaboration, V. M. Abazov et al., *Measurement of the CP-violating phase $\phi_s^{J/\psi\phi}$ using the flavor-tagged decay $B_s^0 \to J/\psi\phi$ in 8 fb^{-1} of $p\bar{p}$ collisions*, Phys.Rev. **D85** (2012) 032006, arXiv:1109.3166 [hep-ex].

[9] LHCb Collaboration, R. Aaij et al., *Measurement of the CP-violating phase ϕ_s in the decay $B_s^0 \to J/\psi\phi$*, Phys.Rev.Lett. **108** (2012) 101803, arXiv:1112.3183 [hep-ex].

[10] ATLAS Collaboration, *The ATLAS Experiment at the CERN Large Hadron Collider*, JINST **3** (2008) S08003.

[11] T. Sjostrand, S. Mrenna, and P. Z. Skands, *PYTHIA 6.4 Physics and Manual*, JHEP **0605** (2006) 026, arXiv:hep-ph/0603175 [hep-ph].

[12] ATLAS Collaboration, *ATLAS tunes of PYTHIA 6 and PYTHIA 8 for MC11*, ATL-PHYS-PUB-2011-009, http://cdsweb.cern.ch/record/1363300 .

[13] ATLAS Collaboration, *The ATLAS Simulation Infrastructure*, Eur.Phys.J. **C70** (2010) 823–874, arXiv:1005.4568 [physics.ins-det].

[14] ATLAS Collaboration, *Measurement of the differential cross-sections of inclusive, prompt and non-prompt J/ψ production in proton-proton collisions at $\sqrt{s} = 7$ TeV*, Nucl.Phys. **B850** (2011) 387–444, arXiv:1104.3038 [hep-ex].

[15] Particle Data Group Collaboration, K. Nakamura et al., *Review of particle physics*, J.Phys.G **G37** (2010) 075021. (And 2011 partial update for the 2012 edition).

[16] ATLAS Collaboration, *Commissioning of the ATLAS high-performance b-tagging algorithms in the 7 TeV collision data*, Tech. Rep. ATLAS-CONF-2011-102, CERN, Geneva, Jul, 2011.

[17] ATLAS Collaboration, G. Aad et al., *Expected Performance of the ATLAS Experiment - Detector, Trigger and Physics*, arXiv:0901.0512 [hep-ex].

[18] A. S. Dighe, I. Dunietz, and R. Fleischer, *Extracting CKM phases and $B_s^0 - \bar{B}_s^0$ mixing parameters from angular distributions of nonleptonic B decays*, Eur.Phys.J. **C6** (1999) 647–662, arXiv:hep-ph/9804253 [hep-ph].

[19] LHCb Collaboration, R. Aaij et al., *Determination of the sign of the decay width difference in the B_s^0 system*, Phys.Rev.Lett. **108** (2012) 241801, arXiv:1202.4717 [hep-ex].

A Pull Plots

To determine whether the likelihood fit is unbiased, the pull distributions of the measured parameters are investigated. To produce a pull distribution 1500 pseudo-experiments are generated. The fit functions are used to generate the pseudo-experiments and the results from the real data fit are taken as input values for the generation. Each of the pseudo-experiments is then fitted with the fit model and the pull distributions are determined. The pull for each parameter and pseudo-experiment is calculated as

$$\frac{fitted\ value - generated\ value}{fitted\ error} \tag{8}$$

and filled into a histogram. these distributions are fitted with a Gaussian as one can see in figure 10. An unbiased fit procedure would show gaussian distributed parameters around 0 with a sigma of 1. All deviations from 0 are included into systematic uncertainty of the default fit model.

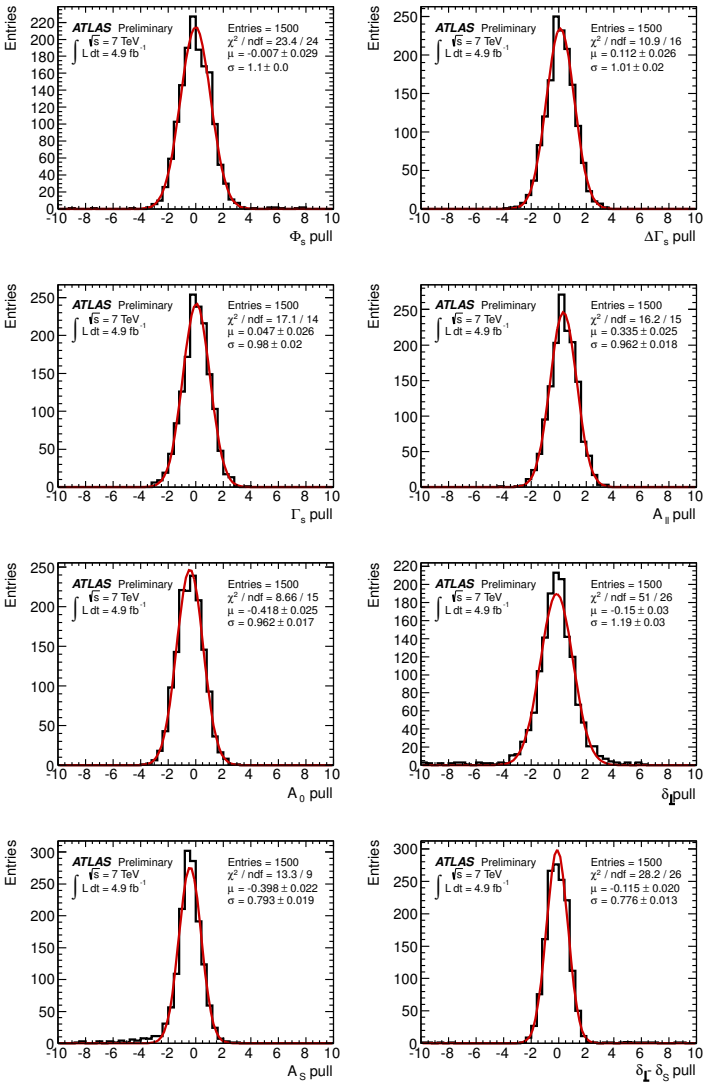

Figure 10: Pull plots from 1500 toy Monte Carlo experiments for the main physics parameters